Selective separation of gases by carboxylate phosphonium ionic liquids

Nicolas Scaglione

THÈSE de DOCTORAT DE L'UNIVERSITÉ DE LYON

opérée par

l'École Normale Supérieure de Lyon

École Doctorale N°206

École Doctorale de Chimie (Chimie, Procédés, Environnement)

Spécialité de doctorat : Chimie

Soutenue le 15/07/2024, par :

Nicolas SCAGLIONE

Selective separation of gases by carboxylate phosphonium ionic liquids

Devant le jury composé de :

Margulis, Claudio	Professeur	University of Iowa, USA	Rapporteur
Bouquillon, Sandrine	Professeure des Universités	Université de Reims Champagne-Ardenne	Rapporteuse
Moura, Leila	Maître de Conférences	Queens University Belfast, UK	Examinatrice
Andrioletti, Bruno	Professeur des Universités	Université Lyon 1	Examinateur
Abécassis, Benjamin	Directeur de Recherche	CNRS, ENS de Lyon	Examinateur
Baylaucq, Antoine	Personnalité Scientifique	R&D TotalEnergies, Pau	Examinateur
Costa Gomes, Margarida	Directrice de Recherche	CNRS, ENS de Lyon	Directrice de thèse
Pádua, Agílio	Professeur des Universités	ENS de Lyon	Co-directeur de thèse

ACKNOWLEDGEMENTS

I would like to thank first Margarida, my supervisor, and Agilio, my co-supervisor, for the opportunity they gave me to do my master internship and then, my PhD in their group. You taughted me all I needed to carry out both experimental and computational experiments as well as the thermodynamics lying behind. When I arrived in the group, learning both experiment and computational chemistry was a stiff double learning curve, but I got over it thank to your support while still respecting and taking into account my views and ideas on the topic.

Margarida, a particular thank you for the countless hours we spent together for the papers, but more particularly, to help me to get better at presenting. It was a long and tumultuous way, but it was truly helpful. I will never forget the working meetings in which we were finally discussing about our gastronomic experiences, it was always a great pleasure.

A special huge thanks to Jocasta, a post-doc in the group when I started my master internship, who explained and showed me all I needed in the lab to be independent and to carry out correctly my experiments.

Another particular thanks to Chiara, my co-bureau, with who I shared so many things during these years.. I don't need to develop more, she knows exactly how important it was.

Obviously, I want to thank as well the whole ionic liquid team, with who I spent a bit more than 3 great years. I learnt a lot with you all, Katya you taught me how to carry out properly molecular dynamics simulations, Ines you showed my how to use the solubility cell, Adriaan your precious advices concerning the DSC and the thermodynamics properties were of great help, Guillaume with all the tips you shared and the good time spent in the lab, Cintia your help was essential for electrochemical experiments. I am citing only a few examples, but you all helped me at some point, and I really hope that I was able you to give back at least as much as you gave me. It was scientifically very enriching, but not only. You all participated to make this journey very pleasant with all the conversations, the laughs, the beers and the good moments we shared. A deep thank you to you all for this.

Of course, I would to thank all the other people in the lab with who I shared very nice moments during these 3 years such as hiking week-ends, board game nights, a drink after work, shared lunch time or just some random discussions through the day. You all helped to make this adventure even better.

I thank as well the permanent members of the lab who were always nice and also helped me with various techniques. In particular, Fred with the TGA and the IR and Sandrine for the NMR.

I thank also the jury members: Sandrine Bouquillon and Claudio Margulis for your reports, and Leila Moura, Benjamin Abécassis, Bruno Andrioletti and Antoine Baylaucq for your attentive reading of this manuscript. Thank you to you all for travelling to Lyon to be physically present to my defence. I was very glad and honoured by your comments and your suggestions, we had a very interesting discussion.

ABSTRACT

The capture of polluting gases such as CO_2 and SO_2 presents a significant challenge in mitigating the environmental impact of human activities. To address this challenge, we propose the development of new materials based on reactive ionic liquids (ILs) as absorbents, with low environmental impact and cost-effectiveness.

ILs are non-volatile compounds with a melting temperature below 100 °C, capable of dissolving a wide range of substances due to their versatile cation-anion combinations. With unique properties like low flammability, high conductivity, and thermal stability, ILs hold promise for various applications, including gas absorption. The wide range of possible combinations of cations and anions allow for the design of a multitude of ionic solvents with tunable properties.

A novel family of ILs comprising carboxylate anions and phosphonium cations for the selective separation of CO_2 and SO_2 has been developed and prepared. Through rigorous experimental and computational analyses, we investigated their physicochemical properties, thermal behavior, and microscopic structure. They notably displayed promising thermal stability and a large liquid window. It was possible to distinguish the microscopic structure of the ILs based on the substituents of the carboxylate anions. $[P_{4,4,4,4}][TetrazC_1COO]$ appeared as an outlier with peculiar anion-anion correlations.

Measurements of gas absorption as a function of temperature and partial pressure revealed the crucial role of carboxylate anion basicity in CO_2 capture capacity, but not in SO_2 capture. The pK_a of corresponding carboxylic acids in water of each carboxylate anion was nonetheless determinant for the reversibility of SO_2 capture, and crucial for achieving high selectivity over CO_2. The related thermodynamics properties were carefully studied and interpreted based on the equilibrium constants and Henry's law constants, obtained from the absorption isotherm fittings, and *ab initio* simulations.

Exploratory projects were carried out to consider other potential applications of these ILs and their mixtures in electrochemistry due to their high electrochemical stability, but also as plastic crystals.

These studies pave the way for understanding the properties of these ILs, guiding future research in this field.

Key words: Ionic liquids, tunable, physico-chemical properties, gas absorption, CO_2, SO_2, selectivity, basicity, molecular dynamics, *ab initio* simulations, porous liquids, electrochemistry

RÉSUMÉ

La capture des gaz polluants tels que le dioxyde de carbone (CO_2) et le dioxyde de soufre (SO_2) reste un défi majeur dans les efforts visant à atténuer l'impact des activités humaines sur l'environnement. Nous proposons le développement de nouveaux matériaux absorbants à base de liquides ioniques (LIs) réactifs, avec un faible impact environnemental et un coût réduit.

Les LIs, des sels dont la température de fusion est inférieure à 100 °C, sont une classe de composés non volatils capables de dissoudre une grande variété de substances. La multitude de combinaisons de cations et d'anions permet de concevoir une large gamme de solvants ioniques aux propriétés modulables. Grâce à leurs propriétés uniques, telles qu'une faible inflammabilité, une volatilité négligeable, une conductivité élevée ainsi qu'une excellente stabilité thermique et électrochimique, les LIs sont des milieux prometteurs pour de nombreuses applications, et plus particulièrement, ils sont des candidats intéressants pour l'absorption de gaz polluants.

Une nouvelle famille de LIs composés d'anions carboxylates et de cations phosphoniums pour la séparation sélective de CO_2 et SO_2 a été conçue et préparée. Leurs propriétés physico-chimiques et thermiques ainsi que leur structure microscopique ont été étudiées en détail à l'aide de méthodes expérimentales et computationnelles. Ils ont notamment démontré une stabilité thermique prometteuse et une large fenêtre liquide. Il a été possible de distinguer la structure microscopique des LIs en fonction des substituants des anions carboxylates. $[P_{4,4,4,4}][TetrazC_1COO]$ est apparu comme un cas particulier avec des corrélations anion-anion singulières.

L'absorption de CO_2 et de SO_2 a été mesurée en fonction de la température et de la pression partielle des gaz pour chacun des LIs. La sélectivité a été calculée à partir du rapport des ratios molaires de chaque gaz absorbé. Les propriétés thermodynamiques d'absorption ont été obtenues à partir des isothermes d'absorption à différentes températures et de simulations *ab initio*.

La basicité de l'anion carboxylate est un facteur déterminant dans la capture de CO_2, mais pas pour SO_2. Le pK_a dans l'eau de l'acide carboxylique correspondant à chaque anion carboxylate a une influence sur la réversibilité de la capture de SO_2, et sur la capture sélective de SO_2 par rapport à CO_2.

Des projets exploratoires ont été menés en parallèle afin d'envisager d'autres applications potentielles de ces LIs et leurs mélanges en électrochimie grâce à leur bonne stabilité électrochimique, mais aussi en tant que cristaux plastiques.

Ces études ouvrent la voie à de futures recherches pour la compréhension des propriétés de ces LIs.

Mots clés : Liquides ioniques, design, propriétés physico-chimiques, absorption de gaz, CO_2, SO_2, sélectivité, basicité, dynamique moléculaire, simulations *ab initio*, liquides poreux, électrochimie

CONTENTS

PUBLICATIONS AND CONFERENCES

Papers that report developments carried out during the present thesis:

— **N. Scaglione**, J. Avila, E. Bakis, A. Padua, M. Costa Gomes. Alkylphosphonium Carboxylate Ionic Liquids with Tuned Microscopic Structures and Properties. *Phys. Chem. Chem. Phys.*, 2023, **25**, 15325–15339.

— **N. Scaglione**, L. Wylie, A. Padua, M. Costa Gomes. Improved reversible and selective SO_2 absorption by a stable phosphonium carboxylate ionic liquid. *ACS Sustain. Chem. Eng.*, 2024.

— **N. Scaglione**, J. Avila, A. Padua, M. Costa Gomes. Tailored Carbon Dioxide Capacity in Carboxylate-Based Ionic Liquids. *Faraday Discuss.*, *Accepted*.

— **N. Scaglione**, A. Padua, M. Costa Gomes. Unlocking the Potential of Carboxylates to Tailor Ionic Liquids for Sustainable Carbon Capture. Effect of Carboxylate basicity on the selective SO_2 absorption by Alkylphosphonium Ionic Liquids, *To be submitted*.

Co-authored papers :

— K. Goloviznina, E. Bakis, F. Philippi, **N. Scaglione**, T. Rekis, L. Laimina, M. Costa Gomes, A. Padua. Attraction Between Like Charged Ions in Ionic Liquids: Unveiling the Enigma of Tetracyanoborate Anions. *J. Phys. Chem. Lett.*, 2024, **15**, 248-253.

— C. Corsini, C.M. Correa, **N. Scaglione**, M. Costa Gomes, A. Padua. How do deep eutectic solvents form porous liquids? The example of methyltriphenylphosphonium bromide : glycerol and ZIF-8. *J. Phys. Chem. B*, 2024, 128, **10**, 2481–2489.

Participation in international conferences:

— **N. Scaglione**, J. Avila, M. Costa Gomes, A. Padua. CO_2 absorption by reactive carboxylate-based Ionic Liquids (ILs). Gordon Research Conference on Ionic Liquids, 7-12 August 2022, Newry, ME, USA. Poster presentation.

— **N. Scaglione**, A. Padua, M. Costa Gomes. Selective SO_2/CO_2 absorption by $[P_{4,4,4,4}]$ $[TetrazC_1COO]$. 9^{th} COIL – Congress on Ionic Liquids, Lyon, France, 24-28 April 2023. Oral communication.

— **N. Scaglione**, A. Padua, M. Costa Gomes. Tuning of the CO_2 absorption by reactive phosphonium-carboxylate ionic liquids. ILMAT2023 – 7^{th} International Conference on Ionic Liquid-Based Materials, Porto, Portugal, 21-24 November 2023. Oral communication.

Co-authored oral communications in international conferences:

— E. Bakis, K. Goloviznina, F. Philippi, **N. Scaglione**, T. Rekis, M. Costa Gomes, A. Padua. Evidence for anion-anion interactions in tetracyanoborate ionic liquids. 9^{th} COIL – Congress on Ionic Liquids, Lyon, France, 24-28 April 2023. Oral communication.

— A. Padua, **N. Scaglione**, M. Costa Gomes. Alkylphosphonium carboxylate ionic liquids for capture of CO_2 and SO_2 modulating chemical and physical sorption. ICCT-2023 - 26^{th} International Conference on Chemical Thermodynamics, Osaka, Japan, 30 July-4 August 2023. Oral communication.

— A. Padua, **N. Scaglione**, J. Avila, E. Bakis, M. Costa Gomes. Modulating chemical and physical sorption of CO_2 and SO_2 in carboxylate ionic liquids to improve capture and selectivity. ACS Spring, New Orleans, USA, 17-21 March 2024. Oral communication.

ACRONYMS

AAD	Average Absolute Deviation
AAIL	Amino Acid-based Ionic Liquid
AHA	Aprotic Heterocyclic Anion
ATR-IR	Attenuated Total Reflection-Infrared
CCS	Carbon Capture and Storage
CCU	Carbon Capture and Utilization
CDF	Combined Distriution Funcition
CHelpG	Charges from Electrostatic Potentials using a Grid-based method
CL&Pol	Canongia Lopes and Padua, polarisable
CM5	Charge Model 5
CN	Coordination Number
COSY	Correlated Spectroscopy
CPCM	Conductor-like polarizable continuum model
CREST	Conformer–Rotamer Ensemble Sampling Tool
DDF	Dihedral Distribution Function
DFT	Density-Functional Theory
DMSO	Dimethyl Sulfoxide
DOSY	Diffusion Ordered Spectroscopy
DSC	Differential Scanning Calorimetry
EDL	Electric Double Layer
ESW	Electrochemical Stability Window
FDG	Flue Gas Desulfurization
GCM	Group Contribution Method
H-bond	Hydrogen Bond
HF	Hartree-Fock
HOMO	Highest Occupied Molecular Orbital
HSQC	Heteronuclear Single Quantum Correlation
IL	Ionic Liquid
LAMMPS	Large-scale Atomic/Molecular Massively Parallel Simulator
LJ	Lennard-Jones
MD	Molecular Dynamics
MEA	Monoethanolamine
MOF	Metal-Organic Framework
MP	Møller–Plesset perturbation theory
MS	Mass Spectroscopy
MSD	Mean Squared Displacement
NMR	Nuclear Magnetic Resonance
NOESY	Nuclear Overhauser Effect Spectroscopy

OCP	Open Circuit Potential
OPLS	Optimized Potentials for Liquid Simulations
PME	Particle–Mesh Ewald
PoIL	Porous Ionic Liquid
PIL	Protic Ionic Liquid
RDF	Radial Distribution Function
r. t.	room temperature
RK	Redlich-Kister
SAXS	Small-Angle X-ray Scattering
SDF	Spatial Distribution Function
SPE	Single-Point Energy
TGA	Thermogravimetric Analysis
TSIL	Task-Specific Ionic Liquid
TraPPE	Transferable Potentials for Phase Equilibria
TRAVIS	Trajectory Analyzer and Visualizer
UV	Ultraviolet
vdW	van de Waals
VTF	Vogel-Fulcher-Tammann
WAXS	Wide-Angle X-ray Scattering

CHEMICAL ABBREVIATIONS

CATIONS

Species	Name	Structural formula
$[P_{4,4,4,4}]^+$	Tetrabutylphosphonium	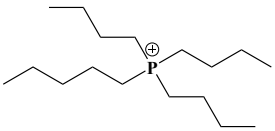
$[P_{6,6,6,14}]^+$	Trihexyl(tetradecyl)phosphonium	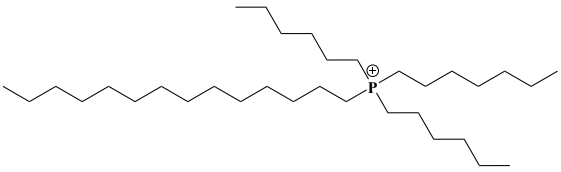
$[C_2C_1Im]^+$	1-Ethyl-3-methylimidazolium	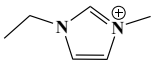
$[C_4C_1Im]^+$	1-Butyl-3-methylimidazolium	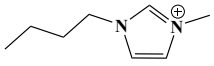
$[OHC_2C_1Im]^+$	1-(2-Hydroxyethyl)-3-methylimidazolium	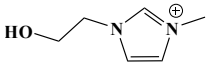
$[NH_2C_3C_4Im]^+$	1-Propylamide-3-butylimidazolium	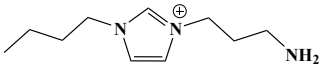
$[C_4Py]^+$	1-Butyl-pyridinium	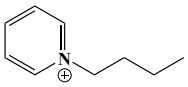
$[N_{2,2,2,2}]^+$	Tetraethylammonium	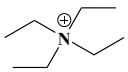
$[N_{2,2,2,4}]^+$	(1-Butyl)triethylammonium	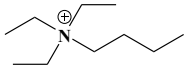
$[TMG]^+$	1,1,3,3-Tetramethylguanidinium	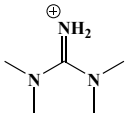

ANIONS

Species	Name	Structural formula
$[AcO]^-$	Acetate	
$[C_5COO]^-$	Hexanoate	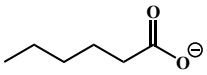
$[C_{11}COO]^-$	Dodecanoate	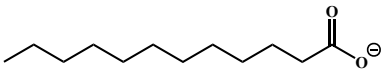
$[MeC_3COO]^-$	Isovalerate	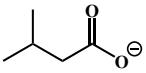
$[Me_4C_4COO]^-$	Tetramethylpentanoate	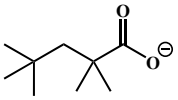
$[Lac]^-$	Lactate	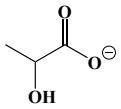
$[Lev]^-$	Levulinate	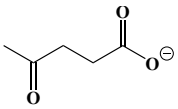
$[c-C_6COO]^-$	Cyclohexanecarboxylate	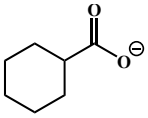
$[p-MeBzCOO]^-$	Para-methylbenzoate	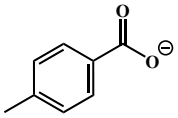
$[p-BrPhCOO]^-$	Para-bromobenzoate	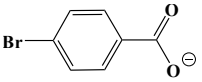
$[p-CNPhCOO]^-$	Para-cyanobenzoate	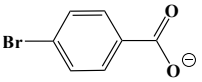
$[PhC_1COO]^-$	Phenylacetate	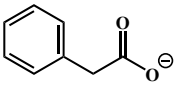
$[PhSC_1COO]^-$	(Phenylthio)acetate	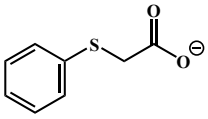
$[2-ClPyCOO]^-$	2-Chloropyridine-3-carboxylate	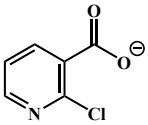
$[2-ClPhC_1OHCOO]^-$	2-(2-Chlorophenyl)-2-hydroxyacetate	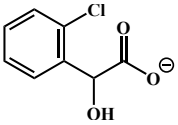
$[TetrazC_1COO]^-$	1-H -tetrazolate-1-acetate	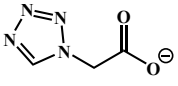

Species	Name	Structural formula
$[Gly]^-$	Glycinate	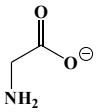
$[Pro]^-$	Prolinate	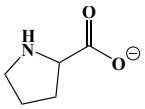
$[Ser]^-$	Serinate	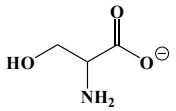
$[Ile]^-$	Isoleucinate	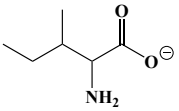
$[Met]^-$	Methioninate	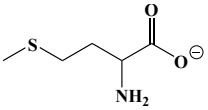
$[PhO]^-$	Phenolate	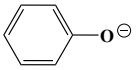
$[Im]^-$	Imidazolate	
$[BenzIm]^-$	Benzimidazolate	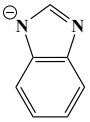
$[1,2,4-Triz]^-$	1,2,4-Triazolide	
$[Tetz]^-$	Tetrazolide	
$[2-CN-Pyr]^-$	2-Cyanopyrrolide	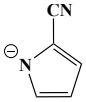
$[2-CF_3-Pyra]^-$	3-(Trifluoromethyl)pyrazolide	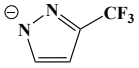
$[Phth]^-$	Ortho-phtalimidate	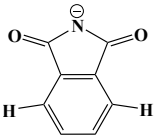
$[DAA]^-$	Diacetamide	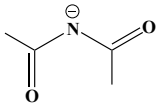
$[BF_4]^-$	Tetrafluoroborate	
$[PF_6]^-$	Hexafluorophosphate	
$[NTf_2]^-$	Bis(trifluoromethane)sulfonimide	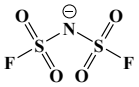
$[TfO]^-$	Trifluoromethanesulfonate, triflate	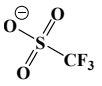

NEUTRAL COMPOUNDS

Species	Name	Structural formula
DBU	(imide-(1,8-diazabicyclo-[5.4.0]undec-7-ene)	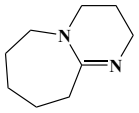
DMSO	dimethylsulfoxyde	
Tol	Toluene	
CO_2	carbon dioxide	
SO_2	sulfur dioxide	
MEA	Monoethanolamine	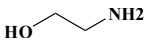

1

INTRODUCTION

1.1 CO_2 AND SO_2 CAPTURE: A GLOBAL CONCERN

In the contemporary landscape of environmental science and engineering, the imperative to address anthropogenic emissions of carbon dioxide (CO_2) and sulfur dioxide (SO_2) stands as a major challenge. The escalating levels of these greenhouse gases in the atmosphere not only contribute significantly to global warming and climate change but also pose grave threats to public health, environmental integrity, and economic stability. As nations strive to mitigate their environmental footprint and uphold commitments outlined in international accords such as the Paris Agreement, the quest for effective strategies to capture and mitigate CO_2 and SO_2 emissions became critical. A huge effort is focused on the reduction of the emission of such gases, especially regarding CO_2, which represents itself about 80 % of global emissions [1] and is the main anthropogenic greenhouse gas.

The rise in atmospheric CO_2 concentrations, driven predominantly by the combustion of fossil fuels for energy production and industrial processes, underscores the urgent need for decisive action to curb emissions and transition to low-carbon energy systems. According to the Global Carbon Project's 2023 report, global CO_2 emissions will probably reach 36.8 $GtCO_2$, marking a worrisome 1.1 % increase from the previous year as illustrated Figure 1.1 [2]. With the current CO_2 emissions, there is 50 % chance that the average temperature on earth rises more than 1.5 °C within 7 years.

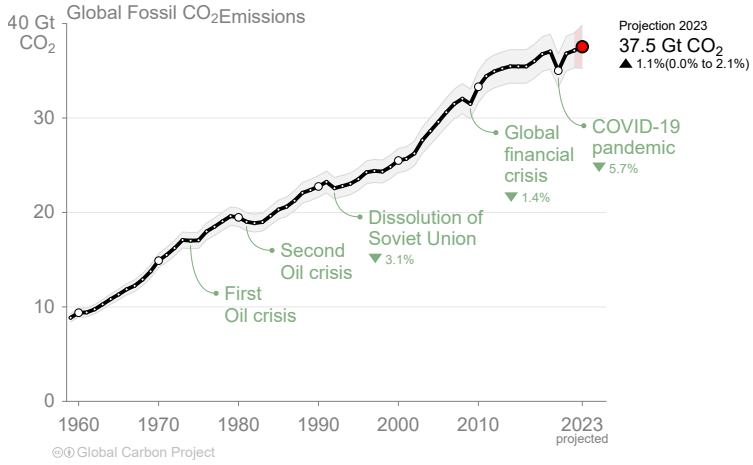

Figure 1.1 – Evolution of global fossil CO_2 emissions over the last decades [2].

Similarly, emissions of SO_2, which is one of the main acid gases, emanating primarily from industrial activities such as coal combustion and metal smelting, continue to plague air quality

and public health, particularly in densely populated urban centers and industrialized regions. Its removal, also known as flue gas desulfurization (FGD), is one of the main environmental concerns. In 2024, European environmental regulations specify that the SOx content of flue gases must be reduced to less than 50–200 mg/Nm^3 depending on the type of plant [3]. Acid gases are the subject of specific regulations in order to control the amount of pollutants sent into the atmosphere.

The reduction of atmospheric emissions of CO_2 and SO_2 is a burning issue. This is why European programs, such as the Strategic Energy Technology plan, are set up in order to reduce greenhouse gas emissions [4]. Many new technologies are already under study in order to reverse the still increasing greenhouse gas emissions. In addition to the difficulties of developing new efficient and sustainable technologies, these projects are facing social, regulatory and financial problems which are obstacles to their development. Therefore, new research programs are required to overcome the current issues and to improve these technologies making them viable for real large-scale applications. One possibility to reduce the emissions of such gases, is the removal of those compounds from industrial flue gas streams. A typical post-combustion flue gas has a volumetric composition of 15 % CO_2, 10 % H_2O, 0.05–0.2 % SO_2, 0.15–0.25 % NO_x and other harmless compounds such as N_2 or O_2 [5].

1.2 OVERVIEW OF ACID GAS CAPTURE TECHNOLOGIES

1.2.1 *Carbon capture technologies*

Technologies for Carbon Capture and Storage (CCS) [1, 6] and Carbon Capture and Utilisation (CCU) [1] are considered as key strategies in order to reduce greenhouse gas emissions. The difference between CCS and CCU is the final processing of CO_2, but they both start with the CO_2 capture, which is the essential step.

The three main ways to capture CO_2 are pre-combustion capture, post-combustion capture and oxy-fuel combustion [7]. The pre-combustion capture consists in capturing the CO_2 generated from an intermediate reaction as a side product. The second method refers to the capture of CO_2 from the flue gas right after combustion. As for the last, application of oxy-fuel combustion capture is only valid for combustion processes using pure oxygen in order to produce flue gases with high CO_2 concentrations so that the following separation is easier [8]. The post-combustion CO_2 capture *via* chemical absorption is considered to be the most promising and mature process [7]. Currently, there are approximately 40 carbon capture facilities around the world [9]. Different ways might be applied to isolate the CO_2 from the gas stream such as chemical looping combustion, membrane separation, cryogenic distillation, adsorption or absorption [10]. Our focus will primarily center on methods employing liquid absorbents.

Amine-based absorbents are the most used due to their remarkable reactivity with CO_2, good thermal stability, low cost and relatively easy production. The main technology for isolating and capturing CO_2 is amine scrubbing [11] in which the sorbent is regenerated in a stripping process by depressurization and/or heating. CO_2 reacts with the amines through a nucleophilic attack of the nitrogen on the carbon leading to carbamate formation in a single step mechanism.

Generally, two amine molecules are involved in the mechanism, as a deprotonation step is required to activate the nucleophilicity of the reacting amine.

Aqueous monoethanolamine (MEA) based absorbents are currently considered as one of the most efficient solvents for flue gases with a low CO_2 partial pressure. Hence, they are currently the most used in post-combustion CO_2 capture processes (Figure 1.2) because they have an efficiency over 90 % and a high rate of reaction with CO_2 compared with other amine-based solvents. The hydroxyl group increases the solubility of MEA in water and it tends to reduce its vapor pressure. On the other hand, the amine function provides the alkaline reactive site necessary to the absorption of the acid gas [12]. Over the years, MEA has become the benchmark amine for CO_2 capture.

$$CO_2 + RNH_2 \rightleftharpoons RNH_2^+COO^-$$

$$RNH_2^+COO^- + RNH_2 \rightleftharpoons RNHCOO^- + RNH_3^+$$

Scheme 1 – Absorption mechanism of CO_2 by MEA.

In a standard post-combustion process, flue gas enters an absorber column at around 40 °C containing a ~ 30 % wt. MEA aqueous solution. The CO_2 is absorbed, forming a CO_2-rich solution which is sent to a stripper column. The temperature is increased up to the solvent's boiling point for the reverse reaction to liberate the CO_2. Finally, the lean solvent is recycled back to the absorber column , while the CO_2-free flue gas is discharged into the atmosphere [12].

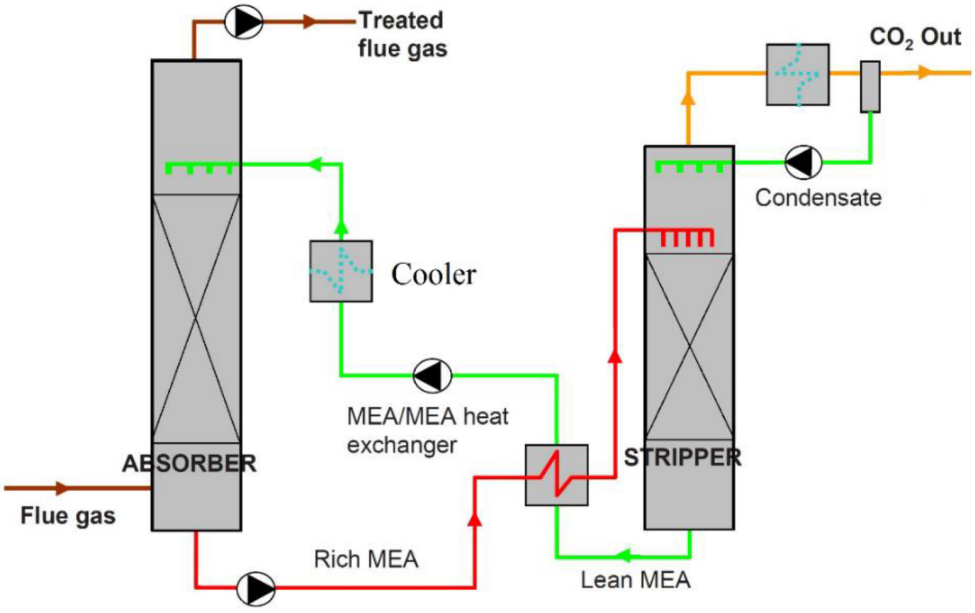

Figure 1.2 – Diagram of a typical absorption-regeneration post-combustion CO_2 capture process [12].

Several drawbacks linked with this process have been highlighted. The aqueous amine solvents have a low CO_2 capacity in real operating conditions because of the low CO_2 partial pressure and of the high flow rates of flue gases. Moreover, the solvent regeneration step is highly energy consuming because of the large negative enthalpy of reaction and the need of heating large

quantities of water. It was found that the total heat of absorption is about $-86\,\mathrm{kJ/mol_{CO_2}}$, which is one of the highest among the available solvent for carbon capture [13]. The sorbent might undergo thermal degradation or react with other oxides or oxygen in the flue gas, leading to solvent loss and potentially increasing the corrosion rate of equipment due to the production of corrosive bicarbonate byproducts.

The majority of large-scale CCS facilities in operation use absorption columns which are based on the utilization of solvents [14] due to the better ratio of gas absorbed over the energy consumed. Physical solvents are efficient for the separation of CO_2 under high-pressure conditions [15], but solvents with a relatively low reactivity towards CO_2 are preferentially employed for gases containing high concentrations of CO_2, such as syngas. Absorbents with a higher reactivity are favoured for gases containing lower concentrations of CO_2, such as coal-fired flue gases. Among the 19 main CCS facilities, 9 are based on amine aqueous solutions, as previously discussed, whereas 6 are using physical absorbents [16]. Figure 1.3 shows that the physical absorbents have a greater contribution to the total quantity of CO_2 absorbed, but it remains far too low to mitigate its effect on climate change [9].

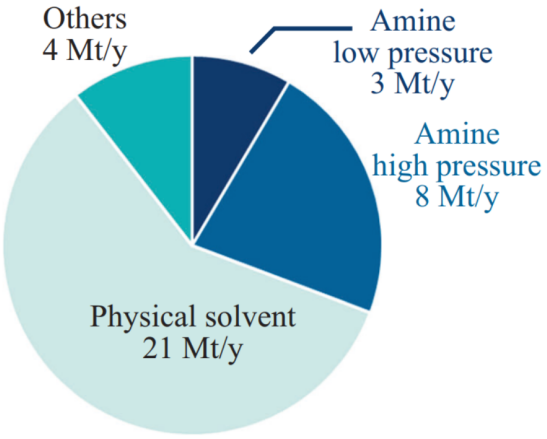

Figure 1.3 – Quantity of CO_2 captured in the 19 main CCS facilities in operation in 2019 using different types of absorbents [14].

The capture of CO_2 is also very important in the purification of biogas to biomethane, suitable for injection into natural gas pipelines or for use as a transportation fuel. A vacuum swing process associated with an adsorbent is currently used in large scale with a removal capacity of approximately $1\,\mathrm{Mt-CO_2/y}$ [14]. Another approach is also the utilization of chemical absorbent, for example based on amine aqueous solution [16]. Additionally, membrane separation techniques are gaining traction, leveraging permeable membranes to selectively separate CO_2 from biogas based on differences in molecular size and solubility. For example, in Brazil, a CCS facility is using this method with a processing capacity of about $7\,\mathrm{Mm^3/d}$ [17].

Enhancing the efficiency of such technologies primarily depends on reducing the cost of the solvent regeneration step, but other factors such as toxicity, biodegradability, stability, and rates of mass transfer, are also pivotal for large-scale applicability [18, 19]. This is why numerous studies are exploring other types of solvents.

1.2.2 *Carbon capture and storage or utilisation*

Once the CO_2 has been captured with a high purity, it is compressed to a supercritical fluid which can be transported through a pipeline, by maritime transports or road tankers in order to be routed either to the storage or to the utilisation site. The first approach mentioned is known as CCS and the second one as CCU.

In the CCS procedure, CO_2 is stored in the ocean or buried underground in depleted oil and gas reservoirs. The main issues related to CO_2 storage are the potential leaks and the damage they can cause to the environment. The availability of safe geological reservoirs is a fundamental requirement in order to make a CCS project available. This is why the United States possess the majority of commercial large-scale CCS units either already operating or in development [20]. Indeed, there is a large availability of safe geological storage in the United States compared with Europe, for instance. A limited geological storage capacity implies increased transportation and injection costs which hinder its viability [21]. Moreover, as CCS is an unprofitable activity, a large financial investment is required which can greatly limit its large-scale application [1].

One of the main advantages of CCU over CCS is the direct recycling of CO_2 waste into valuable compounds to offset the initial costs [1]. CO_2 is a raw material in a broad range of industries as it is required in numerous processes. Indeed, food processing, beverage carbonation packaging [22], mineral carbonation [23], enhanced oil recovery and enhanced coal-bed methane [24, 25], production of biofuels from microalgae [26], utilisation in chemical and fuel syntheses [1] and enhanced geothermal system are the main CO_2 utilisation method considered, and their CO_2 demand might increases in the next years.

Some applications require pressurized CO_2 of very high purity as a feedstock which can greatly increase the cost and limit its utilisation [27]. Hence, in order to make this process financially viable, the development of less demanding CCU technologies is required.

Environmental, economic and technical stakes are the main issues to make both CCS and CCU viable. These technologies both require a significant investment, increasing with the size of the unit. They must be economically profitable in order to be integrated in industrial processes. The environmental consequences have to be examined to ensure that CO_2 emissions are not reduced at the expense of other environmental concerns.

1.2.3 *SO_2 capture*

While CO_2 stands as the primary greenhouse gas, other compounds found in flue gases, such as SO_2, also constitute significant sources of pollution. The strict regulation of its emissions underscores the necessity of its removal from flue gases. The growing concern over air pollution primarily stems from the rising demand for energy which is usually produced from fossil fuels by power plants and other industrial facilities [28], emitting gigatons of SO_2 [29], responsible for approximately 70 % of SO_2 global emissions. When combined with atmospheric moisture, the emitted SO_2 forms sulfuric acid aerosols, leading to the formation of acid rain and contributing to respiratory illnesses such as asthma and bronchitis [30]. SO_2 emissions are a precursor to fine particulate matter (PM2.5) and ground-level ozone, both of which pose serious health risks and

environmental hazards [31]. Effective capture and removal of SO_2 from industrial emissions are essential for mitigating air pollution, protecting public health, and preserving ecosystems.

Traditional methods for removing SO_2 typically utilize ammonia solvents, organic solvents [32], limestones [33], or seawater [34]. These methods suffer from significant drawbacks such as low efficiency, high costs and production of undesirable byproducts such as volatile organic compounds. Finding a material that can effectively and selectively absorb SO_2 in a reversible manner remains a practical challenge for widespread application.

2

IONIC LIQUIDS AS ALTERNATIVE SOLVENTS FOR GAS CAPTURE

2.1 WHAT IS AN IONIC LIQUID?

Ionic Liquids (ILs) emerge as promising absorbents for acid gas capture due to their unique properties. ILs are low-temperature molten salts formed by large organic ions with delocalized electrostatic charge, conformational flexibility, and asymmetric molecular shapes hindering crystallization and lowering the melting point which are often below 100 °C [35–39]. They can be composed by various cations such as imidazolium, quaternary ammonium, phosphonium, pyridinium, pyrrolidinium, with different substituents, associated with a broad range of anions, ranging from symmetrical tetrafluoroborate $[BF_4]^-$ or hexafluorophosphate $[PF_6]^-$, to flexible bistriflimide $[NTf_2]^-$, carboxylates $[RCOO]^-$, or to other aprotic anions such as pyrrolide [Pyr]- or tetrazolide $[Tetraz]^-$ (Figure 2.1).

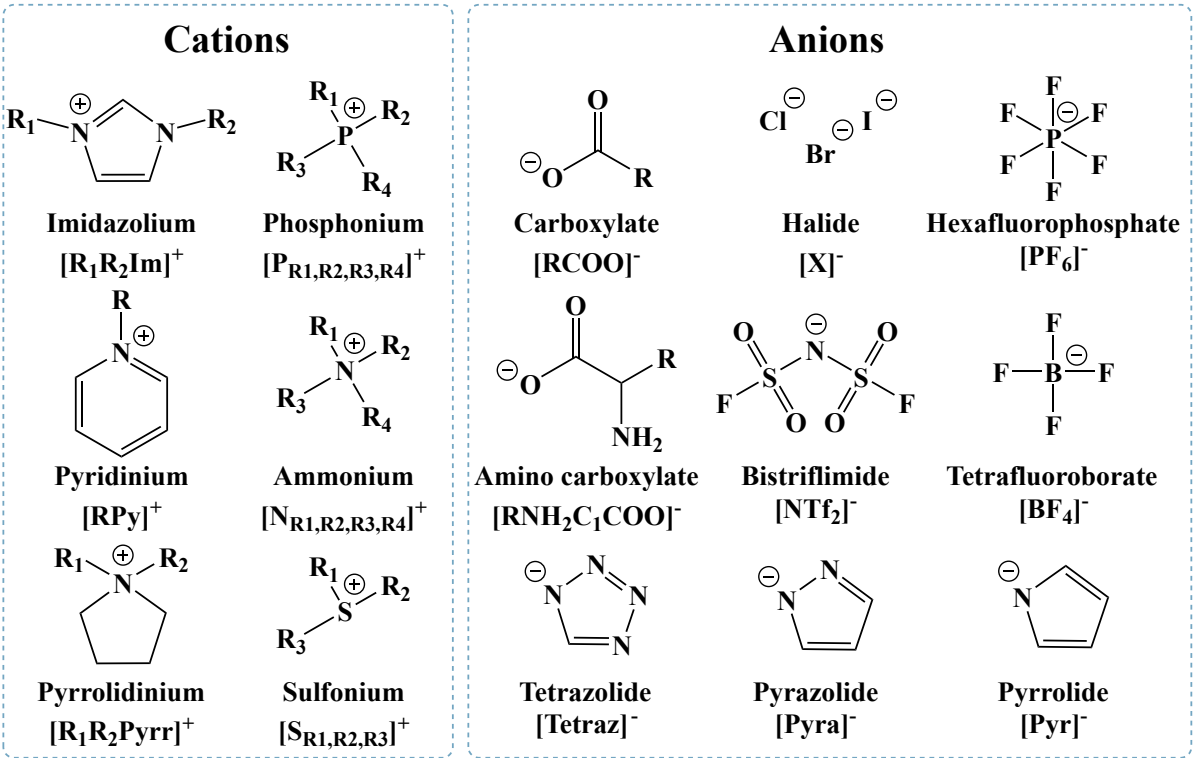

Figure 2.1 – Examples of typical cations and anions used in ionic liquids.

ILs unique properties include a low flammability, negligible vapor pressure, high conductivity, good thermal and electrochemical stability [37, 40–44], making them promising chemicals for methodologies respectful of the environment. Furthermore, they can be designed and optimized to minimize their impact through the combination of different cations and anions or the function-

alization of their side-chains [45, 46]. ILs find application as solvents for reactions, separations, synthesis of materials, as catalysts, as electrolytes in energy-storage devices, as lubricants, optical and magnetic fluids [47–49]. They are known to dissolve a broad range of solutes including carbon dioxide [50], cellulose [51], and water-insoluble dyes [52], making them attractive media for greenhouse gas capturing [53], textile recycling [54], biomass processing [55], and also in pharmaceutical and cosmetic industries [56].

ILs show a variety of intra- and intermolecular interactions such as electrostatic, van der Waals (vdW), π-stacking, H-bonding components. Due to their ionic nature, they are often compared to high-temperature molten salts, and as liquid salts, they exhibit charge alternation and intermediate-range ordering [57]. Although they are liquid, ILs possess a significant self-organization, a glassy nature and some level of heterogeneity at a microscopic scale. It is possible to find polar areas (ionic head groups), as well as non-polar areas leading to nano-domain segregation [58]. Charge delocalization and large ion size lead to weaker interactions between ions, which decreases the long-range ordering, and possible cation-anion hydrogen bonding resulting in a structural orientation, particularly noticeable for ILs in their crystalline phases [59]. The presence of polar and non-polar areas will be very important for the CO_2 and SO_2 absorption.

The possibility of designing the ILs for specific purposes is generally considered as their most important characteristic. An understanding of the link between the chemical structures of the ions and the physico-chemical properties, in addition to their microscopic interactions, is required in order to tailor ILs for acid gas capture processes.

2.2 CO_2 CAPTURE

2.2.1 *Physical absorption*

As stated before, ILs have a heterogeneous microscopic structure which is divided into polar and non polar domains [60] due to strong coulombic forces and weaker vdW interactions [61]. This particular structure is due to the formation of an ion network bound by electrostatic interactions between the anions and the cations, thereby excluding non-polar moieties, such as alkyl side chains, away from these polar areas. It enables the solvation of compounds with different polarities, for examples CO_2 or SO_2 will be preferentially solvated in the polar domains.

Pioneering work on the solubility measurements of CO_2 in $[C_4C_1Im][PF_6]$ [62] has paved the way for further investigations on the physical absorption of CO_2 by ILs. Further studies by Attenuated Total Reflection-Infrared spectroscopy (ATR-IR) [63] and molecular dynamics (MD) simulations [64] were carried out and they demonstrated the existence of weak Lewis acid-base interactions between the anion of the IL as electron donor and CO_2 as electron acceptor. Even tough the presence of fluorinated substituents increase CO_2 solubility [65], their use ILs is now limited because they are not biodegradable, persistent and chemically stable [66], thus, impacting negatively the environment.

Even if CO_2 is preferably solvated in polar areas, it has been shown that increasing the length of the alkyl chains on the cations leads to increased solubility due to vdW interactions. Nevertheless,

if the length of the alkyl chain exceeds eight carbon atoms, the non-polar areas become too large and the CO_2 solubility reaches a plateau [67].

An interesting property of ILs for CO_2 physisorption is the very low volume expansion caused by physisorption compared with traditional organic solvents. For example, in toluene at 40 °C and 70 bar, a CO_2 absorption of 0.74 in mole fraction increases the volume by 134 % whereas in $[C_4C_1Im][PF_6]$ only a small 18 % increase has been found with a CO_2 absorption of 0.69 [68]. This particular feature probably stems from the cohesive structure of the ILs. This is an interesting property in an industrial perspective as it facilitates the process design.

2.2.2 *Chemical absorption*

The solubility of CO_2 in ILs at low partial pressures of gas remains too low, to be applied in large scale capture processes. Consequently, new strategies were developed to improve the carbon dioxide capacity of ILs at low pressures. They are based on the design of ILs able to chemically react with CO_2.

The first IL designed to chemically react with CO_2 (task-specific ionic liquid, TSIL) was developed by inducing a primary amine function on the lateral alkyl chain of imidazolium cation to produce the 1-propylamide-3-butylimidazolium tetrafluoroborate $[NH_2C_3C_4Im][BF_4]$ with a CO_2 capacity of almost 0.33 in mole fraction at room temperature (r. t.) and 1 bar [69]. This capacity is equivalent to that of aqueous MEA as the absorption mechanism is similar and follows a 2:1 stoichiometry as illustrated in Scheme 2. The reaction is reversible and it was possible to regenerate the pure IL upon heating at 80–100 °C for several hours under vacuum. The IL could be reused in up to 5 absorption/desorption cycles with no efficiency loss. On a mass basis, the absorption is nevertheless worse in heavier ILs compared with aqueous amine.

The high viscosity of this first generation of TSILs is a barrier to applications. The viscosity was even higher after the CO_2 absorption [70] hindering their large-scale use. The increase stems from the formation of a strong hydrogen bond network between the ammonium group of the cations and the carbamate products of the reaction [71]. Another drawback of amine-functionalised cations is the electron density decrease at the amine site due to the presence of the nearby cation weakening the interaction with CO_2. Efforts are required not only to improve the absorption capacity and the absorption kinetics, but also to improve physical and chemical properties of the absorbents.

ILs based on amino-acid anions have been proposed to improve the mass transport properties and to decrease the viscosity [72]. Even though tetrabutylphosphonium amino acid-based ILs (AAILs) ($[P_{4,4,4,4}][AA]$) exhibited a higher CO_2 capacity, they are very viscous. This stems from the interactions between the carboxylic acid group of carbamic acid, formed by the reaction with CO_2, and the amino group of the anion. Two trihexyl-(tetradecyl)phosphonium-based ILs ($[P_{6,6,6,14}][Met]$ and $[P_{6,6,6,14}][Pro]$) showed a nearly 1:1 stoichiometric (IL:CO_2) absorption mechanism as no interactions between the amino group and the carboxylic acid group are possible (Scheme 3) [73, 74]. This has been confirmed by IR measurements and also by density functional theory (DFT) calculations at the B3LYP/6-311G++(d,p) level. Other AAILs such as $[P_{6,6,6,14}][Ile]$, $[P_{6,6,6,14}][Gly]$ and $[P_{6,6,6,14}][Sar]$ show nearly equimolar absorption capacities [75,

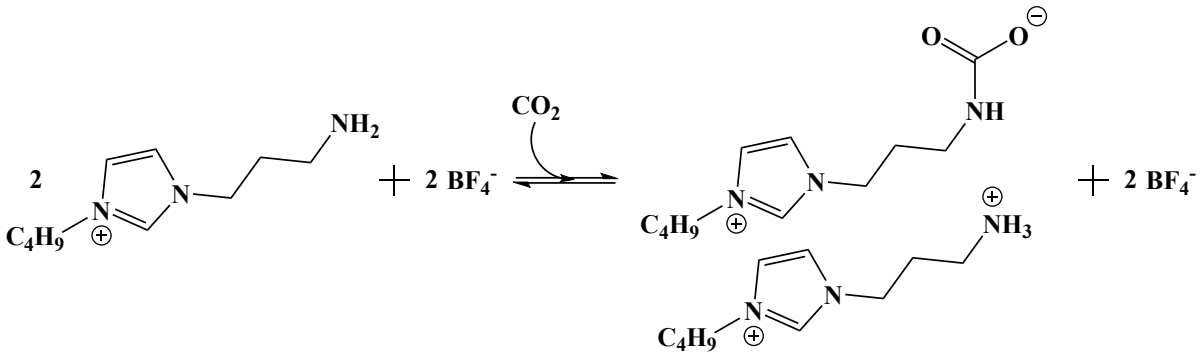

Scheme 2 – Absorption mechanism of CO_2 by $[NH_2C_3C_4Im][BF_4]$. Adapted from [69].

76]. A difficult synthesis, in addition to thermal and chemical instabilities as well as high viscosities hinder their generalized applications. For example, the viscosity of $[P_{6,6,6,14}][Ile]$ increased 240-fold upon CO_2 uptake compared with the pure IL [76]. A slight decrease in CO_2 absorption has been reported when AAILs are mixed with water, probably due to a reprotonation of the anion [77].

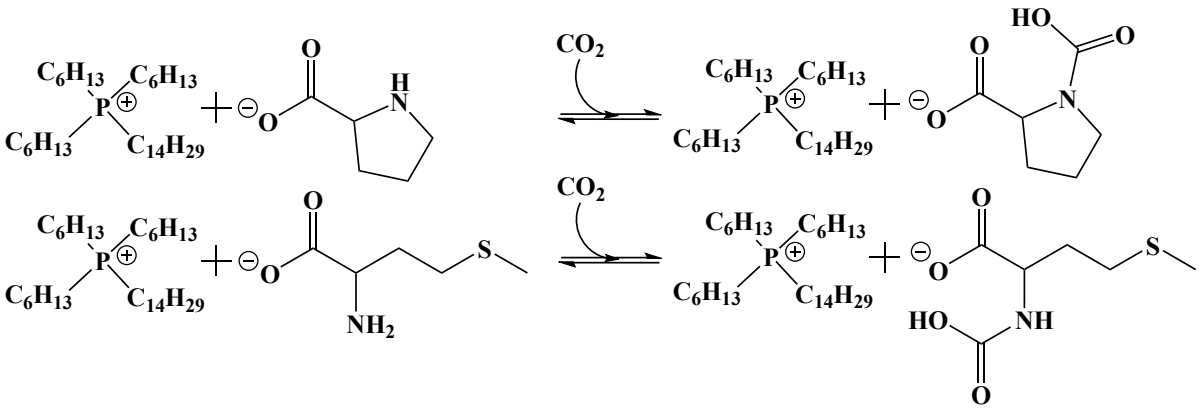

Scheme 3 – Reaction of CO_2 with (top) $[P_{6,6,6,14}][Pro]$ and (bottom) $[P_{6,6,6,14}][Met]$. Adapted from [73].

ILs based on Aprotic Heterocyclic Anions (AHAs) were designed to limit the formation of hydrogen bonds throught the elimination of the hydrogen atoms on the anion [78]. An interesting absorption of about 0.9 mol of CO_2 per mole of IL has been reached with trihexyl-(tetradecyl)phosphonium 2-cyanopyrrolide and 3-(trifluoromethyl)pyrazolide ($[P_{6,6,6,14}][2-CN-Pyr]$ and $[P_{6,6,6,14}][2-CF_3-Pyra]$, respectively). The studies carried out by MD simulations [79], and DFT calculations [78] of the reaction mechanism revealed that the negatively charged nitrogen on the anion was directly reacting with the electrophilic C_{CO_2} through nucleophilic attack (Scheme 4). $[P_{6,6,6,14}][2-CN-Pyr]$ was the most promising candidate due to its low activation energy and its fast binding kinetics with CO_2, which makes it interesting in a recycling prospect [80].

In contrast to AAILs, the presence of water increases the CO_2 absorption of $[P_{6,6,6,14}][2-CN-Pyr]$ as the protonation of the 2-cyanopyrrolide anion is unlikely [81]. It is interesting to note that the viscosity of $[P_{6,6,6,14}][2-CN-Pyr]$ decreased almost by 50 % under wet conditions before CO_2

absorption whereas the viscosity increased dramatically after CO_2 uptake, probably due to the formation of hydrogen bonds between the formed carbamate and water.

Under the same conditions, the CO_2 capacity of the AHA IL is about half of the CO_2 capacity of a 30 % wt. aqueous MEA solvent because of its high molecular weight.

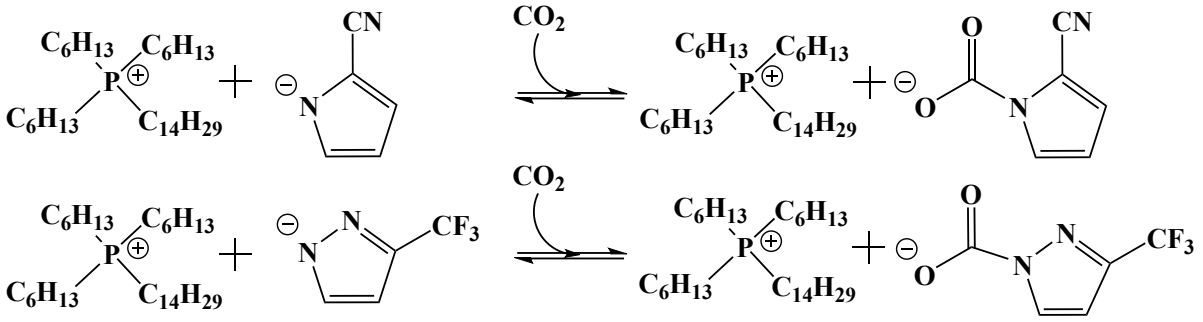

Scheme 4 – Reaction of CO_2 with (top) $[P_{6,6,6,14}][2-CN-Pyr]$ and (bottom) $[P_{6,6,6,14}]$ $[2-CF_3-Pyra]$. Adapted from [82].

Still in the perspective of IL design, it might be interesting to examine the influence of the anion basicity on the CO_2 uptake as it influences the reactivity. In this regard, a series of phosphonium azolate ILs was studied to assess the effect of the anion basicity on the CO_2 absorption capacity [83]. It revealed that when the pK_a of the anions decreased from 19.8 to 8.2 in dimethyl sulfoxide (DMSO), the absorption sharply decreased from 1.02 to 0.08 in mole ratio. On the other hand, the absorption in imidazolate ILs with different cations [84] was similar, clearly indicating that anion basicity is a cornerstone of the CO_2 absorption while the cation has a greater influence on the physico-chemical properties of the ILs.

The utilisation at a large scale of AHA-based ILs seems compromised because of their complex chemical structure and the highly energy consuming regeneration step.

A mixture of an organic alcohol with an amidine superbase was proposed to capture and release CO_2 in a more efficient way than traditional aqueous alkanolamine solutions [85]. Even if a high CO_2 absorption capacity was reported, the high volatility of alcohols leads to an important loss of solvent during the process. Overcoming this issue would require new TSILs with the introduction of the alcohol function directly into the IL, which might be an efficient way to stabilize the absorbent.

Using superbases to prepare ILs appears as a way to improve their reactivity towards CO_2. Various anion-functionalized Protic Ionic Liquids (PILs) were mixed with a superbase resulting in solvents which are able to react stoichiometrically and reversibly with CO_2 [84, 86]. These compounds are good candidates as TSILs due to the wide variety of available organic superbases and weak proton donors, enabling a great number of pairings. PILs have the advantage of being easily synthesized by mixing a Brønsted acid with a Brønsted base.

Consequently, the purpose was to develop new PILs through the deprotonation of weak proton donors (imidazoles, pyrrolidones, phenols or fluorinated alcohols) by a very strong base with such a strong proton affinity that their protonated state cannot be deprotonated by the previously formed anion. This provides a strong thermodynamic driving force to capture CO_2 and a correlation between the pK_a of the superbase and the absorption capacity has been found matching

the previously mentioned effect of anion basicity on the absorption [87]. Nevertheless, we can wonder if the pK_a value of a superbase in an IL medium has the same meaning as that in an aqueous medium.

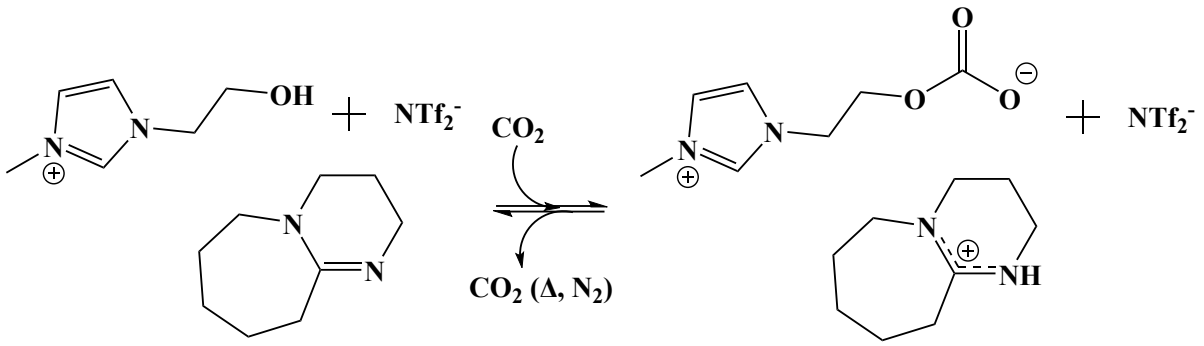

Scheme 5 – Reaction mechanism of the absorption of CO_2 by $[HOC_2C_1Im][NTf_2]$ and DBU. Adapted from [86].

For example, the $[HOC_2C_1Im][NTf_2]$–DBU (imide-(1,8-diazabicyclo-[5.4.0]undec-7-ene) IL exhibited a CO_2 capacity of 1.13 in mole ratio (at 23 °C and 1 bar) with a combination of both chemical and physical absorption (Scheme 5) [86]. It appears that the relatively low viscosity of the superbases improves the absorption rate. The desorption was easily performed by gas stripping at 60 or 120 °C with only a minor loss of absorbent activity after several recycling steps.

In order to make superbase-derived ILS applicable in real carbon capture processes, it is essential to study the influence of water on the CO_2 absorption capacity and also on the viscosity. It has been found in five trihexyltetradecylphoshonium-superbase ILs, that the presence of water can either decrease or increase the CO_2 uptake depending on the anion, but it can also make the IL unusable because of chemical instability under wet conditions. When using phenolate anions ($[P_{6,6,6,14}][PhO]$), the IL is decomposed after reaction with CO_2 under wet conditions. An interesting decrease of the viscosity from 569 to 114 mPa s has been measured in the presence of water after equilibrating CO_2 with the 1,2,4-triazolide anion ($[P_{6,6,6,14}][1,2,4-Triz]$). It was possible to regenerate the $[P_{6,6,6,14}][1,2,4-Triz]$ IL over 6 cycles even under wet conditions by stripping with N_2 at 80 °C for 15 min. A difficult regeneration of superbase-derived ILs was nonetheless reported which greatly hinders their application [20].

ILs based on carboxylate anions were also studied as promising absorbents for CO_2 capture. A solution of $[C_4C_1Im][OAc]$ 14 % wt. in water has a CO_2 absorption capacity intermediate between a typical MEA solution and a physisorbent IL [88]. Moreover, the moderate enthalpy of reaction of CO_2 with an imidazolium acetate IL suggests that the regeneration would be less energy consuming than with a conventional MEA solution.

Nuclear Magnetic Resonance (NMR) analysis showed that the acetate is basic enough to deprotonate the imidazolium ring's C_2 so that the newly formed carbene can attack the electrophilic carbon of CO_2, resulting in the formation of an imidazolium carboxylate zwitterion [89] (Figure 6). A smell of acetic acid after bubbling CO_2 through $[C_4C_1Im][OAc]$ and other 1,3-dialkylimidazolium acetate ILs has been reported [90].

The economic aspect of the CO_2 capture process with this IL has been examined and a 16 % reduction of the energy loss compared with the MEA process was reported, as well as a CO_2 desorption without any degradation of the IL. A 12 % equipment footprint decrease in addition to a 11 % lower investment make this IL-process economically more interesting [91]. However, the synthesis of high purity ILs is generally very expensive compared with a conventional MEA solution, an issue that can be offset if the absorbent is regenerated. The improvement of the IL design requires a better understanding of the absorption mechanism.

The acidic proton located on the C_2 of 1,3-dialkylimidazolium cations can be deprotonated as long as the anion is basic enough, even without the intervention of a strong base [92]. Hence, the formation of a $[C_2C_1Im][H(OAc)_2][C_2C_1Im^+{-}COO^-]$ complex has been proposed. This probably means that a similar complex is produced with $[C_4C_1Im][OAc]$. An extended study of this absorption mechanism by NMR, IR and Raman spectroscopy combined with DFT calculations confirmed the formation of this complex [93]. Moreover, the mole fraction of CO_2 absorbed by $[C_4C_1Im][OAc]$ was very close to the theoretical maximum (0.33) due to the 2:1 stoichiometry of the absorption mechanism.

In order to suppress formation of the imidazolium-2-carboxylate zwitterion as depicted Figure 6, other cations like tetrabutylphosphonium or 1-butyl-pyridinium have been chosen [94]. Indeed, *ab initio* calculations showed that there is a strong interaction between CO_2 and acetate anions if no carbenes are generated, which is very interesting in a IL designing perspective.

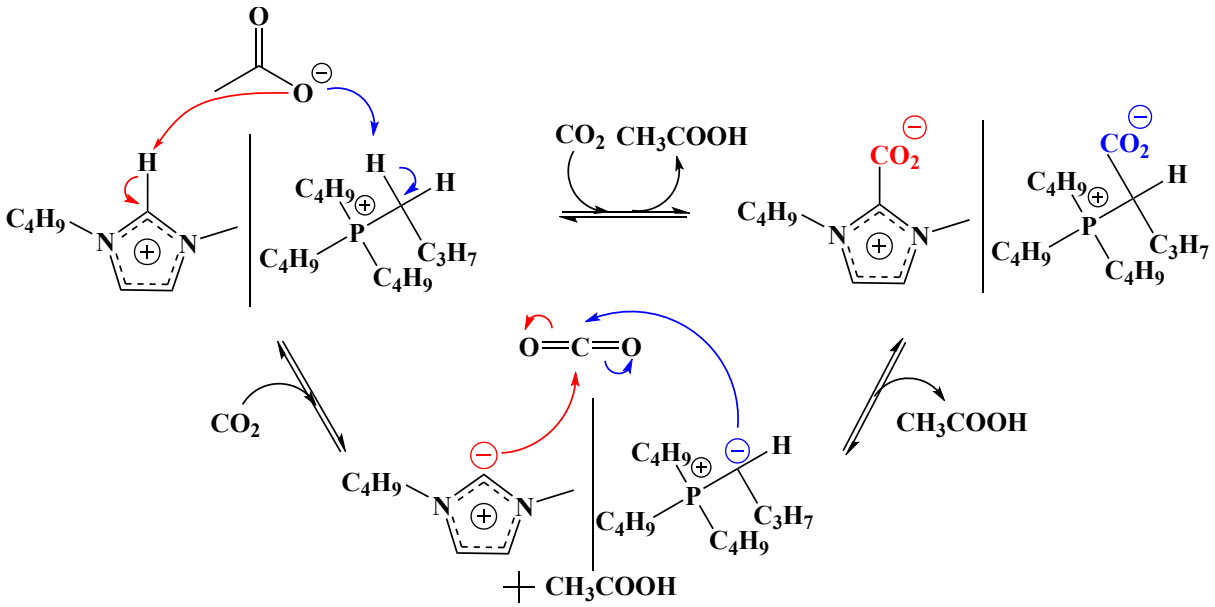

Scheme 6 – Reaction mechanism of the absorption of CO_2 by $[C_4C_1Im][OAc]$ [89] and $[P_{4,4,4,4}][OAc]$ [95, 96].

More recently, to take advantage of the interesting properties of both tetrabutylphosphonium cations and carboxylate anions, three new ILs, $[P_{4,4,4,4}][C_nCOO]$ (n= 1, 2 and 7) were proposed [95]. The anion and the cation are interacting *via* the carboxylate head group of the anion (O_{COO^-}) and the α-H (H_α) of the alkyl side chains of the cation as depicted in Figure 6. Even with a different carboxylate, namely levulinate (4-oxopentanoate), the same absorption mechanism was occurring [96]. These types of ILs showed promising behavior for CO_2 capture. A

similar mechanism was reported for AHA ILs, namely phosphonium cations paired with a 2-cyanopyrrolide ($[2-CNPyr]^-$) anion. At elevated temperatures (338.15 K), the same mechanism occurs inducing a chemical absorption of CO_2 by the ylide intermediate, leading to the formation of a similar phosphonium-carboxylate zwitterion [97]. However, this was considered as a side reaction as the anion is able to directly react with CO_2.

A lower concentration of water led to a smaller decrease of the CO_2 capture capacity $[C_4C_1Im][OAc]$ and $[C_2C_1Im][OAc]$ compared to higher concentrations [98]. The reduction in absorption capacity has been attributed to a competition between H_2O and CO_2 for the solvation sites and to a less favorable chemical reaction between the gas and the IL than with water. A similar effect has been found on $[N_{2,2,2,4}][OAc]$ with a progressive decrease of the CO_2 absorption with increasing water content [99]. However, an important decrease of the viscosity is highlighted in both cases with only a small amount of H_2O, making it a potential interesting trade-off for a real capture process.

Contrary to imidazolium acetate ILs, the addition of 0.5 mole ratio of water to $[P_{4,4,4,4}][HCOO]$ leads to an important increase of the CO_2 capture capacity up to the saturation (0.5 in mole ratio). This increase was due to the direct reaction of H_2O with CO_2 leading to the formation of H_2CO_3 [100]. Interestingly, the formation of unstable carbonic acid was driven by the consecutive formation of a complex between formate anion and formic acid $[(HCOO)_2]^-$, but the reversibility of the reaction was not discussed.

A weaker cation-anion interaction is observed upon addition of water in $[P_{4,4,4,4}][C_nCOO]$ [95], as hydrogen bonds are formed between H_2O and O_{COO^-} resulting in a shift of electronegativity of both oxygen atoms [95]. Proton exchanges between the cation and anion, through the deprotonation of H_α by the anion producing an ylide, are favoured by the basicity of the anions as long as the mass fraction of water lies below 0.75. An extended alkyl chain on the carboxylate appears to hinder the interactions with water due to its hydrophobic effect.

2.3 SO_2 CAPTURE

Even if many ILs exhibit a very good physisorption of SO_2, a large SO_2 partial pressure and a long equilibration time are required, which are limiting conditions in a real process. A chemical reaction between the IL and SO_2 is necessary as well to increase the absorption capacity. The acidic properties and the high polarity of SO_2 indicate that basic functions should be embedded in the ILs in order to increase absorption capacity [101, 102].

The first reported IL capable of chemically reacting with SO_2 was 1,1,3,3-tetramethylguanidinium lactate ([TMG][Lac]) following a 2:1 (IL:SO_2) stoichiometry [103] . A combination of computational methods showed that the lactate anion enhanced and induced the N--S interaction resulting in a ring product with three end-to-end H-bonds [104]. The long time required to reach the absorption equilibrium, due to a slow mass transport and high viscosity, hinders its application. Various ILs such as TMG-based ILs, hydroxyl ammonium-based ILs, imidazolium ILs, cyano-based ILs or azole-based ILs were since reported as SO_2 absorbents.

As is the case with CO_2 chemisorption, the utilisation of basic and electron rich anions seems to improve SO_2 capture in ILs [105, 106]. The desorption of SO_2 appears to be incomplete, and

even impossible in some cases [107], while almost complete reversible absorptions are reported with trihexyl-(tetradecyl)phosphonium tetrazolide ($[P_{6,6,6,14}][Tetz]$) [108]. The regeneration of the IL is important to take into account in its design as the desorption step might be difficult because of the strong bonds formed with SO_2.

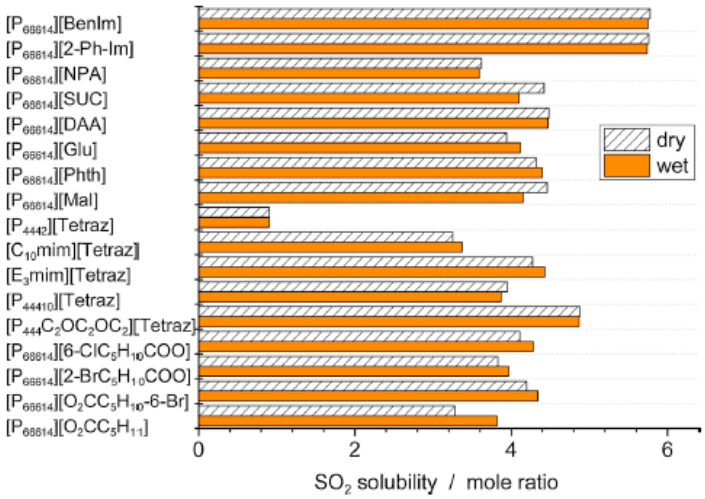

Figure 2.2 – SO_2 absorption in wet and dry ILs at 293.15 K and 1 bar [109].

The effect of water on SO_2 absorption seems to depend on the IL, but most of the time the SO_2 absorption is not strongly influenced by the presence of water as depicted in Figure 2.2 [109]. For example, in two carboxylate-based ILs ([TMG][Lac] [110] and $[N_{2,2,2,2}][Lac]$ [111]), the absorption mechanism changed, but the overall absorption capacity remains similar. Depending on the anion, other compounds can be produced leading to an irreversible reaction, as with $[C_4C_1Im][OAc]$ [112], that leads to a good absorption capacity during the first cycle, but the capacity gradually decreases upon several absorption-desorption cycles. As it was already discussed, water can reduce the viscosity of ILs, which is very interesting for a real application, but this might be accompanied by a higher energy desorption step because of water evaporation.

In what follows, we will mainly consider carboxylate-based ILs as this PhD project is centered on this family of salts and they have a particularly strong affinity with SO_2. It is interesting to note the reduction of cation-anion hydrogen bonding in the ILs seems to increase the SO_2 absorption capacity [113], which is an important factor to take into account to design ILs. Based on the analysis of the SO_2 absorption isotherms of carboxylate imidazolium ILs, it was found that these ILs were reactive towards SO_2 [114]. It was later showed that SO_2 was following a Lewis acid-base reaction mechanism with the carboxylate anion, resulting in a new $O-SO_2^-$ bond [101].

Even if the basicity of the anion is an important factor in SO_2 uptake, it is not determinant [114]. The SO_2 absorption capacity of different carboxylate-based ILs corroborates this observation as the SO_2 absorption capacity is not monotonous with the basicity of the anion ($[Lac]^-$>$[OAc]^-$>$[HCO_3]^-$) [115] and a medium basicity seems to be optimal [116]. The reaction between SO_2 and a highly basic function results in the formation of a strong bond leading to a large desorption enthalpy, which greatly hinders the regeneration step. Consequently, tailoring

the anion basicity might be an interesting method to find a compromise between the absorption and the desorption steps.

The introduction of electron-withdrawing groups appears is a way to adjust the basicity of the anions and to increase the SO_2 uptake. The tethering of a carbonyl next to the reactive site seems to be very effective on various anions such as *o*-phtalimidate $[Phth]^-$, diacetamide $[DAA]^-$ as illustrated in Figure 2.3 (top) [117], but much less efficient on $[PhO]^-$ or benzoate $[PhCOO]^-$, for instance [118]. This appears to be an effective method to increase SO_2 uptake as the carbonyl group moderates the basicity of the reactive function. The additional physical interactions between oxygen and the sulfur (C=O-SO_2), increase even more the absorption capacity. This is probably due to the already weak basicity of these two last anions, indicating that the effect of a carbonyl electron-withdrawing group is not very effective with a moderate basic anion.

The mole ratio of SO_2 absorbed by $[P_{6,6,6,14}][Im]$ has been increased from 4.8 [108] to 5.75 [119] by embedding a phenyl group in the imidazole anion, originating from the increased physical absorption SO_2 through π--S interactions. The presence of a halogen or a nitrile group enhances the SO_2 absorption capacity by physical contributions as depicted Figure 2.3 (bottom) [120].

The presence of a hydroxyl group on a carboxylate anion as been reported to enhance the SO_2 capture capacity of the IL as the -OH group was able to directly interact with SO_2 [113]. It also facilitates the desorption of SO_2 stemming from a reduction of the enthalpy of reaction.

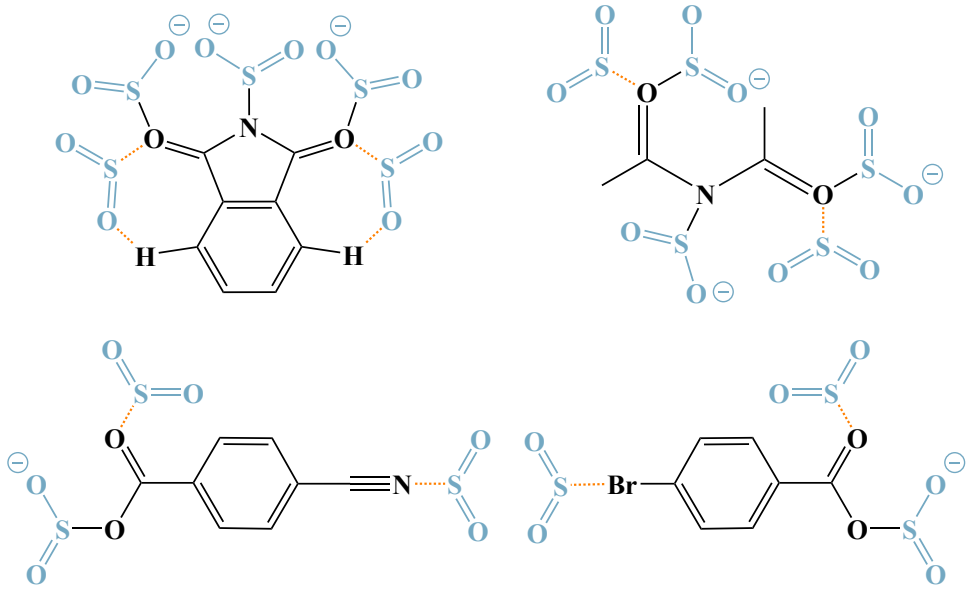

Figure 2.3 – Representation of the interactions between SO_2 and (top left) $[P_{6,6,6,14}][Phth]$, (top right) $[P_{6,6,6,14}][DAA]$, (bottom left) $[P_{6,6,6,14}][p{-}CNPhCOO]$ and (bottom right) $[P_{6,6,6,14}][p{-}BrPhCOO]$. Cations have not been represented as they do not interact with SO_2. Adapted from (top) [117] and (bottom) [120].

Dicarboxylate-based ILs seem promising as they present quite good SO_2 capture ability in addition to a moderate enthalpy of reaction leading to a low desorption energy. Several butyltriethylammonium dicarboxylate ILs were able to capture SO_2 up to approximately 0.8 in mole ratio through a reversible chemical absorption and their capacity was maintained over 3 cycles [121]. The absorption capacity follows the increasing basicity of the anions, which is consistent

with what was stated before (pK_{a1} from 1.92 to 4.16). DFT calculations and FT-IR revealed that SO_2 molecules were also captured by physisorption through the formation of hydrogen bonds between S=O, C=O and adjacent methylene C−H of the anions. The chemisorption is dominant at low pressures while the impact of physisorption increases progressively as pressure rises [122].

Similar results have been found on a new series of functionalized ILs with dicarboxylate anions paired with $[TMG]^+$ cations [123]. The absorption mechanism has been studied by DFT calculations, FT-IR, UV and NMR spectroscopy, revealing that the capture process was also a combination of chemi- and physisorption (Scheme 7) and, the longer the alkyl chain in the anion, the higher the absorption capacity. This is probably due to an increased asymmetry of the ILs resulting in a larger free volume as depicted in Scheme 7. The SO_2 absorption capacity of these types of ILs should be investigated under very low SO_2 pressures to assess whether or not the introduction of various interacting groups as physisorption sites may have a real impact in these conditions.

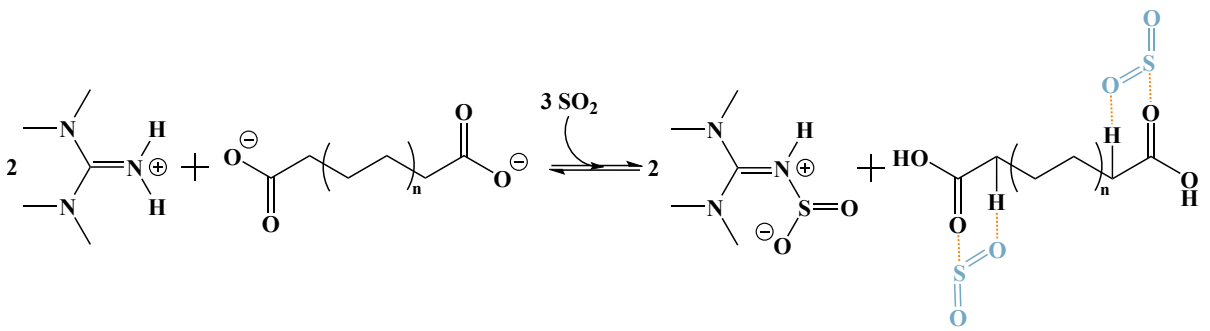

Scheme 7 – Absorption mechanism of SO_2 by $[TMG]_2[COO-(CH_2-CH_2)_n-COO]$ (n= 1, 3 and 5). Adapted from [123].

Carboxylate-based ILs appear as promising candidate for the efficient chemisorption of SO_2 even at low partial pressures. The basicity of the anions should be moderated in order to optimize the SO_2 absorption as well as reducing the desorption enthalpy. The ILs can be designed by introducing electron-withdrawing groups on the anionic moieties. These substituents have also the advantage that they can promote SO_2 absorption through physisorption.

2.4 IS IT POSSIBLE TO REACH A GOOD SELECTIVITY?

In ILs which are able to chemically capture acidic gases, the SO_2 capacity is generally higher than that of CO_2 due to stronger interactions with SO_2. These stronger interactions also lead to a more difficult desorption which can hinder the regeneration of the IL. It is important to consider that the SO_2 partial pressure in a real flue gas is much lower than the one of CO_2. Therefore, even if at equal pressure the SO_2 absorption is prevailing, it might be quite different in real conditions. The tailoring of the physico-chemical properties of ILs to create an efficient, selective and recyclable absorbent is a difficult task.

To be applicable in a real separation process the absorption should be selective. The ILs used as absorbents must maintain their absorption properties even in the presence of other gaseous compounds given that a typical flue gas is composed of many compounds. For example, a

typical MEA aqueous solution used in industrial post-combustion capture presents a lower CO_2 absorption capacity and an increased degradation rate in the presence of SO_2 because of side reactions, even at a very low partial pressure [124]. It is thus essential to consider the competitive absorption of CO_2 and SO_2 in the design of ILs.

The competitive absorption of CO_2 and SO_2 in $[C_2C_1Im][OAc]$ has been reported in the conditions of a typical flue gas, *i.e*, 15 % vol. of CO_2 and 0.2 % vol. of SO_2 [101]. The CO_2 capture was efficient and reversible without SO_2. However, the presence of SO_2 gradually decreased the CO_2 uptake over 5 cycles of regeneration due to a reduction of available absorption sites, resulting in a 48 % decrease absorption capacity. This reduction was attributed, by DFT calculations, FT-IR and NMR spectroscopy, to a better affinity of the acetate anion for SO_2 as well as to a more difficult reverse reaction. This has been corroborated by DFT calculations of the simultaneous capture of CO_2 and SO_2 by five 1-ethyl-3-methylimidazolium-based ILs [125].

More recently, a study on three trihexyltetradecylphoshonium-superbase ILs confirmed the stronger interaction between the basic sites of the ILs and SO_2 [102]. Indeed, SO_2 was able to replace the captured CO_2, but the reverse was not possible (Scheme 8). Despite this competitive reaction, these ILs are able to capture a relatively large amount of CO_2 (mole ratio > 0.7) even in the presence of a low partial pressure of SO_2. Subsequently, a downstream removal of SO_2 is required to preserve the efficiency of the IL.

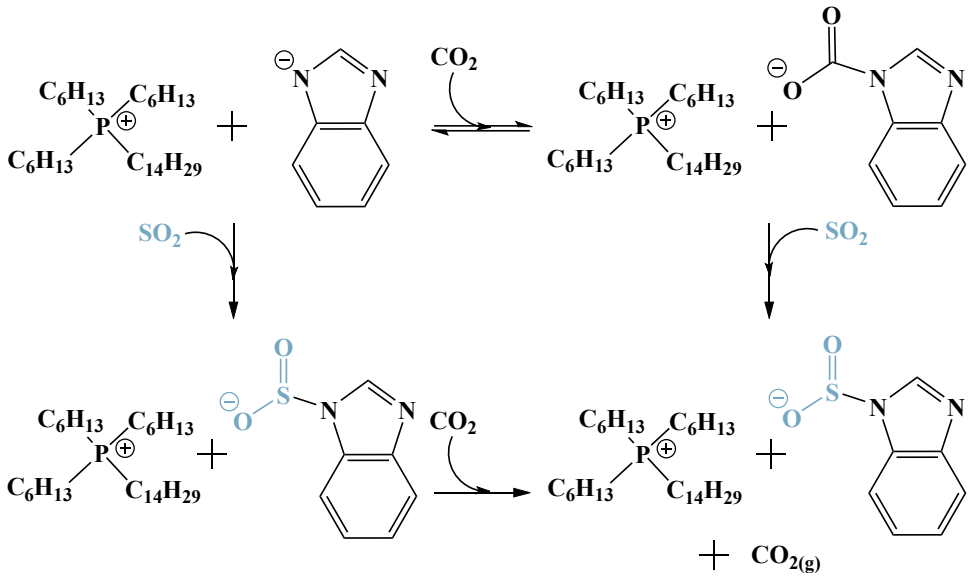

Scheme 8 – Reaction between trihexyl-(tetradecyl)phosphonium benzimidazolide $[P_{6,6,6,14}][BenzIm]$ and both CO_2 and SO_2 showing the better affinity of the IL for SO_2. Adapted from [102].

It would be very useful in a real process to be able to simultaneously capture these two acidic gases to treat the flue gases. To design an appropriate absorbent IL, it is necessary that it reacts reversibly with both gases. A reduction of the absorption enthalpy between SO_2 and the IL would probably lead to a reversible absorption with both gases, but this generally leads to a reduction of the CO_2 absorption capacity. A fine tailoring of the ILs is essential to reach this purpose. Notably, it appears that it can be done by tuning the anion basicity of carboxylate-based ILs,

which seems promising for both CO_2 and SO_2 capture. Molecular simulations can provide useful information about these properties and can contribute to the design of potential ILs as absorbents with the desired properties.

2.5 AIM OF THE PHD THESIS

Many studies using ILs for gas capture are focused on physisorption, which leads to a low capture capacity in real large scale processes. The functionalization of ILs appears as a promising way to increase their CO_2 and SO_2 absorption capacity, especially at low pressures, by taking advantage of chemisorption. However, there are two main issues regarding a large scale application. On one hand, ILs might be difficult and/or expensive to synthesize. On the other hand, the potential high viscosity of the ILs before or after the reaction with CO_2 and SO_2 is a serious obstacle. In this context, the aim of this work is to propose and study a new library of phosphonium carboxylate ILs for the absorption of CO_2 and SO_2, but also for the selective absorption of SO_2/CO_2 by a reversible chemical reaction at low pressures.

ILs based on carboxylate anions were chosen due to their strong physical and chemical interactions with CO_2 leading to an important absorption capacity. They are also likely to react with SO_2 through a different mechanism, paving the way for a selective or simultaneous capture of both gases which would be very interesting in an industrial perspective. Various substituents on the carboxylate anion were chosen to modify its basicity and to study the impact of the pK_a of their conjugated carboxylic acid in water on the gas uptake as well as on the reversibility. In what follows, when the pK_a of the carboxylate anion is mentioned, it will always refer to the one of its conjugated carboxylic acid in water.

Phosphonium carboxylate ILs were chosen due to their promising physico-chemical properties and because they are low cost, environmentally friendly ILs. Moreover, we wanted to take advantage of what was considered an undesirable reaction: the formation of the phosphonium ylide. This reactive intermediate is formed by the deprotonation of the H_α, located on the phosphonium cation, by the carboxylate anion. It might lead to a less favorable reaction with CO_2 resulting in a potential easier regeneration of the IL.

An understanding of the link between the chemical structures of the ions and its properties, in addition to their interactions, is required in order to tailor ILs for acid gas capture. For that purpose, the synthesized ILs were studied by both experimental and computational methods.

2.5.1 *Experimental objectives*

First, it is necessary to develop an easy, efficient, reproducible and economic way to synthesize and purify the phosphonium carboxylate ILs based on commercial, good value, easily accessible and high purity reagents. The purity of the synthesized ILs can be assessed by NMR, IR and Mass Spectroscopy (MS). Once the ILs are obtained with a high purity, the characterization of their physical and chemical properties is required. Notably, density (ρ) and viscosity (η) are very important in a gas capture perspective, as the kinetics of absorption is greatly influenced by these properties.

Thermal analysis by Differential scanning calorimetry (DSC) as well as thermogravimetric analysis (TGA) have been carried out to determine their operating window. It corresponds to the temperature range in which the ILs are liquid and thermally stable.

The objective is to measure the gas absorption capacity of the ILs and also to characterize the reaction products by identification of the absorption mechanism with NMR measurements as well as FT-IR spectroscopy. The analysis of the gas uptake as a function of temperature is also required to have a better understanding of the absorption thermodynamics, which is also essential for the desorption step.

The CO_2 capacity capture of the ILs are measured between 303 and 343 K and up to 5 bar by a gravimetric method with a sorption microbalance.

For safety reasons, SO_2 absorption measurements are run using an apparatus built *in-house* based on an isochoric saturation method under a fume hood at lower pressure (up to 1 bar), but in the same temperature range.

2.5.2 *Computational objectives*

In order to obtain a better insight at the molecular scale of the carboxylate ILs, a computational study at two different scales was carried out. Large systems (300 ion pairs) were investigated by MD using polarizable force fields to provide a better understanding of the microscopic structure and properties of the ILs, but also on the solvation of CO_2 and SO_2. The group has developed a polarizable force field that allows a more accurate description of the liquid structure, energetic and dynamic features brought into play. Even if polarizable simulations are slower than with traditional fixed-charge force fields, the improved accuracy in terms of dynamic quantities is essential to have a reliable description of the IL medium and also of CO_2 and SO_2 solvation environments and transport properties. The first step is to extend the polarizable force field (CL&Pol) [126] as it had not been adapted to the ILs under study. Suitable parameters are determined to minimize the deviations from the experimental properties while preserving the consistency and the transferability of the force field.

At a smaller scale (one or two ion pairs, with one CO_2 or up to five SO_2 molecules), *ab initio* calculations provide a better insight of the thermochemical quantities of the gas chemisorption as well as the interactions involved. This contributes to understand the effect of the basicity of the carboxylate anions on the chemical absorption of CO_2 and SO_2.

Part I

A NEW LIBRARY OF CARBOXYLATE-BASED IONIC LIQUIDS

3

ALKYLPHOSPHONIUM CARBOXYLATE IONIC LIQUIDS WITH TUNED MICROSCOPIC STRUCTURES AND PROPERTIES

Context

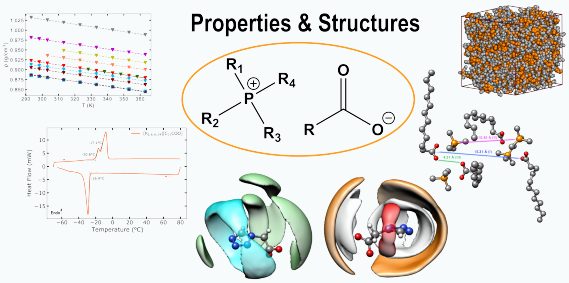

The objective of this first article is the preparation and the characterization of new phosphonium carboxylate ILs on both experimental and computational grounds. This new library of ILs is composed by eleven carboxylate anions, with different basicities, paired with either $[P_{4,4,4,4}]^+$ or $[P_{6,6,6,14}]^+$ cations. This will be used as the foundation of my PhD.

The initial step was to improve and consolidate the synthesis methods to obtain ILs in relatively large quantities with a high purity. The second step was the study of their physico-chemical and thermal properties to determine the temperature window in which the ILs are both thermally stable and liquid.

Their microscopic structures were then studied by SAXS measurements, which permitted the identification of the three characteristic regions in ILs. The analysis of the partial structure factors, computed based on molecular dynamics (MD) simulations, helped to have a better understanding of the different contributions to the total structure factors. An extensive structural analysis by MD simulations provided a better understanding of the spatial arrangement and organization of phosphonium carboxylate ILs at a microscopic scale. The development of new parameters to adapt the already existing CL&Pol polarizable force field to the ILs under study was necessary. A compromise has been made to respect the consistency and the transferability of the force field, but also to obtain density values as close as possible to the experimental ones.

It led to the identification of three distinct IL groups: carboxylate anions with linear, branched or cyclic substituents. $[P_{4,4,4,4}][\text{TetrazC}_1\text{COO}]$ appeared as an outlier due to peculiar anion-anion correlations which are not commonly observed in ILs.

Dr. Avila, a post-doctoral researcher in the group, introduced me to various experimental methods which allowed me to carry out this study. Dr. Bakis, a post-doctoral collaborator, helped with the synthesis of the 2,2,4,4-tetramethylpentanoic acid Me_4C_4COOH, a precursor used to prepare two ionic liquids.

PCCP

ROYAL SOCIETY OF CHEMISTRY

PAPER

Cite this: DOI: 10.1039/d3cp01009k

Alkylphosphonium carboxylate ionic liquids with tuned microscopic structures and properties†

N. Scaglione, [a] J. Avila,[a] E. Bakis, [b] A. Padua *[a] and M. Costa Gomes *[a]

Received 3rd March 2023,
Accepted 29th April 2023

DOI: 10.1039/d3cp01009k

rsc.li/pccp

Eleven pure alkylphosphonium carboxylate ionic liquids (ILs) were synthesised following a reliable and accessible route. Tetrabutylphosphonium and tetradecyltrihexylphosphonium cations were associated to a variety of $[R–COO]^-$ anions with R varying from shorter to longer linear alkyl chains; smaller to bulkier branched alkyl chains; cyclic saturated aliphatic and aromatic moieties; and one heterocyclic aromatic ring containing nitrogen. A combined experimental and molecular simulation study allowed the full characterization of the physico-chemical properties, the structure and the thermal stability of the synthesized ILs. Although slightly more viscous than their imidazolium counterparts, the viscosities of the prepared salts decrease dramatically with temperature and are comparable to other ILs above 50 °C, a manageable temperature as they are thermally stable up to temperatures above 250 °C, even under an oxidizing atmosphere. The microscopic structure of the phophonium ILs is rich and has been studied both experimentally using SAXS and by molecular dynamics simulation using state of the art polarizable force fields whose parameters were determined when necessary. Unique and surprising anion–anion correlations were found for the tetrazolate-based IL allowing to explain some of the unique physical–chemical properties of this phosphonium salt.

1 Introduction

Amongst the large variety of possible cation–anion combinations, ionic liquids (ILs) based on phosphonium cations and carboxylate anions are often considered as promising green solvents[1] and, as such, have been studied for various applications. Tetraalkylphosphonium cations form ILs that are often more stable chemically and in larger temperature ranges than their imidazolium counterparts, especially under basic conditions. This is because their protons on the α-carbon of the alkyl chains are less acidic than those on the C2 position of the imidazolium ring.

Alkyl phosphonium carboxylates can selectively and reversibly absorb large quantities of CO_2,[2–4] SO_2[5–9] and NO[10] and so have been proposed for carbon capture and desulfurization processes. The acid gas absorption involves a reversible chemical reaction[4] with the salt allowing for the easy regeneration of the solvent. The first step of the reactive absorption is the proton transfer from the α-carbon of the alkyl chains of the phosphonium cation to the carboxylate and is determined by the basicity of the anion. The resulting products are a reactive phosphonium ylide and the conjugated carboxylic acid. The phosphonium ylide specifically reacts with gases such as CO_2[4] or SO_2,[9] the reversibility of the reaction depending on the basicity of the anion and on the properties of the carboxylic acid formed. It is thus pertinent to assume that, by appropriately combining phosphonium cations and different carboxylates, it is possible to tailor ILs with controlled reactivity towards different acid gases. The absorption mechanisms can differ with the gas and so a careful design of the carboxylate anions is necessary, with the frequent introduction of chemical functions[5,7,10] in the cation, the anion, or both. The extent of the cation–anion specific interaction also determines the physical properties of the phosphonium carboxylates, in particular their fluidity that affects mass transport and so the kinetics of gas absorption.[11]

Phosphonium carboxylates have also been proposed for metal extraction[12] or for the dissolution of bioactive molecules.[1] When the anion is derived from an appropriate amino-acid,[13–17] the resulting phosphonium ILs are especially appropriate for applications requiring good biocompatibility.[16,18–25] Phosphonium carboxylates can self-aggregate[26] and so favourably interact with organic and aqueous phases[27] as the cations are non-polar and mainly hydrophobic and the anions easily mix with water. The size of alkyl chains in the phosphonium cation can be tuned to design carboxylate ILs with appropriate dynamic properties for their use as electrolytes,[28] heat transfer fluids,[29,30] or lubricants.[31–34] They have also been reported as catalysts[35–37] and curing agents for polymeric materials.[38]

[a] Laboratoire de Chimie, ENS de Lyon and CNRS, 46 Allée D'Italie, Lyon 69364, France. E-mail: margarida.costa-gomes@ens-lyon.fr
[b] Faculty of Chemistry, University of Latvia, Jelgavas 1, Riga, LV-1004, Latvia. E-mail: eduards.bakis@lu.lv

† Electronic supplementary information (ESI) available. See DOI: https://doi.org/10.1039/d3cp01009k

With the aim of understanding the relationship between the basicity of the carboxylate anions and the properties of the corresponding phosphonium ILs, in the present work we decided to prepare a library of salts using anions of different basicities. For this, we made use of the commercial availability, at a relatively low price, of numerous alkyl phosphonium precursors[39] and of a variety of carboxylic acids, often environmentally friendly and biosourced. Combining a commercial aqueous solution of tetrabutylphosphonium hydroxide, $[P_{4,4,4,4}][OH]$, with appropriate carboxylic acids RCOOH, high purity $[P_{4,4,4,4}][RCOO]$ ILs are easily obtained on a multigram scale.[2,4,25,36,40–42] When different phosphonium cations are required, the IL synthesis can proceed starting from a phosphonium halide salt followed by an anion metathesis in solution or using an ion-exchange resin.[43] The family of phosphonium carboxylate-based ILs reported herein includes carboxylate anions chosen to cover different structures and basicities (basicity of the carboxylic acids used as precursors: $2.67 < pK_a < 6.51$). The anions comprise linear, branched, or cycloalkyl, as well as aromatic substituents, all forming salts that we extensively characterize experimentally (chemical, thermodynamic, transport and structural properties) and using theoretical chemistry and molecular simulation to assess their microscopic structure and to understand their molecular interactions.

2 Experimental methods

2.1 Materials

The ionic liquids **(1)** tetrabutylphosphonium acetate, $[P_{4,4,4,4}][C_1COO]$; **(2)** tetrabutylphosphonium isovalerate, $[P_{4,4,4,4}][MeC_3COO]$; **(3)** tetrabutylphosphonium 2,2,4,4-tetramethylpentanoate $[P_{4,4,4,4}][Me_4C_4COO]$; **(4)** trihexyltetradecylphosphonium 2,2,4,4-tetramethylpentanoate $[P_{6,6,6,14}][Me_4C_4COO]$; **(5)** tetrabutylphosphonium hexanoate, $[P_{4,4,4,4}][C_5COO]$; **(6)** tetrabutylphosphonium dodecanoate, $[P_{4,4,4,4}][C_{11}COO]$; **(7)** trihexyltetradecylphosphonium dodecanoate $[P_{6,6,6,14}][C_{11}COO]$; **(8)** tetrabutylphosphonium cyclohexanecarboxylate, $[P_{4,4,4,4}][c\text{-}C_6COO]$; **(9)** tetrabutylphosphonium phenylacetate, $[P_{4,4,4,4}][PhC_1COO]$; **(10)** tetrabutylphosphonium *p*-methylbenzoate, $[P_{4,4,4,4}][p\text{-}MeBzCOO]$; **(11)** tetrabutylphosphonium 1H-tetrazole-1-acetate $[P_{4,4,4,4}][TetrazC_1COO]$ were prepared in-house and characterized following the procedures and methods described in the ESI.† The chemical structures of the phosphonium carboxylate ILs under study are presented in Table 1 that includes their structure, physical state, molecular weight and melting temperature (for the ILs that are solid at room temperature).

Tetrabutylphosphonium hydroxide ($[P_{4,4,4,4}][OH]$), in the form of a 38–42 wt% solution in water, hexanoic acid (>99% pure), dodecanoic acid (>99.5% pure) and 1H-tetrazole-1-acetic acid (>98% pure) were purchased from *Sigma Aldrich*. Isovaleric acid was purchased from *Janssen Chemical* (99% pure). Cyclohexanecarboxylic acid (98% pure) and *p*-methylbenzoic acid (98% pure) were purchased from *Acros Organics*. Phenylacetic acid and dodecanoic acid (99% pure) were purchased from *Alfa Aesar*. Trihexyl(tetradecyl)phosphonium chloride ($[P_{6,6,6,14}][Cl]$, > 95% pure) was provided by *Solvay*.

Before use, the carboxylate ILs were degassed under primary vacuum over 72 h using cycles of solidification and melting. This prevents the alteration of sample composition through promoting the cation–anion proton exchange, as the carboxylate anion can abstract the slightly acidic proton on the α-carbon of the alkyl chains which results in formation of the corresponding carboxylic acid. This proton abstraction is unlikely at ambient conditions and, with the exception of acetic acid, the acids used herein have low vapour pressures.

2.2 Density and viscosity measurements

Density and viscosity measurements were performed in a coupled *Anton Paar* densimeter (DMA 5000 M) and viscometer (LOVIS 2000 ME) in the temperature range 293–363 K at atmospheric pressure.

A U-shaped vibrating-tube is used as the measuring element in the densimeter. The U-tube is electronically excited to oscillate at its characteristic frequency. This specific frequency directly depends on the density of the sample studied. Therefore, the density of the compound is determined *via* the measurement of the characteristic frequency using Equation 1, where A and B are the calibration constants of the densimeter and τ is the oscillation period of the U-tube.

$$\rho = A\tau^2 - B \quad (1)$$

A and B are determined *via* the calibration of the equipment with two fluids of accurately known densities: ultra-pure water provided by *Anton Paar* and air. The measured densities are precise to within 5×10^{-6} g cm^{-3} with the temperature maintained to ± 0.001 K.

The viscometer uses the falling time of a stainless steel ball in a liquid placed inside a glass capillary to assess its viscosity. Two different capillaries with a diameter of 1.8 and 2.5 mm were calibrated with two standard oils, APN26 and APN415 (from *Paragon Scientific Limited*, UK), and two balls in stainless steel, with a known density and size, were used in order to cover the sample viscosity range at various temperatures. The precision of the viscometer is 0.05% in the viscosity and 0.02 K in the temperature.

These two instruments were filled with approximately 1 mL of sample, and the measurements were carried out simultaneously in the liquid range attainable for each IL.

2.3 NMR spectroscopy

The NMR spectra of ^{1}H, ^{13}C, ^{31}P, Correlated Spectroscopy (COSY) and Heteronuclear Single Quantum Correlation (HSQC), as well as diffusion coefficients determined by Diffusion Ordered Spectroscopy (DOSY), were collected on a 400 MHz *Bruker Avance III* spectrometer, with a broadband probe BBO equipped with a temperature control unit BCU II, at 343 K under vacuum. Before analysis, the ILs were degassed and dried under primary vacuum (<0.1 mbar) inside high pressure NE-HP10-M Pyrex NMR tubes (thickness 1 nm, rated to 20 bar) for a few days at a temperature within 303–353 K, depending on the melting point of the IL. A flame-sealed glass capillary containing C_6D_6 was inserted in

Table 1 Abbreviations, chemical structures and properties of the ionic liquids and mixtures of ionic liquids studied

IL	Cation	Anion	Abbreviation	Physical aspect	M (g mol^{-1})	T_m (°C)	pK_a[a]
1	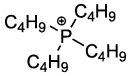		[$P_{4,4,4,4}$][C_1COO]	white solid	318.48	48.80 ± 0.10	4.76
2	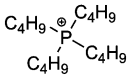	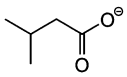	[$P_{4,4,4,4}$][MeC_3COO]	white solid	360.57	48.67 ± 1.00	4.77
3	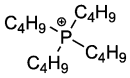	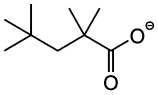	[$P_{4,4,4,4}$][Me_4C_4COO]	colourless liquid	416.66	—	6.51
4	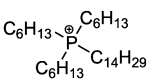	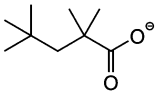	[$P_{6,6,6,14}$][Me_4C_4COO]	brown liquid	641.22	—	6.51
5	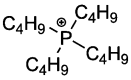	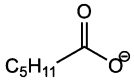	[$P_{4,4,4,4}$][C_5COO]	colourless liquid	374.59	—	4.87
6	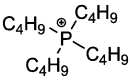	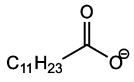	[$P_{4,4,4,4}$][C_{11}COO]	colourless liquid	458.75	—	5.30
7	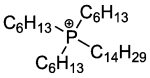	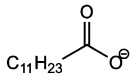	[$P_{6,6,6,14}$][C_{11}COO]	brown liquid	683.13	—	5.30
8	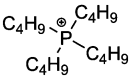	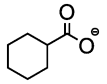	[$P_{4,4,4,4}$][c-C_6COO]	white solid	386.60	64.77 ± 0.29	4.82
9	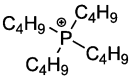	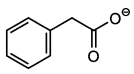	[$P_{4,4,4,4}$][PhC_1COO]	white solid	394.58	43.97 ± 0.42	4.31
10	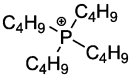	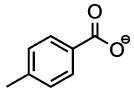	[$P_{4,4,4,4}$][*p*-MeBzCOO]	white solid	386.52	96.41 ± 0.68	4.37
11	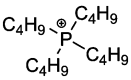	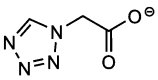	[$P_{4,4,4,4}$][$TetrazC_1$COO]	colourless liquid	386.52	—	2.67

[a] pK_a of the conjugated carboxylic acid in water.

the tube prior to the degassing to act as an internal reference for the compounds [$P_{4,4,4,4}$][MeC_3COO], [$P_{4,4,4,4}$][Me_4C_4COO], [$P_{6,6,6,14}$][Me_4C_4COO], [$P_{4,4,4,4}$][C_5COO], [$P_{4,4,4,4}$][C_{11}COO], [$P_{6,6,6,14}$][C_{11}COO], [$P_{4,4,4,4}$][c-C_6COO] and [$P_{4,4,4,4}$][$TetrazC_1$COO]; and DMSO-d_6 for [$P_{4,4,4,4}$][PhC_1COO] and [$P_{4,4,4,4}$][*p*-MeBzCOO].

2.4 Mass spectrometry

Low-resolution mass spectrometry (LRMS) analyses were performed using an ion trap (*AmaZon* SL, *Bruker*) equipped with an electrospray ion source (ESI†) operated in positive or negative ion mode. The capillary voltage and the end plate offset used were ±4500 V and ±500 V, respectively. The nebulizer gas pressure was fixed at 0.3 bar and the dry gas pressure and temperature were set at 4.0 L min^{-1} and 200 °C, respectively. The measurement was carried out between 20–1000 m/z and the reference employed was a sodium formate cluster solution. To avoid signal saturation, the sample was diluted 10 000 times with a solution of 46.1% methanol, 38.4% dichloromethane, 15.4% Milli-Q water and 0.1% formic acid. The diluted samples have been directly introduced in the source with a flow of 10 μL min^{-1}.

2.5 Infrared spectroscopy

Infrared (IR) spectroscopy measurements were carried out to characterize the neat ILs. IR also served to infer about the presence of water whenever the use of a standard Karl-Fisher titration was inconclusive. The IR spectra of the ILs were obtained in the attenuated total reflection mode (ATR) using a *PerkinElmer* Spectrum 65 FT-IR spectrometer. A small amount of solid or a droplet of the IL was placed on the ATR crystal and the measurements were carried out in the wave number range 550–4000 cm^{-1} accumulating 16 scans with a resolution of 1 cm^{-1}.

2.6 X-ray scattering

Small-angle X-ray scattering (SAXS) and wide-angle X-ray scattering (WAXS) were performed on an X-ray scattering instrument (Xeuss 3.0). The experiment was performed at a wavelength of 1.542 Å. The sample to SAXS detector distance was 42.5 mm which yields a q-range of 0–4 Å^{-1}. Each sample was placed in a capillary and measurements acquired during 6 × 30 min. After the acquisition, beamline-specific corrections were applied to

the SAXS images and the intensity was radially averaged to yield intensity as a function of the wavevector. A background made of an empty capillary was then subtracted from each sample pattern. All data handling was performed using XSACT.

2.7 Thermal analysis

Thermo-gravimetric analysis (TGA) was used to determine the short-term thermal stability of the compounds. When TGA was carried out under a dry nitrogen atmosphere, this was done on a *Mettler Toledo* TGA2 instrument, with the temperature sensor calibrated using indium and zinc standards. When an O_2 atmosphere was used, the measurements were performed on a *Setaram* Labsys Evo TG DTA DSC+ 1600 °C. All samples were accurately weighed, around 5–10 mg in 100 μL aluminium oxide crucibles. The TGA experiments were carried out scanning from 20–500 °C at 10 °C min^{-1} under either a dry nitrogen or an O_2 atmosphere at a flow rate of 30 mL min^{-1}.

A differential-scanning calorimeter (*PerkinElmer* DSC 8500) equipped with a cooling system (Intracooler II) was used to characterize phase transitions. The cell was continuously flushed with 20 mL min^{-1} of argon. Samples of 5–10 mg were crimped into sealed aluminium sample pans of diameter 7 mm. An empty pan was used as a reference. The samples were subjected to a sample-specific heating program through 3 heat–cool cycles (1, 5 and 10 K min^{-1}) with 1 min holding between each ramp. The samples that exhibited a cold crystallization event were exposed to 3 heat-cool cycles at 10 K min^{-1} up to the cold crystallization temperature. This has been found to be an effective means of crystallizing ILs with slow crystallization kinetics in DSC pans.

When the measured signals were broad, the peak temperature of the thermal event was reported instead of the onset, as the determination of the onset in such signals is not accurate. The different temperatures reported are the ones measured at a 10 K min^{-1} heating rate.

A Melting Point System *Mettler Toledo* MP90 was used to determine the melting point of ILs that are solid at room temperature. Three capillaries were filled with *ca.* 3 mg of the sample and were heated at 1 °C min^{-1} starting from 25 °C. The determination of T_m was done by the software in the device, with a threshold defined at 5.0%, and the values were verified visually. The experiment was repeated twice for each sample.

3 Molecular dynamics simulations

3.1 Polarizable force field

The intra- and intermolecular interactions in the IL systems are represented by the CL&Pol force field,[44] a recent polarizable version of the widely adopted CL&P fixed-charge model for ILs.[45,46] The CL&Pol model uses the Drude induce dipole method to represent polarization explicitly. Even though the computational cost is increased, it achieves more consistent predictions of equilibrium and transport properties when compared with fixed-charge force fields.

A Drude dipole is formed by a Drude core (located at a given atomic site) and a Drude particle of opposite charge, bonded by a harmonic spring with zero equilibrium distance. Displacement of the Drude particle due to the electrostatic environment gives rise to an induced dipole. The parameters for the Drude induced dipoles are derived from atomic polarizabilities (α), taken from the literature.[47] The mass of the Drude particles was m_D = 0.4 Da and the force constant of the bond between Drude core and particle was fixed at k_D = 4184 kJ mol^{-1}. The charges on the Drude particules were determined from the polarizabilities according to $\alpha = {q_D}^2/k_D$.[48] Thole damping functions[49,50] were used to provide smearing of electrostatic interactions between induced dipoles at short range, with a universal parameter a = 2.6. A Langevin (for the equilibration) and a Nosé–Hoover (for the production run) dual thermostat were used to regulate the relative motion of the Drude particules with respect to their Drude cores at 1 K.[48,51]

Herein, all the atoms were considered as polarizable except hydrogen atoms, whose polarizability was added to that of the heavy atom the H are bonded to. The polarization effects were handled by the DRUDE package[51] in the OpenMM dynamics code,[52] and input files prepared using the polarizer and scaleLJ tools.[53]

In this work, certain molecular fragments in the phosphonium and carboxylate anions had to be parametrized because they were not available in the CL&Pol parameter database.[44] Fragments are used in order to enable description of entire families of ions through the transferability principle, without need to compute new parameters for each ion individually. These calculations have been performed for a set of molecular fragments, including common cation and anion head-groups and side chains. For example, according to the fragment approach, the $[TetrazC_1COO]^-$ anion was represented by the acetate ($[C_1COO]^-$) anion; and the tetrazole (Tetraz) and $[PhC_1COO]^-$ anions were represented by $[C_1COO]^-$ and Toluene, respectively.

Including polarization effects explicitly involves scaling Lennard-Jones parameters from the original CL&P or from the OPLS-AA force fiels, in order to avoid double counting of induction contributions to the interaction energies, which were included implicitly in the fixed-charge models. As a result, in the polarizable force field, the LJ potential accounts only for repulsive and dispersive interactions. We followed the general predictive scheme published previously,[44] from which a scaling factor is evaluated for the well depth (ε) of the LJ potential (Table S14, ESI†). The predictive scheme requires only simple molecular quantities, namely the total charges of fragments, their dipole moments, polarizabilities and dimer equilibrium distances.

To determine the distance between the centres of mass of the fragments, geometries of isolated molecules, ions and subsequently dimers were optimised using dispersion-corrected density functional theory (DFT-D3)[54] at the B97-D3/cc-pVDZ level, the results of which are reported in Table S11 (ESI†). Atomic partial charges of molecules and ions, as well as the dipole moments of fragments, were computed on optimised geometries (Gaussian[55] or Psi4[56] codes) using the CHelpG method[57] with MP2/cc-pVTZ(-f) densities. Partial charges were determined for carboxylates with aliphatic or

aromatic substituents, namely isovalerate $[MeC_3COO]^-$, 2,2,4,4-tetramethylpentanoate $[Me_4C_4COO]^-$, cyclohexanoate $[c\text{-}C_6COO]^-$, phenylacetate $[PhC_1COO]^-$, *p*-methylbenzoate $[p\text{-}MeBzCOO]^-$ and 1H-tetrazole-1-acetate $[TetrazC_1COO]^-$ are listed in Table S11 (ESI†). The parameters of the dihedral torsion energy profile in the $[TetrazC_1COO]^-$ anion were calculated as in the OPLS-AA and CL&P models.[58]

As previously found for imidazolium carboxylate ILs,[44] when explicit terms of polarization are included in the force fields the calculated densities are slightly underestimated. In the present case, the calculated densities using MD simulations with the CL&Pol force field for the phosphonium-based salts deviated from the experimental values by about 5%. In order to correct for this systematic deviation the force field was modified by choosing charges coherent with the CL&Pol force field (Table S13, ESI†) and by scaling down the σ by a factor of 0.95 while keeping the constancy and transferability of the model. The atomic diameters (LJ σ) have been scaled by a factor 0.985 for most of the ILs studied so far.[44] After correcting the value of σ, the deviations in the calculated density, compared to the experimental values, are within 0.2–3.7% (Table S4, ESI†).

3.2 Simulation setup

Molecular dynamics (MD) simulations of periodic cubic boxes containing 300 ion pairs of the pure ionic liquids were performed with the OpenMM code.[52] Initial configurations were generated using the fftool[53] and Packmol[59] utilities.

A cutoff of 14 Å was considered for the Lennard-Jones (LJ) potential, with tail corrections for energy and pressure. The Particle–Mesh Ewald (PME) was used to evaluate electrostatic energies with the accuracy of 1×10^{-5}. The SHAKE algorithm was used to constrain the bond lengths involving hydrogen atoms, enabling a time-step of 1 fs. The systems were equilibrated for 1 ns at constant *NpT*, using a Langevin duel thermostat and barostat to attain the equilibrium density and liquid structure. The equilibrations were followed by 20 ns production runs in the *NpT* ensemble using Nosé–Hoover dual thermostat and a Monte Carlo barostat.

Temperatures in the range 293–373 K were chosen for different systems according to the availability of experimental data for comparison, while pressure was kept at 1 bar in all runs. The TRAVIS trajectory analysis software was used to compute site–site radial distribution functions (RDF), spatial distribution functions (SDF), combined distribution functions (CDF), dihedral distribution function (DDF) and the partial structure factors.[60,61]

MD simulations were carried out to study physical properties including density and diffusion coefficients of the ILs synthesized, as well as their local structure through RDFs, coordination numbers and SDFs, which were all computed from the 20 ns production trajectories.

4 Results and discussion

4.1 Physico-chemical properties

The experimental values of the densities, ρ, and the calculated molar volumes, V_m, of the eleven synthesised ILs are plotted and listed in the ESI† (Table S1 and Fig. S2, ESI†) together with the deviations of linear fits with the temperature (Tables S2 and S3, ESI†).

For the ILs with $[P_{4,4,4,4}]^+$ as common cation, the density decreases for the different counter ions as: $[TetrazC_1COO]^- > [PhC_1COO]^- > [c\text{-}C_6COO]^- > [C_1COO]^- > [C_5COO]^- \approx [MeC_3COO]^- > [Me_4C_4COO]^- > [C_{11}COO]^-$. Near room temperature, with the exception of $[P_{4,4,4,4}][TetrazC_1COO]$, all the densities are fellow that of water, contrary to many other phosphonium based ILs.[62–64] The density decreases when the alkyl chain of the carboxylate anions increase (as observed when comparing $[P_{4,4,4,4}][C_1COO]$, $[P_{4,4,4,4}][C_5COO]$ and $[P_{4,4,4,4}][C_{11}COO]$) and when the alkyl chains of the phosphonium cations increase (observed when comparing $[P_{4,4,4,4}][C_{11}COO]$ and $[P_{6,6,6,14}][C_{11}COO]$ or $[P_{4,4,4,4}][Me_4C_4COO]$ and $[P_{6,6,6,14}][Me_4C_4COO]$). Density also decreases when the bulkiness of the carboxylate anion increases as from $[MeC_3COO]^-$ to $[Me_4C_4COO]^-$. The presence of cyclohexyl, phenyl or tetrazole ring substituents in the carboxylate anions leads to ILs with higher densities as in $[P_{4,4,4,4}][c\text{-}C_6COO]$, $[P_{4,4,4,4}][PhC_1COO]$ and $[P_{4,4,4,4}][TetrazC_1COO]$, respectively.

As for many families of ILs, the molar volumes of phosphonium carboxylate salts are additive and, as such, can be calculated from a previously developed group contribution method (GCM):[65]

$$V_m^{GCM} = \sum_j n_j \sum_{i=0}^{2} C_i \delta T^i \quad (2)$$

where V_m^{GCM} is the molar volume calculated by the GCM method, n_j are the numbers of groups considered (as indicated in Table S6, ESI†) to calculate each contribution, $C_{j,i}$ are the group contribution parameters (listed in Table S5, ESI†), and $\delta T = T - 298.15$ K. Values for the $C_{j,i}$ have been either taken from the literature or, when not available, calculated from previously reported densities of ILs containing appropriate structural groups. The calculated V_m are compared with the experimental values in Fig. S2 (ESI†). Some typical molar volumes of the ILs studied herein are listed in Table S6 (ESI†) together with the values predicted by the GCM and their deviations from the experimental. The predicted values are accurate within 3%.

The fluidity of the ILs was assessed experimentally by the measurement of their viscosity as a function of temperature (Table S7 and Fig. 1, ESI†) and of their self-diffusion coefficients at 343 K (Table 2). Molecular simulation was also used to calculate the diffusion of the ions (Table S11, ESI†).

The dependence of the experimental viscosities with temperature was adjusted using the Vogel–Fulcher–Tammann (VTF) equations:

$$\eta = A \exp\left(\frac{B}{T - T_0}\right) \quad (3)$$

where η is the dynamic viscosity, T the temperature, and A, B and T_0 are adjustable parameters, whose least-square values are reported in Table S8 (ESI†). As expected, the viscosity decreases as the temperature increases for all ILs under study. Fits using the VFT equation represent the experimental data with an absolute average deviation (AAD) up to 1.8% (Table S8, ESI†).

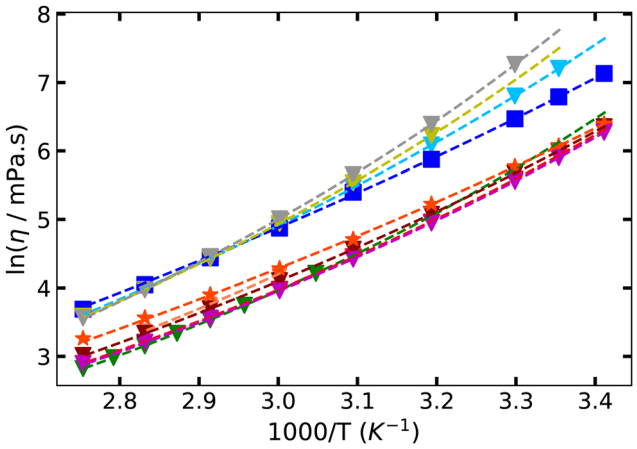

Fig. 1 Experimental viscosity of the phosphonium carboxylate ILs as a function of temperature. Dashed lines represent fits using the VFT equation. Symbols stand for: ▼ $[P_{4,4,4,4}][C_1COO]$; ▼ $[P_{4,4,4,4}][MeC_3COO]$; ▼ $[P_{4,4,4,4}][Me_4C_4COO]$; ■ $[P_{6,6,6,14}][Me_4C_4COO]$; ▼ $[P_{4,4,4,4}][C_5COO]$; ▼ $[P_{4,4,4,4}][C_{11}COO]$; ★ $[P_{6,6,6,14}][C_{11}COO]$; ▼ $[P_{4,4,4,4}][c\text{-}C_6COO]$; ▼ $[P_{4,4,4,4}][PhC_1COO]$; ▼ $[P_{4,4,4,4}][TetrazC_1COO]$.

For the ILs with $[P_{4,4,4,4}]^+$ as common cation, the viscosity decreases as follows: $[TetrazC_1COO]^- > [Me_4C_4COO]^- > [c\text{-}C_6COO]^- > [C_1COO]^- > [C_{11}COO]^- > [C_5COO]^- \approx [PhC_1COO]^- \approx [MeC_3COO]^-$. Around 333 K all the ILs present a viscosity lower than 140 mPa s, a limit important for several applications.

In general, the cations with longer alkyl side-chains lead to ILs with higher viscosities as seen herein when comparing $[P_{4,4,4,4}]$ with $[P_{6,6,6,14}]$-based salts.[66] Strangely enough, $[P_{6,6,6,14}][Me_4C_4COO]$ was found to be less viscous than $[P_{4,4,4,4}][Me_4C_4COO]$. Furthermore, and as observed for other families of ILs, those containing ions with branched organic chains have a higher viscosity than those with linear alkyl-side chains with the same number of carbons.[67] This explains how $[P_{4,4,4,4}][Me_4C_4COO]$, $[P_{6,6,6,14}][Me_4C_4COO]$ and $[P_{4,4,4,4}][c\text{-}C_6COO]$ have amongst the highest viscosities of the group of ILs prepared. $[P_{4,4,4,4}][TetrazC_1COO]$ is the most viscous IL of the group of eleven salts. This result is in line with previously reported ILs comprising tetrazolate-based anions.[68]

The diffusivities determined experimentally by DOSY NMR experiments are listed in Table 2. Although, in general, the ILs with the higher self-diffusion coefficients correspond to those with the lower viscosities and *vice versa*, this is not always the case. The self-diffusion coefficients of $[P_{6,6,6,14}][C_{11}COO]$ and $[P_{6,6,6,14}][Me_4C_4COO]$ are lower than the ones of their $[P_{4,4,4,4}]^+$ counterparts although the viscosity is slightly higher in the first case and lower in the second (see Fig. 1 and Table S7, ESI†). These observations are coherent with the Stokes–Einstein equation as the presence of a bulkier cation or anion increases the radius of the overall ion pair leading to lower self-diffusion coefficients. Very similar diffusivities were measured for each pair of ions, which points towards strong cation–anion correlations. The self-diffusion coefficient of a few carboxylate anions are nevertheless slightly higher than the one of its counter-cation, which is in agreement with the larger hydrodynamic radii of the phosphonium counter ions.[69] This feature is the most noticeable for $[P_{4,4,4,4}][C_1COO]$, as the acetate anion is much smaller than other anions studied.

The self-diffusion coefficients were also calculated by MD simulations (Table S10, ESI†) by fitting the mean squared displacements (MSD) of the MD trajectories after attaining the diffusive regime (typically from 3–18 ns). The calculated coefficients are slightly underestimated when compared to the experimental with typical differences being within 20–30%. The same trends were observed for all the ILs: similar self-diffusion coefficients for the cations and anions in the IL, as well as lower self-diffusion coefficients for the more viscous ILs.

Table 2 Experimental self-diffusion coefficients of various ILs at 343 K determined by DOSY-NMR experiments

Sample (experimental)	T (K)	D_{anion} (1×10^{-11} m^2 s^{-1})	D_{cation} (1×10^{-11} m^2 s^{-1})
$[P_{4,4,4,4}][C_1COO]$	343	5.27 ± 0.01	3.59 ± 0.005
$[P_{4,4,4,4}][MeC3COO]$	343	5.38 ± 0.02	4.97 ± 0.01
$[P_{4,4,4,4}][Me_4C_4COO]$	343	1.33 ± 0.003	1.28 ± 0.002
$[P_{6,6,6,14}][Me_4C_4COO]$	343	0.86 ± 0.002	0.80 ± 0.001
$[P_{4,4,4,4}][C_5COO]$	343	3.07 ± 0.003	2.87 ± 0.002
$[P_{4,4,4,4}][C_{11}COO]$	343	3.79 ± 0.03	3.80 ± 0.02
$[P_{6,6,6,14}][C_{11}COO]$	343	1.19 ± 0.004	1.14 ± 0.004
$[P_{4,4,4,4}][c\text{-}C_6COO]$	343	2.14 ± 0.006	2.04 ± 0.02
$[P_{4,4,4,4}][PhC_1COO]$	343	4.81 ± 0.01	4.00 ± 0.01
$[P_{4,4,4,4}][TetrazC_1COO]$	343	1.69 ± 0.008	1.08 ± 0.003

4.2 Thermal analysis

We used DSC to determine melting points of the ILs, the phase-transition temperatures being reported in Table S9 (ESI†) and the thermograms depicted in Fig. S3 in the ESI.† When the detected signals were broad, the temperature corresponding to the maximum value of the peak of the thermal event was reported instead of the onset as its determination was not accurate enough. The onset and the peak temperatures are indicated in Table S9 (ESI†) by a (o) or a (p), respectively. The values reported were obtained following a 10 K min^{-1} heating rate.

The melting transitions observed are considered as apparent melting points when the signals are very broad. This probably means that several transitions occur simultaneously: solid–solid transitions or solid–liquid transitions that start from different crystal structures. This could be confirmed when using a melting point apparatus: the T_m were coherent when using the two techniques with the melting observed over a large temperature range for the salts that showed broad peaks in DSC. The other transitions appearing in the DSC signals have not been identified visually which corroborates the hypothesis that they correspond to solid–solid transitions. Furthermore, many ILs exist as metastable liquids below their melting point temperatures with no freezing point easily detectable.[70] Several of the ILs listed in Table S9 (ESI†) show this type of behavior, in particular $[P_{4,4,4,4}][p\text{-MeBzCOO}]$ and $[P_{4,4,4,4}][MeC_3COO]$. In most cases, the crystallization temperatures, T_{cr}, could not be determined accurately and were observed to depend on the thermal history of the sample, on the measuring conditions and on the heating rate, contrary to the detected melting points.

Depending on the heating rate used, glass transition temperatures, T_g, could be identified when above −70 °C, which was the lowest temperature of operation for the equipment used. Most of the ILs herein have a glass transition around −65 °C, except for $[P_{4,4,4,4}][MeC_3COO]$, $[P_{4,4,4,4}][Me_4C_4COO]$ and $[P_{4,4,4,4}][c\text{-}C_6COO]$, for which T_g is higher: −52.8 °C, −56.3 °C and −44.6 °C, respectively. The T_g of $[P_{6,6,6,14}][C_{11}COO]$ is probably lower that −70 °C and so could not be measured.

Thermal stability is important if ILs are to be considered as recyclable and reusable when used in temperature swing processes. We have studied the thermal stability of the ILs both under N_2 (for comparison purposes) and O_2 atmospheres as the oxidizing character of O_2 might affect the thermal degradation reaction. The decomposition temperatures, T_{dec}, of ILs are reported Table S10 (ESI†) (thermographs depicted in Fig. S4, ESI†). Under N_2 atmosphere, the thermal stability of the tetrabutylphosphonium $[P_{4,4,4,4}]^+$ – based ILs increases as follows: $[PhC_1COO]^- < [C_{11}COO]^- \sim [MeC_3COO]^- < [C_5COO]^- < [c\text{-}C_6COO]^- < [C_1COO]^- < [p\text{-MeBzCOO}]^-$ while under O_2 this order changes to: $[PhC_1COO]^- < [TetrazC_1COO]^- < [Me_4C_4COO]^- < [C_1COO]^- < [C_5COO]^- \approx [MeC_3COO]^- < [c\text{-}C_6COO]^- < [C_{11}COO]^- < [p\text{-MeBzCOO}]^-$. All ILs present an improved thermal stability of approximately 20–30 °C in O_2 when compared to the data under N_2 atmosphere. Only $[P_{4,4,4,4}][PhC_1COO]$ presents a similar T_{dec}, but its decomposition occurs in one step under O_2 while it follows a two-step process under N_2. Interestingly enough, increasing the alkyl chain-length of the anion decreases thermal stability of the IL in N_2 (as in previously studied 1-ethyl-3-methylimidazolium carboxylate ILs[71]) while under O_2 the reverse trend is observed.

Under both N_2 and O_2 atmosphere, the branching of the alkyl side chain of the anions does not significantly affect the thermal stability of the ILs as observed by comparing the behaviour of, for example, $[P_{4,4,4,4}][C_5COO]$ and $[P_{4,4,4,4}][Me_4C_4COO]$ with similar T_{dec}. The presence of aromatic rings in the carboxylate anions induces a variation in thermal stability of the ILs they form. While $[P_{4,4,4,4}][PhC_1COO]$ is significantly less thermally stable than $[P_{4,4,4,4}][c\text{-}C_6COO]$, $[P_{4,4,4,4}][TetrazC_1COO]$ and $[P_{4,4,4,4}][p\text{-MeBzCOO}]$ are considerably more stable. This behaviour is probably explained by the weak chemical bond between the phenyl ring and the carboxylate head in $[PhC_1COO]^-$, as previously shown using DFT calculations.[72]

In general, an increase of approximately 90 °C or 150 °C in decomposition temperatures is observed for the phosphonium carboxylate ILs (carboxylate anions with linear alkyl chains) compared to their equivalent imidazolium or ammonium counterparts, respectively.[73] When the carboxylate anions are derived from amino acids, the corresponding phosphonium ILs show a lower thermal stability.[74] As expected, shorter alkyl side-chains in the phosphonium cations lead, in general, to higher decomposition temperatures. The high thermal stability of the phosphonium carboxylate ILs point towards their possible utilisation as liquids in wider temperature ranges of approximately 300–400 °C. The T_{dec}, as determined herein, although commonly used to define the thermal stability of ILs it usually overestimates their long-term stability.[71,75,76] Further studies are recommended when the salts are to be used for long periods of time at high temperatures.

4.3 Structural analysis

MD simulations provide insights on the liquid-state microscopic structure of the ILs through calculation of appropriate (site–site) radial or spatial distribution functions: RDFs and SDFs, respectively. The RDFs of the P^+ and H_α sites of the $[P_{4,4,4,4}]^+$ cation around the carboxylate head group $O_{COO}{}^-$ of the anions in $[P_{4,4,4,4}][Me_4C_4COO]$, $[P_{4,4,4,4}][C_5COO]$ and $[P_{4,4,4,4}][PhC_1COO]$ are displayed in Fig. 2 as representative examples of ten of the eleven ILs under study. In fact, only $[P_{4,4,4,4}][TetrazC_1COO]$ presents slightly different RDFs between interacting sites of the cation and the anion (Fig. 6).

The cation–anion site–site RDFs for the three ILs depicted in Fig. 2 present two intense first peaks that reveal a proximity between the carboxylate head group of the anion and the acidic proton (H_α) on the α-carbon of the cation with maxima around 2.2 Å. The P^+ site of the cations is found at slightly larger distances from the $O_{COO}{}^-$ sites of the anions, approximately at 2.8 Å. The corresponding RDFs of $[P_{4,4,4,4}][C_1COO]$, $[P_{4,4,4,4}][C_5COO]$ $[P_{4,4,4,4}][MeC_3COO]$, $[P_{6,6,6,14}][Me_4C_4COO]$, $[P_{6,6,6,14}][C_{11}COO]$, $[P_{4,4,4,4}]$ $[c\text{-}C_6COO]$ and $[P_{4,4,4,4}][p\text{-MeBzCOO}]$ are reported in Fig. S6 (ESI†). They all present the same pattern with similar distances between the cation and anion interacting sites, except for $[P_{4,4,4,4}][C_1COO]$ which presents a slightly shorter distance of 2.75 Å between the two charged moieties resulting from the small size of the acetate anion.

The ILs that include a symmetric phosphonium cation, $[P_{4,4,4,4}]^+$, and those that have a more voluminous asymmetric $[P_{6,6,6,14}]^+$ show the same structure around the carboxylate head groups of the anions, as seen in the site–site RDFs (Fig. S6, ESI†) and on the SDFs of the ILs with the anions $[Me_4C_4COO]^-$ and $[C_{11}COO]^-$ (Fig. S9 (right) and S10 (left), respectively, ESI†). The H_α of the alkyl chains of the cations are found at close proximity of the anion COO^- head group, the identical RDFs proving that there is no preferential acidic proton in the asymmetric phosphonium cations with longer alkyl chains (Fig. S7, ESI†). The differences in peak intensity of the RDFs are due to dilution effects that only depend on the size of the ions. This vision is confirmed by the analysis of the coordination number (CN) $n_{ij}(r)$ in the first solvation shell, obtained by integration of the $g_{ij}(r)$ up to the first minimum. These values are represented in the Fig. S6 (ESI†) where the CN of P^+ and H_α around $O_{COO}{}^-$ is 1 and 4.5 for the ten ILs with similar RDFs, respectively.

The dilution effect stems from the fact that the RDFs are normalized to 1 at large distances according to eqn (4):

$$g_{ij}(r) = \frac{\rho_{ij}(r)}{\langle \rho_{ij} \rangle} \quad (4)$$

where $\rho_{ij}(r)$ is the local density of atom j at a distance r from atom i. Consequently, by increasing the total number of atoms in the IL, the average $\langle \rho_{ij} \rangle$ decreases and the $g_{ij}(r)$ value increases accordingly.

Some differences in the structures of the ten ILs were found after a careful analysis of their spacial distribution functions (SDFs). In Fig. 3, interesting features are highlighted for two ILs containing short or long linear alkyl chains in the carboxylate

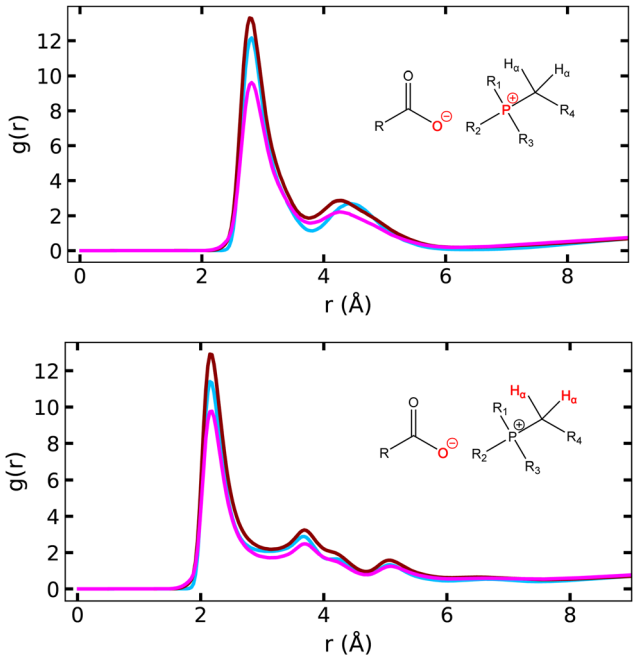

Fig. 2 Comparison of the site–site RDFs, $g_{ij}(r)$, of (top) the P^+ and (bottom) the H_α of the cation around the negatively charged oxygen atoms O_{COO}^- of the carboxylate head of the anion in [$P_{4,4,4,4}$][Me_4C_4-COO], [$P_{4,4,4,4}$][C_{11}COO] and [$P_{4,4,4,4}$][PhC_1COO] at 343 K.

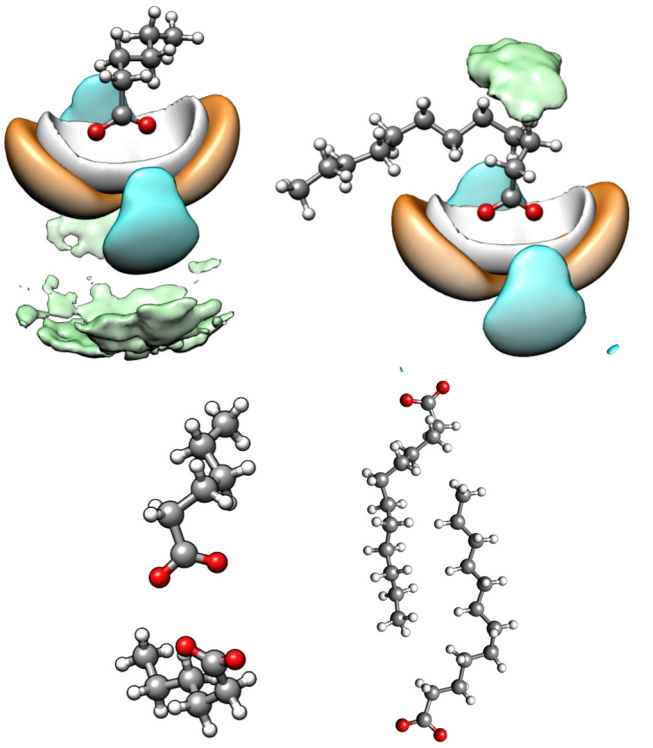

Fig. 3 (Left) SDF of the terminal carbon of the hexanoate alkyl chain belonging to $[C_5COO]^-$ (in green) and (Right) SDF of the terminal carbon of the dodecane alkyl chain belonging to $[C_{11}COO]^-$ (in green), and the SDFs of the P^+ (in orange), of H_α (in white) and the one of the terminal carbon atoms of the alkyl chains of the $[P_{4,4,4,4}]^+$ cation (in blue) around the $[C_5COO]^-$ and the $[C_{11}COO]^-$ anions at 343 K. Isodensity contours at 2.8, 1.7, 5.0, 11.0 and 3.8 times the average density, respectively. (Bottom) The respective snapshot of two anions from the molecular simulation box.

anions – [$P_{4,4,4,4}$][C_5COO] and [$P_{4,4,4,4}$][C_{11}COO]. In the case of the longer anion, $[C_{11}COO]^-$, a head-to-tail configuration is evidenced in the SDF with the terminal atoms of the alkyl chain of neighbouring anions (in green in Fig. 3) appearing at close proximity. The calculated average *anti* and *gauche* conformation percentage for each C–C–C–C dihedral angle in $[C_{11}COO]^-$ (Fig. S10 (right), ESI†) highlight a clear preference for the *anti* conformation, the end of the alkyl chain of the anions being less rigid and more flexible as the percentage of *gauche* conformation increases. The same structural features are not observed for the ILs with shorter alkyl chains in the anion, such as [$P_{4,4,4,4}$][C_5COO] (Fig. 3) or [$P_{4,4,4,4}$][C_1COO], or in those with branched alkyl chains as [$P_{4,4,4,4}$][Me_4C_4COO] (Fig. S9 (left), ESI†) for which the cation intercalates between the alkyl terminal atoms of neighbouring anions. The presence of an asymmetric and bulkier $[P_{6,6,6,14}]^+$ cation does not impact the spatial configuration of the anion as depicted in Fig. S9 (right) and S10 (left) (ESI†).

Herein, the combined distribution functions (CDFs) of the C_α–$H_\alpha\cdots O_{COO}^-$ angle as a function of the distance between the acidic proton H_α and O_{COO}^- in [$P_{4,4,4,4}$][C_1COO], [$P_{4,4,4,4}$][Me_4C_4-COO], [$P_{4,4,4,4}$][C_{11}COO], [$P_{4,4,4,4}$][c-C_6COO], [$P_{4,4,4,4}$][PhC_1COO] and [$P_{4,4,4,4}$][TetrazC_1COO] have been calculated at 343 K (Fig. S8, ESI†). These latter are plots of the angular distribution functions (ADFs) as a function of the RDFs between two atomic sites. The CDFs reveal that in different phosphonium carboxylate ILs, not only the distance between the acidic proton and the carboxylate head are similar, but also the angles between them are identical at around 120.25° ± 0.50° when the substituents of the carboxylate anions are only composed of carbon atoms. These angles are too low when compared with those of a typical hydrogen bond (pointing to a weaker interaction between these two sites) as the carbon atom bearing the acidic proton H_α is not electrogenative enough.

Although the site–site RDFs of the ILs containing cyclic substituents in the carboxylate anion are part of the group of ten salts with similar structures, interesting features appear from a careful analysis of the their SDFs and CDFs. The CDFs together with the respective SDFs are depicted in Fig. 4 for [$P_{4,4,4,4}$][PhC_1COO], in Fig. 5 for [$P_{4,4,4,4}$][c-C_6COO], and in Fig. S11 (ESI†) for [$P_{4,4,4,4}$][*p*-MeBzCOO]. The similarity of the CDFs and SDFs shows that the presence of aliphatic or aromatic rings in the carboxylate anions does not impact the spatial configuration between charged sites of the ions in carboxylate ILs.

The CDF in Fig. 4 points towards an angle between two phenyl groups in neighbour anions in [$P_{4,4,4,4}$][PhC_1COO] compatible with a perpendicular orientation of the rings (as represented schematically in the inset of Fig. 4) and not to π–π stacking. The phenyl rings are situated at the opposite side of the carboxylate head of the anion, as represented in the SDFs. The aromatic rings are quite distant from each other at a distance about 5.60 Å, the alkyl chains of the $[P_{4,4,4,4}]^+$ cation intercalating between the anions (cyan in the SDF of Fig. 4) while the cations are preferentially located around the carboxylate head (orange in the SDF of Fig. 4).

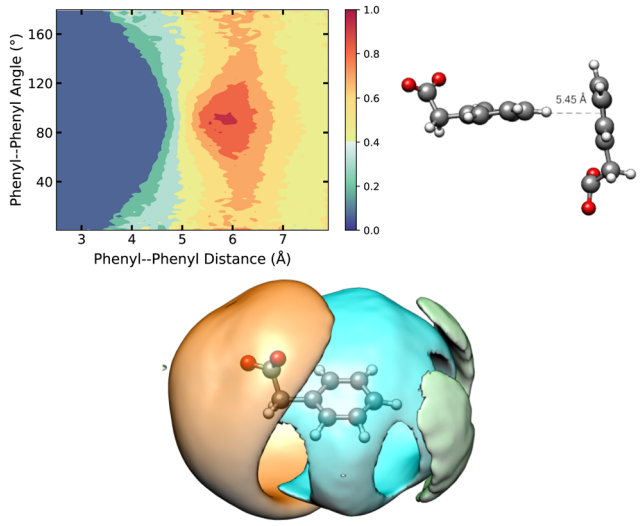

Fig. 4 (Top) CDF of the angle between two adjacent phenyl rings as a function of the RDF between their center of mass in $[P_{4,4,4,4}][PhC_1COO]$ at 343 K with a snapshot from the molecular simulation box showing the most probable spatial configuration of two $[PhC_1COO]^-$ anions. (Bottom) SDF of the center of mass of the phenyl ring of $[PhC_1COO]^-$ (in green), of P^+ (in orange) and of the terminal carbon atoms of the alkyl side chains of $[P_{4,4,4,4}]^+$ (in blue) around the $[PhC_1COO]^-$ anion in $[P_{4,4,4,4}][PhC_1COO]$ at 343 K. Isodensity contours at 2.5, 5.0 and 2.5 times the average density around the central ion, respectively.

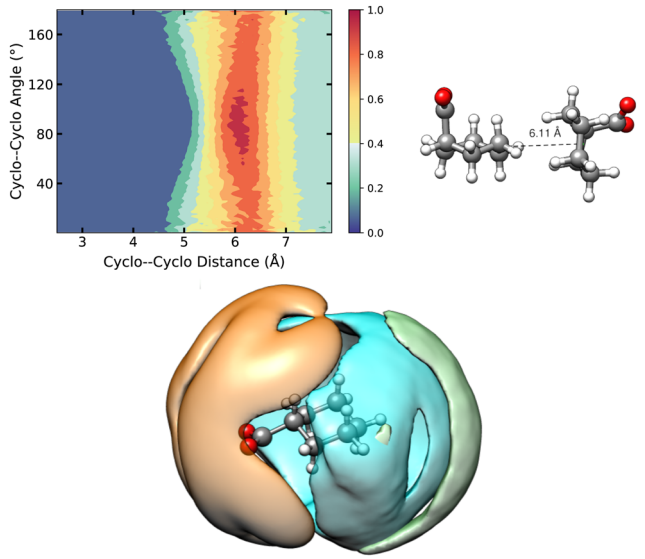

Fig. 5 (Top) CDF of the angle between two adjacent cyclohexyl rings as a function of the RDF between their center of mass in $[P_{4,4,4,4}][c\text{-}C_6COO]$ at 343 K with a snapshot from the molecular simulation box showing the most probable spatial configuration of two $[c\text{-}C_6COO]^-$ anions. (Bottom) SDF of the center of mass of the cyclohexyl ring of $[c\text{-}C_6COO]^-$ (in green), of P^+ (in orange) and of the terminal carbon atoms of the alkyl side chains of $[P_{4,4,4,4}]^+$ (in blue) around the $[c\text{-}C_6COO]^-$ anion in $[P_{4,4,4,4}][c\text{-}C_6COO]$ at 343 K. Isodensity contours at 2.5, 5.0 and 2.5 times the average density around the central ion, respectively.

Likely spatial configurations have been observed in $[P_{4,4,4,4}][p\text{-MeBzCOO}]$ (Fig. S15, ESI†) and in $[P_{4,4,4,4}][c\text{-}C_6COO]$ (Fig. 5) despite the fact that the cyclohexyl ring is more flexible when compared to the phenyl rings. The CDF of the center of mass of the cyclohexyl rings in $[P_{4,4,4,4}][c\text{-}C_6COO]$ presents a slightly wider angle range of 70–110° when compared to phenyl rings in $[P_{4,4,4,4}][PhC_1COO]$ (90–100°) which stems from the less rigid structure of the ring in the former IL. Even if it is wider, it still points towards a preferential perpendicular orientation of the cyclohexyl rings as depicted in Fig. 5. The centers of mass of neighboring anions are found at slightly larger distances in $[P_{4,4,4,4}][c\text{-}C_6COO]$ than in $[P_{4,4,4,4}][PhC_1COO]$ at $\approx$ 6.15 Å but are also intercalated by the alkyl side chains of the phosphonium counterions.

$[P_{4,4,4,4}][TetrazC_1COO]$ is the only IL amongst the eleven under study that already presents different cation–anion site–site RDFs. The RDFs of P^+ and H_α of the cation around the negatively charged oxygen $O_{COO}{}^-$ are depicted Fig. 6 in blue and red, respectively. The first difference is observed in the blue curve, which presents two close maxima at 2.92 Å and 3.38 Å, while the other ten ILs show RDFs of P^+ around $O_{COO}{}^-$ with a single peak at about 2.8 Å and a second peak appearing at a much larger distance above 4.0 Å (Fig. 2). A slight increase in the distance from 2.15–2.18 Å to 2.22 Å is also observed in the RDF of H_α of the phosphonium cations around the $O_{COO}{}^-$ atoms. These points are confirmed by a lower calculated CN that decreases, when comparing $[P_{4,4,4,4}][TetrazC_1COO]$ with the other ten ILs, from 1 to 0.7 for $P^+\cdots O_{COO}{}^-$ and from 4.5 to 2.7 for $H_\alpha\cdots O_{COO}{}^-$, respectively (Fig. S12, ESI†).

These observations point towards weaker interactions between the $[P_{4,4,4,4}]^+$ cation and the $[TetrazC_1COO]^-$ anion compared to the ILs based on other carboxylate anions. This difference in the cation–anion interaction can be explained by the charge delocalisation on the tetrazole ring: two of the nitrogen atoms show a significant partial negative charge of $-0.42e$ (Fig. S5 and Table S14, ESI†); and the partial charge of the oxygen atoms on the carboxylate head group decreases significantly (from $-0.80e$ to $-0.73e$) when compared to the previous ten carboxylate-based salts.

The charge delocalisation from the carboxylate head-group towards the tetrazole ring in the anion also leads to unexpected and unique spatial correlations, which appear clearly in the

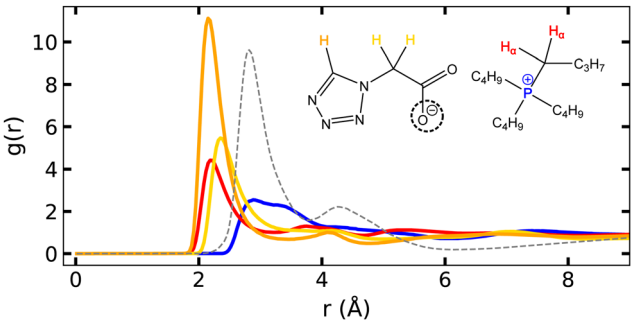

Fig. 6 Site-site RDFs, $g_{ij}(r)$, of P^+ and H_α of the cation and H_{2Z} and H_{RZ} of the anion around $O_{COO}{}^-$ in $[P_{4,4,4,4}][TetrazC_1COO]$ at 343 K. The atom labels of the $[TetrazC_1COO]^-$ anion are listed in the Fig. S9 (ESI†). The dashed line corresponds to the RDF of P^+ site of the cation around the $O_{COO}{}^-$ site in the anion in $[P_{4,4,4,4}][PhC_1COO]$ used as a representative example of the other ILs studied herein.

yellow and orange RDFs in Fig. 6. The orange peak, intense and at short distances (2.15 Å), shows that the proton of the tetrazole ring has a large probability of being near the carboxylate head-group, competing with the H_α of the cation whose RDF (red in Fig. 6) presents a peak at the exact same distance of 2.15 Å. This correlation leads to a CN of 0.65 and a C–H···O_{COO}^- angle of approximately 55–90° (Fig. S12 and S13, ESI†) explained by the small partial positive charge in the H and C sites of the tetrazole ring: +0.115*e* and +0.140*e*, respectively (Fig. S5 and Table S14, ESI†). Similarly, the significant yellow peak in Fig. 6 reveals the proximity of the protons of the side chain of the anion to the O_{COO}^- site at a distance of 2.35 Å. This proximity between sites of the anions in $[P_{4,4,4,4}][TetrazC_1COO]$ is a peculiar structural feature that we tried to explore through representation of other site–site RDFs (Fig. 7).

The most striking feature in Fig. 7 is the light green curve that depicts the site–site RDF of the nitrogen atoms around the proton in the tetrazole ring. This is the signature of the close proximity of neighbouring anions as also shown by the dark green curve – the site–site RDF of the nitrogen in the opposite position of the tetrazole ring around the same proton. Not only these two sites appear at close proximity with a significant probability, but a second and even a third shell of nitrogen atoms of tetrazole around the proton of the ring are clear in the RDF. As expected, the H_α of the cation are also found at close proximity of the tetrazole ring. This is shown by the RDF dark red curve (nitrogen atoms at 2.55 Å and 2.45 Å with CN of 2.1 and 2.3) and also in the SDF depicted in Fig. 7, an observation explained by the important negative partial charges borne by the nitrogen atoms in the tetrazole ring. cation–anion alternation is clear in the SDF and, remarkably, the tetrazole rings of the anions appear at close proximity and orient equatorially, the proton and the neighboring nitrogen of the tetrazole ring being found at a most probable distance of 2.42 Å (5.32 Å for the opposite nitrogen atom in the ring).

The CDF of the center of mass of the tetrazole rings in $[P_{4,4,4,4}][TetrazC_1COO]$, as represented in Fig. 8, reveals that two adjacent rings are located at distances of 4.3–4.6 Å and angles of 90–115° with a higher probability at 4.55 Å and 98.1°. This configuration is determined by the proximity between the H and the opposite nitrogen atom of two neighoring tetrazole rings (also observed in the RDF dark green curve of Fig. 7). Contrary to the other ILs, for $[P_{4,4,4,4}][TetrazC_1COO]$ a second strong signal appears in the CDF, showing that a second spatial configuration is also very likely. In this second case, two tetrazole rings are more distant at 7.0–7.2 Å with an angle ranging from 172 to 180°. This second spatial configuration can be ascribed to the interaction between the O_{COO}^- of a $[TetrazC_1COO]^-$ anion and the H of the adjacent anion as represented in the bottom right of Fig. 8 and illustrated by the SDF in light green in the same Figure (left).

In $[P_{4,4,4,4}][TetrazC_1COO]$, contrary to $[P_{4,4,4,4}][PhC_1COO]$ and $[P_{4,4,4,4}][c\text{-}C_6COO]$, the terminal carbons of the $[P_{4,4,4,4}]^+$

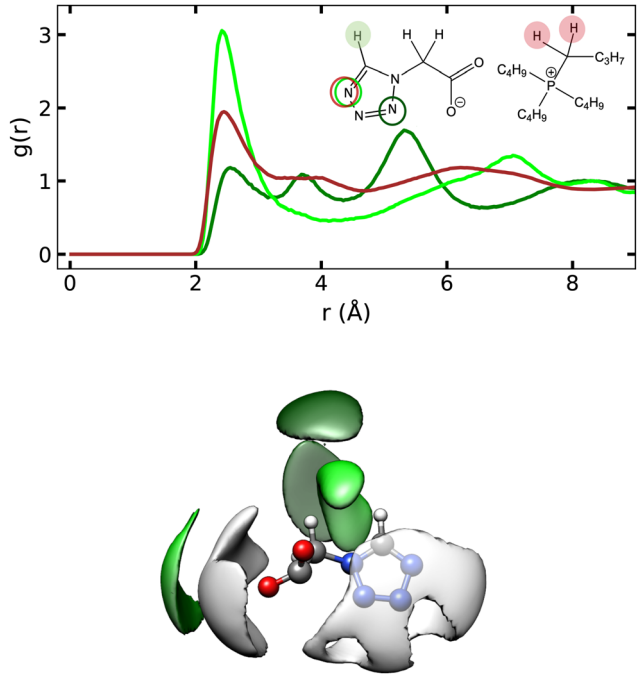

Fig. 7 (Top) Site–site RDFs, $g_{ij}(r)$: in green, two N of tetrazole around the marked H site in the tetrazole ring of the anion; and in dark red, one of the N of tetrazole around the marked H_α sites of the phosphonium cation. (Bottom) SDFs around the $[TetrazC_1COO]^-$ anion in $[P_{4,4,4,4}][TetrazC_1COO]$ at 343 K: two of the N in the tetrazole ring in light and dark green; and H_α of the phosphonium cation in grey. Isodensity contours at 9.0, 10.0 and 4.2 times the average density around the central ion, respectively.

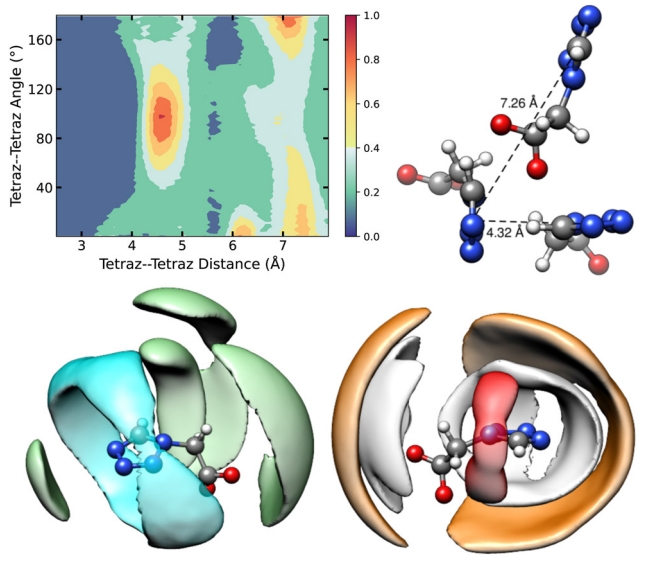

Fig. 8 (Left) CDF of the angle between two adjacent tetrazole rings as a function of the distance between their center of mass in $[P_{4,4,4,4}][TetrazC_1COO]$ at 343 K. (Right) A snapshot from the molecular simulation box showing the most probable spatial configuration of two $[TetrazC_1COO]^-$ anions. (Left) SDF of the center of mass of the tetrazole ring belonging to $[TetrazC_1COO]^-$ around the same anion (in green) and the SDF of the terminal carbon atoms of the alkyl chains of the $[P_{4,4,4,4}]^+$ cation (in blue). (Right) The SDF of the P^+ (in orange), of the H_α (in white) and of the O_{COO}^- (in red) around the $[TetrazC_1COO]^-$ anion, the in $[P_{4,4,4,4}][TetrazC_1COO]$ at 343 K. Isodensity contours at 6.0, 3.0, 6.6, 4.2 and 13.0 times the average density around the central ion, respectively.

alkyl chains are not interposed between two adjacent rings of the anions and do not surround entirely the tetrazole ring of the anion (SDF in Fig. 8 in cyan). This feature comes from the non-symmetric spatial distribution of the tetrazole rings located in a close vicinity in the liquid. These three ILs – $[P_{4,4,4,4}][PhC_1COO]$, $[P_{4,4,4,4}][c\text{-}C_6COO]$ and $[TetrazC_1COO]^-$ – are denser than the other eight carboxylate-based salts prepared herein, a fact probably explained by the efficient packing of the alkyl chains of the $[P_{4,4,4,4}]^+$ cations near the rings of the anions.

We could identify in the eleven ILs the three typical regions in the total structure factors determined experimentally using SAXS.[77] As seen in Fig. 9, a first peak appears at low values of q, at around 0.4–0.6 $Å^{-1}$, a feature observed in only a few classes of amphiphilic materials, like alcohols or ILs and often designated as the pre-peak. A second and third peak is observed at higher values of q and are common for molecular and ionic liquids as they correspond to first neighbour correlations (charge alternation in ILs) and to structural signals (intra or intermolecular) at shorter distances, respectively. In Fig. 9 these two peaks appear at approximately 0.6–0.8 $Å^{-1}$ and 1.5 $Å^{-1}$, and are sometimes named as the shoulder peak and the principal peak, respectively. In some cases the shoulder peak can not be perceived probably because it is hidden by the pre-peak as charge alternation is always present in the ILs.

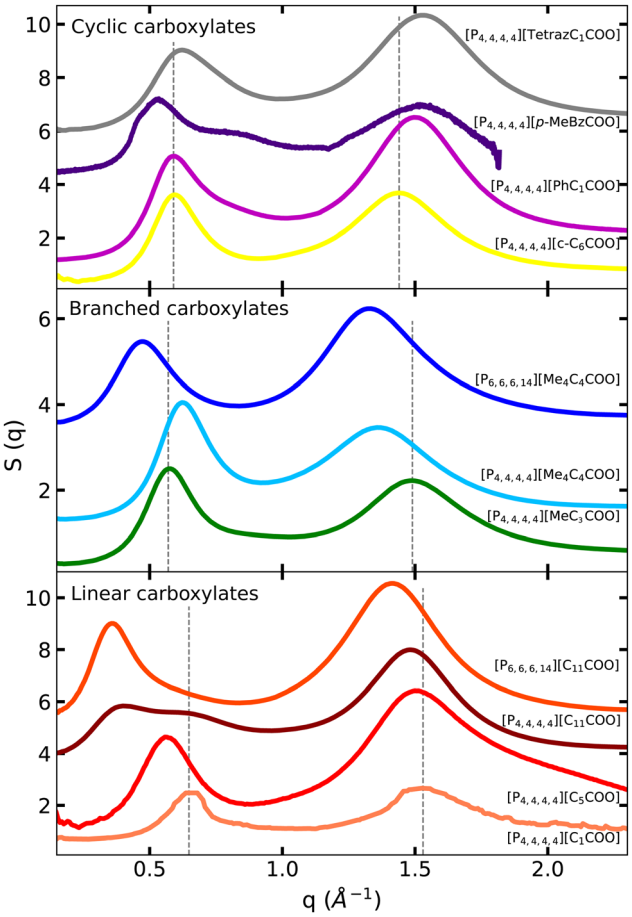

Fig. 9 Experimental X-ray scattering functions, $S(q)$, in the intermolecular region for the ILs with cyclic substituents on the carboxylate anions [$P_{4,4,4,4}$][C_1COO], [$P_{4,4,4,4}$][C_5COO], [$P_{4,4,4,4}$][$C_{11}COO$], [$P_{6,6,6,14}$][$C_{11}COO$], [$P_{4,4,4,4}$][MeC_3COO], [$P_{4,4,4,4}$][Me_4C_4COO], [$P_{6,6,6,14}$][Me_4C_4COO], [$P_{4,4,4,4}$][c-C_6COO], [$P_{4,4,4,4}$][PhC_1COO], [$P_{4,4,4,4}$][p-MeBzCOO] and [$P_{4,4,4,4}$][$TetrazC_1COO$] at 298 K. An offset is applied to each spectrum for the sake of clarity.

The experimental total structure factor of all the ILs based on carboxylate anions with linear side chains include a marked peak at approximately 1.5 $Å^{-1}$. As listed in Table 3, the slightly different q of these principal peaks follows the relative size of the ions in the salts, the smaller q corresponding to the larger ions. The results show that the domains formed by the two charged interacting sites are slightly larger because of steric hindrance between the bulky substituents of the carboxylate anions and the alkyl chains of the phosphonium cations. The pre-peaks, on the other hand, differ for the different ILs based on the linear carboxylates in quite unexpected ways. Their differences can be better understood by the analysis of the partial structure factors calculated by molecular simulation and represented in Fig. S14 (ESI†) where it can be observed that the total $S(q)$ calculated by molecular simulation agrees with the experimental data.

The partial cation–anion structure factors are significantly different for the four ILs with linear alkyl chains in the anions: for [$P_{4,4,4,4}$][C_1COO] it follows the $S(q)$ but as the alkyl side-chain length of the anion increases, the partial cation–anion $S(q)$ becomes negative (often designated as 'anti-peak'[77]) with the lowest values being found for [$P_{4,4,4,4}$][$C_{11}COO$]. This explains the form of the pre-peak in the total structure factors and how it hides or cancels the shoulder peak in some of the salts. The cation–anion partial structure factors are, in their turn, represented in Fig. S17 (ESI†). In this case, the size of the cations determine the importance of the cation–anion correlations with the head–head signals being smaller and the tail–tail signals being larger for the ILs including $[P_{6,6,6,14}]^+$ cations with larger alkyl side-chains. The pre-peaks in the total $S(q)$ appear at lower values of q when the alkyl side-chains of the ions become larger pointing towards larger polar and non-polar domains in these ILs.

The total structure factors of the ILs based on branched carboxylates are also represented in Fig. 9. The maxima of the principal peaks are, as expected, at lower q for the ILs with larger ions. The pre-peaks are found, for the three ILs, at unexpected positions with [$P_{4,4,4,4}$][Me_4C_4COO] appearing at higher q than that of [$P_{4,4,4,4}$][MeC_3COO], while $[Me_4C_4COO]^-$ q is larger than that of $[MeC_3COO]^-$. This can be explained by the partial structure factors in Fig. S14 (ESI†) where it is clear that the anion–anion signal in [$P_{4,4,4,4}$][Me_4C_4COO] is the one that contributes to the higher than expected q for the maximum of the pre-peak. The large negative cation–anion correlations observed in Fig. S14 (ESI†) for the ILs based on the branched carboxylates are easily understood in light of the partial cation–anion structure factors in Fig. S17 (ESI†)—the tail–tail and tail–head correlations are very negative whereas the corresponding head–head are positive peaks, the larger corresponding to

Table 3 SAXS diffraction peak positions, q (Å^{-1}), their corresponding real space length, d (Å), and the ion pair diameter, D (Å), of all the ILs under study. D was estimated by taking the cubic root of the volume of a single ion pair of the IL which was calculated from its molar volume and by assuming a cubic packing geometry[78]

	Pre-peak		Shoulder peak		Principal peak		
Sample	q (Å^{-1})	d (Å)	q (Å^{-1})	d (Å)	q (Å^{-1})	d (Å)	D (Å)
$[P_{4,4,4,4}][C_1COO]$	0.63	10.0	—	—	1.53	4.1	8.3
$[P_{4,4,4,4}][C_5COO]$	0.56	11.2	—	—	1.51	4.2	8.8
$[P_{4,4,4,4}][C_{11}COO]$	0.40	15.7	0.64	9.8	1.49	4.2	9.5
$[P_{6,6,6,14}][C_{11}COO]$	0.36	17.5	0.59	10.6	1.41	4.5	11.0
$[P_{4,4,4,4}][MeC_3COO]$	0.57	11.0	—	—	1.49	4.2	8.7
$[P_{4,4,4,4}][Me_4C_4COO]$	0.62	10.1	—	—	1.37	4.6	9.2
$[P_{6,6,6,14}][Me_4C_4COO]$	0.47	13.4	—	—	1.33	4.7	10.7
$[P_{4,4,4,4}][c\text{-}C_6COO]$	0.59	10.6	—	—	1.44	4.4	8.8
$[P_{4,4,4,4}][PhC_1COO]$	0.62	10.1	0.80	7.9	1.50	4.2	8.8
$[P_{4,4,4,4}][p\text{-}MeBzCOO]$	0.58	10.8	1.07	5.9	1.54	4.1	—[a]
$[P_{4,4,4,4}][TetrazC_1COO]$	0.62	10.1	—	—	1.63	3.9	8.6

[a] Not estimated because no density data available.

$[P_{4,4,4,4}][Me_4C_4COO]$. In Fig. S16 (ESI†), marked differences also appear in the cation–cation partial structure factors for the two ILs based on $[Me_4C_4COO]^-$—the tail–tail correlation peaks are larger and directly linked with the size of the side-chain and structure of the side-chains.

As expected, when the linear and branched side-chains of the anions are of similar size, the microscopic structure of the phosphonium carboxylates is close as it can be observed by the position of the pre-peak and of the main peak in $[P_{4,4,4,4}][MeC_3COO]$ and $[P_{4,4,4,4}][C_5COO]$. Furthermore, the partial structure factors for these two ILs, depicted in Fig. S14–S17 (b) and (e) (ESI†), also reveal the presence of similar shoulder peaks at ≈ 0.8 Å^{-1} being cancelled by a strong anti-peak corresponding to cation–anion correlations.

The experimental total structure factors for the four ILs based on cyclic carboxylates – $[P_{4,4,4,4}][c\text{-}C_6COO]$, $[P_{4,4,4,4}][PhC_1COO]$, $[P_{4,4,4,4}][p\text{-}MeBzCOO]$ and $[P_{4,4,4,4}][TetrazC_1COO]$ – are surprisingly different. The pre-peak that appears at lower values of q is the one for $[P_{4,4,4,4}][p\text{-}MeBzCOO]$ which is probably explained by the rigidity of the anion (clearly appearing in the CDF above) that leads to larger polar and non-polar domains in this IL compared to the others based on cyclic carboxylates studied herein. This rigidity of the $[p\text{-}MeBzCOO]^-$ anion also separates the pre-peak from the shoulder peak (less noticeable in $[PhC_1COO]^-$), making the change of structure linked with the cation–anion charge alternation more clear for $[P_{4,4,4,4}][p\text{-}MeBzCOO]$ when compared with the other IL based on cyclic carboxylates (as also seen in Fig. S14 for the cation–anion partial structure factors and their decomposition in Fig. S15, ESI†).

Interestingly enough, the position of the pre-peak is similar for some of the ILs, independently of being based on linear, branched and or cyclic carboxylate anions. This observation points towards similar polar and non-polar domains and it is the case for $[P_{4,4,4,4}][C_1COO]$, $[P_{4,4,4,4}][Me_4C_4COO]$, $[P_{4,4,4,4}][PhC_1COO]$ and $[P_{4,4,4,4}][TetrazC_1COO]$ with pre-peaks at either 0.62 or 0.63 Å^{-1}; $[P_{4,4,4,4}][C_5COO]$, $[P_{4,4,4,4}][MeC_3COO]$, $[P_{4,4,4,4}][c\text{-}C_6COO]$, $[P_{4,4,4,4}][p\text{-}MeBzCOO]$ with pre-peaks between 0.56 and 0.59 Å^{-1}; and $[P_{4,4,4,4}][C_{11}COO]$ with a pre-peak at 0.40 Å^{-1} corresponding to the larger polar and non-polar domains formed by the longer alkyl side chain (Table 3). An illustrative snapshot of a molecular simulation showing the typical distances of the ions in liquid $[P_{4,4,4,4}][C_{11}COO]$ is depicted in Fig. S18 (ESI†).

The total structure factor of $[P_{4,4,4,4}][TetrazC_1COO]$ appears as an outlier in the group of ILs studied herein. Even if this IL shows a similar total structure factor as $[P_{4,4,4,4}][PhC_1COO]$, the partial structure factors in Fig. S14–S17 (ESI†) show an important contribution from the anion–anion correlation to the pre-peak which is significantly more important in $[TetrazC_1COO]^-$ compared to all the other ILs. This unique feature observed experimentally here was already highlighted in the molecular simulation results expressed by the RDF and SDF for this salt, as well as in the calculated coordination numbers for $[P_{4,4,4,4}][TetrazC_1COO]^-$. This stems directly from the charge delocalization on the tetrazole ring of the $[TetrazC_1COO]^-$ anions which enlarges the polar domain, as the whole anion belongs to these domains, contrary to other ILs whose anion substituents are non-polar. The most important contributions to the shoulder peak come from anion–anion and cationic head–head correlations, but they are totally or partially cancelled by the strong anti-peak from cation–anion correlations. The principal peak, on the other hand, results from cation–anion and cation–cation local ordering due to ions in close contact, the main partial structure factors involved in this peak are from cation tail–tail, cation head–anion head, cation tail–anion head, cation tail–anion tail and, secondly, from anion–anion and cation head–tail correlations.

The ion pair diameter calculated from the experimental SAXS data range from 8.3 to 11.0 Å and increases as follows: $[P_{4,4,4,4}][C_1COO] < [P_{4,4,4,4}][TetrazC_1COO] < [P_{4,4,4,4}][C_1COO] < [P_{4,4,4,4}][MeC_3COO] < [P_{4,4,4,4}][C_5COO] \approx [P_{4,4,4,4}][c\text{-}C_6COO] \approx [P_{4,4,4,4}][PhC_1COO] < [P_{4,4,4,4}][Me_4C_4COO] < [P_{6,6,6,14}][C_{11}COO] < [P_{6,6,6,14}][Me_4C_4COO]$. The values estimated for $[P_{4,4,4,4}][C_{11}COO]$ and $[P_{6,6,6,14}][C_{11}COO]$ correspond to slightly less than the half of the repeat spacing observed by SAXS, which means the local ordering is approximately twice the ion pair dimension, suggesting the ILs are structured in the length scale of the ions with long alkyl chains segregated from the polar domain, as previously reported for protic ionic liquids.[77,79,80] This structuring can be visualized in the snapshots depicted in Fig. 10 (right). The repeated spacing observed for the other ILs does not correspond to twice the ion pair dimension, they are only slightly larger than D in agreement with the differences observed in the analysis of the pre-peaks of the total structure factors.

In general, the major contributions to the pre-peak for all ILs arise from both cation–cation and anion–anion local ordering that result in nano-domain segregation between non-polar and polar domains (Fig. S14–S17, ESI†). These contributions are similar in all ILs with the more important coming from the cation head–head and tail–tail correlations, and the second from the head–head and tail–tail or ring–ring local ordering structure of the anions in the liquid phase. The only exception is observed for $[P_{4,4,4,4}][TetrazC_1COO]$ in which the contribution from the anion–anion correlations are more important to define the polar alternation regime. The shoulder

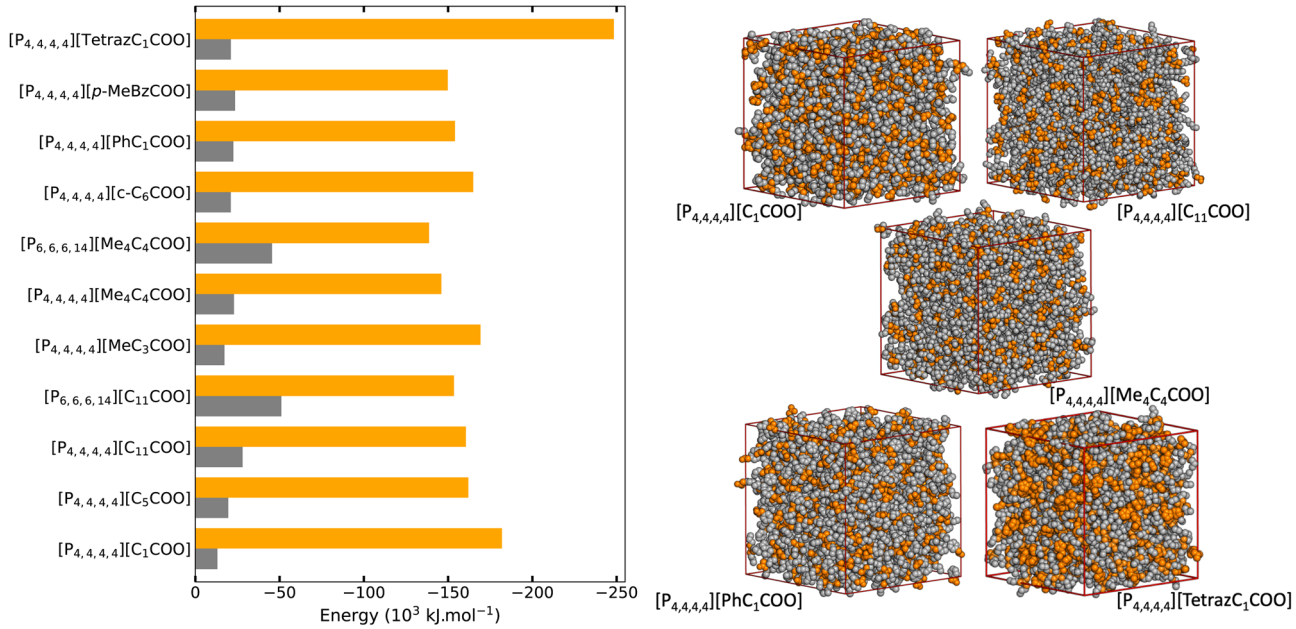

Fig. 10 (Left) Decomposition of the total energy of the ILs from MD simulations in van der Waals energy (accounting for the non-polar domains) and in electrostatic energy (accounting for the polar domains) in kJ mol^{-1}. (Right) Snapshots of simulation boxes of $[P_{4,4,4,4}][C_1COO]$, $[P_{4,4,4,4}][C_{11}COO]$, $[P_{4,4,4,4}][Me_4C_4COO]$, $[P_{4,4,4,4}][PhC_1COO]$ and $[P_{4,4,4,4}][TetrazC_1COO]$. Color codes enable clear identification of the charged and nonpolar domains that form in the ILs with orange atoms holding partial charges and those colored in grey corresponding to the nonpolar moieties of the ions.

peaks, on the other hand, are defined from the spacing between the charged moieties of two cations or two anions. The most important contributions to charge alternation coming from cationic head–head and anion–anion correlations. Finally, the principal peaks are defined from cation–anion (cation head–anion head, cation tail–anion head and cation tail–anion tail) and cation–cation (tail–tail and head–tail of cations) local ordering of ions in a close contact.

A suggestive way of comparing the relative importance of the polar and non-polar domains in the ILs studied is to decompose the total energy of the system, calculated from the MD simulation trajectories, into electrostatic and van der Waals (vdW) contributions (orange and grey in Fig. 10, respectively). The vdW contribution to the total energy increases when the alkyl chain length of linear carboxylate ILs increases (from approximately 6 to 15% for $[C_1COO]^-$ to $[C_{11}COO]^-$, respectively) highlighting the growth of the non-polar domains. The same trend is observed when increasing the bulkiness of the branched carboxylate anion in $[MeC_3COO]^-$ and $[Me_4C_4COO]^-$. This effect is even more important when comparing ILs based on the $[P_{6,6,6,14}]^+$ or $[P_{4,4,4,4}]^+$ cations with a vdW contribution to the total energy approximately 10% higher in the former. The most noticeable feature from this decomposition is the significantly higher electrostatic energy for $[P_{4,4,4,4}][TetrazC_1COO]$ compared to other ILs. The larger polar domains in this IL are linked to the charge distribution though the entire $[TetrazC_1COO]^-$ anion rather than being just localised on the COO^- head as clearly visible (orange regions) in the snapshots in Fig. 10 (right).

5 Conclusions

We have prepared a library of ILs based on alkyl phosphonium cations of different sizes and on carboxylate anions with distinct basicities and molecular structures. We used a simple and reliable synthesis path that allows for an easy preparation of pure salts from available raw materials. The phosphonium-based ILs are slightly more viscous than their imidazolium and ammonium counterparts but have a number of favourable properties that include larger liquid windows and better thermal and chemical stabilities.

The liquid-phase structures of the ILs prepared are rich and were carefully studied experimentally and using molecular simulations. The more complex microscopic structures appear for the ILs where the carboxylate anion has aromatic moieties. The tetrazole-substituted carboxylate anion appears as an outlier as far as the microscopic structure is concerned with anion–anion correlations appearing as unique features that, as far as we know, are not common in other ILs. We are currently exploring the properties of this IL in different applications, namely for gas capture and separation.

Conflicts of interest

There are no conflicts to declare.

Acknowledgements

EB acknowledges funding from the Latvian Council of Science: post-doctoral grant No. 1.1.1.2/VIAA/3/19/549. JA acknowledges funding from IDEXLyon. Solvay graciously provided the ionic liquid $[P_{6,6,6,14}][Cl]$ used. The authors thank S. Denis-Quanquin for her help with NMR data interpretation as well as F. Lerouge and O. Boyron for their assistance with TGA measurements.

Notes and references

1 Y. Ke, W. Jin, Q. Yang, X. Suo, Y. Yang, Q. Ren and H. Xing, *ACS Sustainable Chem. Eng.*, 2018, **6**, 8983–8991.
2 W. Shi, R. L. Thompson, E. Albenze, J. A. Steckel, H. B. Nulwala and D. R. Luebke, *J. Phys. Chem. B*, 2014, **118**, 7383–7394.
3 D. J. Yeadon, J. Jacquemin, N. V. Plechkova, M. Maréchal and K. R. Seddon, *ChemPhysChem*, 2020, **21**, 1369–1374.
4 J. Avila, L. F. Lepre, C. C. Santini, M. Tiano, S. Denis-Quanquin, K. C. Szeto, A. A. H. Padua and M. C. Gomes, *Angew. Chem., Int. Ed.*, 2021, **60**, 12876–12882.
5 G. Cui, J. Zheng, X. Luo, W. Lin, F. Ding, H. Li and C. Wang, *Angew. Chem., Int. Ed.*, 2013, **52**, 10620–10624.
6 G. Cui, F. Zhang, X. Zhou, H. Li, J. Wang and C. Wang, *Chemistry*, 2015, **21**, 5632–5639.
7 G. Cui, Y. Huang, R. Zhang, F. Zhang and J. Wang, *RSC Adv.*, 2015, **5**, 60975–60982.
8 F. Zhang, G. Cui, N. Zhao, Y. Huang, Y. Zhao and J. Wang, *RSC Adv.*, 2016, **6**, 86082–86088.
9 G. Cui, S. Lyu, F. Zhang, H. Wang, Z. Li, Y. Li and J. Wang, *Ind. Eng. Chem. Res.*, 2020, **59**, 21522–21529.
10 N. Cao, L. Gan, Q. Xiao, X. Lv, W. Lin, H. Li and C. Wang, *ACS Sustainable Chem. Eng.*, 2020, **8**, 2990–2995.
11 Y. Zhang, X. Zhao, Q. Yang, Z. Zhang, Q. Ren and H. Xing, *Ind. Eng. Chem. Res.*, 2017, **56**, 7336–7344.
12 L. Fischer, T. Falta, G. Koellensperger, A. Stojanovic, D. Kogelnig, M. S. Galanski, R. Krachler, B. K. Keppler and S. Hann, *Water Res.*, 2011, **45**, 4601–4614.
13 K. Fukumoto, Y. Kohno and H. Ohno, *Chem. Lett.*, 2006, 1252–1253.
14 R. L. Gardas, R. Ge, P. Goodrich, C. Hardacre, A. Hussain and D. W. Rooney, *J. Chem. Eng. Data*, 2010, **55**, 1505–1515.
15 J. Kagimoto, S. Taguchi, K. Fukumoto and H. Ohno, *J. Mol. Liq.*, 2010, **153**, 133–138.
16 T. Makino, M. Kanakubo, T. Matsuki, E. Kamio, H. Takaba and H. Matsuyama, *Fluid Phase Equilib.*, 2016, **420**, 89–96.
17 S. Fujiwara, T. Ichikawa and H. Ohno, *J. Mol. Liq.*, 2016, **222**, 214–217.
18 J. Zhang, S. Zhang, K. Dong, Y. Zhang, Y. Shen and X. Lv, *Chem. – Eur. J.*, 2006, **12**, 4021–4026.
19 Y. Zhang, S. Zhang, X. Lu, Q. Zhou, W. Fan and X. Zhang, *Chem. – Eur. J.*, 2009, **15**, 3003–3011.
20 B. E. Gurkan, J. C. de la Fuente, E. M. Mindrup, L. E. Ficke, B. F. Goodrich, E. A. Price, W. F. Schneider and J. F. Brennecke, *J. Am. Chem. Soc.*, 2010, **132**, 2116–2117.
21 T. Fukuyama, M. T. Rahman, S. Maetani and I. Ryu, *Chem. Lett.*, 2011, **40**, 1027–1029.
22 S. Saravanamurugan, A. J. Kunov-Kruse, R. Fehrmann and A. Riisager, *ChemSusChem*, 2014, **7**, 897–902.
23 S. Kasahara, E. Kamio and H. Matsuyama, *J. Membr. Sci.*, 2014, **454**, 155–162.
24 P. Prakash and A. Venkatnathan, *RSC Adv.*, 2016, **6**, 55438–55443.
25 M. Sivapragasam, J. R. Jaganathan, J.-M. Leveque, M. Moniruzzaman and M. I. Abdul Mutalib, *J. Mol. Liq.*, 2019, **273**, 107–115.
26 S. Duan, Y. Jiang, T. Geng, H. Ju and Y. Wang, *J. Dispers. Sci. Technol.*, 2020, **41**, 148–156.
27 D. J. Yeadon, J. Jacquemin, N. V. Plechkova, M. C. Gomes, K. R. Seddon, D. J. Yeadon, J. Jacquemin, N. V. Plechkova, M. C. Gomes and K. R. Seddon, *Aust. J. Chem.*, 2019, **72**, 144–154.
28 J. Shimada, K. Tsunashima, M. Ue, K. Iwasaki, T. Tsuda, S. Kuwabata, H. Kanematsu, N. Hirai, T. Kogo and A. Ogawa, *ECS Trans.*, 2017, **75**, 105.
29 K. Oster, P. Goodrich, J. Jacquemin, C. Hardacre, A. P. C. Ribeiro and A. Elsinawi, *J. Chem. Thermodyn.*, 2018, **121**, 97–111.
30 A. El-Sinawi, K. Silaipillayarputhur, T. Al-Mughanam and C. Hardacre, *Sustainability*, 2021, **13**, 2949.
31 Y. Zhou, J. Dyck, T. W. Graham, H. Luo, D. N. Leonard and J. Qu, *Langmuir*, 2014, **30**, 13301–13311.
32 H. Duan, W. Li, C. Kumara, Y. Jin, H. M. Meyer, H. Luo and J. Qu, *Tribol. Int.*, 2019, **136**, 342–348.
33 B. C. Stump, Y. Zhou, H. Luo, D. N. Leonard, M. B. Viola and J. Qu, *ACS Appl. Mater. Interfaces*, 2019, **11**, 30484–30492.
34 C. J. Reeves, A. K. Kasar and P. L. Menezes, *J. Cleaner Prod.*, 2021, **279**, 123666.
35 M. Galvan, M. Selva, A. Perosa and M. Noè, *Asian J. Org. Chem.*, 2014, **3**, 504–513.
36 Y. Wu, Y. Zhao, R. Li, B. Yu, Y. Chen, X. Liu, C. Wu, X. Luo and Z. Liu, *ACS Catal.*, 2017, **7**, 6251–6255.
37 S. Malekghasemi, H.-R. Kariminia, N. K. Plechkova and V. C. A. Ward, *Biomass Bioenergy*, 2021, **150**, 106126.
38 T. K. L. Nguyen, S. Livi, B. G. Soares, S. Pruvost, J. Duchet-Rumeau and J.-F. Gérard, *ACS Sustainable Chem. Eng.*, 2016, **4**, 481–490.
39 C. J. Bradaric, A. Downard, C. Kennedy, A. J. Robertson and Y. Zhou, *Green Chem.*, 2003, **5**, 143–152.
40 A. Yokozeki, M. B. Shiflett, C. P. Junk, L. M. Grieco and T. Foo, *J. Phys. Chem. B*, 2008, **112**, 16654–16663.
41 K. Bica and R. D. Rogers, *Chem. Commun.*, 2010, **46**, 1215–1217.
42 S. H. Baharuddin, N. A. Mustahil, A. A. Abdullah, M. Sivapragasam and M. Moniruzzaman, *Proc. Eng.*, 2016, **148**, 401–408.
43 E. Alcalde, I. Dinarès, A. Ibánez and N. Mesquida, *Molecules*, 2012, **17**, 4007–4027.
44 K. Goloviznina, J. N. Canongia Lopes, M. Costa Gomes and A. A. H. Pádua, *J. Chem. Theory Comput.*, 2019, **15**, 5858–5871.
45 J. N. Canongia Lopes, J. Deschamps and A. A. H. Pádua, *J. Phys. Chem. B*, 2004, **108**, 2038–2047.
46 J. N. Canongia Lopes and A. A. H. Pádua, *Theor. Chem. Acc.*, 2012, **131**, 1129.
47 E. Heid, A. Szabadi and C. Schröder, *Phys. Chem. Chem. Phys.*, 2018, **20**, 10992–10996.
48 G. Lamoureux and B. Roux, *J. Chem. Phys.*, 2003, **119**, 3025–3039.
49 B. T. Thole, *Chem. Phys.*, 1981, **59**, 341–350.
50 S. Y. Noskov, G. Lamoureux and B. Roux, *J. Phys. Chem. B*, 2005, **109**, 6705–6713.

51 A. Dequidt, J. Devémy and A. A. H. Pádua, *J. Chem. Inf. Model.*, 2016, **56**, 260–268.
52 P. Eastman, J. Swails, J. D. Chodera, R. T. McGibbon, Y. Zhao, K. A. Beauchamp, L.-P. Wang, A. C. Simmonett, M. P. Harrigan, C. D. Stern, R. P. Wiewiora, B. R. Brooks and V. S. Pande, *PLoS Comput. Biol.*, 2017, **13**, e1005659.
53 *paduagroup/clandpol*, 2021, **https://github.com/paduagroup/clandpol**, original-date: 2019-12-18T10:34:26Z.
54 S. Grimme, J. Antony, S. Ehrlich and H. Krieg, *J. Chem. Phys.*, 2010, **132**, 154104.
55 M. J. Frisch, G. W. Trucks, H. B. Schlegel, G. E. Scuseria, M. A. Robb, J. R. Cheeseman, G. Scalmani, V. Barone, G. A. Petersson, H. Nakatsuji, X. Li, M. Caricato, A. V. Marenich, J. Bloino, B. G. Janesko, R. Gomperts, B. Mennucci, H. P. Hratchian, J. V. Ortiz, A. F. Izmaylov, J. L. Sonnenberg, D. Williams-Young, F. Ding, F. Lipparini, F. Egidi, J. Goings, B. Peng, A. Petrone, T. Henderson, D. Ranasinghe, V. G. Zakrzewski, J. Gao, N. Rega, G. Zheng, W. Liang, M. Hada, M. Ehara, K. Toyota, R. Fukuda, J. Hasegawa, M. Ishida, T. Nakajima, Y. Honda, O. Kitao, H. Nakai, T. Vreven, K. Throssell, J. A. Montgomery, Jr., J. E. Peralta, F. Ogliaro, M. J. Bearpark, J. J. Heyd, E. N. Brothers, K. N. Kudin, V. N. Staroverov, T. A. Keith, R. Kobayashi, J. Normand, K. Raghavachari, A. P. Rendell, J. C. Burant, S. S. Iyengar, J. Tomasi, M. Cossi, J. M. Millam, M. Klene, C. Adamo, R. Cammi, J. W. Ochterski, R. L. Martin, K. Morokuma, O. Farkas, J. B. Foresman and D. J. Fox, *GaussianËœ16 Revision C.01*, Gaussian Inc., Wallingford CT, 2016.
56 J. M. Turney, A. C. Simmonett, R. M. Parrish, E. G. Hohenstein, F. A. Evangelista, J. T. Fermann, B. J. Mintz, L. A. Burns, J. J. Wilke, M. L. Abrams, N. J. Russ, M. L. Leininger, C. L. Janssen, E. T. Seidl, W. D. Allen, H. F. Schaefer, R. A. King, E. F. Valeev, C. D. Sherrill and T. D. Crawford, *Wiley Interdiscip. Rev.: Comput. Mol. Sci.*, 2012, **2**, 556–565.
57 C. M. Breneman and K. B. Wiberg, *J. Comput. Chem.*, 1990, **11**, 361–373.
58 J. N. Canongia Lopes and A. A. H. Padua, *J. Phys. Chem. B*, 2006, **110**, 19586–19592.
59 L. Martínez, R. Andrade, E. G. Birgin and J. M. Martínez, *J. Comput. Chem.*, 2009, **30**, 2157–2164.
60 M. Brehm and B. Kirchner, *J. Chem. Inf. Model.*, 2021, **51**, 2007–2023.
61 M. Brehm, M. Thomas, S. Gehrke and B. Kirchner, *J. Chem. Phys.*, 2020, **152**, 164105.
62 P. Wasserscheid and T. Welton, *Ionic Liquids in Synthesis*, Wiley-VCH, 2002, p. 380.
63 J. S. Wilkes, *J. Mol. Catal.*, 2004, **214**, 11–17.
64 J. Jacquemin, P. Husson, A. A. H. Padua and V. Majer, *Green Chem.*, 2006, **8**, 172–180.
65 J. Jacquemin, R. Ge, P. Nancarrow, D. W. Rooney, M. F. Costa Gomes, A. A. H. Pádua and C. Hardacre, *J. Chem. Eng. Data*, 2008, **53**, 716–726.
66 G. Al Kaisy, M. Mutalib, J. Leveque and T. Rao, *J. Mol. Liq.*, 2017, **230**, 565–573.
67 L. Pison, K. Shimizu, G. Tamas, J. N. C. Lopes, E. L. Quitevis and M. F. C. Gomes, *Phys. Chem. Chem. Phys.*, 2015, **17**, 30328–30342.
68 S. Seo, M. Quiroz-Guzman, M. A. DeSilva, T. B. Lee, Y. Huang, B. F. Goodrich, W. F. Schneider and J. F. Brennecke, *J. Phys. Chem. B*, 2014, **118**, 5740–5751.
69 R. Nanda and K. Damodaran, *Magn. Reson. Chem.*, 2018, **56**, 62–72.
70 P. Wasserscheid and T. Welton, *Org. Process Res. Dev.*, 2003, **7**, 223–224.
71 M. T. Clough, K. Geyer, P. A. Hunt, J. Mertes and T. Welton, *Phys. Chem. Chem. Phys.*, 2013, **15**, 20480–20495.
72 L. Li, H. Fan and H. Hu, *Fuel*, 2015, **153**, 70–77.
73 N. H. Z. O. Zailani, N. M. Yunus, A. H. Ab Rahim and M. A. Bustam, *Molecules*, 2022, **27**, 851.
74 Y. Cao and T. Mu, *Ind. Eng. Chem. Res.*, 2014, **53**, 8651–8664.
75 K. J. Baranyai, G. B. Deacon, D. R. MacFarlane, J. M. Pringle and J. L. Scott, *Aust. J. Chem.*, 2004, **57**, 145–147.
76 T. J. Wooster, K. M. Johanson, K. J. Fraser, D. R. MacFarlane and J. L. Scott, *Green Chem.*, 2006, **8**, 691–696.
77 J. J. Hettige, H. K. Kashyap, H. V. R. Annapureddy and C. J. Margulis, *J. Phys. Chem. Lett.*, 2013, **4**, 105–110.
78 B. Wu, Y. Yamashita, T. Endo, K. Takahashi and E. W. Castner, *J. Chem. Phys.*, 2016, **145**, 244506.
79 A. Triolo, O. Russina, H.-J. Bleif and E. Di Cola, *J. Phys. Chem. B*, 2007, **111**, 4641–4644.
80 R. Hayes, G. G. Warr and R. Atkin, *Chem. Rev.*, 2015, **115**, 6357–6426.

Alkylphosphonium Carboxylate Ionic Liquids with Tuned Microscopic Structures and Properties

Nicolas Scaglione,[†] Jocasta Avila,[†] Eduards Bakis,[‡] Agilio Pádua,[†] and Margarida Costa Gomes*,[†]

†*Laboratoire de Chimie de l'ENS Lyon, CNRS and Université de Lyon, 46 allée d'Italie, 69364 Lyon, France*

‡*Faculty of Chemistry, University of Latvia, Jelgavas 1, Riga, LV-1004, Latvia.*

E-mail: margarida.costa-gomes@ens-lyon.fr

Supplementary Information

Ionic liquids synthesis and characterization

The concentration of $[P_{4,4,4,4}][OH]$ aqueous solution given by the supplier was 41.4 %. The $[P_{4,4,4,4}][RCOO]$ ILs were all synthesized *via* a neutralization reaction of $[P_{4,4,4,4}][OH]$ with the corresponding carboxylic acid of the $[RCOO]^-$ (Figure S1). The carboxylic acids were used without further purification based on the given purity.

General synthesis route of $[P_{4,4,4,4}][RCOO]$: An aqueous solution of $[P_{4,4,4,4}][OH]$ (1 eq) was introduced into a 100 mL round bottom flask, followed by the dropwise addition of a slight excess of the carboxylic acid (1.02 eq) under continuous stirring. The flask was initially placed in a water bath with ice during the addition, then, the mixture was stirred for 3 hours in a water bath at room temperature (r.t.). A slight increase in temperature was noticed upon addition of the acid into the aqueous solution. Then, acetonitrile (ACN) was added to the obtained solution in order to create an azeotrope (% mol ACN : H_2O = 69.26 : 30.74) to facilitate the removal of the water formed under reduced pressure at about 40 mbar and 323 K in a rotary evaporator. Thereafter, the obtained compound was dried either by freeze-drying if it was a liquid at r. t. or under vacuum (1×10^{-4} bar) at a temperature above its melting point. The synthesis was realised on a 5 to 50 mmol scale and the ILs were obtained with a minimum yield of 95 %.

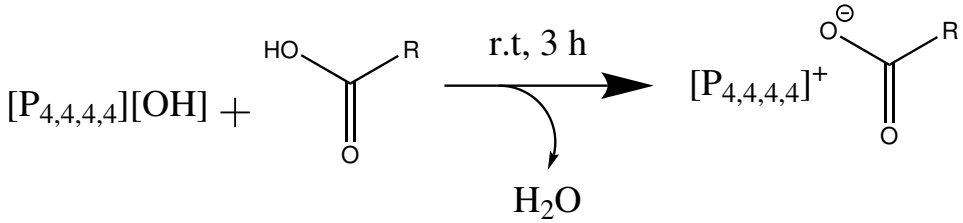

Figure S1 – Scheme of the neutralization reaction of the tetrabutylphosphonium hydroxide ($[P_{4,4,4,4}][OH]$) by the carboxylic acid (RCOOH) to produce the corresponding IL $[P_{4,4,4,4}][RCOO]$.

Tetrabutylphosphonium acetate $[P_{4,4,4,4}][C_1COO]$ was synthesized and characterized as already described in our previous work.[1]

Tetrabutylphosphonium isovalerate $[P_{4,4,4,4}][MeC_3COO]$, the colourless viscous liquid obtained from the rotary evaporator was dried under vacuum (1×10^{-4} bar) at 343 K under stirring (400 rpm). After the water removal, a white solid was obtained.

^{1}H NMR (400 MHz, C_6D_6, 343 K) δ: 0.91 (d, 6H, $^3J_{HH}$ = 6.4 Hz, $(CH_3)_2CHCH_2COO$); 0.96

(t, 12H, $^{3}J_{HH}$ = 7.3 Hz, P($CH_2CH_2CH_2C\mathbf{H_3}$)$_4$); 1.50 (m, 8H, P($CH_2CH_2C\mathbf{H_2}CH_3$)$_4$); 1.60 (m, 8H, P($CH_2C\mathbf{H_2}CH_2CH_3$)$_4$); 1.88 (m, 2H, $(CH_3)_2CHC\mathbf{H_2}COO$); 2.01 (m, 1H, $(CH_3)_2C\mathbf{H}CH_2COO$); 2.63 (m, 8H, P($C\mathbf{H_2}CH_2CH_2CH_3$)$_4$) ppm. ^{13}C NMR (100 MHz, C_6D_6, 298 K) δ: 13.76 (4C, P($CH_2CH_2CH_2\mathbf{C}H_3$)$_4$); 19.21 (4C, P($\mathbf{C}H_2CH_2CH_2CH_3$)$_4$); 23.69 (2C, $(\mathbf{C}H_3)_2CHCH_2COO$); 24.20 – 24.58 (8C, P($CH_2\mathbf{C}H_2\mathbf{C}H_2CH_3$)$_4$); 26.87 (1C, $(CH_3)_2\mathbf{C}HCH_2COO$); 49.35 (1C, $(CH_3)_2CH\mathbf{C}H_2COO$); 175.00 (1C, $(CH_3)_2CHCH_2\mathbf{C}OO$) ppm. ^{31}P NMR (161 MHz, C_6D_6, 298 K) δ: 33.83 (1P, P($CH_2CH_2CH_2CH_3$)$_4$) ppm. ν (cm^{-1}): 2960; 2932; 2874; 2863; 1575; 1466; 1448; 1419; 1362; 1316; 1249; 1210; 1166; 1096; 1002; 970; 908; 884; 833; 817; 723.5. MS ES$^+$ m/z (% Rel. Intensity): 259 (100, [$P_{4,4,4,4}$]$^+$). MS ES$^-$ m/z (% Rel. Intensity): 101 (100, [MeC_3COO]$^-$).

Tetrabutylphosphonium 2,2,4,4-tetramethylpentanoate [$P_{4,4,4,4}$][Me_4C_4COO], the colorless viscous liquid obtained from the rotary evaporator was dried under vacuum (1×10^{-4} bar) at 323 K under stirring (400 rpm). The product was collected as a colourless viscous liquid.

^{1}H NMR (400 MHz, C_6D_6, 343 K) δ: 0.92 – 1.00 (m, 21H, $(C\mathbf{H}_3)_3CCH_2C(CH_3)_2COO$ + P($CH_2CH_2CH_2C\mathbf{H_3}$)$_4$); 1.07 (s, 6H, $(CH_3)_3CCH_2C(C\mathbf{H}_3)_2COO$); 1.50 (m, 8H, P($CH_2CH_2C\mathbf{H_2}CH_3$)$_4$); 1.55 (s, 2H, $(CH_3)_3CC\mathbf{H}_2C(CH_3)_2COO$); 1.59 (m, 8H, P($CH_2C\mathbf{H_2}CH_2CH_3$)$_4$); 2.71 (m, 8H, P($C\mathbf{H_2}CH_2CH_2CH_3$)$_4$) ppm. ^{13}C NMR (100 MHz, C_6D_6, 343 K) δ: 14.21 (4C, P($CH_2CH_2CH_2\mathbf{C}H_3$)$_4$); 19.62 (4C, P($\mathbf{C}H_2CH_2CH_2CH_3$)$_4$); 24.60 – 24.97 (8C, P($CH_2\mathbf{C}H_2\mathbf{C}H_2CH_3$)$_4$); 30.85 (2C, $(CH_3)_3CCH_2C(\mathbf{C}H_3)_2COO$); 32.29 (3C, $(\mathbf{C}H_3)_3CCH_2C(CH_3)_2COO$); 32.55 (1C, $(CH_3)_3\mathbf{C}CH_2C(CH_3)_2COO$); 43.60 (1C, $(CH_3)_3CCH_2\mathbf{C}(CH_3)_2COO$);
57.72 (1C, $(CH_3)_3C\mathbf{C}H_2C(CH_3)_2COO$) 180.28 (1C, $(CH_3)_3CCH_2C(CH_3)_2\mathbf{C}OO$) ppm. ^{31}P NMR (161 MHz, C_6D_6, 343 K) δ: 33.76 (1P, P($CH_2CH_2CH_2CH_3$)$_4$) ppm. ν (cm^{-1}): 2958; 2934; 2906; 2872; 1569; 1476; 1466; 1423; 1394; 1385; 1359; 1346; 1310; 1241; 1226; 1099; 1005; 970; 942; 919; 907; 882; 849; 801; 797; 749; 719; 598. MS ES$^+$ m/z (% Rel. Intensity): 259 (100, [$P_{4,4,4,4}$]$^+$). MS ES$^-$ m/z (% Rel. Intensity): 157 (100, [Me_4C_4COO]$^-$).

Trihexyltetradecylphosphonium 2,2,4,4-tetramethylpentanoate [$P_{6,6,6,14}$][Me_4C_4COO], potassium 2,2,4,4-tetramethylpentanoate (Me_4C_4COOK) was prepared by dissolving stoichiometric quantities of 2,2,4,4-tetramethylpentanoic acid (1 eq) and anhydrous potassium carbonate (2 eq) in methanol, and evaporating the solution to dryness via rotary evaporation at 60 °C. The salt was dried at 80 °C and 10^{-2} mbar for 24 h prior to use. Using the analytical balance,

$[P_{6,6,6,14}][Cl]$ (13.4292 g, 25.8597 mmol, 1 eq) and the potassium salt of 2,2,4,4-tetramethylpentanoic acid (5.0748 g, 25.8485 mmol, 0.9996 eq) were weighed in a flask and combined with ethyl acetate (100 mL). The suspension was stirred at ambient temperature for 24 h. The solids were separated via centrifugation (20 min, 6000 rpm). The solution was evaporated using the rotary evaporator, and the viscous residue stirred at high vacuum (45 °C, 24 h). The brownish viscous liquid was dissolved in ethyl acetate (250 mL) and saturated with small portions of water until two phases persisted after shaking (4 x 3 mL). The mixture was further diluted with ethyl acetate (100 mL), well shaken and left to phase-separate. The aqueous phase was removed, and further extractions with water performed (10 x 3 mL). Between extractions at least 20 min were observed to allow efficient phase separation. After the final extraction the mixture was left to phase-separate overnight, and the clear organic phase evaporated via rotary evaporator (60 °C). Distillation of a cloudy ethyl acetate-water mixture could be observed. In order to further dry the ionic liquid, it was dissolved in benzene (10 mL) and the solvent evaporated at reduced pressure (200 mbar). Finally, the drying with the rotary evaporator was continued at 17 mbar until no more bubbling was observed. Further drying at high vacuum (45 °C, 24 h) provided a viscous brown liquid with a characteristic sweet odour (13.2737 g, 80 %).

^{1}H NMR (400 MHz, C_6D_6, 343 K) δ: 0.89 – 0.98 (m, 12H, $P((CH_2)_5C\mathbf{H}_3)_3((CH_2)_{13}C\mathbf{H}_3)$); 1.01 (s, 9H, $(C\mathbf{H}_3)_3CCH_2C(CH_3)_2COO$); 1.13 (s, 6H, $(CH_3)_3CCH_2C(C\mathbf{H}_3)_2COO$); 1.27 – 1.45 (m, 32H, $P(CH_2CH_2CH_2C\mathbf{H}_2C\mathbf{H}_2CH_3)_3(CH_2CH_2CH_2(C\mathbf{H}_2)_{10}CH_3)$); 1.51 (m, 8H, $P(CH_2CH_2C\mathbf{H}_2CH_2CH_2CH_3)_3(CH_2CH_2C\mathbf{H}_2(CH_2)_{10}CH_3)$); 1.61 (s, 2H, $(CH_3)_3CC\mathbf{H}_2C(CH_3)_2COO$); 1.65 (m, 8H, $P(CH_2C\mathbf{H}_2CH_2CH_2CH_2CH_3)_3(CH_2C\mathbf{H}_2(CH_2)_{11}CH_3)$); 2.76 (m, 8H, $P(C\mathbf{H}_2(CH_2)_4CH_3)_3(C\mathbf{H}_2(CH_2)_{12}CH_3)$) ppm. ^{13}C NMR (100 MHz, C_6D_6, 343 K) δ: 14.29 (3C, $P(CH_2(CH_2)_4\mathbf{C}H_3)_3(CH_2(CH_2)_{12}CH_3)$); 14.67 (3C, $P(CH_2(CH_2)_4CH_3)_3(CH_2(CH_2)_{12}\mathbf{C}H_3)$); 22.37 – 22.67 (5C, $P(CH_2\mathbf{C}H_2(CH_2)_3CH_3)_3(CH_2\mathbf{C}H_2(CH_2)_{11}CH_3) + (CH_3)_3C\mathbf{C}H_2C(CH_3)_2COO$); 22.85, 23.02, 29.52, 29.72, 29.90, 30.03, 30.08, 31.13, 31.47, 31.71, (24C, $P((CH_2)_2(\mathbf{C}H_2)_3CH_3)_3((CH_2)_2(\mathbf{C}H_2)_{11}CH_3)$); 19.64 (4C, $P(\mathbf{C}H_2CH_2CH_2CH_3)_4$); 23.11 – 23.39 (8C, $P(CH_2\mathbf{C}H_2\mathbf{C}H_2CH_2CH_2CH_3)_3(CH_2\mathbf{C}H_2\mathbf{C}H_2(CH_2)_{10}CH_3)$); 30.22 (2C, $(CH_3)_3CCH_2C(\mathbf{C}H_3)_2COO$); 31.98 (3C, $(\mathbf{C}H_3)_3CCH_2C(CH_3)_2COO$); 32.30 (1C, $(CH_3)_3\mathbf{C}CH_2C(CH_3)_2COO$); 43.24 (1C, $(CH_3)_3CCH_2\mathbf{C}(CH_3)_2COO$); 55.19 (1C, $(CH_3)_3C\mathbf{C}H_2C(CH_3)_2COO$) 180.37 (1C, $(CH_3)_3CCH_2C(CH_3)_2\mathbf{C}OO$)

ppm. ^{31}P NMR (161 MHz, C_6D_6, 343 K) δ: 33.73 (1P, **P**$((CH_2)_5CH_3)_3((CH_2)_{13}CH_3)$) ppm. ν (cm^{-1}): 2954; 2924; 2874; 2855; 1568; 1481; 1466; 1395; 1386; 1367; 1359; 1345; 1310: 1266; 1248; 1223; 1181; 1112; 1023; 980; 917; 888; 851; 801; 775; 720; 602; 597; 580; 572; 556. MS ES$^+$ m/z (% Rel. Intensity): 483.5 (100, $[P_{6,6,6,14}]^+$). MS ES$^-$ m/z (% Rel. Intensity): 157 (100, $[Me_4C_4COO]^-$).

Tetrabutylphosphonium hexanoate [$P_{4,4,4,4}$][C_5COO], the colorless liquid obtained from the rotary evaporator was dried under vacuum (1×10^{-4} bar) at 323 K under stirring (400 rpm). The product was collected as a colourless viscous liquid.

^{1}H NMR (400 MHz, C_6D_6, 343 K) δ: 0.92 (t, 3H, $^3J_{HH}$ = 7.0 Hz, C**H**$_3(CH_2)_3CH_2COO$); 1.00 (t, 12H, $^3J_{HH}$ = 7.4 Hz, P($CH_2CH_2CH_2C$**H**$_3$)$_4$); 1.33 (m, 6H, $CH_3(C$**H**$_2)_3CH_2COO$); 1.54 (m, 8H,P(CH_2CH_2C**H**$_2CH_3$)$_4$); 1.64 (m, 8H,P(CH_2C**H**$_2CH_2CH_3$)$_4$); 1.97 (t, 2H, $^3J_{HH}$ = 7.4 Hz, $CH_3(CH_2)_3C$**H**$_2COO$); 2.68 (m, 8H, P(C**H**$_2CH_2CH_2CH_3$)$_4$) ppm. ^{13}C NMR (100 MHz, C_6D_6, 343 K) δ: 13.82 (4C, P($CH_2CH_2CH_2$**C**H_3)$_4$); 14.42 (1C, **C**$H_3(CH_2)_3CH_2COO$) ; 19.07 (4C, P(**C**$H_2CH_2CH_2CH_3$)$_4$); 23.24 (1C, CH_3**C**$H_2(CH_2)_2CH_2COO$); 24.40 (4C, P(CH_2**C**$H_2CH_2CH_3$)$_4$); 24.55 (4C, P(CH_2CH_2**C**H_2CH_3)$_4$); 27.58 (1C, CH_3CH_2**C**$H_2CH_2CH_2COO$); 33.09 (1C, $CH_3(CH_2)_2$**C**H_2CH_2COO ; 38.60 (1C, $CH_3(CH_2)_3$**C**H_2COO); 175.47 (1C, $CH_3(CH_2)_3CH_2$**C**OO) ppm. ^{31}P NMR (161 MHz, C_6D_6, 343 K) δ: 33.81 (1P, **P**$(CH_2CH_2CH_2CH_3)_4$) ppm. ν (cm^{-1}): 2956; 2930; 2872; 2851; 1564; 1466; 1429; 1411; 1382; 1343; 1313; 1288; 1232; 1190; 1098; 1053; 1005; 969; 921; 908; 811; 849; 755; 724. MS ES$^+$ m/z (% Rel. Intensity): 259 (100, $[P_{4,4,4,4}]^+$). MS ES$^-$ m/z (% Rel. Intensity): 115 (100, $[C_5COO]^-$).

Tetrabutylphosphonium dodecanoate [$P_{4,4,4,4}$][C_{11}COO], the colorless liquid obtained from the rotary evaporator was dried under vacuum (1×10^{-4} bar) at 323 K under stirring (400 rpm). The product was collected as a colourless viscous liquid.

^{1}H NMR (400 MHz, C_6D_6, 343 K) δ: 0.91 (t, 3H, $^3J_{HH}$ = 6.6 Hz, C**H**$_3(CH_2)_9CH_2COO$); 0.98 (t, 12H, $^3J_{HH}$ = 7.3 Hz, P($CH_2CH_2CH_2C$**H**$_3$)$_4$); 1.30 (m, 16H, $CH_3CH_2(C$**H**$_2)_8CH_2COO$); 1.52 (m, 8H, P(CH_2CH_2C**H**$_2CH_3$)$_4$); 1.54 (m, 2H, $CH_3(CH_2)_8C$**H**$_2CH_2COO$); 1.61 (m, 8H, P(CH_2C**H**$_2CH_2CH_3$)$_4$); 1.96 (t, 2H, $^3J_{HH}$ = 7.4 Hz, $CH_3(CH_2)_9C$**H**$_2COO$); 2.65 (m, 8H, P(C**H**$_2CH_2CH_2CH_3$)$_4$) ppm. ^{13}C NMR (100 MHz, C_6D_6, 343 K) δ: 13.77 (4C, P($CH_2CH_2CH_2$**C**H_3)$_4$); 14.23 (1C, **C**$H_3(CH_2)_9CH_2COO$); 19.24 (4C, P(**C**$H_2CH_2CH_2CH_3$)$_4$); 22.97 (1C, CH_3**C**$H_2(CH_2)_8CH_2COO$);

24.31 – 24.57 (8C, $P(CH_2\mathbf{C}H_2\mathbf{C}H_2CH_3)_4$); 27.82 (1C, $CH_3(CH_2)_8\mathbf{C}H_2CH_2COO$); 29.63 – 32.30 (8C, $CH_3CH_2(\mathbf{C}H_2)_8CH_2COO$); 39.78 (1C, $CH_3(CH_2)_9\mathbf{C}H_2COO$); 175.58 (1C, $CH_3(CH_2)_9CH_2\mathbf{C}OO$) ppm. ^{31}P NMR (161 MHz, C_6D_6, 298 K) δ: 33.71 (1P, $\mathbf{P}(CH_2CH_2CH_2CH_3)_4$) ppm. ν (cm^{-1}): 2958; 2923; 2872; 2854; 1576; 1466; 1418; 1377; 1306; 1238; 1098; 1042; 1005; 969; 919; 908; 811; 752; 721. MS ES^+ m/z (% Rel. Intensity): 259 (100, $[P_{4,4,4,4}]^+$). MS ES^- m/z (% Rel. Intensity): 199 (100, $[C_{11}COO]^-$).

Trihexyltetradecylphosphonium dodecanoate $[P_{6,6,6,14}][C_{11}COO]$ synthesis began with the formation of potassium dodecanoate ($C_{11}COOK$). To the suspension of a finely ground potassium carbonate K_2CO_3 (10.46 g, 75.68 mol, 1.000 eq) in 96 % ethanol (550 mL), dodecanoic acid was added (30.90 g, 154.28 mol, 2.038 eq), and the mixture stirred under reflux for 12 h. The clear solution was allowed to cool to ambient temperature and then cooled to 5 °C in a fridge. The crystals were collected *via* suction filtration and washed on the filter with ethanol (2 °C, 2 x 50 mL) and petroleum ether (1 x 50 mL). The product was dried in air and then at reduced pressure (0.1 mbar, 80 °C, 24 h) providing white scaly flakes (22.02 g, 61 %).

Thereafter, the trihexyltetradecylphosphonium chloride (10.1566 g, 19.557 mol, 1.000 eq) and potassium dodecanoate (4.6627 g, 19.5575 mol, 1.000 eq) were mixed together and combined with 2-methyltetrahydrofuran (60 mL). After a vigorous stirring (60 °C, 15 min) water was added (10 mL) and the stirring continued for 3 h without additional heating. The solution was cooled to 5 °C and the aqueous (lower) layer removed. The organic layer was further washed with water by vigorous stirring (3 x 10 mL, 30 min per wash), and further in a separatory funnel (3 x 10 mL). The absence of halide ions in washings was checked with the AgCl test by taking 1 mL of the aqueous phase, adding 6 drops of 70 % HNO_3, shaking the mixture with 1 mL of $CHCl_3$, and treating the aqueous phase with 0.5 mL of 0.10 M aqueous $AgNO_3$. In 5 min the solution was visually inspected for cloudiness. The washing was assumed to be complete when the level of cloudiness no longer reduced for further washings. The slightly yellow-brown organic phase was filtered through the hydrophobic filter paper, and the solution was briefly warmed up to 60 °C with a small amount of powdered activated charcoal. The mixture was cooled in an ice bath, filtered via gravity, followed by a 40 µm PTFE membrane filter. No significant decolouration of the solution was achieved. The solvent was removed via rotary evaporation at reduced

pressure (60 °C, 4 mbar) providing a viscous orange liquid (10.56 g, 79.0 %). Further stirred drying (50 °C, 0.1 mbar, 24 h) caused darkening of the liquid without changes in spectroscopic data.

^{1}H NMR (400 MHz, C_6D_6, 343 K) δ: 0.90 – 1.02 (m, 15H, C**H**$_3$(CH$_2$)$_9$CH$_2$COO + P((CH$_2$)$_5$C**H**$_3$)$_3$((CH$_2$)$_{13}$C**H**$_3$)); 1.32 – 1.45 (m, 16H, CH$_3$(C**H**$_2$)$_8$CH$_2$CH$_2$COO + P((CH$_2$)$_3$(C**H**$_2$)$_2$CH$_3$)((CH$_2$)$_3$(C**H**$_2$)$_{10}$CH$_3$)); 1.54 (m, 8H, P((CH$_2$)$_2$C**H**$_2$(CH$_2$)$_2$CH$_3$)$_3$((CH$_2$)$_2$C**H**$_2$(CH$_2$)$_{10}$CH$_3$)); 1.60 (m, 2H, CH$_3$(CH$_2$)$_8$C**H**$_2$CH$_2$COO); 1.67 (m, 8H, P(CH$_2$C**H**$_2$(CH$_2$)$_3$CH$_3$)$_3$(CH$_2$C**H**$_2$(CH$_2$)$_{11}$CH$_3$)); 2.04 (t, 2H, $^{3}J_{HH} = 7.2$ Hz, CH$_3$(CH$_2$)$_9$C**H**$_2$COO); 2.71 (m, 8H, P(C**H**$_2$(CH$_2$)$_4$CH$_3$)$_3$(C**H**$_2$(CH$_2$)$_{12}$CH$_3$)) ppm. ^{13}C NMR (100 MHz, C_6D_6, 343 K) δ: 14.31 (5C, P((CH$_2$)$_{13}$**C**H$_3$)$_3$((CH$_2$)$_5$**C**H$_3$) + **C**H$_3$(CH$_2$)$_9$CH$_2$COO); 19.50 (4C, P(**C**H$_2$(CH$_2$)$_4$CH$_3$)$_3$(**C**H$_2$(CH$_2$)$_{12}$CH$_3$)); 22.40 (4C, P(CH$_2$**C**H$_2$(CH$_2$)$_3$CH$_3$)$_3$(CH$_2$**C**H$_2$(CH$_2$)$_{11}$CH$_3$)); 22.90, 23.06, 29.49 – 32.52 (24C, P((CH$_2$)$_3$(**C**H$_2$)$_2$CH$_3$)$_3$((CH$_2$)$_3$(**C**H$_2$)$_{10}$CH$_3$) + CH$_3$CH$_2$(**C**H$_2$)$_8$CH$_2$COO); 27.69 (1C, CH$_3$(CH$_2$)$_8$**C**H$_2$CH$_2$COO); 31.10 (4C, P((CH$_2$)$_2$**C**H$_2$(CH$_2$)$_2$CH$_3$)$_3$((CH$_2$)$_2$**C**H$_2$(CH$_2$)$_{10}$CH$_3$)); 39.34 (1C, CH$_3$(CH$_2$)$_9$**C**H$_2$COO); 176.04 (1C, CH$_3$(CH$_2$)$_9$CH$_2$**C**OO) ppm. ^{31}P NMR (161 MHz, C_6D_6, 298 K) δ: 33.50 (1P, **P**((CH$_2$)$_5$CH$_3$)$_3$((CH$_2$)$_{13}$CH$_3$)) ppm. ν (cm^{-1}): 2955; 2922; 2874; 2853; 1576; 1466; 1416; 1378; 1302; 1216; 1111; 989; 861; 807; 751; 721; 577. MS ES^{+} m/z (% Rel. Intensity): 483.5 (100, [P$_{6,6,6,14}$]$^{+}$). MS ES^{-} m/z (% Rel. Intensity): 199 (100, [C$_{11}$COO]$^{-}$).

Tetrabutylphosphonium cyclohexanecarboxylate [P$_{4,4,4,4}$][c−C$_6$COO], the colorless liquid obtained from the rotary evaporator was dried under vacuum (1×10^{-4} bar) at 343 K under stirring (400 rpm). After the water removal, a white solid was obtained.

^{1}H NMR (400 MHz, C_6D_6, 343 K) δ: 0.96 (t, 12H, $^{3}J_{HH} = 7.2$ Hz, P(CH$_2$CH$_2$CH$_2$C**H$_3$**)$_4$); 1.20 (m, 1H, (C**H$_{ax}$**H$_{eq}$)(CH$_2$)$_2$(CH$_2$)$_2$CHCOO); 1.23 (m, 2H, CH$_2$(C**H$_{ax}$**H$_{eq}$)$_2$(CH$_2$)$_2$CHCOO); 1.39 (m, 2H, CH$_2$(CH$_2$)$_2$(C**H$_{ax}$**H$_{eq}$)$_2$CHCOO); 1.49 (m, 8H, P(CH$_2$CH$_2$C**H$_2$**CH$_3$)$_4$); 1.57 (m, 1H, (CH$_{ax}$**H$_{eq}$**)(CH$_2$)$_2$(CH$_2$)$_2$CHCOO); 1.59 (m, 8H, P(CH$_2$C**H$_2$**CH$_2$CH$_3$)$_4$); 1.66 (m, 2H, CH$_2$(CH$_{ax}$**H$_{eq}$**)$_2$(CH$_2$)$_2$CHCOO); 1.82 (m, 2H, CH$_2$(CH$_2$)$_2$(CH$_{ax}$**H$_{eq}$**)$_2$CHCOO); 1.92 (m, 1H, CH$_2$(CH$_2$)$_2$(CH$_2$)$_2$C**H**COO); 2.60 (m, 8H, P(C**H$_2$**CH$_2$CH$_2$CH$_3$)$_4$) ppm. ^{13}C NMR (100 MHz, C_6D_6, 343 K) δ: 13.70 (4C, P(CH$_2$CH$_2$CH$_2$**C**H$_3$)$_4$); 19.22 (4C, P(**C**H$_2$CH$_2$CH$_2$CH$_3$)$_4$); 24.14 – 24.45 (8C, P(CH$_2$**C**H$_2$**C**H$_2$CH$_3$)$_4$); 26.99 (2C, CH$_2$(**C**H$_2$)$_2$(CH$_2$)$_2$CHCOO); 27.38 (1C, **C**H$_2$(CH$_2$)$_2$(CH$_2$)$_2$CHCOO); 31.49 (2C, CH$_2$(CH$_2$)$_2$(**C**H$_2$)$_2$CHCOO); 47.23 (1C, CH$_2$(CH$_2$)$_2$(CH$_2$)$_2$**C**HCOO);

178.13 (2C, $CH_2(CH_2)_2(CH_2)_2CH\mathbf{C}OO$) ppm. ^{31}P NMR (161 MHz, C_6D_6, 343 K) δ: 33.62 (1P, $\mathbf{P}(CH_2CH_2CH_2CH_3)_4$) ppm. ν (cm^{-1}): 2959; 2922; 2873; 2849; 1570; 1465; 1447; 1419; 1369; 1346; 1326; 1285; 1274; 1235; 1212; 1135; 1094; 1055; 1005; 968; 921; 909; 893; 887; 833; 813; 799; 764; 751; 721; 657. MS ES^+ m/z (% Rel. Intensity): 259 (100, $[P_{4,4,4,4}]^+$). MS ES^- m/z (% Rel. Intensity): 127 (100, $[c-C_6COO]^-$).

Tetrabutylphosphonium phenylacetate [$P_{4,4,4,4}$][PhC_1COO], the colourless liquid obtained from the rotary evaporator was dried under vacuum (1×10^{-4} bar) at 343 K under stirring (400 rpm). After the water removal, a white solid was obtained.

^1H NMR (400 MHz, DMSO-d_6, 343 K) δ: 0.95 (t, 12H, $^3J_{HH} = 7.2$ Hz, $P(CH_2CH_2CH_2C\mathbf{H_3})_4$); 1.44 (m, 16H, $P(CH_2C\mathbf{H_2}C\mathbf{H_2}CH_3)_4$); 2.40 (m, 8H, $P(C\mathbf{H_2}CH_2CH_2CH_3)_4$); 3.30 (s, 2H, $PhC\mathbf{H_2}COO$; 7.16 (m, 1H, $C\mathbf{H}(CH)_2(CH)_2CCH_2COO$); 7.34 (m, 4H, $CH(C\mathbf{H})_2(C\mathbf{H})_2CCH_2COO$) ppm. ^{13}C NMR (100 MHz, DMSO-d_6, 343 K) δ: 12.35 (4C, $P(CH_2CH_2CH_2\mathbf{C}H_3)_4$); 17.28 (4C, $P(\mathbf{C}H_2CH_2CH_2CH_3)_4$); 22.56 (4C, $P(CH_2CH_2\mathbf{C}H_2CH_3)_4$); 22.79 (4C, $P(CH_2\mathbf{C}H_2CH_2CH_3)_4$); 46.84 (1C $Ph\mathbf{C}H_2COO$); 123.23 (1C, $\mathbf{C}H(CH)_2(CH)_2CCH_2COO$);
126.12 (2C, $CH(\mathbf{C}H)_2(CH)_2CCH_2COO$); 128.33 (2C, $CH(CH)_2(\mathbf{C}H)_2CCH_2COO$); 140.97 (1C, $CH(CH)_2(CH)_2\mathbf{C}CH_2COO$); 170.86 ($PhCH_2\mathbf{C}OO$) ppm. ^{31}P NMR (161 MHz, DMSO-d_6, 343 K) δ: 33.59 (1P, $\mathbf{P}(CH_2CH_2CH_2CH_3)_4$) ppm. ν (cm^{-1}): 3086; 3062; 3029; 2958; 2932; 2872; 1713; 1658; 1602; 1496; 1465; 1454; 1413; 1380; 1160; 1139; 1098; 1075; 1051; 1031; 1004; 968; 918; 646; 599; 589; 570; 564. MS ES^+ m/z (% Rel. Intensity): 259 (100, $[P_{4,4,4,4}]^+$). MS ES^- m/z (% Rel. Intensity): 135 (100, $[PhC_1COO]^-$).

Tetrabutylphosphonium *p*-methylbenzoate [$P_{4,4,4,4}$][*p*−MeBzCOO], the colorless liquid obtained from the rotary evaporator was dried under vacuum (1×10^{-4} bar) at 363 K under stirring (400 rpm). After the water removal, a white solid was obtained.

^1H NMR (400 MHz, DMSO-d_6, 343 K) δ: 0.99 (t, 12H, $^3J_{HH} = 7.1$ Hz, $P(CH_2CH_2CH_2C\mathbf{H_3})_4$); 1.50 (m, 8H, $P(CH_2CH_2C\mathbf{H_2}CH_3)_4$); 1.59 (m, 8H, $P(CH_2C\mathbf{H_2}CH_2CH_3)_4$); 2.27 (m, 8H, $P(C\mathbf{H_2}CH_2CH_2CH_3)_4$); 2.37 (s, 3H, $C\mathbf{H_3}PhCOO$; 7.11 (d, 2H, $^3J_{HH} = 7.9$ Hz, $CH_3C(CH)_2(C\mathbf{H})_2CCOO$); 7.94 (d, 2H, $^3J_{HH} = 7.7$ Hz, $CH_3C(C\mathbf{H})_2(CH)_2CCOO$) ppm. ^{13}C NMR (100 MHz, DMSO-d_6, 343 K) δ: 12.85 ($P(CH_2CH_2CH_2\mathbf{C}H_3)_4$); 17.59 ($P(\mathbf{C}H_2CH_2CH_2CH_3)_4$); 19.98 ($\mathbf{C}H_3C(CH)_2(CH)_2CCOO$); 22.49 ($P(CH_2CH_2\mathbf{C}H_2CH_3)_4$); 22.71 ($P(CH_2\mathbf{C}H_2CH_2CH_3)_4$); 126.97 ($CH_3C(CH)_2(\mathbf{C}H)_2CCOO$)

; 128.66 ($CH_3C(\mathbf{C}H)_2(CH)_2CCOO$); 136.54 ($CH_3\mathbf{C}(CH)_2(CH)_2CCOO$); 137.69 ($CH_3C(CH)_2(CH)_2\mathbf{C}COO$); 168.72 ($CH_3C(CH)_2(CH)_2C\mathbf{C}OO$) ppm. ^{31}P NMR (161 MHz, DMSO-d_6, 343 K) δ: 33.81 (s, $\mathbf{P}(CH_2CH_2CH_2CH_3)_4$) ppm. ν (cm^{-1}):2958; 2931; 2893; 2873; 2730; 1602; 1562; 1465; 1458; 1351; 1230; 1167; 1099; 1092; 1067; 1019; 1005; 971; 918; 911; 897; 855; 838; 824; 813; 769; 752; 732; 720; 693 ; 640; 606. MS ES^+ m/z (% Rel. Intensity): 259 (100, $[P_{4,4,4,4}]^+$). MS ES^- m/z (% Rel. Intensity): 135 (100, $p-[MeBzCOO]^-$).

Tetrabutylphosphonium 1H-tetrazole-1-acetate [$\mathbf{P_{4,4,4,4}}$][$\mathbf{TetrazC_1COO}$], the colorless viscous liquid obtained from the rotary evaporator was dried under vacuum (1×10^{-4} bar) at 323 K under stirring (400 rpm). After the water removal, a colorless liquid was collected. ^{1}H NMR (400 MHz, C_6D_6, 343 K) δ: 0.84 (t, 12H, $^3J_{HH} = 7.3$ Hz, $P(CH_2CH_2CH_2C\mathbf{H_3})_4$); 1.38 (m, 8H, $P(CH_2CH_2C\mathbf{H_2}CH_3)_4$); 1.49 (m, 8H, $P(CH_2C\mathbf{H_2}CH_2CH_3)_4$); 2.33 (m, 8H, $P(C\mathbf{H_2}CH_2CH_2CH_3)_4$); 4.73 (s, 2H, $TetrazC\mathbf{H_2}COO$; 9.40 (s, 1H, $(N_3C\mathbf{H}N)CH_2CCOO$) ppm. ^{13}C NMR (100 MHz, C_6D_6, 343 K) δ: 14.21 ($P(CH_2CH_2CH_2\mathbf{C}H_3)_4$); 19.36 ($P(\mathbf{C}H_2CH_2CH_2CH_3)_4$); 24.45 ($P(CH_2\mathbf{C}H_2CH_2CH_3)_4$); 24.72 ($P(CH_2CH_2\mathbf{C}H_2CH_3)_4$); 53.19 ($TetrazC\mathbf{H}_2CCOO$); 145.85 ($(N_3\mathbf{C}HN)CH_2CCOO$) ; 166.65 ($TetrazCH_2C\mathbf{C}OO$) ppm. ^{31}P NMR (161 MHz, C_6D_6, 343 K) δ: 33.66 (s, $\mathbf{P}(CH_2CH_2CH_2CH_3)_4$) ppm. ν (cm^{-1}): 3081; 2958; 2932; 2908; 2872; 1635; 1486; 1466; 1413; 1380; 1352; 1297; 1241; 1169; 1143; 1102; 1053; 1028; 1006; 970; 923; 908; 820; 795; 749; 721; 684; 658; 568. MS ES^+ m/z (% Rel. Intensity): 259 (100, $[P_{4,4,4,4}]^+$). MS ES^- m/z (% Rel. Intensity): 127 (100, $[TetrazC_1COO]^-$).

Density and viscosity data

Table S1 – Experimental densities and molar volumes of the neat ILs and a few mixtures in the temperature range of 293–363 K. The deviations (δ) reported are relative to the fitting polynomials with coefficients listed in Table S2 and Table S3.

$\frac{T}{\mathrm{K}}$	$\frac{\rho}{\mathrm{g\,cm^{-3}}}$	$\frac{\delta}{\%}$	$\frac{V_m}{\mathrm{cm^3\,mol^{-1}}}$	$\frac{\delta}{\%}$	$\frac{T}{\mathrm{K}}$	$\frac{\rho}{\mathrm{g\,cm^{-3}}}$	$\frac{\delta}{\%}$	$\frac{V_m}{\mathrm{cm^3\,mol^{-1}}}$	$\frac{\delta}{\%}$
	$[P_{4,4,4,4}][C_1COO]$					$[P_{4,4,4,4}][MeC_3COO]$			
303.148	0.935729	0.003	340.35	0.018	-	-	-	-	-
313.148	0.929771	0.001	342.54	0.001	-	-	-	-	-
323.148	0.923802	0.002	344.75	0.010	323.146	0.903840	0.004	398.93	0.009
333.148	0.917847	0.003	346.99	0.013	333.146	0.897580	0.003	401.71	0.0008
343.150	0.911917	0.002	349.24	0.010	343.154	0.891380	0.001	404.51	0.005
353.148	0.905997	0.001	352.24	0.001	353.154	0.885180	0.0009	407.34	0.001
363.151	0.900088	0.004	353.83	0.017	363.154	0.879013	0.003	410.20	0.009
	$[P_{4,4,4,4}][Me_4C_4COO]$					$[P_{6,6,6,14}][Me_4C_4COO]$			
293.150	0.912674	0.01	456.53	0.008	293.149	0.886239	0.009	723.42	0.01
298.152	0.909638	0.008	458.05	0.004	298.152	0.883265	0.003	725.85	0.009
303.152	0.906614	0.0006	459.58	0.001	303.152	0.880298	0.0007	728.30	0.001
313.152	0.900615	0.01	462.64	0.003	313.152	0.874391	0.006	733.22	0.009
323.152	0.894696	0.01	465.70	0.007	323.152	0.86853	0.007	738.17	0.01
333.152	0.888832	0.01	468.77	0.009	333.152	0.862696	0.005	743.16	0.01
343.152	0.882998	0.006	471.87	0.006	343.152	0.856861	0.003	748.22	0.01
353.152	0.877206	0.004	474.99	0.001	353.152	0.851051	0.001	753.33	0.003
363.152	0.871446	0.01	478.12	0.012	363.152	0.845258	0.009	758.49	0.02
	$[P_{4,4,4,4}][C_5COO]$					$[P_{4,4,4,4}][C_{11}COO]$			
293.150	0.922470	0.007	406.07	0.02	293.150	0.904566	0.008	507.15	0.02
298.152	0.919341	0.003	407.45	0.01	298.152	0.901469	0.004	508.89	0.01
303.152	0.916219	0.0005	408.84	0.0003	303.151	0.898381	0.0001	510.64	0.0007
313.152	0.909994	0.003	411.64	0.01	313.152	0.892221	0.005	514.17	0.01
323.152	0.903763	0.007	414.48	0.02	323.152	0.886089	0.007	517.72	0.02
333.152	0.897572	0.007	417.34	0.02	333.152	0.879979	0.007	521.32	0.02
343.152	0.891409	0.004	420.22	0.01	343.152	0.873891	0.004	524.95	0.01
353.152	0.885265	0.001	423.14	0.004	353.152	0.867825	0.001	528.62	0.004
363.152	0.879146	0.01	426.08	0.02	363.152	0.861787	0.01	532.32	0.02
	$[P_{6,6,6,14}][C_{11}COO]$					$[P_{4,4,4,4}][c-C_6COO]$			
293.149	0.886997	0.0042	770.16	0.03	-	-	-	-	-
298.152	0.883890	0.0003	772.87	0.01	-	-	-	-	-
303.152	0.880793	0.003	775.59	0.004	-	-	-	-	-
313.152	0.874637	0.004	781.04	0.01	313.148	0.948335	0.006	407.66	0.008
323.152	0.868513	0.002	786.55	0.03	323.148	0.942133	0.002	410.35	0.001
333.152	0.862393	0.0002	792.13	0.03	333.148	0.935982	0.004	413.04	0.007
343.152	0.856288	0.004	797.78	0.02	343.148	0.929847	0.005	415.77	0.006
353.152	0.850154	0.005	803.54	0.0001	353.148	0.923757	0.001	418.51	0.002
363.152	0.843922	0.005	809.47	0.04	363.152	0.917701	0.007	421.27	0.008
	$[P_{4,4,4,4}][PhC_1COO]$					$[P_{4,4,4,4}][TetrazC_1COO]$			

$\frac{T}{\mathrm{K}}$	$\frac{\rho}{\mathrm{g\,cm^{-3}}}$	$\frac{\delta}{\%}$	$\frac{V_m}{\mathrm{cm^3\,mol^{-1}}}$	$\frac{\delta}{\%}$	$\frac{T}{\mathrm{K}}$	$\frac{\rho}{\mathrm{g\,cm^{-3}}}$	$\frac{\delta}{\%}$	$\frac{V_m}{\mathrm{cm^3\,mol^{-1}}}$	$\frac{\delta}{\%}$
293.148	0.980931	0.01	402.25	0.01	293.15	1.031903	0.005	374.57	0.02
298.148	0.977809	0.006	403.53	0.005	-	-	-	-	
303.148	0.974695	0.0001	404.82	0.0005	303.152	1.025608	0.001	376.87	0.002
313.148	0.968507	0.008	407.41	0.007	313.152	1.019313	0.002	379.20	0.009
323.148	0.962358	0.01	410.01	0.01	323.152	1.013039	0.004	381.55	0.01
333.148	0.956251	0.01	412.63	0.009	333.152	1.006787	0.004	383.91	0.01
343.148	0.950195	0.006	415.26	0.006	343.152	1.000540	0.003	386.31	0.008
353.148	0.944169	0.002	417.91	0.002	353.152	0.994323	0.0004	388.73	0.003
363.152	0.938181	0.01	420.58	0.01	363.152	0.988133	0.006	391.16	0.01

Table S2 – Fitting parameters A_0 and A_1 determined from the linear fitting of the experimental densities to $\rho = A_0 + A_1 T$ and the corresponding absolute average deviation (AAD).

Sample	A_0 / g cm^{-3}	A_1 / g cm^{-3} K^{-1}	AAD / %
$[P_{4,4,4,4}][C_1COO]$	1.1158	-5.9409 x 10^{-4}	0.002
$[P_{4,4,4,4}][MeC_3COO]$	1.1043	-6.2047 x 10^{-4}	0.002
$[P_{4,4,4,4}][Me_4C_4COO]$	1.0852	-5.8903 x 10^{-4}	0.01
$[P_{6,6,6,14}][Me_4C_4COO]$	1.0578	-5.8538 x 10^{-4}	0.005
$[P_{4,4,4,4}][C_5COO]$	1.1039	-6.1924 x 10^{-4}	0.0005
$[P_{4,4,4,4}][C_{11}COO]$	1.0837	-6.1133 x 10^{-4}	0.005
$[P_{6,6,6,14}][C_{11}COO]$	1.0670	-6.1416 x 10^{-4}	0.003
$[P_{4,4,4,4}][c-C_6COO]$	1.1401	-6.1263 x 10^{-4}	0.004
$[P_{4,4,4,4}][PhC_1COO]$	1.1599	-6.1103 x 10^{-4}	0.008
$[P_{4,4,4,4}][TetrazC_1COO]$	1.2152	-6.2545 x 10^{-4}	0.003

Table S3 – Fitting parameters B_0 and B_1 determined from the linear fitting of the experimental molar volumes to $V_m = B_0 + B_1 T$ and the corresponding absolute average deviation (AAD).

Sample	M /g mol^{-1}	B_0/cm^3 mol^{-1}	B_1 /cm^3 mol^{-1} K^{-1}	AAD /%
$[P_{4,4,4,4}][C_1COO]$	318.48	272.20	0.22463	0.01
$[P_{4,4,4,4}][MeC_3COO]$	360.57	307.88	0.28166	0.005
$[P_{4,4,4,4}][Me_4C_4COO]$	416.66	366.15	0.30818	0.006
$[P_{6,6,6,14}][Me_4C_4COO]$	641.22	576.62	0.50029	0.01
$[P_{4,4,4,4}][C_5COO]$	374.59	322.26	0.28561	0.01
$[P_{4,4,4,4}][C_{11}COO]$	458.75	401.73	0.35920	0.01
$[P_{6,6,6,14}][C_{11}COO]$	683.13	605.92	0.59590	0.02
$[P_{4,4,4,4}][c-C_6COO]$	386.60	322.41	0.27214	0.005
$[P_{4,4,4,4}][PhC_1COO]$	394.58	325.50	0.26165	0.007
$[P_{4,4,4,4}][TetrazC_1COO]$	386.52	304.99	0.23707	0.01

Table S4 – Calculated densities of several ILs under study with the CL&Pol polarizable force field at different temperatures with the deviations from experiment densities.

Sample	$\frac{T}{\mathrm{K}}$	$\frac{\rho_{\mathrm{exp}}}{\mathrm{g\,cm^{-3}}}$	$\frac{\rho_{\mathrm{calc}}}{\mathrm{g\,cm^{-3}}}$	$\frac{\delta}{\%}$
$[P_{4,4,4,4}][C_1COO]$	343	0.911917	0.890728	-2.32
$[P_{4,4,4,4}][MeC_3COO]$	333	0.897580	0.876599	-2.33
	343	0.891380	0.866296	-2.81
	353	0.885180	0.863459	-2.45
$[P_{4,4,4,4}][Me_4C_4COO]$	303	0.906614	0.895556	-1.22
	343	0.882998	0.881350	-0.18
$[P_{6,6,6,14}][Me_4C_4COO]$	303	0.880298	0.889108	1.00
	343	0.856861	0.858520	0.19
$[P_{4,4,4,4}][C_5COO]$	303	0.916219	0.904468	-1.28
	323	0.903762	0.888582	-1.67
	343	0.891409	0.858099	-3.73
$[P_{4,4,4,4}][C_{11}COO]$	303	0.898381	0.897265	-0.12
	343	0.873891	0.857305	-1.89
$[P_{6,6,6,14}][C_{11}COO]$	303	0.880793	0.878202	-0.29
	343	0.856288	0.843112	-1.54
$[P_{4,4,4,4}][c-C_6COO]$	333	0.935982	0.901587	-3.67
	343	0.929847	0.897665	-3.46
$[P_{4,4,4,4}][PhC_1COO]$	303	0.974695	0.976053	0.14
	323	0.962358	0.960491	-0.19
	343	0.950195	0.937350	-1.35
$[P_{4,4,4,4}][p-MeBzCOO]$	363	-	0.936795	-
	373	-	0.903211	-
$[P_{4,4,4,4}][TetrazC_1COO]$	303	1.025608	1.035093	0.92
	343	1.000540	1.031101	3.05

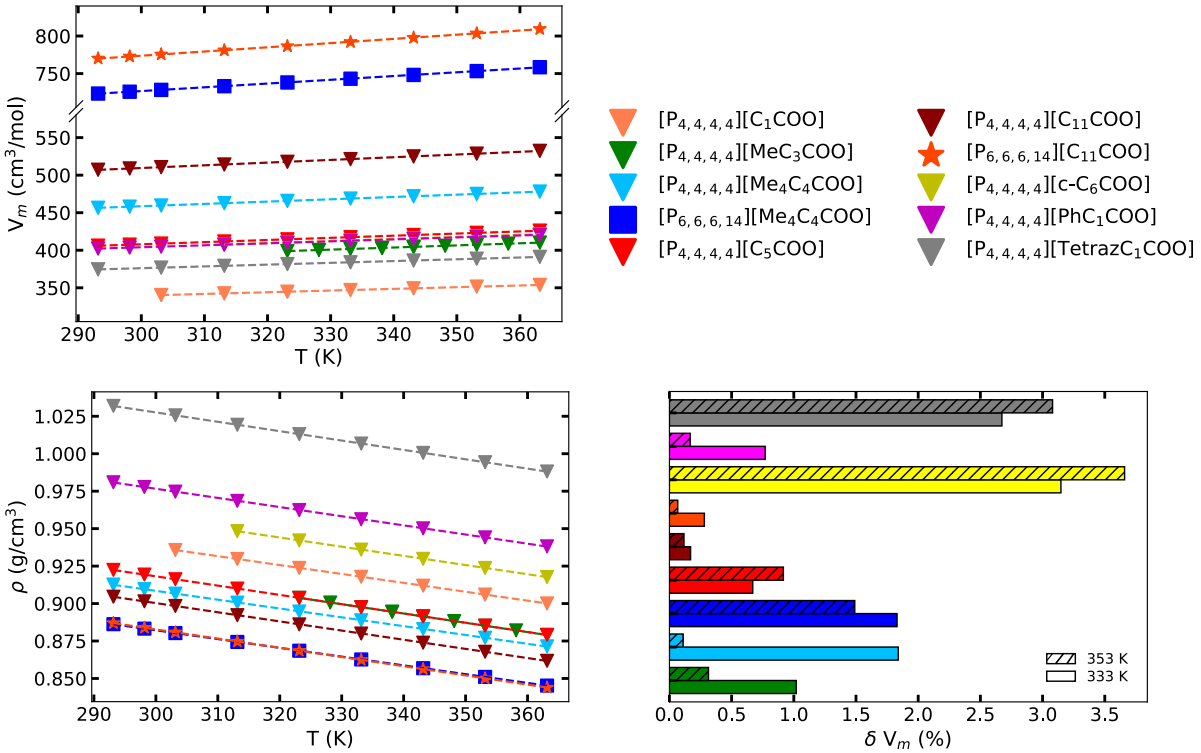

Figure S2 – Experimental molar volumes (top-left) and densities (bottom-left) of the pure ILs as a function of temperature, with linear fits (dashed lines). (Bottom-right) Deviation of the predicted molar volumes (V_m pred.) determined by the GCM from the experimental values (V_m exp.) at 333.15 and 353.15 K.

Table S5 – Group contribution parameters used to calculate the molar volume of cation and anion as a function of temperature.

Group j	C_0 / cm^3 mol^{-1}	C_1 / cm^3 mol^{-1} K	C_2 / cm^3 mol^{-1} K^2	Ref
$-CH_2$	16.967	1.399 x 10^{-3}	-1.946 x 10^{-6}	2
$-CH_3$ (branched compound)	14.460	-3.593 x 10^{-2}	8.574 x 10^{-4}	2⋆
$-C_6H_{11}$	99.909	3.164 x 10^{-2}	5.004 x 10^{-4}	3† 4⋆
$-CH_2-Ph$	80.185	1.344 x 10^{-1}	1.230 x 10^{-4}	2⋆
$-COO^-$	21.680	3.101 x 10^{-2}	-4.333 x 10^{-4}	5
$-CH_3COO^-$	49.177	2.149 x 10^{-2}	-2.775 x 10^{-5}	2
−Tetraz	52.187	-1.791 x 10^{-2}	-5.598 x 10^{-5}	6†
$[P_{4,4,4,4}]^+$	290.987	3.192 x 10^{-1}	1.436 x 10^{-5}	2⋆
$[P_{6,6,6,14}]^+$	560.514	3.904 x 10^{-1}	1.184 x 10^{-4}	2

⋆ Calculated by subtraction of parameters available in the reference.

† Calculated from the density data from the reference with temperatures ranging from 293.15 to 323.15 K for $-C_6H_{11}$ and 283.15 to 353.15 K for −Tetraz.

Table S6 – Number of groups (n_j) considered for the calculation of the molar volume of the studied ILs using the group contribution method (GCM) as well as the experimental molar volumes (V_m exp.) and the predicted ones (V_m pred.) at temperatures ranging from 293.15 to 363.15 K depending on the melting point of the IL.

Group j	n_j	$\frac{T}{K}$	$\frac{V_m \text{ exp.}}{cm^3\ mol^{-1}}$	$\frac{V_m \text{ pred.}}{cm^3\ mol^{-1}}$	$\frac{\delta}{\%}$
		[$P_{4,4,4,4}$][MeC_3COO]			
$-CH_2$	1	323.15	398.93	393.86	1.27
$-CH_3$ (branched)	2	333.15	401.71	397.59	1.02
$-CH_3COO^-$	1	353.15	407.34	406.06	0.31
$[P_{4,4,4,4}]^+$	1	363.15	410.20	410.80	0.14
		[$P_{4,4,4,4}$][Me_4C_4COO]			
$-CH_2$	2	293.15	458.05	445.61	2.39
$-CH_3$ (branched)	5	313.15	462.64	450.51	2.62
$-CH_3COO^-$	1	333.15	468.77	460.12	1.84
$[P_{4,4,4,4}]^+$	1	353.15	474.99	474.43	0.12
		[$P_{6,6,6,14}$][Me_4C_4COO]			
$-CH_2$	2	293.15	723.42	714.85	1.18
$-CH_3$ (branched)	5	313.15	733.22	720.44	1.74
$-CH_3COO^-$	1	333.15	743.16	729.51	1.84
$[P_{6,6,6,14}]^+$	1	353.15	753.33	742.08	1.49
		[$P_{4,4,4,4}$][C_5COO]			
$-CH_2$	4	293.15	406.07	406.30	0.06
$-CH_3COO^-$	1	333.15	417.34	420.13	0.67
$[P_{4,4,4,4}]^+$	1	353.15	423.14	427.01	0.91
		[$P_{4,4,4,4}$][$C_{11}COO$]			
$-CH_2$	10	293.15	507.15	508.06	0.18
$-CH_3COO^-$	1	333.15	521.32	522.21	0.17
$[P_{4,4,4,4}]^+$	1	353.15	528.62	529.24	0.11
		[$P_{6,6,6,14}$][$C_{11}COO$]			
$-CH_2$	10	293.15	770.16	777.23	0.91
$-CH_3COO^-$	1	333.15	792.13	794.35	0.28
$[P_{6,6,6,14}]^+$	1	353.15	803.54	803.00	0.06
		[$P_{4,4,4,4}$][$c-C_6COO$]			
$-C_6H_{11}$	1	313.15	407.66	418.32	2.61
$-COO^-$	1	333.15	413.04	426.04	3.15
$[P_{4,4,4,4}]^+$	1	353.15	418.51	433.82	3.66
		[$P_{4,4,4,4}$][PhC_1COO]			
$-CH_2-Ph$	1	293.15	402.25	390.42	2.94
$-COO^-$	1	333.15	412.63	409.45	0.77
$[P_{4,4,4,4}]^+$	1	353.15	417.91	418.61	0.16
		[$P_{4,4,4,4}$][$TetrazC_1COO$]			
$-CH_2$	1	293.15	374.57	379.96	1.43
$-COO^-$	1	313.15	379.20	387.26	2.12
$-Tetraz$	1	333.15	383.91	394.17	2.67
$[P_{4,4,4,4}]^+$	1	353.15	388.73	400.70	3.08

Table S7 – Experimental viscosities of the ILs in the temperature range of 293–363 K. The deviations (δ) reported are relative to the fitting of the VFT function with coefficients listed in Table S8.

T/K	η/mPa s	δ/%	T/K	η/mPa s	δ/%	T/K	η/mPa s	δ/%
$[P_{4,4,4,4}][C_1COO]$			$[P_{4,4,4,4}][MeC_3COO]$			$[P_{4,4,4,4}][Me_4C_4COO]$		
-	-	-	-	-	-	298.15	1344	0.01
-	-	-	-	-	-	303.15	900.6	0.02
-	-	-	-	-	-	313.15	439.5	0.06
-	-	-	-	-	-	323.15	236.3	0.3
333.16	67.10	0.04	333.15	52.94	0.1	333.15	136.2	0.02
343.15	43.13	0.04	343.15	34.39	0.1	343.15	83.50	0.4
353.15	29.10	0.03	353.15	23.42	0.2	353.15	54.17	0.4
-	-	-	363.15	16.79	0.2	363.15	36.76	0.3
$[P_{6,6,6,14}][Me_4C_4COO]$			$[P_{4,4,4,4}][C_5COO]$			$[P_{4,4,4,4}][C_{11}COO]$		
293.15	1253	0.05	293.15	548.9	0.03	293.15	574.4	0.02
298.15	889.4	0.08	298.15	377.3	0.12	298.15	403.6	0.06
303.15	644.9	0.1	303.15	266.8	0.06	303.15	290.6	0.06
313.15	356.5	0.7	313.15	142.9	0.91	313.15	160.1	0.4
323.15	221.0	3.8	323.15	86.05	1.30	323.15	96.01	0.3
333.15	130.7	1.4	333.15	53.45	0.23	333.15	60.54	0.09
343.15	84.69	2.3	-	-	-	343.15	40.32	0.06
353.15	57.19	2.8	-	-	-	353.15	28.14	0.4
363.15	40.06	3.2	-	-	-	363.15	20.36	0.8
$[P_{6,6,6,14}][C_{11}COO]$			$[P_{4,4,4,4}][c-C_6COO]$			$[P_{4,4,4,4}][PhC_1COO]$		
293.15	598.4	0.05	-	-	-	293.15	529.2	0.03
298.15	434.2	0.07	-	-	-	298.15	365.8	0.1
303.15	321.3	0.1	-	-	-	303.15	259.3	0.07
313.15	185.9	0.5	313.15	505.7	0.01	313.15	140.9	0.1
323.15	110.9	2.2	323.15	254.3	0.1	323.15	83.05	0.2
333.15	72.34	1.0	333.15	140.2	0.1	333.15	52.39	0.3
343.15	49.56	0.7	343.15	83.55	0.3	343.15	35.15	0.2
353.15	35.35	2.7	353.15	53.12	0.2	353.15	24.73	1.0
363.15	26.09	4.8	363.15	36.13	1.3	363.15	18.09	1.9
$[P_{4,4,4,4}][TetrazC_1COO]$								
303.15	1425	0.003						
313.15	595.0	0.07						
323.15	285.1	0.4						
333.15	149.9	0.4						
343.15	86.10	0.6						
353.15	53.31	0.2						
363.15	35.28	1.3						

Table S8 – Fitting parameters A, B and T_0 determined from the fitting of the experimental viscosities to the VFT function and the corresponding absolute average deviation (AAD).

Sample	A (mPa s)	B (K)	T_0 (K)	AAD (%)
$[P_{4,4,4,4}][C_1COO]$	0.0326	1241.10	170.50	0.04
$[P_{4,4,4,4}][MeC_3COO]$	0.0713	940.49	190.91	0.13
$[P_{4,4,4,4}][Me_4C_4COO]$	0.0288	1390.59	168.80	0.19
$[P_{6,6,6,14}][Me_4C_4COO]$	0.0194	1741.66	135.87	1.6
$[P_{4,4,4,4}][C_5COO]$	0.0695	1025.62	178.88	0.04
$[P_{4,4,4,4}][C_{11}COO]$	0.0388	1256.02	162.36	0.20
$[P_{6,6,6,14}][C_{11}COO]$	0.0256	1522.16	141.84	1.3
$[P_{4,4,4,4}][c-C_6COO]$	0.0492	1147.23	188.97	0.40
$[P_{4,4,4,4}][PhC_1COO]$	0.0591	1070.43	175.52	0.47
$[P_{4,4,4,4}][TetrazC_1COO]$	0.0347	1187.17	191.40	0.40

Thermal stability analysis

Table S9 – Glass transition temperatures (T_g), melting points (T_{fus}) and crystallization temperatures (T_{cr}) for the pure ILs and the mixtures prepared. The different temperatures reported were measured using DSC with a 10 K min^{-1} heating rate. In order to facilitate the reading, when the onset temperature is reported, the value will be followed by (o) and when the peak temperature is reported, a (p) marker is used.

Sample	T_g (°C)	T_{trans} (°C) & T_{fus} (°C)	T_{cr} (°C)
$[P_{4,4,4,4}][C_1COO]$	-	22.6 (o) & 49.3 (o)	13.1 (o)
$[P_{4,4,4,4}][MeC_3COO]$	-52.8	-8.0 (p) & 66.0 (p)	-16.6 (p)
$[P_{4,4,4,4}][Me_4C_4COO]$	-56.3	0.7 (p) & 34.2 (p)	-18.3 (p)
$[P_{6,6,6,14}][Me_4C_4COO]$	-65.8	-	-
$[P_{4,4,4,4}][C_5COO]$	-65.1	-	-
$[P_{4,4,4,4}][C_{11}COO]$	-65.3	-	-
$[P_{6,6,6,14}][C_{11}COO]$	-	-20.8 (o) & -17.1 (o)	-26.9 (o)
$[P_{4,4,4,4}][c-C_6COO]$	-44.6	61.8 (p)	46.3 (p)
$[P_{4,4,4,4}][PhC_1COO]$	-63.9	-8.5 (p) & 44.1 (o)	7.2 (o)
$[P_{4,4,4,4}][p-MeBzCOO]$	-	90.7 (o)	11.6 (o)
$[P_{4,4,4,4}][TetrazC_1COO]$	-	9.1 (o)	-37.4 (p)

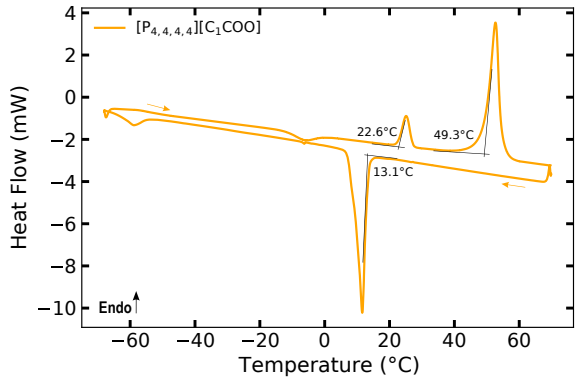
[P4,4,4,4][C1COO]
22.6°C
49.3°C
13.1°C
Endo
Heat Flow (mW)
Temperature (°C)

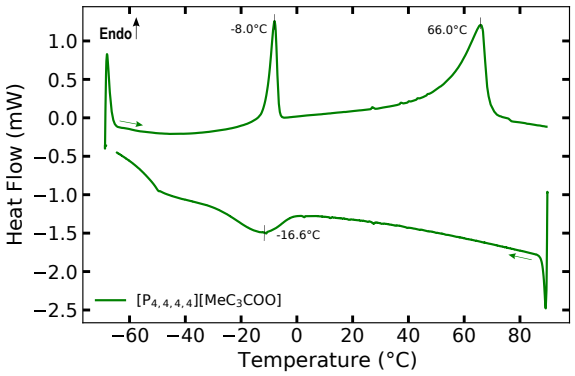
Endo
-8.0°C
66.0°C
-16.6°C
[P4,4,4,4][MeC3COO]
Heat Flow (mW)
Temperature (°C)

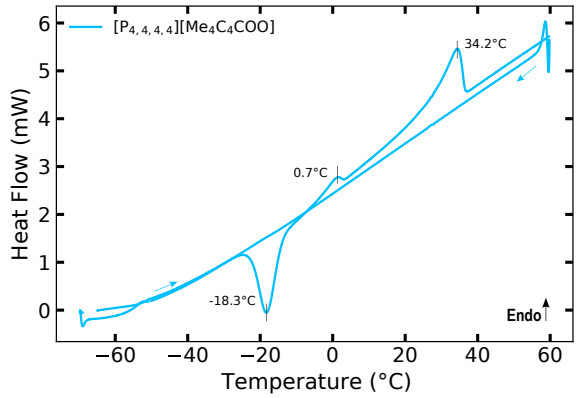
[P4,4,4,4][Me4C4COO]
34.2°C
0.7°C
-18.3°C
Endo
Heat Flow (mW)
Temperature (°C)

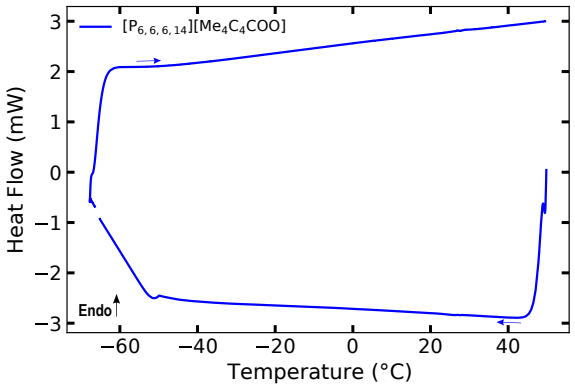
[P6,6,6,14][Me4C4COO]
Endo
Heat Flow (mW)
Temperature (°C)

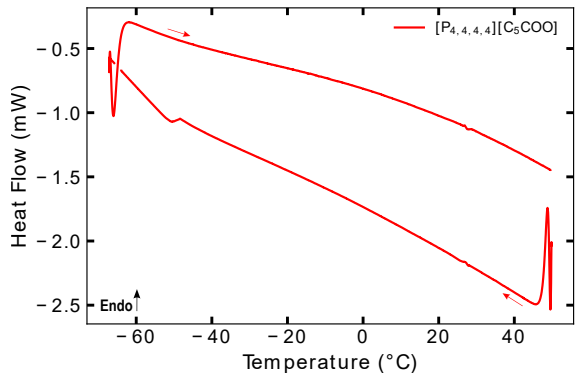
[P4,4,4,4][C5COO]
Endo
Heat Flow (mW)
Temperature (°C)

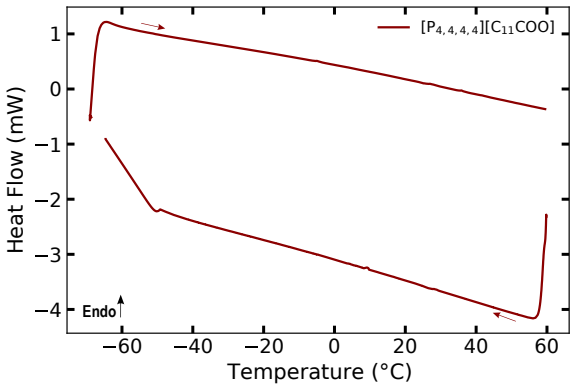
[P4,4,4,4][C11COO]
Endo
Heat Flow (mW)
Temperature (°C)

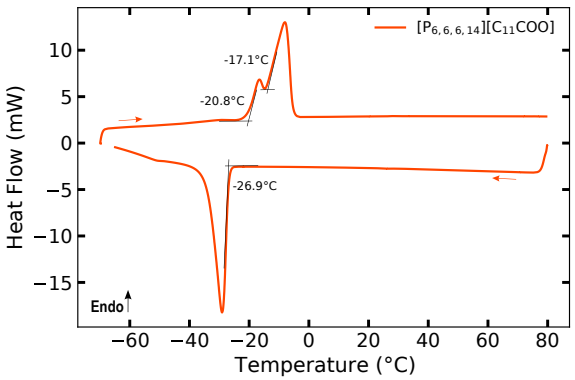
[P6,6,6,14][C11COO]
-17.1°C
-20.8°C
-26.9°C
Endo
Heat Flow (mW)
Temperature (°C)

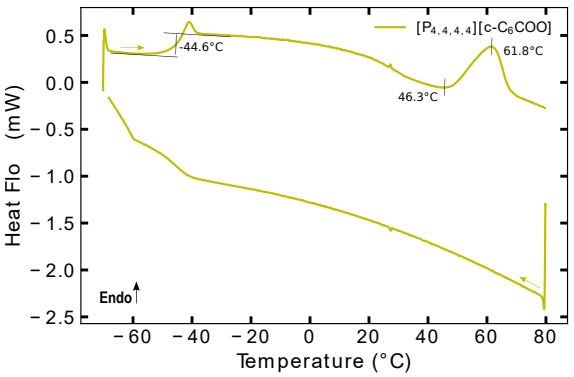
[P4,4,4,4][c-C6COO]
-44.6°C
61.8°C
46.3°C
Endo
Heat Flo (mW)
Temperature (°C)

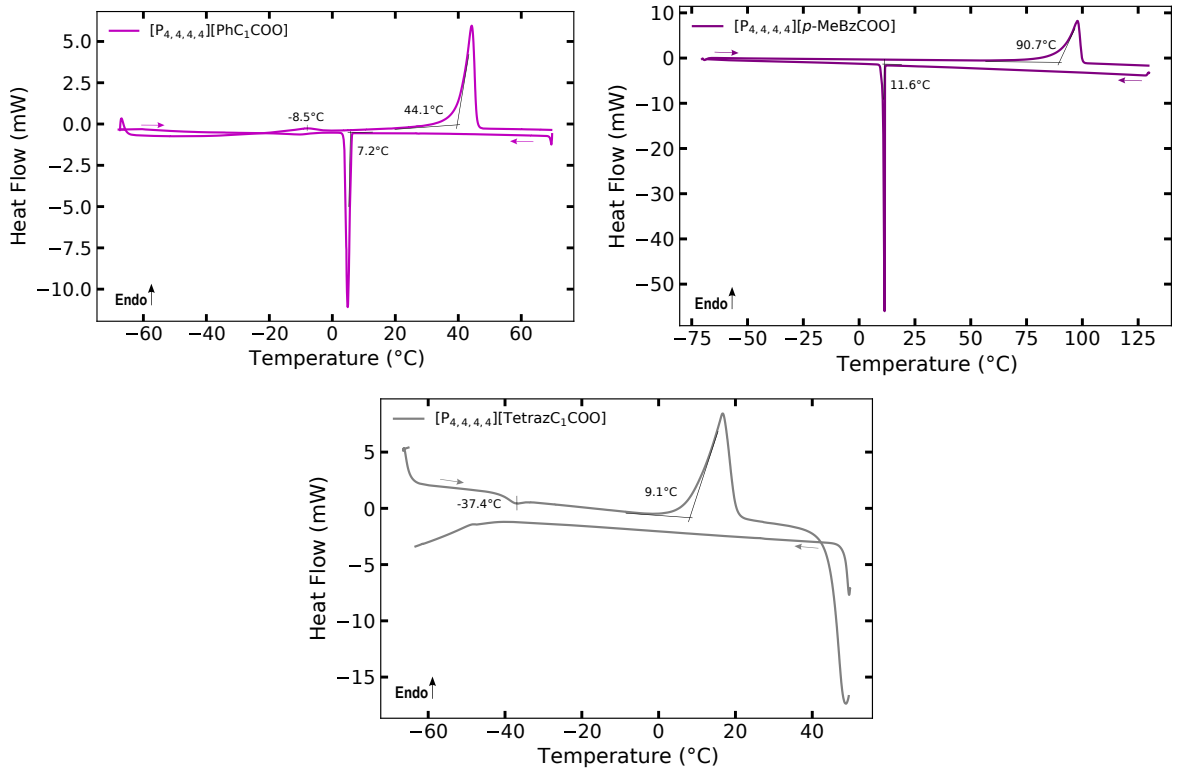

Figure S3 – DSC traces of [$P_{4,4,4,4}$][C_1COO], [$P_{4,4,4,4}$][C_5COO], [$P_{4,4,4,4}$][C_{11}COO], [$P_{6,6,6,14}$][C_{11}COO], [$P_{4,4,4,4}$][MeC_3COO], [$P_{4,4,4,4}$][Me_4C_4COO], [$P_{6,6,6,14}$][Me_4C_4COO], [$P_{4,4,4,4}$][c−C_6COO], [$P_{4,4,4,4}$][PhC_1COO], [$P_{4,4,4,4}$][*p*−MeBzCOO] and [$P_{4,4,4,4}$][TetrazC_1COO] measured at 10 K min^{-1}.

Table S10 – Decomposition temperatures (T_{dec}) for the pure ILs and a few ILs mixtures determined at 10 °C min^{-1} under an atmosphere of N_2 or O_2.

Sample	Atm	$T_{dec,1}$ (°C)	$T_{dec,2}$ (°C)
$[P_{4,4,4,4}][C_1COO]$	N_2[7]	317	-
	O_2	325	-
$[P_{4,4,4,4}][MeC_3COO]$	N_2	292	-
	O_2	328	-
$[P_{4,4,4,4}][Me_4C_4COO]$	O_2	319	-
$[P_{6,6,6,14}][Me_4C_4COO]$	O_2	342	-
$[P_{4,4,4,4}][C_5COO]$	N_2	302	-
	O_2	328	-
$[P_{4,4,4,4}][C_{11}COO]$	N_2	274	-
	O_2	344	-
$[P_{6,6,6,14}][C_{11}COO]$	N_2	318	-
	O_2	345	-
$[P_{4,4,4,4}][c-C_6COO]$	N_2	303	-
	O_2	336	-
$[P_{4,4,4,4}][PhC_1COO]$	N_2	256	358
	O_2	254	-
$[P_{4,4,4,4}][p-MeBzCOO]$	N_2	337	-
	O_2	363	-
$[P_{4,4,4,4}][TetrazC_1COO]$	O_2	291	-

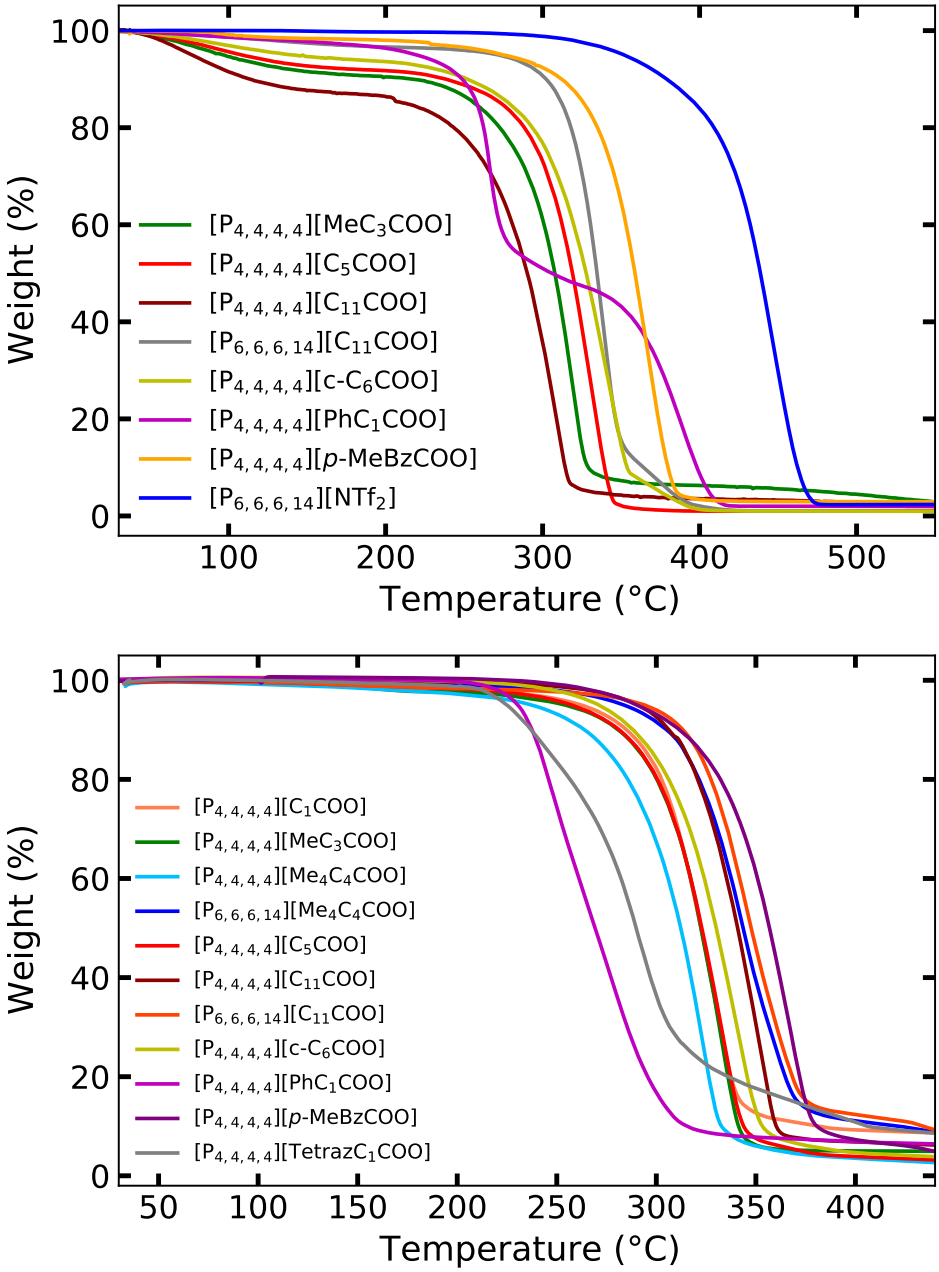

Figure S4 – TGA thermographs of the ILs with a heat rate of 10 °C min^{-1} under: N_2 (top) and O_2 (bottom). The decomposition temperatures were determined by the intersection of the tangents to the lines at low temperature and those corresponding to the rapid mass loss.

Molecular Dynamics Simulations

Table S11 – Simulated self-diffusion coefficients of various ILs at different temperatures by fitting the MSD calculated from MD simulations.

Sample (simulated)	T (K)	D_{anion} (10^{-11} m^2 s^{-1})	D_{cation} (10^{-11} m^2 s^{-1})
$[P_{4,4,4,4}][C_1COO]$	343	1.60 ± 0.02	1.46 ± 0.02
$[P_{4,4,4,4}][MeC_3COO]$	343	2.44 ± 0.01	2.35 ± 0.01
$[P_{4,4,4,4}][Me_4C_4COO]$	343	1.91 ± 0.02	1.75 ± 0.03
$[P_{6,6,6,14}][Me_4C_4COO]$	343	0.98 ± 0.07	1.02 ± 0.04
$[P_{4,4,4,4}][C_5COO]$	303	1.01 ± 0.06	0.99 ± 0.06
	343	4.79 ± 0.02	4.32 ± 0.02
$[P_{4,4,4,4}][C_{11}COO]$	303	1.26 ± 0.04	0.91 ± 0.04
	343	3.50 ± 0.08	3.18 ± 0.09
$[P_{6,6,6,14}][C_{11}COO]$	303	0.67 ± 0.02	0.52 ± 0.01
	343	1.55 ± 0.03	1.58 ± 0.03
$[P_{4,4,4,4}][c-C_6COO]$	333	1.19 ± 0.04	1.00 ± 0.03
	343	1.34 ± 0.03	1.27 ± 0.03
$[P_{4,4,4,4}][PhC_1COO]$	343	4.06 ± 0.02	3.97 ± 0.02
$[P_{4,4,4,4}][p-MeBzCOO]$	373	4.99 ± 0.02	4.16 ± 0.02
$[P_{4,4,4,4}][TetrazC_1COO]$	343	1.40 ± 0.03	2.66 ± 0.01

Table S12 – Distance between the centres of mass between of the fragments used calculated by DFT at the B97-D3/cc-pVDZ level.

Dimers	r (Å)
$[P_{1,1,1,1}]^+$-$[C_1COO]^-$	3.855
$[P_{1,1,1,1}]^+$-Toluene	4.467
$[P_{1,1,1,1}]^+$-Cyclohexane	5.667
$[P_{1,1,1,1}]^+$-Tetrazole	5.789
Toluene-$[C_1COO]^-$ ($[p-MeBzCOO]^-$)	5.561
Toluene-$[C_1COO]^-$ ($[PhC_1COO]^-$)	5.221
Toluene-Toluene	6.383
Cyclohexane-$[C_1COO]^-$	5.311
Cyclohexane-Butane	5.125
Cyclohexane-Cyclohexane	6.062
Tetrazole-$[C_1COO]^-$	4.221
Tetrazole- Butane	5.904
Tetrazole-Tetrazole	4.997

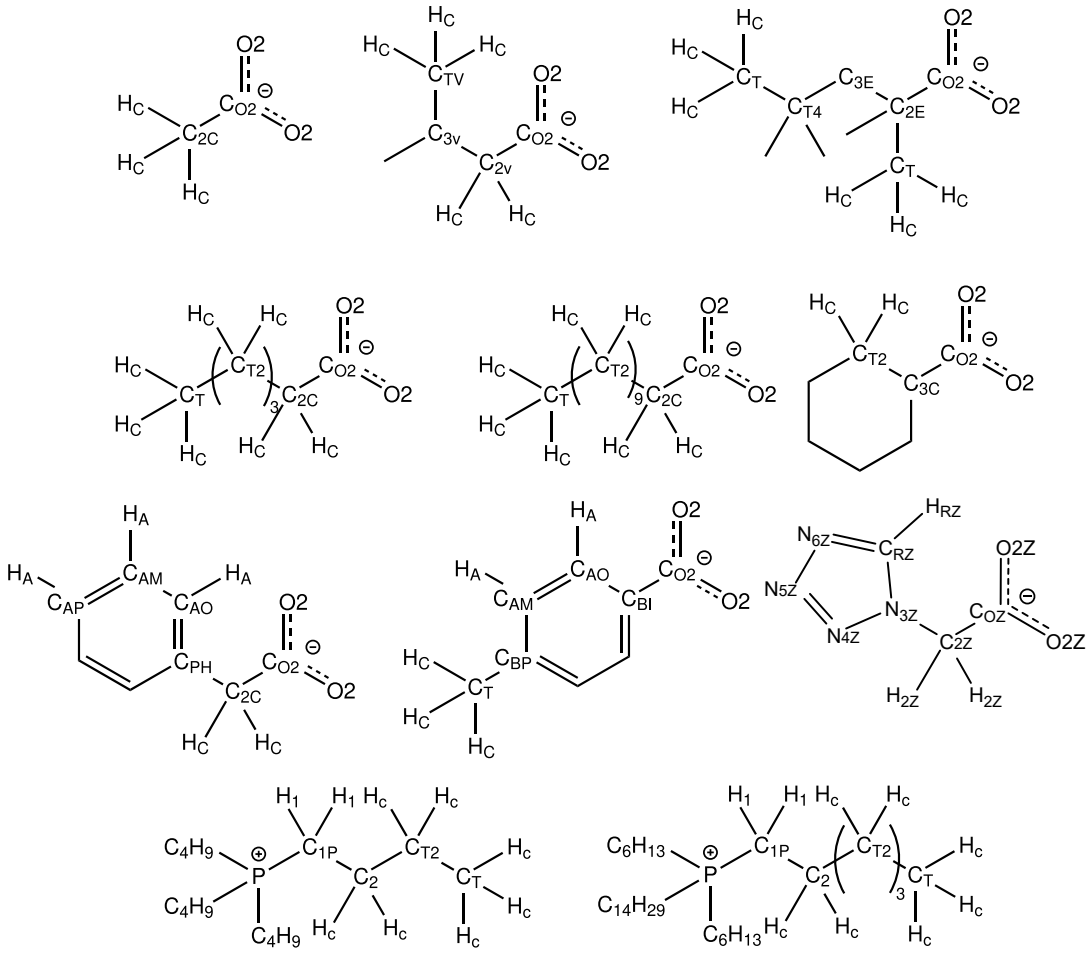

Figure S5 – Atom site labels and structure of the simulated ILs. The unlabelled atoms are the same as the respectively labelled symmetric sites.

Table S13 – New dihedral parameters used for [TetrazC$_1$COO]$^-$. Other atoms use the parameters from OPLS-AA and CL&Pol force fields with the corresponding atom type labels.

Ion	Dihedral	v1	v2	v3	v4
[TetrazC$_1$COO]$^-$	NNCC	-37.0894	5.1348	-1.8911	0.9450
	NCCO	0.10955	-1.2516	-0.101	1.09295

Table S14 – New force field parameters used for $[MeC_3COO]^-$, $[c-C_6COO]^-$, $[PhC_1COO]^-$, $[p-MeBzCOO]^-$ and $[TetrazC_1COO]^-$. Other atoms use the parameters from OPLS-AA and CL&Pol force fields with the corresponding atom type labels.

Ion	Atom type	q (e)	σ (Å)	ϵ (kJ mol^{-1})
$[MeC_3COO]^-$	C_{2V}	-0.300	3.50	0.27614
	C_{3V}	0.420	3.50	0.27614
	C_{TV}	-0.380	3.50	0.27614
$[Me_4C_4COO]^-$	C_{2E}	0.280	3.50	0.27614
	C_{3E}	-0.500	3.50	0.27614
	C_{T4}	0.000	3.50	0.27614
$[c-C_6COO]^-$	C_{3C}	-0.160	3.50	0.27614
$[PhC_1COO]^-$	C_{PH}	0.163	3.55	0.29288
$[p-MeBzCOO]^-$	C_{BI}	-0.040	3.55	0.29288
	C_{BP}	0.064	3.55	0.29288
$[TetrazC_1COO]^-$	O_{2Z}	-0.730	2.96	0.87864
	C_{OZ}	0.840	3.75	0.43932
	C_{2Z}	-0.740	3.50	0.27614
	H_{2Z}	0.180	2.50	0.12552
	C_{RZ}	0.140	3.55	0.29288
	H_{RZ}	0.115	2.42	0.12552
	N_{3Z}	0.685	3.25	0.71128
	N_{4Z}	-0.420	3.25	0.71128
	N_{5Z}	-0.100	3.25	0.71128
	N_{6Z}	-0.420	3.25	0.71128

Table S15 – The scaling factors evaluated for the dispersion energy (ϵ) of the LJ potential.

Dimers	k
$[P_{1,1,1,1}]^+$-$[C_1COO]^-$	0.44
$[P_{1,1,1,1}]^+$-Butane	0.65
$[P_{1,1,1,1}]^+$-Toluene	0.64
$[P_{1,1,1,1}]^+$-Cyclohexane	0.53
$[P_{1,1,1,1}]^+$-Tetrazole	0.52
Toluene-$[C_1COO]^-$	0.42
Butane-$[C_1COO]^-$	0.50
Cyclohexane-$[C_1COO]^-$	0.41
Tetrazole-$[C_1COO]^-$	0.50
Toluene-Butane	0.90
Toluene-Toluene	1.00
Cyclohexane-Butane	1.00
Butane-Butane	0.94
Cyclohexane-Cyclohexane	1.00
Tetrazole-Butane	1.00
Tetrazole-Tetrazole	1.00

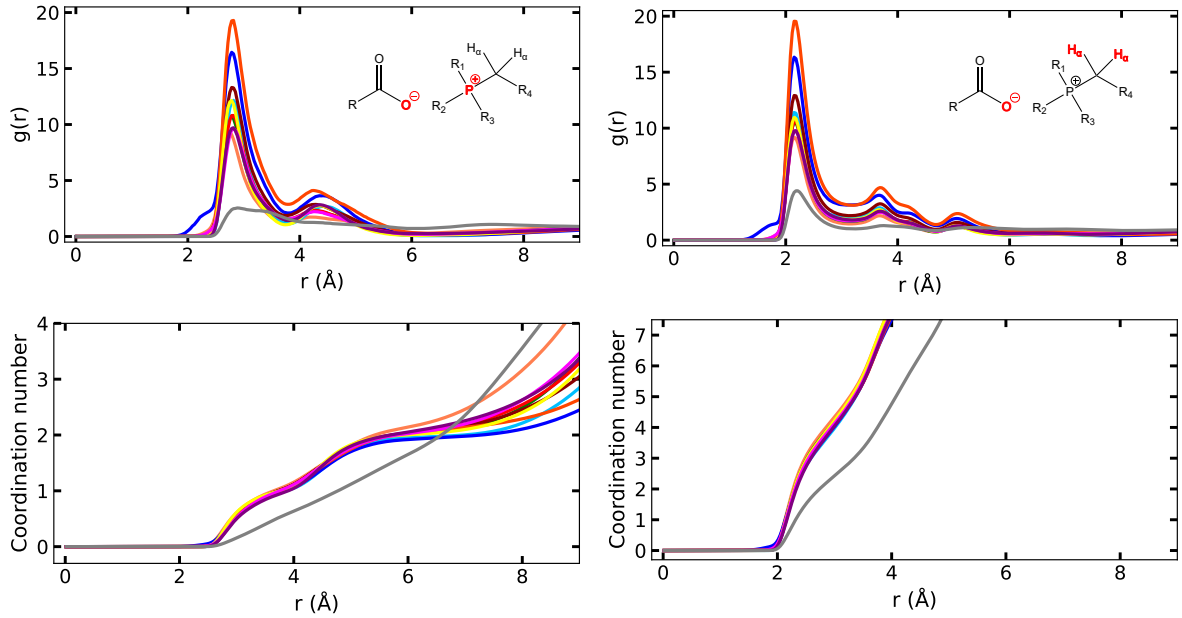

Figure S6 – Comparison of the site-site RDFs, g(r), of (left) the P^+ and (right) the H_α of the cation around the negatively charged oxygen atoms O^-_{COO} of the carboxylate head of the anion and their corresponding coordination numbers in [$P_{4,4,4,4}$][C_1COO], [$P_{4,4,4,4}$][MeC_3COO], [$P_{4,4,4,4}$][Me_4C_4COO], [$P_{6,6,6,14}$][Me_4C_4COO], [$P_{4,4,4,4}$][C_5COO], [$P_{4,4,4,4}$][C_{11}COO], [$P_{6,6,6,14}$][C_{11}COO], [$P_{4,4,4,4}$][c−C_6COO], [$P_{4,4,4,4}$][PhC_1COO] and [$P_{4,4,4,4}$][TetrazC_1COO] at 343 K and at 373 K for [$P_{4,4,4,4}$][*p*−MeBzCOO].

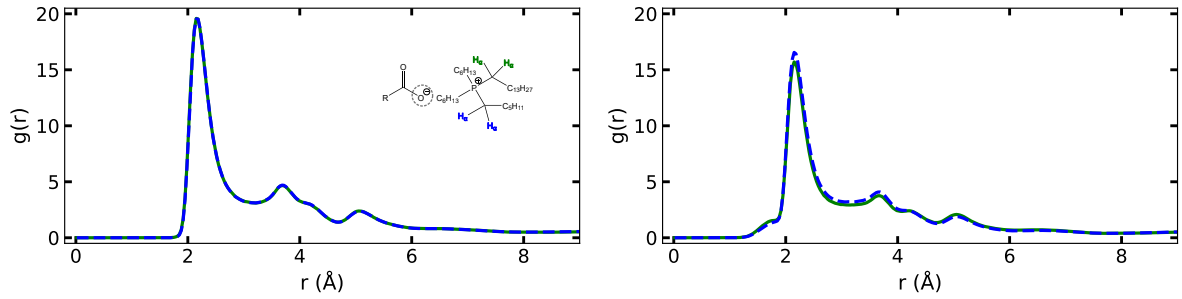

Figure S7 – Site-site RDF, g(r), of the H_α of the tetradecyl (C_{14}) and of the hexyl (C_6) alkyl side chains of the cation around the carboxylate head of the anion in (left) [$P_{6,6,6,14}$][C_{11}COO] and (right) [$P_{6,6,6,14}$][Me_4C_4COO] at 343 K.

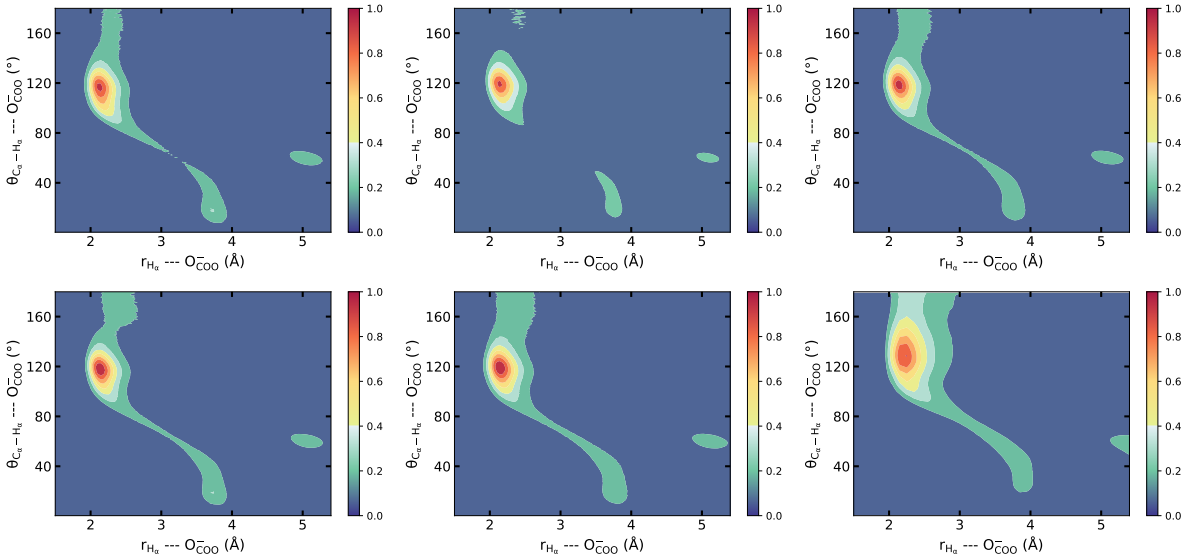

Figure S8 – Combined distribution function (CDF) of the $C_\alpha{-}H_\alpha\cdots O^-_{COO}$ angle as a function of the distance between the acidic proton H_α and the negatively charged O^-_{COO} in (top left) $[P_{4,4,4,4}][C_1COO]$, (top middle) $[P_{4,4,4,4}][Me_4C_4COO]$, (top right) $[P_{4,4,4,4}][C_{11}COO]$, (bottom left) $[P_{4,4,4,4}][c{-}C_6COO]$, (bottom middle) $[P_{4,4,4,4}][PhC_1COO]$ and (bottom right) $[P_{4,4,4,4}][TetrazC_1COO]$ at 343 K.

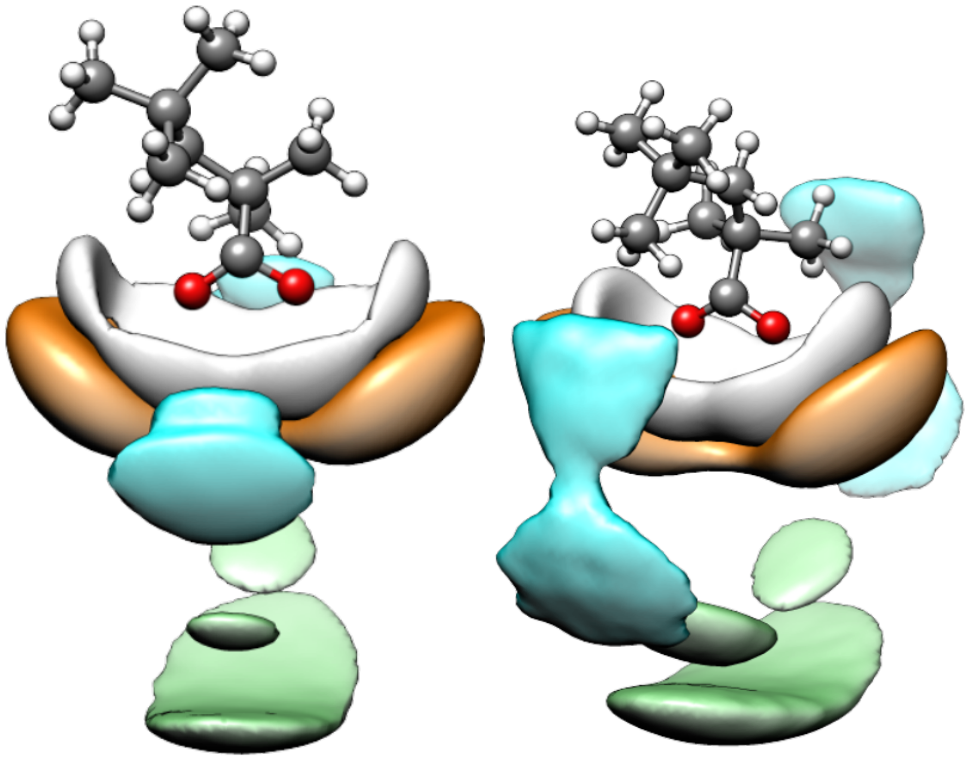

Figure S9 – SDFs of P^+ (in orange), of H_α (in white), of the terminal carbon atoms of the alkyl chains of the cation (in blue) and of the terminal carbon of the branched alkyl chain belonging to $[Me_4C_4COO]^-$ (in green) with (left) $[P_{4,4,4,4}]^+$ cation and (right) $[P_{6,6,6,14}]^+$ cation around O^-_{COO} of the anion at 343 K.

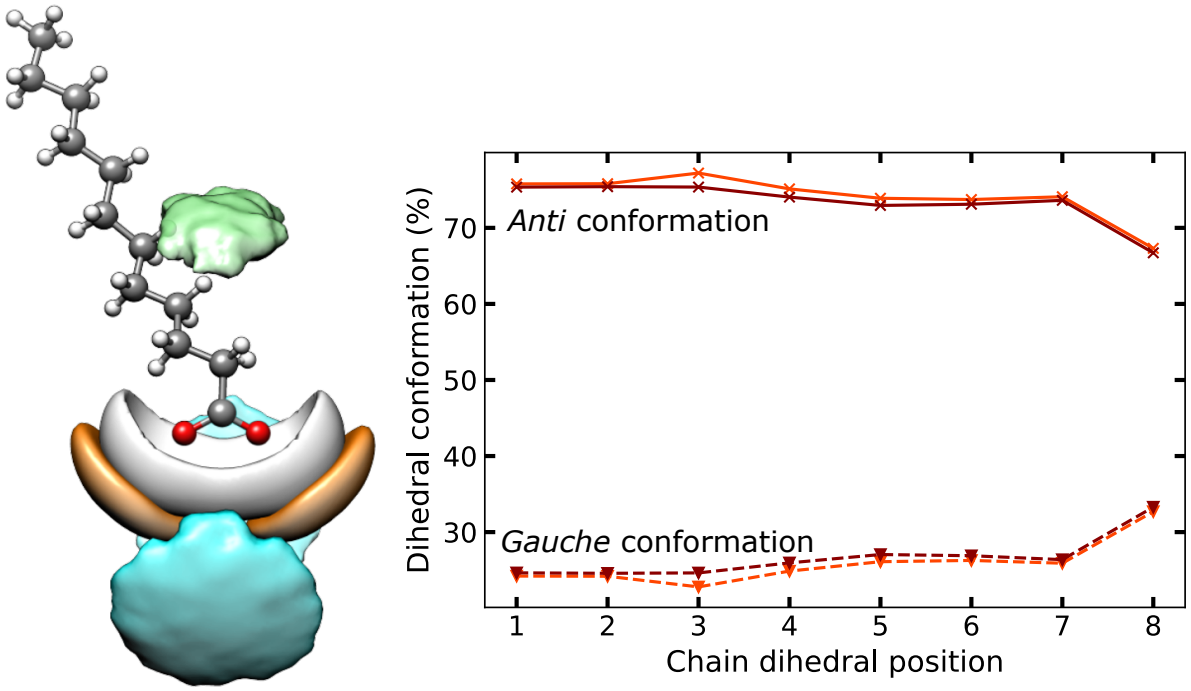

Figure S10 – (Left) SDFs of P^+ (in orange), of H_α (in white), of the terminal carbon atoms of the alkyl chains of $[P_{6,6,6,14}]^+$ (in blue) and of the terminal carbon of $[C_{11}COO]^-$ (in green) around O^-_{COO} of the anion in $[P_{6,6,6,14}][C_{11}COO]$ at 343 K. (Right) Average *gauche* and *anti* conformation percentage for each C−C−C−C dihedral angle along the dodecyl chain of the $[C_{11}COO]^-$ anion in $[P_{4,4,4,4}][C_{11}COO]$ and $[P_{6,6,6,14}][C_{11}COO]$.

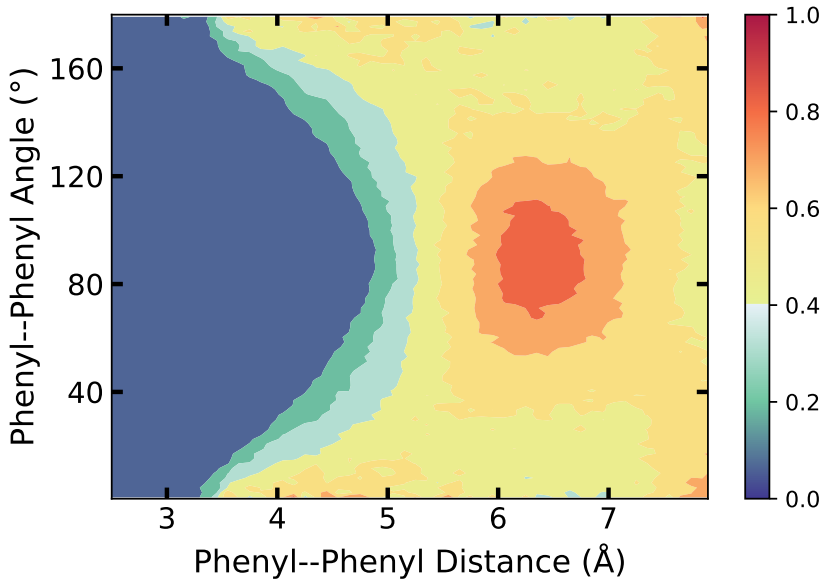

Figure S11 – CDF of the angle between two adjacent phenyl rings as a function of the RDF between their center of mass in $[P_{4,4,4,4}][p-MeBzCOO]$ at 343 K.

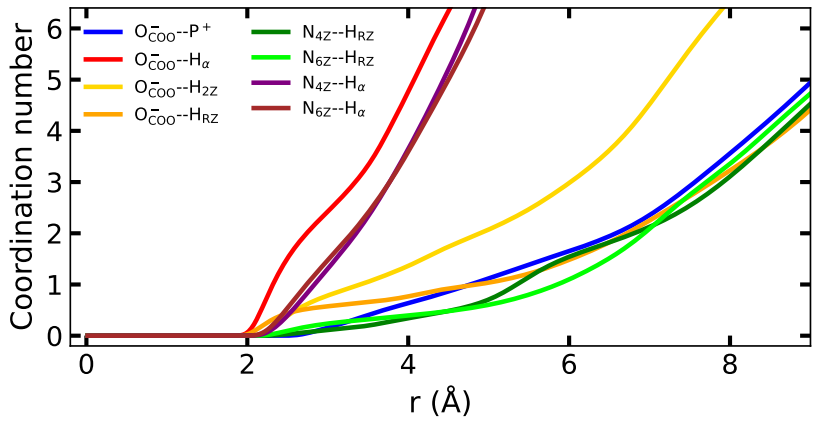

Figure S12 – Coordination number (CN) of (top) P^+, H_α and H_{RZ} around N_{4Z} and N_{6Z} of the $[TetrazC_1COO]^-$ anion, and O^- around H_{RZ} and H_{2Z} in $[P_{4,4,4,4}][TetrazC_1COO]$ at 343 K.

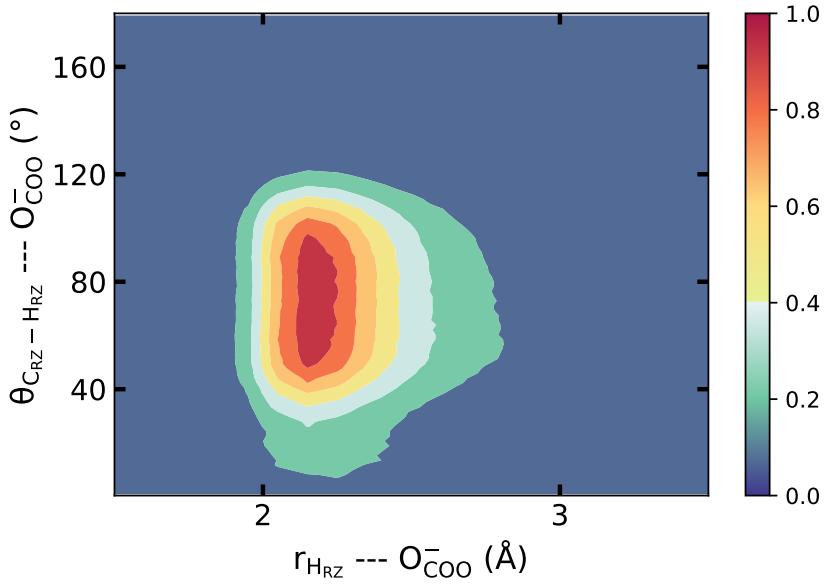

Figure S13 – CDF of the $C_{RZ}{-}H_{RZ}\cdots O^-_{COO}$ angle as a function of the RDF Angular Distribution Function (ADF) as a function of the RDF between the negatively chargedO^-_{COO} of the $[TetrazC_1COO]^-$ anion and the H_{RZ} of a neighbour anion in $[P_{4,4,4,4}][TetrazC_1COO]$ at 343 K.

SAXS data

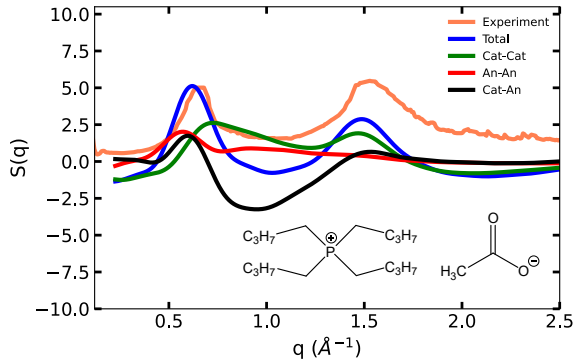

(a)

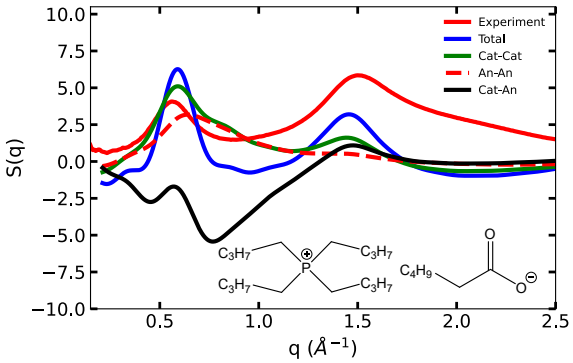

(b)

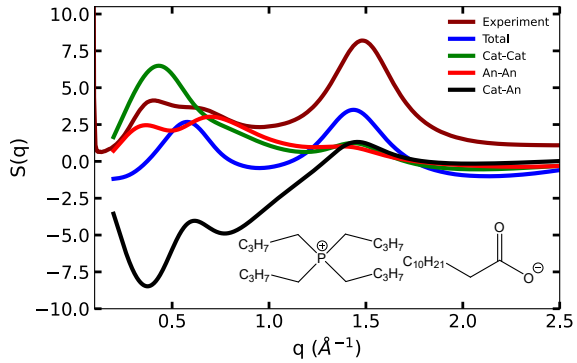

(c)

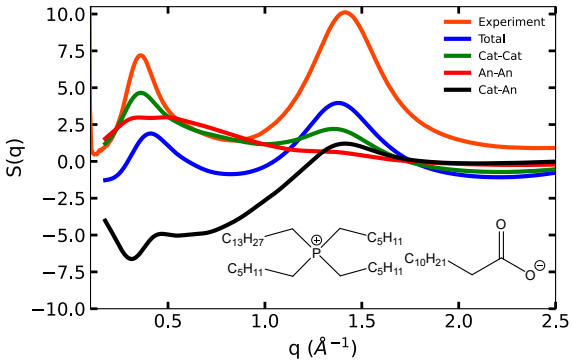

(d)

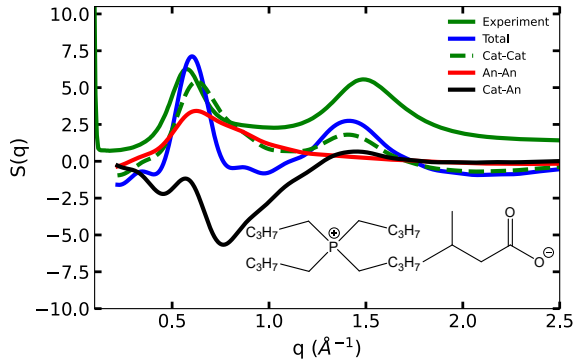

(e)

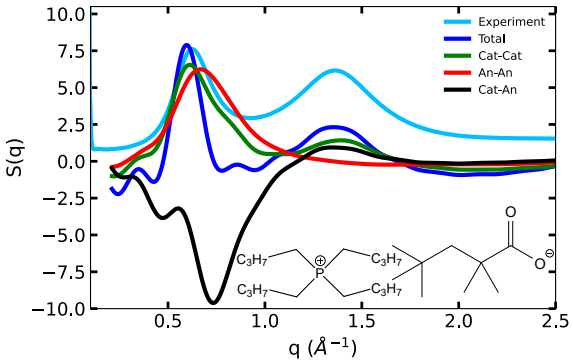

(f)

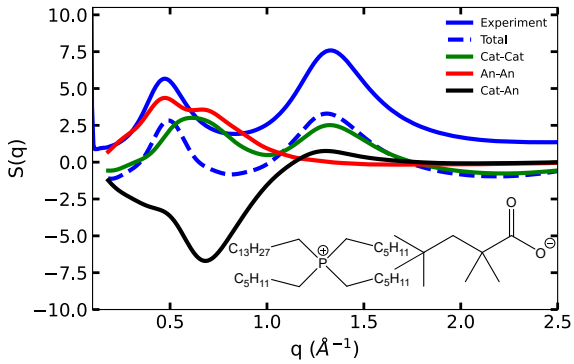

(g)

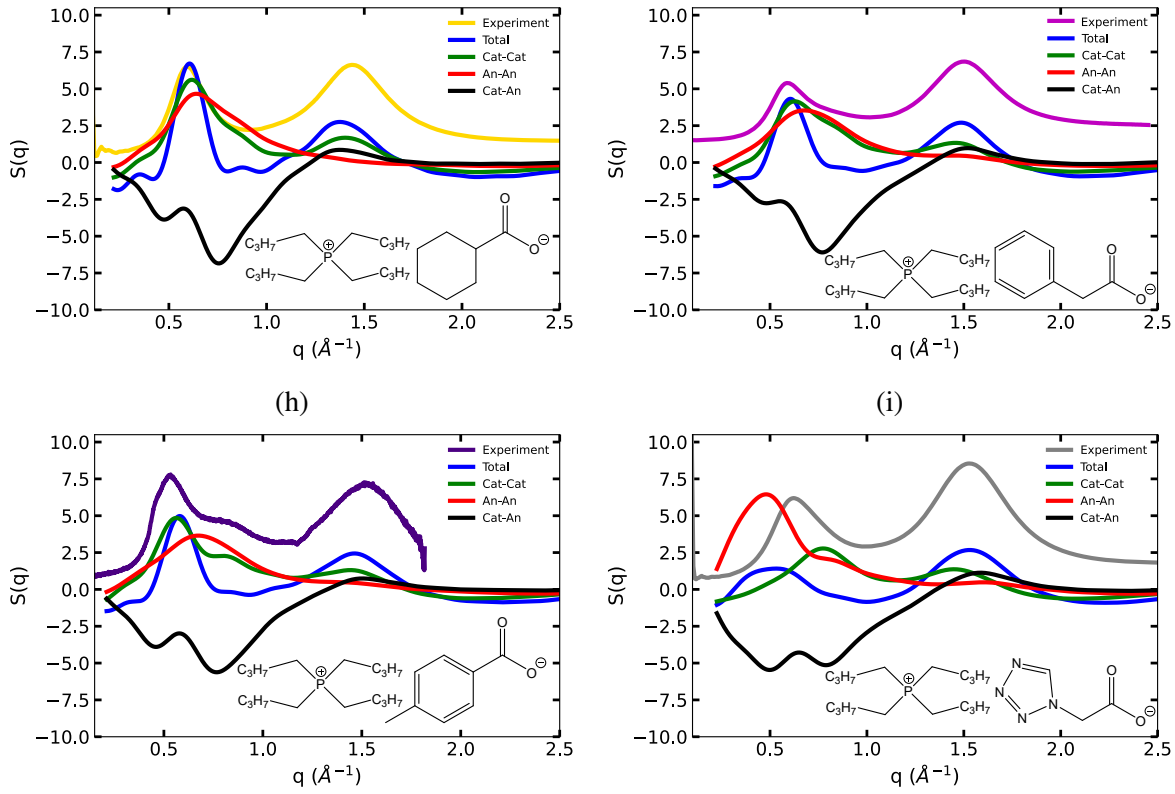

Figure S14 – Comparison of experimental with the total simulated S(q) as well as the partial S(q) for (a) $[P_{4,4,4,4}][C_1COO]$, (b) $[P_{4,4,4,4}][C_5COO]$, (c) $[P_{4,4,4,4}][C_{11}COO]$, (d) $[P_{6,6,6,14}][C_{11}COO]$, (e) $[P_{4,4,4,4}][MeC_3COO]$, (f) $[P_{4,4,4,4}][Me_4C_4COO]$, (g) $[P_{6,6,6,14}][Me_4C_4COO]$, (h) $[P_{4,4,4,4}][c-C_6COO]$, (i) $[P_{4,4,4,4}][PhC_1COO]$, (j) $[P_{4,4,4,4}][p-MeBzCOO]$ and (k) $[P_{4,4,4,4}][TetrazC_1COO]$.

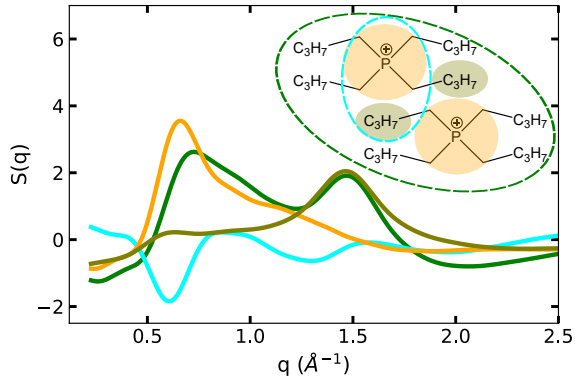
S(q)
q (Å^{-1})
C_3H_7

(a)

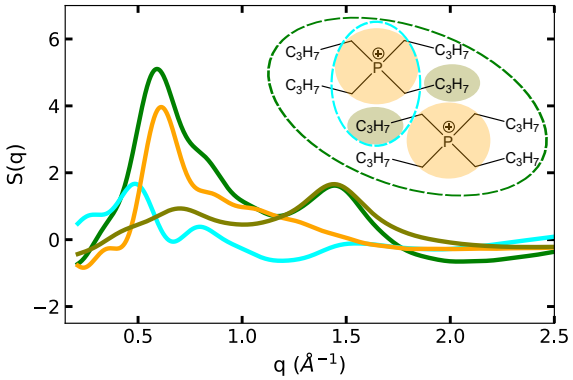
S(q)
q (Å^{-1})
C_3H_7

(b)

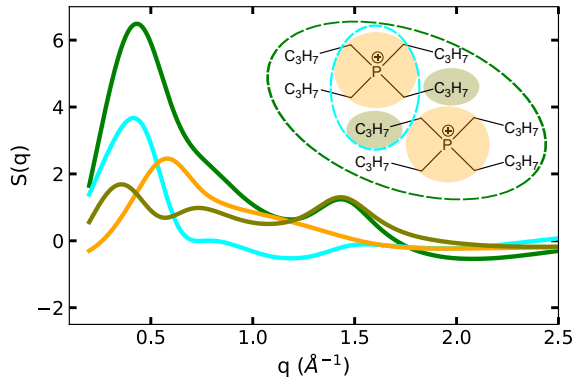
S(q)
q (Å^{-1})
C_3H_7

(c)

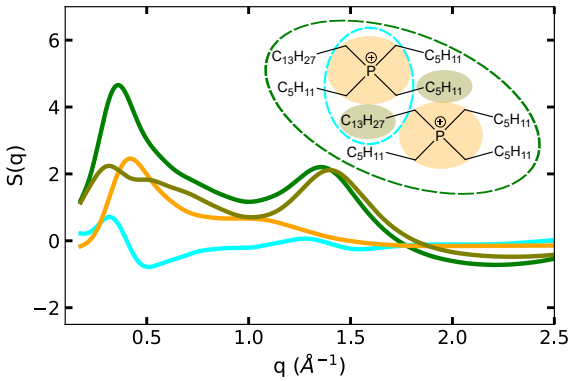
S(q)
q (Å^{-1})
$C_{13}H_{27}$
C_5H_{11}

(d)

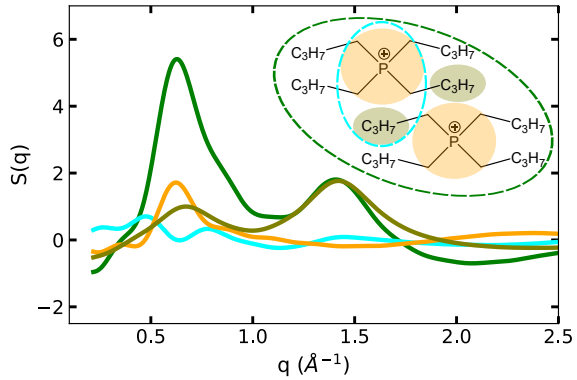
S(q)
q (Å^{-1})
C_3H_7

(e)

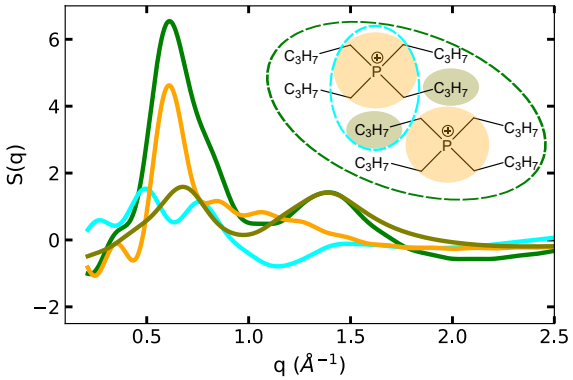
S(q)
q (Å^{-1})
C_3H_7

(f)

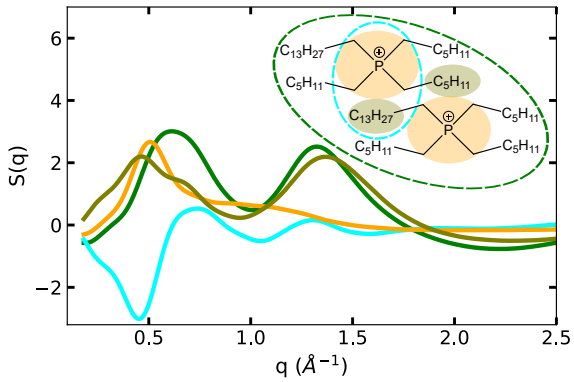
S(q)
q (Å^{-1})
$C_{13}H_{27}$
C_5H_{11}

(g)

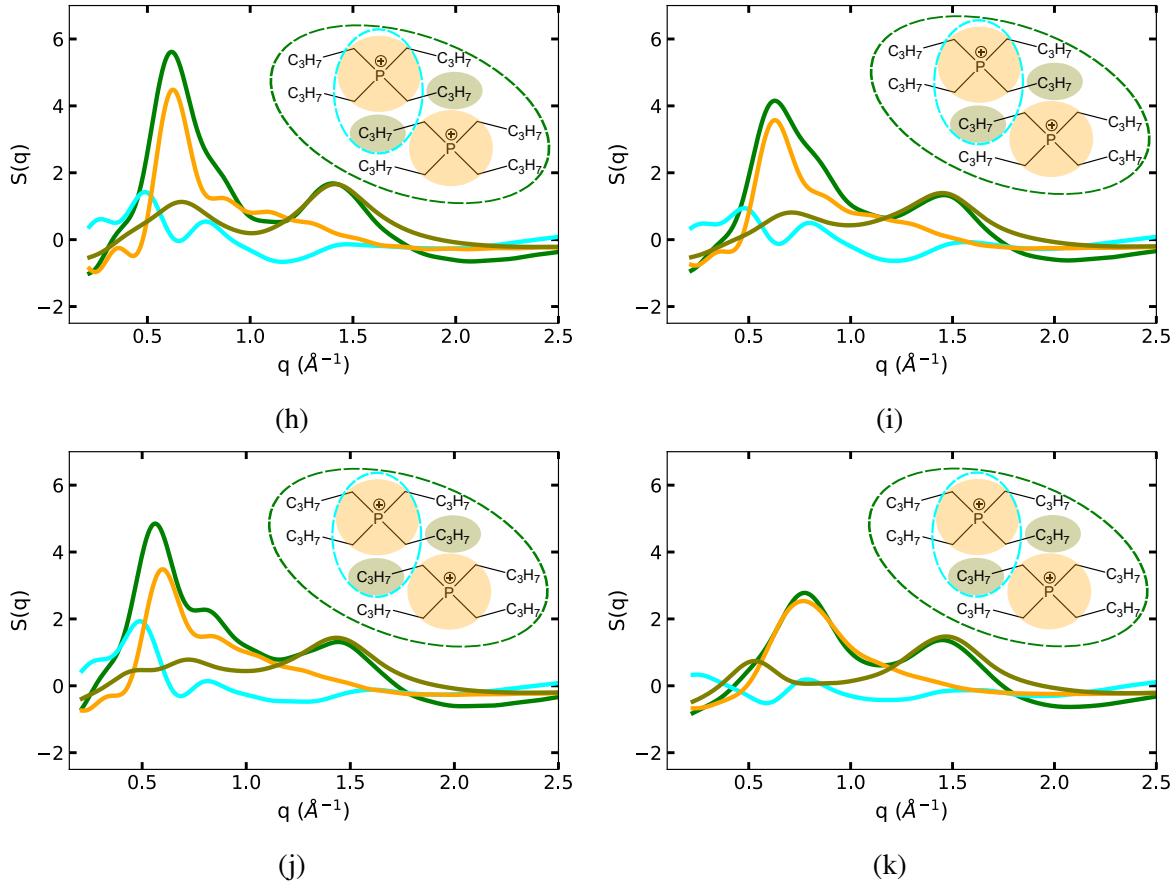

Figure S15 – Cation-cation partial S(q) split into head-tail, head-head and tail-tail components for (a) $[P_{4,4,4,4}][C_1COO]$, (b) $[P_{4,4,4,4}][C_5COO]$, (c) $[P_{4,4,4,4}][C_{11}COO]$, (d) $[P_{6,6,6,14}][C_{11}COO]$, (e) $[P_{4,4,4,4}][MeC_3COO]$, (f) $[P_{4,4,4,4}][Me_4C_4COO]$, (g) $[P_{6,6,6,14}][Me_4C_4COO]$, (h) $[P_{4,4,4,4}][c-C_6COO]$, (i) $[P_{4,4,4,4}][PhC_1COO]$, (j) $[P_{4,4,4,4}][p-MeBzCOO]$ and (k) $[P_{4,4,4,4}][TetrazC_1COO]$.

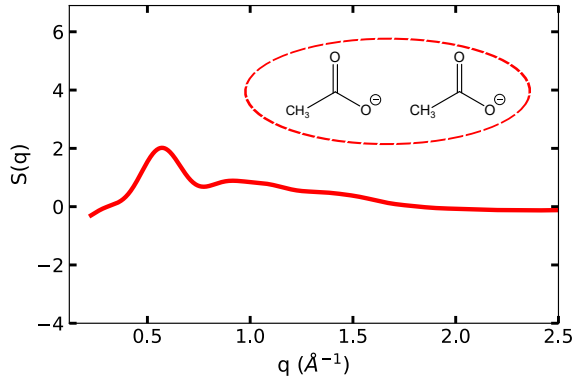

(a)

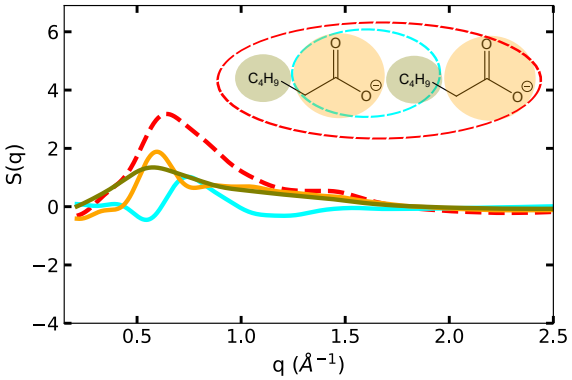

(b)

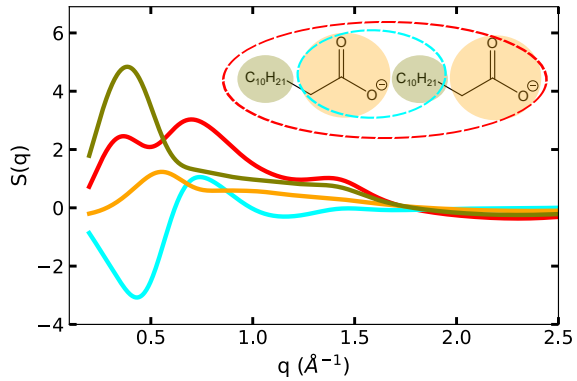

(c)

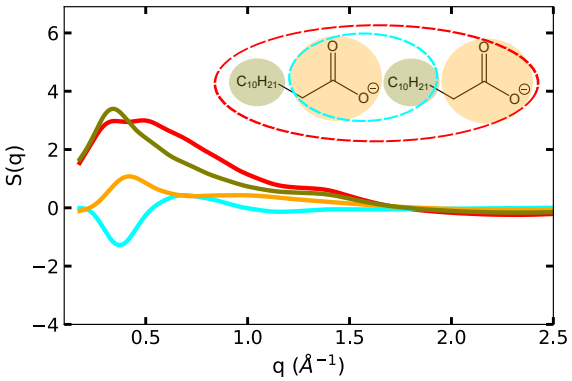

(d)

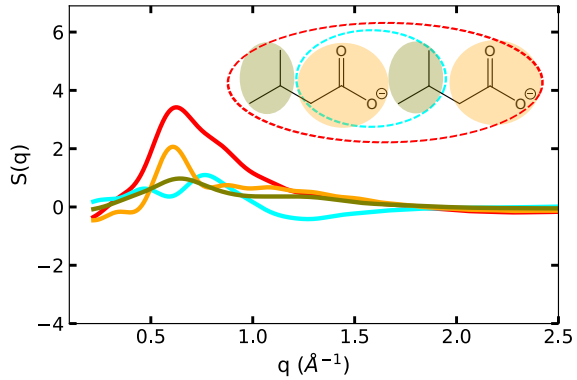

(e)

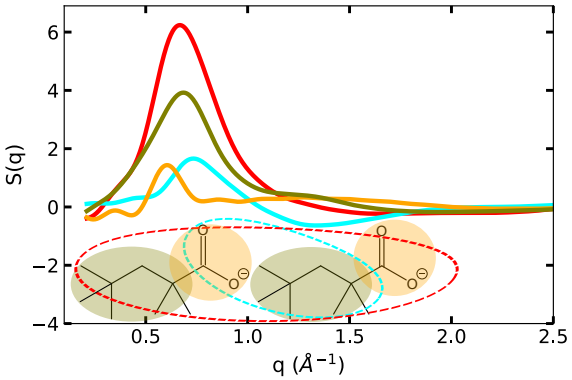

(f)

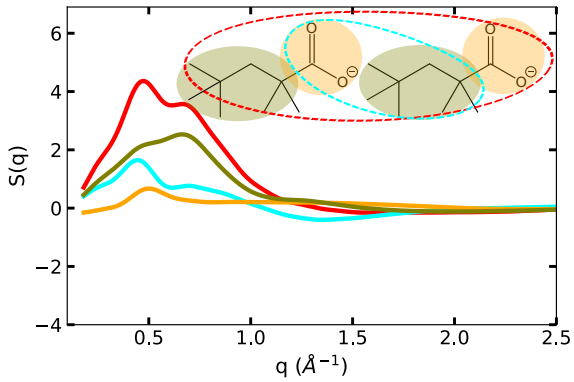

(g)

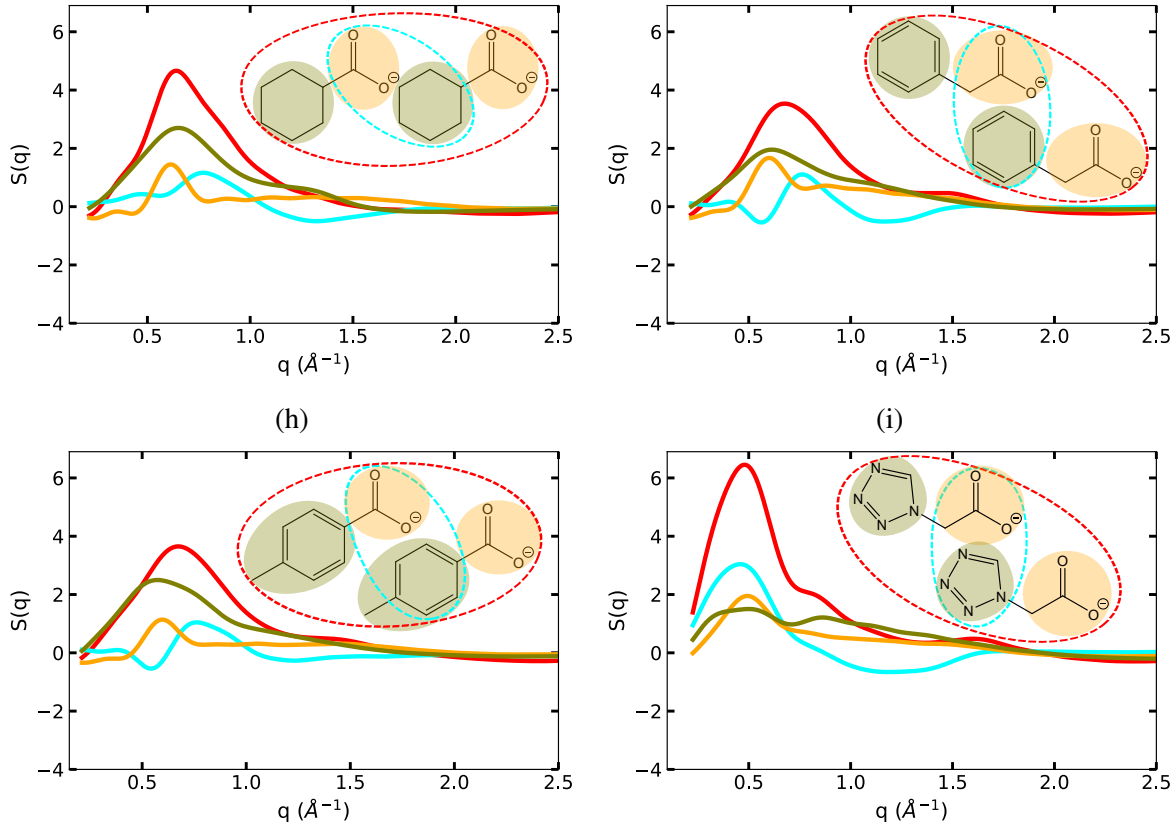

Figure S16 – Anion-anion partial S(q) split into head-tail, head-head and tail-tail or ring-ring components as indicated in the graphs for (a) $[P_{4,4,4,4}][C_1COO]$, (b) $[P_{4,4,4,4}][C_5COO]$, (c) $[P_{4,4,4,4}][C_{11}COO]$, (d) $[P_{6,6,6,14}][C_{11}COO]$, (e) $[P_{4,4,4,4}][MeC_3COO]$, (f) $[P_{4,4,4,4}][Me_4C_4COO]$, (g) $[P_{6,6,6,14}][Me_4C_4COO]$, (h) $[P_{4,4,4,4}][c-C_6COO]$, (i) $[P_{4,4,4,4}][PhC_1COO]$, (j) $[P_{4,4,4,4}][p-MeBzCOO]$ and (k) $[P_{4,4,4,4}][TetrazC_1COO]$.

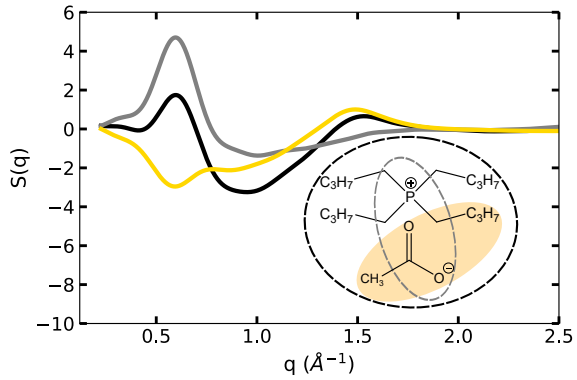
S(q)
q (Å^{-1})
C_3H_7
CH_3

(a)

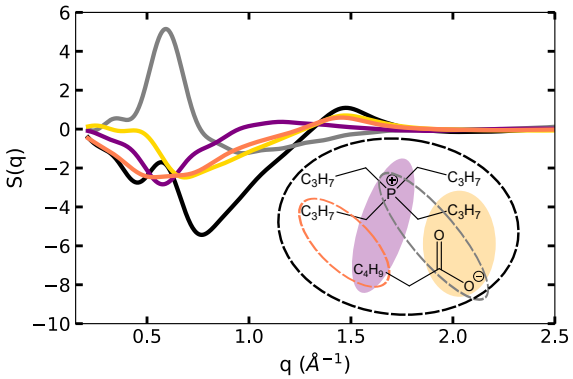
S(q)
q (Å^{-1})
C_3H_7
C_4H_9

(b)

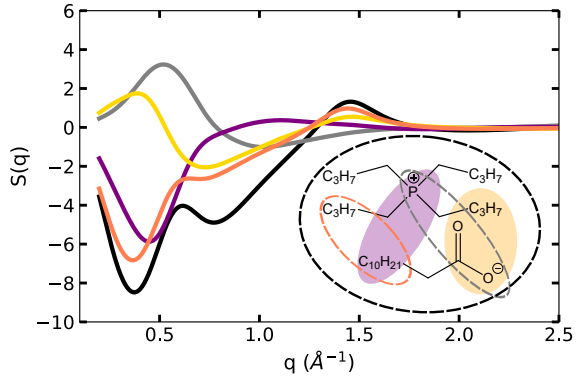
S(q)
q (Å^{-1})
C_3H_7
$C_{10}H_{21}$

(c)

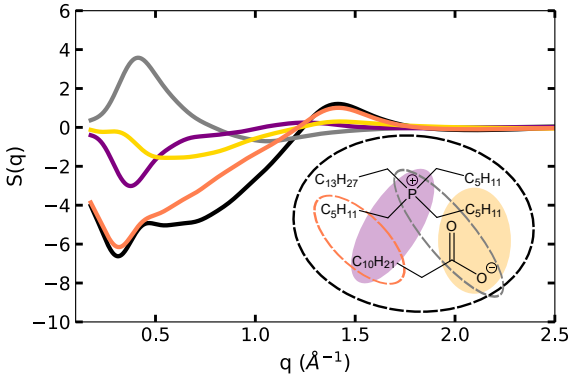
S(q)
q (Å^{-1})
$C_{13}H_{27}$
C_5H_{11}
$C_{10}H_{21}$

(d)

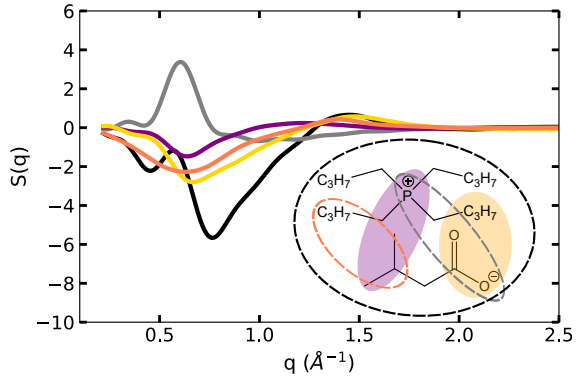
S(q)
q (Å^{-1})
C_3H_7

(e)

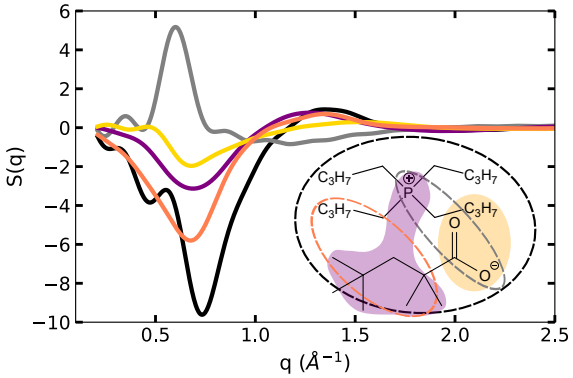
S(q)
q (Å^{-1})
C_3H_7

(f)

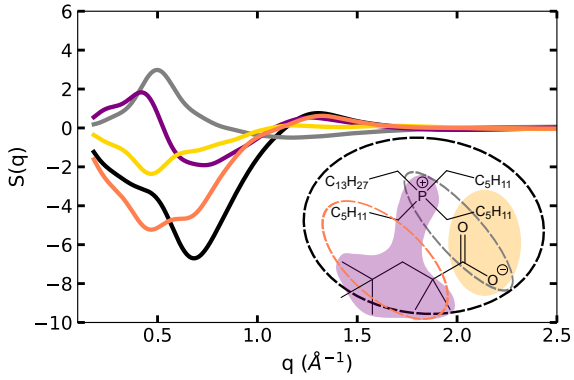
S(q)
q (Å^{-1})
$C_{13}H_{27}$
C_5H_{11}

(g)

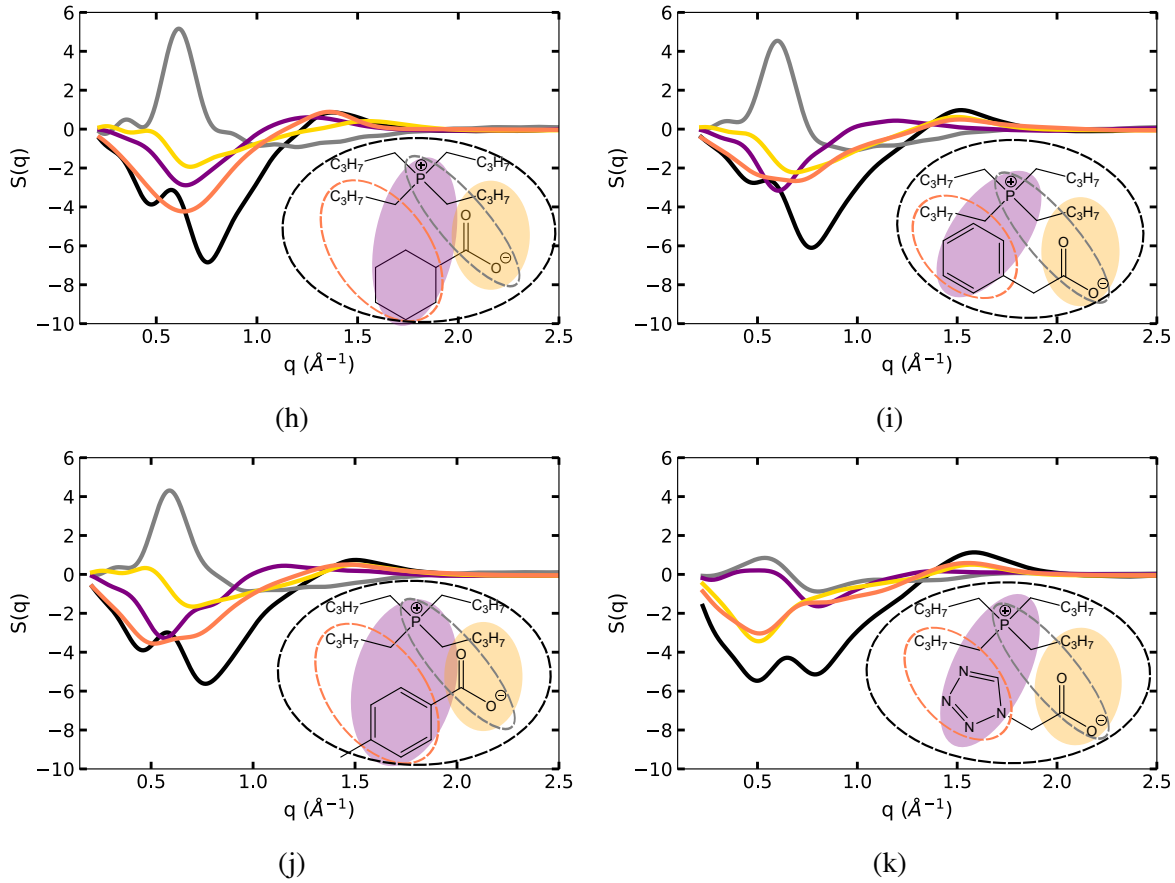

Figure S17 – ■ Cation-anion partial S(q) split into ■ cation head-anion head, ■ cation head-anion ring/tail, ■ cation tail-anion head and ■ cation tail-anion ring/tail components for (a) $[P_{4,4,4,4}][C_1COO]$, (b) $[P_{4,4,4,4}][C_5COO]$, (c) $[P_{4,4,4,4}][C_{11}COO]$, (d) $[P_{6,6,6,14}][C_{11}COO]$, (e) $[P_{4,4,4,4}][MeC_3COO]$, (f) $[P_{4,4,4,4}][Me_4C_4COO]$, (g) $[P_{6,6,6,14}][Me_4C_4COO]$, (h) $[P_{4,4,4,4}][c{-}C_6COO]$, (i) $[P_{4,4,4,4}][PhC_1COO]$, (j) $[P_{4,4,4,4}][p{-}MeBzCOO]$ and (k) $[P_{4,4,4,4}][TetrazC_1COO]$.

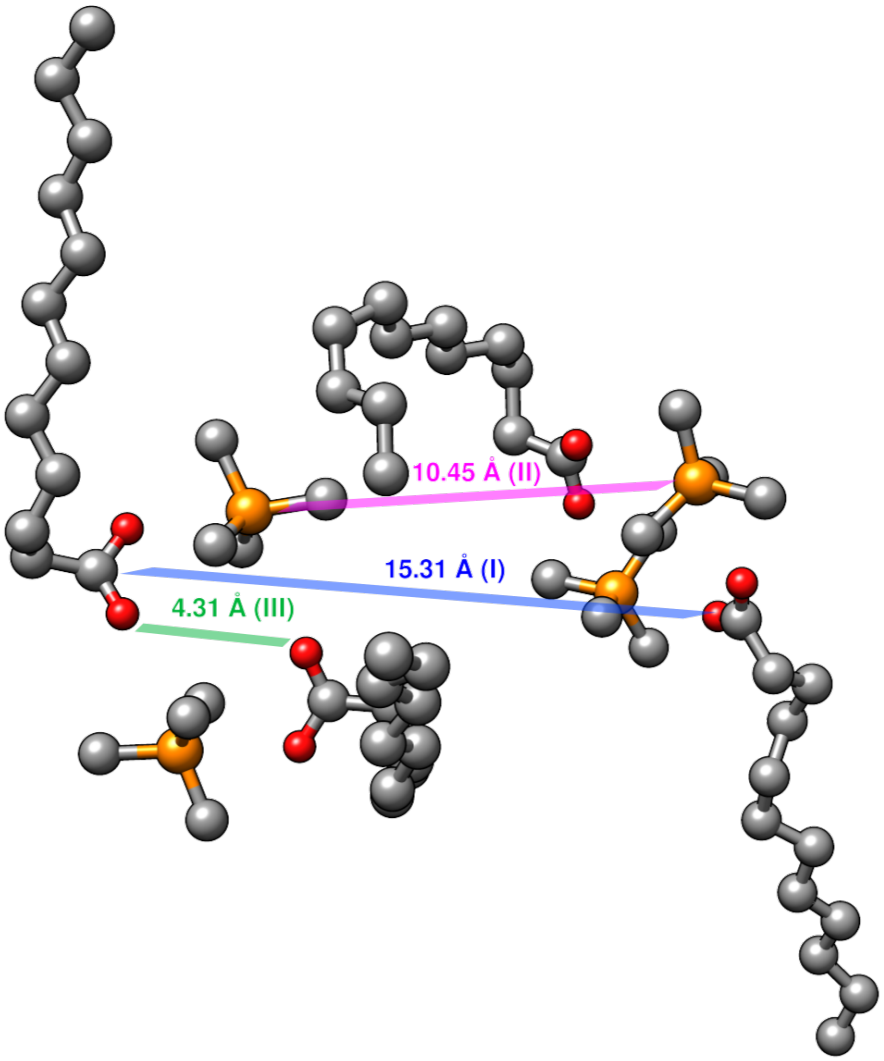

Figure S18 – Snapshot from the $[P_{4,4,4,4}][C_{11}COO]$ molecular simulation box illustrating the three different domains and their size observed by SAXS experiments.

References

(1) Avila, J.; Lepre, L. F.; Santini, C. C.; Tiano, M.; Denis-Quanquin, S.; Szeto, K. C.; Padua, A. A. H.; Gomes, M. C. High-Performance Porous Ionic Liquids for Low-Pressure CO2 Capture. *Angew. Chem. Int. Ed.* **2021**, *60*, 12876–12882.

(2) Jacquemin, J.; Ge, R.; Nancarrow, P.; Rooney, D. W.; Costa Gomes, M. F.; Pádua, A. A. H.; Hardacre, C. Prediction of Ionic Liquid Properties. I. Volumetric Properties as a Function of Temperature at 0.1 MPa. *J. Chem. Eng. Data* **2008**, *53*, 716–726.

(3) Zhou, Q.; Song, Y.; Yu, Y.; He, H.; Zhang, S. Density and Excess Molar Volume for Binary Mixtures of Naphthenic Acid Ionic Liquids and Ethanol. *J. Chem. Eng. Data* **2010**, *55*, 1105–1108.

(4) Zhao, N.; Menegolla, H. B.; Degirmenci, V.; Wagner, Z.; Bendová, M.; Jacquemin, J. Group Contribution Method for Evaluation of Volumetric Properties of Ionic Liquids Using Experimental Data Recommended by Mathematical Gnostics. *Ind. Eng. Chem. Res.* **2017**, *56*, 6827–6840.

(5) Deng, Y.; Morrissey, S.; Gathergood, N.; Delort, A.-M.; Husson, P.; Costa Gomes, M. F. The Presence of Functional Groups Key for Biodegradation in Ionic Liquids: Effect on Gas Solubility. *ChemSusChem* **2010**, *3*, 377–385.

(6) Fillion, J. J.; Xia, H.; Desilva, M. A.; Quiroz-Guzman, M.; Brennecke, J. F. Phase Transitions, Decomposition Temperatures, Viscosities, and Densities of Phosphonium, Ammonium, and Imidazolium Ionic Liquids with Aprotic Heterocyclic Anions. *J. Chem. Eng. Data* **2016**, *61*, 2897–2914.

(7) Pena, C. A.; Soto, A.; King, A. W. T.; Rodríguez, H. Improved Reactivity of Cellulose via Its Crystallinity Reduction by Nondissolving Pretreatment with an Ionic Liquid. *ACS Sustain. Chem. Eng.* **2019**, *7*, 9164–9171.

Part II

ABSORPTION OF ACID GASES

4

REVERSIBLE AND SELECTIVE SO_2 ABSORPTION BY $[P_{4,4,4,4}][TETRAZC_1COO]$

Context

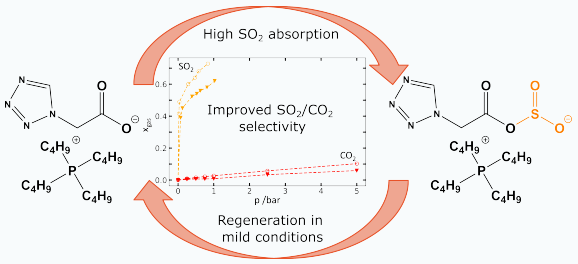

This chapter is focused on $[P_{4,4,4,4}][TetrazC_1COO]$ which was not only depicting peculiar anion-anion interactions, but also a promising ideal selective absorption of SO_2 over CO_2. It has been initially noticed that this IL was not able to react with CO_2, but it was able to reversibly react with SO_2. The IL regeneration was possible in relatively mild conditions which is essential for its applicability.

NMR measurements did not permit to identify the products of reaction with SO_2 as only shifts of the signals were noticed. It nonetheless permits to find that the absorption of CO_2 was fluidifying the IL and the effect was even more important with SO_2. This is a major advantage compared to other ILs suffering from a high increase of viscosity upon absorption of these two gases.

Infrared spectroscopy permitted to elucidate the SO_2 absorption mechanism which is different compared to what was reported for the absorption of CO_2 by phosphonium carboxylate ILs. The absorption isotherms permit to determine the equilibrium constants (K_{eq,SO_2}) and the Henry's law constants (K_{H,SO_2}) assuming a 1:1 stoichiometry. The variation with temperature of the associated gas absorption thermodynamic properties of the reaction.

Molecular dynamics simulations with or without the presence of SO_2 and CO_2 helped to identify the main solvation sites, located preferentially around the negatively charge head of the anion. The peculiar structure of $[P_{4,4,4,4}][TetrazC_1COO]$ provides a second interacting site at the vicinity of the nitrogen atoms.

The energy profile of reaction of $[P_{4,4,4,4}][TetrazC_1COO]$ with both gases were determined by DFT calculations to have a better understanding of the thermodynamics lying behind its reactivity. Another *ab initio* method was used to compute the total interaction energies between $[P_{4,4,4,4}][TetrazC_1COO]$ and up to 5 SO_2 molecules. They were decomposed into electrostatic and dispersion components to have an insight on the chemical or physical absorption contributions.

ACS Sustainable Chemistry & Engineering

pubs.acs.org/journal/ascecg

Research Article

Improved Reversible and Selective SO_2 Absorption by a Stable Phosphonium Carboxylate Ionic Liquid

Nicolas Scaglione, Luke Wylie, Agilio Padua, and Margarida Costa Gomes*

Cite This: https://doi.org/10.1021/acssuschemeng.4c02659

Read Online

ACCESS | Metrics & More | Article Recommendations | Supporting Information

ABSTRACT: The ionic liquid tetrabutylphosphonium 1H-tetrazole-1-acetate, $[P_{4,4,4,4}][TetrazC_1COO]$, appears as promising for the selective and reversible absorption of SO_2 at low pressures and in the presence of CO_2. The ionic liquid reversibly reacts with SO_2 and to a minor extent with CO_2 as shown by high-pressure NMR analysis. High absorption capacities were measured for SO_2 at pressures below 1 bar using an isochoric saturation technique, the CO_2 being measured in a gravimetric microbalance. We could calculate one of the highest SO_2/CO_2 selectivity reported so far. Contrary to previously reported ionic liquids, the solutions have lower viscosities, as inferred by the diffusivities measured by NMR, than that of the pure absorbent—a clear advantage for practical usages. Molecular dynamics simulations using validated polarizable force fields allow for a molecular understanding of the physical absorption of both acidic gases and how they impact of the microscopic structure of the liquid. *Ab initio* calculations provide estimates of the energetics of chemical absorption in line with the experiments confirming that the regeneration of the absorbent can be done at mild conditions of temperature and pressure.

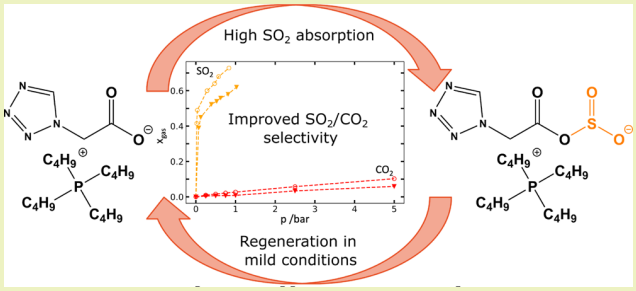

KEYWORDS: *Ionic liquid, gas absorption, SO_2, CO_2, desulfurization, solvent regeneration, chemisorption*

1. INTRODUCTION

Carbon dioxide (CO_2) and sulfur dioxide (SO_2) are acid gases produced during the combustion of fossil fuels or in various industrial processes. Their environmental impact can be diminished through the treatment of flue gases using selective scrubbers eventually allowing for the utilization of the captured gases as raw materials.

Absorption is unquestionably the most common process employed for gas separation and purification. It involves the transfer of a gas phase component into a liquid phase where it is soluble.[1] In some cases, reactions occur between the gaseous species and the liquid absorbent. These chemical processes are considered special cases of absorption, leading to increased gas capacities and selectivity. Moreover, an effective absorbent should facilitate easy regeneration and thus it is crucial to reduce the equilibrium constant and enthalpy of the chemical reaction between the gas and the liquid.

Ionic Liquids (ILs) emerge as promising absorbents for both CO_2 and SO_2 being able to dissolve at 298 K and 1 bar 0.1 and 0.5 mole fraction of gas, respectively.[2] The higher solubility of SO_2 can be explained by its higher polarity and acidity that are linked with more favorable interactions with the ILs. Chemisorption is used to further improve the gas capacity and selectivity either by carefully selecting cations and anions in the IL or by modifying their molecular structure. Gas absorption can then increase to reach mole fractions of 0.6 and 0.8 of CO_2 and SO_2 at 298 K and 1 bar, respectively.[2]

Different strategies have been reported to enhance CO_2 chemisorption in ILs through the careful design of suitable salts with high capacity and low energy requirements, both for gas capture and sorbent regeneration.[3] The first reported IL capable of chemically reacting with CO_2 was based on an amino-functionalized imidazolium salt capable of absorbing the gas following a 1:2 stoichiometry in a reaction mechanism similar to the well-known aqueous amine system.[4] Subsequently, reaction mechanisms were proposed through amine functionalized[5] or amino acid−based anions[6] approaching 1:1 stoichiometry and even 1.5:1 when functionalizing both the cation and the anion with reactive amino groups.[7] Similar results have been reported for protic ILs prepared from the neutralization of a superbase with weak proton donors such as imidazole or phenol.[8] Nonamino anion-functionalized ILs constitute a promising group of chemisorbents allowing for the tuning of CO_2 absorption through the molecular structure and basicity.[3]

The presence of other components such as water, SOx and NOx can impact the capture of CO_2 by the different ILs.

Received: March 29, 2024
Revised: June 10, 2024
Accepted: June 11, 2024

ACS Sustainable Chemistry & Engineering pubs.acs.org/journal/ascecg Research Article

Chemisorption of SO_2 can occur through favorable chemical reactions with the cation[9,10] or the anion[11,12] of the ILs leading to difficult absorbent regeneration. By embedding electron-withdrawing moieties,[13,14] such as carbonyl groups,[15] in the IL anion, the enthalpy of the absorption reaction can be reduced, but this approach is less efficient for anions with low basicity.[16] The presence of an electron-withdrawing group also reduces CO_2 absorption capacity by allowing for the negative charge to be distributed over the anion.[12] Nevertheless, even when introducing a halogen group on a carboxylate anion, SO_2 desorption could only achieved by the IL at relatively high temperatures (393 K for 30 h), highlighting the need to moderate the absorption enthalpy in order to improve reversibility.[17]

When imidazolium acetate ILs are used as absorbents, a reduction in CO_2 uptake in the presence of SO_2 has been observed over a few cycles of absorption and desorption.[18] This has been attributed to the reduction of available absorption sites for CO_2 as SO_2 reacts irreversibly with the acetate anion displacing CO_2. The reverse is not observed and so the concentration of SO_2 increases in the liquid absorbent making its downstream removal necessary especially when the basicity of the IL anion increases, and especially for superbase ILs.[19] This experimental observations have been corroborated by DFT calculations that appear as a useful tool to screening and designing the best ILs as sorbents.[20]

Some of these ILs have a high absorption capacity for SO_2 but their practical use is hindered by difficult and energy-intensive regeneration steps. For example, while tetraalkylphosphonium superbase ILs can capture up to 4.8 mol of SO_2 per mole of IL at 293 K and 1 bar, the complete reverse reaction is not observed at high temperature (353 to 393 K) nor under N_2 stripping,[15,21] pointing again toward the importance of controlling the enthalpy of absorption and the equilibrium constant of the reaction when designing ILs as absorbers.

Inspired by recent studies that reported the promising behavior of tetraalkylphosphonium carboxylate ILs for the capture of CO_2,[22] we aim in this work to carefully choose a low basicity anion and propose an IL with improved selective absorption and capacity toward acid gases such as SO_2 and CO_2. The present study focuses on the previously characterized tetrabutylphosphonium 1H-tetrazole-1-acetate, $[P_{4,4,4,4}][TetrazC_1COO]$, whose anion is derived from the tetrazole-5-carboxylic acid with a pK_a of 2.67 in water. We use a variety of experimental and computational methods to understand the interactions and reaction mechanisms of the liquid salt in the presence of SO_2 or CO_2.

2. EXPERIMENTAL METHODS

2.1. Materials. The tetrabutylphosphonium 1H-tetrazole-1-acetate ionic liquid, abbreviated as $[P_{4,4,4,4}][TetrazC_1COO]$, was synthesized and characterized as described previously.[23] Its chemical structure is reported in Figure 1. Carbon dioxide 4.5 (99.995% pure) and sulfur dioxide 4.0 (99.99% pure) were both purchased from Air Liquide, France. All gases were used as supplied without further purification.

2.2. Gas Absorption Measurements. The absorption of SO_2 in $[P_{4,4,4,4}][TetrazC_1COO]$ was measured using an *in-house* built apparatus based on an isochoric saturation method, that was described in a previous work.[24] The experiments were carried out under a fume hood up to approximately 1 bar, at five different temperatures in the range 303 to 343 K.

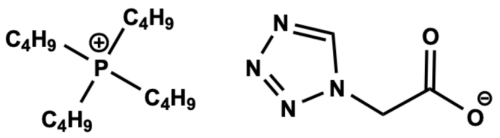

Figure 1. Chemical structure of the IL studied. This salt was was prepared from the corresponding carboxylic acid with a pK_a in water of 2.67 and has a melting point T_m = 9.1 °C and a decomposition temperature T_{dec} = 291 °C.[23]

A glass bulb with a volume V_{bulb} (precisely calibrated) is filled with SO_2 at a known temperature and pressure (T_{ini}, P_{ini}), allowing the determination of the quantity of gas. Prior to the measurement the IL is dried under vacuum (1×10^{-4} bar) and is then introduced in the equilibrium cell (with precisely calibrated volume) and degassed again for 4 h to ensure that no dissolved gas or water remain in the liquid. After the degassing step, the SO_2 is brought in contact with the dried IL and the pressure and temperature are recorded. Once equilibrium is reached, the temperature and pressure (T_{eq}, P_{eq}) are used to calculate the SO_2 solubility in the IL. The quantity of IL introduced in the cell (n_{IL}) is determined gravimetrically with a precision of ± 0.1 mg and its volume (V_{IL}) is obtained from its density, assuming that it does not change significantly upon SO_2 dissolution. The quantity of gas absorbed by the IL ($n_{SO_2}^{IL}$) is obtained from the difference of the two measurements:

$$n_{SO_2}^{IL} = \frac{P_{ini}V_{bulb}}{RT_{ini}Z_{SO_2}(P_{ini}, T_{ini})} - \frac{P_{eq}(V_{tot} - V_{IL})}{RT_{eq}Z_{SO_2}(P_{eq}, T_{eq})} \quad (1)$$

with V_{tot} the total volume of the cell and Z_{SO_2} the SO_2 compressibility factor calculated from the second virial coefficient.[25]

Carbon dioxide absorption was measured using a sorption balance (IGA001) from Hiden Analytical. The experiments were carried out in the range 0.25 to 5 bar, at 303, 323 and 343 K following the procedure previously described.[26]

The measurement proceed along isotherms. At each pressure, the mass of the sample is measured once equilibrium criteria are reached: the samples were kept in contact with the gas for a least 3 h and up to 15 h, at each pressure; the minimum weight change for real-time analysis was set at 1 μg, with the end point set up at 99.5% relaxation (each pressure step along an isotherm is fitted using an exponential decay); the target interval for weight acquisition was set at 1 μg and the acceptable average deviation of the fitted exponential from the acquired data was 7 μg. The raw weight data ($m_{reading}$) is corrected after a blank measurement and for the buoyancy of the gas as reported previously:[26]

$$m_{reading} = m_0 + m_s + m_g + m_g^{EP} - \sum_i \frac{m_i}{\rho_i}\rho_g(T_i, p) + \sum_j \frac{m_j}{\rho_j}\rho_g(T_j, p) - \frac{m_s}{\rho_s(T_s)}\rho_g(T_s, p) \quad (2)$$

where m_g is the mass of gas absorbed by the liquid sample, m_s is the mass of degassed sample and m_g^{EP} is the mass of adsorbed gas on the balance components (EP stands for empty pan). The two sums over *i* and *j* represent the buoyancy effects on the sample and counterweight components of the balance, respectively.

2.3. NMR Measurements. A 400 MHz Bruker Avance III spectrometer, with a broadband probe BBO equipped with a temperature control unit BCU II, was used to collect NMR spectra at 343 K, namely ^1H, ^{13}C, ^{31}P, Correlated Spectroscopy (COSY) and Heteronuclear Single Quantum Correlation (HSQC), Two-dimensional (2D) $^1H-^1H$ Overhauser effect spectroscopy (NOESY), as well as self-diffusion coefficients determined by Diffusion Ordered Spectroscopy (DOSY).

Spectra were collected in samples of $[P_{4,4,4,4}][TetrazC_1COO]$ after degassing before and after exposure to SO_2. The SO_2 exposed samples were also studied after equilibration with 15 bar of CO_2 at 343 K in a

https://doi.org/10.1021/acssuschemeng.4c02659
ACS Sustainable Chem. Eng. XXXX, XXX, XXX−XXX

ACS Sustainable Chemistry & Engineering pubs.acs.org/journal/ascecg Research Article

high pressure NE-HP10-M Pyrex NMR tube (thickness 1 mm, rated to 20 bar). C_6D_6 sealed in a glass capillary was inserted in the tube to act as an internal reference.

$^1H-^1H$ NOESY experiments were conducted with a relaxation delay ($D1$) of 4 s at short mixing times, ranging from 10 to 600 ms, so that the initial rate approximation (IRA) could be applied.[27] The integrated intensities of the NOE cross-peaks were corrected by multiplying them by $(N_{Ha} + N_{Hb})/(N_{Ha} \times N_{Hb})$. This correction accounts for the involvement of multiple protons in each cross-peak, where N_{Ha} and N_{Hb} represent the number of equivalent protons contributing to the observed NOE cross-peak.

2.4. Infrared Spectroscopy. Infrared (IR) spectroscopy was used to characterize the neat IL before and after SO_2 and CO_2 absorption, and also to check for the presence of water. The IR spectra were obtained in the attenuated total reflection mode (ATR) using a PerkinElmer Spectrum 65 FT-IR spectrometer. A droplet of the IL was placed on the ATR crystal and the measurements were carried out in the wavenumber range 550 to 4000 cm^{-1} accumulating scans with a resolution of 2 cm^{-1}.

2.5. Thermal Analysis. Thermogravimetric analysis (TGA) was used to determine the long-term thermal stability of the IL. The measurements were performed on a Setaram Labsys Evo TG DTA DSC+ 1600 °C under O_2 atmosphere. Samples of 20 to 40 mg were weighed in 100 μL^{-1} aluminum oxide crucibles. Prior to the measurements, the samples were heated to 80 °C and placed under vacuum for 30 min to eliminate eventual traces of water. Then, the samples were submitted to isotherms in the range 130 to 190 °C every 10 °C for 5 h.

3. COMPUTATIONAL METHODS

3.1. Molecular Dynamics Simulations. Molecular dynamics (MD) simulations were carried out to study the impact of CO_2 and SO_2 on the IL microscopic structure as well as their solvation of SO_2 in the IL. They were performed using the polarizable CL&Pol force field for ionic liquids,[28,29] which is based on the Drude induced-dipole method, following similar procedures as described previously.[23] MD simulations of periodic cubic boxes containing 300 ion pairs of the pure ionic liquids, and either 30 CO_2 or 300 SO_2 molecules, were performed using the OpenMM code.[30] Initial configurations were generated using the fftool[31] and Packmol[32] utilities. The systems were equilibrated for 2 ns with a Langevin dual thermostat and barostat, followed by 20 ns production runs using specific Nosé–Hoover integrators for force fields with Drude induced dipoles. A temperature of 343 K was chosen while pressure was kept at 1 bar.

The TRAVIS[33] trajectory analysis package was used to compute site–site radial distribution functions (RDF), spatial distribution functions (SDF) and combined distribution functions (CDF).

The explicit introduction of polarization terms to the force field lead to a slight underestimation of the calculated densities of ILs.[28] In order to correct this systematic deviation, the Lennard-Jones atomic diameters (LJ σ) factor has been scaled to 0.985 for most ILs, but with phosphonium-carboxylate ILs it was necessary to use a slightly more significant correction, likely due to the prevalence of alkyl chains. Thus, σ has been scaled by a factor 0.95 in order to correct the systematic underestimation of densities while keeping the constancy and transferability of the model.[23]

The distance between the centers of mass of the fragments, the geometric parameters, the atomic partial charges of molecules and ions, as well as the dipole moments of fragments were taken taken either from the CL&Pol force field[28] or from a previous study in which the missing parameters for the phosphonium carboxylate ILs under study were determined.[23] Only the distance between the centers of mass of CO_2 and SO_2 and the various fragments of $[P_{4,4,4,4}][TetrazC_1COO]$ have been calculated through a geometry optimization using dispersion-corrected density functional theory (DFT-D3)[34] at the B97-D3/cc-pVDZ level (Table S8).

CO_2 was represented by a polarizable version of the Transferable Potentials for Phase Equilibria (TraPPE) force field used to simulate adsorption in MOF materials[35] by scaling the Lennard-Jones energy parameters with respect to their atomic polarizabilities. SO_2 was represented by a model derived from the TraPPE force field parameter set.[36]

3.2. *Ab Initio* Calculations. The energy profiles of the reactions between the IL and either CO_2, SO_2 or a mixture of the two gases were calculated using density functional theory (DFT). The IL was represented by either one or two explicit ion pairs depending on the reaction mechanism. One SO_2 or CO_2 molecule was added in the vicinity of the IL pair in order to generate the initial configuration. Then, the configuration of the following steps were built based on the previous step.

A preoptimization was carried out at each step using the Conformer–Rotamer Ensemble Sampling Tool (CREST),[37] which is a metadynamics-based search algorithm, in order to generate an initial set of 9 conformers. Then, geometry optimizations were performed with Gaussian 16[38] using the M06-2X functional[39] with the cc-pVDZ basis set.[40] Solvent effects were represented by a conductor-like polarizable continuum model (CPCM) with the permittivity of n-octanol. Frequency calculations were made at the same level of theory while single-point energy (SPE) calculations were made with the more extended aug-cc-pVTZ[41] basis set. The enthalpy (H) and the Gibbs free energy (G) of each system were calculated from[42]

$$H = E + ZPVE + E_{TC} \quad (3)$$

$$G = H - TS \quad (4)$$

where E is the electronic energy, $ZPVE$ is the zero point vibrational energy, E_{TC} is the temperature correction,[43] and S the entropy. The quantities S and E_{TC} were calculated with a thermochemistry code[44] at 343 K using the harmonic oscillator approximation. Boltzmann distributions of H and G for the 9 optimized configurations were used to determine the final enthalpy and free energy values for each system.

The CM5 (Charge Model 5) algorithm,[45] based on a Hirshfeld charge scheme,[46] was employed to calculate the partial atomic charges of the most stable conformer for each step using the PBE0 Double Hybrid (PBE0-DH) functional with the cc-pVDZ basis set.[47] Highest occupied molecular orbitals (HOMOs) were also determined for the lowest energy conformer of each IL based on geometry optimization made for the energy profile determination considering a 1:1 stoichiometry (IL:SO_2). Checkpoint files were converted to cube files with a grid size of 80.

Interaction energies between one pair of IL and SO_2 were calculated using the spin ratio scaled Møller-Plesset second-order perturbation theory (SRS-MP2)/cc-pVTZ[48] method. The energies were calculated using the following Equation:

$$E_{int} = E_{IL:SO_2} - (E_{IL} + E_{SO_2}) \quad (5)$$

The Hartree–Fock (HF) contribution to the total interaction energy was calculated with the cc-pVQZ[40] basis set and was corrected with the Boys and Bernardi counterpoise correction to compensate the basis set superposition error.[49] The HF contribution accounts for the electrostatic component while the SRS-MP2 electron correlation was used to determine the dispersion contribution. The interaction energies were calculated between the ILs and up to 5 SO_2 molecules. The SO_2 molecules were added one by one to the system with the energies calculated by the difference with the previous system:

$$E_{int} = E_{IL:xSO_2} - (E_{IL:(x-1)SO_2} + E_{SO_2}) \quad (6)$$

4. RESULTS AND DISCUSSION

The absorptions of SO_2 and CO_2 in $[P_{4,4,4,4}][TetrazC_1COO]$, expressed in mole fraction, x_{gas}, and molality, b_{gas}, measured at temperatures between 303 to 343 K and at different pressures (up to approximately 1 bar for SO_2 and 5 bar for CO_2) are reported in Tables S1 and S3, respectively. Table 1 lists some typical values and in Figure 2 are depicted two of the absorption isotherms for each gas.

https://doi.org/10.1021/acssuschemeng.4c02659
ACS Sustainable Chem. Eng. XXXX, XXX, XXX–XXX

Table 1. SO_2 and CO_2 absorption in $[P_{4,4,4,4}][TetrazC_1COO]$ expressed as mole fraction, x_{gas}, and molality, b_{gas}, at different temperatures and pressures

T (K)	p (bar)	x_{gas}	b_{gas} (mmol g^{-1})
		SO_2	
303.45	0.2838	0.601	3.89
303.45	0.5752	0.675	5.38
303.46	0.8339	0.719	6.62
323.27	0.3381	0.562	3.32
323.28	0.6428	0.616	4.15
323.29	0.9350	0.667	5.19
343.14	0.3911	0.523	2.83
343.13	0.6241	0.544	3.08
343.13	1.0240	0.623	4.27
		CO_2	
303.12	0.2494	0.010	0.02
303.12	0.7480	0.022	0.06
303.22	0.9991	0.027	0.07
323.09	0.2492	0.007	0.02
323.12	0.7490	0.015	0.04
323.14	0.9991	0.018	0.05
343.06	0.2484	0.005	0.01
343.11	0.7488	0.007	0.02
343.13	0.9992	0.008	0.02

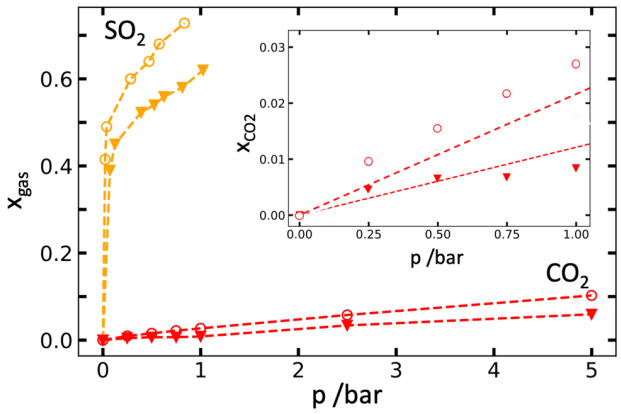

Figure 2. Gas absorption in $[P_{4,4,4,4}][TetrazC_1COO]$: yellow line, SO_2 absorption between 0 to 1 bar at yellow circle 303 K and yellow triangle 343 K; red line, CO_2 between 0 to 5 bar at red circle 303 K and red triangle 343 K. The insert is a zoom of the isotherms for CO_2 between 0 and 1 bar.

The shape of the absorption isotherms of SO_2 in Figure 2, with large deviations from Henry's law at low pressures, points toward a chemisorption of the gas. The mole fraction of SO_2 absorbed by $[P_{4,4,4,4}][TetrazC_1COO]$ is higher than 0.5 at very low partial pressures of the gas, indicating a different absorption mechanism from the 1:2 stoichiometry previously reported for CO_2 in carboxylate-based ionic liquids.[22,50] The isotherms in Figures 2 and S1 also show that SO_2 absorption decreases with increasing temperature, corresponding to an exothermal absorption of the gas. The variation of the gas absorption with temperature is more important at lower partial pressures of gas (chemisorption) than at pressures closer to 1 bar (physical absorption).

In order to identify the products of the chemical reaction, ^1H, ^{13}C and ^{31}P NMR spectra were recorded before and after the IL was exposed to SO_2. They are depicted in Figures S8–S10. No new signals were observed in the NMR spectra but shifts of the peaks after the absorption of the gas when compared with the pure IL are highlighted in Figure S8. The most significant changes appear in two peaks corresponding to two sites of the carboxylate anion, showing its dominant role in the SO_2 absorption process.[51] The signal corresponding to C_{COO^-} is shifted downfield from 166.10 to 168.21 ppm, opposite to what was previously reported, while the signal of the C_α of the anion is shifted upfield from 52.63 to 51.25 ppm, in agreement with the literature.[17,52,53]

FT-IR could thus be used to identify the reaction products as depicted in Figure 3 (supplementary details in Figure S4). The peak assignments were confirmed from quantum chemistry calculations. New bands at 1145 and 1324 cm^{-1} are identified and could be assigned to the symmetric and asymmetric stretching of the S = O bonds of the dissolved SO_2, respectively.[54] At 1353 and 1635 cm^{-1} appear characteristic symmetric and asymmetric vibrations of COO^-, observed in pure $[P_{4,4,4,4}][TetrazC_1COO]$ but absent after the IL has been exposed to SO_2. This confirms that the reaction takes place in the carboxylate group of the anion as depicted in Figure 4. The characteristic bands of the $[P_{4,4,4,4}]^+$ cation remain unchanged.

At 1736 cm^{-1}, the C═O vibration of the carboxyl group is observed in the solution with a blue shift of 101 cm^{-1} compared with that of the pure IL, identified as the COO – SO_2^- adduct formed.[55] New bands assignable to the SO_2^- bending and the $C^-OSO_2^-$ stretching in the adduct are identified at 628 and 952 cm^{-1}, respectively. Additionally, bands related to the symmetric and asymmetric stretching of SOO^- are present at 1047 and 1236 cm^{-1}, respectively.[56−60]

Visible in the spectrum depicted in Figure S4, there is a new signal at 2362 cm^{-1} attributed to the formation of hydrogen bonds between SO_2 and the IL as previously evidenced by the highlighted shifts of the peaks in the ^1H NMR spectrum of Figure S8 (top left). Therein, the peak of H_α of $[P_{4,4,4,4}]^+$ shifts upfield from 2.33 to 2.27, while all other signals related with the cation remain unchanged. This observation seems to contradict the expected deshielding effect of hydrogen bonds on protons but can be explained by the solvation of SO_2 around the O_{COO^-} site that decreases the interaction between the negatively charged headgroup of the anion and the H_α of the cation.[23] The signals related to the anion are shifted downfield, indicating a decrease in electron density, likely due to the electrophilic nature of the sulfur atoms interacting with the carboxylate anion.

By assuming a direct 1:1 nucleophilic addition of the carboxylate anion on SO_2 (Figure 4), the equilibrium constant K_{eq,SO_2} and Henry's law constant K_{H,SO_2} can be calculated from the experimental absorption isotherms using Equations S1 and S2. The resulting fits are depicted in Figure S1, and the calculated values are reported in Table S2. Our approach differs from other models previously reported to describe the isothermic SO_2 absorption in ILs that did not take into account the extent of the reaction chemical reaction. Thus the calculated Henry's law constants were often inaccurate since the composition of the solution significantly changes as the chemisorption of the gas proceeds.[55,61] Other models based on 1:1 or 2:1 stoichiometry have been suggested,[14] but when tested with our experimental data, non-physically sound results were calculated for the 2:1 reaction, further confirming the mechanism assumed herein.

https://doi.org/10.1021/acssuschemeng.4c02659
ACS Sustainable Chem. Eng. XXXX, XXX, XXX−XXX

ACS Sustainable Chemistry & Engineering pubs.acs.org/journal/ascecg Research Article

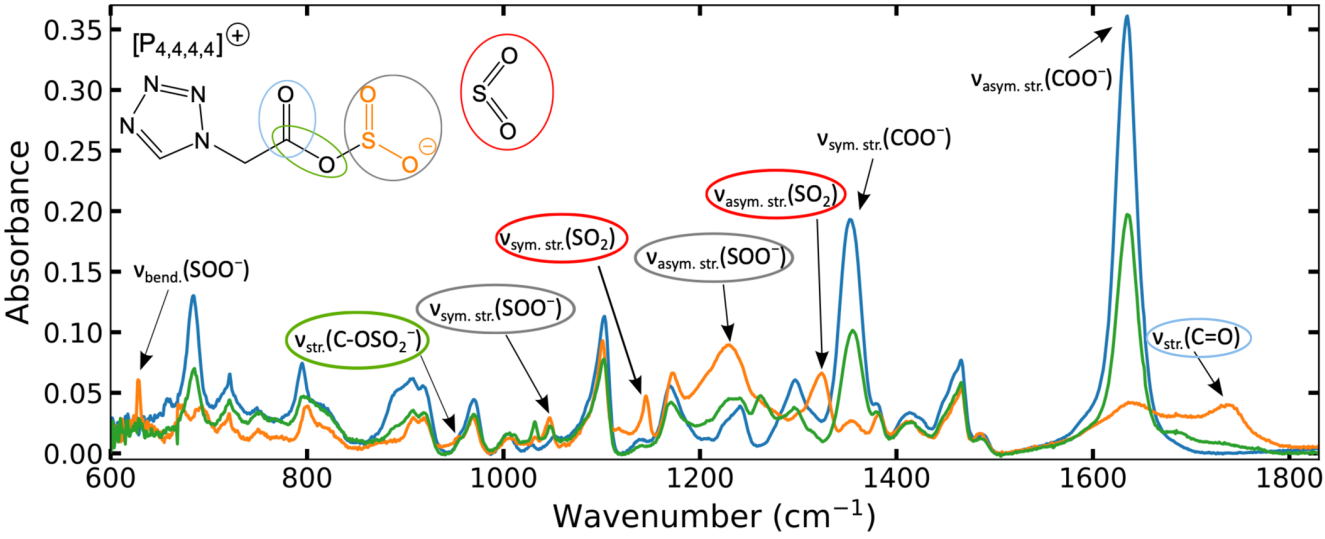

Figure 3. FT-IR spectra: orange line, pure $[P_{4,4,4,4}][TetrazC_1COO]$; blue line, IL after being exposed to SO_2; green line, IL exposed to SO_2 and subsequently regenerated under vacuum at 323 K for 2 h. Bands are assigned to the groups highlighted in color.

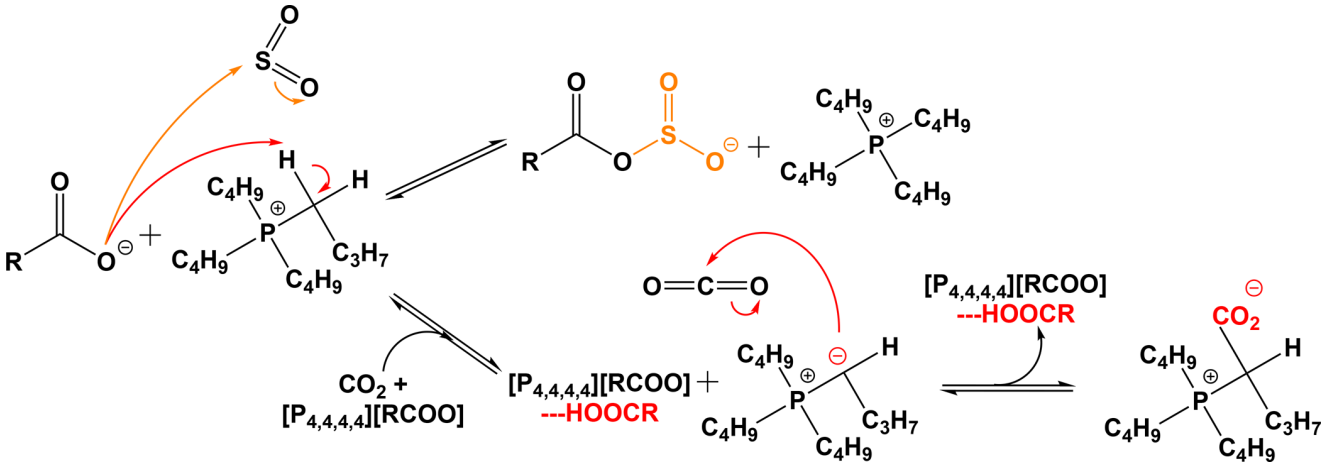

Figure 4. CO_2 and SO_2 absorption mechanism by tetrabutylphosphonium carboxylate ILs ($[P_{4,4,4,4}][RCOO]$). The CO_2 absorption mechanism follows a 2:1 IL:CO_2 stoichiometry that starts by the formation of a phosphonium ylide, $[P^+_{4,4,4,4}\text{-}CO_2^-]$, and a complex between the IL and the formed carboxylic acid $[P_{4,4,4,4}][RCOO] - -$ HOOCR. The ylide subsequently reacts with CO_2. SO_2 absorption follows a 1:1 IL:SO_2 mechanisms through a direct nucleophilic addition of the carboxylate on SO_2.

As expected, K_{H,SO_2} increases with increasing temperature, since the physical absorption of gases is generally an exothermic process. K_{eq,SO_2} decreases with increasing temperature, revealing that the chemical absorption of SO_2 in $[P_{4,4,4,4}][TetrazC_1COO]$ also happens exothermically. Lower temperatures favor SO_2 absorption even if we found that the capacity of the IL remains elevated at 343 K, which is relevant for applications such as for the treatment of flue gases. The calculated enthalpies of reaction, $\Delta_r H°$, and of solvation, $\Delta_{sol} H°$ using equations S4 to S5 are equal to −23.5 kJ mol^{-1} and −8.67 kJ mol^{-1}, respectively. Both are negative as expected, confirming the exothermic and spontaneous chemical reaction of $[P_{4,4,4,4}][TetrazC_1COO]$ with SO_2. The relatively small value of $\Delta_r H°$ suggests a weak chemical bond between the IL and SO_2, making the reverse reaction less energy demanding.

The interaction energies between SO_2 and the IL were calculated and decomposed into dispersion and electrostatic contributions. The values are reported in Table S11 and Figure S27 with the different optimized structures being represented in Figure S28. The strongest calculated SO_2 − IL interaction energy (−108.91 kJ mol^{-1}) corresponds to the electrostatic contribution of the first chemically absorbed SO_2, in agreement with the 1:1 stoichiometry of the reaction. The electrostatic contribution to the interaction energy significantly decreases when additional SO_2 are absorbed with dispersion interactions becoming the main contribution to the total energy of interaction (Table S11). We could identify a clear preference of SO_2 for the carboxylate headgroup and for the tetrazole ring (Figure S28) through the charge delocalization as N2 and N4 carry a significant partial negative charge of −0.4e.[23]

The energy profile of the reaction between SO_2 and the IL was computed using electronic DFT and is represented in Figure 5. The addition of $[TetrazC_1COO]^-$ to SO_2 following the one-step reaction mechanism depicted in Figure 4 corresponds, as expected, to a calculated negative variation of the Gibbs free energy (ΔG (SO_2) = −8.1 kJ mol^{-1}) and, similarly to what was previously reported for other ILs,[17,62,63] a

https://doi.org/10.1021/acssuschemeng.4c02659
ACS Sustainable Chem. Eng. XXXX, XXX, XXX−XXX

ACS Sustainable Chemistry & Engineering pubs.acs.org/journal/ascecg Research Article

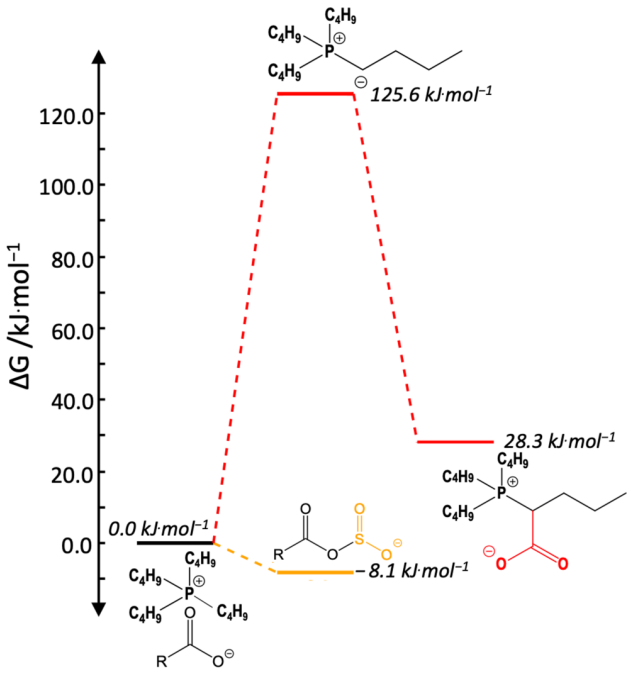

Figure 5. Relative Gibbs free energy, ΔG, at 343 K of the reactions of $[P_{4,4,4,4}][TetrazC_1COO]$ with yellow line, SO_2 following a 1:1 stoichiometry; and red line, CO_2 following a 2:1 stoichiometry.

negative enthalpy of reaction (ΔH (SO_2) = −12.7 kJ mol^{-1}) confirming that the chemical reaction of SO_2 with the IL is thermodynamically favored and exothermic and further validating the reaction model proposed. As shown in Figure S28, the energy of the Highest Occupied Molecular Orbital (HOMO) decreases from −7.79 to −8.32 eV with the nucleophilic addition of the first SO_2 molecule. This lowering in energy is accompanied by an increase in the charge transfer between the cation and the anion of the IL, from 0.18 to 0.28 *e* (Table S12). The new HOMO is spread over the SO_2 moiety added to the carboxylate (see Figure S28). Although the possibility of a second SO_2 reacting with the newly formed $[TetrazC_1COO - SO_2]^-$ adduct through a nucleophilic addition was considered, the calculated energy profile showed that this is unlikely, as the Gibbs free energy change of this reaction is positive (23.6 kJ mol^{-1}) with a less significant stabilization of the HOMO due to the lower interaction energies (Figures S26 and S28).

The complete desorption of SO_2 from $[P_{4,4,4,4}][TetrazC_1COO]$ was achieved using primary vacuum at 303 K for 4 h or at 323 K for only 2 h. These milder conditions than those previously reported for tetrazolate phosphonium-based ILs[60] are explained by the modest interactions between the gas and $[TetrazC_1COO]^-$ when compared with those with tetrazolate. The exothermic nature of the gas absorption explains why the regeneration of the solvent is easier at higher temperatures. The full regeneration of the IL is proven by comparing the FT-IR spectra of the pure IL, the solution of gas and the liquid after being under vacuum (as seen in Figure 3).

MD simulations of $[P_{4,4,4,4}][TetrazC_1COO]$ containing SO_2 were carried out to provide a better understanding of the solvation environment, through the analysis of the radial distribution functions (RDFs), spatial distribution functions (SDFs), and H-bonds. The simulation boxes contain 300 ion pairs and, in order to match the 1:1 chemisorption, 300 SO_2 molecules. Figure 6 (top) shows that the RDFs between the P and the H_α of the cation around the negatively charged oxygen

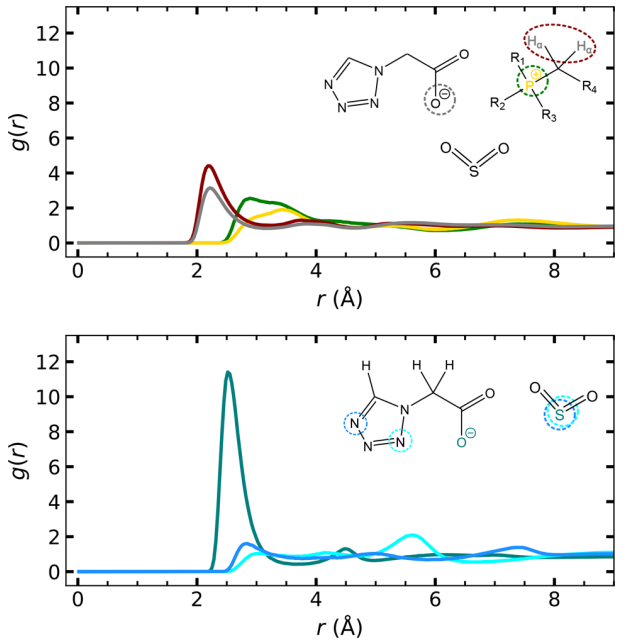

Figure 6. Site−site radial distribution functions, $g(r)$, calculated at 343 K in $[P_{4,4,4,4}][TetrazC_1COO]$. (Top) yellow line, P^+, and gray line, H_α, of the cation in the presence of SO_2, and green line, P^+, and red line, H_α, of the cation around the carboxylate head O_{COO^-} the anion without gas. (Bottom) S_{SO_2} around green line, O_{COO^-}, light blue line, N2, and dark blue line, N4.

atoms O_{COO^-} of the carboxylate anions are similar to those in the neat IL, with two peaks at 2.88 and 3.33 Å for O_{COO^-}...P, and one peak at 2.22 Å for O_{COO^-}...H_α. There was only a decrease in the coordination number (CN) of the first coordination shell, from 0.71 to 0.50 and 2.72 to 1.93 (Figure S19 (left)), respectively. This decrease is due to the intercalation of SO_2 molecules between the two sites (bottom plot), with a very intense peak showing important spatial correlation between O_{COO^-} and S at 2.52 Å (CN of 0.68, Figure S19 (right)) revealing the main site for SO_2 solvation with S pointing toward O_{COO^-}. A second solvation site was found on the N4 of the tetrazolate carboxylate, marked by a peak (bottom), with the S located at 2.85 Å, with a smaller CN of 0.23 (Figure S19 (right)). The spatial correlation of S with N4 appears as more important than with N2. Nonetheless, despite these interactions, there is no modifications in the correlations between these nitrogen atoms and $[P_{4,4,4,4}]^+$ as depicted in Figure S21 (left). In summary, despite the unusual spatial configuration of $[P_{4,4,4,4}][TetrazC_1COO]$, the addition of SO_2 does not have a significant impact on the microscopic structure of the IL.

The strong and unique anion−anion spacial correlations observed in the pure IL[23] remain in the presence of SO_2 with similar distances and CNs, as shown in Figure S22 (right). These are due to the charge delocalization on the tetrazole ring, resulting in an important negative charge on the nitrogen atoms N2 and N4. These anion−anion interactions compete with anion−cation interactions leading to a decrease in CN between O_{COO^-} and H_α compared to other phosphonium carboxylates.[23]

https://doi.org/10.1021/acssuschemeng.4c02659
ACS Sustainable Chem. Eng. XXXX, XXX, XXX−XXX

ACS Sustainable Chemistry & Engineering pubs.acs.org/journal/ascecg Research Article

Previous studies have reported that some carboxylate phosphonium ILs also react chemically with CO_2.[26,64] Strangely enough, it can be seen in Figure 2 that the mole fraction concentration of CO_2 in $[P_{4,4,4,4}][TetrazC_1COO]$ follows approximately Henry's law with only small deviations from linearity at higher temperatures and very low pressures (insert in Figure 2 and ESI) meaning that the IL just barely reacts with CO_2. Experimental cross relaxation rates show a proximity of the α protons of the cation and the carboxylate anion (NOESY results in ESI) indicating the possible activation of the IL (through the formation of the ylide in Figure 4). In contrast with reported observations for similar carboxylate-based ILs,[26] the absorption of CO_2 by $[P_{4,4,4,4}][TetrazC_1COO]$ does not result in the appearance of ^{13}C NMR characteristic signals for the zwitterionic species, $[P^+_{4,4,4,4}-CO_2^-]$, or for the carboxylic acid [TetrazC1COOH] (see reaction mechanism in Figure 4). Instead, only minor shifts in the ^{13}C NMR signals (orange lines in Figure 7) can be

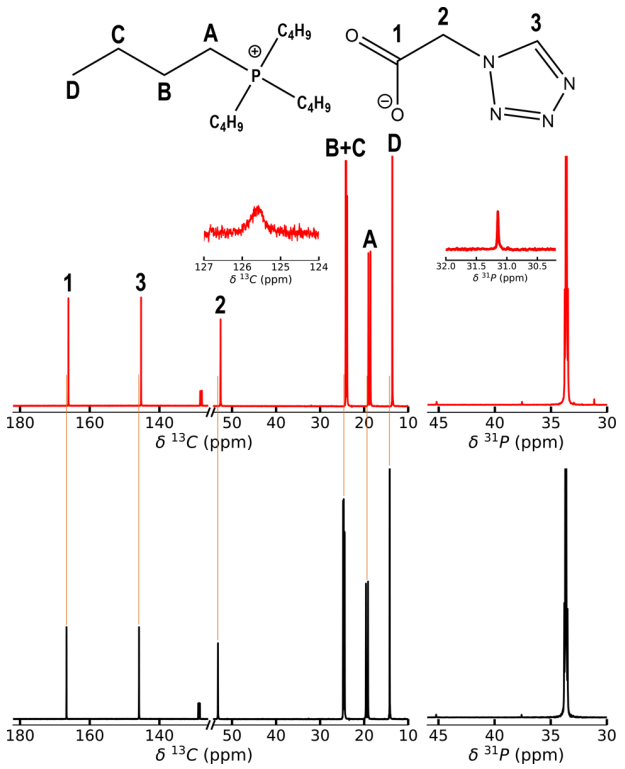

Figure 7. (Left) ^{13}C and (right) ^{31}P NMR spectra of $[P_{4,4,4,4}][TetrazC_1COO]$ before (black line, bottom) and after (red line, CO_2, top) being pressurized with CO_2 at 343 K (C_6D_6 was used as internal reference).

observed due to changes in the chemical environment caused by dissolved CO_2. A CO_2 peak indeed appears at 125.7 ppm (Figure 7 and Table S6). In contrast, a small signal at 31.15 ppm is observed in the ^{31}P NMR spectrum of the IL after contact with CO_2 that can be attributed to the zwitterionic species (Figure 7 (right)) in a quantity too low to be quantified.

The energy profile of the reaction between CO_2 and the IL was also computed using electronic DFT considering the 2:1 absorption mechanism in Figure 4.[22,64] The energy profile for this reaction is also included in Figure 5. The first step of the reaction involves the formation of a high-energy ylide (ΔG (CO_2) = 125.6 kJ mol^{-1} and ΔH (CO_2) = 123.9 kJ mol^{-1} in Figures 5 and S24, respectively). This first step is endothermic and is consistent with the destabilization of the HOMO with its energy increasing from −6.31 to −4.20 eV (Figure S29). The partial atomic charges of the different intermediary compounds are reported in Table S13. A strong net charge transfer of approximately 0.35e is calculated between the cation and the anion in the IL, pointing toward a strong cation−anion interaction. A slight negative charge of −0.11e is calculated for the carboxylic acid formed in this first reaction step probably resulting from a charge transfer from $[TetrazC_1COO]^-$. That charge transfer induces the formation of an hydrogen bond and a complex, $[P_{4,4,4,4}][TetrazC_1COO]$ − − HOOC1Tetraz, with a $d(OH - O^-)$ distance of 1.44 Å and a O−H−O angle of 175.1°. The deprotonation of the H_α of $[P_{4,4,4,4}]^+$ leads to an increase in the HOMO energy from −6.31 to −4.20 eV (Figure S29) indicating that this reaction is not favored.

A negative variation of the Gibbs free energy is calculated for the second step of the CO_2 chemisorption, consisting of the addition of the ylide to CO_2. The calculated energy of the HOMO for this second step decreases from −4.20 to −6.25 ev leading to a HOMO energy in the final state slightly higher than that of the initial state in agreement with the small reactivity of the IL with CO_2. The overall reaction is then thermodynamically unfavorable and endothermic, with positive values for ΔG (CO_2) and ΔH (CO_2), of +28.3 and +15.3 kJ mol^{-1}, respectively. CO_2 chemisorption is therefore unlikely, consistent with the calculated increase in the HOMO energy and with the low gas absorption measured experimentally. A high temperature would then be required for the chemisorption of CO_2, in line with the deviation from Henry's law which is larger at 70 °C than at 30 °C. As measured experimentally, the chemisorption of CO_2 by $[P_{4,4,4,4}][TetrazC_1COO]$ is negligible at low pressures for all the temperatures studied.

The reversibility of CO_2 absorption by $[P_{4,4,4,4}][TetrazC_1COO]$ was also investigated by performing three cycles of absorption and desorption at 303 and 343 K, and two cycles at 323 K, as shown in Figure S5. We observed that even after heating the sample at 343 K for 2 weeks, the capture capacity remained unchanged within the uncertainty of the measurements. The reversibility of the CO_2 absorption was also assessed by ^1H and ^{31}P NMR, by placing the sample previously pressurized with CO_2 under vacuum at 343 K for 48 h (Figure S18). The shifts observed upon carbon capture disappeared, and the peaks returned to the same chemical shifts as in the neat IL. The small peak observed on the ^{31}P NMR spectrum, characteristic of the zwitterion, formed during CO_2 capture, was no longer visible. This suggests that both physical and chemical absorption of CO_2 are reversible without detectable degradation of the IL, even above room temperature.

MD simulations were also carried out for $[P_{4,4,4,4}][TetrazC_1COO]$ containing CO_2. In this case, the calculations were performed in simulation boxes containing 300 ion pairs and 30 CO_2 molecules were included. As seen in the RDFs in Figures 8 (top) and S21 (right), the addition of CO_2 does not alter the structural arrangement of the IL. The O_{COO^-} atoms are still predominantly correlated with P and the H_α of the cations at similar distances than in the neat ILs, although their CN decreases slightly from 0.70 to 0.67 and 2.72 to 2.66 (Figure S20 (left)), respectively. Figure S22 reveals that the

https://doi.org/10.1021/acssuschemeng.4c02659
ACS Sustainable Chem. Eng. XXXX, XXX, XXX−XXX

ACS Sustainable Chemistry & Engineering pubs.acs.org/journal/ascecg Research Article

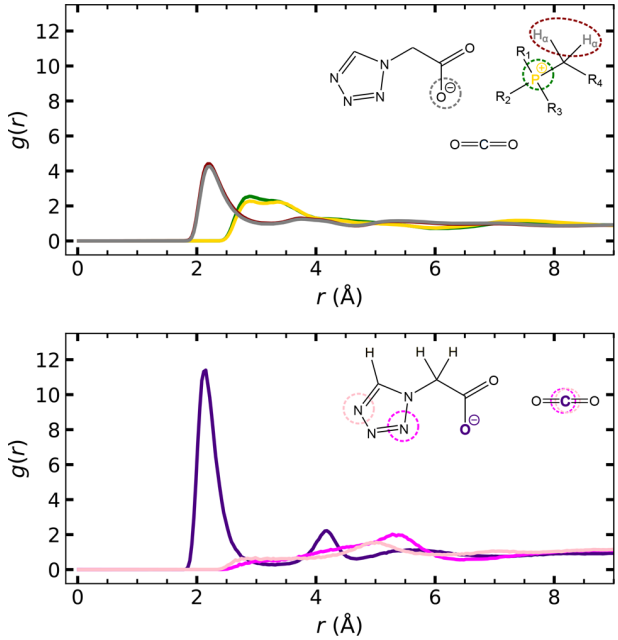

Figure 8. Site−site radial distribution functions, $g(r)$, calculated at 343 K in [$P_{4,4,4,4}$][TetrazC$_1$COO]. (Top) yellow line, P^+, and gray line, H_α, of the cation in the presence of CO_2 and green line, P^+, and red line, H_α, of the cation around the carboxylate head O_{COO^-} the anion without gas. (Bottom) C_{CO_2} around purple line, O_{COO^-}, dark pink line, N2, and light pink line, N4.

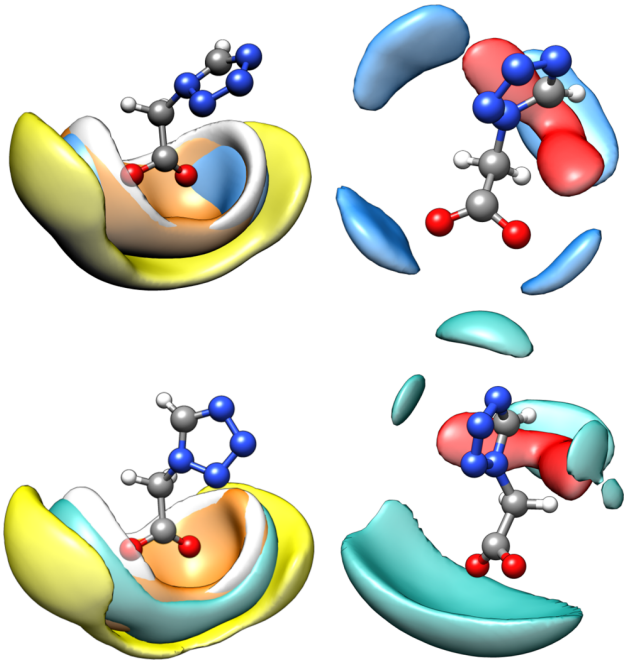

Figure 9. SDFs of yellow box, P^+, and white box, H_α, of the cation, orange box, H_{ring} of the anion and (top left) blue box, C_{CO_2} and (bottom left) teal box, S_{SO_2} around O_{COO^-}. Isodensity contours at 6.2, 5.9, 7.9, 1.4, and 6.1 times the average density around the central anion, respectively. SDFs of red box, O_{COO^-}, and (top right) blue box, C_{CO_2} and (bottom right) teal box, S_{SO_2} around the tetrazole ring in in [$P_{4,4,4,4}$][TetrazC$_1$COO] at 343 K. Isodensity contours at 21.0, 1.3, and 7.5 times the average density around the central anion, respectively.

secondary anion−anion correlations observed in the neat IL[23] are also not affected by the presence of CO_2.

As with SO_2, Figure 8 (bottom) shows that CO_2 is solvated around the carboxylate head of the anion with C_{CO_2} pointing toward O_{COO^-}, but at a closer distance of 2.15 Å with a CN of 0.05 (Figure S20 (right)). However, in Figure 8 (bottom) N2 and N4 show almost no first-shell correlations with C_{CO_2}, with distant first maxima appearing at 5.28 and 5.02 Å, respectively.

The SDFs in Figure 9 show that both CO_2 and SO_2 are inserted between cation−anion and anion−anion sites. The electrophilic C_{CO_2} and S_{SO_2} are preferentially located around O_{COO^-}, while the carboxylate head is also in close proximity of H_α or H_{ring}. The C_{CO_2} are located slightly closer to the carboxylate, probably due to its linear structure. This spatial organization can be visualized in snapshots of the simulation boxes, Figure S23, where CO_2 and SO_2 molecules are preferentially localized in the vicinity of polar domains (colored in orange).

The structural features between the cations and anions are not perturbed by the presence of either CO_2 or SO_2, which is also confirmed by the similar[23] combined distribution functions (CDFs) of the C_α−H_α···O_{COO^-} angle as a function of the distance between H_α of the cation and the negatively charged O_{COO^-} in the presence of CO_2 and SO_2 (Figures 10 (top left) and (top right), respectively). This spatial configuration does not favor the H_α deprotonation by O_{COO^-} as these can not be considered as proper hydrogen bonds.

In Figure 10 (bottom left) there is an angle C_α−H_α...O_{CO_2} of approximately 179.25° and a H_α...O_{CO_2} distance of 2.38 Å, revealing that CO_2 molecules form hydrogen bonds with the phosphonium cations, which favor CO_2 solubility. A similar result is found for SO_2 with an angle of 176.75° and a distance of 2.42 Å (Figure 10 (bottom right)). This result confirms the hydrogen bond formation between SO_2 and the IL observed by FT-IR at 2362 cm^{-1}. Similar hydrogen bond formation between $[P_{2,2,2,1}]^+$ hydrogen atoms and SO_2 had been previously identified in MD simulations as well.[65]

The ideal selectivity of absorption was calculated as the ratio of moles of gas absorbed at a specific pressure with the values reported in Table 2. At 303 K, the quantity of SO_2 absorbed is 60 times higher at 250 mbar (ideal selectivity of 150) and 100 times higher at 343 K (ideal selectivity of 215) than the quantity of CO_2. The decrease of the ideal selectivity is the result of a bigger influence of temperature on the physical absorption of CO_2 than on the chemisorption of SO_2. At lower pressures, the selectivity increases substantially, with values of 289 and 397 at 0.10 bar and 303 and 343 K, respectively. This is explained by the low physical absorption at low pressures and the much stronger chemical absorption at these conditions which results in the increased selectivity. This increased SO_2/CO_2 selectivity at low pressures is pertinent for several applications, since the former gas is often present in lower concentrations in relevant gaseous mixtures.[18,19,66]

To the best of the authors knowledge, only one IL (1-hexyl-3-methylimidazolium 2-nitrobenzoate, [C_6C_1Im][2 − NO_2 − Ben]) has been reported so far as having a larger SO_2/CO_2 selectivity at 1 bar and 333 K — 228[14] compared with 142 for [$P_{4,4,4,4}$][TetrazC$_1$COO] in the same conditions (Table 2). Furthermore, the long-term thermal stability (studied in detail herein as reported in ESI Section 6) of [$P_{4,4,4,4}$]-

https://doi.org/10.1021/acssuschemeng.4c02659
ACS Sustainable Chem. Eng. XXXX, XXX, XXX−XXX

ACS Sustainable Chemistry & Engineering pubs.acs.org/journal/ascecg Research Article

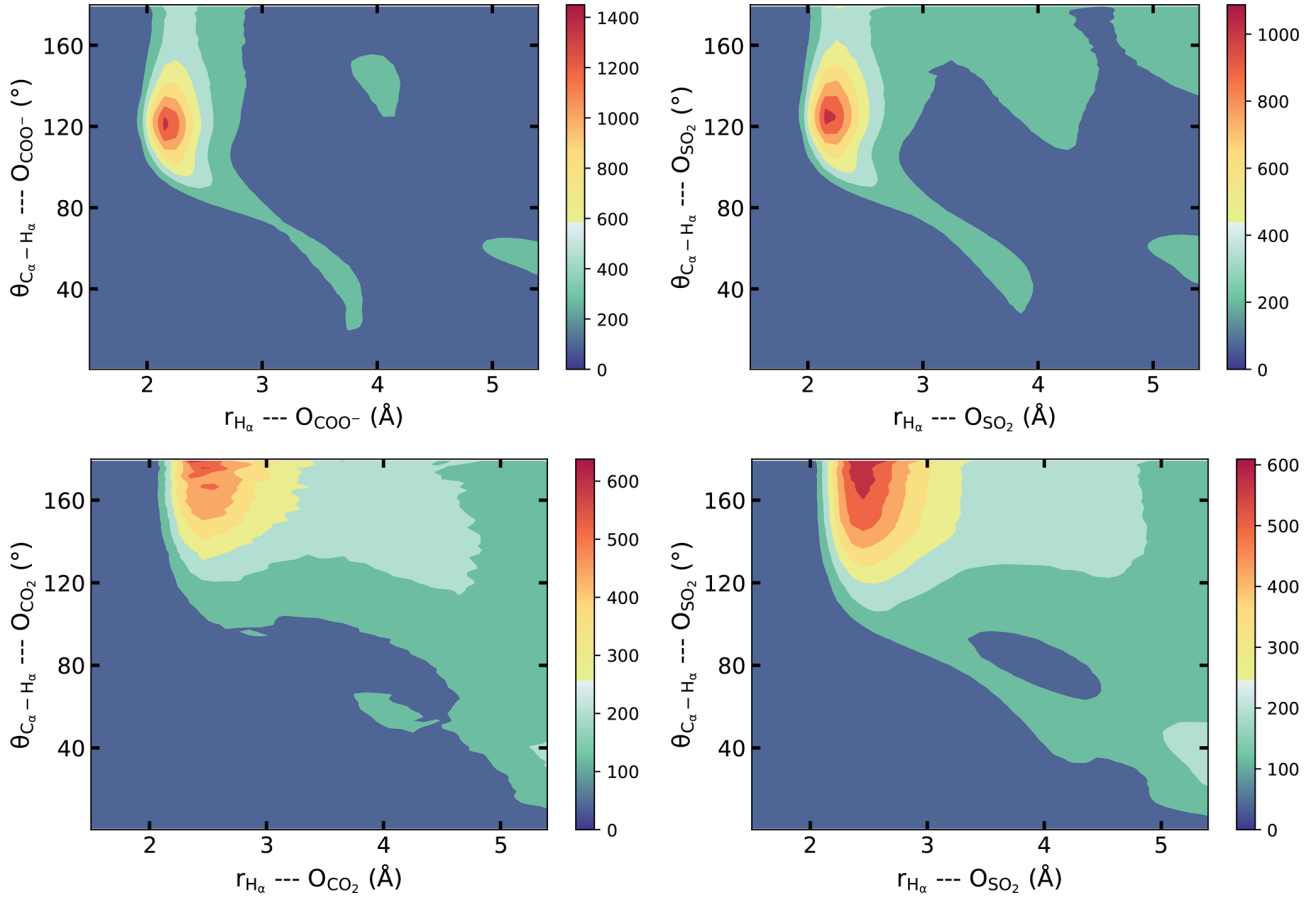

Figure 10. Combined distribution functions (CDFs) of the C_α–H_α...O_{COO^-} angle as a function of the distance between the acidic proton H_α and the negatively charged O_{COO^-} in the presence of (top left) CO_2 and (top right) SO_2. CDF of (bottom left) the C_α–H_α...O_{CO_2} angle and (bottom right) the C_α–H_α...O_{SO_2} as a function of the distance between the acidic proton H_α and O of CO_2 and SO_2 in $[P_{4,4,4,4}][TetrazC_1COO]$ at 343 K, respectively.

Table 2. Absorption capacity and ideal absorption selectivity, *S*, of SO_2 over CO_2 in the ILs: $[P_{4,4,4,4}][TetrazC_1COO]$, this work; $[C_6C_1Im][Ben]$, 1-Hexyl-3-methylimidazolium benzoate;[14] $[C_6C_1Im][2{-}CH_3{-}Ben]$, 1-Hexyl-3-methylimidazolium 2-methylbenzoate;[14] $[C_6C_1Im][2{-}NO_2{-}Ben]$, 1-Hexyl-3-methylimidazolium 2-nitrobenzoate;[14] $[C_6C_1Im][TFA]$, 1-Hexyl-3-methylimidazolium triflate;[14] $[P_{6,6,6,14}][Tetz]$, Trihexyl(tetradecyl)phosphonium tetrazole;[60] $[Et_2NC_2C_1Im][Tetz]$, 1-(2-Diethylaminoethyl)-3-methylimidazolium tetrazole;[68] and $[C_4Py][SCN]$, N-Butylpyridinium Thiocyanate[69a]

Sample	*T* (K)	*S*(0.1/0.1)	*S*(0.25/0.25)	*S*(1.0/1.0)
$[P_{4,4,4,4}][TetrazC_1COO]$	303	289	150	104
	323	349	176	119
	343	397	215	191
	T (K)	b_{SO_2} (mmol g^{-1})	b_{CO_2} (mmol g^{-1})	*S*(1.0/1.0)
$[C_6C_1Im][Ben]$[14]	333	5.44	0.141	39
$[C_6C_1Im][2{-}CH_3{-}Ben]$[14]	333	5.49	0.164	34
$[C_6C_1Im][2{-}NO_2{-}Ben]$[14]	333	3.87	0.017	228
$[C_6C_1Im][TFA]$[14]	333	3.95	0.044	90
$[P_{6,6,6,14}][Tetz]$[60]	293	6.72	0.143	47
$[Et_2NC_2C_1Im][Tetz]$[68]	293	17.12	0.439	39
$[C_4Py][SCN]$[69]	293	13.14	0.234	56

[a]For each ideal selectivity the partial pressure of the gas is indicated in parentheses.

$[TetrazC_1COO]$, even if previously overestimated by more than 150 K,[23] is still significantly higher than that reported for other promising ILs for acid gas separation (such as imidazolium acetate ILs).[67]

The energy profile of the reaction between CO_2 and the IL, after SO_2 absorption is depicted in Figure S25. It reveals a higher energy barrier for the formation of the ylide (activation of the IL for reaction with CO_2 in Figure 4) by approximately 20 kJ mol^{-1} when compared with the pure IL. The reaction with CO_2 is thus less favorable as further confirmed by the calculated positive $\Delta_r G$ (CO_2) and $\Delta_r H$ (CO_2). NMR measurements of $[P_{4,4,4,4}][TetrazC_1COO]$ after SO_2 absorp-

https://doi.org/10.1021/acssuschemeng.4c02659
ACS Sustainable Chem. Eng. XXXX, XXX, XXX−XXX

tion and subsequent pressurization with CO_2 (ESI Figure S11) confirm this. No significant changes are observed in the spectra except for shifts attributed to the presence of dissolved CO_2 which can be clearly visible using ^{13}C NMR with a characteristic signal at 125.23 pm.

The self-diffusion coefficients of the cation and anion, D_{cation} and D_{anion}, in $[P_{4,4,4,4}][TetrazC_1COO]$ were measured both before and after absorption of CO_2 and SO_2, the results being presented in Figure 11 and listed in the ESI Table S7. Both

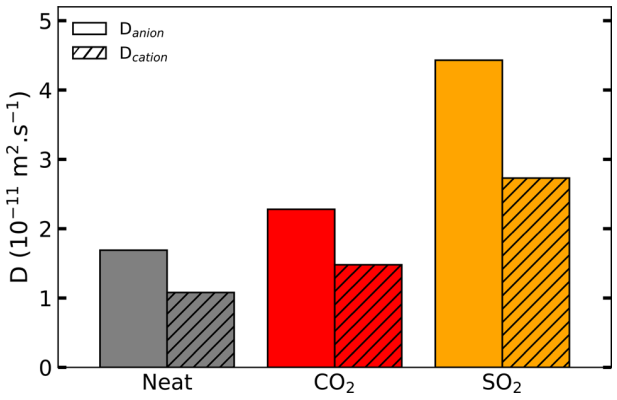

Figure 11. Chart representing the experimental self-diffusion coefficients (D) of $[P_{4,4,4,4}][TetrazC_1COO]$ gray box, before, and after red box, CO_2, and orange box, SO_2 absorption at 343 K by DOSY-NMR experiments.

D_{cation} and D_{anion} increase after CO_2 absorption, and even more significantly after SO_2 absorption. Upon CO_2 absorption, the diffusivity increased by 37% for the cation and by 35% for the anion, and upon SO_2 absorption they increased by 153% and 162% for cation and anion, respectively. These results demonstrate that CO_2 and SO_2 dissolution increases the fluidity $[P_{4,4,4,4}][TetrazC_1COO]$, which is a major advantage for gas capture, as with many ILs dramatic increases in viscosity upon absorption of CO_2 or SO_2 absorption,[51,70] for example imidazolium tetrazolate[71] or diamine polycarboxylate[72] ILs.

5. CONCLUSIONS

In this work the ionic liquid $[P_{4,4,4,4}][TetrazC_1COO]$ emerges as an efficient absorbent for selectively and reversibly absorbing SO_2 in the presence of CO_2. This IL was designed and easily prepared by tuning the basicity of the carboxylate anion which is low enough to allow for a reversible chemical absorption of SO_2 but only physical dissolution of CO_2, as studied by accurate and thouroughly studied gas absorption techniques—an isochoric saturation method used for SO_2 and a gravimetric microbalance for CO_2. As a result it was possible to calculate for this IL one of the highest SO_2/CO_2 selectivity reported to date, associated with a high SO_2 capture capacity at low pressures. These characteristics go in pair with an increase of the fluidity of the liquid upon the absorption of gas reflected in an increased diffusivit (measured using NMR) and a long-term thermal stability determined by a controlled thermogravimetric analysis. This IL appears then as a promising absorbent for the desulfurization of flue gases even when they contain large quantities of SO_2. We showed, experimentally and by quantum-chemical calculations that the complete regeneration of the IL was possible under mild conditions, which constitutes another significant improvement compared to other ILs for SO_2 capture, that also, more often than not, become significantly more viscous when chemically absorbing acid gases.

■ ASSOCIATED CONTENT

Supporting Information

The Supporting Information is available free of charge at https://pubs.acs.org/doi/10.1021/acssuschemeng.4c02659.

Absorption data of SO_2 and CO_2; reversibility and repeatability of SO_2 and CO_2 absorption; NMR of the ionic liquid before and after SO_2 or CO_2 absorption; molecular dynamics simulations; *ab initio* calcultions; long-term thermal stability of the ionic liquid (PDF)

■ AUTHOR INFORMATION

Corresponding Author

Margarida Costa Gomes − *Laboratoire de Chimie, ENS de Lyon and CNRS, Lyon 69364, France;* orcid.org/0000-0001-8637-6057; Email: margarida.costa-gomes@ens-lyon.fr

Authors

Nicolas Scaglione − *Laboratoire de Chimie, ENS de Lyon and CNRS, Lyon 69364, France*

Luke Wylie − *Laboratoire de Chimie, ENS de Lyon and CNRS, Lyon 69364, France*

Agilio Padua − *Laboratoire de Chimie, ENS de Lyon and CNRS, Lyon 69364, France;* orcid.org/0000-0002-7641-6526

Complete contact information is available at: https://pubs.acs.org/10.1021/acssuschemeng.4c02659

Author Contributions

N.S.: preparation of the IL, experimental measurements, MD simulations, DFT calculations, preparation of the manuscript. L.W.: knowledge transfer concerning the *ab initio* methods used. A.P.: project strategy, supervision concerning the simulation methods, manuscript preparation. M.C.G.: project strategy, supervision concerning the experiments, manuscript preparation.

Notes

The authors declare no competing financial interest.

■ REFERENCES

(1) Kohl, A. L., Nielsen, R. B., Eds.; *Gas Purification*, fifth ed.; Gulf Professional Publishing: Houston, 1997; pp ii−iii.

(2) Lei, Z.; Dai, C.; Chen, B. Gas Solubility in Ionic Liquids. *Chem. Rev.* **2014**, *114*, 1289−1326.

(3) Wang, C.; Luo, X.; Zhu, X.; Cui, G.; Jiang, D.; Deng, D.; Li, H.; Dai, S. The strategies for improving carbon dioxide chemisorption by functionalized ionic liquids. *RSC Adv.* **2013**, *3*, 15518.

(4) Bates, E. D.; Mayton, R. D.; Ntai, I.; Davis, J. H. CO_2 Capture by a Task-Specific Ionic Liquid. *J. Am. Chem. Soc.* **2002**, *124*, 926−927.

(5) Zhang, J.; Zhang, S.; Dong, K.; Zhang, Y.; Shen, Y.; Lv, X. Supported Absorption of CO_2 by Tetrabutylphosphonium Amino Acid Ionic Liquids. *Chem. - Eur. J.* **2006**, *12*, 4021−4026.

(6) Gurkan, B. E.; de la Fuente, J. C.; Mindrup, E. M.; Ficke, L. E.; Goodrich, B. F.; Price, E. A.; Schneider, W. F.; Brennecke, J. F. Equimolar CO_2 Absorption by Anion-Functionalized Ionic Liquids. *J. Am. Chem. Soc.* **2010**, *132*, 2116−2117.

(7) Zhang, Y.; Zhang, S.; Lu, X.; Zhou, Q.; Fan, W.; Zhang, X. Dual Amino-Functionalised Phosphonium Ionic Liquids for CO_2 Capture. *Chem. - Eur. J.* **2009**, *15*, 3003−3011.

(8) Tao, D.; Chen, F.; Tian, Z.; Huang, K.; Mahurin, S. M.; Jiang, D.; Dai, S. Highly Efficient Carbon Monoxide Capture by Carbanion-Functionalized Ionic Liquids through C-Site Interactions. *Angew. Chem., Int. Ed.* **2017**, *56*, 6843−6847.
(9) Wu, W.; Han, B.; Gao, H.; Liu, Z.; Jiang, T.; Huang, J. Desulfurization of flue gas: SO_2 absorption by an ionic liquid. *Angew. Chem., Int. Ed. Engl.* **2004**, *43*, 2415−2417.
(10) Shang, Y.; Li, H.; Zhang, S.; Xu, H.; Wang, Z.; Zhang, L.; Zhang, J. Guanidinium-based ionic liquids for sulfur dioxide sorption. *Chem. Eng. J.* **2011**, *175*, 324−329.
(11) Shiflett, M. B.; Yokozeki, A. Chemical Absorption of Sulfur Dioxide in Room-Temperature Ionic Liquids. *Ind. Eng. Chem. Res.* **2010**, *49*, 1370−1377.
(12) Cui, G.; Zheng, J.; Luo, X.; Lin, W.; Ding, F.; Li, H.; Wang, C. Tuning Anion-Functionalized Ionic Liquids for Improved SO_2 Capture. *Angew. Chem., Int. Ed.* **2013**, *52*, 10620−10624.
(13) Yuan, X. L.; Zhang, S. J.; Lu, X. M. Hydroxyl Ammonium Ionic Liquids: Synthesis, Properties, and Solubility of SO_2. *J. Chem. Eng. Data* **2007**, *52*, 596−599.
(14) Huang, K.; Wu, Y.-T.; Hu, X.-B. Effect of alkalinity on absorption capacity and selectivity of SO_2 and H_2S over CO_2: Substituted benzoate-based ionic liquids as the study platform. *Chem. Eng. J.* **2016**, *297*, 265−276.
(15) Cui, G.; Zhang, F.; Zhou, X.; Huang, Y.; Xuan, X.; Wang, J. Acylamido-Based Anion-Functionalized Ionic Liquids for Efficient SO_2 Capture through Multiple-Site Interactions. *ACS Sustain. Chem. Eng.* **2015**, *3*, 2264−2270.
(16) Zhang, F.; Cui, G.; Zhao, N.; Huang, Y.; Zhao, Y.; Wang, J. Improving SO_2 capture by basic ionic liquids in an acid gas mixture (10% vol SO_2) through tethering a formyl group to the anions. *RSC Adv.* **2016**, *6*, 86082−86088.
(17) Cui, G.; Huang, Y.; Zhang, R.; Zhang, F.; Wang, J. Highly efficient and reversible SO_2 capture by halogenated carboxylate ionic liquids. *RSC Adv.* **2015**, *5*, 60975−60982.
(18) Li, X.; Zhang, L.; Zheng, Y.; Zheng, C. Effect of SO_2 on CO_2 Absorption in Flue Gas by Ionic Liquid 1-Ethyl-3-methylimidazolium Acetate. *Ind. Eng. Chem. Res.* **2015**, *54*, 8569−8578.
(19) Taylor, S. F. R.; McClung, M.; McReynolds, C.; Daly, H.; Greer, A. J.; Jacquemin, J.; Hardacre, C. Understanding the Competitive Gas Absorption of CO_2 and SO_2 in Superbase Ionic Liquids. *Ind. Eng. Chem. Res.* **2018**, *57*, 17033−17042.
(20) García, G.; Atilhan, M.; Aparicio, S. Simultaneous CO_2 and SO_2 capture by using ionic liquids: a theoretical approach. *Phys. Chem. Chem. Phys.* **2017**, *19*, 5411−5422.
(21) Cui, G.; Lin, W.; Ding, F.; Luo, X.; He, X.; Li, H.; Wang, C. Highly efficient SO_2 capture by phenyl-containing azole-based ionic liquids through multiple-site interactions. *Green Chem.* **2014**, *16*, 1211−1216.
(22) Avila, J.; Lepre, L. F.; Santini, C. C.; Tiano, M.; Denis-Quanquin, S.; Chung Szeto, K.; Padua, A. A. H.; Costa Gomes, M. High-Performance Porous Ionic Liquids for Low-Pressure CO_2 Capture**. *Angew. Chem., Int. Ed.* **2021**, *60*, 12876−12882.
(23) Scaglione, N.; Avila, J.; Bakis, E.; Padua, A.; Gomes, M. C. Alkylphosphonium carboxylate ionic liquids with tuned microscopic structures and properties. *Phys. Chem. Chem. Phys.* **2023**, *25*, 15325−15339.
(24) Jacquemin, J.; Costa Gomes, M. F.; Husson, P.; Majer, V. Solubility of carbon dioxide, ethane, methane, oxygen, nitrogen, hydrogen, argon, and carbon monoxide in 1-butyl-3-methylimidazolium tetrafluoroborate between temperatures 283 K and 343 K and at pressures close to atmospheric. *J. Chem. Therm.* **2006**, *38*, 490−502.
(25) Dymond, J. H.; Marsh, K. N.; Wilhoit, R. C.; Wong, K. C. In *Virial Coefficients of Pure Gases*; Frenkel, M., Marsh, K. N., Eds.; SpringerMaterials, 2002; Vol. *21*.
(26) Avila, J.; Cervinka, C.; Dugas, P.-Y.; Padua, A. A. H.; Costa Gomes, M. Porous Ionic Liquids: Structure, Stability, and Gas Absorption Mechanisms. *Adv. Mater. Interfaces* **2021**, *8*, 2001982.
(27) Veroutis, E.; Merz, S.; Eichel, R. A.; Granwehr, J. Intra- and inter-molecular interactions in choline-based ionic liquids studied by 1D and 2D NMR. *J. Mol. Liq.* **2021**, *322*, 114934.
(28) Goloviznina, K.; Canongia Lopes, J. N.; Costa Gomes, M.; Pádua, A. A. H. Transferable, Polarizable Force Field for Ionic Liquids. *J. Chem. Theory Comput.* **2019**, *15*, 5858−5871.
(29) Goloviznina, K.; Gong, Z.; Padua, A. A. H. The CL&Pol polarizable force field for the simulation of ionic liquids and eutectic solvents. *WIREs Comput. Mol. Sci.* **2022**, *12*, No. e1572.
(30) Eastman, P.; Swails, J.; Chodera, J. D.; McGibbon, R. T.; Zhao, Y.; Beauchamp, K. A.; Wang, L.-P.; Simmonett, A. C.; Harrigan, M. P.; Stern, C. D.; Wiewiora, R. P.; Brooks, B. R.; Pande, V. S. OpenMM 7: Rapid development of high performance algorithms for molecular dynamics. *PLoS Comput. Biol.* **2017**, *13*, No. e1005659.
(31) Padua, A. github.com/paduagroup/fftool, 2021; https://github.com/paduagroup/clandpol.
(32) Martínez, L.; Andrade, R.; Birgin, E. G.; Martínez, J. M. PACKMOL: A package for building initial configurations for molecular dynamics simulations. *J. Comput. Chem.* **2009**, *30*, 2157−2164.
(33) Brehm, M.; Thomas, M.; Gehrke, S.; Kirchner, B. TRAVIS—A free analyzer for trajectories from molecular simulation. *J. Chem. Phys.* **2020**, *152*, 164105.
(34) Grimme, S.; Antony, J.; Ehrlich, S.; Krieg, H. A consistent and accurate ab initio parametrization of density functional dispersion correction (DFT-D) for the 94 elements H-Pu. *J. Chem. Phys.* **2010**, *132*, 154104.
(35) Becker, T. M.; Lin, L.-C.; Dubbeldam, D.; Vlugt, T. J. H. Polarizable Force Field for CO_2 in M-MOF-74 Derived from Quantum Mechanics. *J. Phys. Chem. C* **2018**, *122*, 24488−24498.
(36) Ketko, M. H.; Kamath, G.; Potoff, J. J. Development of an Optimized Intermolecular Potential for Sulfur Dioxide. *J. Phys. Chem. B* **2011**, *115*, 4949−4954.
(37) Pracht, P.; Bohle, F.; Grimme, S. Automated exploration of the low-energy chemical space with fast quantum chemical methods. *Phys. Chem. Chem. Phys.* **2020**, *22*, 7169−7192.
(38) Frisch, M. J.; Trucks, G. W.; Schlegel, H. B.; Scuseria, G. E.; Robb, M. A.; Cheeseman, J. R.; Scalmani, G.; Barone, V.; Petersson, G. A.; Nakatsuji, H.; Li, X.; Caricato, M.; Marenich, A. V.; Bloino, J.; Janesko, B. G.; Gomperts, R.; Mennucci, B.; Hratchian, H. P.; Ortiz, J. V.; Izmaylov, A. F.; Sonnenber, J. L.; Williams-Young, D.; Ding, F.; Lipparini, F.; Egidi, F.; Goings, J.; Peng, B.; Petrone, A.; Henderson, T.; Ranasinghe, D.; Zakrzewsk, V. G.; Gao, J.; Rega, N.; Zheng, G.; Liang, W.; Hada, M.; Ehara, M.; Toyota, K.; Fukuda, R.; Hasegawa, J.; Ishida, M.; Nakajima, T.; Honda, Y.; Kitao, O.; Nakai, H; Vreven, T.; Throssell, K.; Montgomery, J. A., Jr.; Peralta, J. E.; Ogliaro, F.; Bearpark, M. J.; Heyd, J. J.; Brothers, E. N..; Kudin, K. N.; Staroverov, V. N.; Keith, T. A.; Kobayashi, R.; Normand, J.; Raghavachari, K.; Rendell, A. P.; Burant, J. C.; Iyengar, S. S.; Tomasi, J.; Cossi, M.; Millam, J. M.; Klene, M; Adamo, C.; Cammi, R.; Ochterski, J. W.; Martin, R. L.; Morokuma, K.; Farkas, O.; Foresman, J. B.; Fox, D. J. *Gaussian 16*, Revision C.01; Gaussian, Inc.: Wallingford, CT, 2016.
(39) Zhao, Y.; Truhlar, D. G. The M06 suite of density functionals for main group thermochemistry, thermochemical kinetics, noncovalent interactions, excited states, and transition elements: two new functionals and systematic testing of four M06-class functionals and 12 other functionals. *Theor. Chem. Acc.* **2008**, *120*, 215−241.
(40) Dunning, T. H.; Hay, P. J. In *Methods of Electronic Structure Theory*; Schaefer, H. F., Ed.; Modern Theoretical Chemistry; Springer US: Boston, MA, 1977; pp 1−27.
(41) Papajak, E.; Zheng, J.; Xu, X.; Leverentz, H. R.; Truhlar, D. G. Perspectives on Basis Sets Beautiful: Seasonal Plantings of Diffuse Basis Functions. *J. Chem. Theory Comput.* **2011**, *7*, 3027−3034.
(42) Temelso, B.; Archer, K. A.; Shields, G. C. Benchmark Structures and Binding Energies of Small Water Clusters with Anharmonicity Corrections. *J. Phys. Chem. A* **2011**, *115*, 12034−12046.

https://doi.org/10.1021/acssuschemeng.4c02659
ACS Sustainable Chem. Eng. XXXX, XXX, XXX−XXX

(43) Izgorodina, E. I.; Coote, M. L. Reliable Low-Cost Theoretical Procedures for Studying Addition-Fragmentation in RAFT Polymerization. *J. Phys. Chem. A* **2006**, *110*, 2486−2492.
(44) Wylie, L.; Hakatayama-Sato, K.; Go, C.; Oyaizu, K.; Izgorodina, E. I. Electrochemical characterization and thermodynamic analysis of TEMPO derivatives in ionic liquids. *Phys. Chem. Chem. Phys.* **2021**, *23*, 10205−10217.
(45) Marenich, A. V.; Jerome, S. V.; Cramer, C. J.; Truhlar, D. G. Charge Model 5: An Extension of Hirshfeld Population Analysis for the Accurate Description of Molecular Interactions in Gaseous and Condensed Phases. *J. Chem. Theory Comput.* **2012**, *8*, 527−541.
(46) Spackman, M. A.; Jayatilaka, D. Hirshfeld surface analysis. *CrystEngComm* **2009**, *11*, 19−32.
(47) Brémond, E.; Adamo, C. Seeking for parameter-free double-hybrid functionals: The PBE0-DH model. *J. Chem. Phys.* **2011**, *135*, No. 024106.
(48) Tan, S.; Barrera Acevedo, S.; Izgorodina, E. I. Generalized spin-ratio scaled MP2 method for accurate prediction of intermolecular interactions for neutral and ionic species. *J. Chem. Phys.* **2017**, *146*, No. 064108.
(49) Boys, S.; Bernardi, F. The calculation of small molecular interactions by the differences of separate total energies. Some procedures with reduced errors. *Mol. Phys.* **1970**, *19*, 553−566.
(50) Lepre, L. F.; Szala-Bilnik, J.; Pison, L.; Traikia, M.; Padua, A. A. H.; Ando, R. A.; Costa Gomes, M. F. Can the tricyanomethanide anion improve CO_2 absorption by acetate-based ionic liquids? *Phys. Chem. Chem. Phys.* **2017**, *19*, 12431−12440.
(51) Wang, L.; Zhang, Y.; Liu, Y.; Xie, H.; Xu, Y.; Wei, J. SO_2 absorption in pure ionic liquids: Solubility and functionalization. *J. Hazard. Mater.* **2020**, *392*, 122504.
(52) Zhao, J.; Ren, S.; Hou, Y.; Zhang, K.; Wu, W. SO_2 Absorption by Carboxylate Anion-Based Task-Specific Ionic Liquids: Effect of Solvents and Mechanism. *Ind. Eng. Chem. Res.* **2016**, *55*, 12919−12928.
(53) Deng, D.; Jiang, Y.; Liu, X. Investigation of furoate-based ionic liquid as efficient SO_2 absorbent. *New J. Chem.* **2017**, *41*, 2090−2097.
(54) Lee, H.; Jung, Y. M.; Lee, K. I.; Kim, H. S.; Park, H. S. Understanding the unique interaction of amine-containing ionic compounds with SO_2 for high absorption capacity. *RSC Adv.* **2013**, *3*, 25944−25949.
(55) Huang, K.; Wang, G.-N.; Dai, Y.; Wu, Y.-T.; Hu, X.-B.; Zhang, Z.-B. Dicarboxylic acid salts as task-specific ionic liquids for reversible absorption of SO_2 with a low enthalpy change. *RSC Adv.* **2013**, *3*, 16264−16269.
(56) Schreiber, K. C. Infrared Spectra of Sulfones and Related Compounds. *Anal. Chem.* **1949**, *21*, 1168−1172.
(57) Fujimori, K. The Infrared Spectra of Alkane-1-sulfonates. *BCSJ.* **1959**, *32*, 850−852.
(58) Giguère, P. A.; Savoie, R. Les spectres infrarouges de l'acide sulfurique et des oléums. *Can. J. Chem.* **1960**, *38*, 2467−2476.
(59) Krasovskii, A. N.; Kalnin'sh, K. K. IR spectra of long-chain alkylsulfonic acids. *J. Appl. Spectrosc.* **1977**, *26*, 745−749.
(60) Wang, C.; Cui, G.; Luo, X.; Xu, Y.; Li, H.; Dai, S. Highly Efficient and Reversible SO_2 Capture by Tunable Azole-Based Ionic Liquids through Multiple-Site Chemical Absorption. *J. Am. Chem. Soc.* **2011**, *133*, 11916−11919.
(61) Lu, R.; Ma, S.; Zhai, Y.; Geng, Z.; Jin, Z.; Fu, Y.; Wang, W.; Xu, Y. Acetylcholine-based deep eutectic solvents for highly efficient SO_2 absorption, selective separation from CO_2 and their mechanism. *J. Mol. Liq.* **2023**, *383*, 121937.
(62) Huang, K.; Chen, Y.-L.; Zhang, X.-M.; Xia, S.; Wu, Y.-T.; Hu, X.-B. SO_2 absorption in acid salt ionic liquids/sulfolane binary mixtures: Experimental study and thermodynamic analysis. *Chem. Eng. J.* **2014**, *237*, 478−486.
(63) Liu, P.; Cai, K.; Zhang, X.; Wang, X.; Xu, M.; Liu, F.; Zhao, T. Rich Ether-Based Protic Ionic Liquids with Low Viscosity for Selective Absorption of SO_2 through Multisite Interaction. *Ind. Eng. Chem. Res.* **2022**, *61*, 5971−5983.
(64) Yeadon, D. J.; Jacquemin, J.; Plechkova, N. V.; Maréchal, M.; Seddon, K. R. Induced Protic Behaviour in Aprotonic Ionic Liquids by Anion Basicity for Efficient Carbon Dioxide Capture. *ChemPhysChem* **2020**, *21*, 1369−1374.
(65) Mondal, A.; Balasubramanian, S. Molecular Dynamics Investigation of Efficient SO_2 Absorption by Anion-Functionalized Ionic Liquids. *J. Chem. Sci.* **2017**, *129*, 859−872.
(66) Khatri, R. A.; Chuang, S. S. C.; Soong, Y.; Gray, M. Thermal and Chemical Stability of Regenerable Solid Amine Sorbent for CO_2 Capture. *Energy Fuels* **2006**, *20*, 1514−1520.
(67) Clough, M. T.; Geyer, K.; Hunt, P. A.; Mertes, J.; Welton, T. Thermal decomposition of carboxylate ionic liquids: trends and mechanisms. *Phys. Chem. Chem. Phys.* **2013**, *15*, 20480−20495.
(68) Yang, D.; Hou, M.; Ning, H.; Ma, J.; Kang, X.; Zhang, J.; Han, B. Reversible Capture of SO_2 through Functionalized Ionic Liquids. *ChemSusChem* **2013**, *6*, 1191−1195.
(69) Zeng, S.; Gao, H.; Zhang, X.; Dong, H.; Zhang, X.; Zhang, S. Efficient and reversible capture of SO_2 by pyridinium-based ionic liquids. *Chem. Eng. J.* **2014**, *251*, 248−256.
(70) Ren, S.; Hou, Y.; Zhang, K.; Wu, W. Ionic liquids: Functionalization and absorption of SO_2. *Green Energy Environ.* **2018**, *3*, 179−190.
(71) Jiang, L.; Mei, K.; Chen, K.; Dao, R.; Li, H.; Wang, C. Design and prediction for highly efficient SO_2 capture from flue gas by imidazolium ionic liquids. *Green Energy Environ.* **2022**, *7*, 130−136.
(72) Zhang, H.; Jiang, B.; Yang, N.; Zhang, N.; Zhang, L.; Huang, Z.; Xiao, X.; Tantai, X. Highly Efficient and Reversible Absorption of SO_2 from Flue Gas Using Diamino Polycarboxylate Protic Ionic Liquid Aqueous Solutions. *Energy Fuels* **2019**, *33*, 8937−8945.

https://doi.org/10.1021/acssuschemeng.4c02659
ACS Sustainable Chem. Eng. XXXX, XXX, XXX−XXX

Supporting Information:

Improved reversible and selective SO_2 absorption by a stable phosphonium carboxylate ionic liquid

Nicolas Scaglione, Luke Wylie, Agilio Pádua, and Margarida Costa Gomes*

Laboratoire de Chimie de l'ENS Lyon, CNRS and Université de Lyon, 46 allée d'Italie, 69364 Lyon, France

E-mail: margarida.costa-gomes@ens-lyon.fr

1 Absorption data of SO_2 and CO_2

Table S1 – SO_2 absorption expressed in mole fraction (x_{SO_2}) and molality (b_{SO_2}) in $[P_{4,4,4,4}][TetrazC_1COO]$ as a function of pressure from 0–1 bar at 5 temperatures from 303 K to 343 K.

SO_2 absorption							
$\frac{T}{K}$	$\frac{P}{mbar}$	x_{SO_2}	$\frac{b_{SO_2}}{mmol\ g^{-1}}$	$\frac{T}{K}$	$\frac{P}{mbar}$	x_{SO_2}	$\frac{b_{SO_2}}{mmol\ g^{-1}}$
303.455	22.39	0.436	1.996	313.371	28.13	0.433	1.974
303.444	37.14	0.486	2.444	313.353	50.55	0.480	2.392
303.449	282.66	0.600	3.886	313.356	310.88	0.582	3.600
303.448	283.75	0.601	3.894	313.354	338.97	0.586	3.664
303.628	470.80	0.641	4.621	313.354	510.35	0.617	4.175
303.446	525.58	0.664	5.119	313.371	586.75	0.639	4.586
303.453	575.23	0.675	5.382	313.355	640.75	0.651	4.827
303.462	833.86	0.719	6.620	313.372	890.62	0.687	5.688
323.295	37.29	0.429	1.940	333.220	53.68	0.421	1.878
323.280	69.12	0.473	2.321	333.195	93.65	0.463	2.230
323.274	338.08	0.562	3.322	333.206	365.24	0.542	3.061
323.287	396.87	0.571	3.449	333.202	455.60	0.556	3.242
323.275	549.80	0.593	3.763	333.197	588.14	0.567	3.392
323.281	642.80	0.616	4.145	333.210	695.03	0.593	3.773
323.262	700.01	0.629	4.378	333.176	755.99	0.607	3.991
323.290	935.00	0.667	5.192	333.212	978.25	0.648	4.758
343.143	72.06	0.412	1.812				
343.123	123.04	0.451	2.125				
343.118	391.13	0.523	2.833				

SO_2 absorption							
$\frac{T}{K}$	$\frac{P}{mbar}$	x_{SO_2}	$\frac{b_{SO_2}}{mmol\ g^{-1}}$	$\frac{T}{K}$	$\frac{P}{mbar}$	x_{SO_2}	$\frac{b_{SO_2}}{mmol\ g^{-1}}$
343.063	524.34	0.537	3.003				
343.125	624.11	0.544	3.082				
343.124	744.47	0.572	3.453				
343.100	811.58	0.584	3.631				
343.132	1024.18	0.623	4.268				

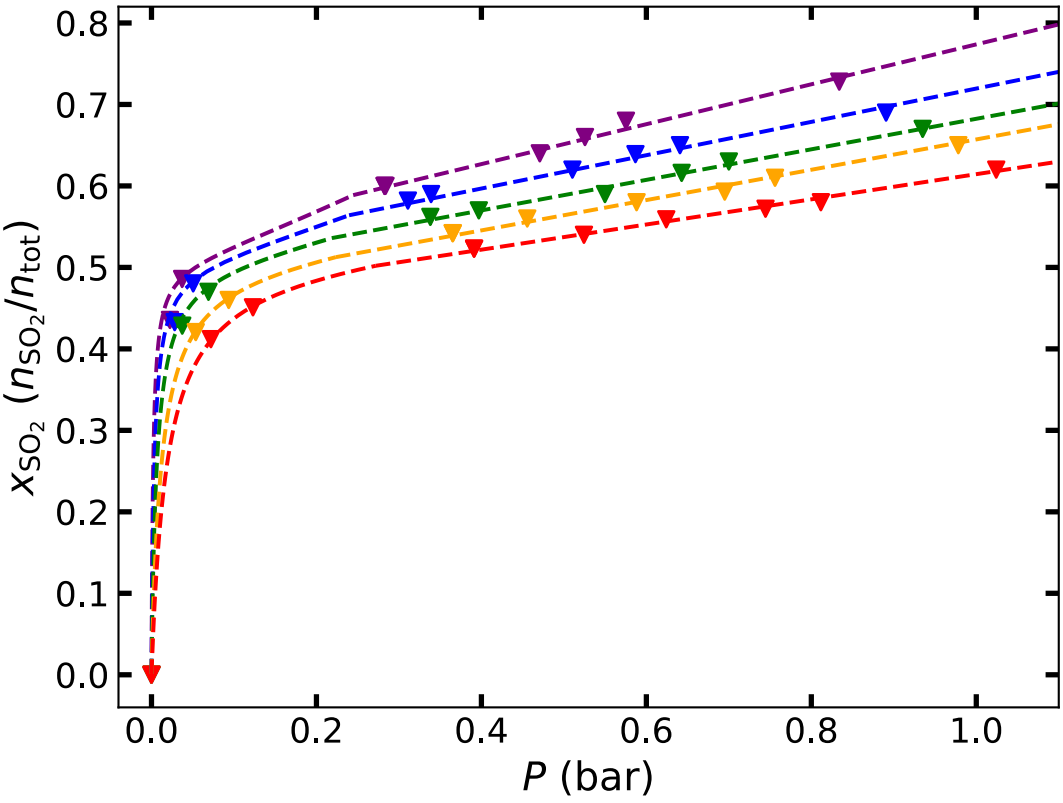

Figure S1 – SO_2 mole fraction absorbed by $[P_{4,4,4,4}][TetrazC_1COO]$ in the 0–1 bar pressure range at ▼ 303.15 K, ▼ 313.15 K, ▼ 323.15 K, ▼ 333.15 K and ▼ 343.15 K. The dashed lines represent fits of Eqs. S1 and S2 to the SO_2 absorption isotherms.

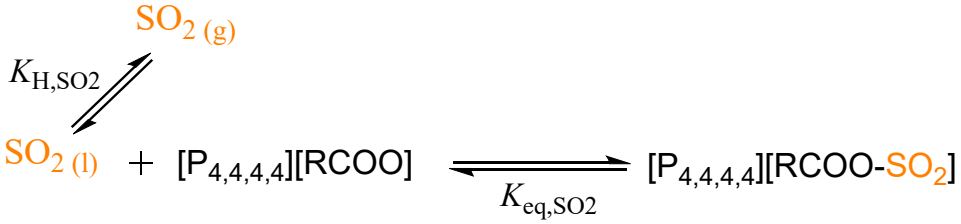

Figure S2 – SO_2 absorption mechanism by phosphonium carboxylate ILs following a 1:1 stoichiometry (IL:SO_2).

$$K_{\mathrm{H,gas}} = \lim_{x_{\mathrm{gas}} \to 0} \frac{\phi_{\mathrm{gas}} P}{x_{\mathrm{gas}}} \approx \frac{P}{x_{\mathrm{gas}}} \tag{S1}$$

where x_{gas} is the mole fraction of gas dissolved. ϕ_{gas} represents the gas fugacity coefficient and P is the equilibrium pressure of the system. The vapor phase was also considered as ideal ($\phi_{\mathrm{gas}} \approx 1$).

Compound	n_{i}
SO_2 (sol)	$n_{SO_2}(1-\xi)$
$[P_{4,4,4,4}][RCOO]$	$n_{IL} - n_{SO_2}\xi$
$[P_{4,4,4,4}][RCOO{-}SO_2]$	$n_{SO_2}\xi$
Total	$n_{SO_2}(1-\xi) + n_{IL}$

$$K_{\mathrm{eq},SO_2} = \frac{\gamma_{IL-SO_2}}{\gamma_{SO_2}\gamma_{IL}} \frac{x_{IL-SO_2}}{x_{SO_2}x_{IL}} \approx \frac{x_{IL-SO_2}}{x_{SO_2}x_{IL}}$$
$$K_{\mathrm{eq},SO_2} = \frac{\xi[n_{SO_2}(1-\xi) + n_{IL}]}{(1-\xi)(n_{IL} - n_{SO_2}\xi)} \tag{S2}$$

where γ_{IL-SO_2}, γ_{SO_2} and γ_{IL} and x_{IL-SO_2}, x_{SO_2} and x_{IL} are the activity coefficients and the mole fraction of $[P_{4,4,4,4}][RCOO{-}SO_2]$, of SO_2 dissolved and of the neat IL in Equation S2. Herein, the solutions are assumed to be ideal, so, the activity coefficients were considered to be independent of the concentration, then, included in K_{eq,SO_2}. Its equation has been rewritten as a function of the amounts of compounds by considering the extent of reaction ξ.

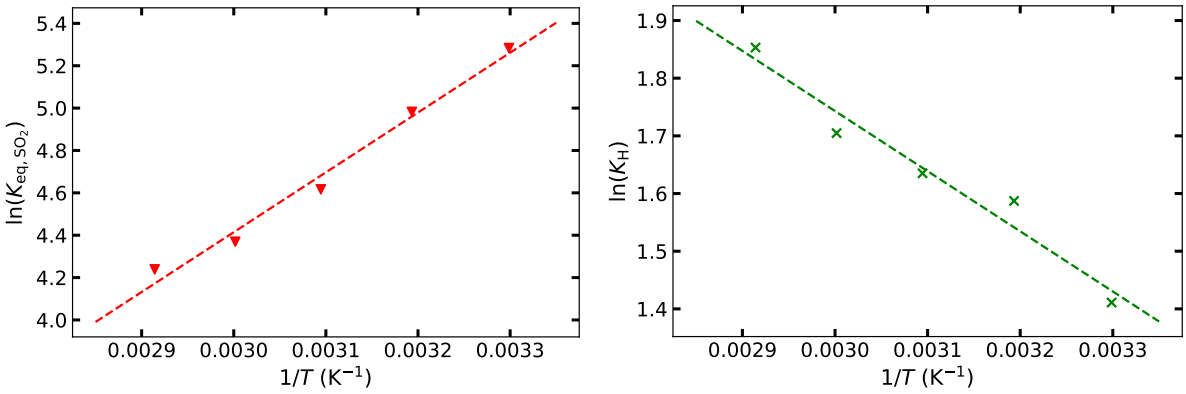

Figure S3 – The linear fit of the logarithm of (left) the equilibrium constant K_{eq,SO_2} and (right) the Henry's law constant K_{H,SO_2} with $1/T$ using van't Hoff equation for $[P_{4,4,4,4}][TetrazC_1COO]$. The points are calculated from the experimental isotherms and the dashed lines the fitting curves.

$$\frac{\partial ln K}{\partial T} = \frac{\Delta H}{RT^2} \tag{S3}$$

$$\Delta_r G^\circ_{exp.}(SO_2) = -RT ln(K_{eq,SO_2}) \tag{S4}$$

$$\Delta_r S^\circ_{exp.}(SO_2) = \frac{\Delta_r H^\circ_{exp.}(SO_2) - \Delta_r G^\circ_{exp.}(SO_2)}{T} \tag{S5}$$

Table S2 – Henry's law constant (K_{H,SO_2}) and equilibrium constant (K_{eq,SO_2}) obtained for SO_2 capture in $[P_{4,4,4,4}][TetrazC_1COO]$ based on the 1:1 mechanism, obtained by fitting the data in Table S1. The derived thermodynamic quantities of SO_2 absorption are also reported.

Gas	$\frac{T}{K}$	K_{eq,SO_2}	$\frac{K_{H,SO_2}}{bar}$	$\frac{\Delta_r H^\circ}{kJ\ mol^{-1}}$	$\frac{\Delta_r G^\circ}{kJ\ mol^{-1}}$	$\frac{\Delta_r S^\circ}{J\ mol^{-1}\ K^{-1}}$	$\frac{\Delta_{sol} H^\circ}{kJ\ mol^{-1}}$
	303	197.09 ± 0.005	4.10 ± 0.09		-13.32	-33.53	
	313	145.82 ± 0.001	4.89 ± 0.09		-12.97	-33.56	
SO_2	323	101.14 ± 0.001	5.13 ± 0.10	-23.48	-12.40	-34.28	-8.67
	333	78.98 ± 0.002	5.50 ± 0.06		-12.10	-34.16	
	343	69.32 ± 0.003	6.38 ± 0.09		-12.09	-33.19	

Table S3 – Absorption and desorption of CO_2 expressed in mole fraction (x_{CO_2}) and molality (b_{CO_2}) in $[P_{4,4,4,4}][TetrazC_1COO]$ as a function of pressure from 0–5 bar at 303 K, 323 K and 343 K.

CO_2 - Absorption				CO_2 - Desorption			
$\frac{T}{K}$	$\frac{P}{bar}$	x_{CO_2}	$\frac{b_{CO_2}}{mmol\ g^{-1}}$	$\frac{T}{K}$	$\frac{P}{bar}$	x_{CO_2}	$\frac{b_{CO_2}}{mmol\ g^{-1}}$
			1st cycle				
303.243	0.0000	0.0000	0.0000	303.243	0.0000	0.0000	0.0000
303.124	0.2494	0.0095	0.0249	303.138	0.2492	0.0103	0.0259
303.110	0.4988	0.0155	0.0408	303.134	0.4986	0.0170	0.0428
303.124	0.7480	0.0217	0.0573	303.148	0.7486	0.0236	0.0599
303.224	0.9991	0.0269	0.0716	303.158	0.9991	0.0296	0.0753
303.134	2.4991	0.0577	0.1584	303.138	2.4991	0.0604	0.1624
303.134	4.9987	0.1026	0.2957	303.134	4.9987	0.1026	0.2957
320.562	0.0000	0.0000	0.0000	320.562	0.0000	0.0000	0.0000
323.086	0.2492	0.0067	0.0175	323.100	0.2498	0.0087	0.0201
323.100	0.4984	0.0112	0.0293	323.105	0.4989	0.0128	0.0314
323.119	0.7490	0.0147	0.0387	323.115	0.7475	0.0158	0.0402
323.139	0.9991	0.0175	0.0461	323.105	0.9986	0.0187	0.0477
323.129	2.4995	0.0419	0.1132	323.153	2.4977	0.0433	0.1151
323.086	4.9987	0.0761	0.2130	323.086	4.9987	0.0761	0.2130
343.024	0.0000	0.0000	0.0000	343.024	0.0000	0.0000	0.0000
343.062	0.2484	0.0046	0.0120	343.178	0.2483	0.0062	0.0161
343.110	0.4985	0.0065	0.0170	343.110	0.4990	0.0077	0.0201
343.110	0.7488	0.0068	0.0176	343.096	0.7483	0.0073	0.0189
343.125	0.9992	0.0084	0.0219	343.091	0.9995	0.0094	0.0247
343.101	2.4987	0.0337	0.0902	343.082	2.4987	0.0367	0.0986

CO_2 - Absorption				CO_2 - Desorption			
$\frac{T}{K}$	$\frac{P}{bar}$	x_{CO_2}	$\frac{b_{CO_2}}{mmol\ g^{-1}}$	$\frac{T}{K}$	$\frac{P}{bar}$	x_{CO_2}	$\frac{b_{CO_2}}{mmol\ g^{-1}}$
343.120	4.9986	0.0593	0.1630	343.120	4.9986	0.0593	0.1630
			2^{nd} cycle				
303.224	0.0000	0.0000	0.0000	303.224	0.0000	0.0000	0.0000
303.148	0.2490	0.0072	0.0189	303.134	0.2491	0.0094	0.0246
303.162	0.4975	0.0145	0.0380	303.153	0.4986	0.0159	0.0418
303.138	0.7488	0.0209	0.0553	303.138	0.7490	0.0218	0.0577
303.134	0.9993	0.0268	0.0714	303.148	0.9963	0.0283	0.0752
303.158	2.4995	0.0592	0.1628	303.134	2.4995	0.0601	0.1656
303.148	4.9990	0.1072	0.3107	303.148	4.9990	0.1072	0.3107
316.887	0.0000	0.0000	0.0000	316.887	0.0000	0.0000	0.0000
323.148	0.2497	0.0069	0.0180	323.167	0.2492	0.0079	0.0207
323.172	0.4986	0.0110	0.0288	323.163	0.4985	0.0119	0.0312
323.177	0.7490	0.0139	0.0366	323.163	0.7491	0.0147	0.0386
323.167	0.9995	0.0165	0.0434	323.177	0.9992	0.0177	0.0465
323.182	2.5002	0.0429	0.1160	323.177	2.4992	0.0437	0.1183
323.153	4.9976	0.0794	0.2233	323.153	4.9976	0.0794	0.2233
335.984	0.0000	0.0000	0.0000	335.984	0.0000	0.0000	0.0000
343.115	0.2492	0.0054	0.0140	343.135	0.2495	0.0067	0.0175
343.096	0.4984	0.0079	0.0206	343.106	0.4978	0.0082	0.0215
343.077	0.7495	0.0080	0.0210	343.120	0.7490	0.0083	0.0215
343.091	0.9989	0.0097	0.0253	343.106	0.9989	0.0101	0.0263
343.135	2.5002	0.0342	0.0917	343.101	2.5006	0.0346	0.0926
343.144	4.9977	0.0631	0.1743	343.144	4.9977	0.0631	0.1743

CO_2 - Absorption				CO_2 - Desorption			
$\frac{T}{K}$	$\frac{P}{bar}$	x_{CO_2}	$\frac{b_{CO_2}}{mmol\,g^{-1}}$	$\frac{T}{K}$	$\frac{P}{bar}$	x_{CO_2}	$\frac{b_{CO_2}}{mmol\,g^{-1}}$
			3rd cycle				
303.153	0.0000	0.0000	0.0000	303.153	0.0000	0.0000	0.0000
303.143	0.2495	0.0075	0.0195	303.153	0.2484	0.0093	0.0242
303.153	0.4978	0.0141	0.0371	303.153	0.4984	0.0157	0.0414
303.148	0.7488	0.0206	0.0544	303.138	0.7488	0.0215	0.0569
303.148	0.9995	0.0266	0.0707	303.153	0.9993	0.0266	0.0708
303.134	2.4998	0.0605	0.1667	303.148	2.4987	0.0573	0.1573
303.162	4.9993	0.1059	0.3065	303.162	4.9993	0.1059	0.3065
334.734	0.0000	0.0000	0.0000	334.734	0.0000	0.0000	0.0000
336.687	0.2480	0.0072	0.0189	343.125	0.2504	0.0071	0.0185
343.086	0.4985	0.0084	0.0219	343.101	0.4989	0.0083	0.0217
343.115	0.7491	0.0090	0.0235	343.13	0.7479	0.0093	0.0243
343.110	1.0000	0.0119	0.0311	343.082	0.9992	0.0132	0.0347
343.115	2.4994	0.0350	0.0938	343.144	2.4992	0.0370	0.0993
343.115	4.9990	0.0608	0.1674	343.115	4.9990	0.0608	0.1674

Table S4 – Henry's law constant (K_{H,CO_2}) obtained for $[P_{4,4,4,4}][TetrazC_1COO]$ by fitting the CO_2 absorption isotherms to Henry's Law at 303 K, 323 K and 343 K. * Too low to be determined accurately.

Gas	$\frac{T}{K}$	$\frac{K_{H,CO_2}}{bar}$
CO_2	303	46.2 ± 1.8
	323	63.2 ± 1.9
	343	82.5 ± 2.9

2 Reversibility and repeatability of SO_2 and CO_2 absorption

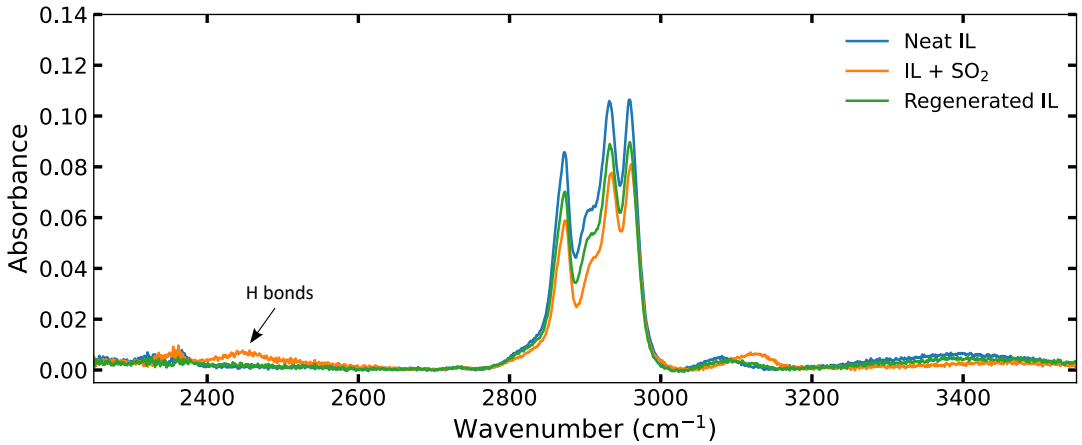

Figure S4 – FT-IR spectra of the — neat $[P_{4,4,4,4}][TetrazC_1COO]$, of the IL after being exposed to — SO_2 and after being under — vacuum at 323 K for 2 h.

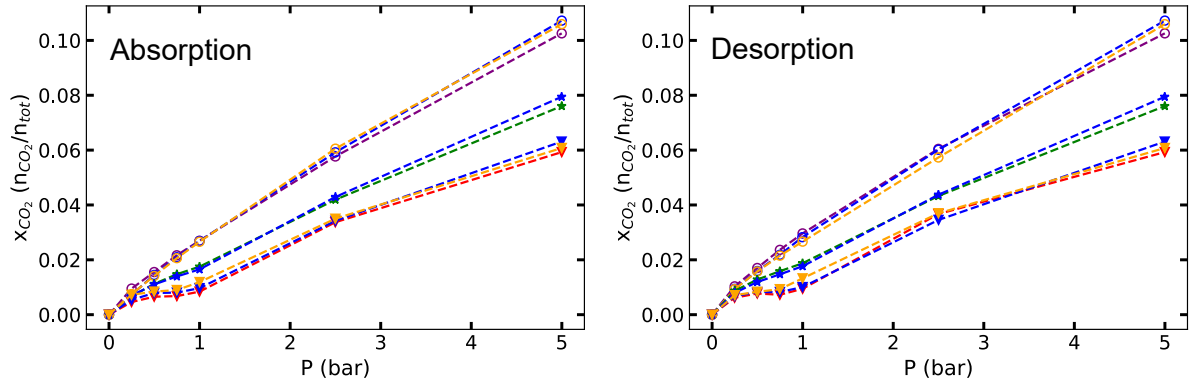

Figure S5 – CO_2 (left) absorption and (right) desorption of $[P_{4,4,4,4}][TetrazC_1COO]$ at ◯ 303.15 K, ★ 323.15 K and ▼ 343.15 K in the pressure range 0–5 bar. The repeatability and sustainability of the CO_2 absorption has been tested over 3 cycles (— 2nd cycle and — 3rd cycle).

Table S5 – Henry's law constant (K_{H,CO_2}) obtained for the successive CO_2 absorption cycles by [$P_{4,4,4,4}$][TetrazC_1COO] at either 303 K, 323 K or 343 K.

Cycle	$\frac{T}{K}$	$\frac{K_{H,CO_2}}{bar}$
2nd	303	44.8 ± 1.3
	323	61.3 ± 1.4
	343	78.1 ± 2.2
3rd	303	45.0 ± 1.4
	343	79.0 ± 2.8

3 NMR of the ionic liquid before and after SO_2 or CO_2 absorption

3.1 ^{1}H-^{1}H NOESY experiments

Valuable insights into the local structure between ions in $[P_{4,4,4,4}][TetrazC_1COO]$ can be obtained by 2D $^1H-^1H$ NOESY NMR experiments, which give information on the spatial proximity of protons, through the cross-relaxation rates, σ_{IRA}, which are higher when two hydrogen atoms are closer (within 5 Å). It is possible to determine cross-relaxation rates by linearly fitting the corrected intensity of the cross-peaks as a function of the mixing time, which we report at 303.15, 323.15 and 343.15 K (Figures S6). To ensure minimal spin diffusion within the observed range, only short mixing times were considered, leading to a linear behavior. It has been shown that the initial rate approximation (IRA) provides results consistent with fitting the complete build-up curve using longer mixing times.[S1] The cross-relaxation rates obtained are listed in Table S5 and allow a qualitative comparison of the rather spatial correlations between the protons on the cations and anions.

The cross-relaxation rates between all all the protons increase at lower temperatures. Intramolecular NOE measurements indicate a preference for a specific conformation at low temperature, resulting in an increase of its population. Higher cross-relaxation rates are related to lower distances between protons, as confirmed by the intramolecular NOEs between protons along the side chain the phosphonium cation, with for example: $\sigma_{IRA}(H_\alpha-H_\beta) > \sigma_{IRA}(H_\alpha-H_\gamma) > \sigma_{IRA}(H_\alpha-H_{CH_3(term)})$. This is logically due to the high conformational flexibility of the alkyl side chains in $[P_{4,4,4,4}]^+$ and to the torsional degree of freedom in $[TetrazC_1COO]^-$ provided by the C_α.

At lower temperatures, intermolecular NOEs also show an enhancement of intermolecular origin, since neighboring species have lower diffusivity, leading to higher ion-ion spatial correlations. The cross-relaxation rates between H_α, H_β, H_γ of the cation, and H_α of the anion are similar within the uncertainty of the measurements. Only $\sigma_{IRA}(H_{CH_3(term)}-H_{C\alpha})$ is slightly higher, showing that the terminal protons are closer to the carboxylate anion, likely due to their higher mobility. With

respect to the H_{ring} of the anion, the closer protons are H_{α}, which was not expected since they are located in the core of the cations. Nonetheless, this feature is in line with the secondary cation-anion interactions previously found by MD simulations, in which N2 of $[TetrazC_1COO]^-$ is in close contact with the acidic H_{α} of $[P_{4,4,4,4}]^+$.

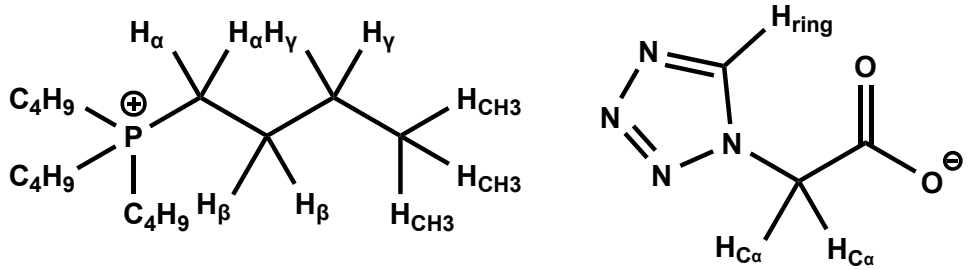

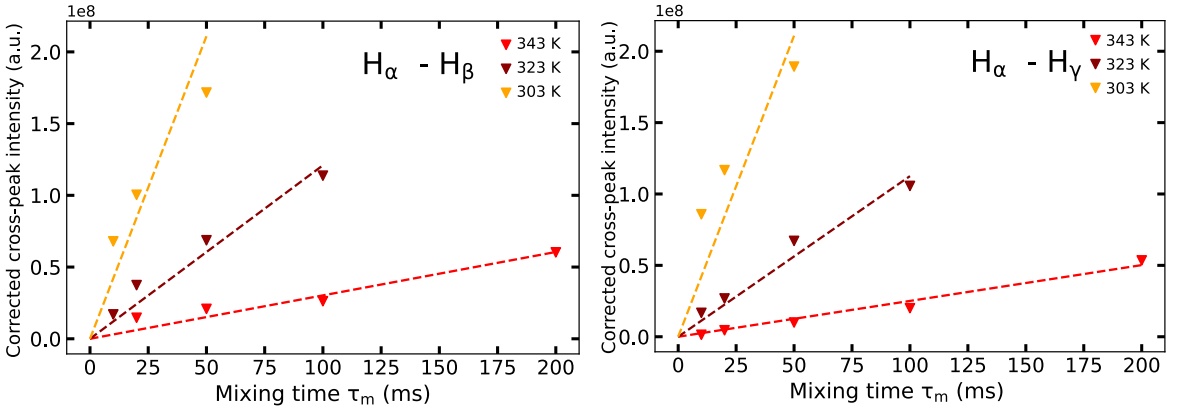

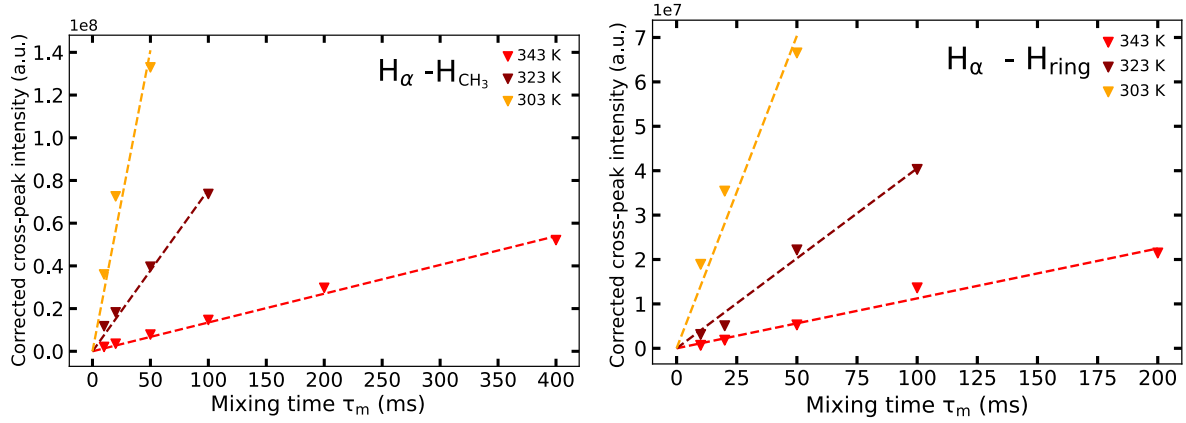

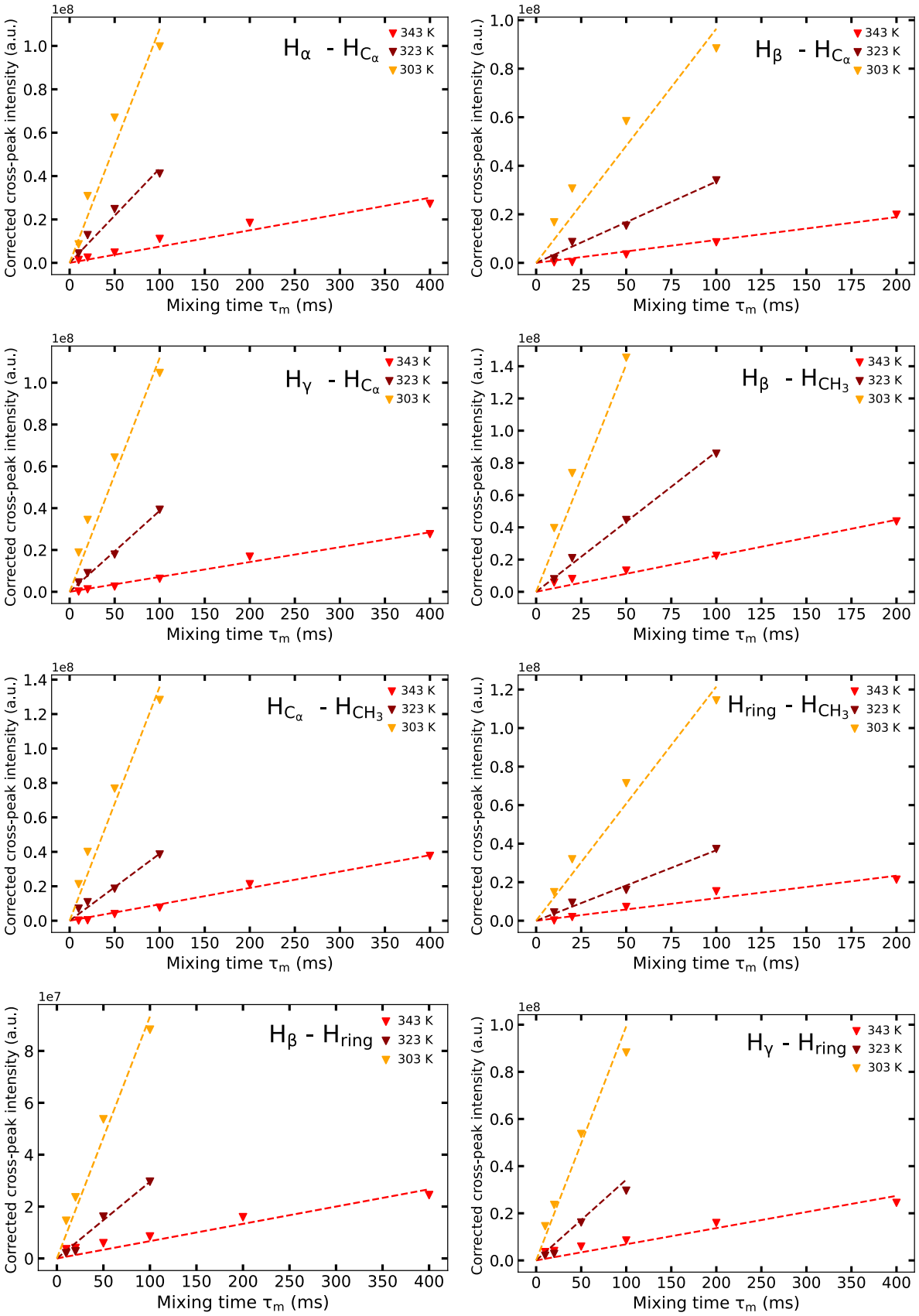
Hα - HCα
Hβ - HCα
Hγ - HCα
Hβ - HCH3
HCα - HCH3
Hring - HCH3
Hβ - Hring
Hγ - Hring
343 K
323 K
303 K
Corrected cross-peak intensity (a.u.)
Mixing time τm (ms)
1e8
1e7

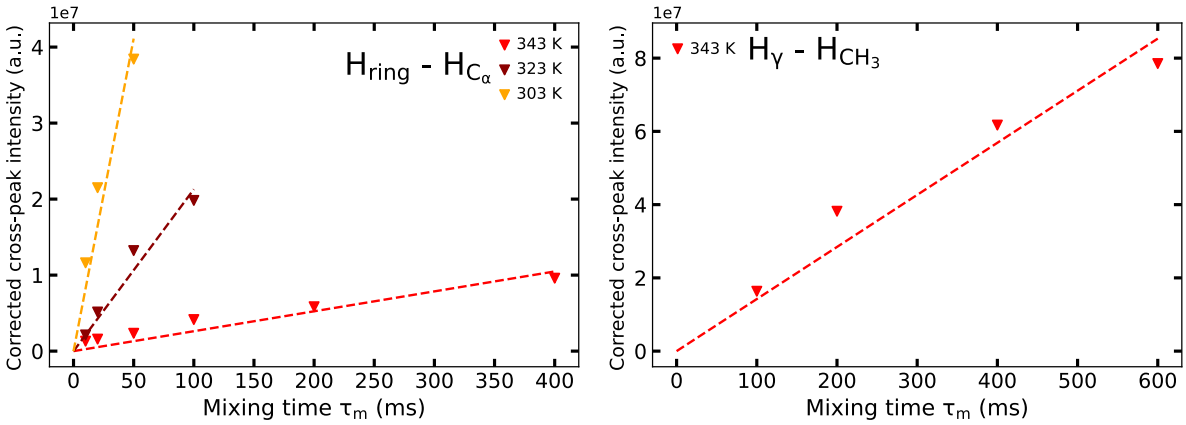

Figure S6 – Build-up curves of the corrected NOE cross-peak volume intensities as a function of mixing time in $[P_{4,4,4,4}][TetrazC_1COO]$ at 303.15, 323.15 and 343.15 K. The dashed lines represent the linear fittings with the coefficient reported in Table S6.

Table S6 – Cross relaxation rates σ_{IRA} for various interacting sites in $[P_{4,4,4,4}][TetrazC_1COO]$ at 303.15, 323.15 and 343.15 K obtained by the linear fit of the build-up curves depicted in the ESI Figure S5.

$\frac{T}{K}$	$\frac{\sigma_{IRA}}{10^5\ ms^{-1}}$				
	$H_\alpha - H_\beta$	$H_\alpha - H_\gamma$	$H_\alpha - H_{CH_3(term)}$	$H_\beta - H_{CH_3(term)}$	$H_\gamma - H_{CH_3(term)}$
343.15	3.03 ± 0.28	2.51 ± 0.15	1.35 ± 0.04	2.23 ± 0.12	1.42 ± 0.01
323.15	12.09 ± 0.90	11.25 ± 0.74	7.56 ± 0.29	8.69 ± 0.20	-
303.15	37.56 ± 5.51	42.18 ± 7.55	28.20 ± 2.54	28.20 ± 2.53	-
	$H_{ring} - H_{CH_3(term)}$	$H_{C_\alpha} - H_{CH_3(term)}$	$H_\alpha - H_{ring}$	$H_\beta - H_{ring}$	$H_\gamma - H_{ring}$
343.15	1.17 ± 0.09	0.95 ± 0.04	1.12 ± 0.06	0.67 ± 0.06	0.68 ± 0.01
323.15	3.65 ± 0.16	3.89 ± 0.22	4.05 ± 0.19	2.95 ± 0.18	3.42 ± 0.09
303.15	12.15 ± 0.77	13.60 ± 0.96	14.08 ± 1.23	9.32 ± 0.57	9.92 ± 1.00
	H_α-H_{C_α}	$H_\beta - H_{C_\alpha}$	$H_\gamma - H_{C_\alpha}$	$H_{ring} - H_{C_\alpha}$	
343.15	0.75 ± 0.06	0.94 ± 0.06	0.71 ± 0.03	0.26 ± 0.03	
323.15	4.34 ± 0.28	3.35 ± 0.15	3.87 ± 0.11	2.13 ± 0.16	
303.15	10.78 ± 0.91	9.62 ± 0.94	11.20 ± 0.91	8.22 ± 0.86	

3.2 NMR and IR spectra of SO_2 absorption

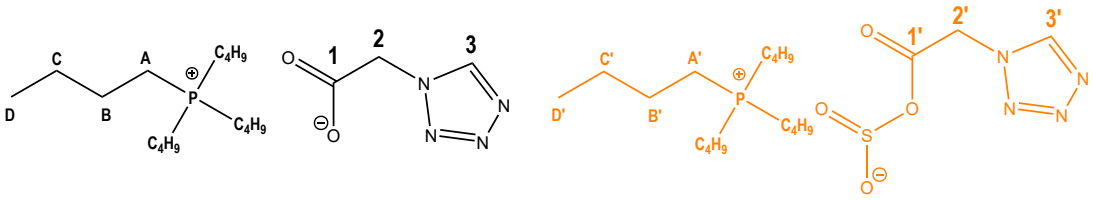

Figure S7 – Chemical structure of the $[P_{4,4,4,4}][TetrazC_1COO]$ (left) before and (right) after SO_2 absorption.

Tetrabutylphosphonium 1H-tetrazole-1-acetate $[P_{4,4,4,4}][TetrazC_1COO]$ after SO_2 absorption:

^{1}H NMR (400 MHz, C_6D_6, 343 K) δ ppm: 0.98 (t, 12H, $^3J_{HH}$ = 7.1 Hz, D'); 1.53 (m, 8H, C'); 1.62 (m, 8H, B'); 2.29 (m, 8H, A'); 5.03 (s, 2H, 2'); 9.17 (s, 1H, 3'). ^{13}C NMR (100 MHz, C_6D_6, 343 K) δ ppm: 13.67 (4C, D'); 18.93 (4C, A'); 23.80, 24.14 (8C, B'+C'); 51.25 (2C, 2'); 145.07 (1C, 3'); 168.21 (1C, 1'). ^{31}P NMR (161 MHz, C_6D_6, 343 K) δ ppm: 33.74 (1P, **P**$((CH_2)_3CH_3)_4$).

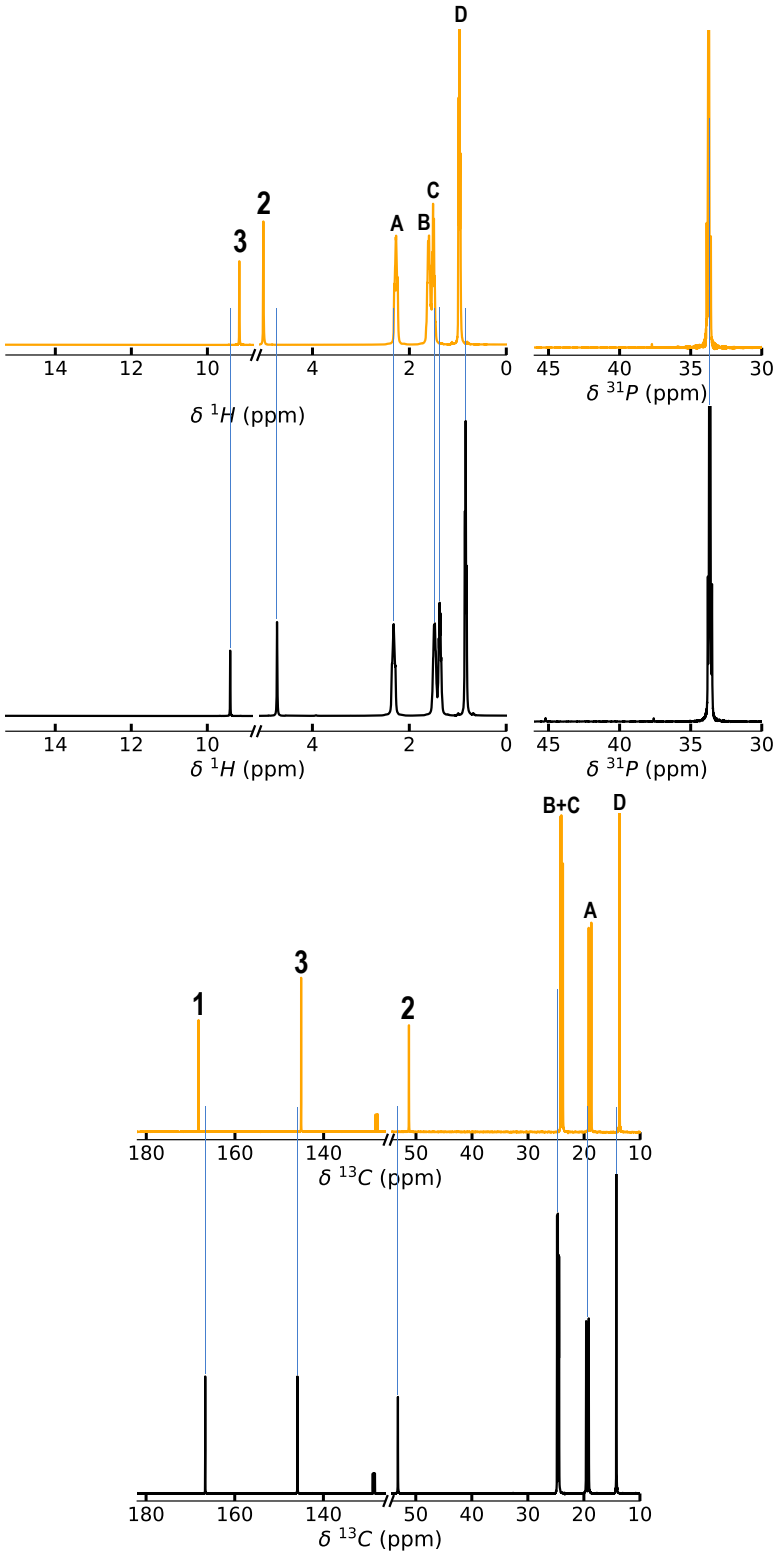

Figure S8 – (Top left) ^{1}H, (top right) ^{31}P and (bottom) ^{13}C NMR spectra of $[P_{4,4,4,4}][TetrazC_1COO]$ — before and — after SO_2 absorption at 343 K with C_6D_6 capillary as internal reference.

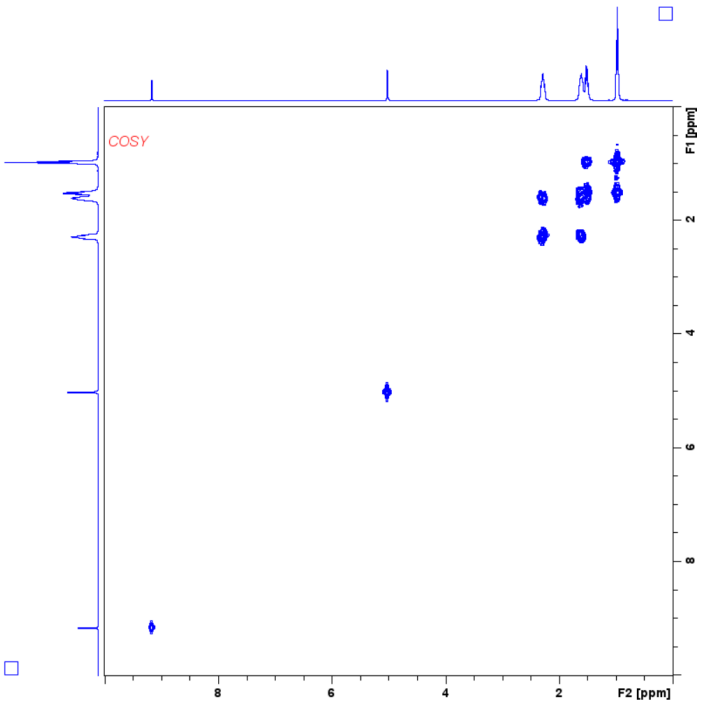

Figure S9 – COSY NMR spectrum of $[P_{4,4,4,4}][TetrazC_1COO]$ after SO_2 absorption at 343 K with C_6D_6 capillary as internal reference.

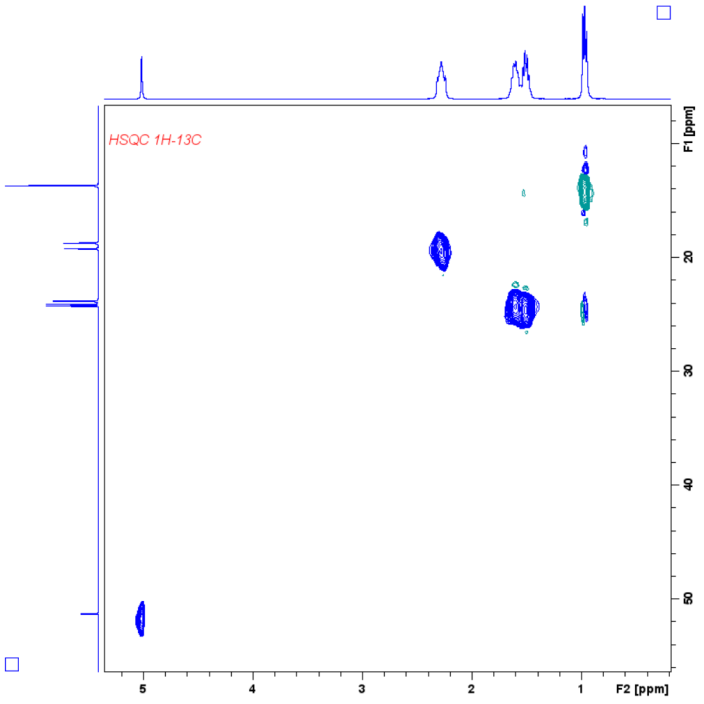

Figure S10 – HSQC NMR spectrum of $[P_{4,4,4,4}][TetrazC_1COO]$ after SO_2 absorption at 343 K with C_6D_6 capillary as internal reference.

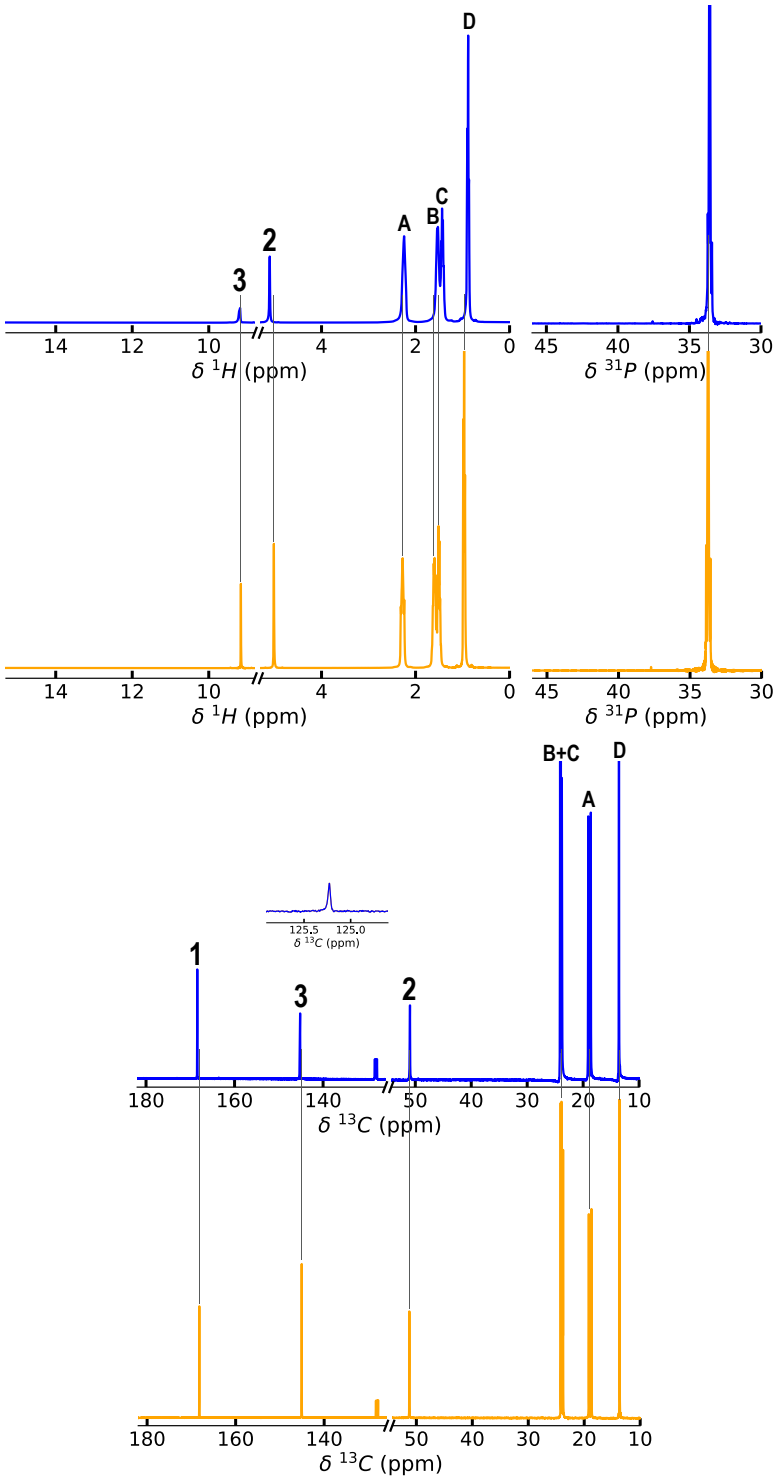

Figure S11 – (Top left) ^{1}H, (top right) ^{13}C and (bottom) ^{13}C NMR spectra of $[P_{4,4,4,4}][TetrazC_1COO]$ after — SO_2 absorption and — after being pressurized with CO_2 at 343 K with C_6D_6 capillary as internal reference.

3.3 NMR spectra of CO_2 absorption

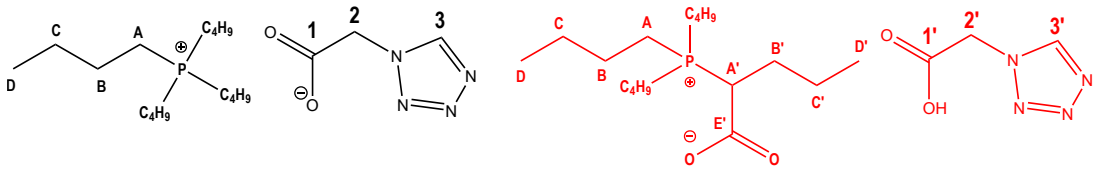

Figure S12 – Chemical structure of the $[P_{4,4,4,4}][TetrazC_1COO]$ (left) before and (right) after CO_2 absorption.

Tetrabutylphosphonium 1H-tetrazole-1-acetate $[P_{4,4,4,4}][TetrazC_1COO]$ after CO_2 absorption: ^1H NMR (400 MHz, C_6D_6, 343 K) δ ppm: 0.86 (t, 12H, $^3J_{HH}$ = 7.1 Hz, D); 1.40 (m, 8H, C); 1.50 (m, 8H, B); 2.35 (m, 8H, A); 4.75 (s, 2H, 2); 9.40 (s, 1H, 3). ^{13}C NMR (100 MHz, C_6D_6, 343 K) δ ppm: 13.61 (4C, D); 18.80 (4C, A); 23.65-24.43 (8C, B+C); 52.60 (2C, 2); 125.58 (1C, CO_2); 145.26 (1C, 3); 166.11 (1C, 1). ^{31}P NMR (161 MHz, C_6D_6, 343 K) δ ppm: 31.15 (1P, **P**$(CHCO_2(CH_2)_2CH_3)((CH_2)_3CH_3)_3)$; 33.65 (1P, **P**$((CH_2)_3CH_3)_4)$.

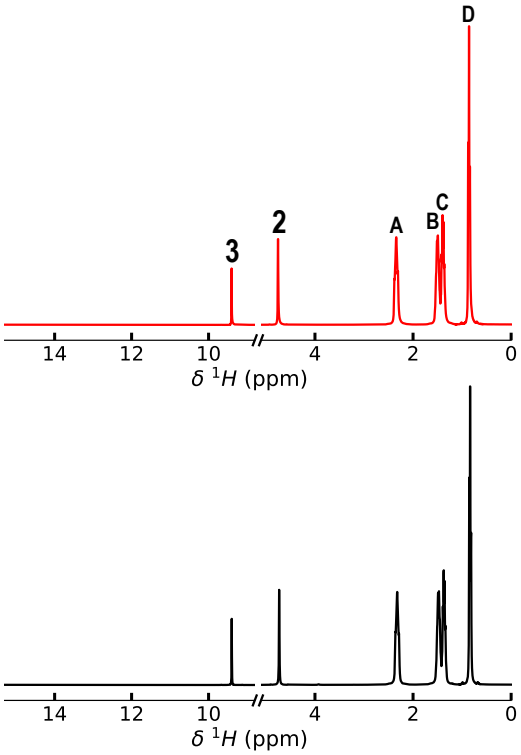

Figure S13 – ^1H NMR spectrum of $[P_{4,4,4,4}][TetrazC_1COO]$ — before and — after being pressurized with CO_2 at 343 K with C_6D_6 capillary as internal reference.

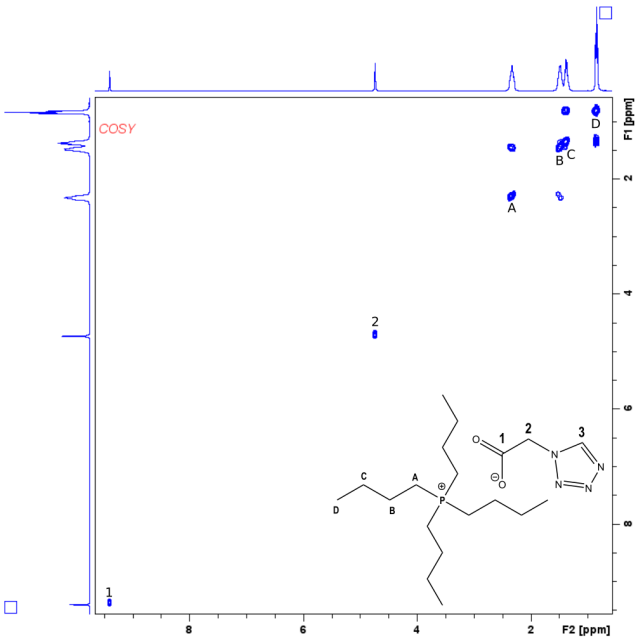

Figure S14 – COSY NMR spectrum of $[P_{4,4,4,4}][TetrazC_1COO]$ at 343 K with C_6D_6 capillary as internal reference.

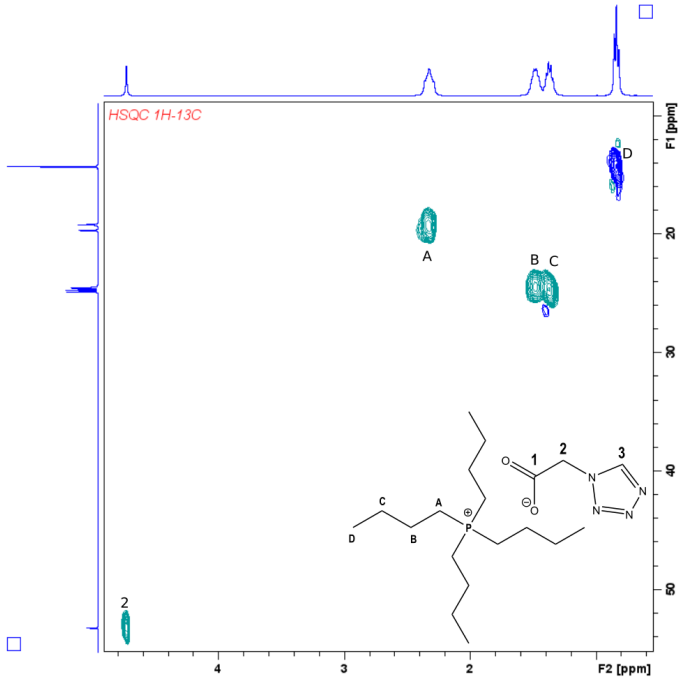

Figure S15 – HSQC NMR spectrum of $[P_{4,4,4,4}][TetrazC_1COO]$ at 343 K with C_6D_6 capillary as internal reference.

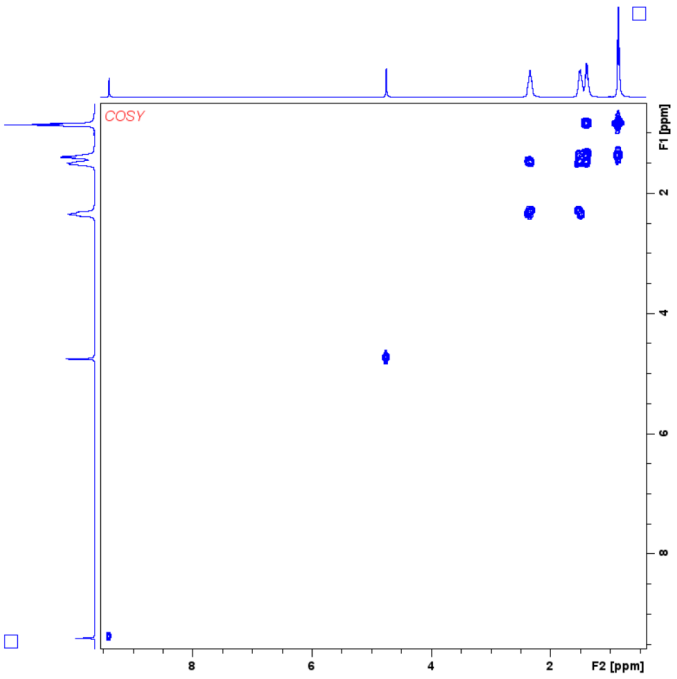

Figure S16 – COSY NMR spectrum of $[P_{4,4,4,4}][TetrazC_1COO]$ after being pressurized with CO_2 at 343 K with C_6D_6 capillary as internal reference.

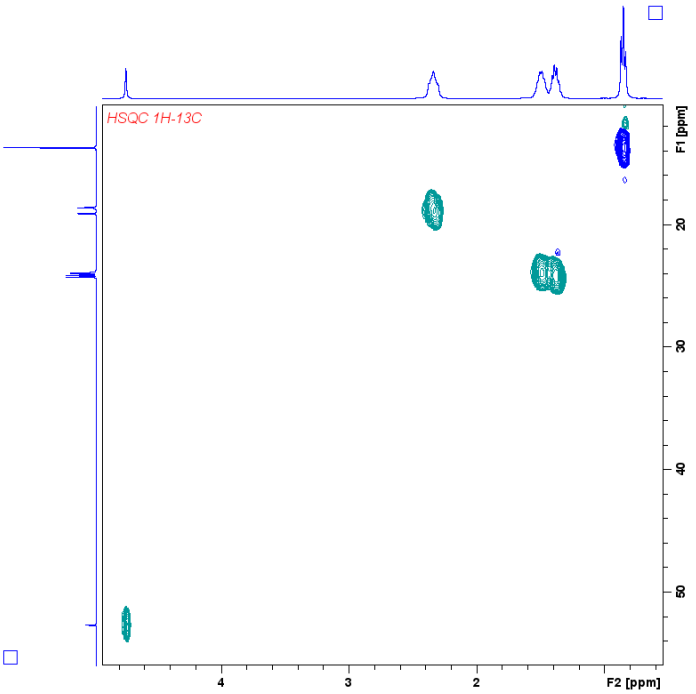

Figure S17 – HSQC NMR spectrum of $[P_{4,4,4,4}][TetrazC_1COO]$ after being pressurized with CO_2 absorption at 343 K with C_6D_6 capillary as internal reference.

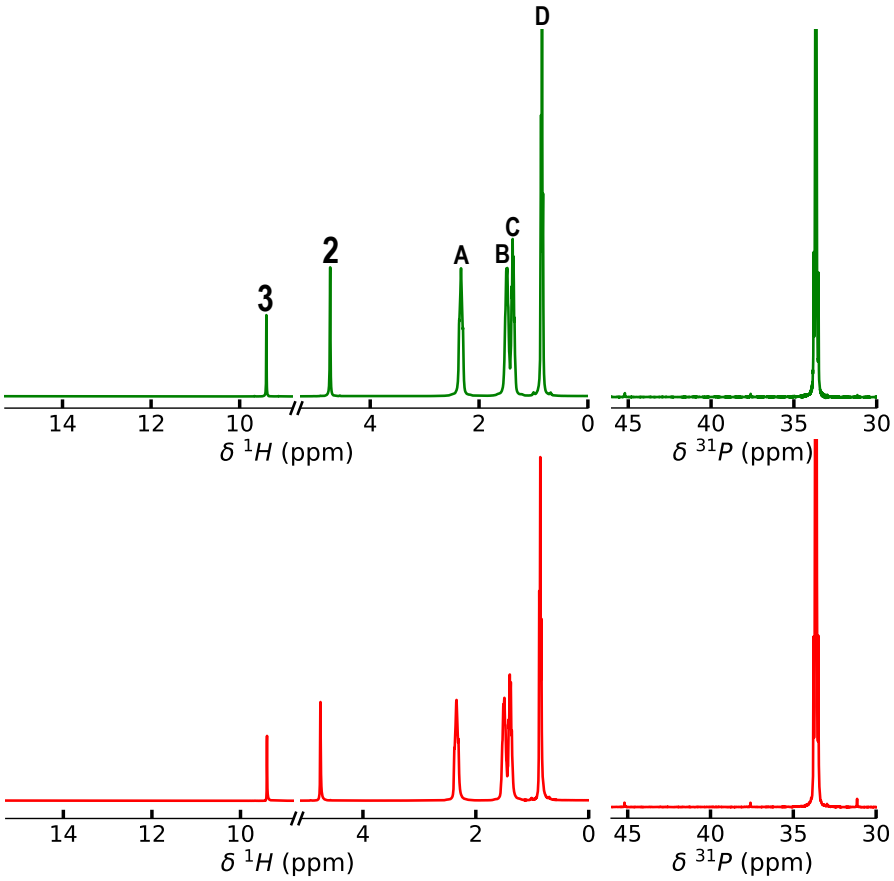

Figure S18 – (Left) ^{1}H and (right) ^{31}P NMR spectra of $[P_{4,4,4,4}][TetrazC_1COO]$ — after being pressurized with CO_2 and — after being place under vacuum at 343 K for 48 hours with C_6D_6 capillary as internal reference.

Table S7 – Chemical shifts of characteristics atoms involved in the absorption mechanism of $[P_{4,4,4,4}][TetrazC_1COO]$ with CO_2 or SO_2. The NMR measurements have been carried out on the pure ILs with an insert filled with a deuterated solvent as internal reference at 343 K.

Sample	$\delta^{31}P$ ppm	$\delta^{1}H_{\alpha([P_{4,4,4,4}]^+)}$ ppm	$\delta^{13}C_{COO^-}$ ppm
$[P_{4,4,4,4}][TetrazC_1COO]$	33.66	2.34	166.10
$[P_{4,4,4,4}][TetrazC_1COO] + CO_2$	31.15 & 33.64	2.34	166.11
$[P_{4,4,4,4}][TetrazC_1COO] + SO_2$	33.74	2.28	168.21
$[P_{4,4,4,4}][TetrazC_1COOSO_2] + CO_2$	33.58	2.25	168.42

3.4 Self-diffusion coefficients

Table S8 – Experimental self-diffusion coefficients of $[P_{4,4,4,4}][TetrazC_1COO]$ at 343 K by DOSY-NMR experiments.

Sample	D_{anion} / $10^{-11}m^2\,s^{-1}$	D_{cation} / $10^{-11}m^2\,s^{-1}$
$[P_{4,4,4,4}][TetrazC_1COO]$	1.69 ± 0.008	1.08 ± 0.003
$[P_{4,4,4,4}][TetrazC_1COO] + CO_2$	2.28 ± 0.01	1.48 ± 0.009
$[P_{4,4,4,4}][TetrazC_1COO] + SO_2$	4.43 ± 0.01	2.73 ± 0.008
$[P_{4,4,4,4}][TetrazC_1COO] + SO_2$ after vacuum	1.77 ± 0.008	1.15 ± 0.004

4 Molecular Dynamics Simulations

Table S9 – Distance between the centres of mass of the fragments and either CO_2 or SO_2 calculated by DFT at the B97-D3/cc-pVDZ level.

Dimers	r / Å
$[P_{1,1,1,1}]^+$-CO_2	4.831
$[P_{1,1,1,1}]^+$-SO_2	4.313
$[C_1COO]^-$-CO_2	6.228
$[C_1COO]^-$-SO_2	2.981
Butane-CO_2	3.785
Butane-SO_2	3.443
Tetrazole-CO_2	5.045
Tetrazole-SO_2	3.882
CO_2-CO_2	5.255
SO_2-SO_2	3.390

Table S10 – The scaling factors evaluated for the dispersion energy (ϵ) of the LJ potential.

Dimers	k
$[P_{1,1,1,1}]^+$-$[C_1COO]^-$	0.44
$[P_{1,1,1,1}]^+$-Butane	0.65
$[P_{1,1,1,1}]^+$-Tetrazole	0.61
$[P_{1,1,1,1}]^+$-CO_2	0.61
$[P_{1,1,1,1}]^+$-SO_2	0.62
Butane-$[C_1COO]^-$	0.50
Tetrazole-$[C_1COO]^-$	0.50
CO_2-$[C_1COO]^-$	0.34
SO_2-$[C_1COO]^-$	0.59
Tetrazole-Butane	1.00
Tetrazole-Tetrazole	1.00
Tetrazole-CO_2	1.00
Tetrazole-SO_2	0.91
Butane-CO_2	1.00
Butane-SO_2	0.91
CO_2-CO_2	1.00
SO_2-SO_2	0.84

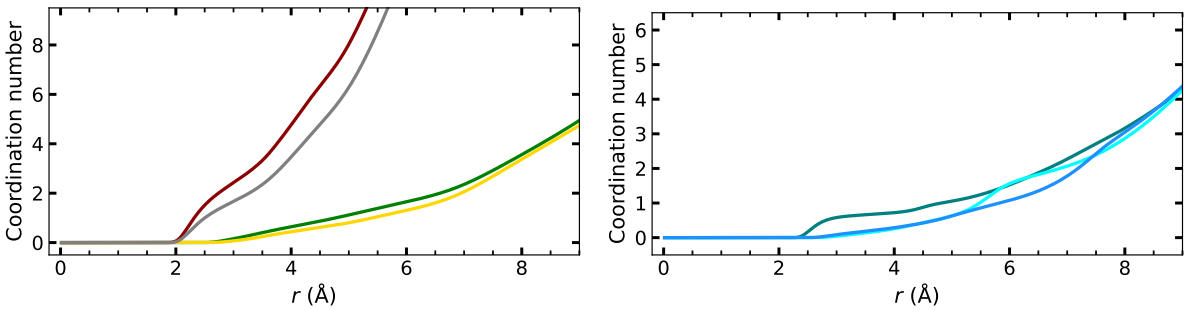

Figure S19 – Coordination numbers (CNs) calculated at 343 K in $[P_{4,4,4,4}][TetrazC_1COO]$. (Left) — P^+ and — H_α of the cation in presence of SO_2 and — P^+ and — H_α of the cation around the carboxylate head O_{COO^-} the anion without gas. (Right) S_{SO_2} around— O_{COO^-}, — N2, and — N4.

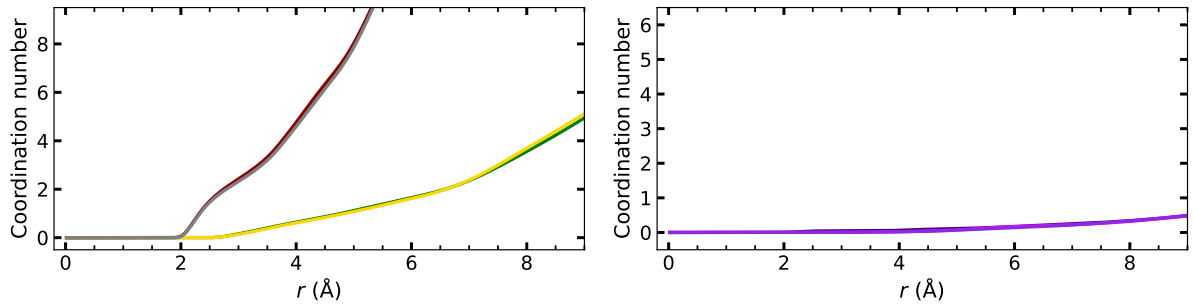

Figure S20 – Coordination numbers (CNs) calculated at 343 K in $[P_{4,4,4,4}][TetrazC_1COO]$. (Left) — P^+ and — H_α of the cation in presence of CO_2 and — P^+ and — H_α of the cation around the carboxylate head O_{COO^-} the anion without gas. (Right) C_{CO_2} around — O_{COO^-}, — N2, and — N4.

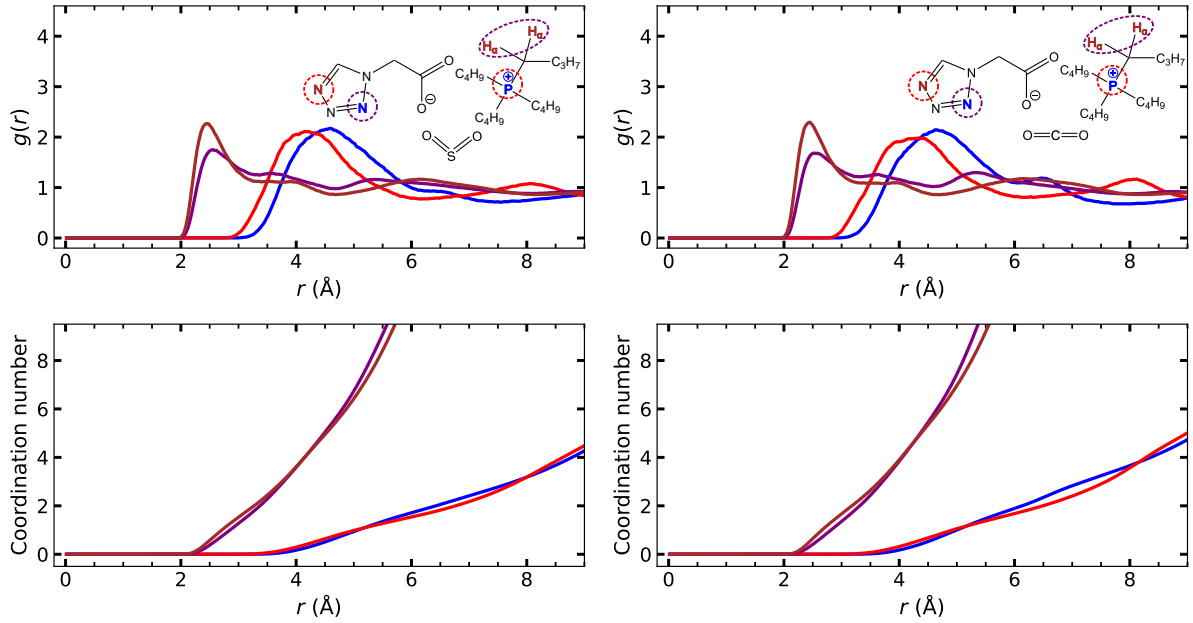

Figure S21 – (Top) Site-site radial distribution functions, $g(r)$, and (bottom) coordination numbers (CNs) calculated at 343 K in $[P_{4,4,4,4}][TetrazC_1COO]$. In presence of (left) SO_2 and (right) CO_2, —, — P^+ and —, — H_α of the cation around N2 and N4, respectively.

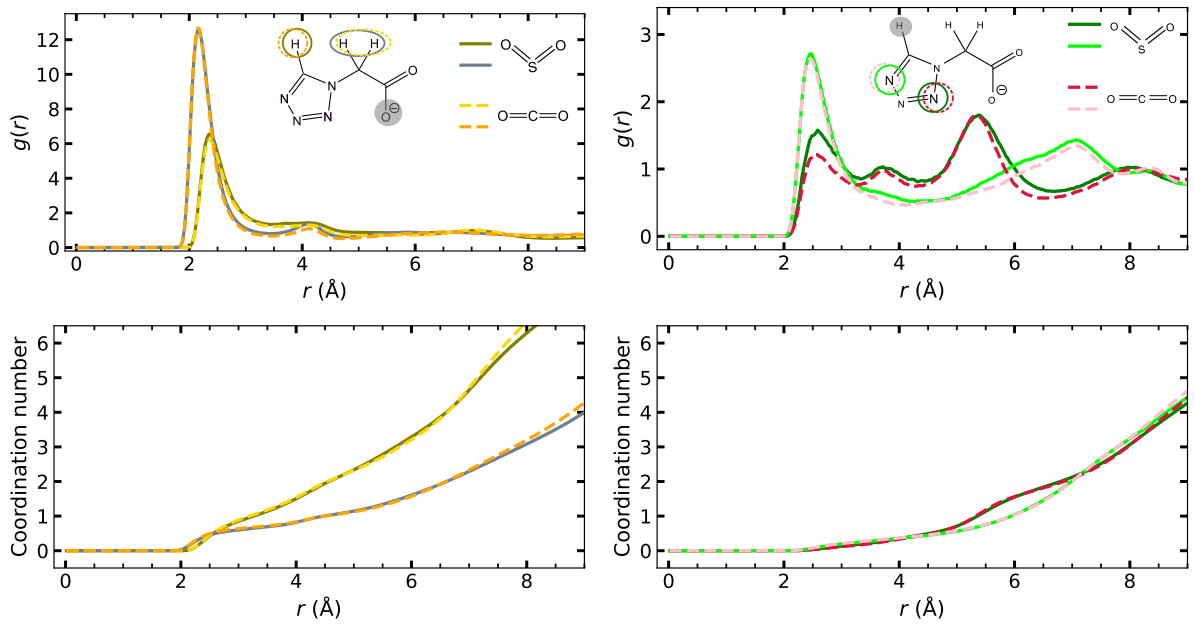

Figure S22 – (Top) Site-site radial distribution functions, $g(r)$, and (bottom) coordination numbers (CNs) calculated at 343 K in $[P_{4,4,4,4}][TetrazC_1COO]$. In presence of SO_2 (solid lines) or CO_2 (dashed lines), (left) —, — H_{C_α} and —, — H_{ring} around O_{COO^-}; (right) of —, — N2 and —, — N4 around H_{ring} of the $[TetrazC_1COO]^-$ anion, respectively.

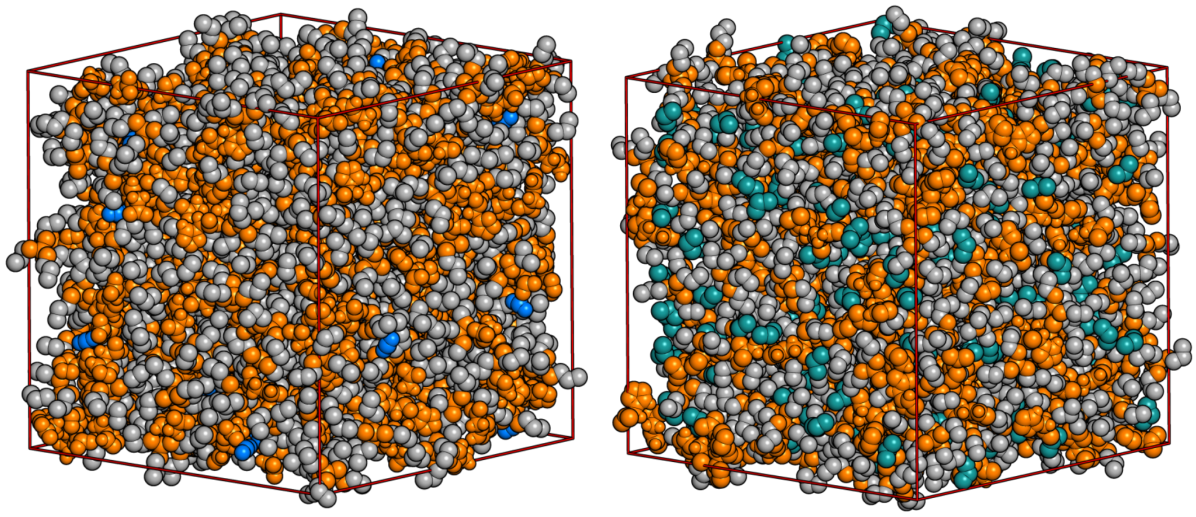

Figure S23 – Snapshots of simulation boxes of $[P_{4,4,4,4}][TetrazC_1COO]$ with (left) ■ CO_2 and (right) ■ SO_2. Color codes enable clear identification of the charged and nonpolar domains that form in the ILs with orange atoms holding partial charges and those colored in grey corresponding to the nonpolar moieties of the ions.

5 *Ab initio* calculations

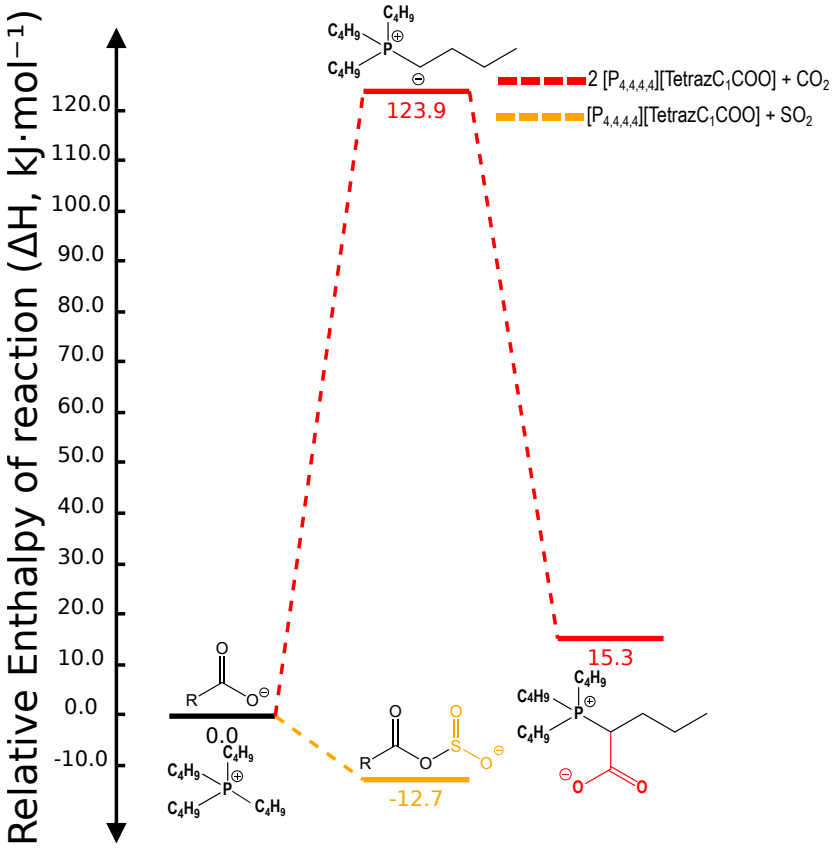

Figure S24 – Relative Enthalpy of the reactions leading to the chemical capture of — SO_2 with a 1:1 stoichiometry (IL:SO_2) and — CO_2 with a 2:1 stoichiometry (IL:CO_2) by $[P_{4,4,4,4}][TetrazC_1COO]$ at 343 K.

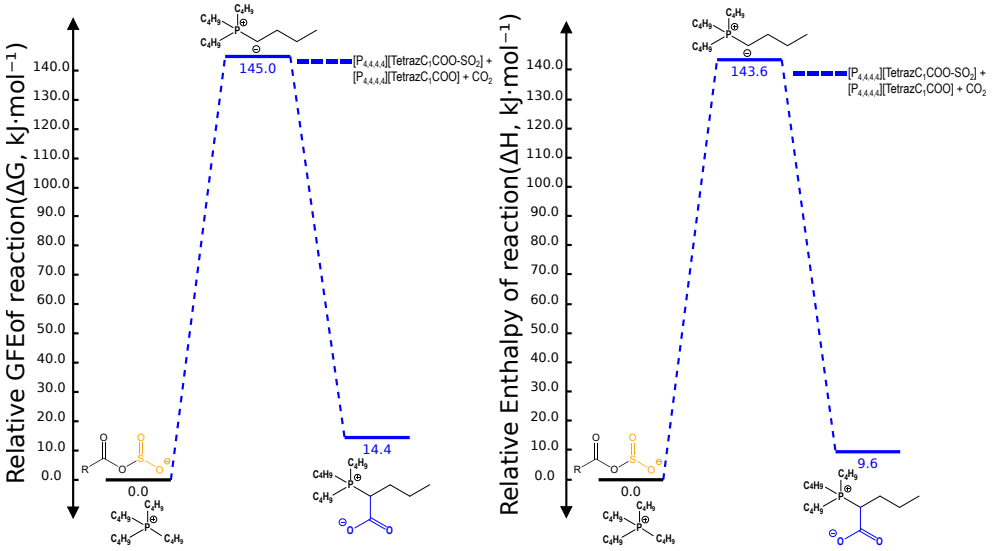

Figure S25 – Relative GFE and Enthalpy of the reactions leading to the chemical capture of — CO_2 with a 2:1 stoichiometry (IL:CO_2) in $[P_{4,4,4,4}][TetrazC_1COO{-}SO_2]$ which corresponds to $[P_{4,4,4,4}][TetrazC_1COO]$ after SO_2 absorption, at 343 K.

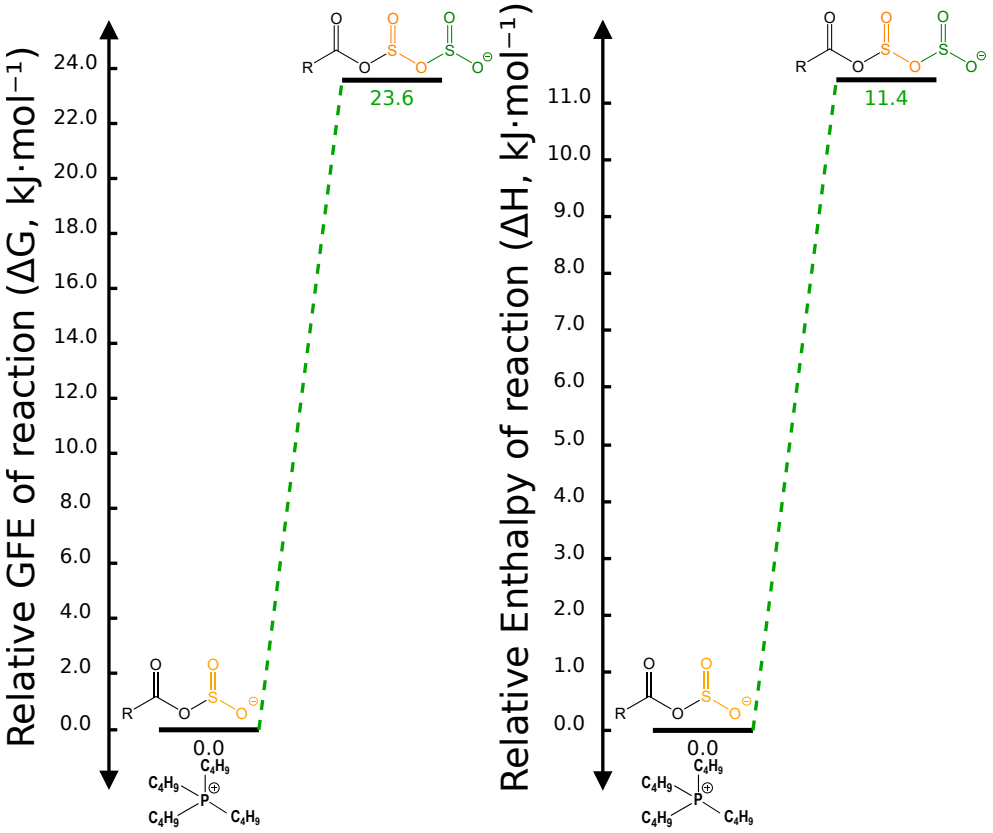

Figure S26 – Relative GFE and Enthalpy of the reactions leading to the chemical capture of — a second SO_2 with a 1:1 stoichiometry (IL:SO_2) in $[P_{4,4,4,4}][TetrazC_1COO{-}SO_2]$ at 343 K.

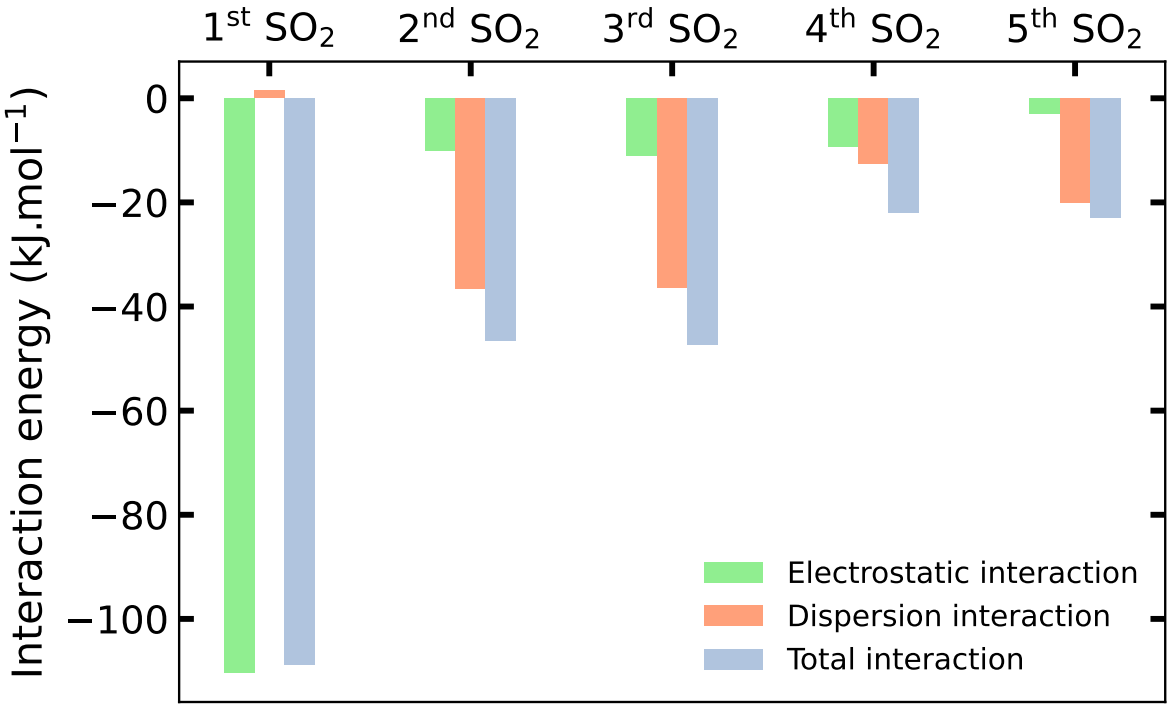

Figure S27 – Comparison of the electrostatic, dispersion and total interaction energy between up to 5 SO_2 molecules and $[P_{4,4,4,4}][TetrazC_1COO]$.

Table S11 – Electrostatic interaction, dispersion interaction as well as the total interaction energies between $[P_{4,4,4,4}][TetrazC_1COO]$ and up to 5 SO_2 molecules. The indicated energies correspond to the interactions of 1 SO_2.

Sample	$E_{electrostat.}$ / kJ mol^{-1}	$E_{disp.}$ / kJ mol^{-1}	$E_{tot.}$ / kJ mol^{-1}
$[P_{4,4,4,4}][TetrazCOO-SO_2]$	-110.37	1.46	-108.91
$[P_{4,4,4,4}][TetrazCOO-SO_2]$ + 1 SO_2	-10.03	-36.57	-46.60
$[P_{4,4,4,4}][TetrazCOO-SO_2]$ + 2 SO_2	-10.98	-36.44	-47.41
$[P_{4,4,4,4}][TetrazCOO-SO_2]$ + 3 SO_2	-9.31	-12.65	-21.96
$[P_{4,4,4,4}][TetrazCOO-SO_2]$ + 4 SO_2	-2.90	-19.99	-22.89

Table S12 – Atomic charges (q) of $[P_{4,4,4,4}][TetrazC_1COO]$ with different number of SO_2 in the system.

Sample	$q([P_{4,4,4,4}]^+)$	q(Anion)	$q(2^{nd}\ SO_2)$	$q(3^{rd}\ SO_2)$	$q(4^{th}\ SO_2)$	$q(5^{th}\ SO_2)$
	e	e	e	e	e	e
$[P_{4,4,4,4}][TetrazC_1COO]$	0.82	-0.82	-	-	-	-
$[P_{4,4,4,4}][TetrazC_1COO{-}SO_2]$	0.72	-0.72	-	-	-	-
$[P_{4,4,4,4}][TetrazC_1COO{-}SO_2] + 1\ SO_2$	0.72	-0.73	0.01	-	-	-
$[P_{4,4,4,4}][TetrazC_1COO{-}SO_2] + 2\ SO_2$	0.65	-0.61	-0.02	-0.02	-	-
$[P_{4,4,4,4}][TetrazC_1COO{-}SO_2] + 3\ SO_2$	0.64	-0.52	-0.03	-0.01	-0.08	-
$[P_{4,4,4,4}][TetrazC_1COO{-}SO_2] + 4\ SO_2$	0.65	-0.51	0.01	-0.04	-0.08	-0.03

$[P_{4,4,4,4}][TetrazC_1COO]$	$[P_{4,4,4,4}][TetrazC_1COO{-}SO_2]$	$[P_{4,4,4,4}][TetrazC_1COO{-}SO_2] + 1\ SO_2$
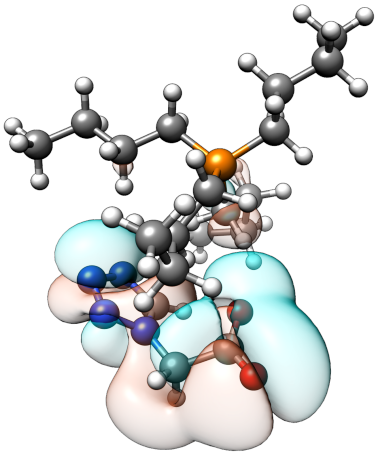	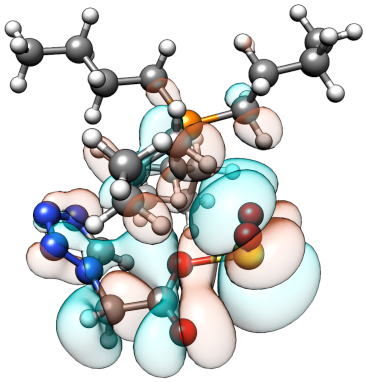	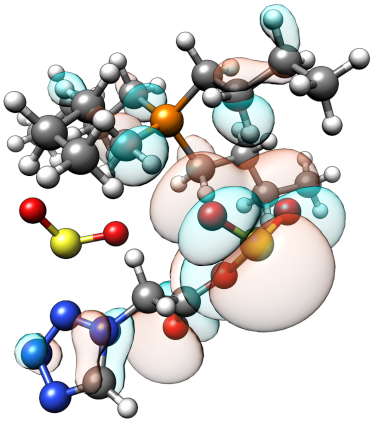
$E(\text{HOMO}) = -7.79\,\text{eV}$	$E(\text{HOMO}) = -8.32\,\text{eV}$	$E(\text{HOMO}) = -8.39\,\text{eV}$
$[P_{4,4,4,4}][TetrazC_1COO{-}SO_2] + 2\ SO_2$	$[P_{4,4,4,4}][TetrazC_1COO{-}SO_2] + 3\ SO_2$	$[P_{4,4,4,4}][TetrazC_1COO{-}SO_2] + 4\ SO_2$
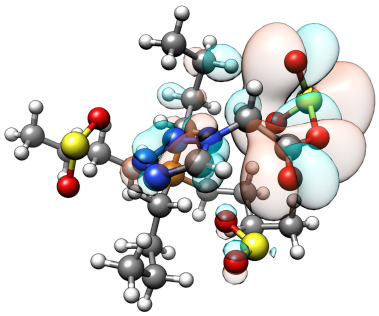	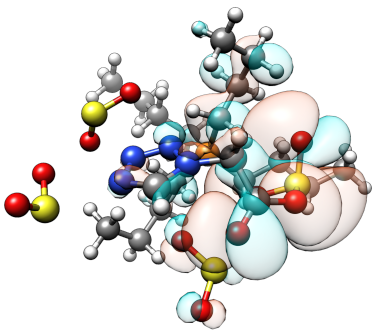	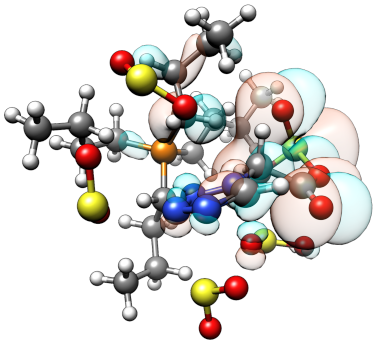
$E(\text{HOMO}) = -8.82\,\text{eV}$	$E(\text{HOMO}) = -8.87\,\text{eV}$	$E(\text{HOMO}) = -8.89\,\text{eV}$

Figure S28 – Highest Occupied Molecular Orbital (HOMO) of the neat $[P_{4,4,4,4}][TetrazC_1COO]$ and also in presence of between 1 and 5 SO_2 molecules as well as the related HOMO energy.

Table S13 – Atomic charges (q) of $[P_{4,4,4,4}][TetrazC_1COO]$ in the initial state, intermediate state and final state of the CO_2 absorption mechanism with a 2:1 stoichiometry (IL:CO_2).

Sample	$q([P_{4,4,4,4}]^+)$	$q([TetrazC_1COO]^-)$	$q(CO_2)$	q(Ylide)	$q(TetrazC_1COOH)$	$q(P^+_{4,4,4,4}-CO_2^-)$
	e	e	e	e	e	e
Initial state	0.68 & 0.63	-0.64 & -0.67	0.00	-	-	-
Intermediate state	0.72	-0.54	-0.02	-0.05	-0.11	-
Final state	0.73	-0.65	-	-	-0.11	0.03

Initial state	Intermediate state	Final state
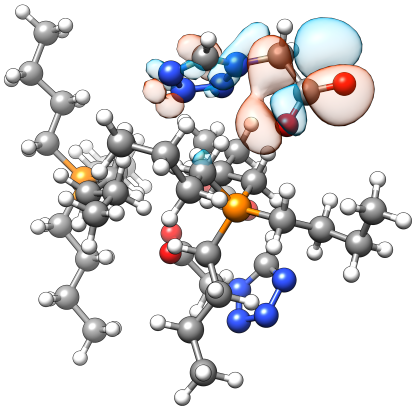	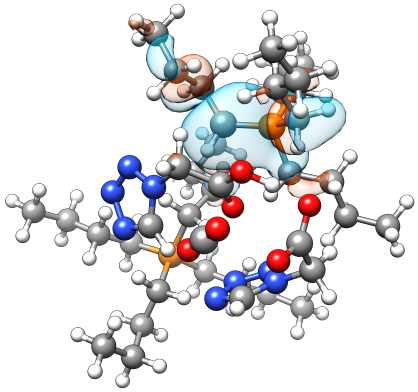	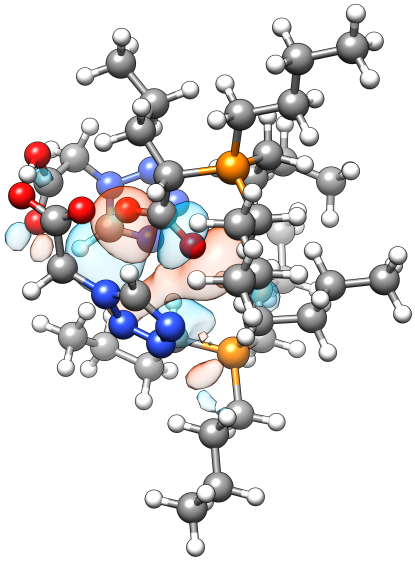
$E(\text{HOMO}) = -6.31\,\text{eV}$	$E(\text{HOMO}) = -4.20\,\text{eV}$	$E(\text{HOMO}) = -6.25\,\text{eV}$

Figure S29 – Highest Occupied Molecular Orbital (HOMO) of $[P_{4,4,4,4}][TetrazC_1COO]$ in the initial state, intermediate state and final state of the CO_2 absorption mechanism with a 2:1 stoichiometry (IL:CO_2) as well as the the related HOMO energy.

6 Long-term thermal stability of the ionic liquid

The thermal stability of $[P_{4,4,4,4}][TetrazC_1COO]$ was investigated in a previous study, where the decomposition temperature (T_{dec}) was determined to be 291 °C under an O_2 atmosphere.[S2] However, T_{dec} measurements are known to overestimate the long-term stability of ILs.[S3,S4] To evaluate the thermal stability more accurately, it is advisable to determine the $T_{0.01/10}$ value, rather than T_{dec}. The $T_{x/z}$ value represents the temperature at which x percent of the total weight (here 1 %) is lost in z hours (here 10 h).

The $T_{0.01/10}$ value is determined through measurement of decomposition curves under isothermal conditions at various temperatures, using thermogravimetric analysis (TGA).[S3] The decomposition rate (k_{dec}) is then calculated from the slope of the isotherms, assuming the pseudo-zero order decomposition behavior of the ILs. From extrapolation of the isotherms at each temperature, $t_{0.99}$, the time required for 1 % sample decomposition, can be determined. The values of $t_{0.99}$ at different temperatures are presented in Figure S27 (left) of the ESI and are fitted to an exponential function (Equation S6), so that $T_{0.01/10}$ can be calculated by extrapolation or interpolation.

$$t_z = ae^{-\frac{T_z}{b}} \tag{S6}$$

The rate of decomposition k_{dec} of the IL can be determined by a pseudo-zero order reaction, where the amount of decomposed IL (α) is proportional to the time $\frac{d\alpha}{dt}$ (Equation (S7)). To determine the activation energy, E_a, and the pre-exponential factor, A, the quantity $\ln(\frac{d\alpha}{dt})$ can be plotted as a function of $1000/T$ (Figure S27 right). The pre-exponential factor A, also known as the frequency factor, represents the collision frequency of the molecules, regardless of whether these collisions lead to a chemical reaction.

$$\frac{d\alpha}{dt} = Ae^{\frac{-Ea}{RT}} \tag{S7}$$

The thermal stability of $[P_{4,4,4,4}][TetrazC_1COO]$ was investigated by comparing the temperature-ramped TGA measurements to isothermal measurements. The results showed a significant decrease

in temperature from T_{dec} to $T_{0.01/10}$ (292 to 133 °C) and confirmed the overestimation of temperature-ramped TGA measurements. In any case, $[P_{4,4,4,4}][TetrazC_1COO]$ exhibited better long-term thermal stability compared to imidazolium acetate ILs,[S5] with an improvement of approximately 30 °C. The pre-exponential factor A of $[P_{4,4,4,4}][TetrazC_1COO]$ was determined to be 2.03×10^{10}, indicating a higher ion mobility than $[C_2C_1im][OAc]$ and $[C_2C_1C_1im][OAc]$ (2.98×10^9 and 2.19×10^7, respectively). Despite both the cation and anion being bulkier, the activation energy E_a was in the same range (115.0 kJ mol^{-1}) as that of the imidazolium ILs. Moreover, the $T_{0.01/10}$ of $[P_{4,4,4,4}][TetrazC_1COO]$ was found to be similar to the reported estimated values for phosphonium salicylate and benzoate ILs.[S6] Overall, $[P_{4,4,4,4}][TetrazC_1COO]$ displayed a long-term thermal stability suitable for various applications.

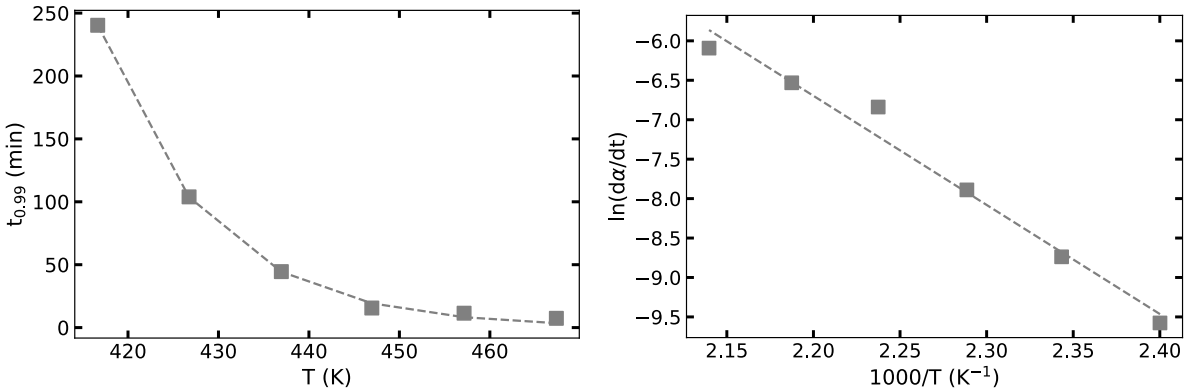

Figure S30 – Plot of (left) $t_{0.99}$, which is the time required to observe a decomposition of 1 % of the sample mass, as a function of temperature (T) and (right) of $\ln(\frac{d\alpha}{dt})$ as a function of $1000/T$ for $[P_{4,4,4,4}][TetrazC_1COO]$. ■ are experimental data and dashed lines are the fitted curves.

Bibliography

(S1) Veroutis, E.; Merz, S.; Eichel, R. A.; Granwehr, J. Intra- and inter-molecular interactions in choline-based ionic liquids studied by 1D and 2D NMR. *J. Mol. Liq.* **2021**, *322*, 114934.

(S2) Scaglione, N.; Avila, J.; Bakis, E.; Padua, A.; Gomes, M. C. Alkylphosphonium carboxylate ionic liquids with tuned microscopic structures and properties. *Phys. Chem. Chem. Phys.* **2023**, *25*, 15325–15339.

(S3) Baranyai, K. J.; Deacon, G. B.; MacFarlane, D. R.; Pringle, J. M.; Scott, J. L. Thermal Degradation of Ionic Liquids at Elevated Temperatures. *Aust. J. Chem.* **2004**, *57*, 145–147.

(S4) Wooster, T. J.; Johanson, K. M.; Fraser, K. J.; MacFarlane, D. R.; Scott, J. L. Thermal degradation of cyano containing ionic liquids. *Green Chem.* **2006**, *8*, 691–696.

(S5) Clough, M. T.; Geyer, K.; Hunt, P. A.; Mertes, J.; Welton, T. Thermal decomposition of carboxylate ionic liquids: trends and mechanisms. *Phys. Chem. Chem. Phys.* **2013**, *15*, 20480–20495.

(S6) Khajeh, A.; Rahman, M. H.; Liu, T.; Panwar, P.; Menezes, P. L.; Martini, A. Thermal decomposition of phosphonium salicylate and phosphonium benzoate ionic liquids. *J. Mol. Liq.* **2022**, *352*, 118700.

5

TAILORED CARBON DIOXIDE CAPACITY IN CARBOXYLATE-BASED IONIC LIQUIDS

Context

Following the study of gas absorption in a particular IL, we wanted to take advantage of our library of phosphonium carboxylate ILs to evaluate their CO_2 capture at various temperatures up to 5 bar, but also the effect of the carboxylate anion basicity on CO_2 absorption.

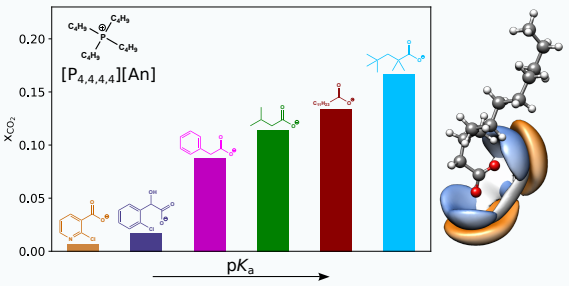

The basicity scale of carboxylate anions we already had, was expanded with 3 new ILs: $[P_{4,4,4,4}][2\text{–ClPyCOO}]$, $[P_{4,4,4,4}][2\text{–ClPhC}_1\text{OHCOO}]$ and $[P_{4,4,4,4}][\text{PhSC1}_1\text{COO}]$. They were carefully characterized as described in Chapter 3 for the other ILs. We now have a series of carboxylate ILs with the pK_a of the corresponding carboxylic acid in water ranging from 2.07 to 6.51.

Two groups were identified: the non-reactive and the reactive ILs, with a clear correlation between the basicity of the carboxylate anions and the ability of ILs to capture CO_2. Some exceptions were found, highlighting as well the importance of the structure of the ions involved. The absorption mechanism was confirmed by NMR spectroscopy and *in situ* IR measurements in presence of CO_2. Interestingly, it was possible to clearly identified the presence of solvated CO_2 in the non-reactive ILs.

Ab initio calculations provided a better comprehension of the thermodynamics lying behind the chemical absorption reaction. Whereas molecular dynamics simulations helped to understand the physical absorption process and the influence of CO_2 solvation on the microscopic structures of the ILs.

An increase of the self-diffusion coefficients of both the cation and the anion was found upon CO_2 absorption in most cases, similarly to what was observed in the previous chapter. It means that the viscosity is decreasing upon carbon capture which overcomes the dramatic increase of viscosity that many ILs suffer from upon CO_2 absorption.

The long-term thermal stability of all these ILs were evaluated, following a similar protocol as carried out for $[P_{4,4,4,4}][\text{TetrazC}_1\text{COO}]$, to get a better overview of their applicability in real conditions.

Faraday Discussions

Cite this: DOI: 10.1039/d4fd00052h

PAPER View Article Online View Journal

Tailored carbon dioxide capacity in carboxylate-based ionic liquids†

Nicolas Scaglione, Jocasta Avila, Agilio Padua and Margarida Costa Gomes *

Received 6th March 2024, Accepted 16th April 2024

DOI: 10.1039/d4fd00052h

We have used a library of thermally stable tetraalkylphosphonium carboxylate ionic liquids that were easily prepared from available carboxylic acids. Depending on the pK_a in water of the precursor acids, the resulting ionic liquids either dissolve or reversibly chemically absorb CO_2, with some exhibiting notable gas capacities, reaching a CO_2 mole fraction of 0.2 at 1 bar and 343 K. While equilibrium constants and ionic liquid capacities generally correlate with the pK_a of the acids, certain exceptions underscore the influence of liquid structure and physical properties of the ionic liquids, elucidated through molecular dynamics simulations and density functional theory calculations. Unlike the trends observed in other CO_2-absorbing ILs, phosphonium carboxylates do not experience increased viscosity upon gas absorption; instead, enhanced diffusivities are observed, facilitating efficient gas–liquid transfer.

1 Introduction

Carboxylate anions are accessible building blocks used to prepare stable ionic liquids (ILs) *via* anion exchange reactions using readily available carboxylic acids with distinct acidity.[1] As a result, large libraries of carboxylate ILs comprising diverse cations—mono or divalent,[2] functionalized[3] or unmodified—are made available, exhibiting a range of interesting and sometimes unexpected properties.[1,4]

The dissolution of cellulose stands out as the most extensively investigated application of carboxylate ILs.[4] The discovery of liquid salts capable of dissolving cellulose under mild conditions,[5] including those based in carboxylate anions,[6,7] opened an area of study spanning across various domains. These include, for example, the advancement of environmentally friendly cellulose processing, the selective extraction of biomass components, and the promotion of textile fiber recycling.

Laboratoire de Chimie de l'ENS Lyon, CNRS, Université de Lyon, 46 allée d'Italie, 69364 Lyon, France. E-mail: margarida.costa-gomes@ens-lyon.fr

† Electronic supplementary information (ESI) available. See DOI: https://doi.org/10.1039/d4fd00052h

Carboxylate-based ILs have also been proposed as sustainable absorbents for environmentally harmful substances, such as sulfur dioxide[8] or carbon dioxide.[9] Imidazolium acetate ILs are known to chemically react with CO_2 through a nucleophilic attack following the formation of a carbamate in the imidazolium C_2 position.[10] The reversible absorption mechanism follows a 2 : 1 stoichiometry with formation of a zwitterion and a complex between the IL and the newly formed carboxylic acid.[11] 1-Butyl-3-methyl imidazolium acetate has compared favourably with conventional amine-based absorbers for carbon capture[12] even though the synthesis of the IL is still relatively expensive.

Tetraalkylphosphonium carboxylates react with CO_2 through a similar mechanism with a first step involving the formation of a reactive phosphorous ylide through the acid–base reaction between the carboxylate anion and one of the two acidic protons on the α-carbon of the cation.[13,14] This easily reversible acid–base equilibrium is displaced in the presence of CO_2 that reacts with the formed ylide, the cation being, in general, chemically stable.[15,16] We hypothesise that the equilibrium constant and the enthalpy of the chemical reaction of CO_2 with the IL can be precisely adjusted by altering the basicity of the carboxylate anions as was proposed by Wang *et al.* for azole-based ILs.[17] We propose to follow this approach for alkylphosphonium carboxylate ILs and thus validate a methodological strategy for engineering absorbents with reduced energy requirements.[18] In addition to regulating the extent and energetics of the chemical reaction with CO_2, the use of phosphonium cations has several advantages[19,20] as the properties of the stable phosphonium carboxylate ILs can be further modulated. For example, the hydrophobicity of these salts depends on the length of the alkyl chains in the cation, enabling control over their performance as absorbents in the presence of water.[13,21]

We decided to test these approaches by extensively studying the absorption of CO_2 in an existing library of phosphonium carboxylate ILs, extended herein, synthesised from carboxylic acids covering a large range of pK_a in water.[1]

2 Materials and methods

2.1 Materials

The ionic liquids studied are listed in Table 1. Tetrabutylphosphonium 2-chloropyridine-3-carboxylate, [$P_{4,4,4,4}$][2-ClPyCOO], tetrabutylphosphonium 2-(2-chlorophenyl)-2-hydroxyacetate, [$P_{4,4,4,4}$][2-ClPhC_1OHCOO], and tetrabutylphosphonium (phenylthio)acetate, [$P_{4,4,4,4}$][$PhSC_1$COO], were synthesised and characterised as described in the ESI.† The other ILs in Table 1 were previously prepared as described by Scaglione *et al.*[1] Before use, the ILs were degassed by cycles of solidification and melting under primary vacuum.

Carbon dioxide (CO_2) was purchased from Air Liquide with a mole fraction purity of 99.995% and was used as received.

2.2 Gas absorption

The absorption of carbon dioxide in the ILs was measured in an Intelligent Gravimetric Analyzer (IGA001) manufactured by Hiden Analytical. The experiments were conducted in isotherms from 0.25 bar to 5 bar, at 303 K, 323 K, and

Table 1 Chemical structures and abbreviations of the anions of the tetrabutylphosphonium, $[P_{4,4,4,4}]$, ILs studied including their melting and decomposition temperatures as well as the pK_a of the corresponding carboxylic acids in water: 2-chloropyridine-3-carboxylate, [2-ClPyCOO]; 1*H*-tetrazolate-1-acetate, ch[TetrazC1COO]; 2-(2-chlorophenyl)-2-hydroxyacetate, $[2\text{-ClPhC}_1\text{OHCOO}]$; (phenylthio)acetate, $[\text{PhSC}_1\text{COO}]$; phenylacetate, $[\text{PhC}_1\text{COO}]$; acetate, $[\text{C}_1\text{COO}]$; isovalerate, $[\text{MeC}_3\text{COO}]$; cyclohexanecarboxylate, $[\text{c-C}_6\text{COO}]$; hexanoate, $[\text{C}_5\text{COO}]$; dodecanoate, $[\text{C}_{11}\text{COO}]$; and tetramethylpentanoate, $[\text{Me}_4\text{C}_4\text{COO}]$

Anion	T_m/K	T_{dec}/K	pK_a	Anion	T_m/K	T_{dec}/K	pK_a
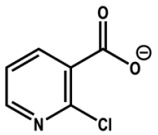 $[2\text{-ClPyCOO}]^-$		534	2.07	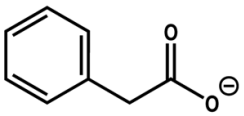 $[\text{PhC}_1\text{COO}]^-$	317	527	4.31
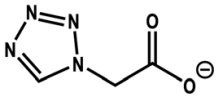 $[\text{TetrazC}_1\text{COO}]^-$	282	564	2.67	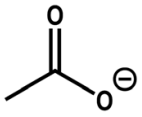 $[\text{C}_1\text{COO}]^-$	322	598	4.76
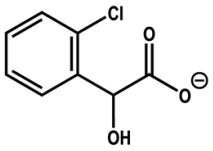 $[2\text{-ClPhC}_1\text{OHCOO}]^-$		534	3.30	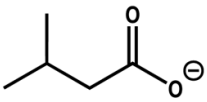 $[\text{MeC}_3\text{COO}]^-$	322	601	4.77
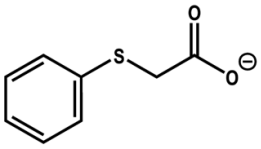 $[\text{PhSC}_1\text{COO}]^-$	329	549	3.70	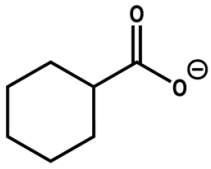 $[\text{c-C}_6\text{COO}]^-$	338	609	4.82
				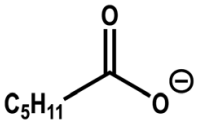 $[\text{C}_5\text{COO}]^-$		601	4.87
				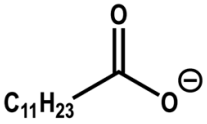 $[\text{C}_{11}\text{COO}]^-$		617 618[a]	5.30
				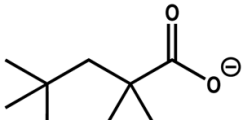 $[\text{Me}_4\text{C}_4\text{COO}]^-$	301 256[a]	592 615[a]	6.51

[a] Properties of the ILs based on the trihexyltetrabutylphosphonium, $[P_{6,6,6,14}]$, cation.

343 K depending on the melting point of the ILs. The experimental setup, experimental procedure and data analysis have been described previously.[22]

2.3 NMR measurements

^{1}H, ^{13}C and ^{31}P NMR spectra, Correlated Spectroscopy (COSY) and Heteronuclear Single Quantum Correlation (HSQC) were collected on a 400 MHz Bruker Avance III spectrometer with a broadband probe BBO equipped with a temperature control unit BCU II set at 343 K. Diffusion Ordered Spectroscopy (DOSY) was used to measure the self-diffusion coefficients of the species before and after saturation with CO_2.

The pure ILs were first inserted into high-pressure NE-HP10-M Pyrex NMR tubes (thickness 1 mm, rated to 20 bar) and were subsequently degassed and dried under primary vacuum (<0.1 mbar) for 24 h to 72 h at temperatures between 303 K and 353 K. After obtaining the NMR spectra of the pure ILs, the samples were placed under a CO_2 pressure of 15 bar for several days until no pressure drop was observed after closing the gas cylinder (the pressure was followed by a digital pressure gauge with an uncertainty of 0.4 bar). The ILs saturated with CO_2 were then studied in a similar way. C_6D_6 in a sealed capillary was used as an internal reference for all the ILs except for $[P_{4,4,4,4}][PhC_1COO]$ for which DMSO-d_6 was employed.

The COSY and HSQC NMR spectra served for the attributions of the peaks before and after CO_2 absorption for all the ILs (as shown in the ESI† for the example of tetrabutylphosphonium 2,2,4,4-tetramethylpentanoate $[P_{4,4,4,4}][Me_4C_4COO]$).

2.4 X-ray scattering

Small-angle X-ray scattering (SAXS) measurements were performed on an Xeuss 3.0 instrument at a wavelength of 1.542 Å. The sample to SAXS detector distance was 42.5 mm yielding a q-range of 0 $Å^{-1}$ to 4 $Å^{-1}$. A capillary tube was filled with each sample and measurements were acquired six times during 30 min. Beamline-specific corrections were applied after the acquisition to the SAXS signals and the intensity was radially averaged to obtain the intensity of scattering as a function of the wavevector. A background measurement was made for an empty capillary and was subtracted from each sample pattern.

2.5 Infrared spectroscopy

Infrared (IR) spectroscopy was used to quantify the presence of water in the IL samples and to verify the purity of $[P_{4,4,4,4}][C_{11}COO]$ after several cycles of CO_2 absorption and desorption. The IR spectra were obtained in the attenuated total reflection mode (ATR) using a PerkinElmer Spectrum 65 FT-IR spectrometer. A small amount of solid or a droplet of the IL was placed on the ATR crystal and the measurements were carried out in the wave number range 550 cm^{-1} to 4000 cm^{-1} accumulating 16 scans with a resolution of 2 cm^{-1}.

IR spectra of $[P_{4,4,4,4}][C_5COO]$ under CO_2 pressure were measured over time in an integrated system comprising high temperature, mass flow controllers (Brooks), an air-tight reaction chamber (Harrick Scientific) with a 4-way valve and a pressure regulating valve. The reaction chamber was equipped with ZnSe windows and fitted into the Praying Mantis optical unit also provided by Harrick

Scientific. All the lines were extensively purged before CO_2 was introduced in the chamber. The FT-IR spectra were collected in a Thermo Scientific FTIR 6700 spectrophotometer in diffuse reflectance mode equipped with a MCT detector. A thin film of the IL was placed on the surface of a wafer and the spectra were recorded in the range 550 cm^{-1} to 4000 cm^{-1}, accumulating 64 scans with a resolution of 4 cm^{-1}, up to 15 bar at room temperature.

2.6 Thermal analysis

The thermal stability of the ILs was assessed using thermo-gravimetric analysis (TGA) on a Setaram Labsys Evo TG DTA DSC+ 1600 °C instrument under an O_2 atmosphere. Precise weighted samples of 20 mg to 40 mg were placed in 100 μL aluminum oxide crucibles and underwent a preheating step at 80 °C under vacuum for 30 min to ensure the removal of any potential water traces. Subsequently, the samples were subjected to isothermal conditions, with temperatures varying between 130 and 190 °C at intervals of 10 °C for a duration of 5 h. The data were treated for all the ILs as previously explained (details included in the ESI†).[23,24]

2.7 Molecular dynamics simulations

Molecular dynamics (MD) simulations were performed using the OpenMM code[25] with the ILs being described by the CL&Pol force field[1] and CO_2 by the TraPPE force field.[26] Periodic cubic boxes with 300 ion pairs and 30 CO_2 molecules were prepared using fftool[27] and Packmol[28] and were equilibrated for 2 ns at 343 K and 1 bar followed by 20 ns production runs. Site–site radial distribution functions (RDFs), spatial distribution functions (SDFs), and combined distribution functions (CDFs) were obtained using the TRAVIS trajectory analysis software.[29,30]

Specifics regarding the development and testing of the force field for the new ILs are provided in the ESI,† including density calculations, self-diffusion coefficients, and their comparisons with experimental values (Tables S9 and S10†). MD simulations using the developed force field were used to assess the microscopic structure of the ILs and to calculate partial structure factors after validation of the simulated total structure factors against experimentally obtained X-ray patterns (Fig. S11†).

2.8 *Ab initio* calculations

Density functional theory (DFT) was used to study the interactions between the ILs and CO_2 following a procedure previously described.[24] The ILs are explicitly represented by either one or two ion pairs with one CO_2 molecule. The Conformer–Rotamer Ensemble Sampling Tool (CREST) code[31] was used to pre-optimize the geometry at each step and generate an initial set of nine conformers. Each step was optimized based on the equilibrium geometry of the previous step using Gaussian16[32] with the Dunning's double-ζ basis set (cc-pVDZ)[33] and the M062-2X DFT functional.[34] A conductor-like polarizable continuum model (CPCM), with the permittivity of *n*-octanol, was used to represent solvent effects. Single-point energy (SPE) calculations were made at a higher level of theory (aug-cc-pVTZ[35]). The enthalpy (H) and the Gibbs free energy (G) of each system were determined as previously described.[24,36]

Partial atomic charges for the most stable conformers for each IL were calculated by the algorithm charge model 5[37] based on a Hirshfeld charge scheme,[38] using a cc-pVDZ basis set with a PBE0 functional.[39] Highest occupied molecular orbitals (HOMOs) were also determined for the lowest energy conformer of each IL based on geometry optimization made for the energy profile determination considering a reaction stoichiometry validated experimentally. Checkpoint files were converted to cube files with a grid size of 80.

3 Results and discussion

Data for the absorption of CO_2 for all the ILs up to 5 bar and at temperatures from 303 K to 343 K are listed in Table S12.† The isotherms at 343 K for the ILs based on the $[P_{4,4,4,4}]$ cation are depicted in Fig. 1 together with the values measured at 1 bar pressure of gas.

Two distinct groups of ILs emerge in their ability to absorb CO_2. ILs containing the anions [2-ClPyCOO], $[TetrazC_1COO]$,[24] $[2\text{-}ClPhC_1OHCOO]$ and $[PhSC_1COO]$ show a relatively limited CO_2 capacity, demonstrating a behaviour consistent with Henry's law. Conversely, the remaining ILs demonstrate significantly enhanced absorption capacities, particularly evident at lower pressures, suggestive of chemisorption of the gas.[13,14]

In order to identify the products present in solution after exposure of the ILs to CO_2, NMR spectra (^1H, ^{13}C and ^{31}P) were recorded before and after gas absorption. The typical spectra recorded for the non-reacting ILs are represented in Fig. 3 (left) for $[P_{4,4,4,4}]$[2-ClPyCOO]. Except for a new peak appearing in the ^{13}C spectrum, easily attributed to the dissolved CO_2, no other new signals are identified after the IL was equilibrated with the gas. Similar signals are obtained for the other three non-reacting ILs as shown in the ESI† and reported elsewhere for $[P_{4,4,4,4}][TetrazC_1COO]$.[24]

For some of the non-reactive ILs, such as $[P_{4,4,4,4}][PhSC_1COO]$, a new small signal can be observed at 30.97 ppm in the ^{31}P NMR spectrum, as shown in Fig. 2

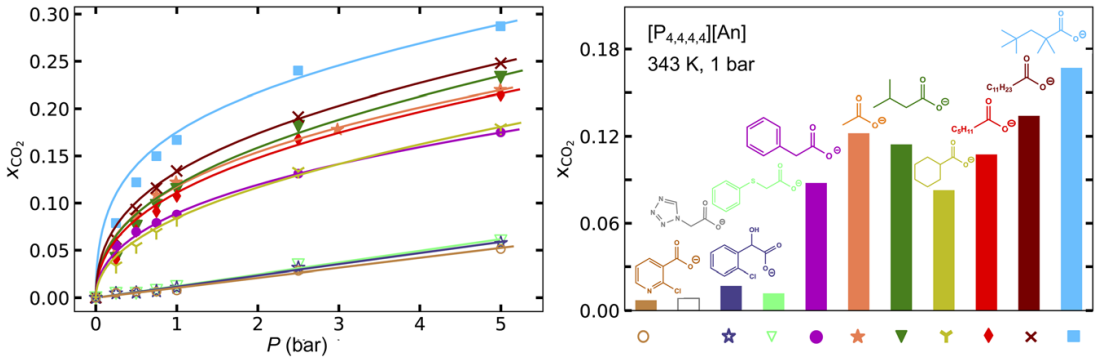

Fig. 1 (Left) Isotherms at 343 K of the CO_2 mole fraction absorbed up to a pressure of 5 bar by the ionic liquids based on the tetrabutylphosphonium cation: ○ $[P_{4,4,4,4}]$[2-ClPyCOO], ☆ $[P_{4,4,4,4}][2\text{-}ClPhC_1OHCOO]$, ▽ $[P_{4,4,4,4}][PhSC_1COO]$, ● $[P_{4,4,4,4}][PhC_1COO]$, ★ $[P_{4,4,4,4}][C_1COO]$; ▼ $[P_{4,4,4,4}][MeC_3COO]$, Y $[P_{4,4,4,4}][c\text{-}C_6COO]$, ♦ $[P_{4,4,4,4}][C_5COO]$, × $[P_{4,4,4,4}][C_{11}COO]$ and ■ $[P_{4,4,4,4}][Me_4C_4COO]$. The lines are fits of the experimental points using the absorption model described below. (Right) Mole fraction CO_2 absorption by the ionic liquids based on the tetrabutylphosphonium cation at 343 K and 1 bar partial pressure of gas. The data for $[P_{4,4,4,4}][TetrazC_1COO]$ are included for comparison.[24]

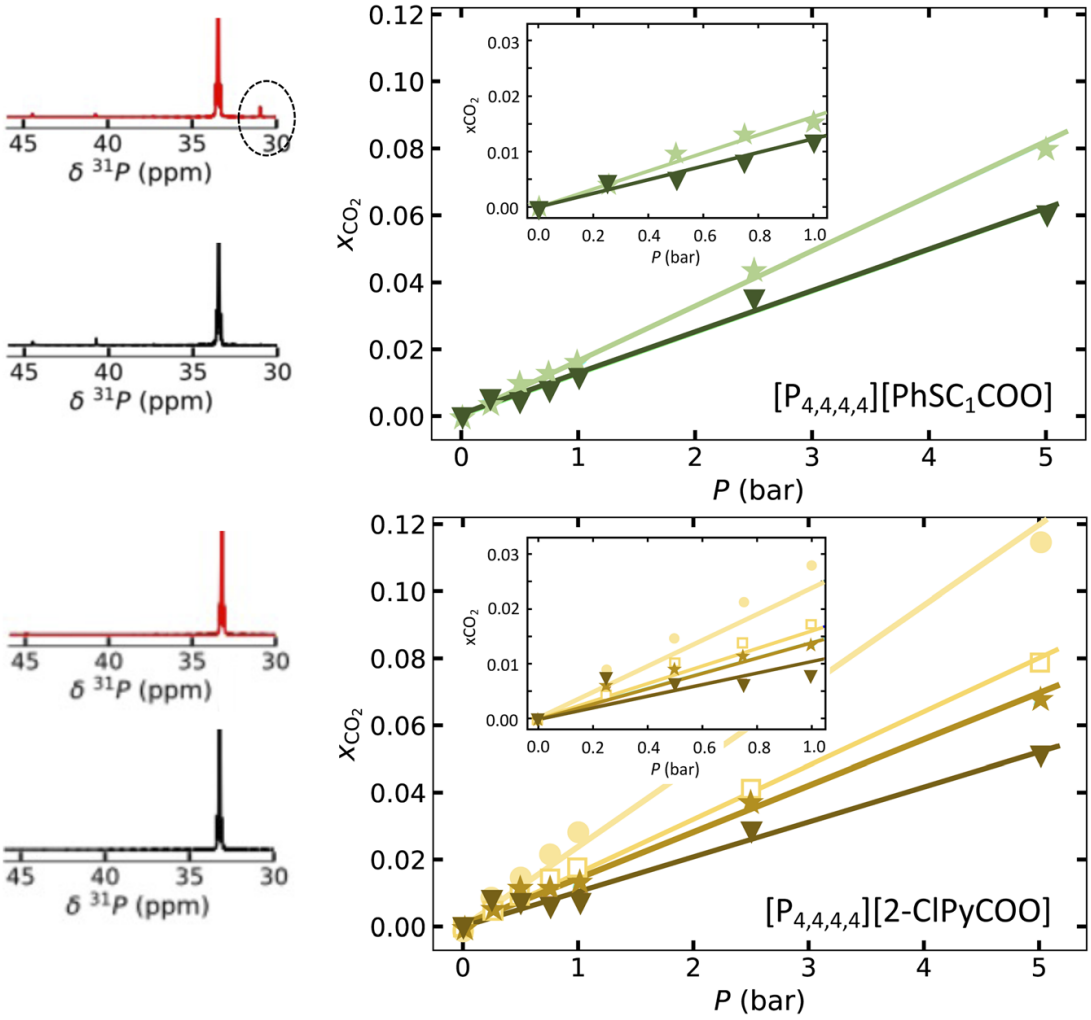

Fig. 2 Left: ^{31}P NMR signals of $[P_{4,4,4,4}][PhSC_1COO]$ pure (black) and after equilibration with CO_2 (red) with a new small signal visible at 30.97 ppm. Right: Absorption isotherms at 323 K, ★ and 343 K, ▼, for CO_2 in $[P_{4,4,4,4}][PhSC_1COO]$.

(the full spectra are included in the ESI†). Deviations from Henry's law could be detected at the higher temperature studied as depicted in Fig. 2 for both $[P_{4,4,4,4}][PhSC_1COO]$ and $[P_{4,4,4,4}][2\text{-ClPyCOO}]$ (although no NMR signal was detected for this last IL). These deviations at low pressures suggest a chemical reaction between gas and IL, albeit occurring only to a limited extent, possibly explaining the weak NMR signals. As expected for non-reactive gases in liquids, the solubility of CO_2 decreases with increasing temperatures.

Typical NMR spectra for ILs that react with CO_2 are depicted in Fig. 3 for the example of $[P_{4,4,4,4}][c\text{-}C_6COO]$ (the spectra for the other reactive ILs are included in the ESI†). The NMR signals after equilibration with CO_2 reveal, as expected, new chemicals compatible with the known reaction mechanism depicted in Fig. 4.[13,22] In the ^{1}H NMR spectrum, a characteristic signal at 11.54 ppm corresponds to the carboxylic acid formed in the pure IL as a result of the cation–anion proton exchange. This proton transfer is favoured by the presence of CO_2 that combines with the phosphorous ylide to form a zwitterionic species. This last is revealed by the peak at 15.97 ppm in the ^{1}H NMR spectrum and by the low intensity triplet at 2.74 ppm (A′ in Fig. 3) that refers to the single proton in the α-carbon of the zwitterion. The chemical shift of the acidic proton corresponds to the average of

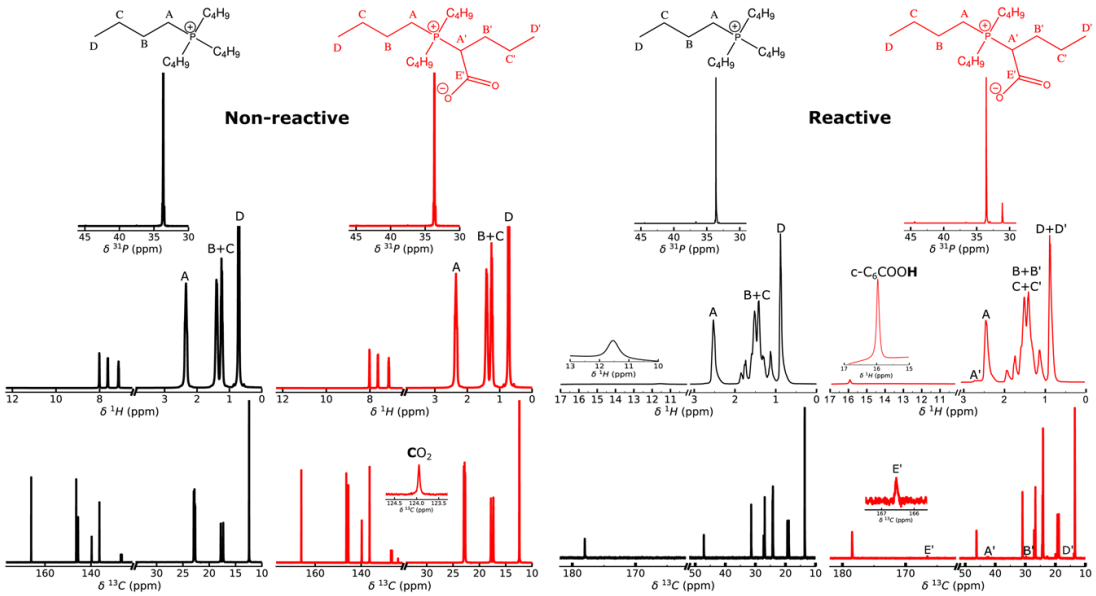

Fig. 3 ^{13}C, ^{1}H and ^{31}P and NMR spectra of (left) $[P_{4,4,4,4}][2\text{-ClPyCOO}]$ and (right) $[P_{4,4,4,4}][c\text{-}C_6COO]$ before (—) and after (—) CO_2 absorption at 343 K. For the sake of clarity, only the signals related to the cation and the newly formed zwitterion have been highlighted here.

the two carboxylate protons present in solution. More generally, the signal of the acidic protons of the phosphonium cation at around 2.5 ppm is shifted upfield while the others are shifted downfield upon CO_2 absorption due to a shielding effect of the carboxylate moiety in the zwitterion. As expected and due to the charge neutralization, the peaks of the newly formed carboxylic acid are shifted downfield.

The ^{13}C NMR spectrum in Fig. 3 shows a new peak at 166.99 ppm, corresponding to a new carboxylate, and a new doublet at 43.96 ppm, attributed to the carbon in the α position, C_α, of the formed phosphonium-carboxylate zwitterion. The ^{31}P NMR spectrum after CO_2 absorption reveals two different phosphonium species, with a new peak at 31.11 ppm. These peak assignments are further confirmed by the downfield shift of the signals of C_α and of the carbon of the carboxylate group, C_{COO^-}, in the ^{13}C NMR spectrum, while all the others are shifted upfield. The 36.65 ppm and at 44.43 ppm signals in the ^{31}P NMR spectrum, present before and after CO_2 absorption, have been assigned to phosphine oxide impurities (also present in some of the other ILs as shown in the ESI†). The

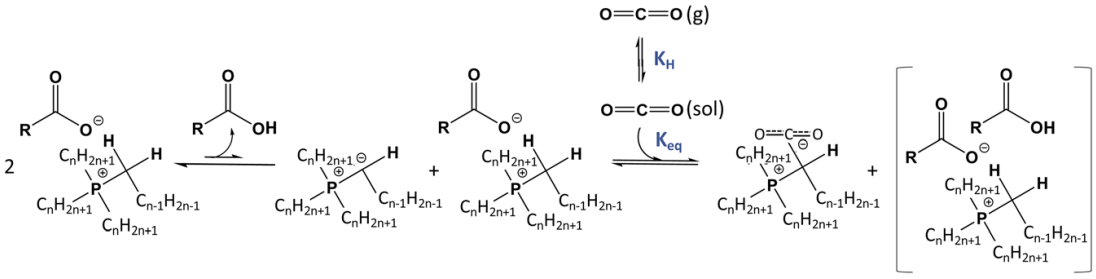

Fig. 4 Mechanism of CO_2 absorption by a tetraalkylphosphonium carboxylate ionic liquid.[14]

peak corresponding to the phosphonium cation on the ^{31}P NMR spectrum is, as expected, shifted upfield after the CO_2 absorption.

The gas chemisorption was further monitored over time using FT-IR under pressurized CO_2 over $[P_{4,4,4,4}][C_5COO]$, chosen as a convenient example of a reactive IL (see complete spectra in the ESI†). Two significant changes can be identified over time—the broadening of the COO^- stretching mode between 1500 cm^{-1} and 1800 cm^{-1} due to the reaction of the carboxylate anions, whose characteristic band appears at 1570 cm^{-1}, and the formation of the new zwitterion with the vibrational band of its carboxylate group now appearing at 1714 cm^{-1}.

The equilibrium constant (K_{eq}) and the Henry's law constant (K_H) in Fig. 4 can be calculated for all the ILs studied at 343 K by fitting the mole fraction of CO_2 absorbed as a function of pressure. The equations used as well as the gas absorption data for the different ILs are reported in the ESI.† The resulting fits are the lines plotted in Fig. 1 together with the experimental points, and the corresponding constants are reported in Table 2.

All the studied ILs have similar Henry's law constants at 343 K, regardless of their ability to chemically absorb CO_2. Their values vary between $47 < K_H/\text{bar} < 105$, roughly corresponding to mole fraction CO_2 solubilities of 0.01–0.02 at 1 bar. This observation confirms the site–site radial distribution functions (RDFs) and spatial distribution functions (SDFs) represented in Fig. 5 calculated for CO_2 dissolved in two ILs based on anions with very different basicities. For the RDF of the IL based

Table 2 Henry's law constant (K_H) and equilibrium constant (K_{eq}) obtained for the ILs under study by fitting the gas absorption data

Non-reactive $[P_{4,4,4,4}]$ ILs	T/K	K_H/bar	Reactive $[P_{4,4,4,4}]$ ILs	T/K	K_{eq}	K_H/bar
[2-ClPyCOO]	303	42 ± 1	[PhC$_1$COO]	323	1.5 ± 0.2	47 ± 2
	313	62 ± 1		343	1.2 ± 0.1	105 ± 6
	323	72 ± 2	[C$_1$COO]	343	1.7 ± 0.3	71 ± 6
	343	95 ± 3	[MeC$_3$COO]	343	1.2 ± 0.4	52 ± 7
[TetrazC$_1$COO][24]	303	46 ± 2	[c-C$_6$COO]	343	0.6 ± 0.1	72 ± 8
	323	63 ± 2	[C$_5$COO]	343	1.3 ± 0.4	65 ± 9
	343	83 ± 3	[C$_{11}$COO]	303		36.1 ± 0.8
[2-ClPhC$_1$OHCOO]	303	48 ± 1		343	1.8 ± 0.2	53 ± 3
	313	58 ± 1	[Me$_4$C$_4$COO]	343	5 ± 1	48 ± 6
	323	66 ± 1				
	343	85 ± 2				
[PhSC$_1$COO]	323	61 ± 1				
	343	81 ± 2				

Reactive $[P_{6,6,6,14}]$ ILs	T/K	K_{eq}	K_H/bar
[C$_{11}$COO]	303	1.0 ± 0.2	50 ± 4
	343	1.81 ± 0.03	55.7 ± 0.4
[Me$_4$C$_4$COO]	303	1.1 ± 0.2	60 ± 4
	323	1.8 ± 0.3	68 ± 5
	343	4.1 ± 0.4	70 ± 3

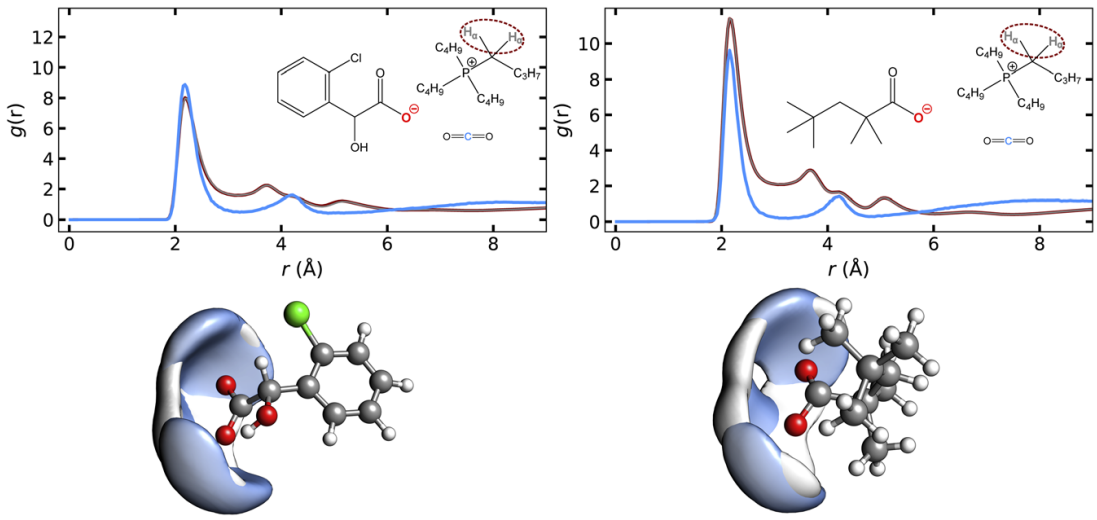

Fig. 5 Left: Site–site RDFs of the H_α of the $[P_{4,4,4,4}]$ (—) and of the carbon atom of CO_2 around the charged oxygen atom of the carboxylate anion (—) in $[P_{4,4,4,4}][2\text{-}ClPhC_1OHCOO]$. SDFs of □ H_α of the cation and ■ C_{CO_2} around the carboxylate head in $[P_{4,4,4,4}][2\text{-}ClPhC_1OHCOO]$. Isodensity contours at 9.6 and 0.5 times the average density around the anion. Right: Site–site RDFs of the H_α of the $[P_{4,4,4,4}]$ (—) and of the carbon atom of CO_2 around the charged oxygen atom of the carboxylate anion (—) in $[P_{4,4,4,4}][Me_4C_4COO]$. SDFs of □ H_α of the cation and ■ C_{CO_2} around the carboxylate head in $[P_{4,4,4,4}][Me_4C_4COO]$. Isodensity contours at 12 and 0.5 times the average density around the anion.

on the anion with low pK_a, $[P_{4,4,4,4}][2\text{-}ClPhC_1OHCOO]$, a stronger correlation is observed between the oxygen atom of the carboxylate and the dissolved CO_2 when compared with the hydrogen atoms in the α position of the cation. For the IL with the more basic anion, $[P_{4,4,4,4}][Me_4C_4COO]$, a contrary result is observed with a weaker correlation of the carboxylate oxygen and the dissolved CO_2.

Tetrabutylphosphonium ILs based on carboxylate anions with linear or branched alkyl chains have a lower K_H than those with aromatic or cyclic carboxylate anions, meaning that they are capable of dissolving larger quantities of CO_2. For the tetrabutylphosphonium ILs, the larger the alkyl chain in the

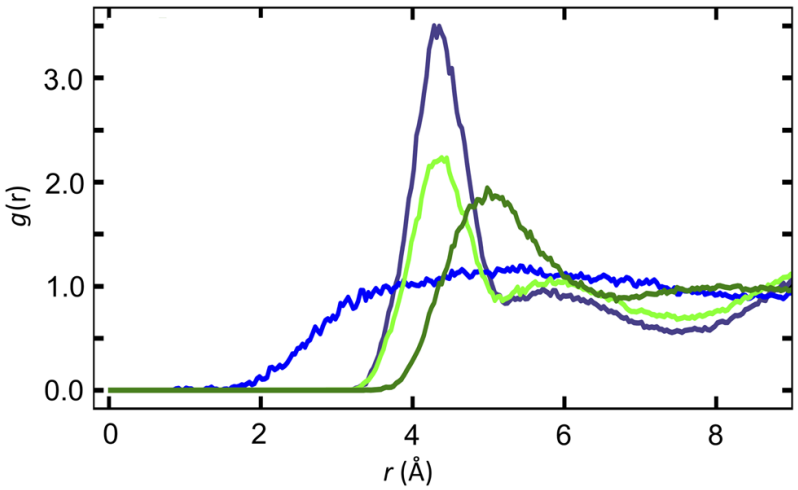

Fig. 6 Centre-of-mass radial distribution functions of the cation and anion around dissolved CO_2 at 343 K for $[P_{4,4,4,4}][Me_4C_4COO]$ — and —, respectively; and $[P_{6,6,6,14}][Me_4C_4COO]$ — and —, respectively.

anions, the lower the calculated value of K_H—71 bar for $[C_1COO]^-$, 65 bar for $[C_5COO]^-$ and 53 bar for $[C_{11}COO]^-$ for the linear anions, and 52 bar for $[MeC_3COO]^-$ and 48 bar for $[Me_4C_4COO]^-$ in the case of the branched anions. The effect of the size of the alkyl side chains of the cation is opposite as K_H is higher for $[P_{6,6,6,14}][C_{11}COO]$ (56 bar) and $[P_{6,6,6,14}][Me_4C_4COO]$ (70 bar) when compared with $[P_{4,4,4,4}][C_{11}COO]$ (53 bar) and $[P_{4,4,4,4}][Me_4C_4COO]$ (48 bar), respectively. The MD simulations confirm these experimental observations as can be seen in Fig. 6—while the cation and the anion approach CO_2 in the case of $[P_{4,4,4,4}][Me_4C_4COO]$, the solute is surrounded preferentially by the anion when dissolved in $[P_{6,6,6,14}][Me_4C_4COO]$.

A similar behavior has been previously observed for the solubility of CO_2 in 1-alkyl-3-methylimidazolium bis(trifluoro methylsulfonyl)imide ILs, wherein it increases with the lengthening of the alkyl side chain of the cation, but only up to a certain chain length. Beyond this point, the solubility either remains constant or even slightly decreases. Indeed, molecular dynamics (MD) simulations reveal that CO_2 tends to solvate preferentially near the charged regions of the liquid. The augmentation of non-polar domains enhances favorable van der Waals interactions, but only to a certain extent where the gas becomes too distant from the polar segments of the ionic liquid.[40] The same arguments apply herein for phosphonium carboxylate ILs whose microscopic structures have been studied experimentally through SAXS experiments (reported in the ESI† for $[P_{4,4,4,4}][2\text{-ClPyCOO}]$, $[P_{4,4,4,4}][2\text{-ClPhC}_1\text{OHCOO}]$ and $[P_{4,4,4,4}][PhSC_1COO]$ and elsewhere[1] for the other ILs). Those reveal the existence of a pre-peak at low q values, typical the presence of nanoscale polar and non-polar domains.

The thermodynamic properties of solvation were calculated from the variation of the Henry's law constants with temperature as previously explained.[40] Surprisingly enough, for the non-reactive ILs, the more negative enthalpy of solvation ($\Delta_{solv}H = -18$ kJ mol^{-1}) is calculated for $[P_{4,4,4,4}][2\text{-ClPyCOO}]$ even if it concerns the IL with the higher K_H value, corresponding to the lower CO_2 solubility. This means that, although the interactions between the gas and the IL are more favourable than for the other non-reactive salts, the CO_2 solubility is lower probably because of a less favourable entropic contribution. For the other non-reactive ILs, values of $\Delta_{solv}H$ are similar: −13, −12 and −13 kJ mol^{-1} were calculated for $[P_{4,4,4,4}][TetrazC_1COO]$,[24], $[P_{4,4,4,4}][2\text{-ClPhC}_1\text{OHCOO}]$ and $[P_{4,4,4,4}]$-[PhSC1COO], respectively. As far as the reactive ILs are concerned, the enthalpies of solvation could be calculated for $[P_{4,4,4,4}][PhC_1COO]$ and $[P_{4,4,4,4}]$ $[C_{11}COO]$ and, although K_H is higher for the former (corresponding to a lower gas solubility), the enthalpy of solvation is more negative pointing towards more favourable interactions between the gas and the IL. Of course, in the case of the reactive ILs, the quantity of gas chemisorbed is significantly more important than its solubility.

Equilibrium constants, K_{eq}, for the chemical reaction of CO_2 with the ILs could also be calculated from the experimental isotherms and are reported in Table 2. The equilibrium constants are relatively low and vary from 0.6 to 5. ILs based on the acetate anion and the 1-butyl-3-methylimidazolium cation, $[C_4C_1Im]^+$, have been previously studied and a much higher equilibrium constant of $K_{eq} = 70$ has been determined for $[C_4C_1Im][C_1COO]$[11] compared with $K_{eq} = 1.7$ for $[P_{4,4,4,4}]$ $[C_1COO]$. The thermodynamics of the CO_2 chemisorption could be determined for the three ILs studied at different temperatures. For $[P_{4,4,4,4}][PhC_1COO]$, CO_2 is

absorbed exothermically with $\Delta_{abs}H = -5$ kJ mol^{-1} in the temperature range studied. For both $[P_{6,6,6,14}][C_{11}COO]$ and $[P_{6,6,6,14}][Me_4C_4COO]$, in contrast, CO_2 is absorbed endothermically with $\Delta_{abs}H = +11$ kJ mol^{-1} and $\Delta_{abs}H = +25$ kJ mol^{-1}, respectively.

The chemisorption of CO_2 is reversible as evaluated over up to 8 cycles of gas absorption and pressure swing desorption at different temperatures. No significant changes in capture capacity were observed for several reactive and non-reactive ILs within the measurement uncertainty, even after heating the sample at 343 K for 2 weeks. Some variations of the kinetics of absorption and desorption as well as variations of the absorption at higher pressures were observed over the cycles. The K_{eq} and K_H values determined in successive cycles were very similar to those obtained in the first cycle, except for $[P_{6,6,6,14}][Me_4C_4COO]$. Infrared spectra of $[P_{4,4,4,4}][C_{11}COO]$ were compared before and after two cycles of CO_2 absorption and desorption at 303 and 343 K (full spectra are available in the ESI†). The comparison reveals that $[P_{4,4,4,4}][C_{11}COO]$ is completely regenerated after its utilization as a CO_2 absorbent. For the ILs with endothermic absorption of CO_2, the pressure swing regeneration at high temperatures is, as expected, not very efficient. These are, however, the most promising liquids for applications as absorbents at high temperatures, such as flue gas scrubbers or to treat any other gas mixtures at high temperatures.

Fig. 7 illustrates the absorption of CO_2 at various temperatures for ILs featuring common anions and different cations: $[P_{4,4,4,4}][C_{11}COO]$, $[P_{6,6,6,14}][C_{11}COO]$, $[P_{4,4,4,4}][Me_4C_4COO]$ and $[P_{6,6,6,14}][Me_4C_4COO]$. Both ILs containing the $[C_{11}COO]^-$ anion exhibit increased CO_2 absorption when raising the temperature. However, at 303 K, CO_2 is merely physically absorbed by $[P_{4,4,4,4}][C_{11}COO]$, with a slight deviation from Henry's law evident in Fig. 7 and consistently observed across multiple measurements detailed in Table S12.† At 343 K, an equilibrium constant for the reaction between $[P_{4,4,4,4}][C_{11}COO]$ and CO_2 could be calculated as expected in view of the significantly higher CO_2 absorption at low pressures. In contrast, CO_2 is chemically absorbed by $[P_{6,6,6,14}][C_{11}COO]$ at both temperatures, with the gas absorption also increasing at higher temperatures, indicative of an endothermic reaction. Notably, at 343 K, the mole fraction of absorbed CO_2 is approximately equal in both ILs. As shown before,[1] the size of the alkyl side chains

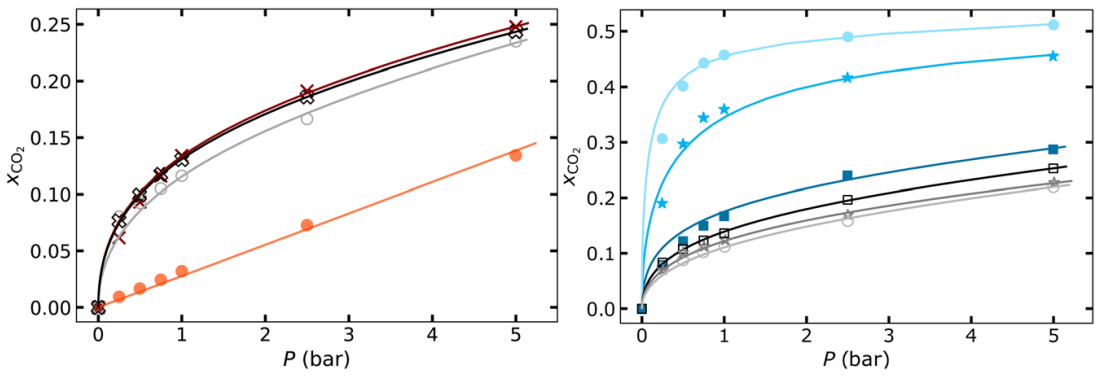

Fig. 7 CO_2 absorption as a function of pressure at different temperatures. Left: $[P_{4,4,4,4}][C_{11}COO]$ at 303 K, ●, and at 343 K, ×; $[P_{6,6,6,14}][C_{11}COO]$ at 303 K, ○, and at 343 K, ⊗. Right: $[P_{4,4,4,4}][Me_4C_4COO]$ at 303 K, ●, at 323 K, ★, and at 343 K, ■; $[P_{6,6,6,14}][Me_4C_4COO]$ at 303 K, ○, at 323 K, and at 343 K, □.

in the phosphonium cations does not significantly affect the microscopic structure or the acidity of the protons in the position of the phosphonium cations, H_α.

As far as the ILs based on the more basic $[Me_4C_4COO]^-$ anion are concerned, the behaviour with temperature is surprisingly different. For $[P_{4,4,4,4}][Me_4C_4COO]$, the amount of CO_2 absorbed decreases dramatically with increasing temperature, the sign of a very exothermic chemical reaction between the gas and the IL. A different behaviour has been observed for $[P_{6,6,6,14}][Me_4C_4COO]$ as, in this case, the quantity of CO_2 absorbed is lower and increases with increasing temperature, with a positive enthalpy of reaction, $\Delta_{abs}H = +11$ kJ mol^{-1}, being calculated from the experimental data.

At first glance, the equilibrium constants, and hence the CO_2 absorption amounts, increase with the increasing basicity of the carboxylate anions, as measured by the pK_a in water of the anions' conjugate carboxylic acid, listed in Table 1. The variation of the quantity of CO_2 absorbed at 343 K with the pK_a is represented in Fig. 8. A closer look reveals slight discrepancies for the anions with an intermediary basicity that, nevertheless, follow the general trend. The discrepancies point towards the importance of other factors, besides the basicity of the anion, to explain the reactivity of CO_2. For example, $[P_{4,4,4,4}][C_1COO]$, with a pK_a of 4.76, absorbs a larger quantity of CO_2 than $[P_{4,4,4,4}][c\text{-}C_6COO]$ (p$K_a = 4.82$), $[P_{4,4,4,4}][MeC_3COO]$ (p$K_a = 4.77$) or $[P_{4,4,4,4}][C_5COO]$ (p$K_a = 4.87$).

The hypothesis suggesting that the smaller size of the anion $[C_1COO]$ might enhance its ability to access the acidic proton of the cation, thereby facilitating the formation of the phosphorous ylide, is not supported by the MD simulations conducted on the pure ionic liquids (ILs). Fig. 9 illustrates the radial distribution functions for three ILs with distinct anions, all exhibiting strong correlation peaks of the hydrogen in the α position of the cation alkyl chains, H_α, around the

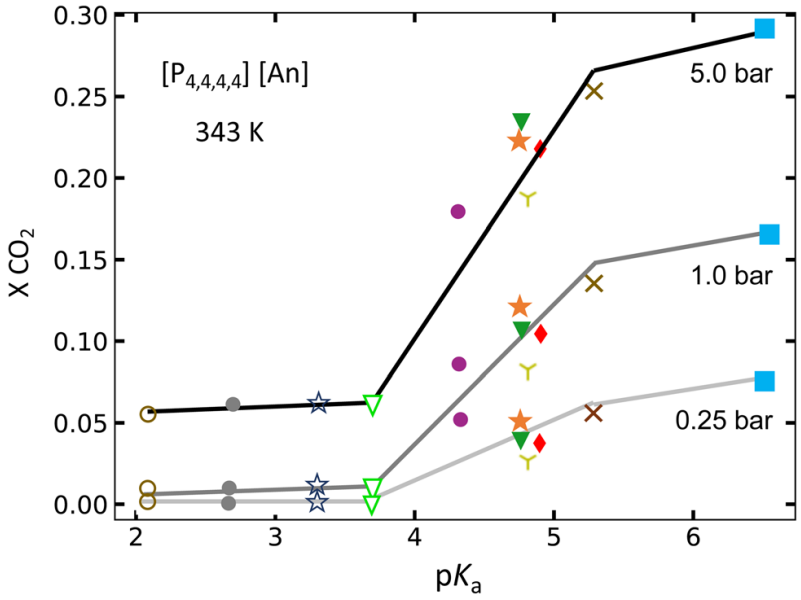

Fig. 8 CO_2 absorbed by the ILs at 343 K as a function of the basicity of the anions measured by the pK_a of the conjugated carboxylic acid in water: ○ $[P_{4,4,4,4}][2\text{-}ClPyCOO]$; ● $[P_{4,4,4,4}][TetrazC_1COO]$;[24] ☆ $[P_{4,4,4,4}][2\text{-}ClPhC_1OHCOO]$; ▽ $[P_{4,4,4,4}][PhSC_1COO]$; ● $[P_{4,4,4,4}][PhC_1COO]$; ★ $[P_{4,4,4,4}][C_1COO]$; ▼ $[P_{4,4,4,4}][MeC_3COO]$; Y $[P_{4,4,4,4}][c\text{-}C_6COO]$; ♦ $[P_{4,4,4,4}][C_5COO]$; × $[P_{4,4,4,4}][C_{11}COO]$; and ■ $[P_{4,4,4,4}][Me_4C_4COO]$. Lines are guides to the eye.

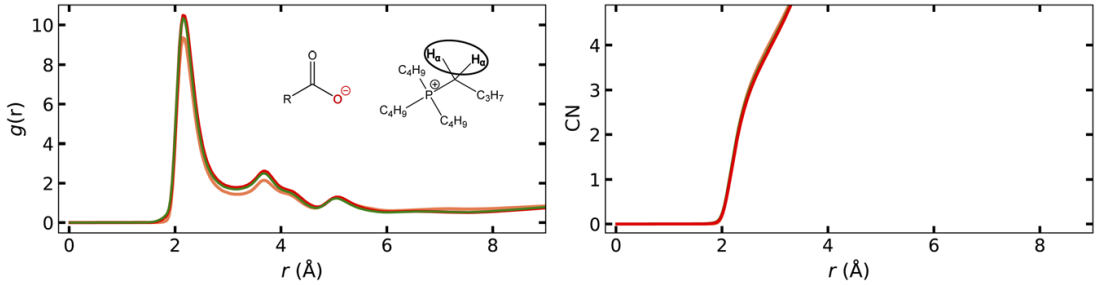

Fig. 9 Comparison of the site–site RDFs, $g_{ij}(r)$, of H_α of the cation around the negatively charged oxygen atoms O_{COO^-} of the carboxylate head of the anion and their corresponding coordination numbers in — $[P_{4,4,4,4}][C_1COO]$; — $[P_{4,4,4,4}][MeC_3COO]$; and — $[P_{4,4,4,4}][C_5COO]$.

carboxylate group at the same distance and of similar intensity. Furthermore, the calculated coordination numbers are identical across the three ILs. The explanation for the stronger than expected reactivity of the $[C_1COO]^-$ ion cannot come from the size of the anion and it does not fully correlate with pK_a so it has to be linked with the stability of the zwitterionic species formed by the reaction of CO_2 with the phosphorous ylide or to the stabilisation provided by the complexation of the carboxylate acid formed by a second ion pair.

Table 3 lists the relative Gibbs energies of reaction, calculated using DFT, facilitating a comparison among different ILs and providing insights into their respective behaviors. The calculated ΔG concerns the cation–anion proton transfer leading to the formation of the phosphorous ylide. The calculated values exhibit a trend that correlates with the experimentally measured CO_2 capacities. For instance, $[P_{4,4,4,4}][Me_4C_4COO]$ shows the lowest energy barrier (65.0 kJ mol^{-1}) and the highest capture capacity, while $[P_{4,4,4,4}][c\text{-}C_6COO]$ and $[P_{4,4,4,4}][PhC_1COO]$ display higher energy barriers (110.9 kJ mol^{-1} and 105.9 kJ mol^{-1}, respectively) and exhibit lower CO_2 capture capacities.

The $\Delta_r G°$ values concern the chemical reaction of the phosphorous ylide with CO_2. A slightly positive value is observed for $[P_{4,4,4,4}][PhC_1COO]$, indicating

Table 3 Relative enthalpy and Gibbs free energy of the reaction of CO_2 with the phosphonium carboxylate ILs calculated by DFT. ΔG and ΔH refer to the formation of the phosphonium ylide while $\Delta_r G°$ and $\Delta_r H°$ correspond to the subsequent formation of the zwitterion $[P_{4,4,4,4}{}^+–CO_2{}^-]$

Sample	ΔG/kJ mol^{-1}	ΔH/kJ mol^{-1}	$\Delta_r G°$/kJ mol^{-1}	$\Delta_r H°$/kJ mol^{-1}
$[P_{4,4,4,4}][2\text{-}ClPyCOO]$	137.4	129.9	35.1	20.5
$[P_{4,4,4,4}][TetrazC_1COO]$ [24]	125.6	123.9	28.3	15.3
$[P_{4,4,4,4}][2\text{-}ClPhC_1OHCOO]$	102.7	111.5	17.7	1.3
$[P_{4,4,4,4}][PhSC_1COO]$	102.6	103.7	21.2	7.1
$[P_{4,4,4,4}][PhC_1COO]$	105.9	103.7	1.7	−7.5
$[P_{4,4,4,4}][C_1COO]$	95.8	94.0	−13.6	−37.3
$[P_{4,4,4,4}][MeC_3COO]$	89.3	91.2	−18.5	−22.4
$[P_{4,4,4,4}][c\text{-}C_6COO]$	110.9	114.0	−6.0	−6.7
$[P_{4,4,4,4}][C_5COO]$	98.2	94.0	−16.1	−19.6
$[P_{4,4,4,4}][C_{11}COO]$	84.6	82.5	−6.0	−19.7
$[P_{4,4,4,4}][Me_4C_4COO]$	65.0	63.3	−21.5	−31.5

a modest reactivity compared to the other reactive ILs, for which negative $\Delta_r G°$ values have been calculated. All other factors remaining constant—cation structure and presence of the reactive phosphorous ylide—the more negative values of $\Delta_r G°$ can only be explained by the stability of the $[P_{4,4,4,4}][RCOO]$–HOOCR complex formed in the reaction. Interestingly enough, the less negative $\Delta_r G°$ values correspond to the ILs capable of absorbing lower quantities of gas, namely $[P_{4,4,4,4}][c\text{-}C_6COO]$ and $[P_{4,4,4,4}][C_{11}COO]$; this last one only reacting at the higher temperatures studied (as shown in Fig. 7). The four non-reactive ILs all present a positive $\Delta_r G°$ confirming their low likelihood of reaction with CO_2.

A positive enthalpy of reaction, ΔH, is calculated for the formation of the phosphorous ylide in all the ILs, confirming this reaction as the controlling step in the CO_2 absorption mechanism (with a positive ΔG also). The presence of an additional ion pair plays a crucial role in stabilizing the intermediate products of this first reaction (see Fig. S46†). A sufficiently high temperature or the presence of an excess of CO_2 is necessary to displace the reaction towards the chemisorption of the gas with the formation of the zwitterion. As for this last reaction, an exothermic enthalpy, $\Delta_r H°$, is calculated and a balance is necessary to choose the optimum reaction temperature. These observations are supported by the calculation of the partial charges and molecular orbital energies of all the species present in solution as reported in Table S15.†

The overall enthalpy of CO_2 absorption in the ILs, calculated from experimental gas absorptions at various temperatures, is not quantitatively matched by the DFT-calculated values. Nevertheless, certain general trends emerge. In ILs based on more basic anions such as $[P_{4,4,4,4}][C_{11}COO]$ and $[P_{4,4,4,4}][Me_4C_4COO]$, CO_2 absorption is endothermic in the former and exothermic in the latter (see Fig. 7). This trend aligns with the DFT predictions as a more negative $\Delta_r H°$ is found for $[P_{4,4,4,4}][Me_4C_4COO]$, as shown in Table 3. In the case of $[P_{4,4,4,4}][PhC_1COO]$, although a small negative $\Delta_r H°$ was calculated (listed in Table 3), consistent with the measured exothermic CO_2 absorption, it is largely offset by a positive ΔH calculated for the formation of the phosphorous ylide.

Unlike in previously reported ILs for the chemisorption of CO_2,[41–44] the self-diffusion coefficients of the cation and anion measured in the ILs are generally higher after the absorption of CO_2, with the exception of $[P_{4,4,4,4}][C_1COO]$, $[P_{4,4,4,4}][Me_4C_4COO]$, and $[P_{6,6,6,14}][Me_4C_4COO]$ (Table S14 and Fig. S38†). All the other ILs become more fluid upon CO_2 absorption, following a physical or chemical process, with higher measured self-diffusion coefficients and lower viscosities. Furthermore, at temperatures below their melting points, ILs such as $[P_{4,4,4,4}][MeC_3COO]$, $[P_{4,4,4,4}][c\text{-}C_6COO]$, $[P_{4,4,4,4}][PhC_1COO]$ and $[P_{4,4,4,4}][PhSC_1COO]$ liquefy upon CO_2 absorption.

4 Conclusions

In conclusion, tetraalkylphosphonium carboxylate ILs can be prepared following a straightforward synthesis route using readily available carboxylic acids, selected for their low environmental impact, yielding chemically and thermally stable salts with customizable physical properties. Depending on the pK_a of the acid precursors, these ILs can dissolve or chemically absorb CO_2, with some displaying high gas capacities at relatively low pressures, reaching a CO_2 mole fraction of up to 0.2 at 1 bar and 343 K.

ILs that solely dissolve CO_2 are derived from anions with acid precursors featuring low pK_a values. Regardless, in all ILs, CO_2 is solvated near the polar regions of the liquid, particularly in proximity to the carboxylate group of the anion. Chemisorption of CO_2 occurs with anions prepared from acids possessing a pK_a in water of approximately 4. This chemisorption process is readily reversible, with low equilibrium constants and weakly exothermic, or even endothermic, enthalpies of reaction.

While equilibrium constants and IL capacities roughly correlate with pK_a, certain outliers emphasize the influence of liquid structure and physical properties on how CO_2 is absorbed. These deviations could be partially elucidated by the microscopic structure of the liquid, as determined by MD simulations, or by the electronic structure of reaction products, as assessed by DFT calculations.

In contrast to reported behaviors in other CO_2-absorbing ILs, phosphonium carboxylates do not exhibit increased viscosity upon CO_2 absorption; instead, higher diffusivities are observed. This fluidity enhancement is advantageous for gas absorption, facilitating efficient gas–liquid transfer and reducing energy requirements in separation or carbon-capture processes.

Carboxylate-based ILs emerge as a promising liquid family for carbon capture, boasting high capacities, environmentally friendly attributes such as low vapor pressures and viscosities, and stability across wide temperature ranges. The diverse range of precursor acids enables tailored properties and selectivities for gas capture. By controlling equilibrium constants and energetics through the selection of acids with different pK_a values, the reactivity and efficiency of CO_2 absorption can be finely tuned, optimizing carbon-capture conditions and absorber regeneration.

Conflicts of interest

There are no conflicts to declare.

Acknowledgements

The authors thank K. C. Szeto for his help and assistance with IR measurements under CO_2 pressure.

Notes and references

1 N. Scaglione, J. Avila, E. Bakis, A. Padua and M. C. Gomes, *Phys. Chem. Chem. Phys.*, 2023, **25**, 15325–15339.
2 J. Avila, L. F. Lepre, K. Goloviznina, L. Guazzelli, C. S. Pomelli, C. Chiappe, A. Pádua and M. Costa Gomes, *Phys. Chem. Chem. Phys.*, 2021, **23**, 23130–23140.
3 N. Bagány, A. Tot, M. Vraneš and S. Gadžurić, *J. Mol. Liq.*, 2021, **328**, 115474.
4 A. Xu and F. Wang, *Green Chem.*, 2020, **22**, 7622–7664.
5 R. P. Swatloski, S. K. Spear, J. D. Holbrey and R. D. Rogers, *J. Am. Chem. Soc.*, 2002, **124**, 4974–4975.
6 J.-M. Andanson, E. Bordes, J. Devémy, F. Leroux, A. A. H. Padua and M. C. Gomes, *Green Chem.*, 2014, **16**, 2528.

7 J.-M. Andanson, A. A. H. Pádua and M. F. C. Gomes, *Chem. Commun.*, 2015, **51**, 4485–4487.
8 K. Huang, Y.-T. Wu and X.-B. Hu, *Chem. Eng. J.*, 2016, **297**, 265–276.
9 A. Yokozeki, M. B. Shiflett, C. P. Junk, L. M. Grieco and T. Foo, *J. Phys. Chem. B*, 2008, **112**, 16654–16663.
10 G. Gurau, H. Rodríguez, S. P. Kelley, P. Janiczek, R. S. Kalb and R. D. Rogers, *Angew. Chem., Int. Ed.*, 2011, **50**, 12024–12026.
11 L. F. Lepre, J. Szala-Bilnik, L. Pison, M. Traïkia, A. A. H. Pádua, R. A. Ando and M. F. C. Gomes, *Phys. Chem. Chem. Phys.*, 2017, **19**, 12431–12440.
12 M. B. Shiflett, D. W. Drew, R. A. Cantini and A. Yokozeki, *Energy Fuels*, 2010, **24**, 5781–5789.
13 D. J. Yeadon, J. Jacquemin, N. V. Plechkova, M. Maréchal and K. R. Seddon, *ChemPhysChem*, 2020, **21**, 1369–1374.
14 J. Avila, L. F. Lepre, C. C. Santini, M. Tiano, S. Denis-Quanquin, K. C. Szeto, A. A. H. Padua and M. C. Gomes, *Angew. Chem., Int. Ed.*, 2021, **60**, 12876–12882.
15 W. Shi, R. L. Thompson, E. Albenze, J. A. Steckel, H. B. Nulwala and D. R. Luebke, *J. Phys. Chem. B*, 2014, **118**, 7383–7394.
16 Y. Yasaka, M. Ueno and Y. Kimura, *Chem. Lett.*, 2014, **43**, 626–628.
17 C. Wang, X. Luo, H. Luo, D. Jiang, H. Li and S. Dai, *Angew. Chem., Int. Ed.*, 2011, **50**, 4918–4922.
18 C. Wang, X. Luo, X. Zhu, G. Cui, D.-e. Jiang, D. Deng, H. Li and S. Dai, *RSC Adv.*, 2013, **3**, 15518.
19 R. Cuéllar-Franca, P. García-Gutiérrez, S. Taylor, C. Hardacre and A. Azapagic, *Faraday Discuss.*, 2016, **192**, 283–301.
20 R. Cuéllar-Franca, P. García-Gutiérrez, J. Hallett and N. Mac Dowell, *React. Chem. Eng.*, 2021, **6**, 258–278.
21 K. Anderson, M. P. Atkins, J. Estager, Y. Kuah, S. Ng, A. A. Oliferenko, N. V. Plechkova, A. V. Puga, K. R. Seddon and D. F. Wassell, *Green Chem.*, 2015, **17**, 4340–4354.
22 J. Avila, C. Červinka, P.-Y. Dugas, A. A. H. Pádua and M. C. Gomes, *Adv. Mater. Interfaces*, 2021, **8**, 2001982.
23 K. J. Baranyai, G. B. Deacon, D. R. MacFarlane, J. M. Pringle and J. L. Scott, *Aust. J. Chem.*, 2004, **57**, 145–147.
24 N. Scaglione, L. Wylie, A. Padua and M. Costa Gomes, *ACS Sustainable Chem. Eng.*, 2024, **12**(28), 10486–10497.
25 P. Eastman, J. Swails, J. D. Chodera, R. T. McGibbon, Y. Zhao, K. A. Beauchamp, L.-P. Wang, A. C. Simmonett, M. P. Harrigan, C. D. Stern, R. P. Wiewiora, B. R. Brooks and V. S. Pande, *PLoS Comput. Biol.*, 2017, **13**, e1005659.
26 T. M. Becker, L.-C. Lin, D. Dubbeldam and T. J. H. Vlugt, *J. Phys. Chem. C*, 2018, **122**, 24488–24498.
27 A. H. Padua, *fftool v1.2.1*, accessed 2021, **https://github.com/paduagroup/fftool**.
28 L. Martínez, R. Andrade, E. G. Birgin and J. M. Martínez, *J. Comput. Chem.*, 2009, **30**, 2157–2164.
29 M. Brehm and B. Kirchner, *J. Chem. Inf. Model.*, 2011, **51**, 2007–2023.
30 M. Brehm, M. Thomas, S. Gehrke and B. Kirchner, *J. Chem. Phys.*, 2020, **152**, 164105.

31 P. Pracht, F. Bohle and S. Grimme, *Phys. Chem. Chem. Phys.*, 2020, **22**, 7169–7192.
32 M. J. Frisch, G. W. Trucks, H. B. Schlegel, G. E. Scuseria, M. A. Robb, J. R. Cheeseman, G. Scalmani, V. Barone, G. A. Petersson, H. Nakatsuji, X. Li, M. Caricato, A. V. Marenich, J. Bloino, B. G. Janesko, R. Gomperts, B. Mennucci, H. P. Hratchian, J. V. Ortiz, A. F. Izmaylov, J. L. Sonnenberg, D. Williams-Young, F. Ding, F. Lipparini, F. Egidi, J. Goings, B. Peng, A. Petrone, T. Henderson, D. Ranasinghe, V. G. Zakrzewski, J. Gao, N. Rega, G. Zheng, W. Liang, M. Hada, M. Ehara, K. Toyota, R. Fukuda, J. Hasegawa, M. Ishida, T. Nakajima, Y. Honda, O. Kitao, H. Nakai, T. Vreven, K. Throssell, J. A. Montgomery Jr, J. E. Peralta, F. Ogliaro, M. J. Bearpark, J. J. Heyd, E. N. Brothers, K. N. Kudin, V. N. Staroverov, T. A. Keith, R. Kobayashi, J. Normand, K. Raghavachari, A. P. Rendell, J. C. Burant, S. S. Iyengar, J. Tomasi, M. Cossi, J. M. Millam, M. Klene, C. Adamo, R. Cammi, J. W. Ochterski, R. L. Martin, K. Morokuma, O. Farkas, J. B. Foresman and D. J. Fox, *Gaussian 16 Revision C.01*, Gaussian Inc., Wallingford CT, 2016.
33 T. H. Dunning and P. J. Hay, *Methods of Electronic Structure Theory*, Springer US, 1977, pp. 1–27.
34 Y. Zhao and D. G. Truhlar, *Theor. Chem. Acc.*, 2008, **120**, 215–241.
35 E. Papajak, J. Zheng, X. Xu, H. R. Leverentz and D. G. Truhlar, *J. Chem. Theory Comput.*, 2011, **7**, 3027–3034.
36 B. Temelso, K. A. Archer and G. C. Shields, *J. Phys. Chem. A*, 2011, **115**, 12034–12046.
37 A. V. Marenich, S. V. Jerome, C. J. Cramer and D. G. Truhlar, *J. Chem. Theory Comput.*, 2012, **8**, 527–541.
38 M. A. Spackman and D. Jayatilaka, *CrystEngComm*, 2009, **11**, 19–32.
39 C. Adamo and V. Barone, *J. Chem. Phys.*, 1999, **110**, 6158–6170.
40 D. Almantariotis, T. Gefflaut, A. Pádua, J.-Y. Coxam and M. F. Costa Gomes, *J. Phys. Chem. B*, 2010, **114**, 3608–3617.
41 E. D. Bates, R. D. Mayton, I. Ntai and J. H. Davis, *J. Am. Chem. Soc.*, 2002, **124**, 926–927.
42 K. E. Gutowski and E. J. Maginn, *J. Am. Chem. Soc.*, 2008, **130**, 14690–14704.
43 B. E. Gurkan, J. C. de la Fuente, E. M. Mindrup, L. E. Ficke, B. F. Goodrich, E. A. Price, W. F. Schneider and J. F. Brennecke, *J. Am. Chem. Soc.*, 2010, **132**, 2116–2117.
44 S. Seo, M. Quiroz-Guzman, M. A. DeSilva, T. B. Lee, Y. Huang, B. F. Goodrich, W. F. Schneider and J. F. Brennecke, *J. Phys. Chem. B*, 2014, **118**, 5740–5751.

Tailored Carbon Dioxide Capacity in Carboxylate-Based Ionic Liquids

Nicolas Scaglione, Jocasta Avila, Agilio Pádua, and Margarida Costa Gomes*

Laboratoire de Chimie de l'ENS Lyon, CNRS and Université de Lyon, 46 allée d'Italie, 69364 Lyon, France

E-mail: margarida.costa-gomes@ens-lyon.fr

Supplementary Information

1 Synthesis and Characterisation of the ILs

1.1 Ionic liquids synthesis

$[P_{4,4,4,4}][2-ClPyCOO]$, $[P_{4,4,4,4}][2-ClPhC_1OHCOO]$ and $[P_{4,4,4,4}][PhSC_1COO]$, whose structures are represented in Figure S1 were synthesized and characterized as described in our previous work.[1]

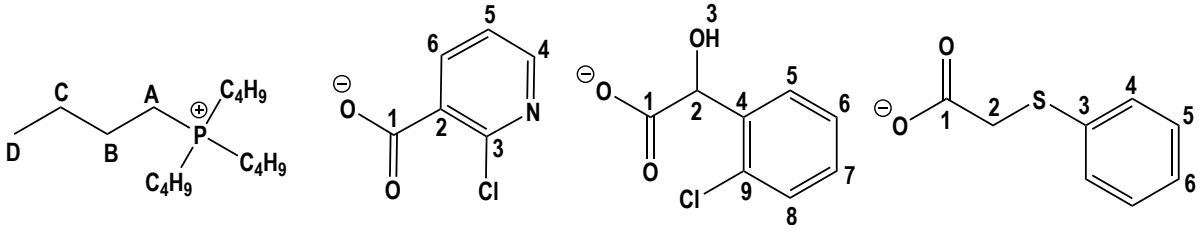

Figure S1 – Chemical structure of the newly prepared ILs: $[P_{4,4,4,4}][2-ClPyCOO]$, $[P_{4,4,4,4}][2-ClPhC_1OHCOO]$ and $[P_{4,4,4,4}][PhSC_1COO]$.

Tetrabutylphosphonium 2-chloropyridine-3-carboxylate $[P_{4,4,4,4}][2-ClPyCOO]$, the yellowish liquid obtained from the rotary evaporator was dried under vacuum (1×10^{-4} bar) at 323 K under stirring (400 rpm). The product was collected as a yellowish viscous liquid. ^{1}H NMR (400 MHz, C_6D_6, 343 K) δ ppm: 0.71 (t, 12H, $^{3}J_{HH} = 7.2$ Hz, D); 1.25 (m, 8H, C); 1.40 (m, 8H, B); 2.34 (m, 8H, A); 7.14 (t, 1H, $^{3}J_{HH} = 4.9$ Hz, 5); 7.63 (d, 1H, $^{3}J_{HH} = 7.0$ Hz, 6); 8.02 (m, 1H, 4). ^{13}C NMR (100 MHz, C_6D_6, 343 K) δ ppm: 12.43 (4C, D); 17.57 (4C, A); 22.70 (7C, B); 22.88 (4C, C); 121.54 (1C, 5); 136.33 (1C, 6); 139.71 (1C, 2); 145.60 (1C, 4); 146.43 (1C, 3); 166.01 (1C, 1). ^{31}P NMR (161 MHz, C_6D_6, 343 K) δ ppm: 33.66 (1P, $\mathbf{P}((CH_2)_3CH_3)_4$). ν (cm^{-1}): 2959; 2932; 2903; 2872; 1609; 1570; 1466; 1410; 1386; 1349; 1321; 1281; 1232; 1191; 1157; 1118; 1099; 1062; 1035; 1005; 969; 919; 909; 828; 812; 779; 752; 727; 643; 567; 554. MS ES^+ m/z (% Rel. Intensity): 259 (100, $[P_{4,4,4,4}]^+$). MS ES^- m/z (% Rel. Intensity): 156 (100, $[2-ClPyCOO]^-$).

Tetrabutylphosphonium 2-(2-chlorophenylacetate)-2-hydroxyacetate $[P_{4,4,4,4}][2-ClPhC_1OHCOO]$, the yellowish viscous liquid obtained from the rotary evaporator was dried under vacuum (1×10^{-4} bar) at 323 K under stirring (400 rpm). The product was collected as a dark yellowish viscous liquid.

^{1}H NMR (400 MHz, C_6D_6, 343 K) δ ppm: 0.71 (t, 12H, $^{3}J_{HH} =$ Hz, D); 1.20 (m, 14H, B+C); 2.04 (m, 8H, A); 4.79 (s, 1H, 2); 5.55 (s, 1H, 3); 6.95 (m, 2H, 7+8); 7.05 (m, 1H, 5); 7.24 (m,

1H, 6). ^{13}C NMR (100 MHz, C_6D_6, 343 K) δ ppm: 12.37 (4C, D); 17.33 (4C, A); 22.51 (4C, B); 22.80 (4C, C); 70.10 (1C, 2); 125.25 (1C, 7); 126.30 (1C, 8); 127.52 (1C, 6); 127.77 (1C, 5); 132.77 (1C, 4); 142.59 (1C, 9); 171.85 (1C, 1). ^{31}P NMR (161 MHz, C_6D_6, 343 K) δ ppm: 33.23 (1P, **P**$((CH_2)_3CH_3)_4$). ν (cm^{-1}): 3070; 2959; 2932; 2903; 2873; 1632; 1615; 1581; 1466; 1442; 1413; 1381; 1346; 1330; 1291; 1249; 1192; 1126; 1098; 1067; 1045; 1030; 1002; 969; 950; 925; 906; 871; 824; 782; 752; 722; 699; 609; 585; 570; 554. MS ES$^+$ m/z (% Rel. Intensity): 259 (100, $[P_{4,4,4,4}]^+$). MS ES$^-$ m/z (% Rel. Intensity): 185 (100, [2 $-$ClPhC$_1$OHCOO]$^-$).

Tetrabutylphosphonium (thiophenyl)acetate [$P_{4,4,4,4}$][$PhSC_1COO$], the dark orange viscous liquid obtained from the rotary evaporator was dried under vacuum (1×10^{-4} bar) at 323 K under stirring (400 rpm). The product was collected as a orange-brown solid after drying under vacuum.

^{1}H NMR (400 MHz, C_6D_6, 343 K) δ ppm: ^{1}H NMR (400 MHz, C_6D_6, 343 K) δ ppm: 0.76 (t, 12H, $^3J_{HH} = 7.4$ Hz, D); 1.29 (m, 8H, C); 1.37 (m, 8H, B); 2.33 (m, 8H, A); 3.34 (s, 1H, 2); 6.87 (t, 1H, $^3J_{HH} = 7.4$ Hz, 6); 7.02 (m, 2H, $^3J_{HH} = 7.6$ Hz, 5); 7.14 (d, 2H, $^3J_{HH} = 7.8$ Hz, 4). ^{13}C NMR (100 MHz, C_6D_6, 343 K) δ ppm: 13.82 (4C, D); 18.87 (4C, A); 24.11, 24.29 (8C, B+C); 41.44 (1C, 2); 124.36 (1C, 6); 127.22 (2C, 4); 128.80 (2C, 5); 141.43 (1C, 3); 168.69 (1C, 1). ^{31}P NMR (161 MHz, C_6D_6, 343 K) δ ppm: 33.49 (1P, **P**$((CH_2)_3CH_3)_4$). ν (cm^{-1}): 2957; 2930; 2908; 2872; 1609; 1585; 1560; 1480; 1465; 1443; 1405; 1380; 1343; 1321; 1239; 1204; 1180; 1090; 1068; 1048; 1026; 1009; 968; 912; 907; 808; 737; 701; 691; 581; 575; 570; 561; 556. MS ES$^+$ m/z (% Rel. Intensity): 259 (100, $[P_{4,4,4,4}]^+$). MS ES$^-$ m/z (% Rel. Intensity): 167 (100, [$PhSC_1COO$]$^-$).

1.2 Density and molar volume

The experimental densities (ρ) and molar volumes (V_m) of the three new ILs are plotted in Figure S2 and listed in Table S1 along with the deviations of linear fits with temperature whose coefficients are listed in Tables S2 and S3, respectively. The presence of aromatic ring substituents in the carboxylate anions appears to result in denser ILs.

The V_m of these newly prepared ILs is additive and could be predicted using a group contribution method (GCM).[2] The calculated V_m agree with experimental values to within 2 % as

represented in Figure S2. The group contribution parameters are reported in Table S4.

Table S1 – Experimental densities and molar volumes of $[P_{4,4,4,4}][2-ClPyCOO]$, $[P_{4,4,4,4}][2-ClPhC_1OHCOO]$ and $[P_{4,4,4,4}][PhSC_1COO]$ in the temperature range of 293–363 K. The deviations (δ) reported are relative to the fitting polynomials with coefficients listed in Table S2 and Table S3.

T/K	ρ/g cm^{-3}	δ/%	V_m/cm^3 mol^{-1}	δ/%	T/K	ρ/g cm^{-3}	δ/%	V_m/cm^3 mol^{-1}	δ/%
	$[P_{4,4,4,4}][2-ClPyCOO]$					$[P_{4,4,4,4}][2-ClPhC_1OHCOO]$			
293.149	1.06170	0.003	391.81	0.02	293.151	1.06261	0.001	418.80	0.02
298.152	1.05860	0.005	392.96	0.00	298.150	1.05966	0.01	419.96	0.0005
303.151	1.05546	0.003	394.13	0.002	303.152	1.05653	0.005	421.21	0.004
313.152	1.04917	0.003	396.49	0.01	313.152	1.05030	0.004	423.71	0.008
323.152	1.04291	0.006	398.87	0.01	323.152	1.04412	0.008	426.21	0.01
333.152	1.03667	0.007	401.27	0.01	333.152	1.03799	0.008	428.73	0.01
343.152	1.03046	0.005	403.69	0.006	343.151	1.03188	0.005	431.27	0.005
353.152	1.02430	0.0006	406.12	0.003	353.152	1.02580	0.0003	433.83	0.004
363.152	1.01817	0.01	408.57	0.02	363.152	1.01977	0.01	436.39	0.01
	$[P_{4,4,4,4}][PhSC_1COO]$								
313.148	1.01071	0.007	422.12	0.006					
323.148	1.00451	0.001	424.72	0.002					
333.148	0.99834	0.006	427.35	0.004					
343.148	0.99223	0.006	429.98	0.004					
353.148	0.98616	0.001	432.63	0.001					
363.152	0.98012	0.007	435.29	0.006					

Table S2 – Fitting parameters A_0 and A_1 determined from the linear fitting of the experimental densities to $\rho = A_0 + A_1 T$ and the corresponding absolute average deviation (AAD).

Sample	A_0/g cm^{-3}	A_1/g cm^{-3} K	AAD/%
$[P_{4,4,4,4}][2-ClPyCOO]$	1.2443	-6.2290 x 10^{-4}	0.004
$[P_{4,4,4,4}][2-ClPhC_1OHCOO]$	1.2425	-6.1377 x 10^{-4}	0.005
$[P_{4,4,4,4}][PhSC_1COO]$	1.2022	-6.1173 x 10^{-4}	0.004

Table S3 – Fitting parameters B_0 and B_1 determined from the linear fitting of the experimental molar volumes to $M_v = B_0 + B_1 T$ and the corresponding absolute average deviation (AAD).

Sample	M/g mol^{-1}	B_0/cm^3 mol^{-1}	B_1/cm^3 mol^{-1} K	AAD/%
$[P_{4,4,4,4}][2-ClPyCOO]$	415.99	321.56	0.23940	0.009
$[P_{4,4,4,4}][2-ClPhC_1OHCOO]$	445.02	344.91	0.25174	0.009
$[P_{4,4,4,4}][PhSC_1COO]$	426.64	339.59	0.26340	0.004

Table S4 – Group contribution parameters used to calculate the molar volume of cation and anion as a function of temperature.

Group j	C_0 / $cm^3\ mol^{-1}$	C_1 / $cm^3\ mol^{-1}\ K$	C_2 / $cm^3\ mol^{-1}\ K^2$	Ref.
$-CH_2$	16.967	1.399 x 10^{-3}	-1.946 x 10^{-6}	2
$-CH_2-Ph$	80.185	1.344 x 10^{-1}	1.230 x 10^{-4}	2⋆
$-OH$	10.624	-3.319 x 10^{-2}	-4.034 x 10^{-5}	2⋆
$-Cl$	26.830	-7.000 x 10^{-4}	-4.250 x 10^{-5}	2
$-S-$	23.361	-1.814 x 10^{-1}	2.770 x 10^{-3}	3† ⋆
$-ClPy$	78.449	7.872 x 10^{-2}	4.3316 x 10^{-4}	2⋆
$-COO^-$	21.680	3.101 x 10^{-2}	-4.333 x 10^{-4}	4
$-CH_3COO^-$	49.177	2.149 x 10^{-2}	-2.775 x 10^{-5}	2
$[P_{4,4,4,4}]^+$	290.987	3.192 x 10^{-1}	1.436 x 10^{-5}	2⋆

⋆ Calculated by subtraction of parameters available in the reference.

† Calculated from the density data from the reference with temperatures ranging from 283 to 343 K.

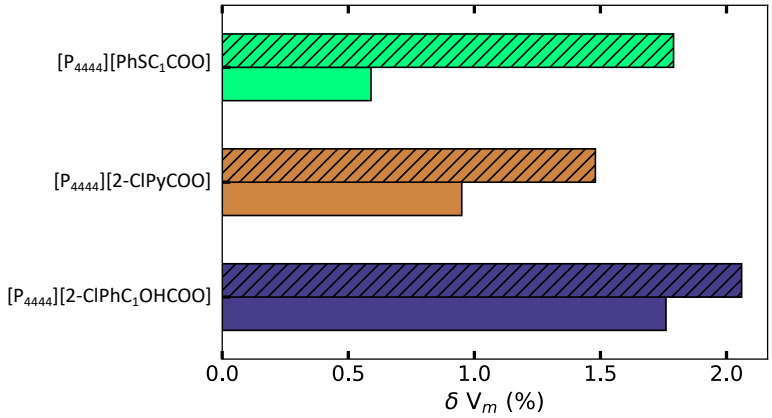

Figure S2 – Deviation of the predicted molar volumes[2] (V_m pred.) from the experimental values (V_m exp.) at 333 K (plain bars) and 353 K (textured bars).

1.3 Viscosity

The measured viscosity of the newly prepared ILs are listed in Table S5.

The experimental viscosities were fitted with temperature by using the Vogel-Fulcher-Tammann (VTF) equation:

$$\eta = A \exp\left(\frac{B}{T - T_0}\right) \tag{S1}$$

where η is the dynamic viscosity, T the temperature, and A, B, and T_0 are adjustable parameters. Their values for the ILs newly prepared are provided in Table S6. The experimental data are well repre-

sented by the fits with absolute average deviations (AAD) of up to 2.7 %.

Table S5 – Experimental viscosities of $[P_{4,4,4,4}][PhSC_1COO]$, $[P_{4,4,4,4}][2-ClPyCOO]$ and $[P_{4,4,4,4}][2-ClPhC_1OHCOO]$ in the temperature range of 303–363 K. The deviations (δ) reported are relative to the fitting of the VFT function with coefficients listed in Table S6.

T/K	η/mPa s	δ/%	T/K	η/mPa s	δ/%	T/K	η/mPa s	δ/%
$[P_{4,4,4,4}][2-ClPyCOO]$			$[P_{4,4,4,4}][2-ClPhC_1OHCOO]$			$[P_{4,4,4,4}][PhSC_1COO]$		
303.15	1222	0.07						
313.15	533.4	1.1	313.15	752.5	0.01			
323.15	282.0	3.11	323.15	377.2	0.1	323.15	119.1	0.005
333.15	156.3	1.6	333.15	205.8	0.2	333.15	72.90	0.03
343.15	89.20	5.4	343.15	121.2	0.3	343.15	47.49	0.04
353.15	59.54	3.1	353.15	76.06	0.03	353.15	32.60	0.08
363.15	40.52	4.4	363.15	50.73	1.2	363.15	23.42	0.1

Table S6 – Fitting parameters A, B and T_0 determined from the fitting of the experimental viscosities to the VFT function and the corresponding absolute average deviation (AAD).

Sample	A/mPa s	B/K	T_0/K	AAD/%
$[P_{4,4,4,4}][2-ClPyCOO]$	0.1635	884.18	204.01	2.7
$[P_{4,4,4,4}][2-ClPhC_1OHCOO]$	0.0346	1341.83	178.81	0.31
$[P_{4,4,4,4}][PhSC_1COO]$	0.0973	958.06	188.41	0.06

1.4 Thermal analysis

The melting points (T_{fus}) and phase-transition temperatures (T_{trans}) of the three newly synthesized ILs are listed in Table S7, and the corresponding thermograms are depicted in Figure S3. A meting point was only detected for $[P_{4,4,4,4}][PhSC_1COO]$ at $T_{fus} = 57.4$ °C and a solid-solid transition at $T_{trans} = 48.9$ °C. The melting point of $[P_{4,4,4,4}][PhSC_1COO]$ was verified using a melting point apparatus, providing an observable verification. For $[P_{4,4,4,4}][2-ClPyCOO]$ and $[P_{4,4,4,4}][2-ClPhC_1OHCOO]$, glass transition temperatures (T_g) were observed at −45.9 °C and −44.0 °C, respectively. $[P_{4,4,4,4}][PhSC_1COO]$ also exhibits a glass transition, but at a lower temperature of −53.0 °C.

Table S7 – Glass transition temperatures (T_g), melting points (T_{fus}) and crystallization temperatures (T_{cr}) for $[P_{4,4,4,4}][PhSC_1COO]$, $[P_{4,4,4,4}][2-ClPyCOO]$ and $[P_{4,4,4,4}][2-ClPhC_1OHCOO]$ measured in a DSC with a 10 K min^{-1} heating or cooling rate.

Sample	T_g / °C	T_{trans} & T_{fus} / °C	T_{cr} / °C
$[P_{4,4,4,4}][2-ClPyCOO]$	-45.9	-	-
$[P_{4,4,4,4}][2-ClPhC_1OHCOO]$	-44.0	-	-
$[P_{4,4,4,4}][PhSC_1COO]$	-53.4	46.1 & 57.6	-19.1

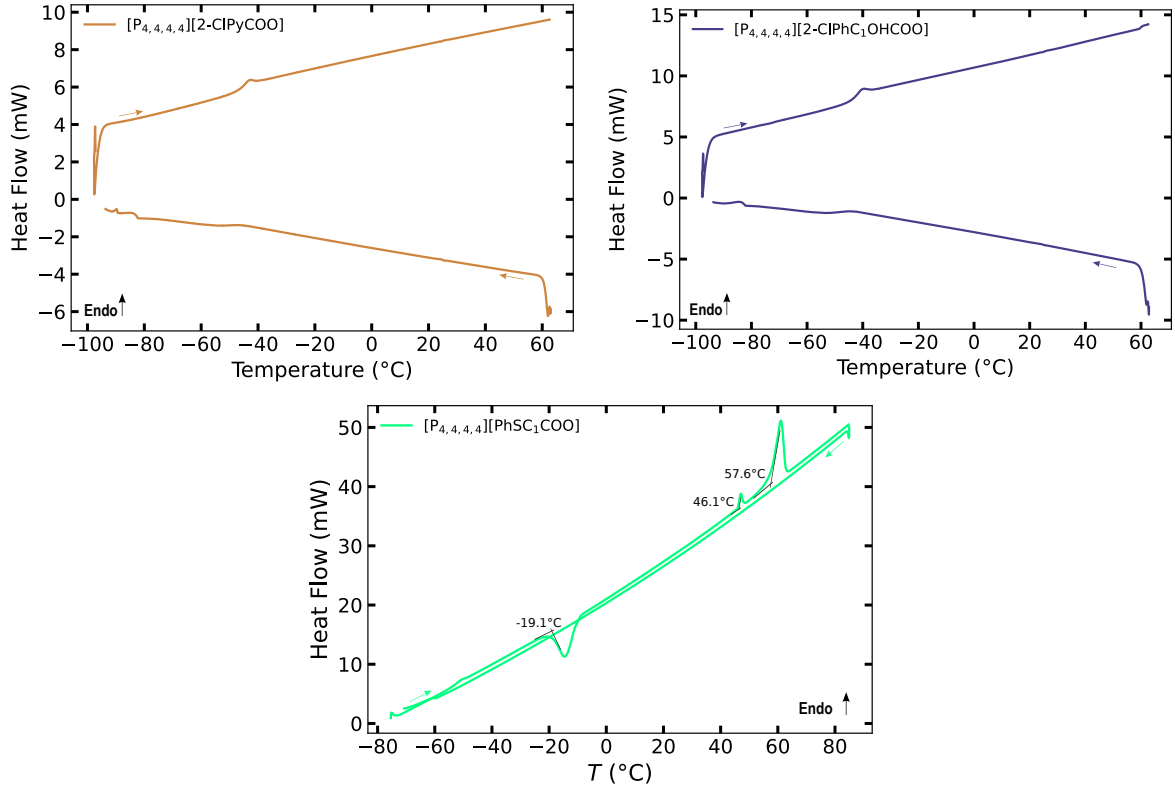

Figure S3 – Thermograms of — $[P_{4,4,4,4}][2-ClPyCOO]$, — $[P_{4,4,4,4}][2-ClPhC_1OHCOO]$ and — $[P_{4,4,4,4}][PhSC_1COO]$ measured at 10 K min^{-1}.

The thermal stability of the three newly synthesized ILs was investigated under an O_2 atmosphere, as the presence of O_2 can potentially affect IL stability due to its oxidizing properties. The decomposition temperatures (T_{dec}) of the ILs are listed in Table 1, and their corresponding thermographs are shown in Figure S4. Both $[P_{4,4,4,4}][2-ClPyCOO]$ and $[P_{4,4,4,4}][2-ClPhC_1OHCOO]$ exhibited a similar T_{dec} (261 °C), indicating comparable thermal stability. On the other hand, the T_{dec} of $[P_{4,4,4,4}][PhSC_1COO]$ was slightly higher at (276 °C). Their decomposition temperatures are close to those of other ILs containing carboxylate anions containing aromatic moieties.[1]

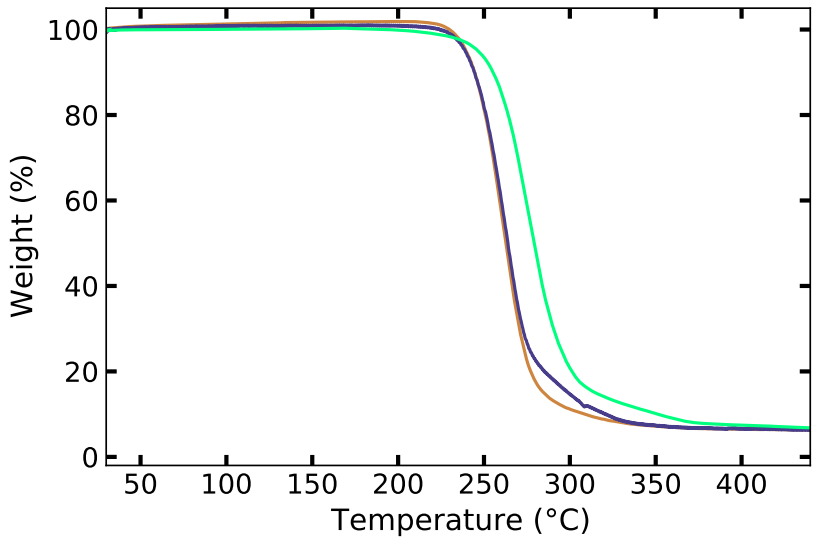

Figure S4 – TGA thermographs of — $[P_{4,4,4,4}][2-ClPyCOO]$, — $[P_{4,4,4,4}][2-ClPhC_1OHCOO]$ and — $[P_{4,4,4,4}][PhSC_1COO]$ with a heat rate of 10 °C min^{-1} under O_2. The decomposition temperatures were determined by the intersection of the tangents to the lines at low temperature and those corresponding to the rapid mass loss.

A considerable decrease in temperature was found from T_{dec} (254–345 °C) to $T_{0.01/10}$ (103–157 °C), confirming the overestimation of temperature-ramped TGA measurements. The long-term stability order of the ILs is also different and increases as follows: $[C_1COO]^- < [MeC_3COO]^- < [Me_4C_4COO]^- < [C_5COO]^- < [C_{11}COO]^- < [c-C_6COO]^- < [PhSC_1COO]^- < [PhC_1COO]^- < [TetrazC_1COO]^- < [2-ClPyCOO]^- < [2-ClPhC_1OHCOO]^-$ with $[P_{4,4,4,4}]^+$ as common cation. When aromatic moieties are part of the carboxylate anions, higher $T_{0.01/10}$ values were found while their T_{dec} values are significantly lower. These results highlight the importance of studying both long-term and short-term thermal stability when designing ILs for a given application. Interestingly enough, some trends remain consistent, such as the increased stability with the elongation of alkyl chain length in either the carboxylate anion or the phosphonium cation.

The pre-exponential factor A of the ILs containing $[P_{4,4,4,4}]^+$ as cation increases following a different trend: $[C_{11}COO]^- < [PhSC_1COO]^- < [C_1COO]^- \approx [c-C_6COO]^- \approx [C_5COO]^- < [MeC_3COO]^- < [Me_4C_4COO]^- < [TetrazC_1COO]^- < [PhC_1COO]^- < [2-ClPhC_1OHCOO]^- < [2-ClPyCOO]^-$, with a difference of nearly 14 orders of magnitude between the two extremes. It indicates that the structure of the carboxylate anion substituent significantly influences the value of the pre-exponential factor A, with higher values corresponding to more mobile ions. However, the size of the cation does not play a decisive role, as $[P_{6,6,6,14}][C_{11}COO]$ exhibits a higher A value than $[P_{4,4,4,4}][C_{11}COO]$, while the reverse trend is observed for $[P_{6,6,6,14}][Me_4C_4COO]$ and $[P_{4,4,4,4}][Me_4C_4COO]$. Despite the superior long-term

thermal stability of ILs compared to $[C_2C_1im][C_1COO]$ and $[C_2C_1C_1im][C_1COO]$, their activation energy (E_a) values were either lower or within a similar range, with the exception of $[P_{4,4,4,4}][PhC_1COO]$, $[P_{4,4,4,4}][2-ClPyCOO]$, and $[P_{4,4,4,4}][2-ClPhC_1OHCOO]$, which exhibited significantly higher E_a.

Table S8 – Long-term decomposition temperatures ($T_{0.01/10}$), the activation energy (E_a) and pre-exponential factor (A) determined for all the ILs under study following the MacFarlane method[5] under an atmosphere of O_2.

Sample	$T_{0.01/10}$ / °C	E_a / kJ mol^{-1}	A
$[P_{4,4,4,4}][2-ClPyCOO]$	156.8	194.56	1.27×10^{19}
$[P_{4,4,4,4}][TetrazC_1COO]$[6]	132.5	115.00	2.03×10^{10}
$[P_{4,4,4,4}][2-ClPhC_1OHCOO]$	145.4	153.30	4.26×10^{14}
$[P_{4,4,4,4}][C_1COO]$	102.9	92.86	1.23×10^{8}
$[P_{4,4,4,4}][PhSC_1COO]$	122.9	83.83	2.72×10^{6}
$[P_{4,4,4,4}][PhC_1COO]$	124.0	143.38	1.21×10^{14}
$[P_{4,4,4,4}][C_1COO]$	102.9	92.86	1.23×10^{8}
$[P_{4,4,4,4}][MeC_3COO]$	108.8	97.88	5.30×10^{8}
$[P_{4,4,4,4}][c-C_6COO]$	118.0	95.22	1.26×10^{8}
$[P_{4,4,4,4}][C_5COO]$	112.3	93.51	1.31×10^{8}
$[P_{4,4,4,4}][C_{11}COO]$	114.1	85.06	6.25×10^{5}
$[P_{6,6,6,14}][C_{11}COO]$	123.0	93.77	7.92×10^{7}
$[P_{4,4,4,4}][Me_4C_4COO]$	110.7	105.06	6.34×10^{9}
$[P_{6,6,6,14}][Me_4C_4COO]$	124.9	95.59	1.28×10^{8}

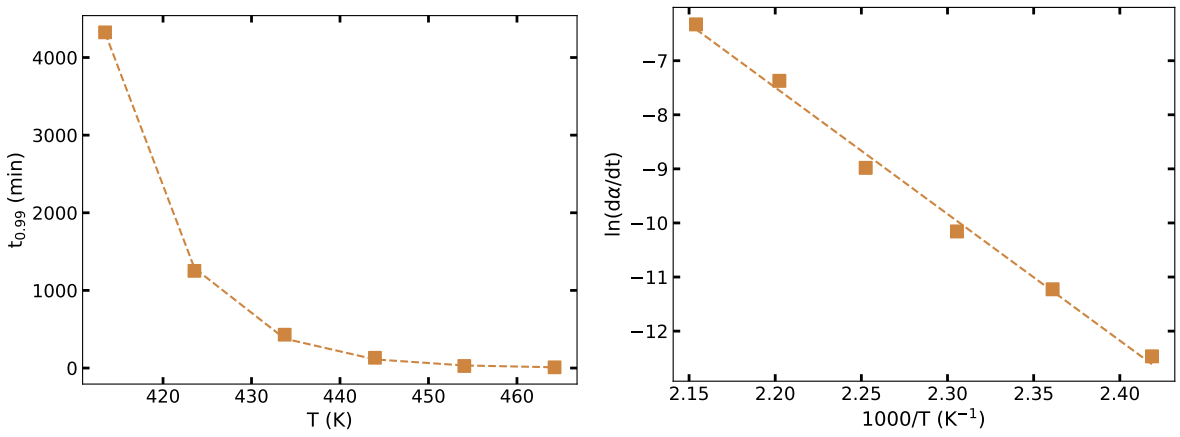

Figure S5 – Typical plot of (left) $t_{0.99}$, which is the time required to observe a decomposition of 1 % of the sample mass, as a function of temperature and (right) of $\ln(\frac{d\alpha}{dt})$ as a function of $1000/T$ for ■ $[P_{4,4,4,4}][2-ClPyCOO]$. Similar behaviours are found for the other ILs studied. Points are experimental and dashed lines are fitted curves.

1.5 Force field

Table S9 – Calculated densities of $[P_{4,4,4,4}][PhSC_1COO]$, $[P_{4,4,4,4}][2-ClPyCOO]$ and $[P_{4,4,4,4}][2-ClPhC_1OHCOO]$ with the new CL&Pol polarizable force field parameters[7] at different temperatures with the deviations from experimental densities.

Sample	$\frac{T}{K}$	$\frac{\rho_{exp}}{g\,cm^{-3}}$	$\frac{\rho_{calc}}{g\,cm^{-3}}$	$\frac{\delta}{\%}$
$[P_{4,4,4,4}][2-ClPyCOO]$	303	1.05546	1.04927	-0.59
	343	1.03047	1.02150	-0.87
$[P_{4,4,4,4}][2-ClPhC_1OHCOO]$	303	1.05653	1.05777	0.11
	343	1.03188	1.02356	-0.81
$[P_{4,4,4,4}][PhSC_1COO]$	343	0.99223	0.98264	-0.97

The force field was also employed to determine the self-diffusion coefficients of the ILs by fitting the mean squared displacements (MSD) obtained from the MD trajectories. The MSD analysis was performed after reaching the diffusive regime, typically observed between 3 and 18 ns. The calculated coefficients were found to be slightly underestimated compared to the experimental values (Table S14), with differences typically ranging from 20–30 % (Table S10). Similar self-diffusion coefficients for both cations and anions were also calculated for all the ILs confirming this feature. Furthermore, the more viscous ILs exhibited lower self-diffusion coefficients compared to their less viscous counterparts.

Table S10 – Simulated self-diffusion coefficients of $[P_{4,4,4,4}][2-ClPyCOO]$, $[P_{4,4,4,4}][2-ClPhC_1OHCOO]$ and $[P_{4,4,4,4}][PhSC_1COO]$ at 343 K by fitting the MSD calculated from MD simulations.

Sample (simulated)	$\frac{T}{K}$	$\frac{D_{anion}}{m^2\,s^{-1}}$	$\frac{D_{cation}}{m^2\,s^{-1}}$
$[P_{4,4,4,4}][2-ClPyCOO]$	343	1.05 ± 0.003	0.99 ± 0.002
$[P_{4,4,4,4}][2-ClPhC_1OHCOO]$	343	0.84 ± 0.002	0.85 ± 0.003
$[P_{4,4,4,4}][PhSC_1COO]$	343	0.96 ± 0.003	1.00 ± 0.002

1.6 Microscopic structure of the ILs

Appropriate radial or spatial distribution functions (RDFs and SDFs, respectively) were calculated for the three ILs synthesized herein. The RDFs of the P^+ and H_α sites of the $[P_{4,4,4,4}]^+$ cation around the carboxylate head group O_{COO^-} of the anions in $[P_{4,4,4,4}][PhSC_1COO]$, $[P_{4,4,4,4}][2-ClPyCOO]$, and $[P_{4,4,4,4}][2-ClPhC_1OHCOO]$ are shown in Figure S6 and compared with $[P_{4,4,4,4}][PhC_1COO]$ as a representative example of the carxoxylate ILs previously studied.[1]

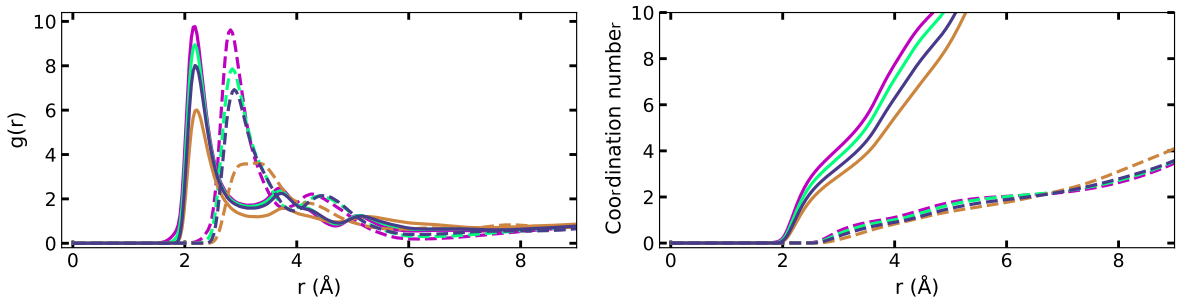

Figure S6 – Comparison of the site-site RDFs, $g_{ij}(r)$, of (dashed lines) P^+ and (solid lines) H_α of the cation around the negatively charged oxygen atoms O_{COO^-} of the carboxylate head of the anion and their corresponding coordination numbers in — $[P_{4,4,4,4}][PhC_1COO]$, — $[P_{4,4,4,4}][2-ClPyCOO]$, — $[P_{4,4,4,4}][2-ClPhC_1OHCOO]$ and — $[P_{4,4,4,4}][PhSC_1COO]$ at 343 K. The RDFs of $[P_{4,4,4,4}][PhC_1COO]$ were used as a representative example of the other ILs previously studied.[1]

Only $[P_{4,4,4,4}][2-ClPyCOO]$ exhibits slightly different RDFs between P^+ and H_α and O_{COO^-}, indicating a less significant correlation between these sites. This is further supported by the lower calculated coordination numbers (CNs) from approximately 1 and 4.5 to 0.79 and 3.35, respectively. Figure S7 (left) demonstrates that these reduced correlations arise from the presence of new correlations between the N of the carboxylate anion and P^+ and H_α of the phosphonium cation, as well as between Cl and H_α as illustrated on the SDF Figure S8. In $[P_{4,4,4,4}][2-ClPhC_1OHCOO]$, Figure S7 (right) reveals a low correlation between the O_{OH} of the carboxylate anion and H_α although it is not important enough to significantly affect the main interacting sites. These MD simulations provide valuable insights into the structural properties of the investigated ILs and offer a deeper understanding of their intermolecular interactions.

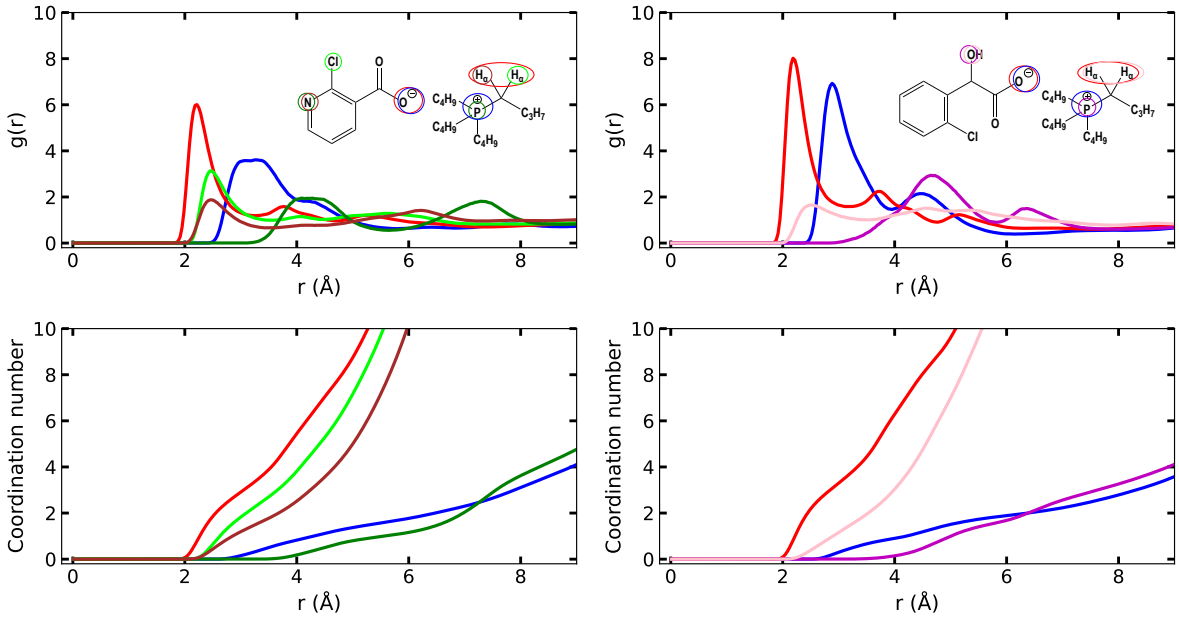

Figure S7 – Site-site RDFs, $g_{ij}(r)$, of — P^+ and — H_α of the cation around O_{COO^-} of the carboxylate anion and (left) H_α around — Cl and — N, — P^+ around N in $[P_{4,4,4,4}][2-ClPyCOO]$; (right) — P^+ and — H_α of the cation around O_{OH} in $[P_{4,4,4,4}][2-ClPhC_1OHCOO]$ at 343 K.

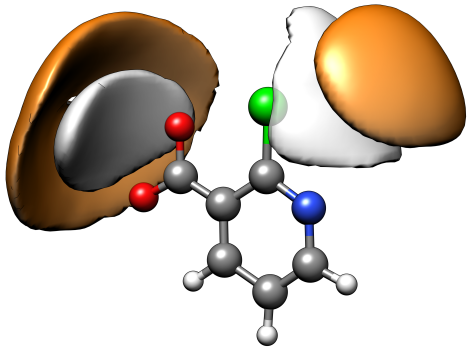

Figure S8 – The spatial distribution functions (SDFs) of P^+ (in orange) and of the acidic protons H_α (in white) around the O_{COO^-} of the $[2-ClPyCOO]^-$ anion in $[P_{4,4,4,4}][2-ClPyCOO]$ at 343 K. Isodensity contours at 14.7 and 7.9 times the average density around the central anion, respectively.

The combined distribution functions (CDFs) of the $C_\alpha-H_\alpha\cdots O_{COO^-}$ angle as a function of the distance between the acidic proton H_α and O_{COO^-} have also been calculated at 343 K (Figure S9). The CDFs reveal that not only the distance between the acidic proton and the carboxylate head are similar, but also the angles between them are identical at around 120 ° in these 3 new ILs. These angles are too low to be considered as proper hydrogen bonds.

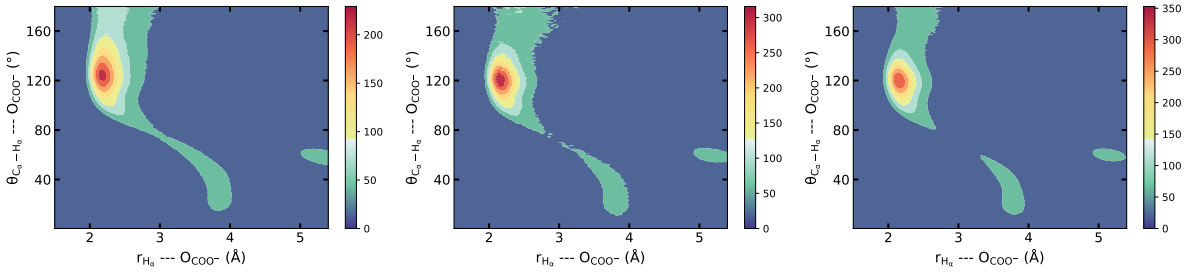

Figure S9 – Combined distribution functions (CDFs) of the $C_\alpha{-}H_\alpha\cdots O_{COO^-}$ angle as a function of the distance between the acidic proton H_α and the negatively charged O_{COO^-} in (left) $[P_{4,4,4,4}][2\ {-}ClPyCOO]$, (middle) $[P_{4,4,4,4}][2\ {-}ClPhC_1OHCOO]$ and (right) $[P_{4,4,4,4}][PhSC_1COO]$ at 343 K.

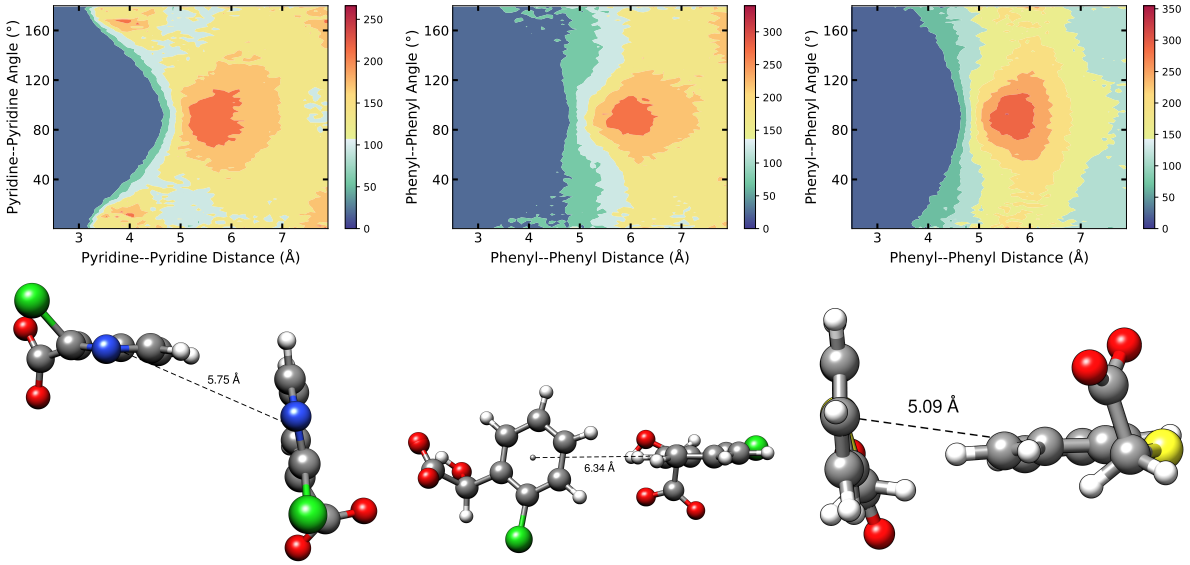

Figure S10 – CDFs of the angle between (left) two adjacent pyrridine rings in $[P_{4,4,4,4}][2\ {-}ClPyCOO]$, two adjacent phenyl rings (middle) in $[P_{4,4,4,4}][2\ {-}ClPhC_1OHCOO]$ and (right) in $[P_{4,4,4,4}][PhSC_1COO]$ as a function of the RDF between their center of mass at 343 K. (Bottom) Snapshots from the molecular simulation box showing the most probable spatial configuration of two neighbour anions.

$[P_{4,4,4,4}][PhSC_1COO]$, $[P_{4,4,4,4}][2\ {-}ClPyCOO]$ and $[P_{4,4,4,4}][2\ {-}ClPhC_1OHCOO]$ are presenting peculiar spatial configurations that can be attributed to the presence of aromatic moieties in the carboxylate anions. While one could expect a π-π stacking, the aromatic rings of the carboxylate anions are perpendicular to each other at a distance of 5.09, 5.75 and 6.34 Å, respectively. It is showed on the CDFs of the angle between two adjacent aromatic rings as a function of the RDF between their center of mass and illustrated by the snapshot from their molecular simulation box (Figure S10). This particular spatial configuration has also been found previously in the other ILs containing aromatic or aliphatic rings in the carboxylate anions.[1]

1.7 Small angle X-ray scattering

The experimental total structure factors of the three synthesised ILs are represented in Figure S11. The positions of the pre-peak, the shoulder and the principal peak are reported in Table S11. The total $S(q)$ calculated by MD simulations agree with the experimental data and so the calculated partial structure factors can be used to get further insights about the structure of the ILs. No particular features could be identified in the three ILs prepared herein when compared with the ones previously characterized.[1]

Table S11 – SAXS diffraction peak positions, q, their corresponding real space length, d, and the ion pair diameter, D, of $[P_{4,4,4,4}][2-ClPyCOO]$, $[P_{4,4,4,4}][2-ClPhC_1OHCOO]$ and $[P_{4,4,4,4}][PhSC_1COO]$. D was estimated by taking the cubic root of the volume of a single ion pair of the IL which was calculated from its molar volume and by assuming a cubic packing geometry.[8]

Sample	Pre-peak		Shoulder peak		Principal peak		
	q / Å^{-1}	d / Å	q / Å^{-1}	d / Å	q / Å^{-1}	d / Å	D / Å
$[P_{4,4,4,4}][2-ClPyCOO]$	0.57	11.0	0.72	8.7	1.38	4.6	8.7
$[P_{4,4,4,4}][2-ClPhC_1OHCOO]$	0.59	10.6	0.67	9.4	1.38	4.6	8.9
$[P_{4,4,4,4}][PhSC_1COO]$	0.58	10.8	-	-	1.46	4.3	8.9

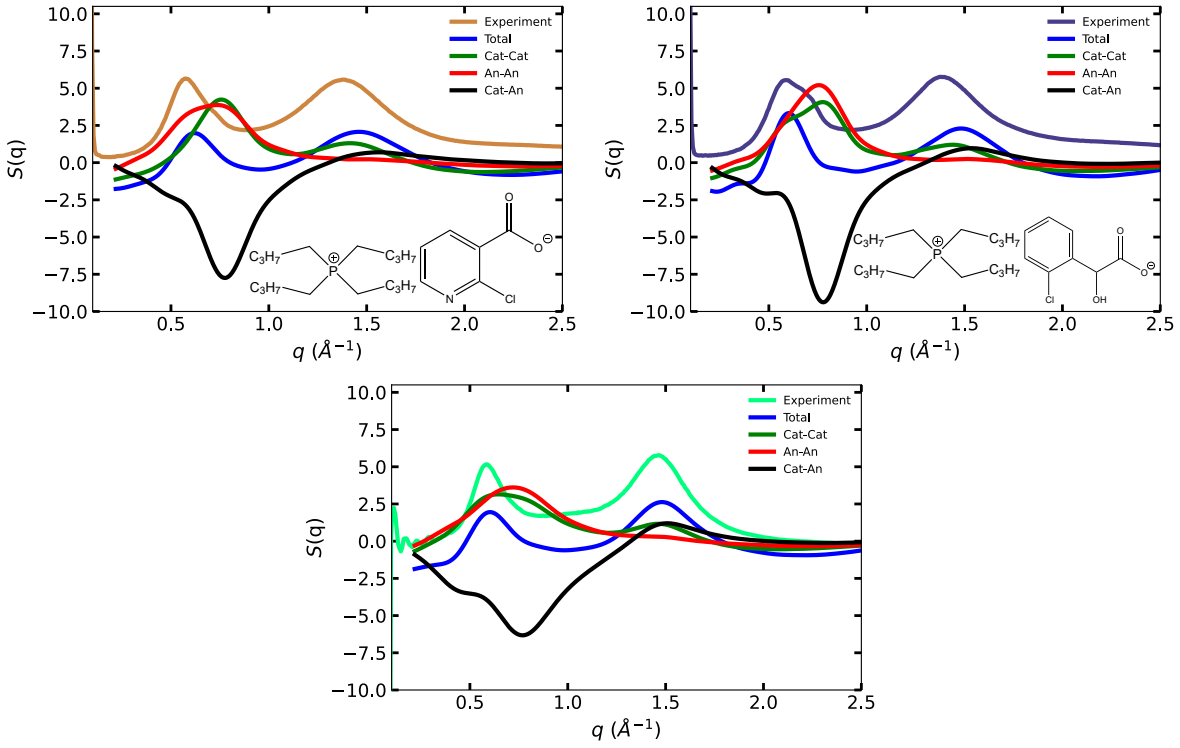

Figure S11 – Comparison of experimental with the total simulated $S(q)$ as well as the partial $S(q)$ for (top left) $[P_{4,4,4,4}][2-ClPyCOO]$, (top right) $[P_{4,4,4,4}][2-ClPhC_1OHCOO]$ and (bottom) $[P_{4,4,4,4}][PhSC_1COO]$.

2 Gas absorption data

Table S12 – Absorption and desorption of CO_2 in the ILs as a function of pressure from 0–5 bar at either 303 K or 343 K.

CO_2 - Absorption			CO_2 - Desorption		
$\frac{T}{K}$	$\frac{P}{bar}$	x_{CO_2}	$\frac{T}{K}$	$\frac{P}{bar}$	x_{CO_2}
		$[P_{4,4,4,4}][2-ClPyCOO]$			
		1st cycle			
303.13	0.0000	0.0000	303.13	0.0000	0.0000
303.14	0.2495	0.0090	303.15	0.2488	0.0115
303.16	0.4982	0.0148	303.16	0.4982	0.0191
303.15	0.7491	0.0213	303.15	0.7491	0.0262
303.14	0.9995	0.0280	303.15	1.000	0.0328
303.15	2.500	0.0646	303.13	2.499	0.0702
303.14	4.999	0.1150	303.14	4.999	0.115
312.29	0.0000	0.0000	312.29	0.0000	0.0000
313.13	0.2494	0.0045	313.12	0.2484	0.0063
313.12	0.4977	0.0103	313.12	0.4978	0.0107
313.12	0.7497	0.0140	313.14	0.7490	0.0149
313.11	0.9979	0.0174	313.11	0.9995	0.0187
313.11	2.500	0.0411	313.12	2.499	0.0428
313.13	4.999	0.0789	313.13	4.999	0.0789
320.11	0.0000	0.0000	320.16	0.0000	0.0000
323.11	0.2483	0.0059	323.12	0.2495	0.0061
323.12	0.4984	0.0092	323.10	0.4978	0.0094
323.12	0.7487	0.0115	323.12	0.7488	0.0122
323.11	0.9991	0.0135	323.11	0.9991	0.0144
323.12	2.500	0.0372	323.10	2.500	0.0367
323.12	4.998	0.0680	323.12	4.998	0.0680
336.53	0.0000	0.0000	336.53	0.0000	0.0000
343.13	0.2499	0.0052	343.08	0.2487	0.0036
343.07	0.4981	0.0065	343.04	0.4986	0.0048
343.15	0.7480	0.0065	343.09	0.7499	0.0051
343.11	0.9992	0.0078	343.08	0.9988	0.0064
343.05	2.499	0.0286	343.10	2.499	0.0282
343.05	4.998	0.0513	343.05	4.998	0.0513
		$[P_{4,4,4,4}][2-ClPhC_1OHCOO]$			
		1st cycle			
303.14	0.0000	0.0000	303.14	0.0000	0.0000
303.14	0.2492	0.0087	303.14	0.2494	0.0048
303.15	0.4974	0.0134	303.16	0.4978	0.0109
303.14	0.7488	0.0186	303.14	0.7486	0.0170
303.15	0.9992	0.0236	303.16	0.9989	0.0225
303.14	2.500	0.0545	303.13	2.499	0.0555
303.15	4.998	0.1022	303.15	4.998	0.1022
312.73	0.0000	0.0000	312.73	0.0000	0.0000

CO_2 - Absorption			CO_2 - Desorption		
$\frac{T}{K}$	$\frac{P}{bar}$	x_{CO_2}	$\frac{T}{K}$	$\frac{P}{bar}$	x_{CO_2}
313.09	0.2474	0.0033	313.09	0.2487	0.0056
313.13	0.4972	0.0101	313.14	0.4985	0.0104
313.10	0.7490	0.0142	313.12	0.7488	0.0153
313.14	0.9993	0.0180	313.11	0.9997	0.0194
313.12	2.499	0.0438	313.09	2.500	0.0455
313.10	4.998	0.0851	313.10	4.998	0.0851
318.41	0.0000	0.0000	318.41	0.0000	0.0000
323.11	0.2492	0.0061	323.12	0.2474	0.0064
323.14	0.4985	0.0100	323.14	0.4986	0.0102
323.12	0.7477	0.0125	323.13	0.7490	0.0126
323.12	0.9993	0.0149	323.12	0.9996	0.0152
323.08	2.500	0.0393	323.13	2.499	0.0399
323.13	5.000	0.0750	323.13	5.000	0.0750
335.86	0.0000	0.0000	335.86	0.0000	0.0000
343.12	0.2488	0.0048	343.11	0.2486	0.0047
343.12	0.4993	0.0055	343.09	0.4979	0.0059
343.10	0.7486	0.0070	343.09	0.7486	0.0070
343.08	0.9991	0.0108	343.12	0.9995	0.0108
343.09	2.500	0.0316	343.12	2.500	0.0326
343.06	4.999	0.0578	343.06	4.999	0.0578
$[P_{4,4,4,4}][PhSC_1COO]$ 1st cycle					
320.14	0.0000	0.0000	320.14	0.0000	0.0000
323.11	0.2487	0.0041	323.12	0.2494	0.0065
323.12	0.4984	0.0099	323.11	0.4977	0.0106
323.12	0.7490	0.0126	323.12	0.7486	0.0143
323.11	1.0002	0.0155	323.12	0.9995	0.0171
323.12	2.500	0.0434	323.10	2.500	0.0441
323.12	4.999	0.0801	323.12	4.999	0.0801
337.78	0.0000	0.0000	337.78	0.0000	0.0000
343.06	0.2498	0.0047	343.12	0.2483	0.0097
343.08	0.4986	0.0048	343.10	0.4981	0.0099
343.07	0.7488	0.0078	343.10	0.7491	0.0113
343.11	0.9986	0.0119	343.09	0.9991	0.0143
343.14	2.500	0.0345	343.13	2.500	0.0359
343.37	4.999	0.0599	343.37	4.999	0.0599
$[P_{4,4,4,4}][PhC_1COO]$ 1st cycle					
323.04	0.0000	0.0000	323.04	0.0000	0.0000
323.12	0.2501	0.0669	323.11	0.2491	0.0884
323.11	0.4986	0.0944	323.11	0.4986	0.1119
323.11	0.7490	0.1171	323.12	0.7470	0.1288
323.12	0.9992	0.1308	323.10	0.9999	0.1452
323.09	2.499	0.1947	323.14	2.500	0.2086
323.09	4.999	0.2540	323.10	4.999	0.254

CO_2 - Absorption			CO_2 - Desorption		
$\frac{T}{K}$	$\frac{P}{bar}$	x_{CO_2}	$\frac{T}{K}$	$\frac{P}{bar}$	x_{CO_2}
343.10	0.0000	0.0000	343.10	0.0000	0.0000
343.12	0.2490	0.0552	343.13	0.2501	0.0609
343.12	0.4981	0.0695	343.12	0.4975	0.0849
343.10	0.7490	0.0790	343.12	0.7488	0.0943
343.10	0.9992	0.0878	343.09	0.9995	0.1116
343.13	2.500	0.1312	343.15	2.498	0.1449
343.11	4.998	0.1750	343.11	4.998	0.1750
		2^{nd} cycle			
326.72	0.0000	0.0000	326.72	0.0000	0.0000
323.12	0.2495	0.0357	323.11	0.2490	0.0865
323.12	0.4990	0.0668	323.12	0.4986	0.1060
323.12	0.7490	0.0919	323.15	0.7493	0.1246
323.10	0.9991	0.1134	323.13	0.9997	0.1423
323.12	2.499	0.1738	323.10	2.500	0.2015
323.09	4.999	0.2342	323.09	4.999	0.2342
340.35	0.0000	0.0000	340.35	0.0000	0.000
343.08	0.2490	0.0522	343.06	0.2490	0.0535
343.12	0.4984	0.0658	343.11	0.4982	0.0850
343.09	0.7483	0.0744	343.12	0.7477	0.0943
343.11	0.9995	0.0818	343.11	0.9993	0.1020
343.10	2.499	0.1119	343.13	2.500	0.1290
343.14	4.998	0.1547	343.14	4.998	0.1547
		3^{rd} cycle			
343.11	0.0000	0.0000	343.11	0.0000	0.0000
343.11	0.2494	0.0496	343.10	0.2468	0.0636
343.11	0.4984	0.0633	343.09	0.4985	0.0805
343.12	0.7488	0.0717	343.11	0.7480	0.0888
343.11	0.9992	0.0794	343.10	0.9984	0.0956
343.10	2.499	0.1187	343.07	2.500	0.1235
343.08	4.999	0.1503	343.08	4.999	0.1503
		$[P_{4,4,4,4}][C_1COO]$			
339.45	0.0000	0.0000	340.35	0.0000	0.0000
343.00	0.2484	0.0516	343.10	0.2437	0.1382
343.18	0.4921	0.0870	343.13	0.5004	0.1599
343.18	0.7488	0.1084	343.13	0.7496	0.1651
343.01	0.9903	0.1221	343.04	0.9976	0.1791
343.078	2.983	0.1780	343.07	2.998	0.2057
343.07	4.993	0.2199	343.07	4.993	0.2199
		$[P_{4,4,4,4}][MeC_3COO]$			
342.44	0.0000	0.0000	334.52	0.0000	0.0000
343.11	0.2497	0.0413	343.07	0.2488	0.0465
343.09	0.4984	0.0754	343.10	0.4992	0.0817
343.14	0.7483	0.0974	343.12	0.7490	0.1015
343.09	1.0002	0.1144	343.10	0.9991	0.1214

CO_2 - Absorption			CO_2 - Desorption		
$\frac{T}{K}$	$\frac{P}{bar}$	x_{CO_2}	$\frac{T}{K}$	$\frac{P}{bar}$	x_{CO_2}
336.36	2.500	0.1814	336.44	2.498	0.1877
336.55	4.998	0.2329	336.55	4.998	0.2329
		$[P_{4,4,4,4}][c-C_6COO]$			
338.21	0.0000	0.0000	333.25	0.0000	0.0000
343.11	0.2501	0.0335	336.91	0.2487	0.0384
343.13	0.4986	0.0541	343.14	0.4990	0.0567
343.12	0.7468	0.0691	343.09	0.7483	0.0714
343.11	0.9996	0.0828	343.09	0.9979	0.0865
343.14	2.499	0.1338	343.13	2.499	0.1355
343.11	4.998	0.1800	343.11	4.998	0.1800
		$[P_{4,4,4,4}][C_5COO]$			
325.87	0.0000	0.0000	331.59	0.0000	0.0000
343.16	0.2495	0.0406	343.14	0.2498	0.0494
343.14	0.4984	0.0705	340.23	0.4966	0.0831
343.14	0.7488	0.0912	343.15	0.7490	0.1030
343.16	0.9999	0.1075	336.83	0.9997	0.1402
343.14	4.998	0.2145	343.14	4.998	0.2145
		$[P_{4,4,4,4}][C_{11}COO]$			
		1st cycle			
330.73	0.0000	0.0000	303.15	0.0000	0.0000
303.17	0.2494	0.0093	303.15	0.2488	0.0202
303.13	0.4981	0.0166	303.14	0.4990	0.0257
303.19	0.7486	0.0244	303.15	0.7490	0.0315
303.13	0.9993	0.0320	303.16	1.0002	0.0374
303.14	2.499	0.0728	303.07	2.499	0.0760
303.12	4.998	0.1343	303.12	4.998	0.1343
331.79	0.0000	0.0000	331.22	0.0000	0.0000
343.16	0.2484	0.0616	343.15	0.2494	0.0871
343.15	0.4981	0.0932	343.16	0.4981	0.1118
343.16	0.7486	0.1159	343.19	0.7491	0.1291
343.12	0.9982	0.1341	343.15	1.0000	0.1475
343.19	2.499	0.1913	343.14	2.498	0.1993
343.29	4.999	0.2479	343.29	4.999	0.2479
		2nd cycle			
303.13	0.0000	0.0000	303.13	0.0000	0.0000
303.15	0.2492	0.0089	303.16	0.2490	0.0176
303.14	0.4982	0.0167	303.14	0.4979	0.0238
303.16	0.7491	0.0242	303.15	0.7488	0.0298
303.16	0.9986	0.0317	303.11	0.9986	0.036
303.15	2.500	0.0722	303.14	2.500	0.0746
303.14	4.998	0.1330	303.14	4.998	0.1330
340.35	0.0000	0.0000	340.35	0.0000	0.0000
343.12	0.2491	0.0634	343.11	0.2491	0.0691
343.11	0.4979	0.0914	343.11	0.4981	0.0955

CO_2 - Absorption			CO_2 - Desorption		
$\frac{T}{K}$	$\frac{P}{bar}$	x_{CO_2}	$\frac{T}{K}$	$\frac{P}{bar}$	x_{CO_2}
343.12	0.7486	0.1088	343.18	0.7479	0.1167
343.09	0.9984	0.1245	336.92	0.9996	0.1418
343.11	2.499	0.1854	343.11	2.499	0.1873
343.09	4.998	0.2362	343.09	4.998	0.2362
		$[P_{6,6,6,14}][C_{11}COO]$			
299.87	0.0000	0.0000	303.16	0.0000	0.0000
303.15	0.2492	0.0803	303.14	0.2494	0.0938
303.14	0.4993	0.0924	303.15	0.4982	0.1111
303.14	0.7488	0.1050	303.15	0.7483	0.1214
303.15	0.9989	0.1162	303.18	0.9993	0.1296
303.14	2.500	0.1665	303.15	2.498	0.1734
303.15	4.999	0.2349	303.15	4.999	0.2349
336.95	0.0000	0.0000	327.27	0.0000	0.0000
343.12	0.2481	0.0766	343.12	0.2491	0.0787
343.11	0.4938	0.0992	343.13	0.4970	0.1062
337.43	0.7475	0.1175	343.12	0.7487	0.1189
343.11	0.9991	0.1305	343.10	0.9992	0.1346
343.12	2.499	0.1859	343.11	2.499	0.1894
343.08	4.999	0.2435	343.08	4.999	0.2435
		$[P_{4,4,4,4}][Me_4C_4COO]$			
		1st cycle			
303.21	0.0000	0.0000	303.21	0.0000	0.0000
303.15	0.2497	0.3074	303.19	0.2494	0.4045
303.12	0.4984	0.4015	303.17	0.4979	0.4341
303.16	0.7493	0.4419	303.14	0.7494	0.4452
303.16	0.9991	0.4578	303.12	0.9988	0.4522
303.16	2.498	0.4897	303.13	2.498	0.4904
303.16	4.999	0.5129	303.16	4.999	0.5129
323.12	0.0000	0.0000	323.12	0.0000	0.0000
323.10	0.2488	0.1911	323.11	0.2497	0.2382
323.11	0.4985	0.2979	323.11	0.4971	0.2917
323.12	0.7487	0.3448	323.12	0.7490	0.3120
323.11	0.9991	0.3602	323.13	0.9995	0.3236
323.09	2.498	0.4176	323.11	2.501	0.4019
323.14	4.993	0.4555	323.14	4.993	0.4555
343.03	0.0000	0.0000	343.03	0.0000	0.0000
343.13	0.2491	0.0788	343.08	0.2490	0.0720
343.12	0.4993	0.1220	343.13	0.4988	0.1107
343.10	0.7476	0.1498	343.20	0.7459	0.1301
343.08	0.9989	0.1670	343.10	0.9985	0.1396
343.07	2.497	0.2401	343.04	2.498	0.2252
343.16	4.996	0.2871	343.16	4.996	0.2871
		2nd cycle			
341.60	0.0000	0.0000	341.60	0.0000	0.0000
343.12	0.2491	0.0915	343.10	0.2497	0.0962

CO_2 - Absorption			CO_2 - Desorption		
$\frac{T}{K}$	$\frac{P}{bar}$	x_{CO_2}	$\frac{T}{K}$	$\frac{P}{bar}$	x_{CO_2}
343.12	0.4988	0.1270	343.11	0.4984	0.1283
343.09	0.7480	0.1504	343.12	0.7490	0.1521
343.14	0.9995	0.1695	343.14	0.9978	0.1706
343.14	2.499	0.2390	336.54	2.499	0.2624
343.09	4.998	0.2833	343.09	4.998	0.2833
$[P_{6,6,6,14}][Me_4C_4COO]$					
1^{st} cycle					
303.52	0.0000	0.0000	303.52	0.0000	0.0000
303.11	0.2491	0.0721	303.15	0.2498	0.0829
303.18	0.4984	0.0882	303.17	0.4982	0.0993
303.15	0.7487	0.1009	303.14	0.7477	0.1101
303.15	0.9995	0.1118	303.14	0.9989	0.1188
303.15	2.500	0.1586	303.15	2.498	0.1617
303.15	4.999	0.2202	303.15	4.999	0.2202
318.54	0.0000	0.0000	318.54	0.0000	0.0000
323.16	0.2985	0.1011	323.06	0.4975	0.1243
323.17	0.7490	0.1127	323.17	0.7469	0.1339
323.18	0.9989	0.1237	323.16	1.0003	0.1419
323.15	2.499	0.1695	323.15	2.499	0.1817
323.16	4.999	0.2268	323.16	4.999	0.2268
334.22	0.0000	0.0000	334.22	0.0000	0.0000
342.65	0.2504	0.0833	343.10	0.2492	0.0851
343.35	0.4979	0.1078	343.08	0.4979	0.1088
343.08	0.7486	0.1232	343.12	0.7490	0.1245
343.18	0.9993	0.1363	343.13	0.9988	0.1389
342.93	2.499	0.1966	343.14	2.500	0.2139
342.99	4.997	0.2528	342.99	4.997	0.2528
2^{nd} cycle					
303.14	0.0000	0.0000	303.14	0.0000	0.0000
303.14	0.2488	0.0735	303.14	0.2491	0.0788
303.14	0.4975	0.0931	303.15	0.4992	0.0976
303.14	0.7476	0.1073	303.15	0.7488	0.1110
303.13	0.9992	0.1190	303.18	0.9989	0.1218
303.15	2.499	0.1684	303.15	2.500	0.1696
303.15	4.999	0.2292	303.15	4.999	0.2292
333.39	0.0000	0.0000	333.39	0.0000	0.0000
343.14	0.2494	0.1200	343.14	0.2490	0.1203
343.07	0.4979	0.1420	343.20	0.4971	0.1414
343.20	0.7481	0.1568	343.24	0.7487	0.1566
343.23	0.9986	0.1696	343.08	0.9999	0.1695
343.16	2.500	0.2223	343.18	2.500	0.2289
343.13	4.998	0.2761	343.13	4.998	0.2761

3 CO_2 absorption model

$$K_H = \lim_{x_{CO_2} \to 0} \frac{\phi_{CO_2} P}{x_{CO_2}} \approx \frac{P}{x_{CO_2}} \tag{S2}$$

Compound	n_i
CO_2 (sol)	$n_{CO_2}(1-\xi)$
$[P_{4,4,4,4}][RCOO]$	$n_{IL} - 2n_{CO_2}\xi$
$[P^+_{4,4,4,4}\text{-}CO_2^-]$	$n_{CO_2}\xi$
$[P_{4,4,4,4}][RCOO]$ - - HOOCR	$n_{CO_2}\xi$
Total	$n_{CO_2}(1-\xi) + n_{IL}$

$$K_{eq,1:2} = \frac{\gamma_{zwi}\gamma_{compl}}{\gamma_{CO_2}\gamma_{IL}} \frac{x_{zwi}x_{compl}}{x_{CO_2}x_{IL}^2}$$
$$K_{eq,1:2} \approx \frac{x_{zwi}x_{compl}}{x_{CO_2}x_{IL}^2} \tag{S3}$$
$$K_{eq,1:2} = \frac{n_{CO_2}\xi^2[n_{CO_2}(1-\xi) + n_{IL}]}{(1-\xi)(n_{IL} - 2n_{CO_2}\xi)^2}$$

where γ_{zwi}, γ_{compl}, γ_{CO_2}, and γ_{IL} represent the activity coefficients, while x_{zwi}, x_{compl}, x_{CO_2}, and x_{IL} denote the mole fractions of the zwitterion, complex, dissolved CO_2, and neat IL in Equation S3 , respectively. In Equation S2, ϕ_{CO_2} corresponds to the fugacity coefficient of CO_2, and P represents the equilibrium pressure of the system. Ideal solutions are assumed, implying that the activity coefficients are concentration-independent and are thus incorporated into the K_{eq} value. is considered ideal ($\phi_{CO_2} \approx 1$). The K_{eq} equation is reformulated as a function of the compound amounts, taking into account the extent of reaction ξ.

Table S13 – Henry's law constant (K_H) and the equilibrium constant (K_{eq}) obtained for various ILs by fitting the data in Table S12 of the successive cycles at either 303 K, 323 K or 343 K.

Sample	Cycle	$\frac{T}{K}$	K_{eq}	$\frac{K_H}{bar}$
$[P_{4,4,4,4}][PhC_1COO]$	2nd	323	0.8 ± 0.2	45 ± 4
	2nd	343	1.2 ± 0.2	139 ± 29
	3rd	343	1.2 ± 0.3	144 ± 35
$[P_{4,4,4,4}][C_{11}COO]$	2nd	303		36.4 ± 0.8
	2nd	343	1.8 ± 0.3	59 ± 4
$[P_{4,4,4,4}][Me_4C_4COO]$	2nd	343	5 ± 1	53 ± 6
$[P_{6,6,6,14}][Me_4C_4COO]$	2nd	303	1.3 ± 0.2	58 ± 3
	2nd	343	5.3 ± 0.5	58 ± 2

4 NMR before and after CO_2 absorption

4.1 $[P_{4,4,4,4}][2-ClPyCOO]$

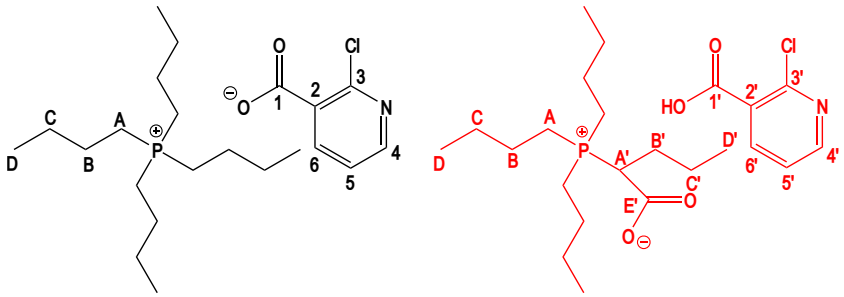

Figure S12 – Chemical structure of the $[P_{4,4,4,4}][2-ClPyCOO]$ (left) before and (right) after CO_2 absorption.

Tetrabutylphosphonium 2-chloropyridine-3-carboxylate $[P_{4,4,4,4}][2-ClPyCOO]$ after CO_2 absorption: ^{1}H NMR (400 MHz, C_6D_6, 343 K) δ ppm: 0.73 (m, 12H, D); 1.25 (m, 8H, C); 1.41 (m, 8H, B); 2.35 (m, 8H, A); 7.14 (t, 1H, 5); 7.63 (d, 1H, 6); 8.02 (m, 1H, 4). ^{13}C NMR (100 MHz, C_6D_6, 343 K) δ ppm: 12.41 (4C, D); 17.57 (4C, A); 22.71 (7C, B); 22.89 (4C, C); 121.54 (1C, 5); 136.33 (1C, 6); 139.72 (1C, 2); 145.58 (1C, 4); 146.45 (1C, 3); 166.03 (1C, 1). ^{31}P NMR (161 MHz, C_6D_6, 343 K) δ ppm: 33.65 (1P, $\mathbf{P}((CH_2)_3CH_3)_4$).

4.2 $[P_{4,4,4,4}][2-ClPhC_1OHCOO]$

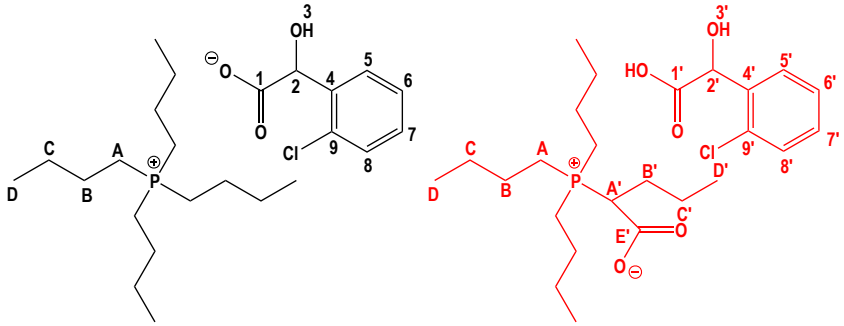

Figure S13 – Chemical structure of the $[P_{4,4,4,4}][2-ClPhC_1OHCOO]$ (left) before and (right) after CO_2 absorption.

Tetrabutylphosphonium 2-(2-chlorophenylacetate)-2-hydroxyacetate $[P_{4,4,4,4}][2-ClPhC_1OHCOO]$ after CO_2 absorption: ^{1}H NMR (400 MHz, C_6D_6, 343 K) δ ppm: 0.73 (t, 12H, $^{3}J_{HH} = 6.8$ Hz, D); 1.22 (m, 16H, B+C); 2.05 (m, 8H, A); 4.81 (s, 1H, 2); 5.56 (s, 1H, 3); 6.96 (m, 2H, 7+8); 7.06 (m, 1H,

5); 7.26 (m, 1H, 6). ^{13}C NMR (100 MHz, C_6D_6, 343 K) δ ppm: 12.33 (4C, D); 17.35 (4C, A); 22.51 (4C, B); 22.80 (4C, C); 70.11 (1C, 2); 125.24 (1C, 7); 126.28 (1C, 8); 127.55 (1C, 6); 127.76 (1C, 5); 132.79 (1C, 4); 142.60 (1C, 9); 171.90 (1C, 1). ^{31}P NMR (161 MHz, C_6D_6, 343 K) δ ppm: 33.22 (1P, **P**$((CH_2)_3CH_3)_4$). 3

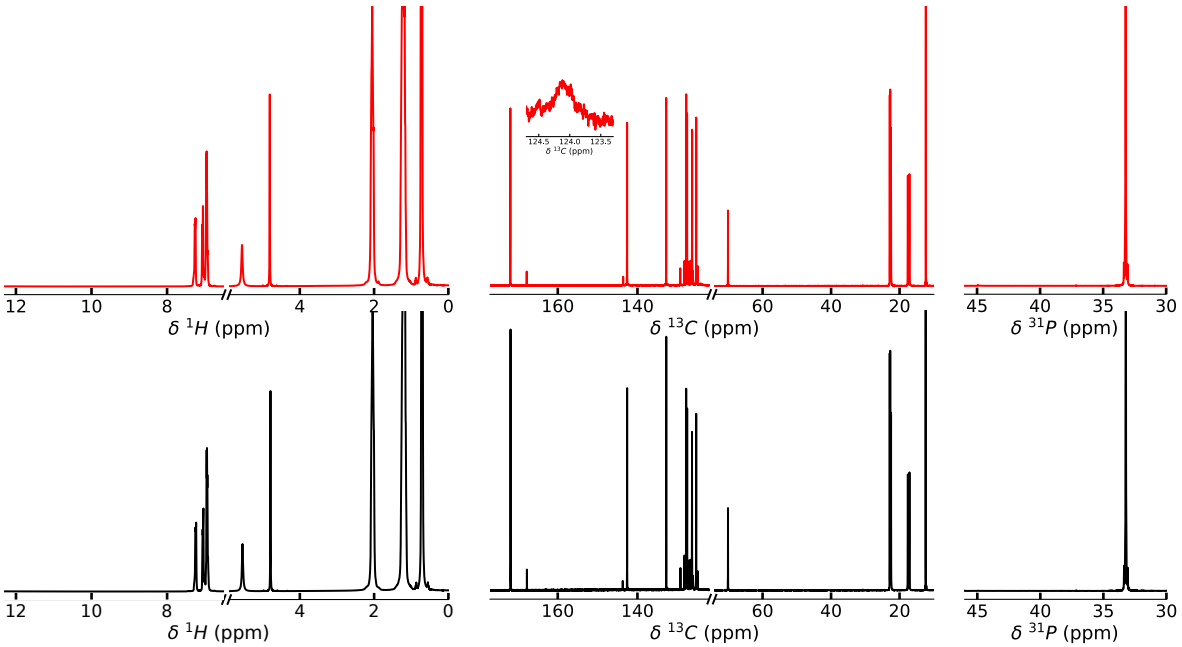

Figure S14 – (Left) ^{1}H, (middle) ^{13}C and (right) ^{31}P NMR spectra of $[P_{4,4,4,4}][2-ClPhC_1OHCOO]$ — before and — after CO_2 absorption at 343 K.

4.3 $[P_{4,4,4,4}][PhSC_1COO]$

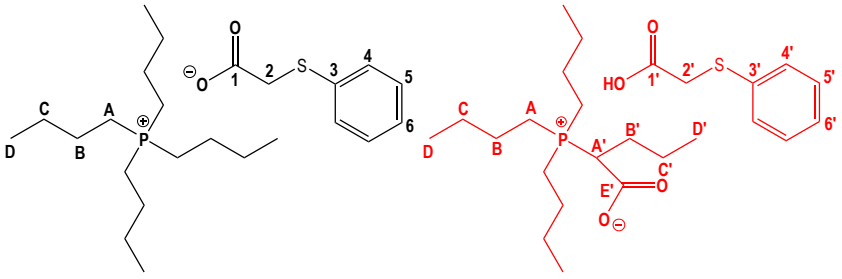

Figure S15 – Chemical structure of the $[P_{4,4,4,4}][PhSC_1COO]$ (left) before and (right) after CO_2 absorption.

Tetrabutylphosphonium (thiophenyl)acetate $[P_{4,4,4,4}][PhSC_1COO]$ after CO_2 absorption: ^{1}H NMR (400 MHz, C_6D_6, 343 K) δ ppm: 0.77 (t, 12H, $^{3}J_{HH}$ = 7.8 Hz, D); 1.30 (m, 8H, C); 1.38 (m, 8H, B); 2.34 (m, 8H, A); 3.36 (s, 1H, 2); 6.87 (t, 1H, $^{3}J_{HH}$ = 7.2 Hz, 6); 7.02 (m, 2H, $^{3}J_{HH}$ = 7.5 Hz, 5); 7.15 (d, 2H, $^{3}J_{HH}$ = 7.1 Hz, 4). ^{13}C NMR (100 MHz, C_6D_6, 343 K) δ ppm: 13.79 (4C, D); 18.88 (4C, A); 24.11,

24.29 (8C, B+C); 41.38 (1C, 2); 124.35 (1C, 6); 127.24 (2C, 4); 128.78 (2C, 5); 141.42 (1C, 3); 168.77 (1C, 1). ^{31}P NMR (161 MHz, C_6D_6, 343 K) δ ppm: 33.47 (1P, **P**$((CH_2)_3CH_3)_4$).

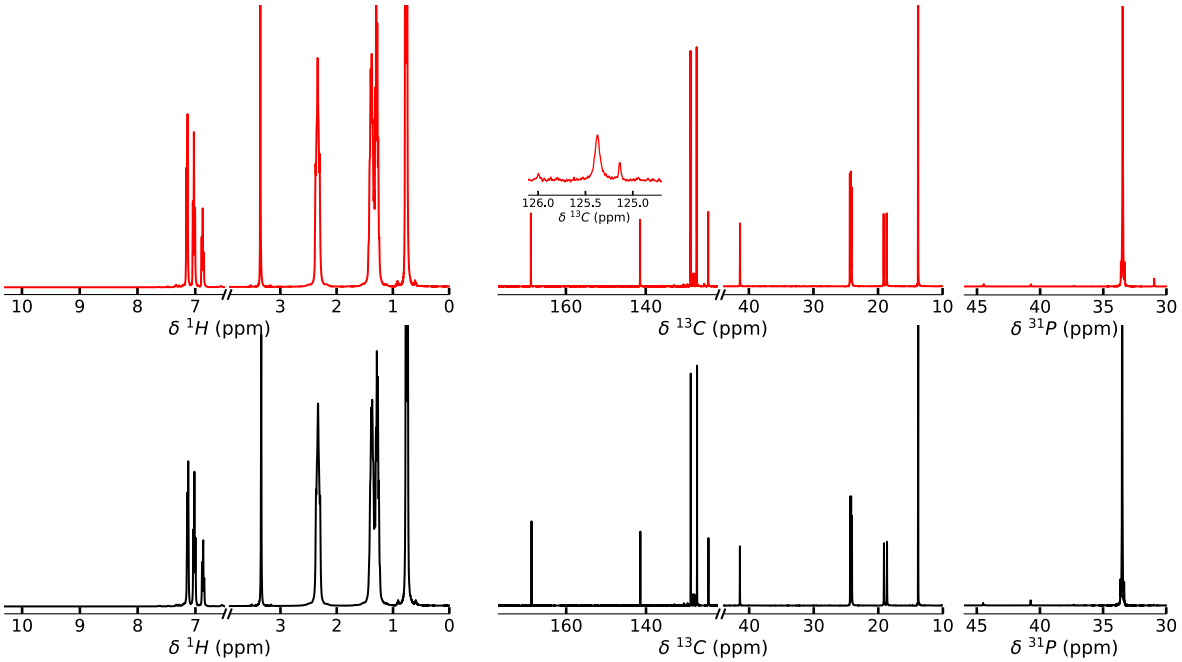

Figure S16 – (Left) ^{1}H, (middle) ^{13}C and (right) ^{31}P NMR spectra of $[P_{4,4,4,4}][PhSC_1COO]$ — before and — after CO_2 absorption at 343 K.

4.4 $[P_{4,4,4,4}][PhC_1COO]$

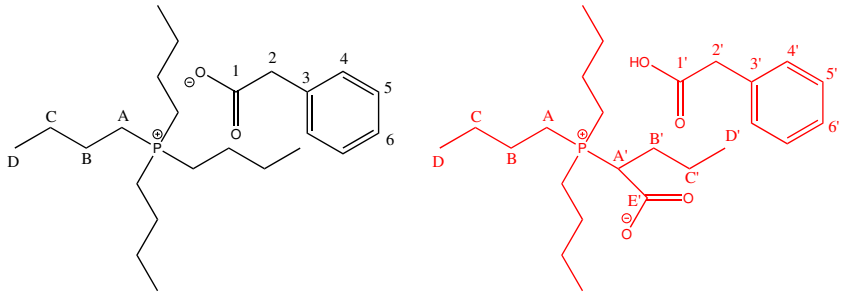

Figure S17 – Chemical structure of the $[P_{4,4,4,4}][PhC_1COO]$ (left) before and (right) after CO_2 absorption.

Tetrabutylphosphonium phenylacetate $[P_{4,4,4,4}][PhC_1COO]$ after CO_2 absorption: ^{1}H NMR (400 MHz, DMSO-d_6, 343 K) δ ppm: 0.97 (t, 12H, $^{3}J_{HH} = 6.8$ Hz, D+D'); 1.40-1.56 (m, 14H, B+B'+C+C'); 1.96 (m, 2H, B'); 2.26 (m, 6H, A); 2.35 (m, 8H, A); 2.87 (t, 1H, $^{3}J_{HH} = 11.8$ Hz, A'); 3.48 (s, 2H, 2'); 7.14 (t, 1H, $^{3}J_{HH} = 7.3$ Hz, 6'); 7.23 (t, 2H, $^{3}J_{HH} = 7.4$ Hz, 5'); 7.37 (d, 2H, $^{3}J_{HH} = 7.5$ Hz, 4'); 14.12 (1H, RCOO**H**). ^{13}C NMR (100 MHz, DMSO-d_6, 343 K) δ ppm: 12.28 (3C, D); 12.31 (4C,

D); 12.69 (1C, D'); 17.35 (4C, A); 18.10 (3C, A); 21.33 (1C, C'); 22.41-23.10 (7C, B+C+C'); 28.38 (1C, B'); 40.98 (1C, A'); 44.74 (1C, 2'); 124.09 (1C, 6'); 126.57 (2C, 5'); 128.46 (2C, 4'); 138.97 (1C, 3'); 165.36 (1C, E'); 172.49 (1C, 1'). ^{31}P NMR (161 MHz, DMSO-d_6, 343 K) δ ppm: 31.25 (1P, **P**($CHCO_2(CH_2)_2CH_3$)($(CH_2)_3CH_3$)$_3$); 33.57 (1P, **P**($(CH_2)_3CH_3$)$_4$).

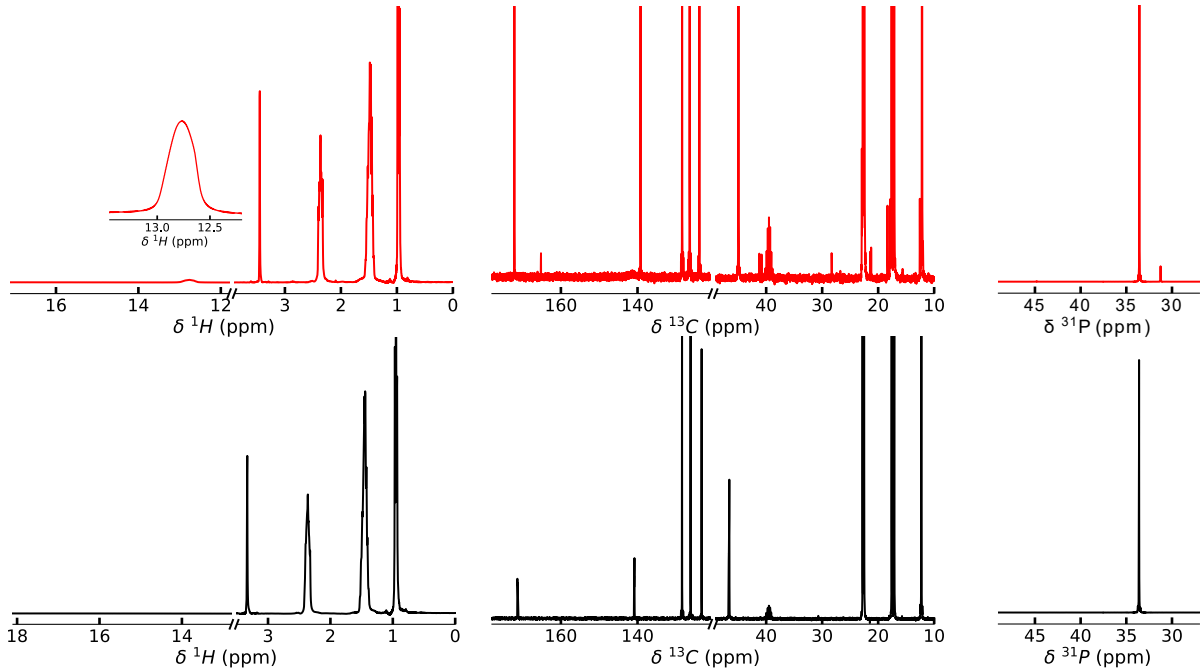

Figure S18 – (Left) ^{1}H, (middle) ^{13}C and (right) ^{31}P NMR spectra of [$P_{4,4,4,4}$][PhC_1COO] — before and — after CO_2 absorption at 343 K.

4.5 [$P_{4,4,4,4}$][C_1COO]

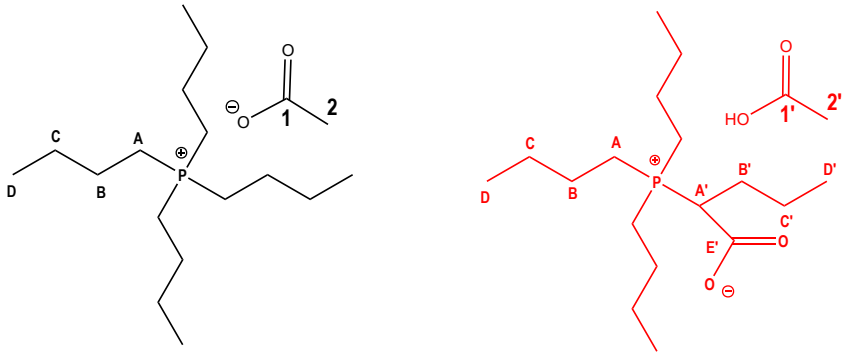

Figure S19 – Chemical structure of the [$P_{4,4,4,4}$][C_1COO] (left) before and (right) after CO_2 absorption.

Tetrabutylphosphonium acetate [$P_{4,4,4,4}$][C_1COO] after CO_2 absorption: ^{1}H NMR (400 MHz, C_6D_6, 343 K) δ ppm: 0.99 (t, 12H, $^{3}J_{HH}$ = 6.9 Hz, D + D'); 1.53 (m, 8H, C + C'); 1.64 (m, 8H, B + B'); 1.82

(m, 2H, 2'); 2.42 (m, 6H, A); 2.54 (m, 8H, A); 2.87 (t, 1H, $^{3}J_{HH}$ = 11.1 Hz, A'); 15.86 (1H, RCOO**H**). ^{13}C NMR (100 MHz, C_6D_6, 343 K) δ ppm: 13.71 (4C, D); 14.10 (1C, D'); 18.91 (4C, A); 19.60 (3C, A); 24.11 (8C, B+B'); 24.27 (8C, C+C'); 24.42 (1C, 2'); 42.64 (1C, A'); 166.82 (1C, E'); 173.68 (1C, 1'). ^{31}P NMR (161 MHz, C_6D_6, 343 K) δ ppm: 31.18 (1P, **P**($CHCO_2(CH_2)_2CH_3$)($(CH_2)_3CH_3$)$_3$); 33.66 (1P, **P**($(CH_2)_3CH_3$)$_4$).

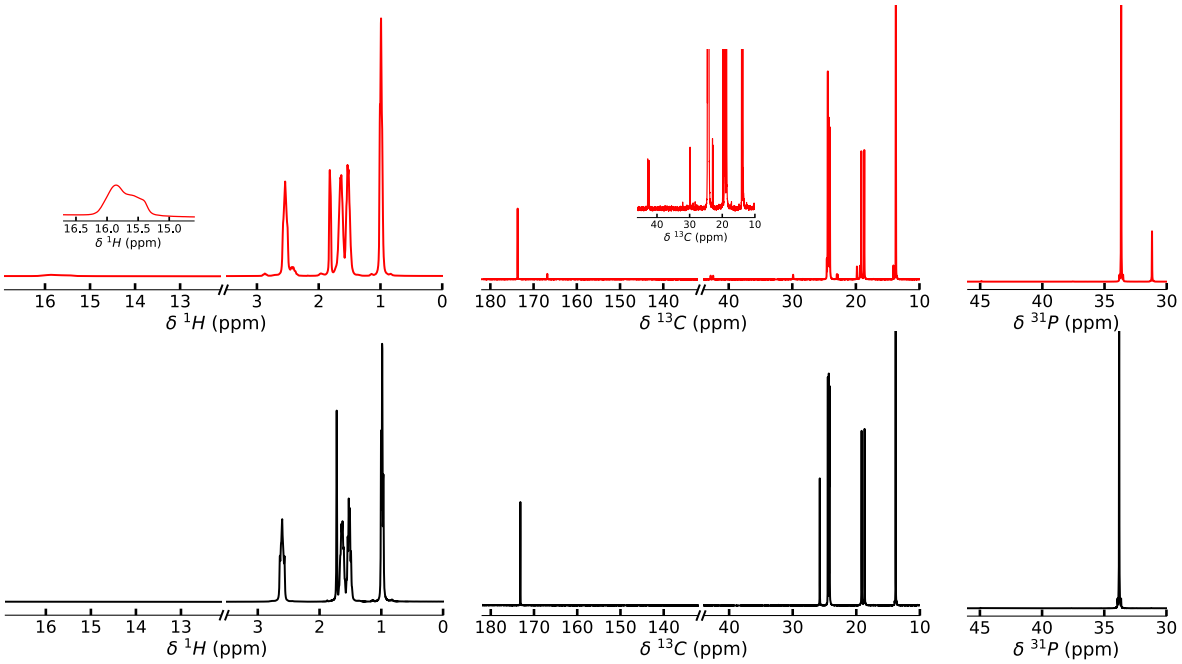

Figure S20 – (Left) ^{1}H, (middle) ^{13}C and (right) ^{31}P NMR spectra of $[P_{4,4,4,4}][C_1COO]$ — before and — after CO_2 absorption at 343 K.

4.6 $[P_{4,4,4,4}][MeC_3COO]$

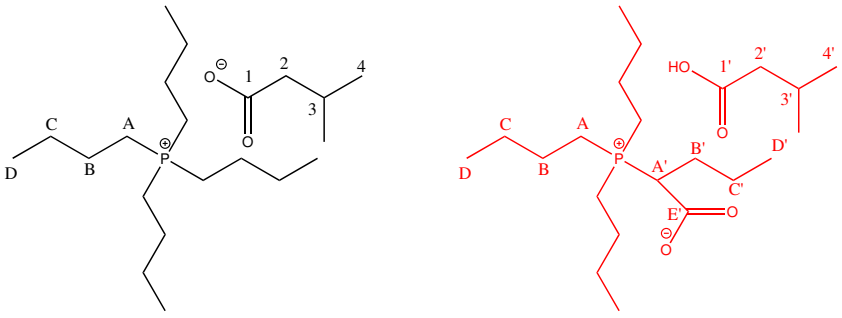

Figure S21 – Chemical structure of the $[P_{4,4,4,4}][MeC_3COO]$ (left) before and (right) after CO_2 absorption.

Tetrabutylphosphonium isovalerate $[P_{4,4,4,4}][MeC_3COO]$ after CO_2 absorption: ^{1}H NMR (400 MHz, C_6D_6, 343 K) δ ppm: 0.94 (d, 6H, $^{3}J_{HH}$ = 6.4 Hz, 4'); 0.97 (t, 12H, $^{3}J_{HH}$ = 7.3 Hz, D + D'); 1.51 (m,

8H, C + C'); 1.62 (m, 8H, B + B'); 1.99 (m, 2H, 2'); 2.05 (m, 1H, 3'); 2.44 (m, 6H, A); 2.57 (m, 8H, A); 2.85 (t, 1H, $^{3}J_{HH}$ = 11.7 Hz, A'); 17.52 (1H, RCOO**H**). ^{13}C NMR (100 MHz, C_6D_6, 343 K) δ ppm: 13.64 (3C, D); 13.68 (4C, D); 14.06 (1C, D'); 19.19 (4C, A); 19.86 (3C, A); 23.27 (1C, C'): 23.44 (2C, 4'); 24.18-24.66 (7C, B+C+C'); 26.58 (1C, 3'); 29.97 (1C, B'); 42.74 (1C, A'); 48.03 (1C, 2'); 166.68 (1C, E'); 175.42 (1C, 1'). ^{31}P NMR (161 MHz, C_6D_6, 343 K) δ ppm: 31.23 (1P, **P**($CHCO_2(CH_2)_2CH_3$)($(CH_2)_3CH_3$)$_3$); 33.75 (1P, **P**($(CH_2)_3CH_3$)$_4$).

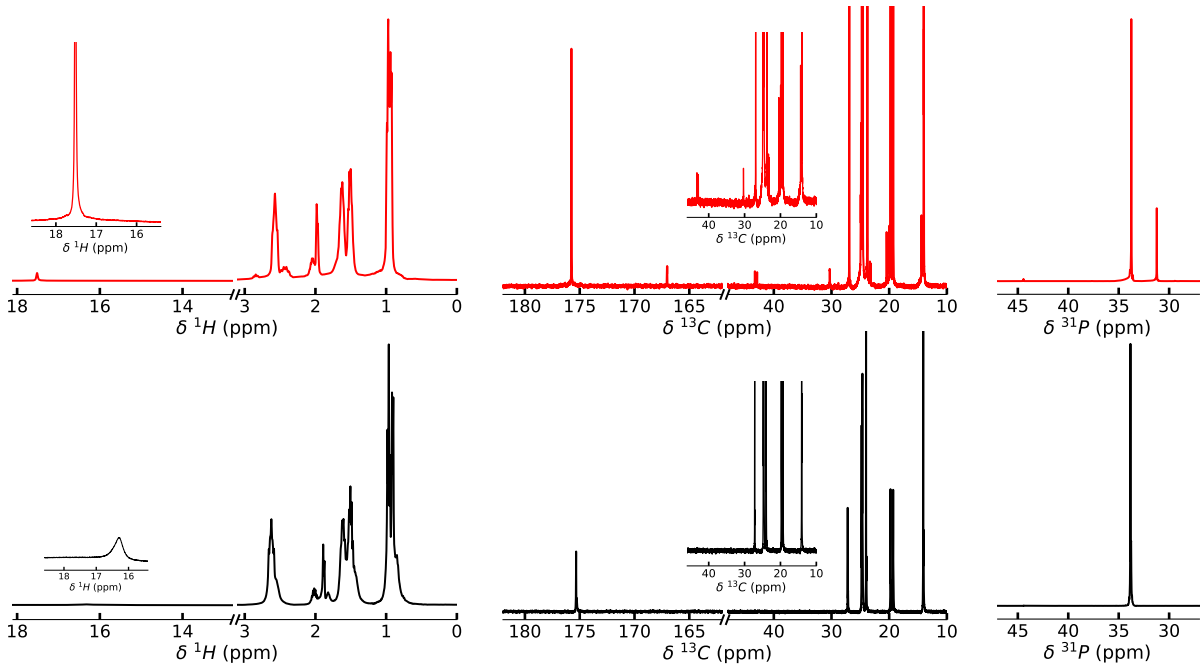

Figure S22 – (Left) ^{1}H, (middle) ^{13}C and (right) ^{31}P NMR spectra of [$P_{4,4,4,4}$][MeC_3COO] — before and — after CO_2 absorption at 343 K.

4.7 [$P_{4,4,4,4}$][c−C_6COO]

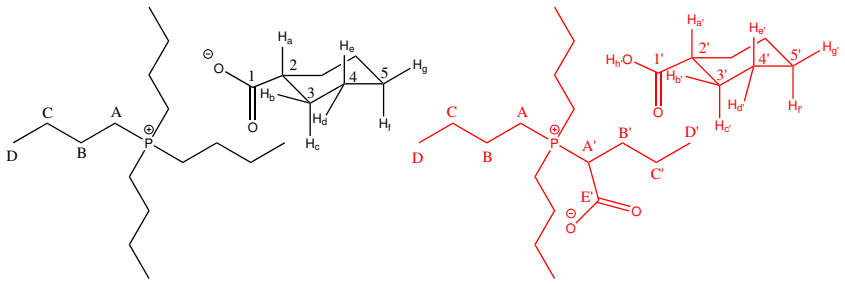

Figure S23 – Chemical structure of the [$P_{4,4,4,4}$][c−C_6COO] (left) before and (right) after CO_2 absorption.

Tetrabutylphosphonium cyclohexanecarboxylate [$P_{4,4,4,4}$][c−C_6COO] after CO_2 absorption: ^{1}H NMR (400 MHz, C_6D_6, 343 K) δ ppm: 0.94 (m, 12H, D+D'); 1.20 (m, 1H, 5', $H_{f'}$); 1.24 (m, 2H, 4',

$H_{e'}$); 1.38 (m, 2H, 5', $H_{c'}$); 1.48 (m, 8H, C+C'); 1.57 (m, 1H, 5', $H_{g'}$); 1.58 (m, 8H, B+B'); 1.66 (m, 2H, 4', $H_{d'}$); 1.82 (m, 2H, 3', $H_{b'}$); 2.02 (m, 1H, 2', $H_{a'}$); 2.55 (m, 6H, A); 2.81 (t, 1H, $^{3}J_{HH}$ = 11.2 Hz, A'); 16.04 (1H, RCOO**H**). ^{13}C NMR (100 MHz, C_6D_6, 343 K) δ ppm: 13.58 (3C, D); 13.63 (4C, D); 13.97 (1C, D'); 19.17 (4C, A); 19.81 (3C, A); 24.04-24.60 (6C, B+C+C'); 26.76 (2C, 4'); 27.20 (1C, 5'); 29.91 (1C, B'); 31.06 (2C, 3'); 42.89 (1C, A'); 46.36 (1C, 2'); 166.65 (1C, E'); 178.57 (1C, 1'). ^{31}P NMR (161 MHz, C_6D_6, 343 K) δ ppm: 31.11 (1P, **P**($CHCO_2(CH_2)_2CH_3$)($(CH_2)_3CH_3$)$_3$); 33.56 (1P, **P**($(CH_2)_3CH_3$)$_4$).

4.8 [$P_{4,4,4,4}$][C_5COO]

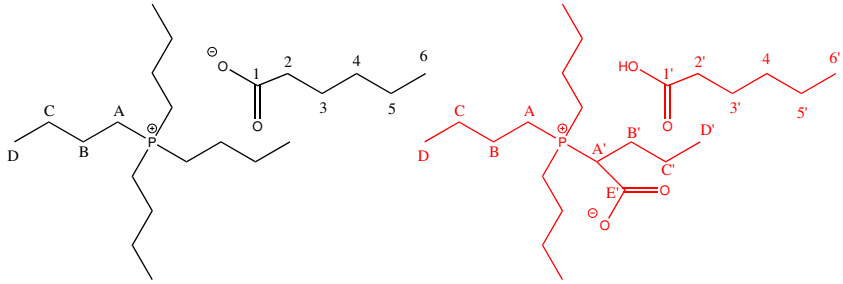

Figure S24 – Chemical structure of the [$P_{4,4,4,4}$][C_{11}COO] (left) before and (right) after CO_2 absorption.

Tetrabutylphosphonium hexanoate [$P_{4,4,4,4}$][C_5COO] after CO_2 absorption: ^{1}H NMR (400 MHz, C_6D_6, 343 K) δ ppm: 0.93 (m, 3H, 6'); 1.00 (m, 12H, D+D'); 1.35 (m, 4H, 4'+5'); 1.54 (m, 8H, C + C'); 1.58 (m, 2H, 3'); 1.65 (m, 8H, B+B'); 2.09 (t, 2H, $^{3}J_{HH}$ = 7.6 Hz, 2'); 2.45 (m, 6H, A); 2.62 (m, 8H, A); 2.87 (t, 1H, $^{3}J_{HH}$ = 11.5 Hz, A'); 16.92 (1H, RCOO**H**). ^{13}C NMR (100 MHz, C_6D_6, 343 K) δ ppm: 13.68 (3C, D); 13.73 (4C, D); 14.08 (1C, D'); 14.31 (1C, 6'); 19.04 (4C, A); 19.74 (3C, A); 23.09 (1C, 5'); 24.17-24.39 (3C, B); 24.39-24.68 (4C, C+C'); 26.78 (1C, 3'); 29.95 (1C, B'); 37.71 (1C, 4'); 38.26 (1C, 2'); 42.61 (1C, A'); 166.75 (1C, E'); 176.12 (1C, 1'). ^{31}P NMR (161 MHz, C_6D_6, 343 K) δ ppm: 31.17 (1P, **P**($CHCO_2(CH_2)_2CH_3$)($(CH_2)_3CH_3$)$_3$); 33.69 (1P, **P**($(CH_2)_3CH_3$)$_4$).

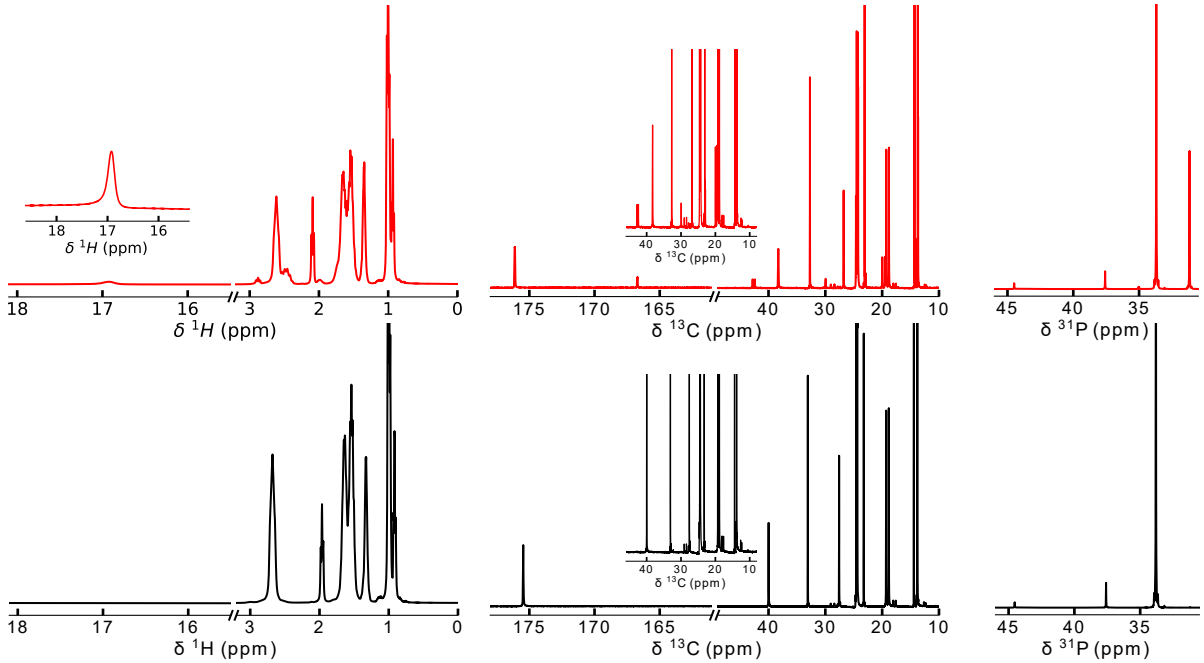

Figure S25 – (Left) ^{1}H, (middle) ^{13}C and (right) ^{31}P NMR spectra of $[P_{4,4,4,4}][C_5COO]$ — before and — after CO_2 absorption at 343 K.

4.9 $[P_{4,4,4,4}][C_{11}COO]$

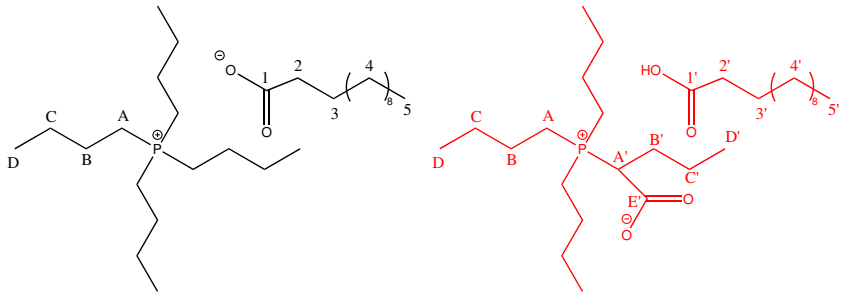

Figure S26 – Chemical structure of the $[P_{4,4,4,4}][C_{11}COO]$ (left) before and (right) after CO_2 absorption.

Tetrabutylphosphonium dodecanoate $[P_{4,4,4,4}][C_{11}COO]$ after CO_2 absorption: ^{1}H NMR (400 MHz, C_6D_6, 343 K) δ ppm: 0.93 (t, 3H, $^{3}J_{HH}$ = 6.1 Hz, 5'); 1.00 (t, 12H, $^{3}J_{HH}$ = 7.4 Hz, D+D'); 1.33 (m, 18H, 4'); 1.55 (m, 8H, C + C'); 1.59 (m, 2H, 3'); 1.66 (m, 8H, B+B'); 2.10 (t, 2H, $^{3}J_{HH}$ = 7.2 Hz, 2'); 2.45 (m, 6H, A); 2.60 (m, 8H, A); 2.88 (t, 1H, $^{3}J_{HH}$ = 11.5 Hz, A'); 17.04 (1H, RCOO**H**). ^{13}C NMR (100 MHz, C_6D_6, 343 K) δ ppm: 13.60 (3C, D); 13.66 (4C, D); 14.00 (1C, D'); 14.17 (1C, 5'); 19.21 (4C, A); 19.91 (3C, A); 22.98, 29.62-30.48, 32.31 (8C, 4'); 24.19-24.68 (7C, B+C+C'); 27.09 (1C, 3'); 30.29 (1C, B'); 38.19 (1C, 2'); 42.62 (1C, A'); 166.68 (1C, E'); 176.20 (1C, 1'). ^{31}P NMR (161 MHz, C_6D_6,

343 K) δ ppm: 31.22 (1P, **P**($CHCO_2(CH_2)_2CH_3$)($(CH_2)_3CH_3$)$_3$); 33.71 (1P, **P**($(CH_2)_3CH_3$)$_4$).

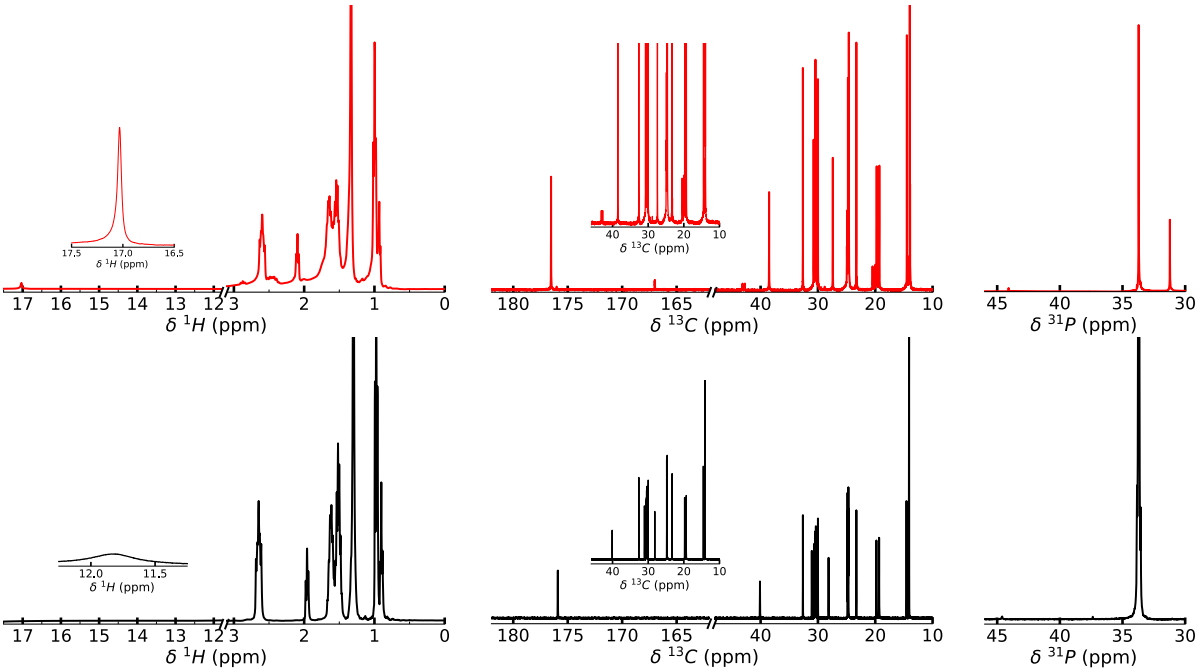

Figure S27 – (Left) ^{1}H, (middle) ^{13}C and (right) ^{31}P NMR spectra of [$P_{4,4,4,4}$][$C_{11}COO$] — before and — after CO_2 absorption at 343 K.

4.10 [$P_{6,6,6,14}$][$C_{11}COO$]

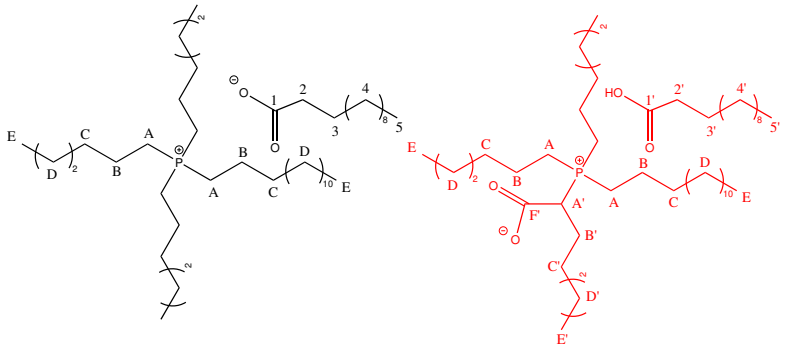

Figure S28 – Chemical structure of the [$P_{6,6,6,14}$][$C_{11}COO$] (left) before and (right) after CO_2 absorption. For the sack of clarity, the CO_2 absorbed has been represented on one of the hexyl alkyl chain of the phosphonium cation, but it also could be grafted on the tetradecyl alkyl chain without any clear preference.

Trihexyltetradecylphosphonium dodecanoate [$P_{6,6,6,14}$][$C_{11}COO$] after CO_2 absorption: ^{1}H NMR (400 MHz, C_6D_6, 343 K) δ ppm: 0.94-1.02 (m, 15H, 5'+E+E'); 1.34-1.46 (m, 48H, D+D'+4'); 1.56 (m, 8H, C + C'); 1.63 (m, 2H, 3'); 1.69 (m, 8H, B+B'); 2.15 (t, 2H, $^{3}J_{HH}$ = 7.3 Hz, 2'); 2.45 (m, 6H, A); 2.64 (m, 8H, A); 2.88 (t, 1H, $^{3}J_{HH}$ = 11.4 Hz, A'); 14.40 (1H, RCOO**H**). ^{13}C NMR (100 MHz,

C_6D_6, 343 K) δ ppm: 14.26 (5C, E+E'+5'); 19.50 (4C, A); 20.24 (3C, A); 22.31 (3C, B); 22.87, 23.06, 29.44-32.44 (24C, D+D'+4'); 30.82 (1C, B'); 31.01 (4C, C+C'); 26.89 (1C, 3'); 37.70 (1C, 2'); 42.49 (1C, A'); 166.81 (1C, E'); 177.00 (1C, 1'). ^{31}P NMR (161 MHz, C_6D_6, 343 K) δ ppm: 31.19 (1P, **P**($CHCO_2(CH_2)_2CH_3$)($(CH_2)_3CH_3$)$_3$); 33.36 (1P, **P**($(CH_2)_3CH_3$)$_4$).

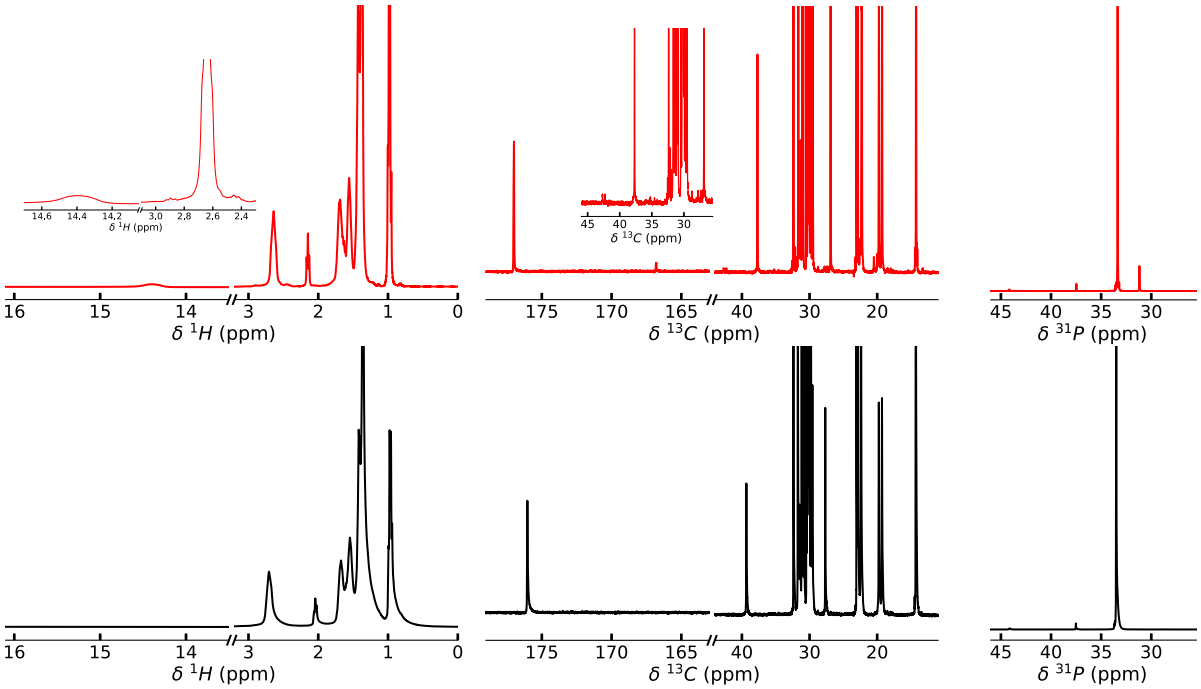

Figure S29 – (Left) ^{1}H, (middle) ^{13}C and (right) ^{31}P NMR spectra of $[P_{6,6,6,14}][C_{11}COO]$ — before and — after CO_2 absorption at 343 K.

4.11 $[P_{4,4,4,4}][Me_4C_4COO]$

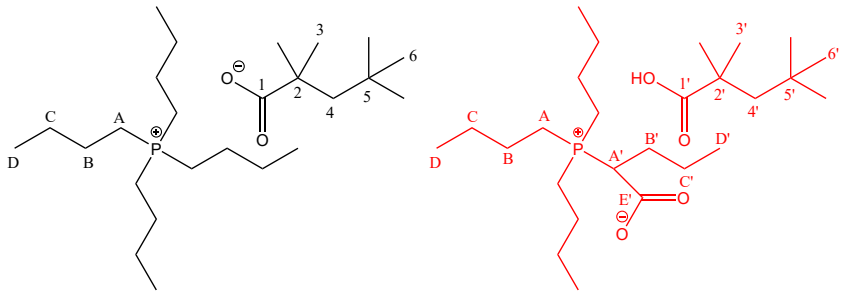

Figure S30 – Chemical structure of the $[P_{4,4,4,4}][Me_4C_4COO]$ (left) before and (right) after CO_2 absorption.

Tetrabutylphosphonium 2,2,4,4-tetramethylpentanoate $[P_{4,4,4,4}][Me_4C_4COO]$ after CO_2 absorption: ^{1}H NMR (400 MHz, C_6D_6, 343 K) δ ppm: 0.93-1.01 (m, 21H, 6 + D + D'); 1.11 (s, 6H, 3'); 1.51 (m, 8H, C + C'); 1.58 (s, 2H, 4'); 1.62 (m, 8H, B + B'); 2.52 (m, 6H, A); 2.69 (m, 8H, A); 2.85 (t, 1H, $^3J_{HH}$

= 12.0 Hz, A'); 17.68 (1H, RCOO**H**). ^{13}C NMR (100 MHz, C_6D_6, 343 K) δ ppm: 13.79 (3C, D); 13.85 (4C, D); 14.20 (1C, D'); 19.24 (4C, A); 19.82 (3C, A); 24.12-24.75 (8C, B + B' + C + C'); 30.05 (2C, 3'); 31.86 (3C, 6'); 32.18 (1C, 5'); 42.61 (1C, A'); 43.13 (1C, 2'); 55.05 (1C, 4'); 166.76 (1C, E'); 180.39 (1C, 1'). ^{31}P NMR (161 MHz, C_6D_6, 343 K) δ ppm: 31.24 (1P, **P**($CHCO_2(CH_2)_2CH_3$)($(CH_2)_3CH_3$)$_3$); 33.73 (1P, **P**($(CH_2)_3CH_3$)$_4$).

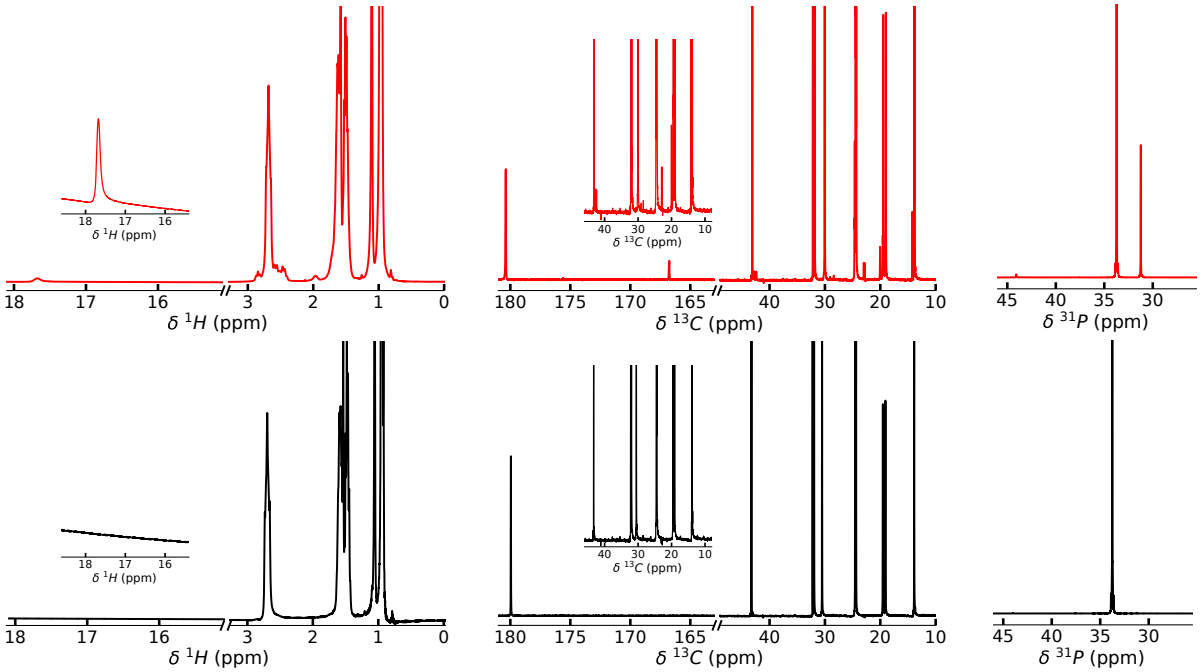

Figure S31 – (Left) ^{1}H, (middle) ^{13}C and (right) ^{31}P NMR spectra of [$P_{4,4,4,4}$][Me_4C_4COO] — before and — after CO_2 absorption at 343 K.

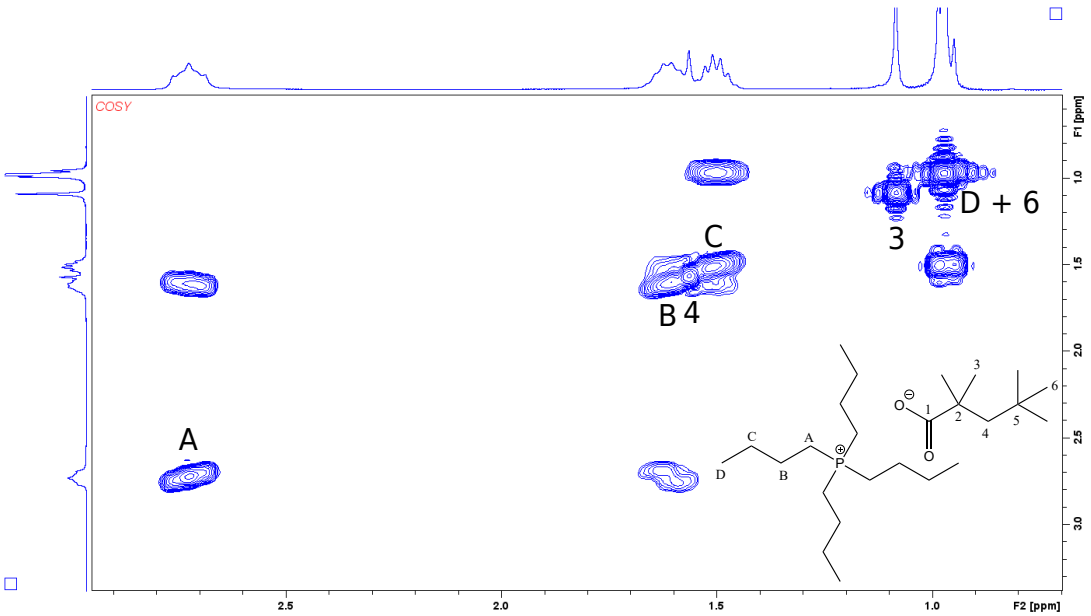

Figure S32 – COSY NMR spectrum of [$P_{4,4,4,4}$][Me_4C_4COO] at 343 K.

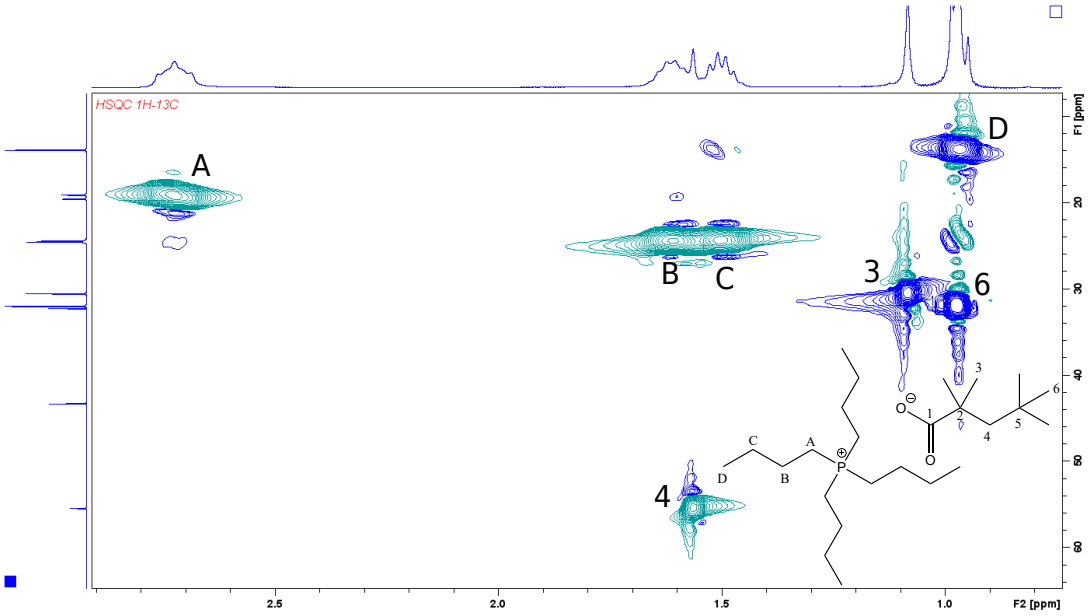

Figure S33 – HSQC NMR spectrum of $[P_{4,4,4,4}][Me_4C_4COO]$ at 343 K.

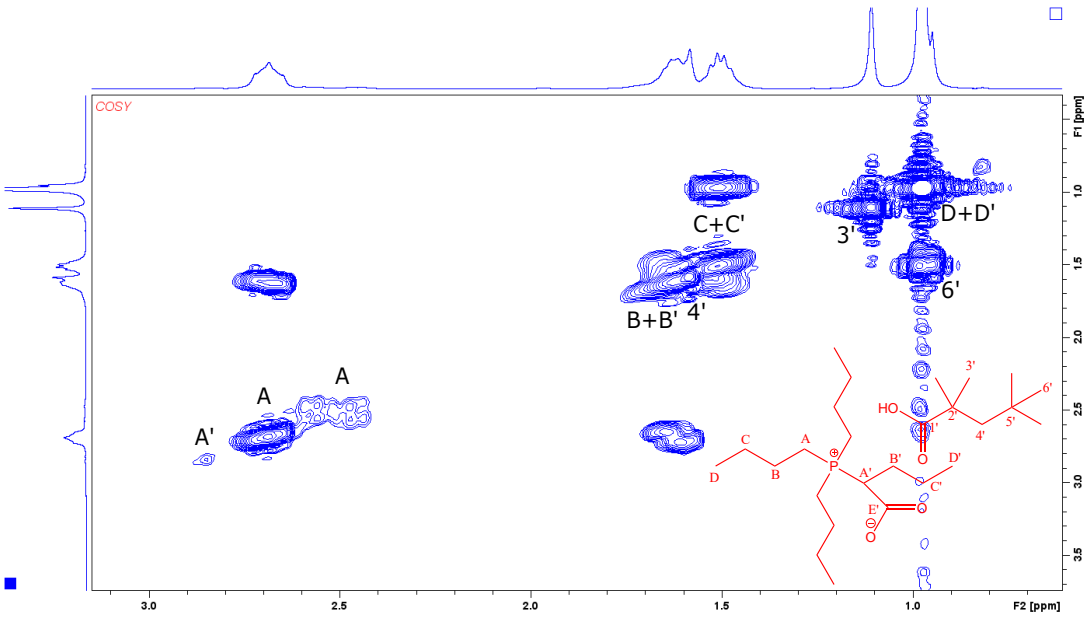

Figure S34 – COSY NMR spectrum of $[P_{4,4,4,4}][Me_4C_4COO]$ after CO_2 absorption at 343 K.

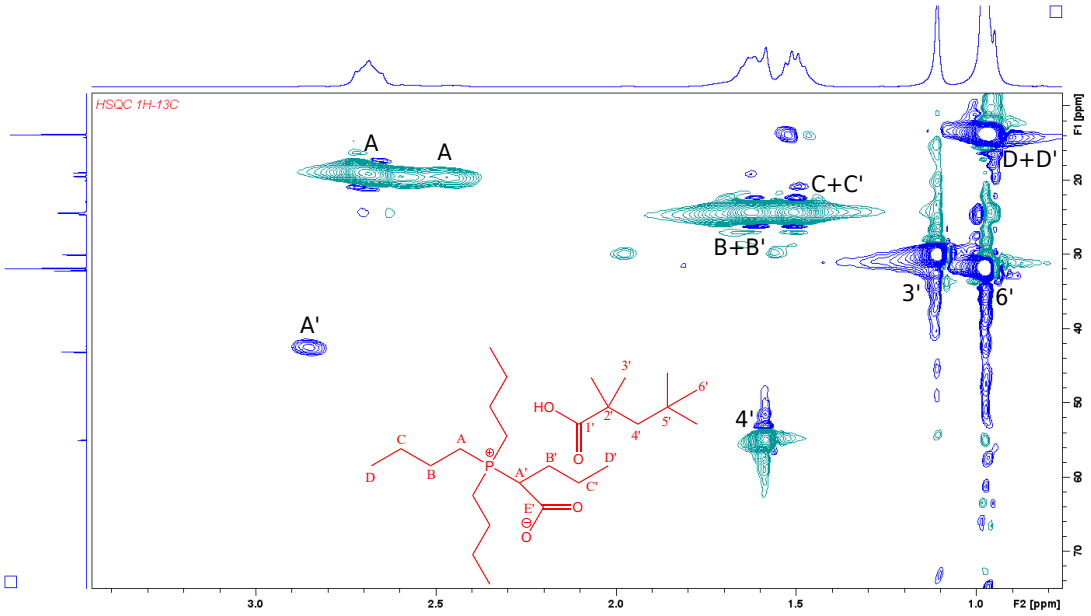

Figure S35 – HSQC NMR spectrum of $[P_{4,4,4,4}][Me_4C_4COO]$ after CO_2 absorption at 343 K.

4.12 $[P_{6,6,6,14}][Me_4C_4COO]$

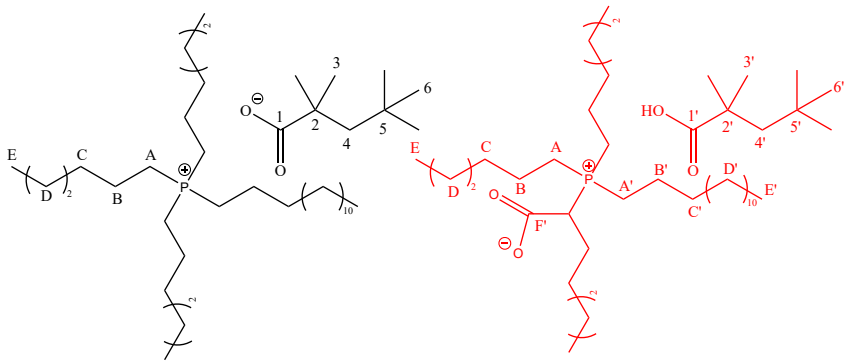

Figure S36 – Chemical structure of the $[P_{6,6,6,14}][Me_4C_4COO]$ (left) before and (right) after CO_2 absorption. For the sack of clarity, the CO_2 absorbed has been represented on one of the hexyl alkyl chain of the phosphonium cation, but it also could be grafted on the tetradecyl alkyl chain without any clear preference.

Trihexyltetradecylphosphonium $[P_{6,6,6,14}][Me_4C_4COO]$ after CO_2 absorption: ^{1}H NMR (400 MHz, C_6D_6, 343 K) δ ppm: 0.89-0.99 (m, 12H, E+E'); 1.02 (s, 9H, 6'); 1.17 (s, 6H, 3'); 1.27-1.46 (m, 32H, D+D'); 1.52 (m, 8H, C + C'); 1.64 (s, 2H, 4'); 1.68 (m, 8H, B+B'); 2.48 (m, 6H, A); 2.73 (m, 8H, A); 2.89 (m, 1H, A'); 17.08 (1H, RCOO**H**). ^{13}C NMR (100 MHz, C_6D_6, 343 K) δ ppm: 14.27, 14.33 (4C, E + E'); 19.55 (4C, A); 20.28 (3C, A); 22.29-22.67 (4C, B+B'); 22.85, 23.02, 29.28-30.25, 31.27-32.53 (25C, D + D'+ 5'); 29.90 (2C, 3'); 30.88-31.25 (4C, C+C'); 31.88 (3C, 6'); 42.42 (1C, A'); 43.06 (1C, 2'); 54.84 (1C, 4'); 166.83 (1C, E'); 180.77 (1C, 1'). ^{31}P NMR (161 MHz, C_6D_6, 343 K) δ ppm: 31.36

(1P, **P**($CHCO_2(CH_2)_2CH_3$)($(CH_2)_3CH_3$)$_3$); 33.64 (1P, **P**($(CH_2)_3CH_3$)$_4$).

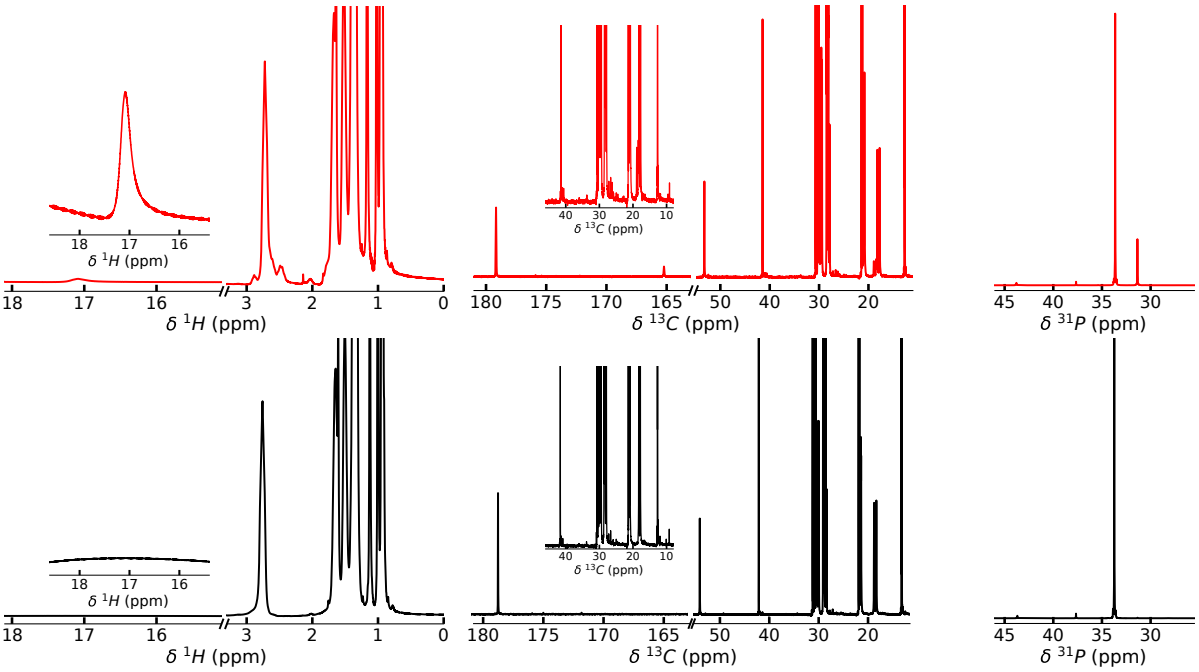

Figure S37 – (Left) ^{1}H, (middle) ^{13}C and (right) ^{31}P NMR spectra of [$P_{6,6,6,14}$][Me_4C_4COO] — before and — after CO_2 absorption at 343 K.

4.13 DOSY experiments

DOSY NMR experiments were conducted on ^{1}H atoms to determine the self-diffusion coefficients (D) of the ions before and after the absorption of CO_2. These measurements aimed to gain insights into the dynamic properties of the ILs. The obtained results are presented in Figure S38, and the exact values can be found in Table S14. As previously emphasized in a relevant study,[1] the self-diffusion coefficients of both the anion and cation in the neat ILs were found to be similar. This observation suggests the presence of strong cation-anion associations, despite the substantial difference in their masses.

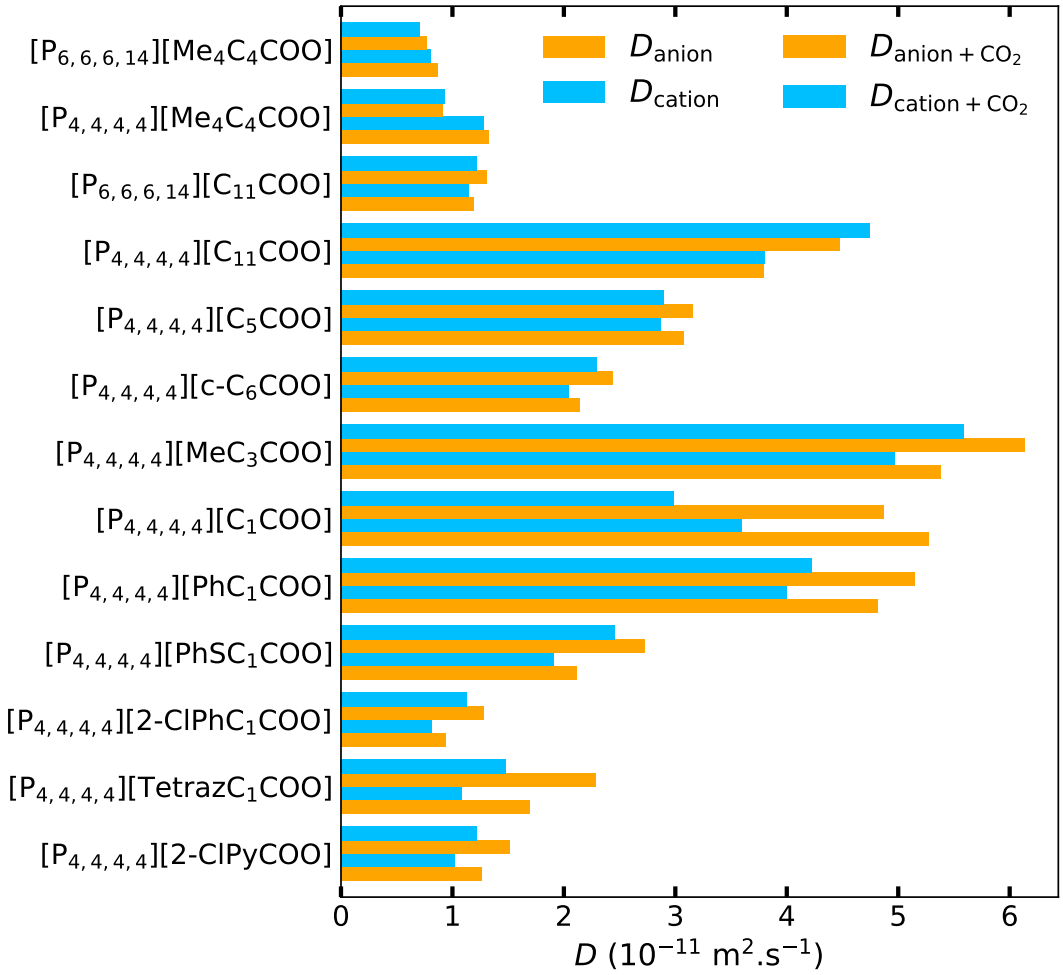

Figure S38 – Histogram representing the experimental self-diffusion coefficients (D) of both the anion and the cation in the ILs before and after being pressurized by CO_2 at 343 K by DOSY-NMR experiments.

Table S14 – Self-diffusion coefficients (D) of the ILs under study at 343 K by DOSY-NMR experiments. The D values of the neat ILs were determined in a previous study.[1]

Sample	$\frac{T}{\mathrm{K}}$	$\frac{D_{\mathrm{anion}}}{10^{-11}\mathrm{m^2\,s^{-1}}}$	$\frac{D_{\mathrm{cation}}}{10^{-11}\mathrm{m^2\,s^{-1}}}$
$[P_{4,4,4,4}][2-ClPyCOO]$	343	1.26 ± 0.04	1.02 ± 0.02
$[P_{4,4,4,4}][2-ClPyCOO] + CO_2$	343	1.51 ± 0.03	1.22 ± 0.02
$[P_{4,4,4,4}][TetrazC_1COO]$	343	1.69 ± 0.008	1.08 ± 0.003
$[P_{4,4,4,4}][TetrazC_1COO] + CO_2$[6]	343	2.28 ± 0.01	1.48 ± 0.009
$[P_{4,4,4,4}][2-ClPhC_1OHCOO]$	343	0.94 ± 0.008	0.81 ± 0.004
$[P_{4,4,4,4}][2-ClPhC_1OHCOO] + CO_2$	343	1.28 ± 0.003	1.13 ± 0.007
$[P_{4,4,4,4}][PhSC_1COO]$	343	2.11 ± 0.007	1.91 ± 0.005
$[P_{4,4,4,4}][PhSC_1COO] + CO_2$	343	2.72 ± 0.005	2.45 ± 0.004
$[P_{4,4,4,4}][PhC_1COO]$	343	4.81 ± 0.01	4.00 ± 0.01
$[P_{4,4,4,4}][PhC_1COO] + CO_2$	343	5.15 ± 0.03	4.22 ± 0.02
$[P_{4,4,4,4}][C_1COO]$	343	5.27 ± 0.01	3.59 ± 0.005
$[P_{4,4,4,4}][C_1COO] + CO_2$	343	4.87 ± 0.02	2.98 ± 0.007
$[P_{4,4,4,4}][MeC_3COO]$	343	5.38 ± 0.02	4.97 ± 0.01
$[P_{4,4,4,4}][MeC_3COO] + CO_2$	343	6.13 ± 0.03	5.59 ± 0.02
$[P_{4,4,4,4}][c-C_6COO]$	343	2.14 ± 0.006	2.04 ± 0.02
$[P_{4,4,4,4}][c-C_6COO] + CO_2$	343	2.44 ± 0.03	2.29 ± 0.01
$[P_{4,4,4,4}][C_5COO]$	343	3.07 ± 0.003	2.87 ± 0.002
$[P_{4,4,4,4}][C_5COO] + CO_2$	343	3.15 ± 0.01	2.89 ± 0.01
$[P_{4,4,4,4}][C_{11}COO]$	343	3.79 ± 0.03	3.80 ± 0.02
$[P_{4,4,4,4}][C_{11}COO] + CO_2$	343	4.47 ± 0.01	4.74 ± 0.02
$[P_{6,6,6,14}][C_{11}COO]$	343	1.19 ± 0.004	1.14 ± 0.004
$[P_{6,6,6,14}][C_{11}COO] + CO_2$	343	1.31 ± 0.003	1.22 ± 0.001
$[P_{4,4,4,4}][Me_4C_4COO]$	343	1.33 ± 0.003	1.28 ± 0.002
$[P_{4,4,4,4}][Me_4C_4COO] + CO_2$	343	0.91 ± 0.002	0.93 ± 0.001
$[P_{6,6,6,14}][Me_4C_4COO]$	343	0.86 ± 0.002	0.80 ± 0.001
$[P_{6,6,6,14}][Me_4C_4COO] + CO_2$	343	0.77 ± 0.002	0.70 ± 0.001

5 FT-IR measurements

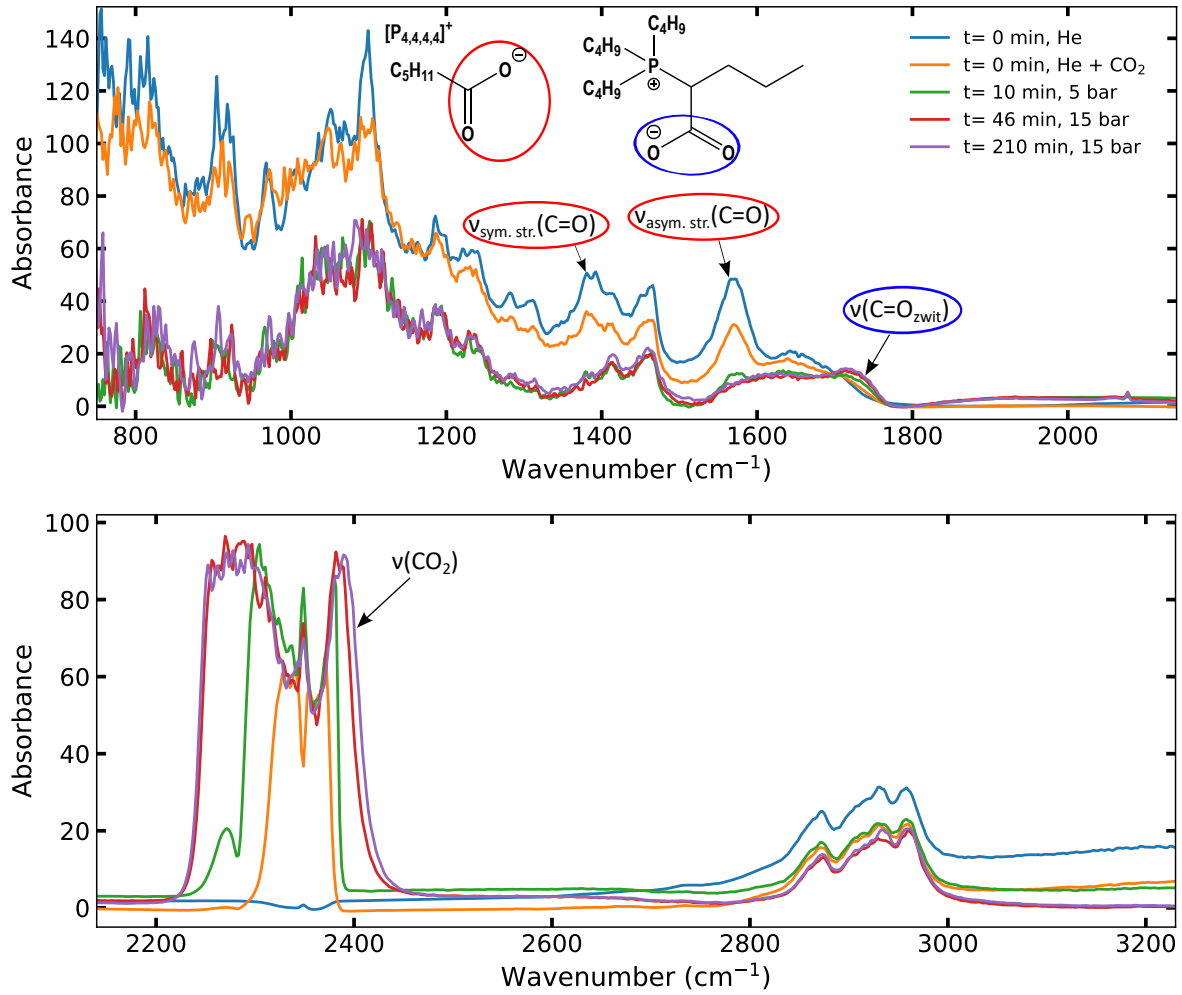

Figure S39 – FT-IR spectrum of $[P_{4,4,4,4}][C_5COO]$ at different time exposure under CO_2 pressure at 303 K from 750 to 3230 cm^{-1}.

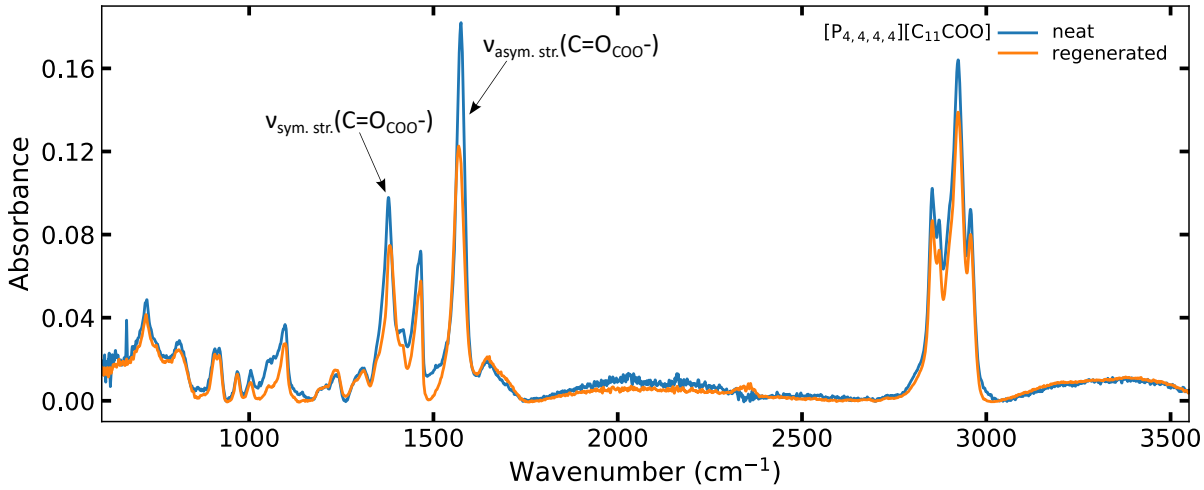

Figure S40 – Comparison of the full FT-IR spectra between the — neat $[P_{4,4,4,4}][C_{11}COO]$ and — post regeneration after 2 cycles of absorption and desorption at 303 K and 343 K.

6 Molecular Dynamics Simulations

MD simulations of the ILs in presence of CO_2 have been carried out as they allow further insights into the molecular structure of the systems to have a better understanding of how CO_2 is solvated. The RDFs of $[P_{4,4,4,4}][C_{11}COO]$ in presence of CO_2, depicted in Figure 8 as representative example of the other ILs, show that there is no modification of the structural organization of the IL induced by the presence of CO_2. Indeed, the distances between the negatively charged O_{COO^-} of the carboxylate anions and the P^+ and the H_α of the phosphonium cation remain the same. The CN of these two different interacting sites remain almost identical to the case without CO_2 as they slightly decrease from 1.01 to 1.00 and 4.53 to 4.51, respectively. The presence of CO_2 into the system does not seem to perturb the interaction between the two ions. The CO_2 molecules are preferentially located around the carboxylate head of the anion with the carbon atoms oriented toward the negatively charged oxygen atoms at 2.183 Å with a coordination number of about 0.04 in $[P_{4,4,4,4}][C_{11}COO]$. More generally, the RDFs and the CNs of these two interacting sites are similar in all the ILs even in the presence of CO_2 (Figure S43). Even the microscopic structures of $[P_{4,4,4,4}][2-ClPyCOO]$ (Figure S44) and $[P_{4,4,4,4}][TetrazC_1COO]$,[6] which were presenting slightly different RDFs because of secondary intermolecular interactions, are not impacted by the presence of CO_2.

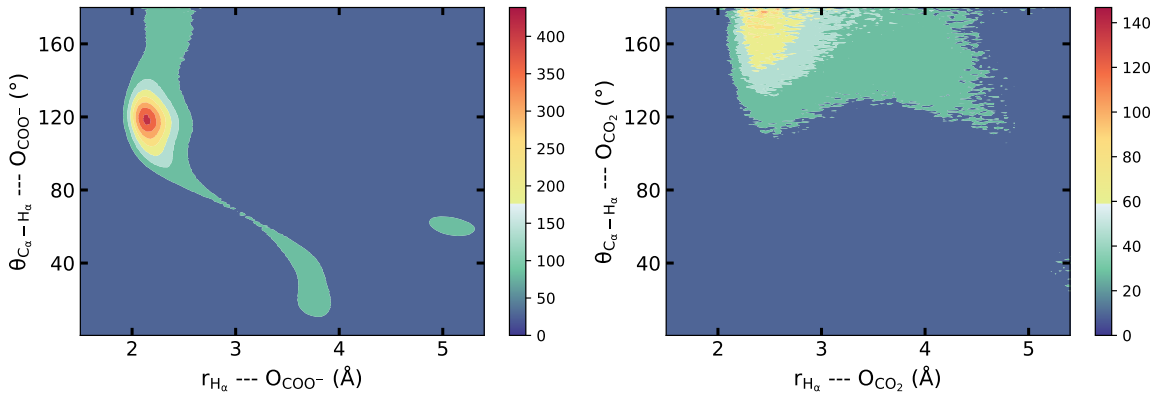

Figure S41 – Combined distribution function of the Angular Distribution Function (ADF) as a function of the RDF in $[P_{4,4,4,4}][C_{11}COO]$ showing the angle between (left) $C_\alpha{-}H_\alpha$ of the $[P_{4,4,4,4}]^+$ cation, (right) the oxygen atoms of CO_2 with the oxygen atoms O_{COO^-} of the carboxylate anion as a function of the distance between the acidic proton H_α and the O_{CO_2} with the negatively charged O_{COO^-} at 343 K, respectively.

The CDFs of the $C_\alpha{-}H_\alpha\cdots O_{COO^-}$ angle as a function of the distance between the acidic proton H_α and O_{COO^-}, and the CDFs of the $C_\alpha{-}H_\alpha\cdots O_{CO_2}$ angle as a function of the distance between the acidic proton H_α and O_{CO_2} in all the ILs under study have been calculated at 343 K, but only the ones of

$[P_{4,4,4,4}][C_{11}COO]$ are depicted Figure S41 for the sack of clarity as they are all similar.

Even in presence of CO_2, the CDFs are similar to the ones of the neat ILs with an $C_\alpha{-}H_\alpha\cdots O_{COO^-}$ angle of approximately 120 ° at a distance about 2.15–2.18 Å at the exception of $[P_{4,4,4,4}][TetrazC_1COO]$ and $[P_{4,4,4,4}][2-ClPyCOO]$ which exhibit larger angles of about 123.3 °[6] and 124.5 °, respectively. The angles are too low to be considered as proper hydrogen bonds which means that the H_α abstraction is not driven by this interaction. The acid-base equilibrium is not favored by this particular spatial configuration as it is the case with imidazolium carboxylate ILs. Therefore, the differences of absorption capacity are not explained by a particular spatial configuration between the interacting sites revealing that the differences are probably due to thermodynamic features. In imidazolium carboxylate ILs, the proton located on the C_2 position of the 1,3-dialkylimidazolium rings is more acidic. It induces a strong H-bond interaction between O_{COO^-} of the carboxylate and this proton resulting in a more favorable initial deprotonation.[9] It is in line with the higher K_{eq} determined for these imidazolium ILs.[10]

A $C_\alpha{-}H_\alpha\cdots O_{CO_2}$ angle of approximately 179° and a distance of 2.26 Å has been found in all the ILs as illustrated in Figure S41 (right). It indicates the formation of H-bonds between CO_2 and the phosphonium cations, confirming that the most favourable CO_2 solubilization site in phosphonium carboxylate ILs is located between the O_{COO^-} of the anion and the H_α of the cation.

It is interesting to note that in the initial state, the CO_2 molecule is in close proximity to O_{COO^-} and H_α of the phosphonium cation. This observation is consistent with both DFT calculations and MD simulations (Figure S42) indicating that CO_2 is preferentially solvated around the carboxylate head of the anions. This finding suggests that increasing the bulkiness of both the cation and the anion may impede accessibility to the interacting sites, thereby reducing its solubility. This could explain why $[P_{6,6,6,14}][Me_4C_4COO]$ exhibits a lower CO_2 capture capacity compared to its $[P_{4,4,4,4}]^+$ counterparts.

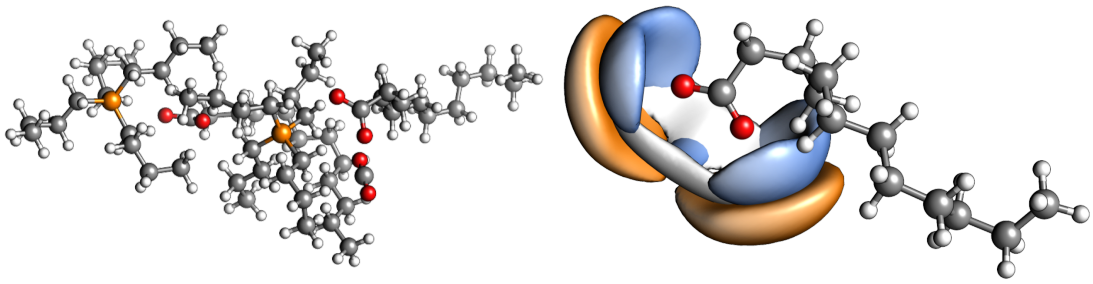

Figure S42 – (Left) The most favorable optimized structure of the initial state in $[P_{4,4,4,4}][C_{11}COO]$ from *ab initio* calculations. (Right) The SDFs of ■ P^+, of □ the acidic protons H_α and of ■ C_{CO_2} around the O_{COO^-} of the $[C_{11}COO]^-$ anion in $[P_{4,4,4,4}][C_{11}COO]$ at 343 K. Isodensity contours at 11.6, 14.1 and 0.8 times the average density around the central anion, respectively.

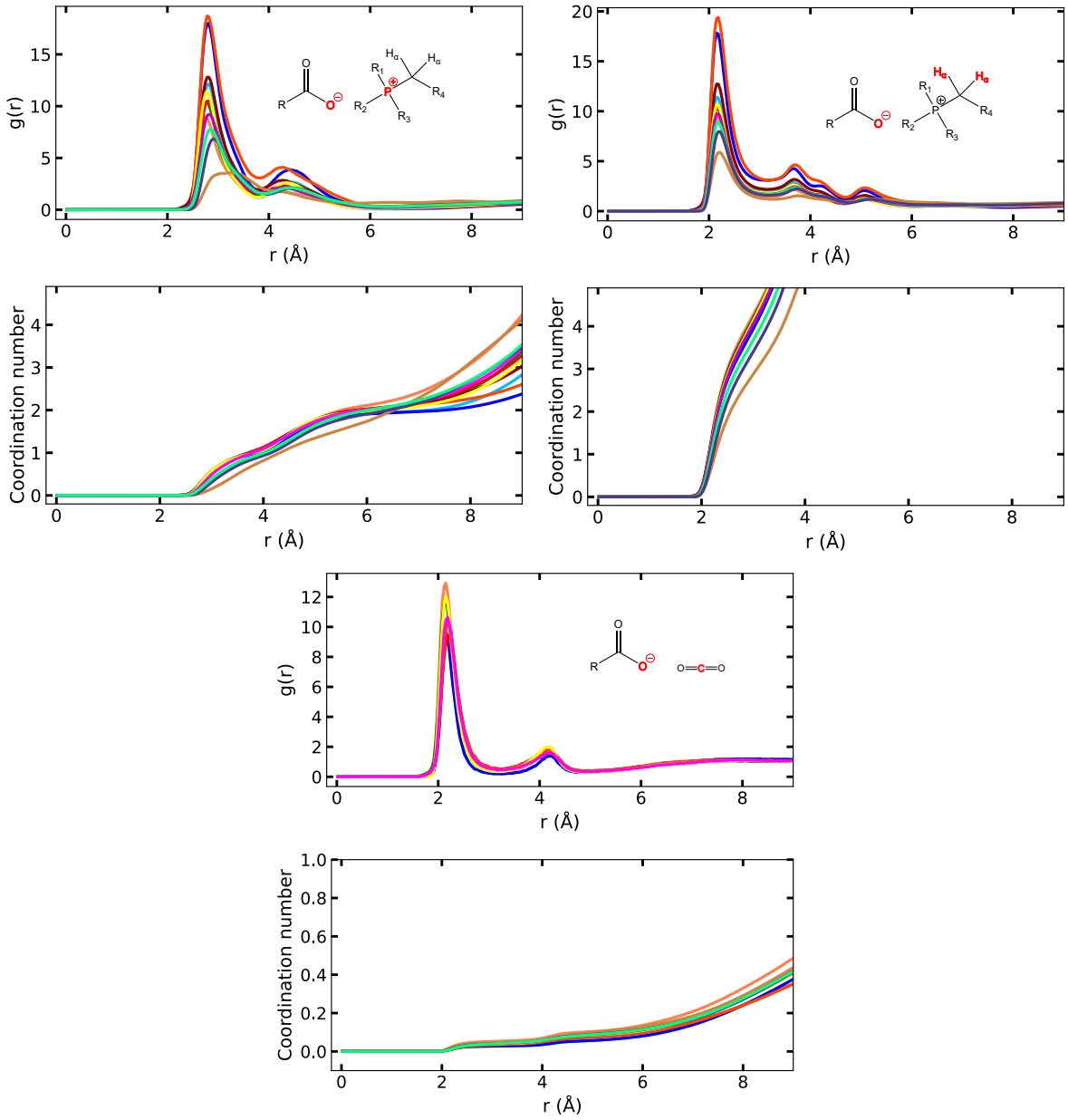

Figure S43 – Comparison of the site-site RDF, $g(r)$, of (top left) P^+ and (top right) H_α of the cation and (bottom) C_{CO_2} of the CO_2 around O_{COO^-} of the carboxylate anion and their corresponding coordination number in carboxylate head of the anion and their corresponding coordination numbers in — $[P_{4,4,4,4}][2-ClPyCOO]$, — $[P_{4,4,4,4}][2-ClPhC_1OHCOO]$, — $[P_{4,4,4,4}][PhSC_1COO]$, — $[P_{4,4,4,4}][PhC_1COO]$, — $[P_{4,4,4,4}][C_1COO]$, — $[P_{4,4,4,4}][MeC_3COO]$, — $[P_{4,4,4,4}][c-C_6COO]$, — $[P_{4,4,4,4}][C_5COO]$, — $[P_{4,4,4,4}][C_{11}COO]$, — $[P_{6,6,6,14}][C_{11}COO]$, — $[P_{4,4,4,4}][Me_4C_4COO]$ and — $[P_{6,6,6,14}][Me_4C_4COO]$ in presence of CO_2 at 343 K.

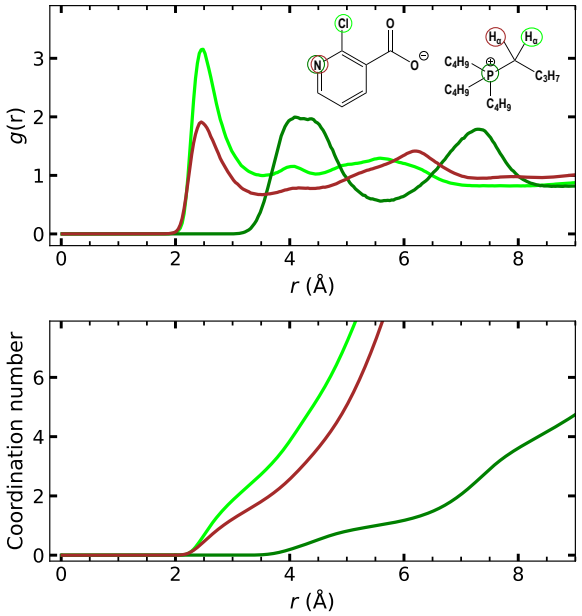

Figure S44 – Site-site RDFs, $g_{ij}(r)$, of H_α around — Cl and — N, — P^+ around N in $[P_{4,4,4,4}][2-ClPyCOO]$ in presence of CO_2 at 343 K.

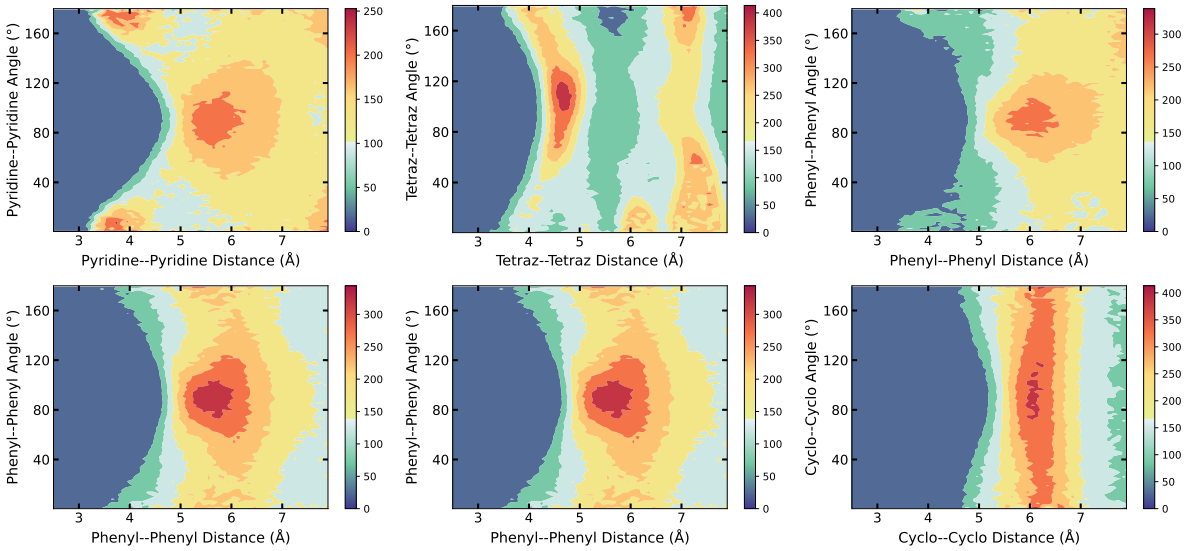

Figure S45 – CDFs of the angle between (top left) two adjacent pyrridine rings in $[P_{4,4,4,4}][2-ClPyCOO]$, (top middle) two adjacent tetrazole rings in $[P_{4,4,4,4}][TetrazC_1COO]$, two adjacent phenyl rings (top right) in $[P_{4,4,4,4}][2-ClPhC_1OHCOO]$, (bottom left) in $[P_{4,4,4,4}][PhSC_1COO]$, (bottom middle) in $[P_{4,4,4,4}][PhC_1COO]$ and (bottom right) two adjacent cyclohexane in $[P_{4,4,4,4}][c-C_6COO]$ as a function of the RDF between their center of mass at 343 K in presence of CO_2.

7 *Ab initio* calculations

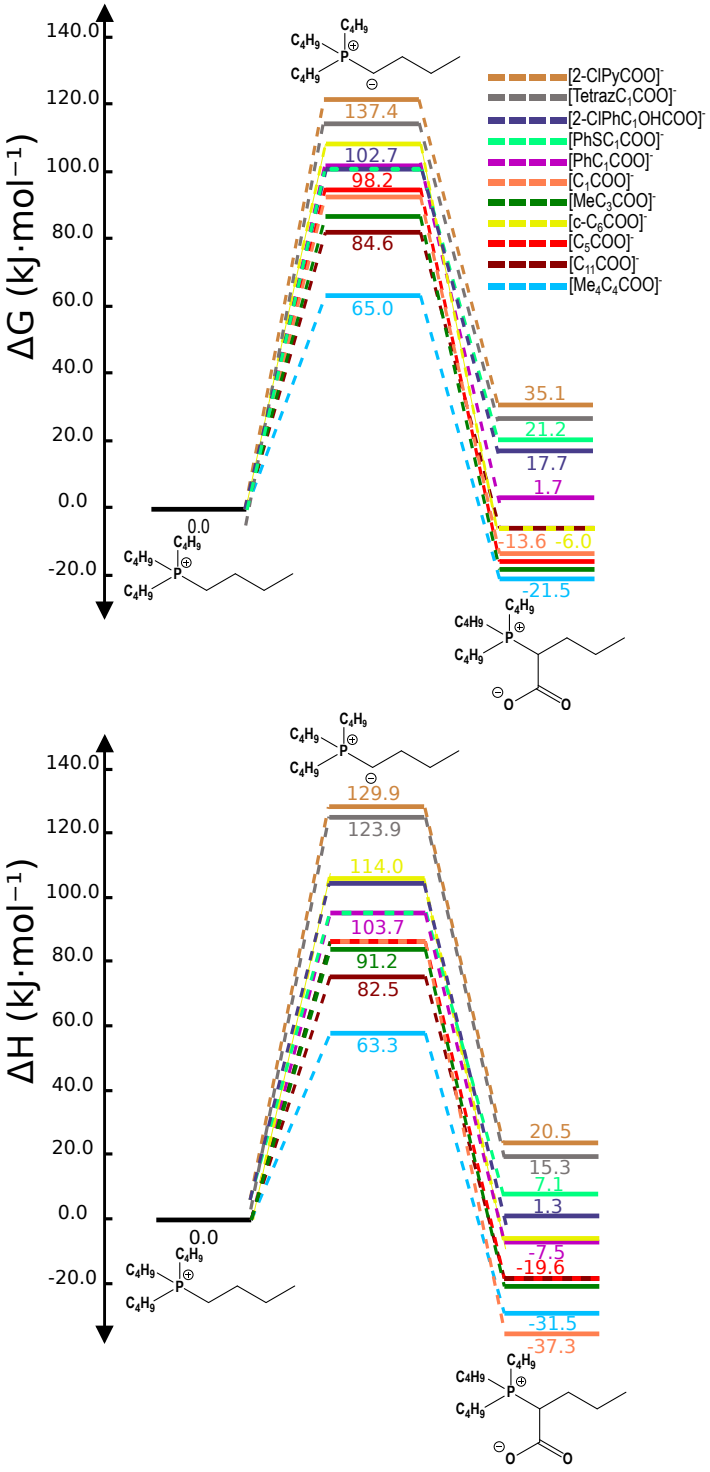

Figure S46 – Relative (top) Gibbs free energy and (bottom) enthalpy of the reactions leading to the chemical capture of CO_2 in — $[P_{4,4,4,4}][2-ClPyCOO]$, — $[P_{4,4,4,4}][TetrazC_1COO]$,[6] — $[P_{4,4,4,4}][2-ClPhC_1OHCOO]$, — $[P_{4,4,4,4}][PhSC_1COO]$, — $[P_{4,4,4,4}][PhC_1COO]$, — $[P_{4,4,4,4}][C_1COO]$, — $[P_{4,4,4,4}][MeC_3COO]$, — $[P_{4,4,4,4}][c-C_6COO]$, — $[P_{4,4,4,4}][C_5COO]$, — $[P_{4,4,4,4}][C_{11}COO]$ and — $[P_{4,4,4,4}][Me_4C_4COO]$ at 343 K with 2:1 stoichiometry (IL:CO_2).

Table S15 – Atomic charges (q) of the different ILs in the initial state (I.S.), intermediate (Interm.) and the final state (F.S.) of the CO_2 absorption mechanism with a 2:1 stoichiometry (IL:CO_2) as well as the related HOMO energy. All the anions are paired with the $[P_{4,4,4,4}]^+$ cation. As the charges carried by the $[P^+_{4,4,4,4}{-}CO_2^-]$ zwitterion and the free CO_2 are approximately 0, they are not displayed for the sack of clarity.

Sample	$q([P_{4,4,4,4}]^+)$	$q([RCOO]^-)$	q(Ylide)	q(RCOOH)	E(HOMO)
	e	e	e	e	eV
[2 −ClPyCOO] I.S.	0.58 & 0.65	-0.60 & -0.63	-	-	-8.02
[2 −ClPyCOO] Interm.	-0.73	-0.52	-0.08	-0.10	-5.57
[2 −ClPyCOO] F.S.	0.57	-0.42	-	-0.08	-7.94
[TetrazC$_1$COO] I.S.[6]	0.78 & 0.53	-0.60 & -0.71	-	-	-6.31
[TetrazC$_1$COO] Interm.[6]	0.72	-0.54	-0.05	-0.11	-4.20
[TetrazC$_1$COO] F.S.[6]	0.73	-0.65	-	-0.11	-6.25
[2 −ClPhC$_1$OHCOO] I.S.	0.71 & 0.58	-0.61 & -0.62	-	-	-7.43
[2 −ClPhC$_1$OHCOO] Interm.	0.61	-0.49	0.00	-0.08	-5.56
[2 −ClPhC$_1$OHCOO] F.S.	0.62	-0.47	-	-0.12	-7.55
[PhSC$_1$COO] I.S.	0.65 & 0.56	-0.58 & -0.62	-	-	-6.84
[PhSC$_1$COO] Interm.	0.52	-0.49	0.09	-0.07	-5.04
[PhSC$_1$COO] F.S.	0.65	-0.54	-	-0.11	-6.94
[PhC$_1$COO] I.S.	0.58 & 0.63	-0.62 & -0.58	-	-	-6.07
[PhC$_1$COO] Interm.	0.70	-0.48	-0.06	-0.17	-4.26
[PhC$_1$COO] F.S	0.57	-0.49	-	-0.10	-6.58
[C$_1$COO] I.S.	0.61 & 0.62	-0.61 & -0.61	-	-	-6.13
[C$_1$COO] Interm.	0.68	-0.51	0.01	-0.16	-4.47
[C$_1$COO] F.S.	0.65	-0.51	-	-0.13	-6.57
[MeC$_3$COO] I.S.	0.62 & 0.65	-0.62 & -0.64	-	-	-6.12
[MeC$_3$COO] Interm.	0.65	-0.54	0.07	-0.17	-4.44
[MeC$_3$COO] F.S.	0.67	-0.52	-	-0.15	-6.52
[c−C$_6$COO] I.S.	0.63 & 0.66	-0.61 & -0.68	-	-	-5.95
[c−C$_6$COO] Interm.	0.76	-0.50	-0.08	-0.15	-4.31
[c−C$_6$COO] F.S.	0.61	-0.49	-	-0.13	-6.53
[C$_5$COO] I.S.	0.63 & 0.62	-0.62 & -0.61	-	-	-6.12
[C$_5$COO] Interm.	0.63	-0.54	0.12	-0.17	-4.72
[C$_5$COO] F.S.	0.71	-0.52	-	-0.13	-6.46
[C$_{11}$COO] I.S.	0.64 & 0.65	-0.62 & -0.64	-	-	-6.02
[C$_{11}$COO] Interm.	0.72	-0.52	-0.01	-0.15	-4.43
[C$_{11}$COO] F.S.	0.64	-0.57	-	-0.11	-6.42
[Me$_4$C$_4$COO] I.S.	0.69 & 0.58	-0.62 & -0.64	-	-	-6.04
[Me$_4$C$_4$COO] Interm.	0.65	-0.57	0.12	-0.17	-4.67
[Me$_4$C$_4$COO] F.S.	0.62	-0.53	-	-0.13	-6.44

In the intermediate state, the formation of the $[P_{4,4,4,4}]$[RCOO]-HOOCR complex is supported by the presence of a slight negative charge on the carboxylic acid between -0.07 and $-0.17e$ with specific values

for each IL reported in Table S15. This charge arises from a transfer of charge from the carboxylate anion to the neutral carboxylic acid, facilitated by the formation of a hydrogen bond. The negative charge carried by $[RCOO]^-$ decreases from approximately $-0.6e$ to $-0.53e$. In the final state, although the partial charge on HOOCR is slightly less negative, the presence of the complex linked by a hydrogen bond is still evident due to a similar charge transfer (between -0.08 and $-0.15e$). The positive charge on the phosphonium cation increases upon the formation of this complex, as the hydrogen bond formation reduces the charge transfer between the cation and the anion.

Molecular orbital analysis was performed on the HOMOs of the CO_2 absorption mechanism steps for each IL, and their corresponding energies are reported in Table S15. This analysis provides insight into the stabilization of ILs upon CO_2 capture. In all cases, the HOMO is destabilized due to the acid-base reaction between the phosphonium cation and the carboxylate anion, as indicated by the positive ΔE. Among the ILs, $[P_{4,4,4,4}][Me_4C_4COO]$ exhibits the smallest ΔE (1.37 eV), which aligns with the most favorable intermediate step discussed earlier. The ΔE values for the other ILs fall within an intermediate range, at the exception of $[P_{4,4,4,4}][TetrazC_1COO]$, $[P_{4,4,4,4}][PhSC_1COO]$, $[P_{4,4,4,4}][2-ClPyCOO]$ and $[P_{4,4,4,4}][2-ClPhC_1OHCOO]$ with higher ΔE. It is in agreement with their highly positive ΔG and the lower basicity of their carboxylate anions. Upon the addition of the ylide to CO_2, a significant stabilization of the HOMOs is observed, leading to a decrease in E(HOMO) by approximately 0.4–0.5 eV compared to the initial state. This decrease indicates that the final state is more energetically favorable compared to the initial state. It aligns with the negative $\Delta_r G°$ values calculated for most ILs, expect for the four previously mentioned ILs, which exhibit almost no reactivity towards CO_2. Only a slightly positive or near-zero variation in E(HOMO) between the final and initial states is noticed which is consistent with the positive $\Delta_r G°$ determined.

The optimized structures of the intermediate step and the final step are shown in Figure S47. In the intermediate state, following the abstraction of the acidic proton by the carboxylate anion, it is possible to observe the newly formed complex between the free pair of IL and the carboxylic acid $[P_{4,4,4,4}][RCOO]$-HOOCR as illustrated in Figure S47 (left). The formation of this complex is driven by the establishment of a hydrogen bond between the negatively charged oxygen atom of the carboxylate and the $-OH$ group of the carboxylic acid. This complex in still present after the addition of the ylide on CO_2 (Figure S47 (right)). In the $[P_{4,4,4,4}][C_{11}COO]$-$HOOCC_{11}$ complex, the distance between the acidic proton and the oxygen atom ($d(OH-OCOO^-)$) is 1.36 Å, while the corresponding angle ($\widehat{OHO}$) is 178.2°, satisfying the hydrogen bond criteria. The values of $d(OH-O_{COO^-})$ and $\widehat{OHO}$ for the other ILs all fall within a similar

range, without any specific correlation between these parameters and the basicity of the carboxylate anion in water.

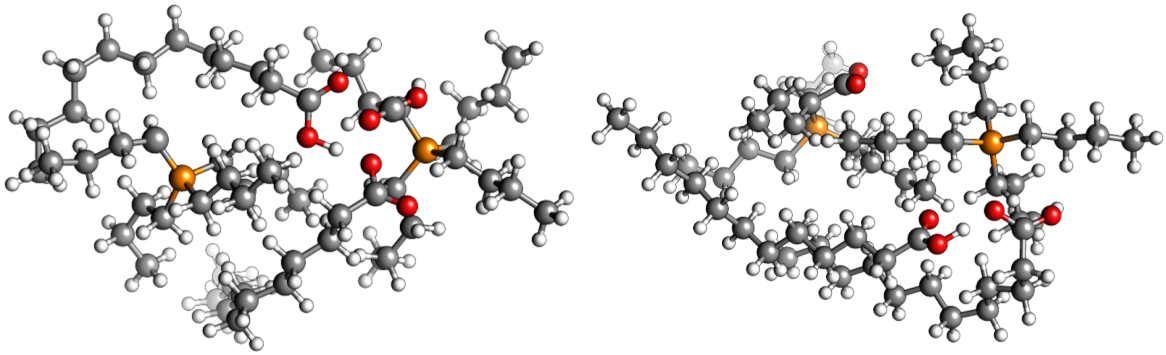

Figure S47 – The most favorable optimized structures of (left) the intermediate state and (right) the product of the reaction between $[P_{4,4,4,4}][C_{11}COO]$ and CO_2 as well as the $[P_{4,4,4,4}][RCOO]$-HOOCR complex.

The peculiar spatial configurations found in the neat ILs containing rings in the carboxylate anions [1] were similar even in presence of CO_2 as depicted on the CDFs of the angle between two adjacent rings as a function of the RDF between their center of mass in the ESI Figure S45.

References

(1) Scaglione, N.; Avila, J.; Bakis, E.; Padua, A.; Gomes, M. C. *Phys. Chem. Chem. Phys.* **2023**, *25*, 15325–15339.

(2) Jacquemin, J.; Ge, R.; Nancarrow, P.; Rooney, D. W.; Costa Gomes, M. F.; Pádua, A. A. H.; Hardacre, C. *J. Chem. Eng. Data* **2008**, *53*, 716–726.

(3) Goodrich, B. F.; de la Fuente, J. C.; Gurkan, B. E.; Lopez, Z. K.; Price, E. A.; Huang, Y.; Brennecke, J. F. *J. Phys. Chem. B* **2011**, *115*, 9140–9150.

(4) Deng, Y.; Morrissey, S.; Gathergood, N.; Delort, A.-M.; Husson, P.; Costa Gomes, M. F. *ChemSusChem* **2010**, *3*, 377–385.

(5) Baranyai, K. J.; Deacon, G. B.; MacFarlane, D. R.; Pringle, J. M.; Scott, J. L. *Aust. J. Chem.* **204**, *57*, 145–147.

(6) Scaglione, N.; Wylie, L.; Padua, A.; Costa Gomes, M. Improved Reversible and Selective SO2 Absorption by a Stable Phosphonium Carboxylate Ionic Liquid. *ACS Sustainable Chem. Eng.* **2024**, Publisher: American Chemical Society.

(7) Padua, A. H. Cl&Pol. (accessed 2021); `https://github.com/paduagroup/clandpol`.

(8) Wu, B.; Yamashita, Y.; Endo, T.; Takahashi, K.; Castner, E. W. *J. Chem. Phys.* **2016**, *145*, 244506.

(9) Gurau, G.; Rodríguez, H.; Kelley, S. P.; Janiczek, P.; Kalb, R. S.; Rogers, R. D. Demonstration of Chemisorption of Carbon Dioxide in 1,3-Dialkylimidazolium Acetate Ionic Liquids. *Angew. Chem. Int. Ed.* **2011**, *50*, 12024–12026.

(10) Lepre, L. F.; Szala-Bilnik, J.; Pison, L.; Traïkia, M.; Pádua, A. a. H.; Ando, R. A.; Gomes, M. F. C. Can the tricyanomethanide anion improve CO2 absorption by acetate-based ionic liquids? *Phys. Chem. Chem. Phys.* **2017**, *19*, 12431–12440.

6

INFLUENCE OF CARBOXYLATE ANION BASICITY ON SO_2 ABSORPTION IN CARBOXYLATE-BASED IONIC LIQUIDS

What to expect

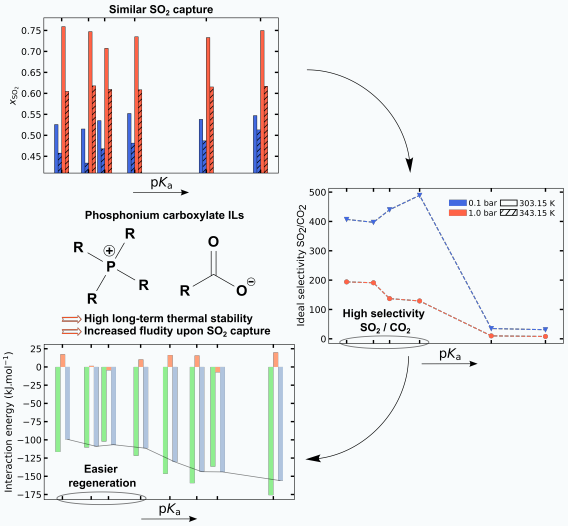

This study provides a comprehensive investigation into the SO_2 absorption by phosphonium carboxylate ILs. Through a combination of experimental measurements and computational simulations, we discovered key insights into the mechanisms driving SO_2 absorption by ILs.

The high selectivity and capture capacity of $[P_{4,4,4,4}][TetrazC_1COO]$ towards SO_2 and the impact of the carboxylate basicity on CO_2 capture triggered our interest to pursue the study on the absorption of SO_2. The ILs were chosen to assess the effect of the anion basicity and its structure as well as the cation size on the SO_2 uptake and the ideal selectivity of SO_2 over CO_2. The pK_a of the corresponding carboxylic acid in water are ranging from 2.07 to 6.51.

The basicity of the carboxylate anion does not significantly influence the SO_2 absorption at both low and high pressures, and at temperatures between 303–343 K. The chemical absorption is predominant at low pressures, while physical absorption becomes more important at higher pressures. FT-IR and NMR measurements supported the proposed SO_2 absorption mechanism observed in prior studies. Thermodynamic analysis of the isotherms indicated that the chemical capture of SO_2 is exothermic and thermodynamically favored, with regeneration of the ILs feasible under mild conditions. The substitution of $[P_{4,4,4,4}]^+$ by a bulkier cation, $[P_{6,6,6,14}]^+$, had a minimal impact on the SO_2 capture capacity. It appeared that the ILs based on the carboxylate anions with the lowest basicity have the highest ideal selectivity of SO_2 over CO_2.

Molecular dynamics simulations provided insights into the solvation of SO_2 in ILs, showing that SO_2 molecules are preferentially solvated in the polar domains of the ILs, at the vicinity of the carboxylate head of the anion.

Overall, this work contributes to a deeper understanding of the factors governing SO_2 absorption in ILs and provides valuable insights for the design of efficient and economically viable SO_2 capture systems.

Journal Name

ARTICLE TYPE

Cite this: DOI: 00.0000/xxxxxxxxxx

Influence of Carboxylate Anion Basicity on SO_2 Absorption in Phosphonium Carboxylate Ionic Liquids †

N. Scaglione,[a] A. Padua*[a] and M. Costa Gomes*[a]

Received Date
Accepted Date

DOI: 00.0000/xxxxxxxxxx

This study explores how the basicity of carboxylate anions and the size of the phosphonium cations affect the absorption of sulfur dioxide (SO_2) in phosphonium carboxylate ionic liquids (ILs). SO_2 absorption capacity was measured at temperatures between 303–343 K up to approximately 1 bar, revealing a combination of thermodynamically favored chemical and physical absorption processes. Surprisingly, both the carboxylate anion basicity and the alkyl chain length of the phosphonium cation had minimal impact on total SO_2 uptake, but it was crucial for reversibility and also to reach a high ideal selectivity of SO_2 over CO_2. *Ab initio* studies supported the favorable thermodynamics of the chemical reaction between the anion and SO_2. Molecular dynamics simulations showed that the SO_2 solvation was not impacted by anion basicity or cation size.

1 Introduction

Sulfur dioxide (SO_2) poses significant environmental and health concerns due to its role as a major air pollutant emitted from various industrial processes, including fossil fuel combustion and metal smelting. New effective mitigation strategies for SO_2 emissions are crucially needed to safeguard both environmental quality and public health.

Conventional flue-gas desulfurization (FGD) processes use organic solvents often based on ammonia,[1] limestones,[2] or seawater.[3] However, these methods suffer from drawbacks such as low performance, high cost, generation of large amounts of wastewater, production of undesirable byproducts, and the emission of volatile organic compounds, which hinder their application and sustainability.

Ionic Liquids (ILs) have emerged as promising alternative absorbents due to their unique properties. The customizable nature of ILs, stemming from their chemical structures, allows the tailoring of their physical and chemical properties by choosing a specific combination of cation and anion and also by the possibility to functionalize them.

The low partial pressure of SO_2 in flue gases (up to 2×10^{-3} atm) necessitates the development of efficient absorbents. While many ILs demonstrate excellent physisorption of SO_2, achieving high absorption capacity often requires a large SO_2 partial pressure and extended equilibration times, posing limitations in real processes. Therefore, a chemical reaction between the IL and SO_2 becomes essential to enhance absorption capacity.

The first reported reactive IL for SO_2 capture, 1,1,3,3-tetramethylguanidinium lactate ([TMG][Lac]), was able to react with SO_2 through the cation, leading to a reaction with a 1:1 stoichiometry,[4] but slow mass transport and high viscosity limited its application. The acidic properties and high polarity of SO_2 suggest that basic functionalities should be incorporated into ILs to increase absorption capacity.[5,6] Subsequent research focused on synthesizing ILs with basic and electron-rich anions, which appeared to enhance SO_2 absorption.[7,8] However, challenges in desorbing SO_2 remain,[9,10] underscoring the importance of the careful design of ILs.

It is possible to create new interaction sites with SO_2, through physical contribution, by including extra functional groups into the IL, such as carbonyl,[11,12] phenyl,[13] halogen[14] or nitrile.[15] The introduction of a second chemical active sites by using, for example, pyridinecarboxylate anions ($[PyCOO]^-$), appears as a promising way to improve SO_2 capture.[16] It seems that the anions play a key role in SO_2 capture while cations have a secondary role if they do not carry reactive sites.

The basicity of the anion in carboxylate-based ILs appears to be an important factor to take into account for SO_2 uptake, but it is not determinant.[17] Indeed, the SO_2 absorption capacity does not increase necessarily with the basicity of the anion ($[Lac]^- > [C_1COO]^- > [HCO_3]^-$)[18] and a medium basicity seems to be optimal for SO_2 absorption.[19] The introduction of electron-withdrawing groups appears to be a promising way to adjust the basicity of the anions with for example a hydroxyle[20] or a carbonyl group next to the reactive site. The enhancement seems to be very effective on various anions such as *o*-phtalimidate $[Phth]^-$, diacetamide $[DAA]^-$,[11] but much less efficient on phe-

[a] *Laboratoire de Chimie, ENS de Lyon and CNRS, 46 Allée D'Italie, Lyon 69364, France. E-mail: margarida.costa-gomes@ens-lyon.fr*

† Electronic Supplementary Information (ESI) available: [details of any supplementary information available should be included here]. See DOI: 00.0000/00000000.

nolate $[PhO]^-$ or benzoate $[PhCOO]^-$, for instance.[12] It is probably due to the weak basicity of these two last anions, indicating that the presence of a electron-withdrawing group on a moderately basic carboxylate anion is not very efficient. More particularly, tetraalkylphosphonium carboxylate ILs have been reported to have a favorable properties for SO_2 capture through the direct reaction of the carboxylate anion on SO_2.[21]

We have recently analysed how the nature of carboxylate anions determine the CO_2 capture capacity of phosphonium-based ILs as reversible CO_2 absorbent. An increase of the CO_2 capture capacity with the pK_a of the conjugated carboxylic acid in water of the carboxylate anion has been found.[22] Among them, tetrabutylphosphonium 1H-tetrazole-1-acetate ($[P_{4,4,4,4}][TetrazC_1COO]$) exhibited a promising selective and reversible absorption of SO_2 over CO_2 at low pressures.[23] As the absorption mechanism of these two acid gases follow different pathways, we propose to assess the effect of the basicity of the carboxylate anion on SO_2 absorption and to design ILs with increase SO_2 selectivity.

2 Experimental methods

2.1 Materials

The ionic liquids studied are: tetrabutylphosphonium 2-chloropyridine-3-carboxylate, $[P_{4,4,4,4}][2-ClPyCOO]$; tetrabutylphosphonium 2-(2-chlorophenyl)-2-hydroxyacetate, $[P_{4,4,4,4}][2-ClPhC_1OHCOO]$; tetrabutylphosphonium (phenylthio)acetate, $[P_{4,4,4,4}][PhSC_1COO]$; tetrabutylphosphonium phenylacetate, $[P_{4,4,4,4}][PhC_1COO]$;tetrabutylphosphonium hexanoate, $[P_{4,4,4,4}][C_5COO]$; tetrabutylphosphonium dodecanoate, $[P_{4,4,4,4}][C_{11}COO]$; trihexyltetradecylphosphonium dodecanoate $[P_{6,6,6,14}][C_{11}COO]$; tetrabutylphosphonium 2,2,4,4-tetramethylpentanoate $[P_{4,4,4,4}][Me_4C_4COO]$; trihexyltetradecylphosphonium 2,2,4,4-tetramethylpentanoate $[P_{6,6,6,14}][Me_4C_4COO]$ (Table 1). They were synthesized and characterized as described previously.[22,24]

Table 1 Chemical structures and abbreviations of the two cations and the seven anions used in this study. The indicated pK_a corresponds to the one of the corresponding carboxylic acid in water.

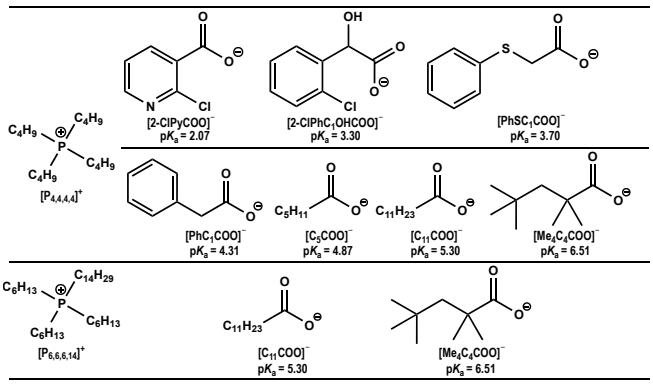

2.2 Gas absorption measurements

The SO_2 absorption of ILs were measured using an *in-house* built apparatus which is based on an isochoric saturation method. The experiments were carried out up to approximately 1 bar, at 5 different temperatures between 303.15 K and 343.15 K under a fume hood. The setup has been described in detail in a previous work.[25] The same experimental protocol as used for $[P_{4,4,4,4}][TetrazC_1COO]$ was followed.[23]

2.3 NMR measurements

A 400 MHz Bruker Avance III spectrometer, with a broadband probe BBO equipped with a temperature control unit BCU II, was used to record ^1H, ^{13}C, ^{31}P, Correlated Spectroscopy (COSY) and Heteronuclear Single Quantum Correlation (HSQC) NMR spectra and also the self-diffusion coefficients by Diffusion Ordered Spectroscopy (DOSY) at 343 K.

NMR spectra of the neat ILs were reported in previous articles.[22,24] After SO_2 absorption, the sample was transferred inside a high pressure NE-HP10-M Pyrex NMR tubes (thickness 1 mm, rated to 20 bar). NMR spectra were collected in similar conditions with a C_6D_6 sealed glass capillary as internal reference. The COSY and the HSQC spectra were used for the attribution of peaks and only the ones of $[P_{4,4,4,4}][2-ClPhC_1OHCOO]$ are depicted in the ESI Figure S8 and the others are omitted for the sack of clarity.

2.4 Infrared spectroscopy

Infrared (IR) spectroscopy measurements were carried out in the ILs before and after SO_2 absorption. IR also served to infer about the presence of water. The IR spectra of the ILs were obtained in the attenuated total reflection mode (ATR) using a Perkin Elmer Spectrum 65 FT-IR spectrometer. A small amount of solid or a droplet of the IL was placed on the ATR crystal and the measurements were carried out in the wave number range 550–4000 cm^{-1} accumulating 16 scans with a resolution of 1 cm^{-1}.

3 Computational methods

3.1 Molecular dynamics simulations

Molecular dynamics (MD) simulations were performed using the OpenMM code[26] to assess the effect of the presence of SO_2 on the IL microscopic structure as well as the solvation of SO_2 in the IL. The polarizable CL&Pol force field for ionic liquids,[27,28] which is based on the Drude induced-dipole method, was used following similar procedures as described previously for the neat ILs,[24] but also in presence of SO_2.[23] The simulated system consists of 300 ion pairs of the ILs and 300 SO_2 molecules in a periodic cubic box. The fftool[29] and Packmol[30] utilities were used to generate the initial configurations. A specific Nosé-Hoover integrator was used for force fields with Drude induced dipoles at 343.15 K while pressure was kept at 1 bar. Site-site radial distribution functions (RDFs), spatial distribution functions (SDFs) and combined distribution functions (CDFs) were computed with the TRAVIS[31] trajectory analysis package.

The parameters were taken taken either from the CL&Pol force field[27] or from previous studies on phosphonium carboxylate ILs.[22,24] The distance between SO_2 and the all the fragments

was determine with a geometry optimization using dispersion-corrected density functional theory (DFT-D3)[32] at the B97-D3/cc-pVDZ level.[33] Polarizable force field parameters for SO_2 are derived from the Transferable Potentials for Phase Equilibria (TraPPE) force field parameter set.[34]

3.2 *Ab initio* calculations

Density functional theory (DFT) was used to calculate the energy profile of the reaction between the ILs and SO_2 according to a previously described procedure.[23]

Gaussian16[35] has been used to optimize the geometries with a Dunning's double-ζ basis set (cc-pVDZ)[36] and a M062-2X DFT functional.[37] A conductor-like polarizable continuum model (CPCM) was used to represent the solvent effects with the permittivity of n-octanol. Frequency calculations were carried out at the same level and Single-point energy (SPE) calculations were made at a higher level of theory (aug-cc-pVTZ[38]).

The 9 optimized configurations were used to determine the final enthalpy (H) and free energy (G) values for each system with Boltzmann distributions.

The algorithm charge model 5[39] (CM5) has been used to compute the partial atomic charges of the more stable configuration of the IL with up to 5 SO_2. Highest occupied molecular orbitals (HOMOs) were calculated on the same conformer with a conversion of the checkpoint files to cube files with a grid size of 80.

The spin ratio scaled Møller-Plesset second-order perturbation theory (SRS-MP2)[40]/cc-pVTZ[36] method has been used to determine the interaction energies between one pair of IL and up to 5 SO_2 molecules as previously described.[23] The Hartree–Fock (HF) contribution was calculated at a higher level of theory (cc-pVQZ[36]) with a compensation of the basis set superposition error with the Boys and Bernardi counterpoise correction.[41]

4 Results and discussion

To investigate the impact of anion basicity on SO_2 uptake, we selected $[P_{4,4,4,4}]^+$ as cation paired with seven carboxylate anions with aqueous pK_a of the anion ranging from 2.07 to 6.51 from our recently reported library of phosphonium carboxylate ILs.[22,24]

The SO_2 absorption capacity of the phosphonium carboxylate ILs under study are reported in the ESI Table S1 from 303 to 343 K every 10 K at pressures of gas up to 1 bar. They are expressed in different units and are listed in Table S1. Examples of the SO_2 absorption isotherms in $[P_{4,4,4,4}][2-ClPhC_1OHCOO]$ are depicted Figure 1, the isotherms for the other ILs being reported in ESI.

The IL SO_2 absorption isotherms present a large deviation from Henry's law at low pressures suggesting a chemisorption process. Up to 0.5 mole fraction of SO_2 absorbed, chemical absorption predominates, and past this threshold, the isotherms follow Henry's law, indicating a physical absorption at higher pressures. This observation is in agreement with prior findings on $[P_{4,4,4,4}][TetrazC_1COO]$, which was able to capture SO_2 in a 1:1 stoichiometry (IL:SO_2).[23] The SO_2 uptake is decreasing with increasing temperature for all the ILs pointing towards an exothermic gas absorption. This effect is more pronounced at higher pressures, indicating a greater sensitivity of physical absorption

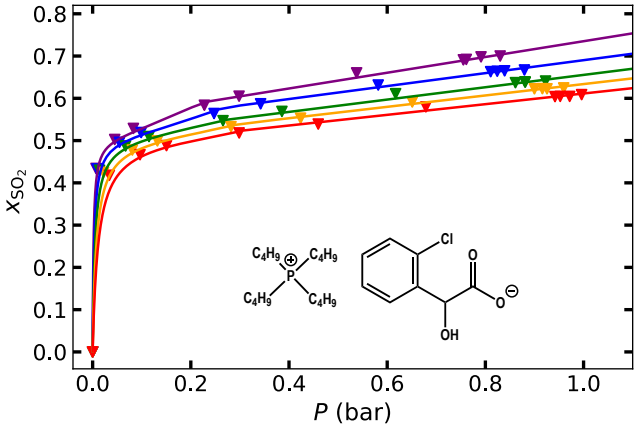

Figure 1 SO_2 absorption isotherms of $[P_{4,4,4,4}][2-ClPhC_1OHCOO]$ in the pressure range of 0–1 bar at ▼ 303 K, ▼ 313 K, ▼ 323 K, ▼ 333 K and ▼ 343 K. The solid lines represent fits of the model previously described[23] to the SO_2 absorption isotherms.

to temperature variation.

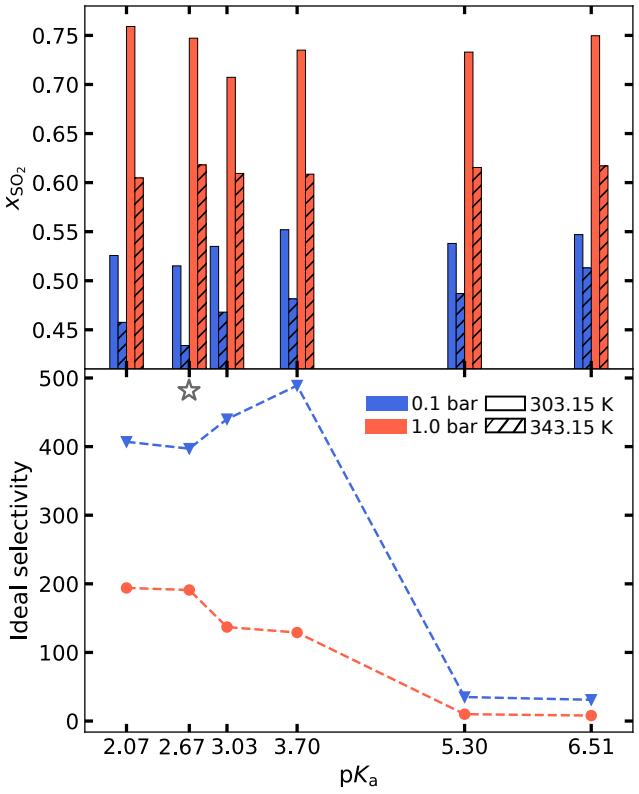

Figure 2 (Top) SO_2 capture capacity of the ILs at 303 (plain bars) and 343 K (textured bars) and (bottom) the ideal selectivity of SO_2/CO_2 at 343 K, calculated as the ratio of quantity of gas absorbed at ■ 0.1 and ■ 1 bar as a function of pK_a. ☆ highlights $[P_{4,4,4,4}][TetrazC_1COO]$ which is used for comparison.[23]

As observed in Figure 2 (top), the basicity of the carboxylate anion does not significantly influence the SO_2 uptake ($2.07 <$ pK_a < 6.51) as suggested by the similar SO_2 absorption capacity

at both low and high pressures for all the temperatures in all the ILs.

To verify if the gas is being absorbed following the previously reported mechanism,[23] the products of the reaction were identified by FT-IR measurements as depicted in Figure 4 for $[P_{4,4,4,4}][2-ClPhC_1OHCOO]$ and in the ESI Figure S3 for all the other ILs.

The bands associated to the $[P_{4,4,4,4}]^+$ cation are unaltered, whereas the characteristic symmetric and asymmetric stretching bands of COO^- (at about 1346 and 1631 cm^{-1}, respectively) disappeared which confirms the reaction of SO_2 with the anion. The direct addition of the negatively charged oxygen of the anion O_{COO^-} on S_{SO_2} is evidenced by the apparition of new bands at 882 and 1733 cm^{-1} attributed to the stretching of $C-OSO_2^-$ and of C=O in the newly formed $COO-SO_2^-$ moiety, respectively. Two other bands related to the symmetric and asymmetric stretching of SOO^- are located at 986 and 1221 cm^{-1}, proving the formation of the adduct as illustrated in orange in Figure 3.

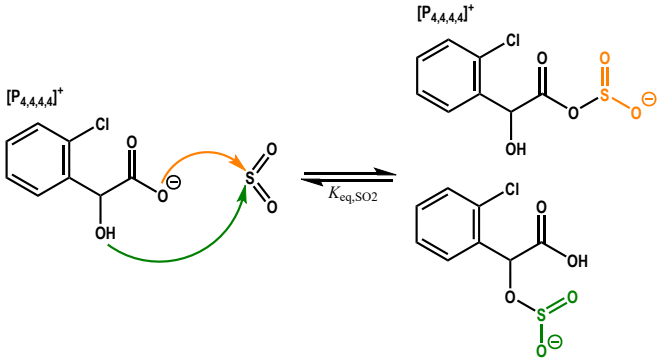

Figure 3 SO_2 absorption mechanism by $[P_{4,4,4,4}][2-ClPhC_1OHCOO]$. The direct reaction of O_{COO^-} on S_{SO_2} (in orange) is similar for all the ILs under study,[23] whereas the direct addition of O_{OH} (in green) in specific to this IL.

The presence of free solvated SO_2 was identified by the apparition of 2 new bands at 1145 and 1325 cm^{-1} assigned to the symmetric and asymmetric stretching of the S=O bonds, respectively.[42] This observation is directly associated to a signal at 2459 cm^{-1} originating from hydrogen bonds between O_{SO_2} and the acidic proton located of the α-carbon (H_α) of the $[P_{4,4,4,4}]^+$ cation. This is supported by the up-field shift of H_α from 2.04 to 1.93 ppm in the ^1H NMR spectrum of $[P_{4,4,4,4}][2-ClPhC_1OHCOO]$ depicted in Figure 5.

A particular feature has been observed in the FT-IR spectra of $[P_{4,4,4,4}][2-ClPhC_1OHCOO]$ in Figure 4 (bottom). The large band at 3240 cm^{-1} which is attributed to the O−H bond disappeared after reacting with SO_2. This modification was also noticed by comparison of the ^1H spectrum before and after absorption of SO_2 in Figure 5. The peak (labeled 3) related to the alcohol function at 5.54 ppm was not present after SO_2 exposure while a new peak appeared at 9.81 ppm. It is the result of the direct addition of O_{OH} on S_{SO_2} as depicted in Figure 3. It consequently induces a large shift of the signal of the proton (labeled 2) due to the important modification of the chemical environment.

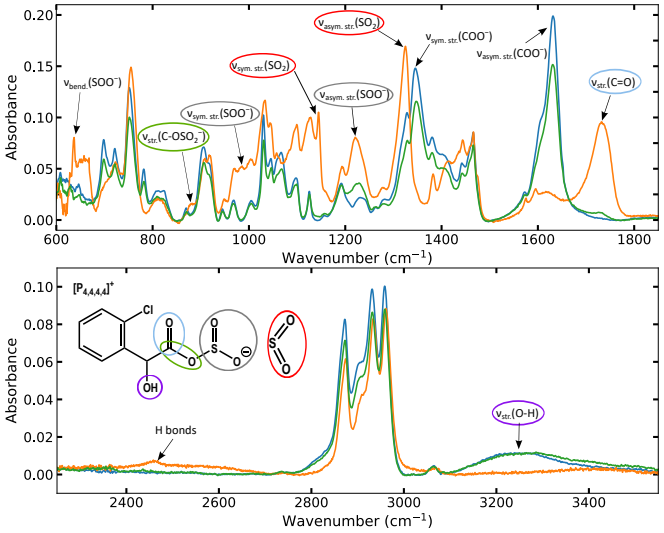

Figure 4 FT-IR spectra of — the neat $[P_{4,4,4,4}][2-ClPhC_1OHCOO]$, — after being exposed to SO_2 and — after being regenerated under vacuum at 343 K for 72 h. Bend. stands for bending; str. for stretching; sym. for symmetric and asym. for asymmetric.

The other peaks of the ^1H NMR spectrum (Figure 5), attributed to both the phosphonium cation the anion, are shifted down-field. It indicates a decrease in electron density, likely due to the strong electrophilic nature of S_{SO_2}. Similar features were found in the ^1H NMR spectra of the other ILs (reported in ESI), confirming that they all follow a similar SO_2 absorption mechanism.

The comparison of the ^{13}C and ^{31}P NMR spectra of all the ILs (plotted in ESI) before and after SO_2 capture only show shifts of the peaks induced by the presence of solvated SO_2 and the formation of a new adduct modifying the chemical environment. For all the anions, the signal of the α-carbon (C_α) is shifted up-field. Whereas the C_{COO^-} peak is shifted down-field for almost all the ILs, which is in agreement with what we reported for $[P_{4,4,4,4}][TetrazC_1COO]$.[23] A up-field shift of the signal related to C_{COO^-} is only noticed in $[P_{4,4,4,4}][2-ClPhC_1OHCOO]$, similarly to what was previously observed for other phosphonium carboxylate ILs.[14,20,43,44]

Based on the NMR and IR spectroscopy, the SO_2 absorption mechanism occurring is similar to that of $[P_{4,4,4,4}][TetrazC_1COO]$. The isotherms are consequently adjusted assuming a 1:1 reaction mechanism.[23] The resulting equilibrium constants K_{eq,SO_2} and Henry's law constants K_{H,SO_2} are reported in Table 2.

K_{H,SO_2} of all the ILs are increasing with temperature as expected for the exothermic physical absorption of gases. This is also confirmed by the negative enthalpies of solvation ($\Delta_{solv}H°(SO_2)$) calculated by using the van't Hoff equation reported in the ESI Table S2. Considering the ILs with $[P_{4,4,4,4}]^+$ as cation, all the K_{H,SO_2} fall within the same range showing the minimal impact of the anion structure and basicity on the solvation of SO_2. K_{H,SO_2} is ranging from 4.2 to 5.5 bar at 303 K, and from 7.3 to 9.7 bar at 343 K roughly corresponding to $0.018 < x_{SO_2} < 0.024$, and $0.010 < x_{SO_2} < 0.014$ at 0.1 bar and ten times higher at 1 bar, respectively.

Table 2 Henry's law constant (K_{H,SO_2}) and the equilibrium constant (K_{eq,SO_2}) obtained by fitting the previously described model[23] to the experimental data (Table S1) as well as the related thermodynamic properties of SO_2 chemisorption at 5 temperatures from 303 K to 343 K.

Sample	$\frac{T}{K}$	K_{eq,SO_2}	$\frac{K_{H,SO_2}}{bar}$	Sample	$\frac{T}{K}$	K_{eq,SO_2}	$\frac{K_{H,SO_2}}{bar}$
	303	185.5 ± 0.6	4.2 ± 0.1		303	252 ± 10	4.3 ± 0.1
	313	154 ± 12	5.1 ± 0.1		313	205 ± 3	5.0 ± 0.1
$[P_{4,4,4,4}][2-ClPyCOO]$	323	121 ± 8	6.1 ± 0.2	$[P_{4,4,4,4}][C_{11}COO]$	323	187 ± 23	5.5 ± 0.1
	333	105 ± 7	7.3± 0.2		333	171 ± 27	6.3 ± 0.1
	343	95 ± 5	8.3 ± 0.3		343	140 ± 23	7.3 ± 0.2
	303	210 ± 11	5.5 ± 0.1		303	259 ± 5	3.9 ± 0.2
	313	169.5 ± 0.1	6.5 ± 0.1		313	218 ± 2	4.6 ± 0.2
$[P_{4,4,4,4}][2-ClPhC_1OHCOO]$	323	141 ± 2	7.1 ± 0.1	$[P_{6,6,6,14}][C_{11}COO]$	323	188 ± 7	5.1± 0.2
	333	115 ± 2	7.4 ± 0.1		333	167 ± 8	6.0 ± 0.2
	343	104.84 ± 0.02	7.9 ± 0.1		343	139 ± 12	6.6 ± 0.2
	303	267.80 ± 0.03	4.6 ± 0.3		303	274.6 ± 0.3	5.0 ± 0.1
	313	239.36 ± 0.02	5.6 ± 0.3		313	244.7 ± 0.2	5.6 ± 0.1
$[P_{4,4,4,4}][PhSC_1COO]$	323	206.62 ± 0.01	6.3 ± 0.3	$[P_{4,4,4,4}][Me_4C_4COO]$	323	211.8 ± 0.1	7.0 ± 0.1
	333	186.68 ± 0.01	7.1 ± 0.4		333	195.1 ± 0.1	8.3 ± 0.1
	343	169.45 ± 0.01	7.6 ± 0.6		343	178.5 ± 0.2	9.7 ± 0.1
					303	272.81 ± 0.02	4.9 ± 0.2
					313	257.54 ± 0.02	5.7 ± 0.1
				$[P_{6,6,6,14}][Me_4C_4COO]$	323	237.38 ± 0.01	6.63 ± 0.03
					333	223.74 ± 0.01	7.8 ± 0.1
					343	203.49 ± 0.01	8.9 ± 0.1

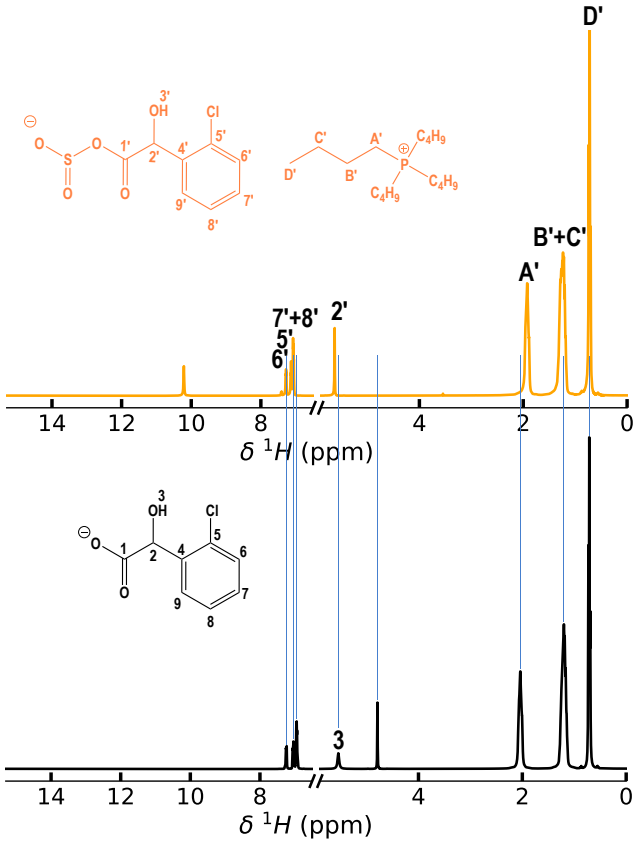

Figure 5 ^1H NMR spectrum of $[P_{4,4,4,4}][2-ClPhC_1OHCOO]$ — before and — after SO_2 absorption at 343 K.

The chemical capture of SO_2 is the result of an exothermic reaction as K_{eq,SO_2} is decreasing with temperature like it was reported for $[P_{4,4,4,4}][TetrazC_1COO]$.[23] It shows that a low temperature is more favorable for SO_2 capture, the gas uptake remaining relatively high even at 343 K. The K_{eq,SO_2} are not increasing linearly with pK_a as the one of $[P_{4,4,4,4}][C_{11}COO]$ is lower than the one of $[P_{4,4,4,4}][PhSC_1COO]$. A clear trend can still be noticed by looking at the ILs with the less and more basic anions ($[P_{4,4,4,4}][2-ClPyCOO]$ and $[P_{4,4,4,4}][Me_4C_4COO]$), with a clear increase of K_{eq,SO_2} from 186 to 273, respectively.

Van't Hoff equation was used to determine the enthalpies of reaction ($\Delta_r H°(SO_2)$) also reported in the ESI Table S2. The negative Gibbs free energies of reaction ($\Delta_r G°(SO_2)$) show that this reaction is thermodynamically favored. The regeneration of the ILs should not be too difficult as the calculated $\Delta_r H°(SO_2)$ are relatively small and negative.

Negative Gibbs free energy and enthalpy of the direct addition of the carboxylate anion on SO_2 ($\Delta G(SO_2)$ and $\Delta H(SO_2)$, respectively) were computed by DFT calculations and the energy profile of the reaction for all the ILs under study are depicted in Figures 6 and S22. Even tough SO_2 absorption capacity of $[P_{4,4,4,4}][PhC_1COO]$ and $[P_{4,4,4,4}][C_5COO]$ were not measured, they were utilized as supplementary compounds in our computational analysis.

The $\Delta G(SO_2)$ and $\Delta H(SO_2)$ of $[P_{4,4,4,4}][Me_4C_4COO]$ (the most basic anion) are equal to −52.3 and −45.3 kJ mol^{-1}, respectively, whereas for $[P_{4,4,4,4}][TetrazC_1COO]$ (one of the less basic anion) they are equal to −8.1 and −12.7 kJ mol^{-1}, respectively. It suggests that increasing the basicity of the carboxylate anion leads to a more favourable and more exothermic reaction with SO_2. It is still worth keep in mind that ranking their reactivity based solely on the calculated $\Delta G(SO_2)$ and $\Delta H(SO_2)$ is difficult due to the uncertainty of the calculations (about 10 kJ mol^{-1}), but a clear trend emerges for the more extreme pK_a.

The reaction between the IL and SO_2 also leads to the stabilization of the Highest Occupied Molecular Orbital (HOMO)

(from approximately −0.4 to −0.6 eV, Table S6) which highlights the likelihood of SO_2 chemical capture. A dispersion of the HOMO over the newly grafted SO_2 on the carboxylate anion is noticed for all the ILs, but they were not represented for the sack of clarity as similar features were previously reported for $[P_{4,4,4,4}][TetrazC_1COO]$.[23] The addition of extra SO_2 molecules, corresponding to the physical absorption of SO_2, is also accompanied by a stabilization of the HOMO, but to a lesser extent.

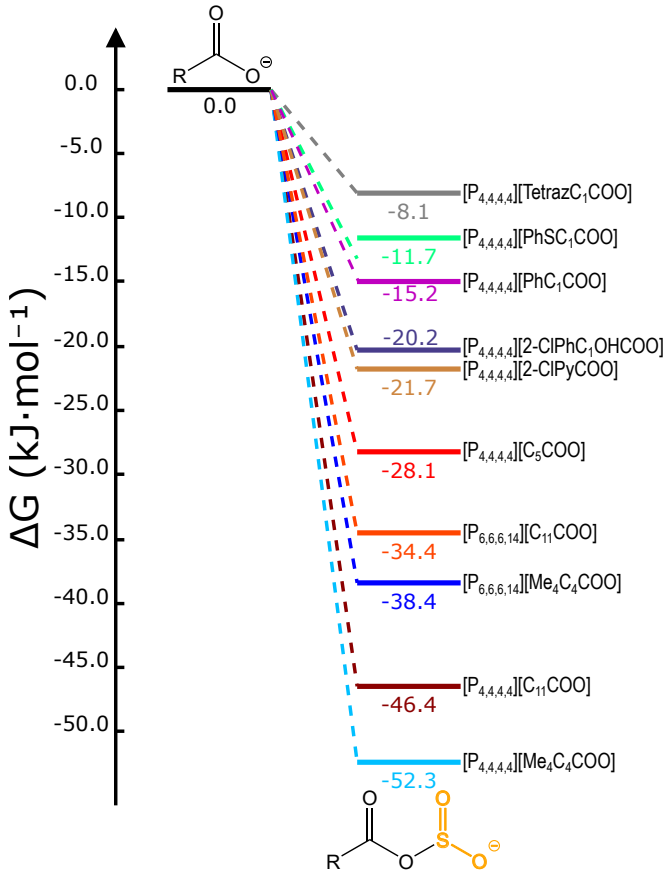

Figure 6 Relative Gibbs Free Energy (GFE) of the reaction between SO_2 and — $[P_{4,4,4,4}][2-ClPyCOO]$, — $[P_{4,4,4,4}][TetrazC_1COO]$,[23] — $[P_{4,4,4,4}][2-ClPhC_1OhCOO]$, — $[P_{4,4,4,4}][PhSC_1COO]$, — $[P_{4,4,4,4}][PhC_1COO]$, — $[P_{4,4,4,4}][C_5COO]$, — $[P_{4,4,4,4}][C_{11}COO]$, — $[P_{6,6,6,14}][C_{11}COO]$, — $[P_{4,4,4,4}][Me_4C_4COO]$ and — $[P_{6,6,6,14}][Me_4C_4COO]$ at 343 K

The analysis of the interaction energies, decomposed into electrostatic and dispersion contributions, between the ILs and SO_2 were carried out using the SRS-MP2 method with the values detailed in ESI Table S5. Figure 7 reveals that there is a clear predominance of the electrostatic interactions for the addition of the first SO_2 in all the ILs with $[P_{4,4,4,4}]^+$ as cation. This is in agreement with the proposed SO_2 absorption mechanism in a 1:1 stoichiometry, suggesting a chemical interaction. Only $[P_{4,4,4,4}][C_{11}COO]$ presents a negative dispersion interaction contribution resulting from the presence of the long dodecyl chain. It is observable by the comparison of its HOMO before and after reaction with SO_2 depicted in the ESI Figure S24 (left) and (middle), respectively. In all the cases, the addition of up to 5 SO_2 molecules lead to a decrease of the electrostatic interactions, while the contribution of dispersion interactions increases as showed in the ESI Figure S23. It shows that the physisorption becomes the main process for more than 1 SO_2 molecule captured.

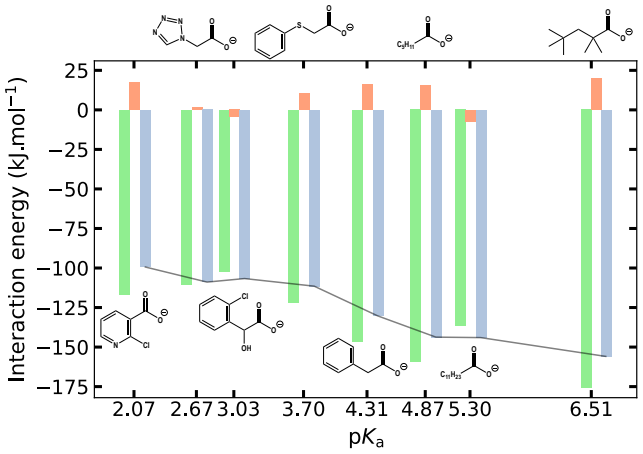

Figure 7 Comparison of the electrostatic, dispersion and total interactions between all the ILs (ranked following the basicity of the carboxylate anion) and 1 SO_2 molecule. The solid line is a guideline to show the variation of the electrostatic interaction energy as a function of the pK_a of the conjugated carboxylic acid in water.

The role of the cation in the SO_2 absorption can be observed by comparing the behaviors of $[P_{4,4,4,4}]^+$-based ILs with $[P_{6,6,6,14}]^+$-based salts. No major changes of the SO_2 capacity capture in mole fraction were observed, even tough a slightly higher uptake is noticed for $[P_{6,6,6,14}][C_{11}COO]$ compared to $[P_{4,4,4,4}][C_{11}COO]$ as depicted in Figure 8 (top). The SO_2 uptake in molality is nonetheless much lower for $[P_{6,6,6,14}]^+$-based ILs compared to their $[P_{4,4,4,4}]^+$ counterparts because of the presence of a bulkier cation.

As expected, the K_{eq,SO_2} determined for these 4 ILs are very similar (Table 2). The K_{H,SO_2} are also comparable which shows that increasing the size of the non-polar domains through longer alkyl chains on the cation is not beneficial for the SO_2 physical absorption. This means that the main interactions are not based on van der Waals (vdW) interactions. The corresponding thermodynamic properties of solvation and reaction are falling in the same range as listed in the ESI Table S2. The increase of the size of the non-polar domains through longer alkyl chains on the cation is not beneficial for the SO_2 physical absorption.

Figure 8 (bottom) shows that longer alkyl side chains on the cations lead to a decrease of the electrostatic contribution to the total interaction energy, while the dispersion contribution is more significant. This stems from the presence of longer alkyl side chains on the phosphonium cation and this effect can be visualized in their HOMOs depicted in ESI Figure S24. This feature is also found upon the addition of up to 5 SO_2 molecules showing stronger dispersion interactions (Figure S23). A similar effect was noticed in $[P_{4,4,4,4}][C_{11}COO]$ by increasing the alkyl chain length of the carboxylate anion.

The impact of the carboxylate basicity on the selective cap-

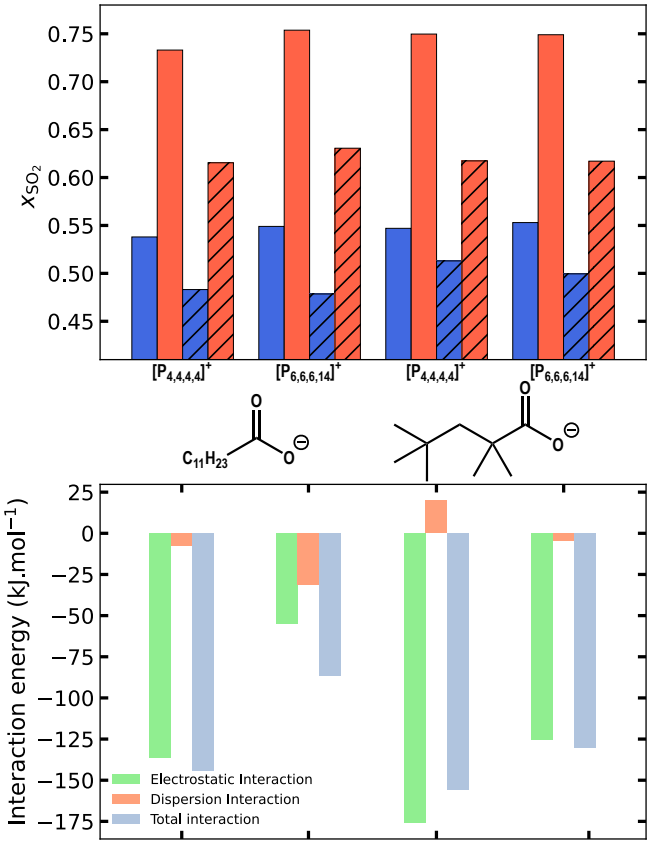

Figure 8 (Top) Influence of the size of the phosphonium cation on the SO_2 capture capacity at 303 (plain bars) and 343 K (textured bars) and at 0.1 and 1 bar. (Bottom) Comparison of the electrostatic, dispersion and total interactions between $[P_{4,4,4,4}][C_{11}COO]$, $[P_{6,6,6,14}][C_{11}COO]$, $[P_{4,4,4,4}][Me_4C_4COO]$, $[P_{6,6,6,14}][Me_4C_4COO]$ and 1 SO_2 molecule.

ture of acidic gases was explored through the determination of the ideal selectivity SO_2 / CO_2 (S) of the ILs under study. It is calculated as the ratio of mole fraction of gas absorbed at a specific temperature and pressure. The CO_2 capture capacity of these phosphonium carboxylate ILs were determined in a previous study.[22] The results are reported in the ESI Table S3 at 0.10, 0.25 and 1.0 bar at different temperatures.

Figure 2 (bottom) shows that at 343 K, the ideal selectivity at 1.0 bar (in orange) decreases as a function of pK_a which underscores the essential role of the carboxylate anion basicity to reach a selective absorption. The increase of S with decreasing pK_a results from the non-reactivity with CO_2 of the ILs containing the less basic carboxylate anions.

On the other hand, S also increases with temperature and this trend is even more significant for carboxylate anions with low basicity and at low pressures (ESI Table S3). This is due to the important decrease of the physical absorption of CO_2 with increasing temperatures for non-reactive ILs. Whereas the chemical capture of SO_2 at low pressures is almost not impacted by the variation of temperature. The variations are in agreement with what was observed for $[P_{4,4,4,4}][TetrazC_1COO]$,[23]

Interestingly, at 0.1 bar, S is not following the same trend for low pK_a carboxylate anions resulting from the higher SO_2 uptake of $[P_{4,4,4,4}][PhSC_1COO]$ and $[P_{4,4,4,4}][2-ClPhC_1OHCOO]$ compared to $[P_{4,4,4,4}][2-ClPyCOO]$ at 0.1 bar. This inversion of trend stems from the more favorable physical absorption of SO_2 in $[P_{4,4,4,4}][2-ClPyCOO]$ at 1.0 bar due to the presence of a second solvation site for SO_2 which will be further discussed later (Figure 10).

Overall, a lower pressure and a higher temperature is beneficial for the selective absorption of SO_2 over CO_2 by phosphonium ILs associated to low pK_a carboxylate anions, while the reverse is usually reported with a higher selectivity at lower temperatures.[21] Although $[P_{4,4,4,4}][TetrazC_1COO]$ was considered as a promising candidate for the selective absorption of SO_2,[23] ILs with even higher selectivity are reported. This increased selectivity at low pressures is crucial for applications, as SO_2 is in a minority in real flue gases.

The ideal selectivity of $[P_{4,4,4,4}][C_{11}COO]$ and $[P_{4,4,4,4}][Me_4C_4COO]$ are different than their $[P_{6,6,6,14}]^+$ counterparts despite their similar SO_2 capacity capture (Table S3). This is the consequence of their particular reactivity towards CO_2. For example, $[P_{4,4,4,4}][Me_4C_4COO]$ exhibits a very high CO_2 uptake at 303 K, whereas the CO_2 capture capacity of $[P_{6,6,6,14}][Me_4C_4COO]$ is much lower at this temperature.[22] Nonetheless, their selectivity remain very low compared to the ILs involving less basic anions showing that the pK_a of the carboxylate anion is the cornerstone of the selective capture of SO_2 over CO_2.

The regeneration of the ILs was assessed by comparing the FT-IR spectra of the ILs before and after SO_2 capture, and also after being placed under primary vacuum at different temperatures. $[P_{4,4,4,4}][2-ClPhC_1OHCOO]$ is used as a representative example (Figure 4) and the other spectra are reported in the ESI Figure S3.

To realise the almost complete regeneration of $[P_{4,4,4,4}][Me_4C_4COO]$, containing the most basic anion, it was necessary to heat it at 343 K for approximately 72 h under primary vacuum, while less basic carboxylate anions required milder conditions. For instance, regeneration of $[P_{4,4,4,4}][2-ClPyCOO]$ and $[P_{4,4,4,4}][2-ClPhC_1OHCOO]$ was achievable faster under primary vacuum at lower temperatures (323 K for 1.5 and 5 h, respectively). Interestingly, the regeneration of $[P_{4,4,4,4}][TetrazC_1COO]$ required a duration intermediate (2 h) between the two previously mentioned, also under primary vacuum at 323 K[23] which is in accordance with the aqueous pK_a of $[TetrazC_1COO]^-$ falling between that of $[2-ClPyCOO]^-$ and $[2-ClPhC_1OHCOO]^-$. This trend was also corroborated by the more difficult regeneration of $[P_{4,4,4,4}][PhSC_1COO]$. Indeed, it was not possible to regenerate it completely under similar conditions probably because of its slightly more basic anion.

The correlation between the basicity of the carboxylate and the difficulty in regenerating the IL after SO_2 capture can be attributed to the increasing interaction energy between the IL and SO_2 with pK_a (Figure 7), as well as the more negative $\Delta H(SO_2)$ calculated for the more basic anion.

The presence of $[P_{6,6,6,14}]^+$ as cation led to an easier regeneration as the SO_2 desorption required less time. For example,

$[P_{4,4,4,4}][C_{11}COO]$ had to be placed under primary vacuum at 323 K for 40 h, while 23 h was sufficient for $[P_{6,6,6,14}][C_{11}COO]$. Similarly, only 48 h was necessary for $[P_{6,6,6,14}][Me_4C_4COO]$ at 343 K. This is reflected by a decrease of the total interaction energy in $[P_{6,6,6,14}]^+$-based ILs (Figure 8), in agreement with the less favorable thermodynamic properties computed by *ab initio* calculations (Figures 6 and S22).

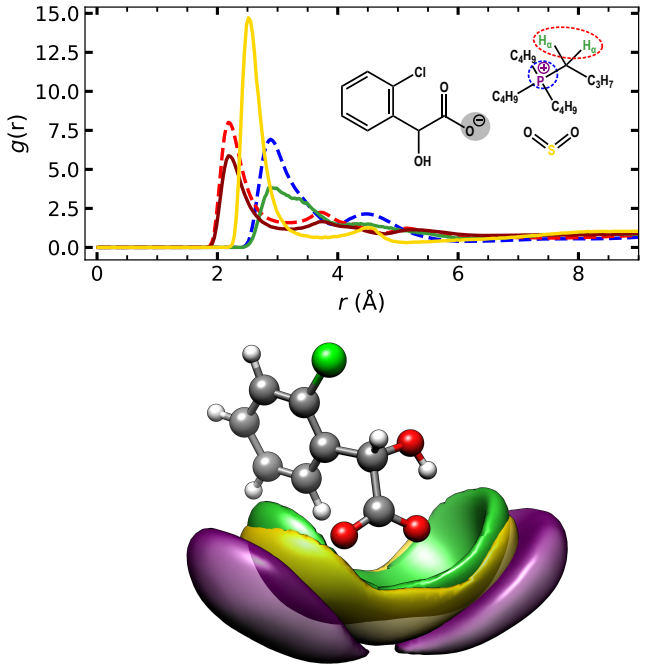

Figure 9 (Top) Site-site radial distribution functions (RDFs), $g(r)$, of – – P^+ and – – H_α of the cation without SO_2, and — P^+ and — H_α of the cation and — S_{SO_2} in presence of SO_2 and around O_{COO^-} of the anion in $[P_{4,4,4,4}][2-ClPhC_1OHCOO]$ at 343 K. (Bottom) The corresponding spatial distribution functions (SDFs) in presence of SO_2 with isodensity contours at 7.1, 7.5, and 10.4 times the average density around the central anion, respectively.

The solvation of SO_2 into these ILs was further explored by MD simulations of the ILs in presence of 300 SO_2 molecules. The comparison of the radial distribution functions (RDFs) in $[P_{4,4,4,4}][2-ClPhC_1OHCOO]$ with and without SO_2 in Figure 9 (top) shows that the presence of SO_2 only leads to a decrease of the coordination numbers (CNs) between P^+ and H_α of the cation around O_{COO^-} of the anion (from 0.91 to 0.68 and from 3.82 to 2.58, respectively), without disruption of the microscopic structure of the IL. This is confirmed by the combined distribution functions (CDFs) of the $C_\alpha{-}H_\alpha\cdots O_{COO^-}$ angle as a function of the distance between H_α of the cation and O_{COO^-} with SO_2 (ESI Figure S20 (left)) in comparison with the ones of the pure ILs previously reported.[22,24]

SO_2 is intercalated between the anion and the cation (with a CN of 0.75) as illustrated by the corresponding spatial distribution functions (SDFs) in Figure 9 (bottom), with S_{SO_2} oriented towards O_{COO^-}. There is also the formation of H-bonds between the solvated SO_2 and the H_α of the cation is clearly visible in the CDFs of the $C_\alpha{-}H_\alpha\cdots O_{SO_2}$ angle as a function of the $H_\alpha\cdots O_{SO_2}$ distance as depicted in ESI Figure S20 (right). A distance of approximately 2.4 Å associated with an angle of 178–180° was found for all the phosphonium carboxylate ILs under study independently of the anion basicity or the cation size, consistent with the previously reported data.[23]

Similar structural features were found in the RDFs of all the ILs under study (ESI Figure S20), which is in agreement with what we previously reported for $[P_{4,4,4,4}][TetrazC_1COO]$.[23]

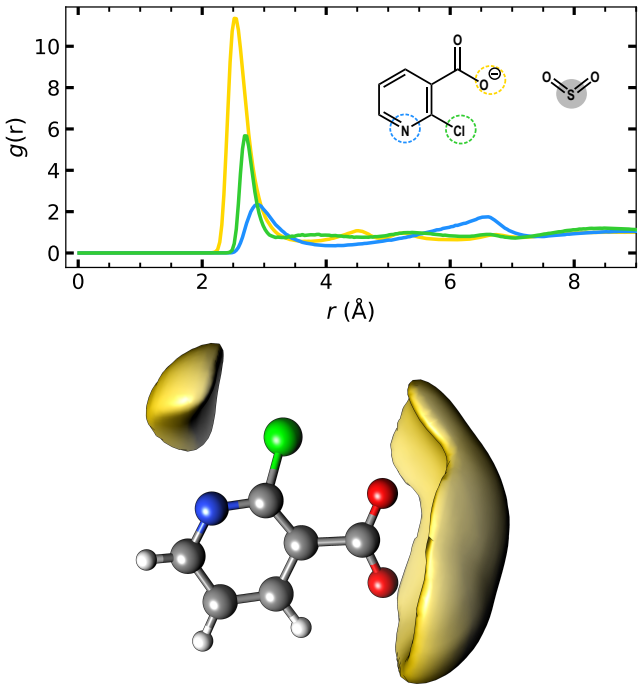

Figure 10 (Top) Site-site radial distribution functions (RDFs), $g(r)$, of S_{SO_2} around — O_{COO^-}, — Cl and — N of the anion in $[P_{4,4,4,4}][2-ClPyCOO]$ at 343 K. (Bottom) The corresponding spatial distribution function (SDFs) of S_{SO_2} around $[2-ClPyCOO]^-$. Isodensity contours at 7.6 times the average density around the central anion.

The secondary interactions previously reported for $[P_{4,4,4,4}][2-ClPyCOO]$ between H_α of the cation and the Cl and N of the anion were not affected by the presence of SO_2,[22] and they were also providing another solvation site for SO_2 as illustrated in Figure 10.

The basicity of the carboxylate anion or the size of the phosphonium does not seem to influence the solvation of SO_2. This is in agreement with the experimental observations as no significant variation of K_{H,SO_2} was noticed by modification of either the cation or the anion.

Similarly to $[P_{4,4,4,4}][TetrazC_1COO]$,[23] the ILs are fluidized by the absorption of SO_2 which is marked by the significant increase of the self-diffusion coefficients of both the anion and the cation (D_{anion} and D_{cation}, respectively) as depicted in Figure S19 with the exact values reported in Table S4 in the ESI. The increase is even more important on the anion, resulting from the fact that SO_2 is preferentially absorbed and solvated around the carboxylate. The confirmation that SO_2 has a fluidifying effect on

this entire family of phosphonium carboxylate ILs, and not only on $[P_{4,4,4,4}][TetrazC_1COO]$, is a major improvement compared to many other ILs that suffer from high viscosity upon SO_2 capture.[21]

5 Conclusions

The total SO_2 uptake is not significantly influenced by neither the basicity of the carboxylate anion nor the size of the phosphonium cation. The absorption of SO_2 is governed by physical and chemical processes, which are both exothermic and thermodynamically favored. Nonetheless, the choice of the carboxylate anion appears to be crucial for the IL regeneration as milder conditions were found for the lower pK_a. It was also determinant to reach a high ideal selectivity of SO_2 over CO_2, with the highest S found for ILs based on the least basic carboxylate anions (with aqueous pK_a below 3.7).

SO_2 molecules are preferentially solvated at the vicinity of the negatively charged head of the carboxylate anions, in the polar areas of the ILs, independently of their basicity. The formation of hydrogen bonds between the acidic H_α of the phosphonium cation and O_{SO_2} favors its solvation. A secondary solvation site was noticed in $[P_{4,4,4,4}][2-ClPyCOO]$ resulting in a slightly higher physical absorption.

An increase of the self-diffusion coefficients of both the cations and the anions was found upon SO_2 capture which overcomes the dramatic increase of viscosity that many other types of ILs suffer from. This is a major improvement as it might facilitate their utilization in real processes.

Overall, the carboxylate anions with lower basicity emerge as preferable candidates for the reversible and selective capture of SO_2, provided it is basic enough to capture SO_2 in significant quantities at low pressures. This study provides valuable insights for the design of efficient and environmentally sustainable technologies for mitigating SO_2 emissions.

Conflicts of interest

Acknowledgements

Notes and references

[1] J. Yang, H. Gao, G. Hu, S. Wang and Y. Zhang, *Energy Fuels*, 2016, **30**, 3205–3218.

[2] F. J. Gutiérrez Ortiz, F. Vidal, P. Ollero, L. Salvador, V. Cortés and A. Giménez, *Ind. Eng. Chem. Res.*, 2006, **45**, 1466–1477.

[3] J. Rodríguez-Sevilla, M. Álvarez, M. C. Díaz and M. C. Marrero, *J. Chem. Eng. Data*, 2004, **49**, 1710–1716.

[4] W. Wu, B. Han, H. Gao, Z. Liu, T. Jiang and J. Huang, *Angew. Chem. Int. Ed. Engl.*, 2004, **43**, 2415–2417.

[5] X. Li, L. Zhang, Y. Zheng and C. Zheng, *Ind. Eng. Chem. Res.*, 2015, **54**, 8569–8578.

[6] S. F. R. Taylor, M. McClung, C. McReynolds, H. Daly, A. J. Greer, J. Jacquemin and C. Hardacre, *Ind. Eng. Chem. Res.*, 2018, **57**, 17033–17042.

[7] K. Huang, J.-F. Lu, Y.-T. Wu, X.-B. Hu and Z.-B. Zhang, *Chem. Eng. J.*, 2013, **215-216**, 36–44.

[8] K. Huang, G.-N. Wang, Y. Dai, Y.-T. Wu, X.-B. Hu and Z.-B. Zhang, *RSC Adv.*, 2013, **3**, 16264–16269.

[9] C. Wang, G. Cui, X. Luo, Y. Xu, H. Li and S. Dai, *J. Am. Chem. Soc.*, 2011, **133**, 11916–11919.

[10] G. Cui, J. Zheng, X. Luo, W. Lin, F. Ding, H. Li and C. Wang, *Angew. Chem. Int. Ed.*, 2013, **52**, 10620–10624.

[11] G. Cui, F. Zhang, X. Zhou, Y. Huang, X. Xuan and J. Wang, *ACS Sustain. Chem. Eng.*, 2015, **3**, 2264–2270.

[12] F. Zhang, G. Cui, N. Zhao, Y. Huang, Y. Zhao and J. Wang, *RSC Adv.*, 2016, **6**, 86082–86088.

[13] G. Cui, W. Lin, F. Ding, X. Luo, X. He, H. Li and C. Wang, *Green Chem.*, 2014, **16**, 1211–1216.

[14] G. Cui, Y. Huang, R. Zhang, F. Zhang and J. Wang, *RSC Adv.*, 2015, **5**, 60975–60982.

[15] G. Cui, F. Zhang, X. Zhou, H. Li, J. Wang and C. Wang, *Chemistry*, 2015, **21**, 5632–5639.

[16] G. Cui, S. Lyu, F. Zhang, H. Wang, Z. Li, Y. Li and J. Wang, *Ind. Eng. Chem. Res.*, 2020, **59**, 21522–21529.

[17] M. B. Shiflett and A. Yokozeki, *Ind. Eng. Chem. Res.*, 2010, **49**, 1370–1377.

[18] X. L. Yuan, S. J. Zhang and X. M. Lu, *J. Chem. Eng. Data*, 2007, **52**, 596–599.

[19] K. Huang, Y.-T. Wu and X.-B. Hu, *Chem. Eng. J.*, 2016, **297**, 265–276.

[20] J. Zhao, S. Ren, Y. Hou, K. Zhang and W. Wu, *Ind. Eng. Chem. Res.*, 2016, **55**, 12919–12928.

[21] L. Wang, Y. Zhang, Y. Liu, H. Xie, Y. Xu and J. Wei, *J. Hazard. Mater.*, 2020, **392**, 122504.

[22] N. Scaglione, J. Avila, A. A. H. Padua and M. C. Gomes, *Faraday Discuss.*, 2024.

[23] N. Scaglione, L. Wylie, A. Padua and M. Costa Gomes, *Submitted*, 2024, **00**, 000–000.

[24] N. Scaglione, J. Avila, E. Bakis, A. Padua and M. C. Gomes, *Phys. Chem. Chem. Phys.*, 2023, **25**, 15325–15339.

[25] J. Jacquemin, M. F. Costa Gomes, P. Husson and V. Majer, *J. Chem. Therm.*, 2006, **38**, 490–502.

[26] P. Eastman, J. Swails, J. D. Chodera, R. T. McGibbon, Y. Zhao, K. A. Beauchamp, L.-P. Wang, A. C. Simmonett, M. P. Harrigan, C. D. Stern, R. P. Wiewiora, B. R. Brooks and V. S. Pande, *PLOS Computational Biology*, 2017, **13**, e1005659.

[27] K. Goloviznina, J. N. Canongia Lopes, M. Costa Gomes and A. A. H. Pádua, *J. Chem. Theory Comput.*, 2019, **15**, 5858–5871.

[28] K. Goloviznina, Z. Gong and A. A. H. Padua, *WIREs Comput. Mol. Sci.*, 2022, **12**, e1572.

[29] A. H. Padua, *fftool v1.2.1*, (accessed 2021), `https://github.com/paduagroup/fftool`.

[30] L. Martínez, R. Andrade, E. G. Birgin and J. M. Martínez, *J. Comput. Chem.*, 2009, **30**, 2157–2164.

[31] M. Brehm, M. Thomas, S. Gehrke and B. Kirchner, *J. Chem. Phys.*, 2020, **152**, 164105.

[32] S. Grimme, J. Antony, S. Ehrlich and H. Krieg, *J. Chem. Phys.*, 2010, **132**, 154104.

[33] A. H. Padua, *Cl&Pol*, (accessed 2021), `https://github.com/paduagroup/clandpol`.

[34] M. H. Ketko, G. Kamath and J. J. Potoff, *J. Phys. Chem. B*, 2011, **115**, 4949–4954.

[35] M. J. Frisch, G. W. Trucks, H. B. Schlegel, G. E. Scuseria, M. A. Robb, J. R. Cheeseman, G. Scalmani, V. Barone, G. A. Petersson, H. Nakatsuji, X. Li, M. Caricato, A. V. Marenich, J. Bloino, B. G. Janesko, R. Gomperts, B. Mennucci, H. P. Hratchian, J. V. Ortiz, A. F. Izmaylov, J. L. Sonnenberg, D. Williams-Young, F. Ding, F. Lipparini, F. Egidi, J. Goings, B. Peng, A. Petrone, T. Henderson, D. Ranasinghe, V. G. Zakrzewski, J. Gao, N. Rega, G. Zheng, W. Liang, M. Hada, M. Ehara, K. Toyota, R. Fukuda, J. Hasegawa, M. Ishida, T. Nakajima, Y. Honda, O. Kitao, H. Nakai, T. Vreven, K. Throssell, J. A. Montgomery, Jr., J. E. Peralta, F. Ogliaro, M. J. Bearpark, J. J. Heyd, E. N. Brothers, K. N. Kudin, V. N. Staroverov, T. A. Keith, R. Kobayashi, J. Normand, K. Raghavachari, A. P. Rendell, J. C. Burant, S. S. Iyengar, J. Tomasi, M. Cossi, J. M. Millam, M. Klene, C. Adamo, R. Cammi, J. W. Ochterski, R. L. Martin, K. Morokuma, O. Farkas, J. B. Foresman and D. J. Fox, *Gaussian~16 Revision C.01*, 2016, Gaussian Inc. Wallingford CT.

[36] T. H. Dunning and P. J. Hay, *Methods of Electronic Structure Theory*, Springer US, Boston, MA, 1977, pp. 1–27.

[37] Y. Zhao and D. G. Truhlar, *Theor. Chem. Account.*, 2008, **120**, 215–241.

[38] E. Papajak, J. Zheng, X. Xu, H. R. Leverentz and D. G. Truhlar, *J. Chem. Theory Comput.*, 2011, **7**, 3027–3034.

[39] A. V. Marenich, S. V. Jerome, C. J. Cramer and D. G. Truhlar, *J. Chem. Theory Comput.*, 2012, **8**, 527–541.

[40] S. Tan, S. Barrera Acevedo and E. I. Izgorodina, *J. Chem. Phys.*, 2017, **146**, 064108.

[41] S. Boys and F. Bernardi, *Molecular Physics*, 1970, **19**, 553–566.

[42] H. Lee, Y. M. Jung, K. I. Lee, H. S. Kim and H. S. Park, *RSC Adv.*, 2013, **3**, 25944–25949.

[43] D. Deng, Y. Jiang and X. Liu, *New J. Chem.*, 2017, **41**, 2090–2097.

[44] L. Wei, Y. Wang, Z. Fan, R. Wang, Y. Wang, J. Chen and Y. Xu, *Chem. Phys. Lett.*, 2019, **724**, 67–72.

Influence of Carboxylate Anion Basicity on SO_2 Absorption in Phosphonium Carboxylate Ionic Liquids

Nicolas Scaglione, Agilio Pádua, and Margarida Costa Gomes*

Laboratoire de Chimie de l'ENS Lyon, CNRS and Université de Lyon, 46 allée d'Italie, 69364 Lyon, France

E-mail: margarida.costa-gomes@ens-lyon.fr

Supplementary Information

1 Gas absorption data

Table S1 – SO_2 absorption expressed in mole fraction (x_{SO_2}) and molality (b_{SO_2}) in the ILs under study as a function of pressure from 0–1 bar at 5 temperatures from 303 K to 343 K.

SO_2 absorption							
$\frac{T}{K}$	$\frac{P}{mbar}$	x_{SO_2}	$\frac{b_{SO_2}}{mmol\ g^{-1}}$	$\frac{T}{K}$	$\frac{P}{mbar}$	x_{SO_2}	$\frac{b_{SO_2}}{mmol\ g^{-1}}$
[$P_{4,4,4,4}$][2 −ClPyCOO]							
303.44	8.49	0.446	1.938	313.35	11.69	0.445	1.927
303.46	94.54	0.523	2.636	313.37	111.45	0.513	2.536
303.45	204.09	0.576	3.270	313.36	238.15	0.561	3.071
303.46	267.09	0.602	3.635	313.37	306.97	0.586	3.408
303.46	384.72	0.646	4.391	313.36	424.04	0.622	3.957
303.44	417.22	0.653	4.526	313.36	456.99	0.628	4.061
303.45	488.17	0.666	4.803	313.36	545.28	0.642	4.304
303.45	695.53	0.704	5.716	313.36	754.47	0.674	4.974
323.25	16.93	0.443	1.909	333.18	24.99	0.439	1.883
323.28	128.75	0.504	2.439	333.20	146.57	0.494	2.344
323.28	271.52	0.546	2.888	333.19	302.13	0.532	2.735
323.29	348.21	0.570	3.185	333.19	385.00	0.556	3.005
323.29	458.35	0.602	3.628	333.20	490.66	0.582	3.347
323.29	491.86	0.607	3.707	333.20	524.37	0.587	3.413
323.28	597.18	0.618	3.896	333.22	643.27	0.598	3.578
323.27	807.86	0.646	4.387	333.20	855.23	0.622	3.950
343.10	37.46	0.434	1.844				
343.12	166.15	0.483	2.243				
343.13	332.08	0.519	2.595				
343.10	421.66	0.541	2.836				
343.13	520.04	0.565	3.126				

SO_2 absorption							
$\frac{T}{\mathrm{K}}$	$\frac{P}{\mathrm{mbar}}$	x_{SO_2}	$\frac{b_{SO_2}}{\mathrm{mmol\,g^{-1}}}$	$\frac{T}{\mathrm{K}}$	$\frac{P}{\mathrm{mbar}}$	x_{SO_2}	$\frac{b_{SO_2}}{\mathrm{mmol\,g^{-1}}}$
343.14	554.39	0.569	3.176				
343.15	681.60	0.583	3.363				
343.09	900.47	0.598	3.575				
$[P_{4,4,4,4}][2-ClPhC_1OHCOO]$							
303.47	6.85	0.434	1.724	313.38	8.87	0.433	1.715
303.46	44.95	0.503	2.270	313.37	54.68	0.496	2.210
303.46	83.00	0.529	2.521	313.39	98.86	0.519	2.425
303.46	227.63	0.584	3.149	313.37	247.35	0.564	2.910
303.45	236.37	0.583	3.148	313.38	255.28	0.566	2.930
303.47	298.28	0.605	3.437	313.37	342.16	0.587	3.189
303.46	537.75	0.660	4.364	313.37	581.70	0.631	3.849
303.45	755.16	0.691	5.036	313.35	810.73	0.663	4.415
303.46	761.07	0.692	5.051	313.36	824.12	0.664	4.440
303.46	791.12	0.698	5.188	313.38	839.15	0.665	4.453
303.45	830.11	0.700	5.233	313.37	879.53	0.667	4.493
323.28	14.10	0.430	1.693	333.21	22.32	0.425	1.660
323.28	67.02	0.487	2.135	333.20	80.86	0.478	2.054
323.29	114.78	0.509	2.334	333.22	131.94	0.499	2.240
323.29	265.59	0.547	2.714	333.17	281.84	0.533	2.565
323.28	274.56	0.548	2.719	333.18	291.20	0.533	2.568
323.28	385.56	0.569	2.961	333.18	423.56	0.553	2.782
323.29	617.13	0.611	3.528	333.20	651.09	0.591	3.251
323.25	861.21	0.637	3.935	333.20	899.93	0.623	3.705
323.29	880.65	0.639	3.974	333.21	916.10	0.623	3.711
323.27	881.17	0.638	3.965	333.16	925.46	0.623	3.705

SO_2 absorption							
$\frac{T}{\mathrm{K}}$	$\frac{P}{\mathrm{mbar}}$	x_{SO_2}	$\frac{b_{SO_2}}{\mathrm{mmol\,g^{-1}}}$	$\frac{T}{\mathrm{K}}$	$\frac{P}{\mathrm{mbar}}$	x_{SO_2}	$\frac{b_{SO_2}}{\mathrm{mmol\,g^{-1}}}$
323.29	922.55	0.641	4.008	333.21	959.50	0.625	3.738
343.09	34.04	0.418	1.613				
343.11	96.53	0.467	1.965				
343.11	150.44	0.488	2.142				
343.09	298.46	0.518	2.417				
343.10	308.07	0.519	2.421				
343.08	459.53	0.539	2.627				
343.07	678.76	0.580	3.099				
343.10	941.79	0.604	3.427				
343.14	952.39	0.605	3.435				
343.11	971.67	0.605	3.435				
343.14	996.00	0.609	3.496				
$[P_{4,4,4,4}][PhSC_1COO]$							
303.45	39.09	0.519	2.530	313.35	47.08	0.514	2.447
303.46	106.64	0.555	2.926	313.36	119.46	0.541	2.760
303.45	114.57	0.557	2.950	313.35	132.63	0.544	2.798
303.46	159.02	0.580	3.234	313.36	184.19	0.567	3.063
303.46	203.27	0.600	3.512	313.36	228.59	0.584	3.283
303.46	312.84	0.639	4.152	313.36	331.91	0.614	3.724
303.47	492.50	0.682	5.014	313.38	522.30	0.653	4.412
303.45	705.13	0.705	5.587	313.36	762.51	0.677	4.417
323.25	56.32	0.501	2.356	333.20	67.33	0.490	2.250
323.27	133.70	0.525	2.585	333.19	147.85	0.508	2.422
323.26	153.79	0.529	2.630	333.18	170.85	0.517	2.511
323.27	211.69	0.552	2.889	333.19	238.43	0.538	2.732

SO_2 absorption							
$\frac{T}{\mathrm{K}}$	$\frac{P}{\mathrm{mbar}}$	x_{SO_2}	$\frac{b_{SO_2}}{\mathrm{mmol\,g^{-1}}}$	$\frac{T}{\mathrm{K}}$	$\frac{P}{\mathrm{mbar}}$	x_{SO_2}	$\frac{b_{SO_2}}{\mathrm{mmol\,g^{-1}}}$
323.29	254.84	0.567	3.066	333.20	280.64	0.550	2.866
323.28	349.32	0.593	3.408	333.21	366.64	0.571	3.113
323.29	549.47	0.629	3.972	333.20	574.42	0.609	3.644
323.26	812.75	0.653	3.590	333.18	862.96	0.628	3.962
343.10	79.21	0.477	2.140				
343.13	160.85	0.494	2.286				
343.08	190.66	0.503	2.372				
343.09	268.25	0.522	2.560				
343.13	305.23	0.534	2.690				
343.12	382.70	0.552	2.887				
343.12	597.33	0.593	3.411				
343.08	909.74	0.605	3.590				
$[P_{4,4,4,4}][C_{11}COO]$							
303.44	3.35	0.423	1.598	313.35	3.53	0.423	1.597
303.45	38.56	0.484	2.045	313.35	44.51	0.482	2.028
303.45	49.17	0.499	2.167	313.36	58.91	0.492	2.110
303.45	92.71	0.535	2.504	313.36	112.05	0.525	2.408
303.43	141.99	0.556	2.726	313.34	168.23	0.546	2.619
303.46	203.48	0.580	3.006	313.36	230.52	0.563	2.811
303.44	310.19	0.609	3.390	313.35	359.09	0.594	3.191
303.43	597.22	0.676	4.553	313.33	657.43	0.654	4.114
303.45	809.33	0.706	5.246	313.35	861.60	0.679	4.613
303.42	827.59	0.712	5.397	313.33	883.40	0.684	4.718
323.25	3.77	0.423	1.597	333.17	4.14	0.423	1.596
323.24	52.34	0.479	2.005	333.15	60.58	0.476	1.983

SO_2 absorption							
$\frac{T}{K}$	$\frac{P}{mbar}$	x_{SO_2}	$\frac{b_{SO_2}}{mmol\ g^{-1}}$	$\frac{T}{K}$	$\frac{P}{mbar}$	x_{SO_2}	$\frac{b_{SO_2}}{mmol\ g^{-1}}$
323.26	65.61	0.488	2.076	333.16	73.50	0.483	2.037
323.26	131.28	0.515	2.319	333.19	150.07	0.506	2.237
323.26	194.50	0.536	2.518	333.16	220.47	0.527	2.425
323.27	254.42	0.549	2.657	333.16	276.23	0.537	2.530
323.27	409.37	0.579	2.997	333.18	457.37	0.565	2.826
323.24	710.52	0.634	3.775	333.15	761.60	0.615	3.476
323.27	905.59	0.659	4.215	333.19	951.06	0.636	3.805
323.22	930.31	0.663	4.283	333.11	977.45	0.639	3.867
343.10	4.81	0.422	1.594				
343.09	69.99	0.473	1.958				
343.14	81.12	0.479	2.002				
343.08	168.15	0.498	2.164				
343.15	245.64	0.518	2.340				
343.04	298.42	0.525	2.407				
343.10	501.32	0.552	2.683				
343.10	804.15	0.601	3.279				
343.08	993.33	0.615	3.487				
343.03	1023.63	0.616	3.496				
$[P_{6,6,6,14}][C_{11}COO]$							
303.45	53.25	0.518	1.571	313.36	62.93	0.507	1.507
303.46	92.56	0.546	1.758	313.37	105.50	0.532	1.662
303.45	109.28	0.553	1.812	313.35	127.03	0.540	1.715
303.46	222.01	0.604	2.236	313.37	245.49	0.585	2.060
303.46	454.03	0.658	2.812	313.35	485.82	0.633	2.530
303.46	458.15	0.659	2.834	313.38	518.99	0.638	2.583

SO_2 absorption							
$\frac{T}{\mathrm{K}}$	$\frac{P}{\mathrm{mbar}}$	x_{SO_2}	$\frac{b_{SO_2}}{\mathrm{mmol\,g^{-1}}}$	$\frac{T}{\mathrm{K}}$	$\frac{P}{\mathrm{mbar}}$	x_{SO_2}	$\frac{b_{SO_2}}{\mathrm{mmol\,g^{-1}}}$
303.46	695.30	0.701	3.427	313.36	743.04	0.675	3.034
323.27	74.86	0.494	1.428	333.17	84.08	0.484	1.375
323.29	117.68	0.519	1.578	333.17	129.12	0.507	1.506
323.24	144.07	0.527	1.628	333.14	160.45	0.514	1.551
323.29	267.26	0.566	1.912	333.21	287.06	0.550	1.792
323.25	511.58	0.610	2.287	333.18	535.56	0.589	2.098
323.29	580.97	0.619	2.380	333.16	640.05	0.601	2.201
323.26	786.46	0.651	2.730	333.17	828.06	0.628	2.470
343.07	93.10	0.475	1.326				
343.13	140.03	0.496	1.443				
343.05	176.22	0.503	1.481				
343.13	305.93	0.536	1.688				
343.07	558.57	0.570	1.939				
343.10	694.62	0.5840	2.052				
343.11	865.23	0.610	2.288				
$[P_{4,4,4,4}][Me_4C_4COO]$							
303.45	48.16	0.524	2.640	313.36	57.75	0.520	2.604
303.44	103.00	0.548	2.911	313.35	122.37	0.541	2.833
303.42	258.93	0.611	3.773	313.34	295.89	0.595	3.522
303.44	270.66	0.614	3.816	313.33	319.54	0.599	3.584
303.43	459.27	0.661	4.681	313.34	524.14	0.641	4.293
303.46	491.36	0.670	4.878	313.36	556.03	0.649	4.430
303.44	751.17	0.709	5.852	313.34	815.98	0.682	5.157
303.44	786.26	0.715	6.017	313.35	839.11	0.686	5.238
323.28	67.65	0.517	2.569	333.20	77.10	0.514	2.537

SO_2 absorption							
$\frac{T}{K}$	$\frac{P}{mbar}$	x_{SO_2}	$\frac{b_{SO_2}}{mmol\ g^{-1}}$	$\frac{T}{K}$	$\frac{P}{mbar}$	x_{SO_2}	$\frac{b_{SO_2}}{mmol\ g^{-1}}$
323.27	141.63	0.535	2.759	333.16	159.98	0.529	2.694
323.25	330.55	0.579	3.306	333.16	360.99	0.567	3.137
323.24	364.20	0.585	3.390	333.19	406.19	0.573	3.221
323.26	584.79	0.623	3.959	333.16	638.16	0.606	3.699
323.27	613.71	0.629	4.071	333.16	667.58	0.611	3.766
323.26	875.03	0.657	4.600	333.16	927.04	0.636	4.189
323.27	887.86	0.658	4.619	333.19	930.86	0.636	4.191
343.10	86.35	0.511	2.508				
343.10	177.33	0.524	2.638				
343.11	389.66	0.555	2.992				
343.08	444.78	0.562	3.079				
343.08	688.32	0.592	3.475				
343.08	717.62	0.594	3.510				
343.10	976.21	0.616	3.847				
343.11	971.69	0.616	3.843				
$[P_{6,6,6,14}][Me_4C_4COO]$							
303.45	35.45	0.509	1.615	313.35	43.50	0.505	1.590
303.45	111.15	0.560	1.988	313.36	130.15	0.549	1.902
303.46	157.15	0.582	2.174	313.37	177.21	0.566	2.037
303.44	169.25	0.584	2.193	313.36	202.85	0.572	2.087
303.43	341.83	0.632	2.679	313.34	395.95	0.612	2.462
303.94	372.06	0.642	2.796	313.36	407.88	0.613	2.471
303.45	559.52	0.669	3.158	313.36	601.52	0.645	2.839
303.45	786.94	0.710	3.827	313.36	835.36	0.683	3.358
323.25	52.28	0.501	1.565	333.15	61.78	0.497	1.539

SO_2 absorption							
$\frac{T}{\mathrm{K}}$	$\frac{P}{\mathrm{mbar}}$	x_{SO_2}	$\frac{b_{SO_2}}{\mathrm{mmol\,g^{-1}}}$	$\frac{T}{\mathrm{K}}$	$\frac{P}{\mathrm{mbar}}$	x_{SO_2}	$\frac{b_{SO_2}}{\mathrm{mmol\,g^{-1}}}$
323.26	148.78	0.539	1.823	333.17	166.08	0.530	1.756
323.28	194.85	0.553	1.930	333.17	211.50	0.541	1.837
323.26	235.70	0.561	1.990	333.18	265.40	0.551	1.910
323.28	438.10	0.590	2.245	333.17	463.68	0.573	2.090
323.26	448.24	0.593	2.268	333.17	490.04	0.578	2.134
323.27	641.95	0.621	2.559	333.18	678.32	0.601	2.347
323.27	879.32	0.658	3.006	333.18	921.56	1.736	2.707
343.05	71.95	0.492	1.512				
343.10	183.28	0.520	1.693				
343.10	226.77	0.530	1.761				
343.09	294.62	0.541	1.837				
343.14	487.21	0.558	1.969				
343.12	531.48	0.563	2.010				
343.07	709.13	0.587	2.213				
343.07	961.19	0.613	2.471				

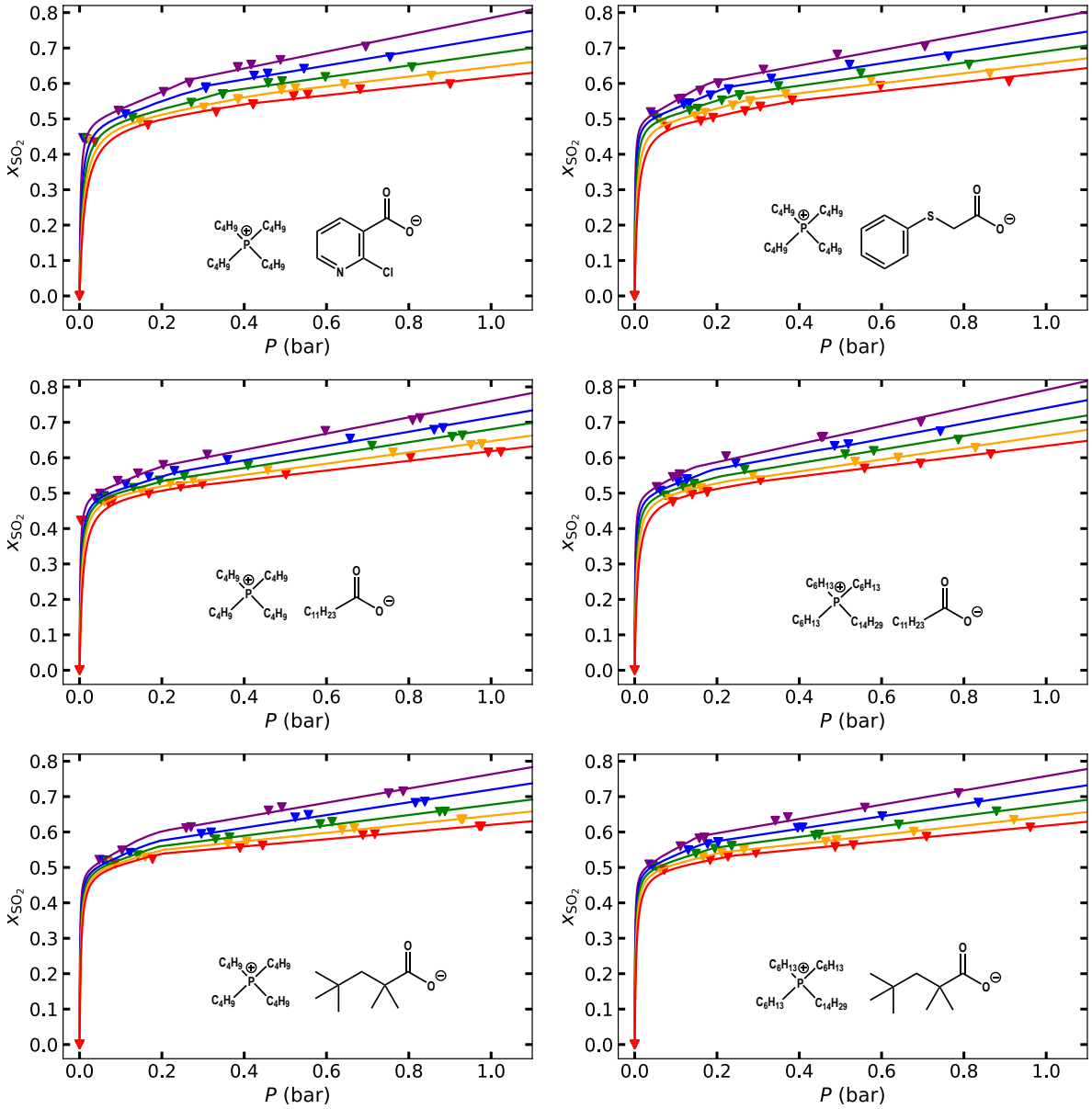

Figure S1 – SO_2 absorption isotherms of (top left) $[P_{4,4,4,4}][2-ClPyCOO]$, (top right) $[P_{4,4,4,4}][PhSC_1COO]$, (middle left) $[P_{4,4,4,4}][C_{11}COO]$, (middle right) $[P_{6,6,6,14}][C_{11}COO]$, (bottom left) $[P_{4,4,4,4}][Me_4C_4COO]$ and (bottom right) $[P_{6,6,6,14}][Me_4C_4COO]$ in the pressure range of 0–1 bar at ▼ 303 K, ▼ 313 K, ▼ 323 K, ▼ 333 K and ▼ 343 K.

Table S2 – Thermodynamic properties of SO_2 reaction and solvation between 303 and 343 K.

Sample	$\frac{T}{K}$	$\frac{\Delta_r H^\circ}{kJ\ mol^{-1}}$	$\frac{\Delta_r G^\circ}{kJ\ mol^{-1}}$	$\frac{\Delta_r S^\circ}{J\ mol^{-1}\ K^{-1}}$	$\frac{\Delta_{solv} H^\circ}{kJ\ mol^{-1}}$	$\frac{\Delta_{solv} G^\circ}{kJ\ mol^{-1}}$	$\frac{\Delta_{solv} S^\circ}{J\ mol^{-1}\ K^{-1}}$
$[P_{4,4,4,4}][2-ClPyCOO]$	303	-11.47	-13.16	5.60	-11.31	-3.62	-25.38
	313	-12.24	-13.12	2.82	-12.07	-4.25	-24.98
	323	-13.03	-12.88	-0.46	-12.85	-4.86	-24.73
	333	-13.85	-12.90	-2.85	-13.66	-5.49	-24.52
	343	-14.69	-12.98	-5.00	-14.49	-6.03	-24.66
$[P_{4,4,4,4}][2-ClPhC_1OHCOO]$	303	-11.79	-13.48	5.56	-5.62	-4.30	-4.36
	313	-12.58	-13.36	2.50	-5.99	-4.89	-3.54
	323	-13.40	-13.30	-0.32	-6.38	-5.28	-3.41
	333	-14.24	-13.14	-3.31	-6.78	-5.55	-3.70
	343	-15.11	-13.27	-5.35	-7.20	-5.88	-3.83
$[P_{4,4,4,4}][PhSC_1COO]$	303	-7.70	-14.09	21.07	-8.35	-3.84	-14.87
	313	-8.22	-14.26	19.30	-8.91	-4.47	-14.16
	323	-8.75	-14.32	17.24	-9.49	-4.94	-14.08
	333	-9.30	-14.49	15.56	-10.08	-5.43	-13.96
	343	-9.87	-14.64	13.92	-10.70	-5.79	-14.28
$[P_{4,4,4,4}][C_{11}COO]$	303	-8.98	-13.94	16.36	-8.71	-3.66	-16.66
	313	-9.58	-13.87	13.68	-9.29	-4.17	-16.36
	323	-10.20	-14.06	11.92	-9.90	-4.58	-16.46
	333	-10.85	-14.24	10.19	-10.52	-5.10	-16.27
	343	-11.51	-14.10	7.56	-11.16	-5.68	-15.95
$[P_{6,6,6,14}][C_{11}COO]$	303	-9.96	-14.01	13.35	-8.75	-3.44	-17.53
	313	-10.63	-14.01	10.82	-9.34	-3.95	-17.23
	323	-11.32	-14.07	8.54	-9.95	-4.39	-17.19
	333	-12.03	-14.19	6.49	-10.57	-4.94	-16.91
	343	-12.76	-14.07	3.83	-11.22	-5.40	-16.95
$[P_{4,4,4,4}][Me_4C_4COO]$	303	-7.21	-14.15	22.90	-11.39	-4.04	-24.24
	313	-7.70	-14.32	21.15	-12.15	-4.49	-24.46
	323	-8.20	-14.39	19.17	-12.94	-5.23	-23.86
	333	-8.71	-14.61	17.70	-13.76	-5.86	-23.69
	343	-9.24	-14.79	16.17	-14.59	-6.48	-23.65
$[P_{6,6,6,14}][Me_4C_4COO]$	303	-4.79	-14.14	30.83	-9.88	-4.01	-19.39
	313	-5.11	-14.45	29.83	-10.55	-4.53	-19.21
	323	-5.44	-14.70	28.63	-11.23	-5.08	-19.03
	333	-5.79	-14.99	27.62	-11.94	-5.68	-18.77
	343	-6.14	-15.17	26.31	-12.66	-6.22	-18.77

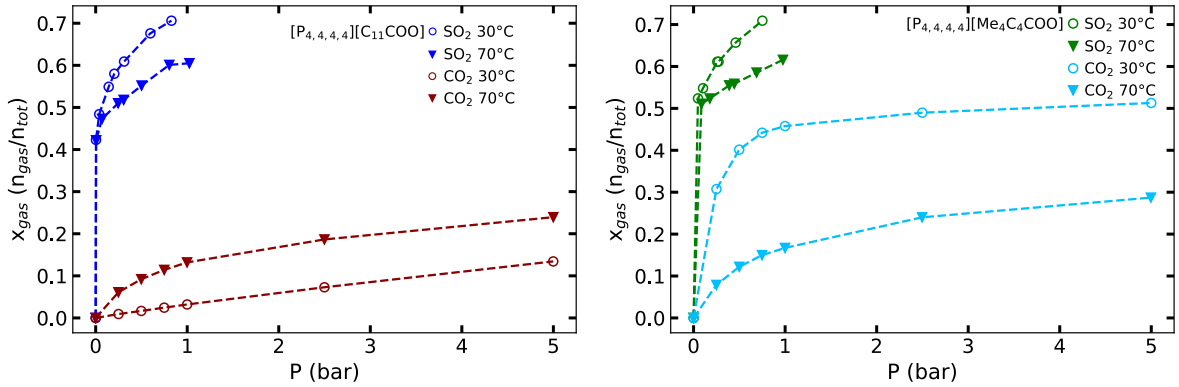

Figure S2 – Comparison of the CO_2 absorption in the pressure range of 0–5 bar[1] and SO_2 absorption in the pressure range of 0–1 bar at 303 K and 343 K for (left) $[P_{4,4,4,4}][C_{11}COO]$ and (right) $[P_{4,4,4,4}][Me_4C_4COO]$.

Table S3 – Ideal selectivity of SO_2 over CO_2 for the ILs under study at 0.10, 0.25 and 1.0 bar at 303, 323 and 343 K calculated as the ratio of mole of gas absorbed at a certain pressure and temperature.

Sample	$\frac{T}{K}$	$S(0.1/0.1)$	$S(0.25/0.25)$	$S(1.0/1.0)$
$[P_{4,4,4,4}][2-ClPyCOO]$	303	303	161	102
	323	396	191	147
	343	407	229	194
$[P_{4,4,4,4}][TetrazC_1COO]$[2]	303	289	150	104
	323	349	176	119
	343	397	215	191
$[P_{4,4,4,4}][2-ClPhC_1OHCOO]$	303	328	162	100
	323	412	185	120
	343	440	206	137
$[P_{4,4,4,4}][PhSC_1COO]$	323	405	199	116
	343	489	226	129
$[P_{4,4,4,4}][C_{11}COO]$	303	64	156	81
	343	35	16	10
$[P_{6,6,6,14}][C_{11}COO]$	303	18	8	5.8
	343	15	6.5	5.4
$[P_{4,4,4,4}][Me_4C_4COO]$	303	6.8	3.5	3.5
	323	12	5.4	3.5
	343	31	13	8.0
$[P_{6,6,6,14}][Me_4C_4COO]$	303	40	20	23
	323	35	17	15
	343	28	13	10

2 FT-IR measurements

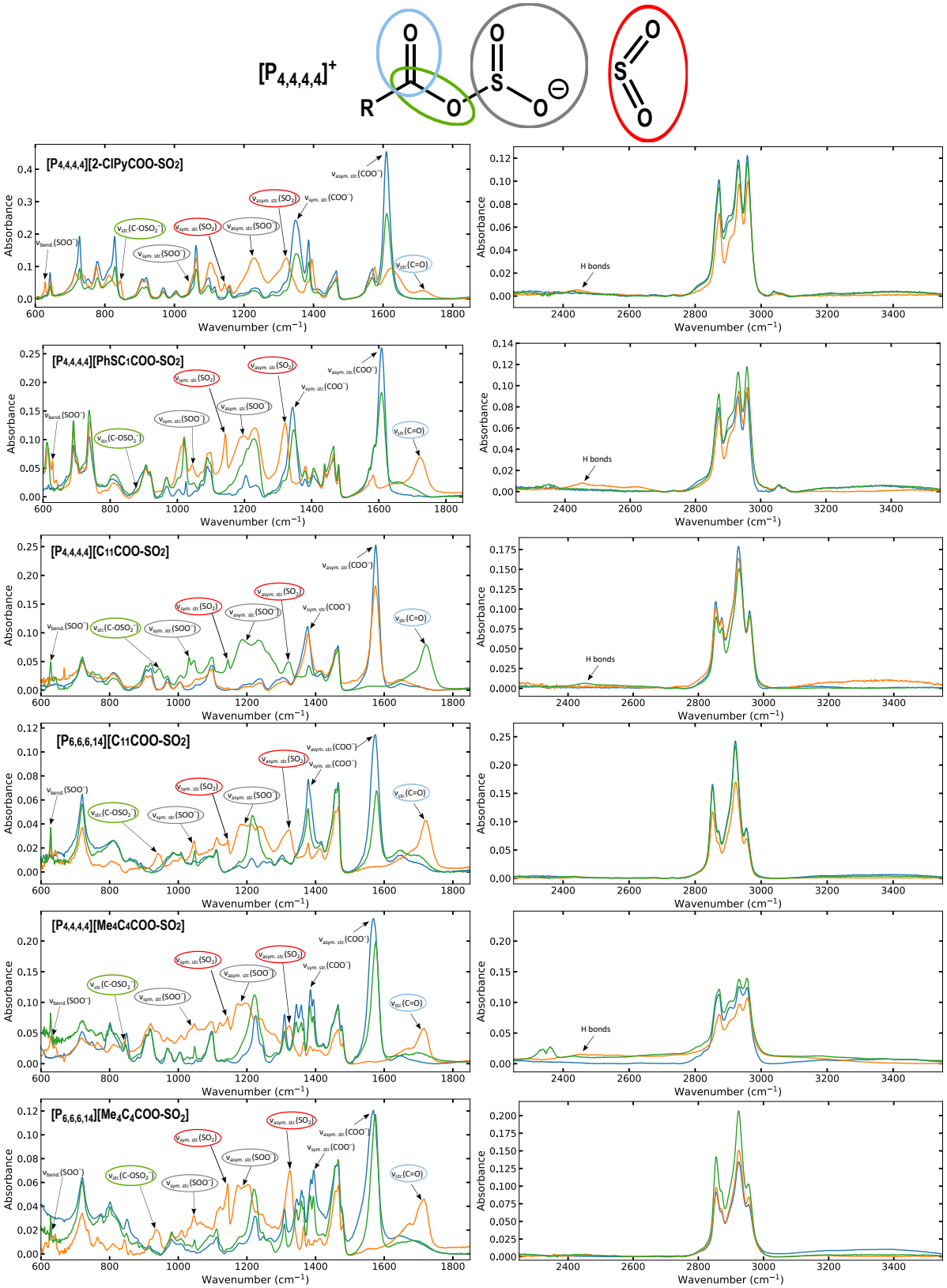

Figure S3 – FT-IR spectra of — the neat ILs, — after being exposed to SO_2 and — after being regenerated under primary vacuum with various conditions. Bend. stands for bending; str. for stretching; sym. for symmetric and asym. for asymmetric.

3 NMR before and after SO_2 absorption

3.1 $[P_{4,4,4,4}][2-ClPyCOO]$

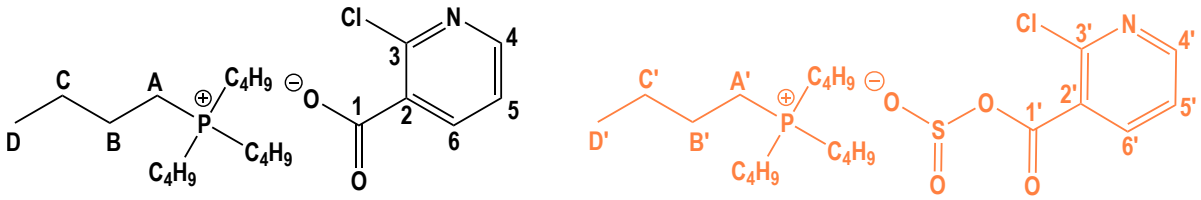

Figure S4 – Chemical structure of the $[P_{4,4,4,4}][2-ClPyCOO]$ (left) before and (right) after SO_2 absorption.

Tetrabutylphosphonium 2-chloropyridine-3-carboxylate $[P_{4,4,4,4}][2-ClPyCOO]$ after SO_2 absorption: ^{1}H NMR (400 MHz, C_6D_6, 343 K) δ ppm: 0.22 (t, 12H, $^{3}J_{HH}$ = 7.2 Hz, D'); 1.38 (m, 8H, C'); 1.53 (m, 8H, B'); 2.24 (m, 8H, A'); 7.34 (t, 1H, $^{3}J_{HH}$ = 5.9 Hz, 5'); 7.81 (d, 1H, $^{3}J_{HH}$ = 7.5 Hz, 6'); 8.26 (m, 1H, 4'). ^{13}C NMR (100 MHz, C_6D_6, 343 K) δ ppm: 11.93 (4C, D'); 17.29 (4C, A'); 22.12 (4C, B'); 22.39 (4C, C'); 121.54 (1C, 5'); 133.51 (1C, 6'); 137.01 (1C, 2'); 146.37 (1C, 3'); 147.45 (1C, 1'). ^{31}P NMR (161 MHz, C_6D_6, 343 K) δ ppm: 33.27 (1P, **P**$((CH_2)_3CH_3)_4$).

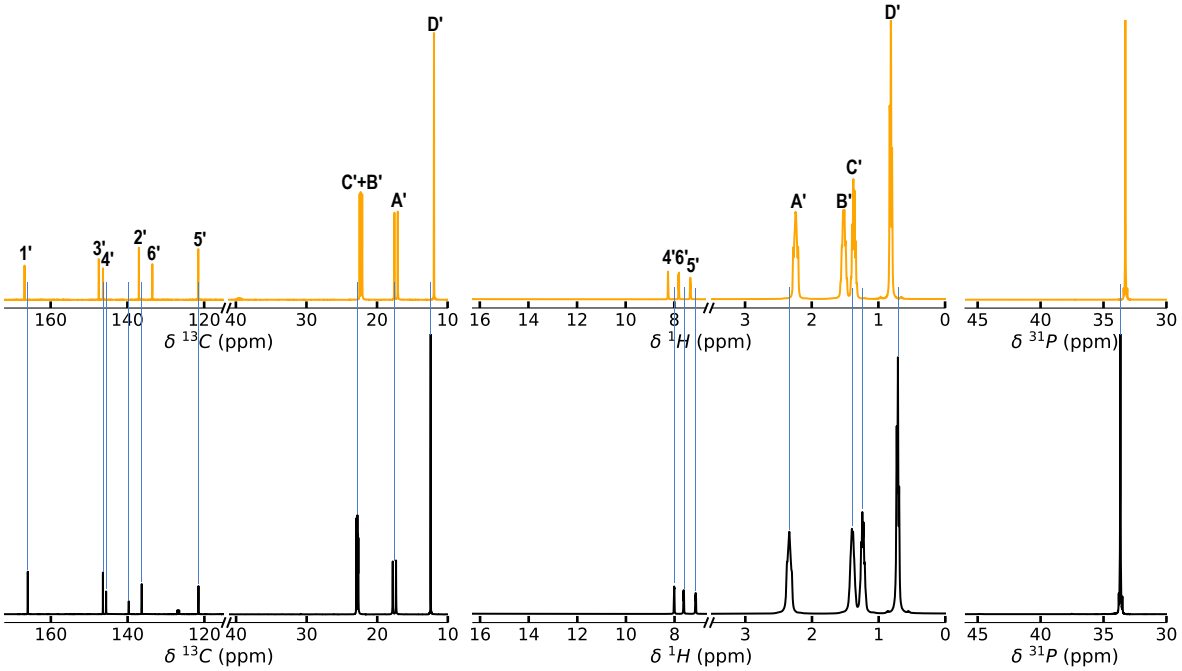

Figure S5 – (Left) ^{13}C, (middle) ^{1}H and (right) ^{31}P NMR spectra of $[P_{4,4,4,4}][2-ClPyCOO]$ — before and — after SO_2 absorption at 343 K.

3.2 $[P_{4,4,4,4}][2-ClPhC_1OHCOO]$

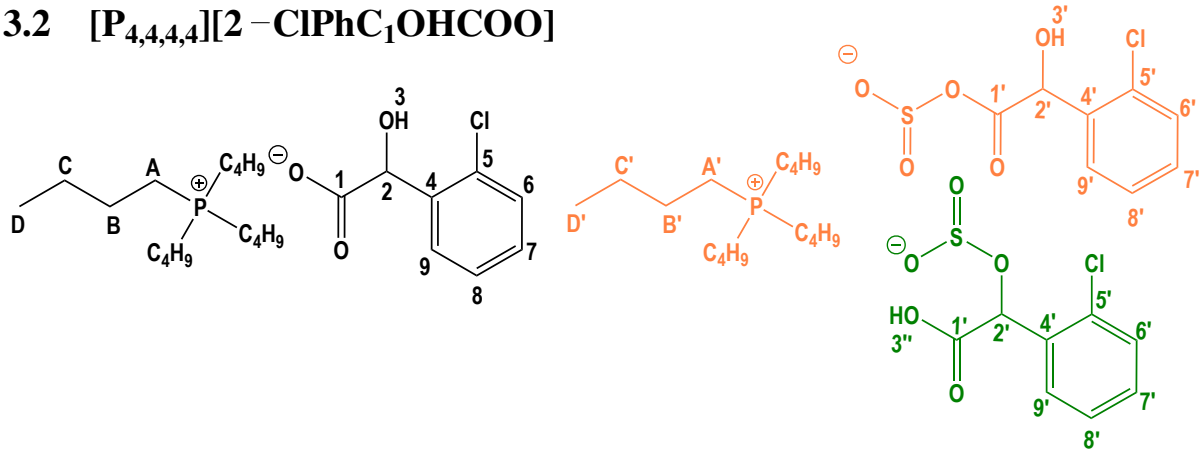

Figure S6 – Chemical structure of the $[P_{4,4,4,4}][2-ClPhC_1OHCOO]$ (left) before and (right) after SO_2 absorption.

Tetrabutylphosphonium 2-(2-chlorophenylacetate)-2-hydroxyacetate $[P_{4,4,4,4}][2-ClPhC_1OHCOO]$ after SO_2 absorption: ^{1}H NMR (400 MHz, C_6D_6, 343 K) δ ppm: 0.72 (t, 12H, $^{3}J_{HH} = 7.0$ Hz, D'); 1.24 (m, 16H, B'+C'); 1.93 (m, 8H, A); 5.63 (s, 1H, 2'); 7.07 (m, 2H, 7'+8'); 7.13 (m, 1H, 5'); 7.28 (m, 1H, 6'); 10.21 (s, 1H, 3''). ^{13}C NMR (100 MHz, C_6D_6, 343 K) δ ppm: 11.87 (4C, D'); 17.00 (4C, A'); 21.92 (4C, C'); 22.28 (4C, C'); 66.13 (1C, 2'); 125.41 (1C, 7'); 127.53 (1C, 8'); 127.68 (1C, 6'); 127.96 (1C, 5'); 132.06 (1C, 4'); 137.49 (1C, 9'); 171.61 (1C, 1'). ^{31}P NMR (161 MHz, C_6D_6, 343 K) δ ppm: 32.88 (1P, **P**$((CH_2)_3CH_3)_4$).

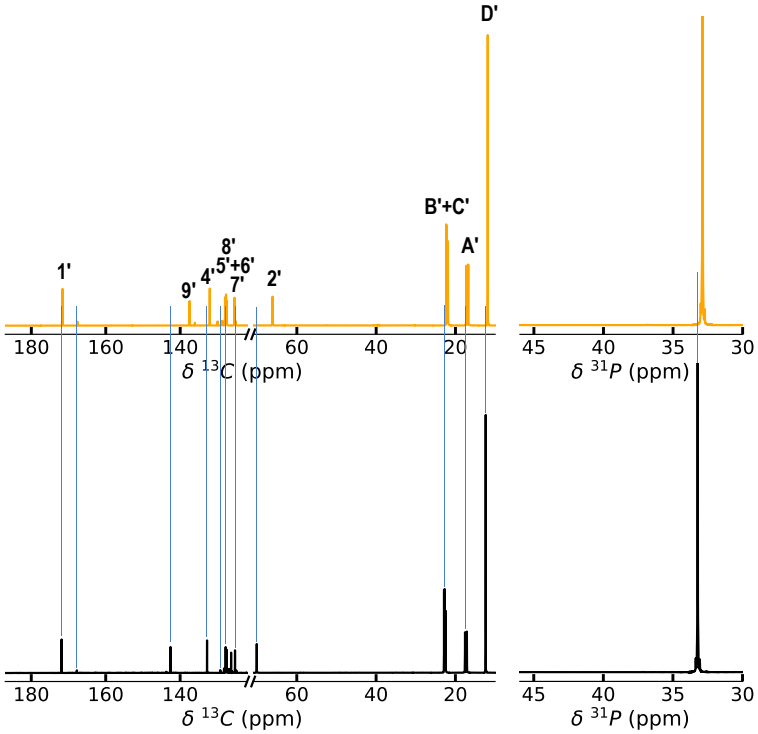

Figure S7 – (Left) ^{13}C and (right) ^{31}P NMR spectra of $[P_{4,4,4,4}][2-ClPhC_1OHCOO]$ — before and — after SO_2 absorption at 343 K.

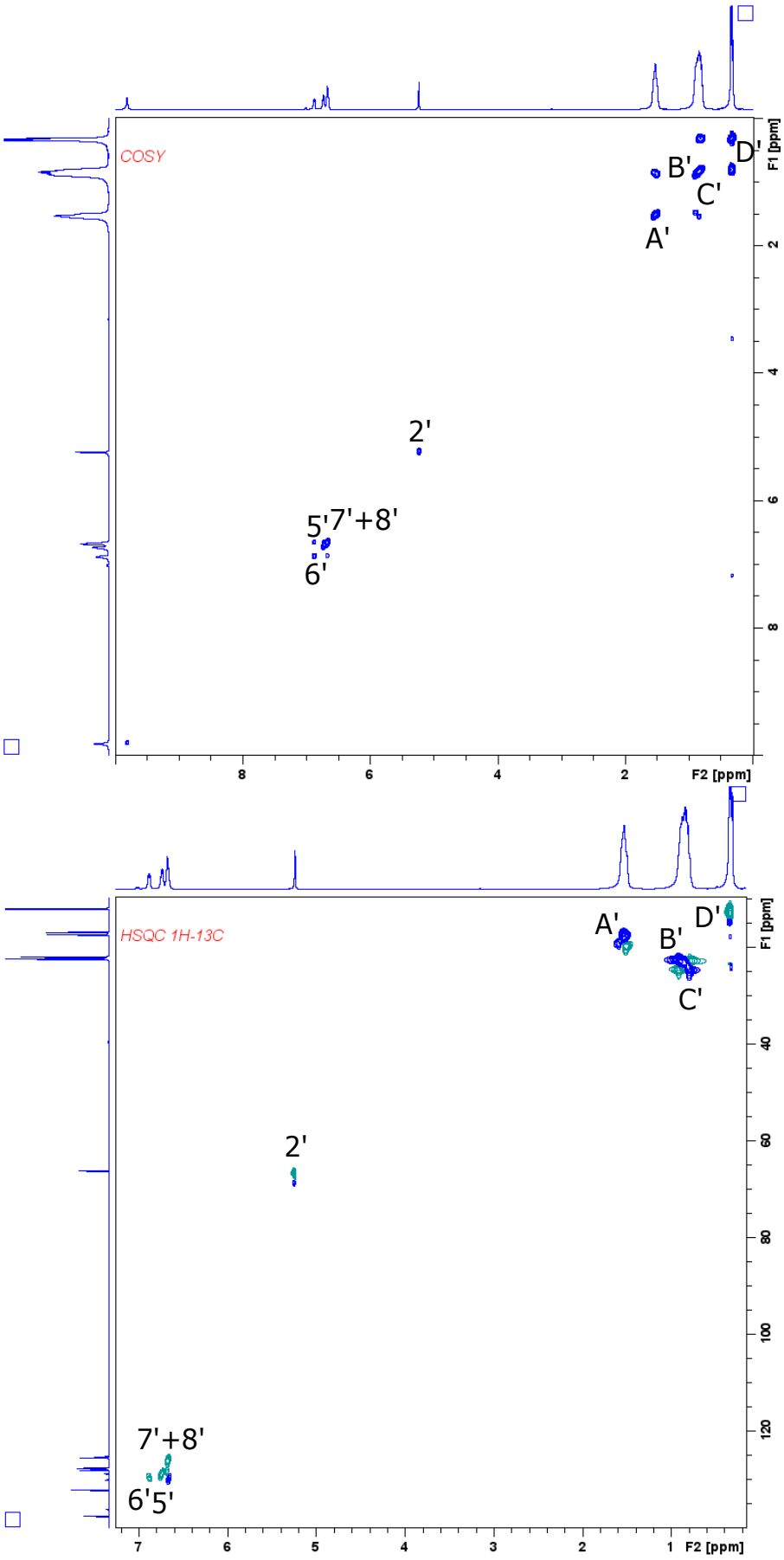

Figure S8 – (Top) COSY and (bottom) HSQC NMR spectra of $[P_{4,4,4,4}][2-ClPhC_1OHCOO]$ after SO_2 absorption at 343 K.

3.3 $[P_{4,4,4,4}][PhSC_1COO]$

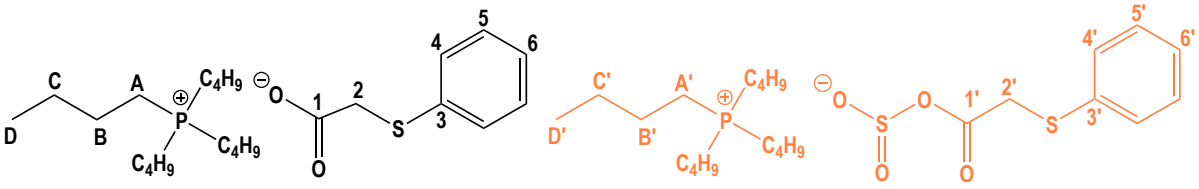

Figure S9 – Chemical structure of the $[P_{4,4,4,4}][PhSC_1COO]$ (left) before and (right) after SO_2 absorption.

Tetrabutylphosphonium (thiophenyl)acetate $[P_{4,4,4,4}][PhSC_1COO]$ after SO_2 absorption: ^{1}H NMR (400 MHz, C_6D_6, 343 K) δ ppm: 0.80 (t, 12H, $^3J_{HH}$ = 7.3 Hz, D'); 1.33 (m, 8H, C'); 1.41 (m, 8H, B'); 2.29 (m, 8H, A'); 3.39 (s, 1H, 2'); 6.91 (t, 1H, $^3J_{HH}$ = 7.3 Hz, 6'); 7.06 (m, 2H, $^3J_{HH}$ = 7.4 Hz, 5'); 7.18 (d, 2H, $^3J_{HH}$ = 7.3 Hz, 4'). ^{13}C NMR (100 MHz, C_6D_6, 343 K) δ ppm: 13.50 (4C, D'); 18.51 (4C, A'); 23.78, 24.93 (8C, B'+C'); 41.12 (1C, 2'); 124.04 (1C, 6'); 126.90 (2C, 4'); 128.48 (2C, 5'); 141.11 (1C, 3'); 168.85 (1C, 1'). ^{31}P NMR (161 MHz, C_6D_6, 343 K) δ ppm: 33.34 (1P, **P**$((CH_2)_3CH_3)_4$).

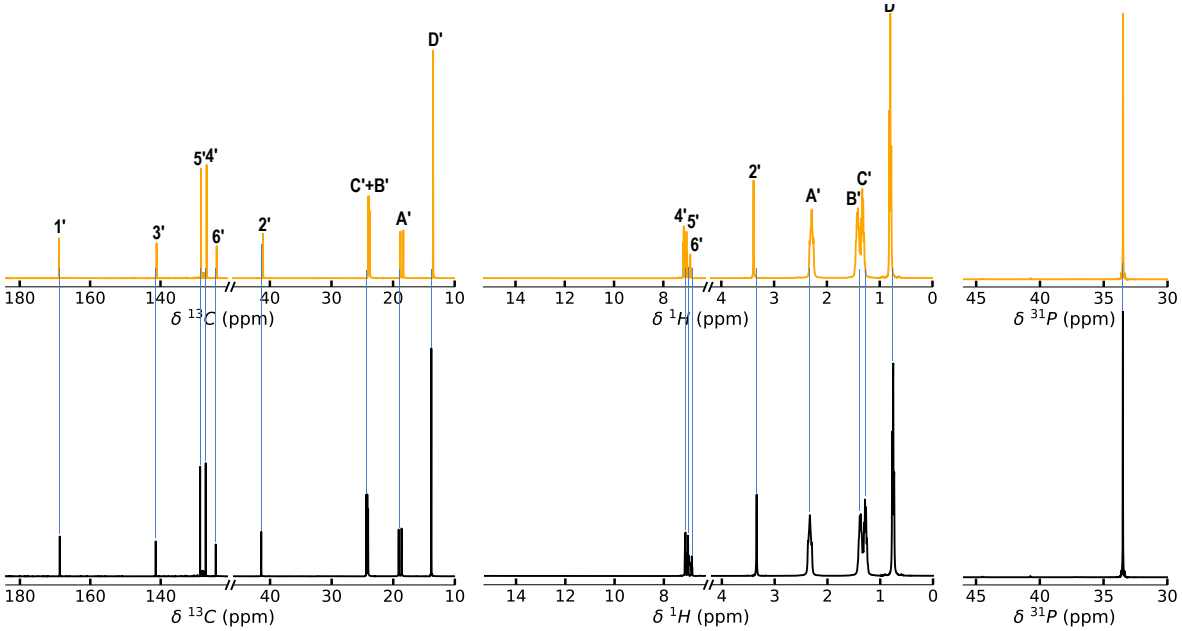

Figure S10 – (Left) ^{13}C, (middle) ^{1}H and (right) ^{31}P NMR spectra of $[P_{4,4,4,4}][PhSC_1COO]$ — before and — after SO_2 absorption at 343 K.

3.4 $[P_{4,4,4,4}][C_{11}COO]$

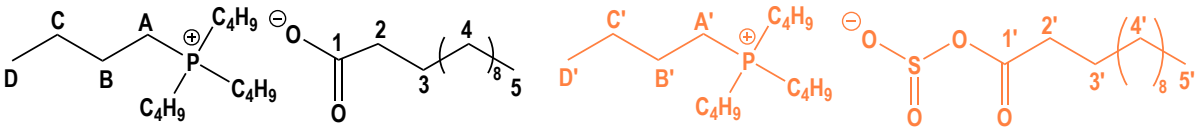

Figure S11 – Chemical structure of the $[P_{4,4,4,4}][C_{11}COO]$ (left) before and (right) after SO_2 absorption.

Tetrabutylphosphonium dodecanoate $[P_{4,4,4,4}][C_{11}COO]$ after SO_2 absorption: ^{1}H NMR (400 MHz, C_6D_6, 343 K) δ ppm: 0.96 (t, 3H, $^{3}J_{HH} = 6.0$ Hz, 5'); 1.03 (t, 12H, $^{3}J_{HH} = 7.0$ Hz, D'); 1.36 (m, 18H, 4'); 1.59 (m, 8H, C'); 1.61 (m, 2H, 3'); 1.70 (m, 8H, B'); 2.13 (t, 2H, $^{3}J_{HH} = 7.1$ Hz, 2'); 2.49 (m, 8H, A'). ^{13}C NMR (100 MHz, C_6D_6, 343 K) δ ppm: 13.75 (4C, D'); 14.33 (1C, 5'); 19.11 (4C, A'); 23.03, 29.72, 29.96-30.27, 32.33 (8C, 4'); 24.12 (4C, C'); 24.31 (4C, B'); 26.28 (1C, 3'); 36.95 (1C, 2'); 175.91 (1C, 1'). ^{31}P NMR (161 MHz, C_6D_6, 343 K) δ ppm: 33.56 (1P, $\mathbf{P}((CH_2)_3CH_3)_4$).

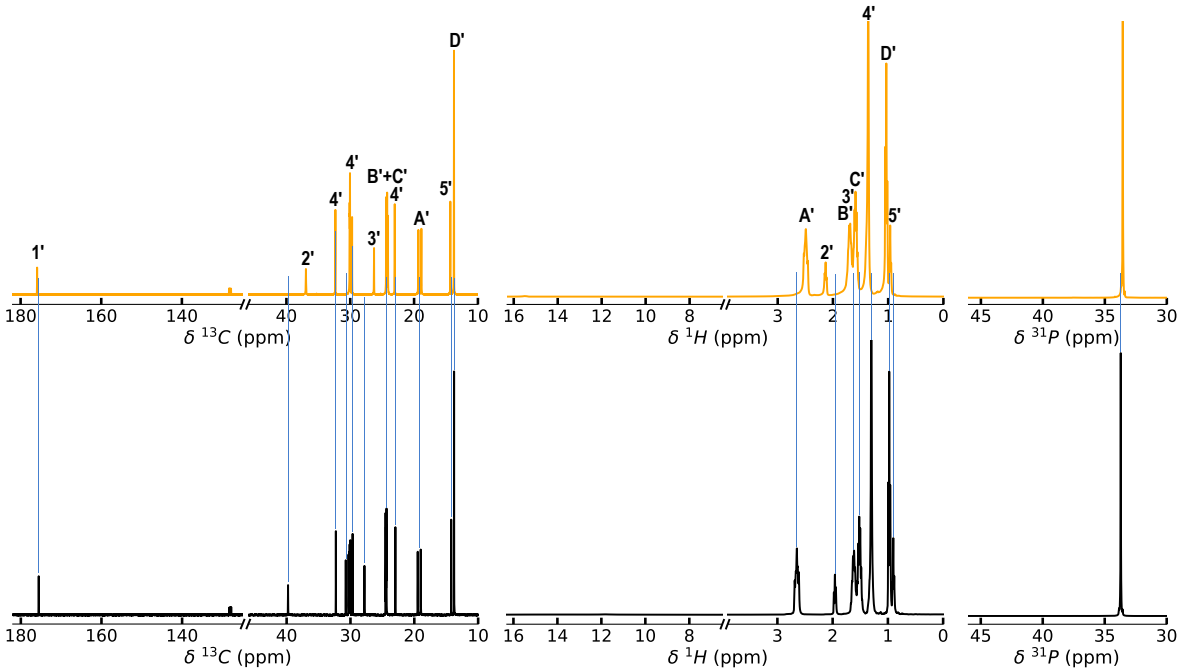

Figure S12 – (Left) ^{13}C, (middle) ^{1}H and (right) ^{31}P NMR spectra of $[P_{4,4,4,4}][C_{11}COO]$ — before and — after SO_2 absorption at 343 K.

3.5 $[P_{6,6,6,14}][C_{11}COO]$

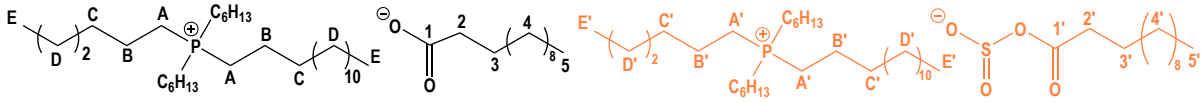

Figure S13 – Chemical structure of the $[P_{6,6,6,14}][C_{11}COO]$ (left) before and (right) after SO_2 absorption.

Trihexyltetradecylphosphonium dodecanoate $[P_{6,6,6,14}][C_{11}COO]$ after SO_2 absorption: ^{1}H NMR (400 MHz, C_6D_6, 343 K) δ ppm: 1.01-1.11 (m, 15H, 5'+E'); 1.38-1.57 (m, 48H, D'+4'); 1.65 (m, 8H, C'); 1.70 (m, 2H, 3'); 1.77(m, 8H, B'); 2.25 (t, 2H, $^{3}J_{HH}$ = 7.5 Hz, 2'); 2.52 (m, 8H, A'). ^{13}C NMR (100 MHz, C_6D_6, 343 K) δ ppm: 14.34, 14.41(5C, E'+5'); 19.54 (4C, A'); 22.12, 22.17 (4C, B'); 22.88, 23.14, 29.45, 29.85, 29.95, 30.17, 30.24, 31.59, 32.45 (24C, D'+4'); 30.88 (4C, C'); 26.25 (1C, 3'); 36.72 (1C, 2'); 176.30 (1C, 1'). ^{31}P NMR (161 MHz, C_6D_6, 343 K) δ ppm: 33.49 (1P, $\mathbf{P}((CH_2)_3CH_3)_4$).

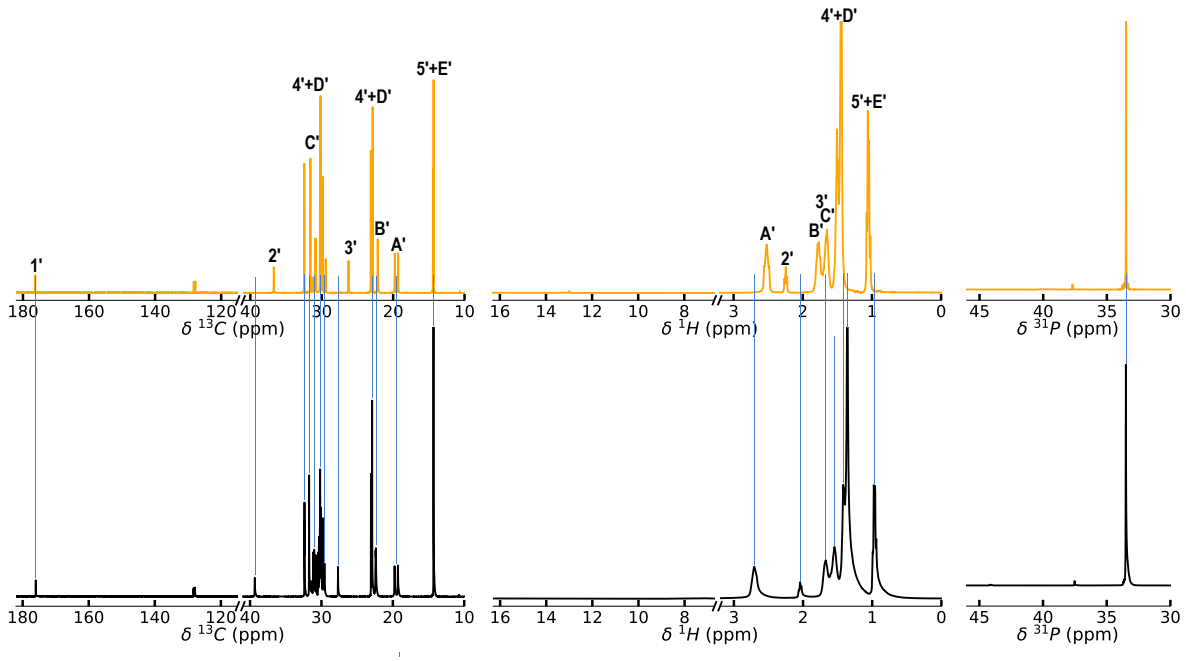

Figure S14 – (Left) ^{13}C, (middle) ^{1}H and (right) ^{31}P NMR spectra of $[P_{6,6,6,14}][C_{11}COO]$ — before and — after SO_2 absorption at 343 K.

3.6 $[P_{4,4,4,4}][Me_4C_4COO]$

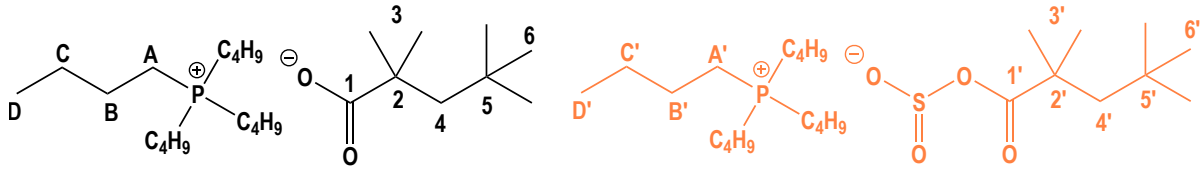

Figure S15 – Chemical structure of the $[P_{4,4,4,4}][Me_4C_4COO]$ (left) before and (right) after SO_2 absorption.

Tetrabutylphosphonium 2,2,4,4-tetramethylpentanoate $[P_{4,4,4,4}][Me_4C_4COO]$ after SO_2 absorption: ^{1}H NMR (400 MHz, C_6D_6, 343 K) δ ppm: 1.09 (t, 12H, $^{3}J_{HH}$ = 7.5 Hz, 6' + D'); 1.23 (s, 6H, 3'); 1.65 (m, 8H, C'); 1.68 (s, 2H, 4'); 1.74 (m, 8H, B'); 2.49 (m, 8H, A'). ^{13}C NMR (100 MHz, C_6D_6, 343 K) δ ppm: 13.86 (4C, D'); 19.22 (4C, A'); 24.10 (8C, C'); 24.30 (4C, B'); 28.75 (2C, 3'); 31.83 (3C, 6'); 32.34 (1C, 5'); 43.16 (1C, 2'); 54.22 (1C, 4'); 180.50 (1C, 1'). ^{31}P NMR (161 MHz, C_6D_6, 343 K) δ ppm: 33.63 (1P, **P**$((CH_2)_3CH_3)_4$).

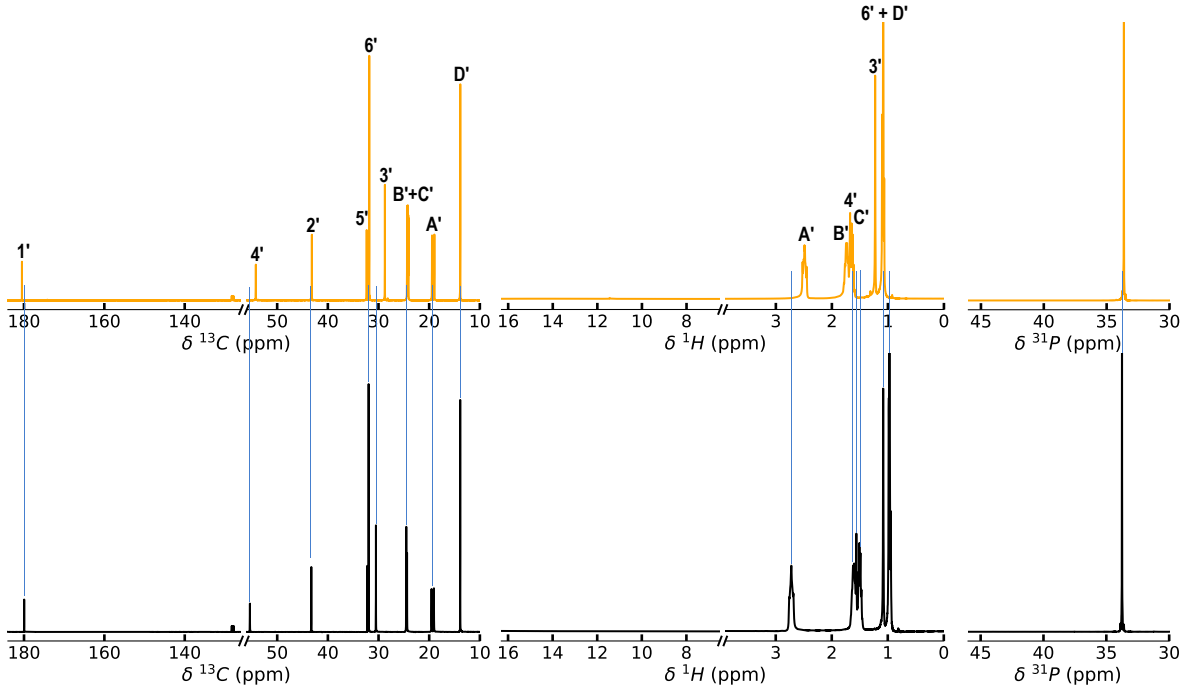

Figure S16 – (Left) ^{13}C, (middle) ^{1}H and (right) ^{31}P NMR spectra of $[P_{4,4,4,4}][Me_4C_4COO]$ — before and — after SO_2 absorption at 343 K.

3.7 $[P_{6,6,6,14}][Me_4C_4COO]$

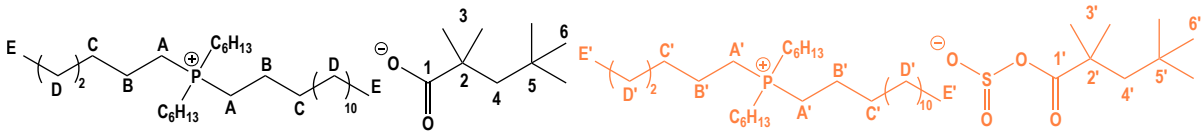

Figure S17 – Chemical structure of the $[P_{6,6,6,14}][Me_4C_4COO]$ (left) before and (right) after SO_2 absorption.

Trihexyltetradecylphosphonium $[P_{6,6,6,14}][Me_4C_4COO]$ after SO_2 absorption: ^{1}H NMR (400 MHz, C_6D_6, 343 K) δ ppm: 1.02 (m, 12H, E'); 1.09 (s, 9H, 6'); 1.25 (s, 6H, 3'); 1.35-1.53 (m, 32H, D'); 1.62 (m, 8H, C'); 1.70 (s, 2H, 4'); 1.75 (m, 8H, B'); 2.52 (m, 8H, A'). ^{13}C NMR (100 MHz, C_6D_6, 343 K) δ ppm: 14.34, 14.43 (4C, E'); 19.52 (4C, A'); 22.15 (4C, B'); 22.83, 23.08, 29.39, 29.78, 29.86, 30.05, 30.10, 30.14, 31.56, 32.35 (25C, D'+ 5'); 28.73 (2C, 3'); 30.86 (4C, C+C'); 31.77 (3C, 6'); 42.97 (1C, 2'); 54.27 (1C, 4'); 180.39 (1C, 1'). ^{31}P NMR (161 MHz, C_6D_6, 343 K) δ ppm: 33.45 (1P, **P**$((CH_2)_3CH_3)_4$).

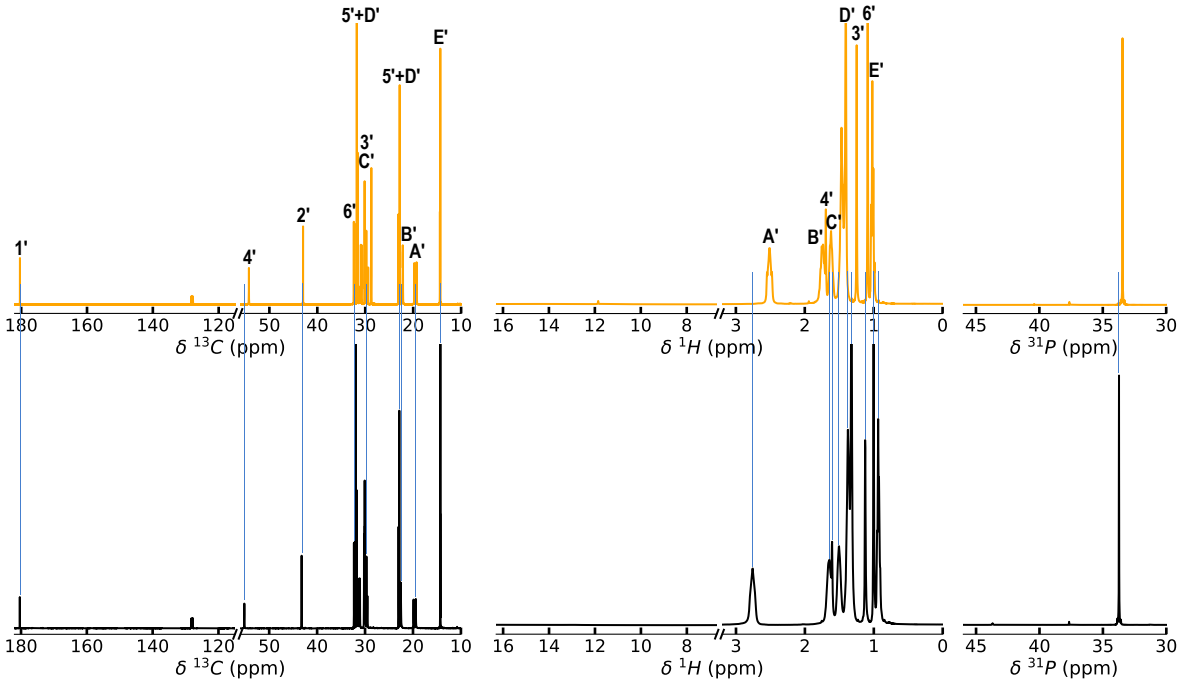

Figure S18 – (Left) ^{13}C, (middle) ^{1}H and (right) ^{31}P NMR spectra of $[P_{6,6,6,14}][Me_4C_4COO]$ — before and — after SO_2 absorption at 343 K

3.8 DOSY experiments

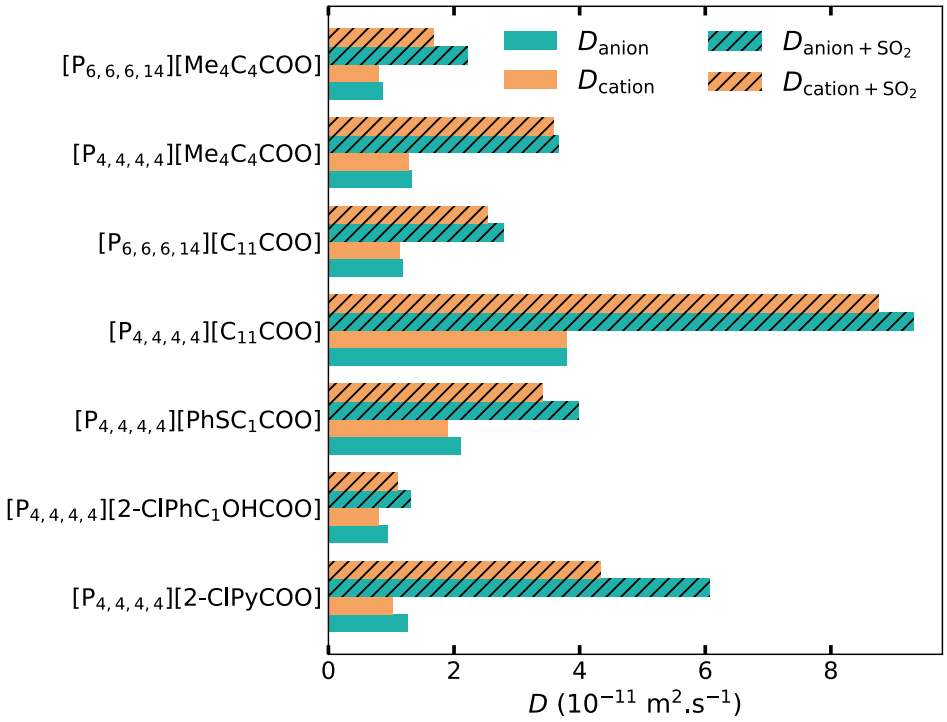

Figure S19 – Histogram representing the experimental self-diffusion coefficients (D) of both the anion and the cation in the ILs before and after SO_2 capture at 343 K measured by DOSY-NMR experiments.

Table S4 – Self-diffusion coefficients (D) of the ILs under study at 343 K by DOSY-NMR experiments. The D values of the neat ILs were determined in a previous study.[3]

Sample	D_{anion} / 1×10^{-11} m^2 s^{-1}	D_{cation} / 1×10^{-11} m^2 s^{-1}
$[P_{4,4,4,4}][2-ClPyCOO]$	1.26 ± 0.04	1.02 ± 0.02
$[P_{4,4,4,4}][2-ClPyCOO] + SO_2$	6.06 ± 0.008	4.33 ± 0.009
$[P_{4,4,4,4}][2-ClPhC_1OHCOO]$	0.94 ± 0.008	0.81 ± 0.004
$[P_{4,4,4,4}][2-ClPhC_1OHCOO] + SO_2$	1.31 ± 0.01	1.10 ± 0.02
$[P_{4,4,4,4}][PhSC_1COO]$	2.11 ± 0.007	1.91 ± 0.005
$[P_{4,4,4,4}][PhSC_1COO] + SO_2$	3.98 ± 0.02	3.41 ± 0.01
$[P_{4,4,4,4}][C_{11}COO]$	3.79 ± 0.03	3.80 ± 0.02
$[P_{4,4,4,4}][C_{11}COO] + SO_2$	9.31 ± 0.05	8.76 ± 0.04
$[P_{6,6,6,14}][C_{11}COO]$	1.19 ± 0.004	1.14 ± 0.004
$[P_{6,6,6,14}][C_{11}COO] + SO_2$	2.79 ± 0.007	2.54 ± 0.003
$[P_{4,4,4,4}][Me_4C_4COO]$	1.33 ± 0.003	1.28 ± 0.002
$[P_{4,4,4,4}][Me_4C_4COO] + SO_2$	3.66 ± 0.04	3.58 ± 0.03
$[P_{6,6,6,14}][Me_4C_4COO]$	0.86 ± 0.002	0.80 ± 0.001
$[P_{6,6,6,14}][Me_4C_4COO] + SO_2$	2.21 ± 0.01	1.67 ± 0.01

4 Molecular Dynamics Simulations

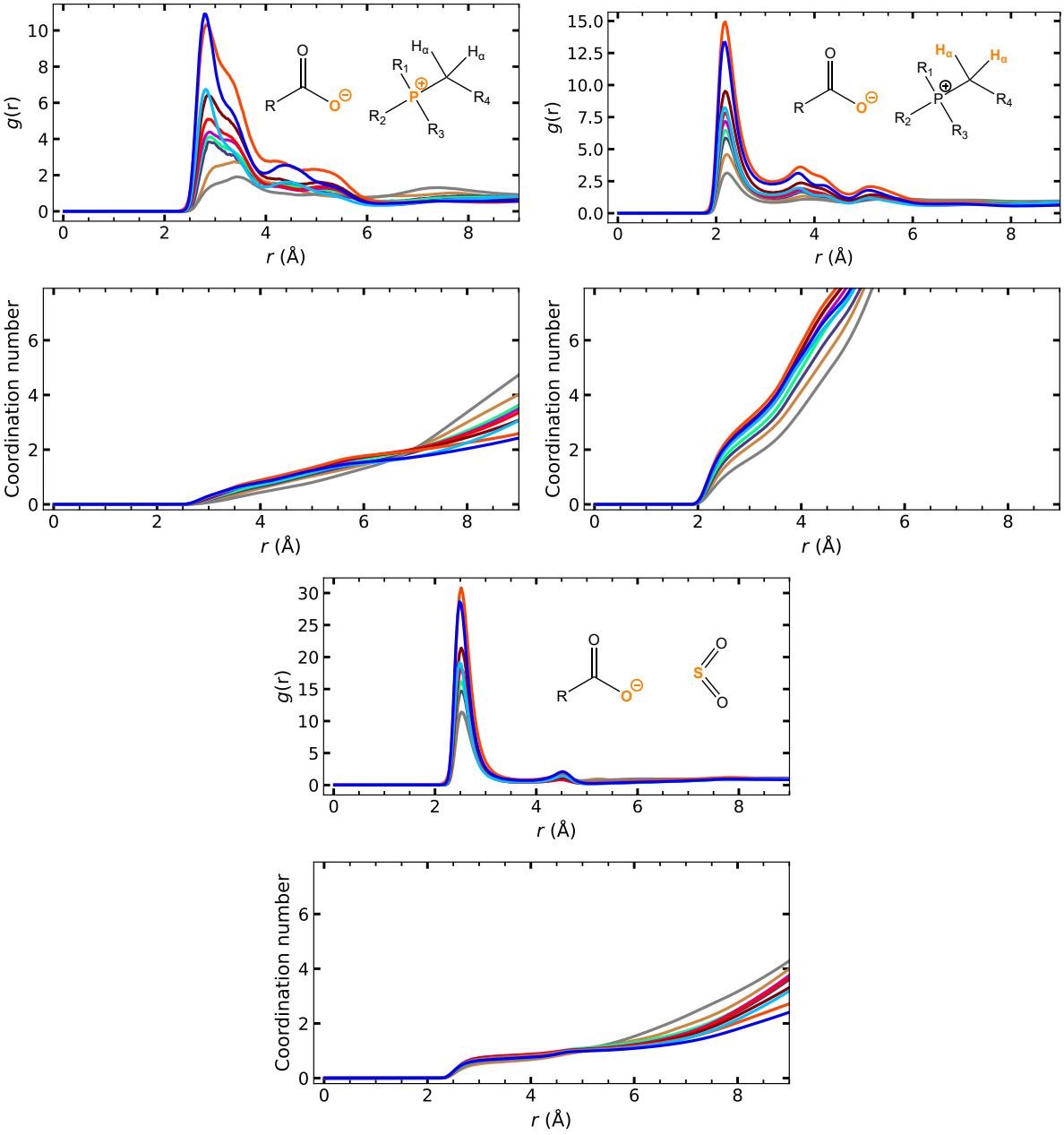

Figure S20 – Comparison of the site-site RDFs, $g(r)$, of (top left) P^+ and (top right) H_α of the cation and (bottom) S_{SO_2} of the SO_2 around O_{COO^-} of the carboxylate anion and their corresponding coordination number (CN) in — $[P_{4,4,4,4}][2\text{-}ClPyCOO]$, — $[P_{4,4,4,4}][TetrazC_1COO]$,[2] — $[P_{4,4,4,4}][2\text{-}ClPhC_1OHCOO]$, — $[P_{4,4,4,4}][PhSC_1COO]$, — $[P_{4,4,4,4}][PhC_1COO]$, — $[P_{4,4,4,4}][C_5COO]$, — $[P_{4,4,4,4}][C_{11}COO]$, — $[P_{6,6,6,14}][C_{11}COO]$, — $[P_{4,4,4,4}][Me_4C_4COO]$ and — $[P_{6,6,6,14}][Me_4C_4COO]$ in presence of SO_2 at 343 K.

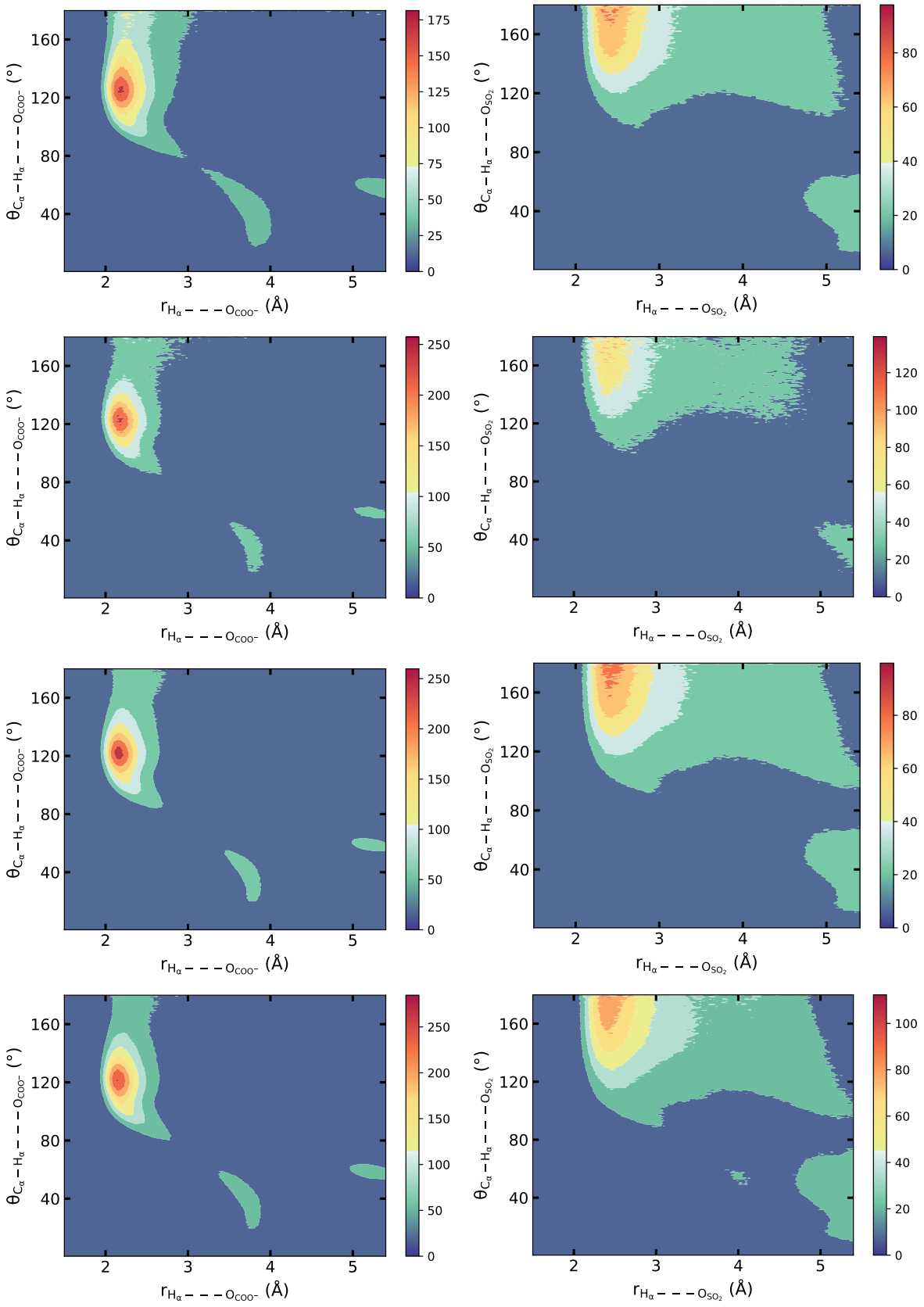
θ Cα – Hα – – – OCOO- (°)
rHα – – – OCOO- (Å)
θ Cα – Hα – – – OSO2 (°)
rHα – – – OSO2 (Å)

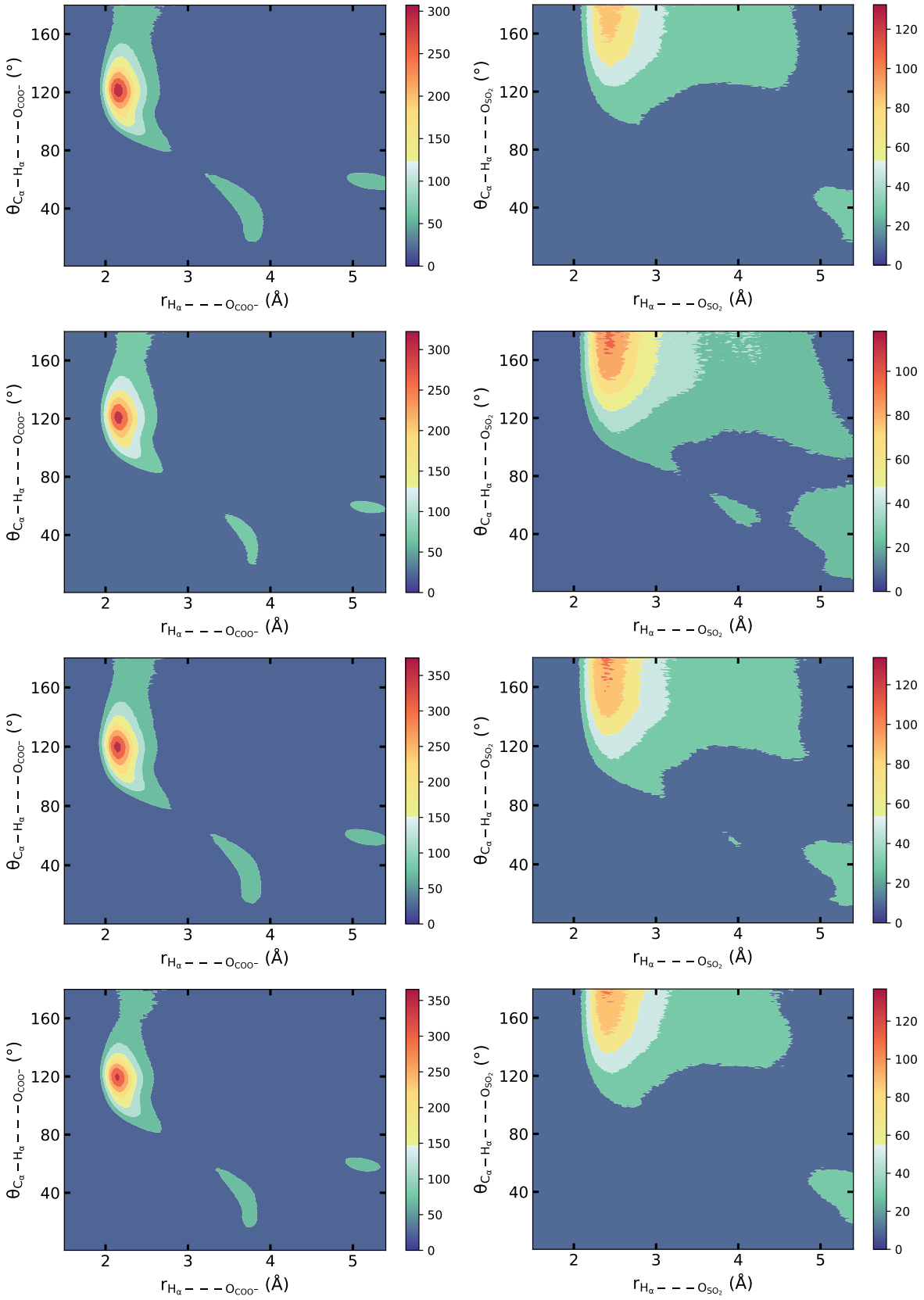
θ$_{C_\alpha-H_\alpha---O_{COO^-}}$ (°)
r$_{H_\alpha---O_{COO^-}}$ (Å)
θ$_{C_\alpha-H_\alpha---O_{SO_2}}$ (°)
r$_{H_\alpha---O_{SO_2}}$ (Å)

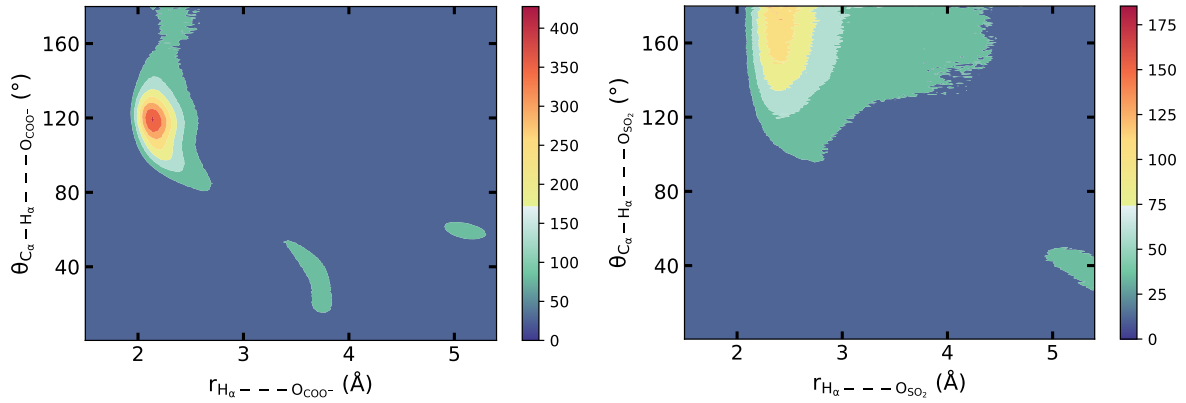

Figure S20 – Combined distribution functions (CDFs) of the Angular Distribution Function (ADF) as a function of the RDF showing the angle between $C_\alpha-H_\alpha$ of the cation (left) and O_{COO^-} of the carboxylate anion, (right) and O_{SO_2} as a function of the distance between $H_\alpha-O_{COO^-}$ and $H_\alpha-O_{SO_2}$ at 343 K, respectively. The ILs are from (top to bottom) $[P_{4,4,4,4}][2-ClPyCOO]$, $[P_{4,4,4,4}][2-ClPhC_1OHCOO]$, $[P_{4,4,4,4}][PhSC_1COO]$, $[P_{4,4,4,4}][PhC_1COO]$, $[P_{4,4,4,4}][C_5COO]$, $[P_{4,4,4,4}][C_{11}COO]$, $[P_{6,6,6,14}][C_{11}COO]$, $[P_{4,4,4,4}][Me_4C_4COO]$ and $[P_{6,6,6,14}][Me_4C_4COO]$.

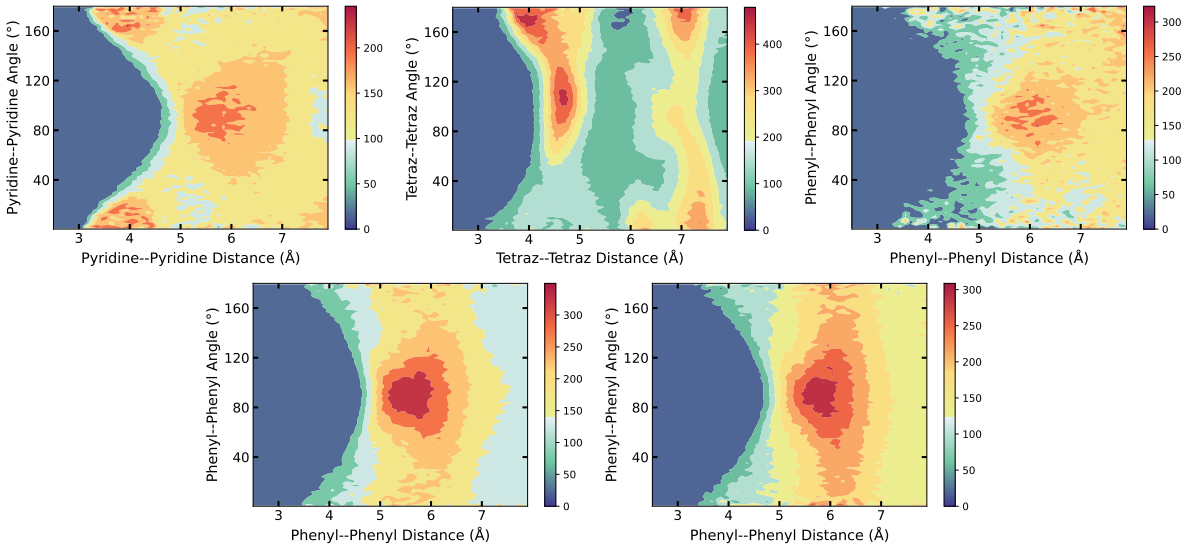

Figure S21 – CDFs of the ADF between (top left) two adjacent pyrridine rings in $[P_{4,4,4,4}][2-ClPyCOO]$, (top middle) two adjacent tetrazole rings in $[P_{4,4,4,4}][TetrazC_1COO]$, two adjacent phenyl rings (top right) in $[P_{4,4,4,4}][2-ClPhC_1OHCOO]$, (bottom left) in $[P_{4,4,4,4}][PhSC_1COO]$ and (bottom right) in $[P_{4,4,4,4}][PhC_1COO]$ as a function of the RDF between their center of mass at 343 K.

5 *Ab initio* simulations

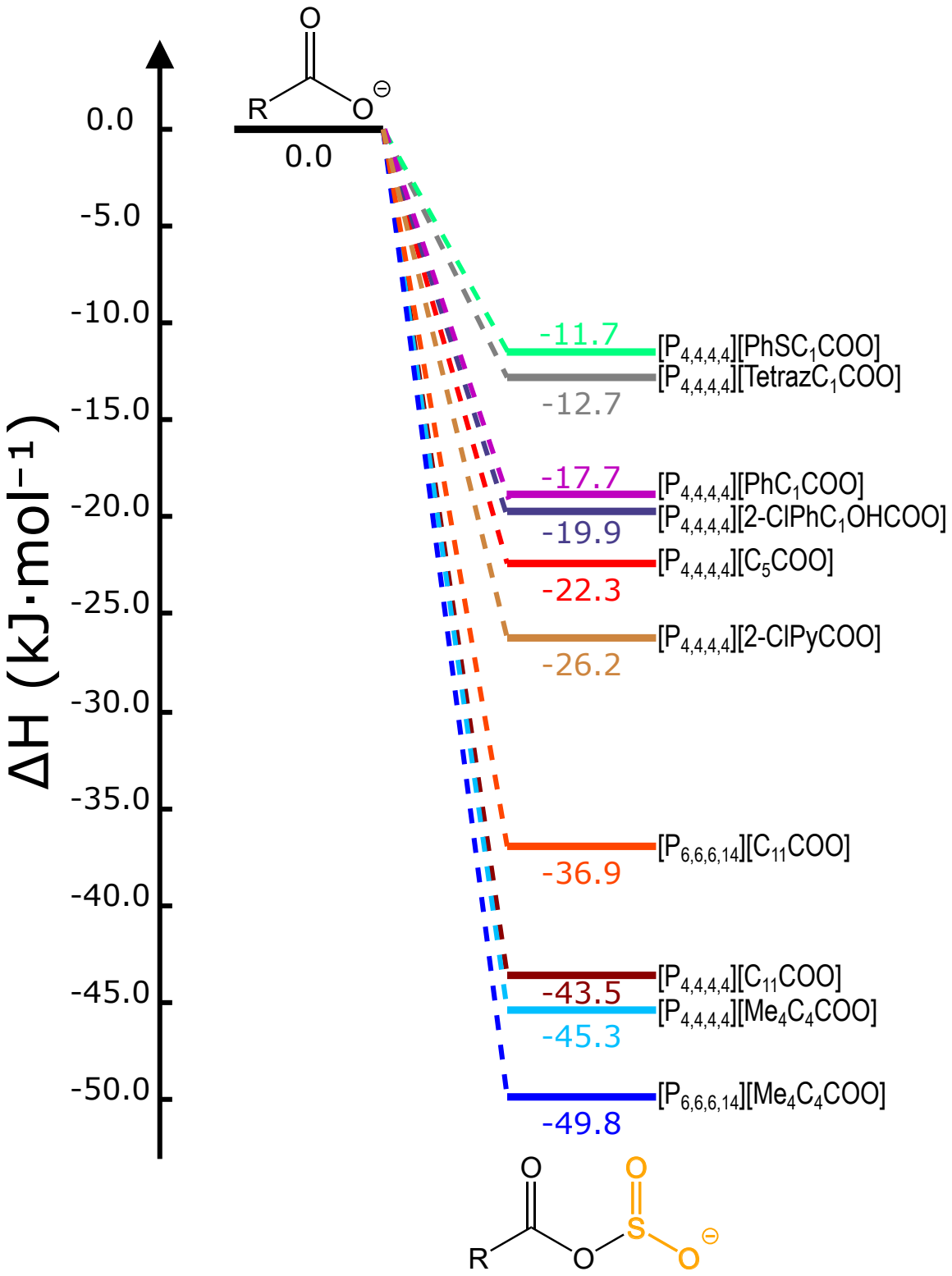

Figure S22 – Enthalpy of the reaction leading to the chemical capture of SO_2 in — $[P_{4,4,4,4}][2\text{-ClPyCOO}]$, — $[P_{4,4,4,4}][TetrazC_1COO]$,[2] — $[P_{4,4,4,4}][2\text{-ClPhC}_1OhCOO]$, — $[P_{4,4,4,4}][PhSC_1COO]$, — $[P_{4,4,4,4}][PhC_1COO]$, — $[P_{4,4,4,4}][C_5COO]$, — $[P_{4,4,4,4}][C_{11}COO]$, — $[P_{6,6,6,14}][C_{11}COO]$, — $[P_{4,4,4,4}][Me_4C_4COO]$ and — $[P_{6,6,6,14}][Me_4C_4COO]$ at 343 K.

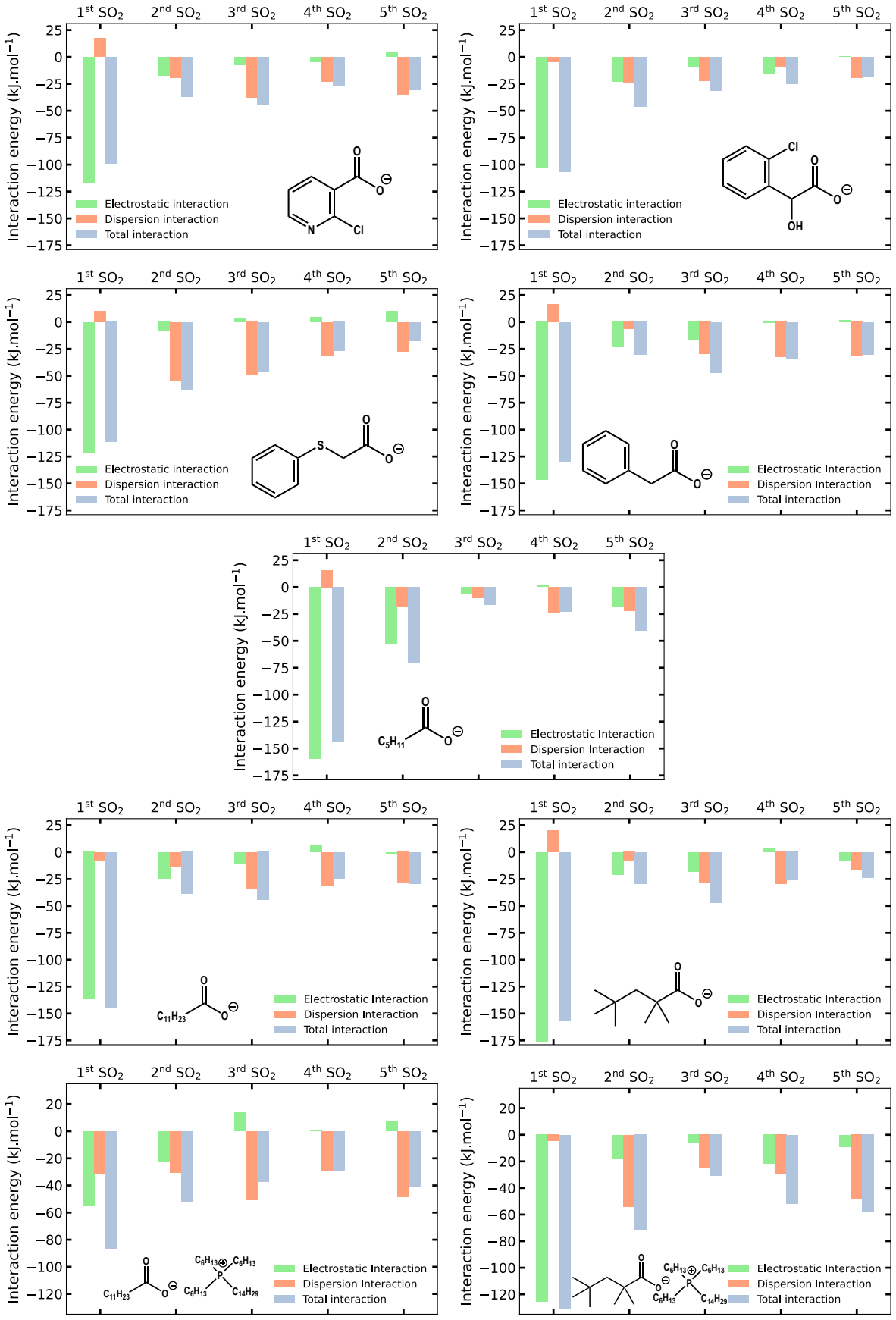

Figure S23 – Comparison of the electrostatic, dispersion and total interactions between up to 5 SO_2 molecules and $[P_{4,4,4,4}][2-ClPyCOO]$, $[P_{4,4,4,4}][2-ClPhC_1OHCOO]$, $[P_{4,4,4,4}][PhSC_1COO]$, $[P_{4,4,4,4}][PhC_1COO]$, $[P_{4,4,4,4}][C_5COO]$, $[P_{4,4,4,4}][C_{11}COO]$, $[P_{6,6,6,14}][C_{11}COO]$, $[P_{4,4,4,4}][Me_4C_4COO]$ and $[P_{6,6,6,14}][Me_4C_4COO]$.

Table S5 – Total interaction energies ($E_{\text{tot.}}$) decomposed into electrostatic and dispersion contributions ($E_{\text{electrostat.}}$ and $E_{\text{disp.}}$, respectively) between the IL and SO_2. The indicated energies correspond to the interactions with 1 SO_2 molecule.

Sample	$E_{\text{electrostat.}}$ / kJ mol^{-1}	$E_{\text{disp.}}$ / kJ mol^{-1}	$E_{\text{tot.}}$ / kJ mol^{-1}
$[P_{4,4,4,4}][2-ClPyCOO-SO_2]$	-116.6	17.3	-99.3
$[P_{4,4,4,4}][2-ClPyCOO-SO_2] + 1\,SO_2$	-17.6	-19.1	-36.6
$[P_{4,4,4,4}][2-ClPyCOO-SO_2] + 2\,SO_2$	-7.4	-37.6	-44.9
$[P_{4,4,4,4}][2-ClPyCOO-SO_2] + 3\,SO_2$	-4.5	-22.6	-27.0
$[P_{4,4,4,4}][2-ClPyCOO-SO_2] + 4\,SO_2$	4.9	-35.2	-30.3
$[P_{4,4,4,4}][TetrazCOO-SO_2]$	-110.4	1.5	-108.9
$[P_{4,4,4,4}][TetrazCOO-SO_2] + 1\,SO_2$	-10.0	-36.6	-46.6
$[P_{4,4,4,4}][TetrazCOO-SO_2] + 2\,SO_2$	-11.0	-36.4	-47.4
$[P_{4,4,4,4}][TetrazCOO-SO_2] + 3\,SO_2$	-9.3	-12.7	-22.0
$[P_{4,4,4,4}][TetrazCOO-SO_2] + 4\,SO_2$	-2.9	-20.0	-22.9
$[P_{4,4,4,4}][2-ClPhC_1OHCOO-SO_2]$	-121.9	4.9	-112.6
$[P_{4,4,4,4}][2-ClPhC_1OHCOO-SO_2] + 1\,SO_2$	-22.7	-23.3	-46.0
$[P_{4,4,4,4}][2-ClPhC_1OHCOO-SO_2] + 2\,SO_2$	-9.6	-22.0	-31.6
$[P_{4,4,4,4}][2-ClPhC_1OHCOO-SO_2] + 3\,SO_2$	-15.4	-9.7	-25.1
$[P_{4,4,4,4}][2-ClPhC_1OHCOO-SO_2] + 4\,SO_2$	0.67	-19.1	-18.5
$[P_{4,4,4,4}][PhSC_1COO-SO_2]$	-121.8	10.3	-111.5
$[P_{4,4,4,4}][PhSC_1COO-SO_2] + 1\,SO_2$	-8.7	-54.0	-62.6
$[P_{4,4,4,4}][PhSC_1COO-SO_2] + 2\,SO_2$	2.9	-48.7	-45.8
$[P_{4,4,4,4}][PhSC_1COO-SO_2] + 3\,SO_2$	4.7	-31.6	-27.0
$[P_{4,4,4,4}][PhSC_1COO-SO_2] + 4\,SO_2$	9.9	-27.4	-17.5
$[P_{4,4,4,4}][C_5COO-SO_2]$	-159.4	15.7	-143.7
$[P_{4,4,4,4}][C_5COO-SO_2] + 1\,SO_2$	-53.4	-17.7	-71.1
$[P_{4,4,4,4}][C_5COO-SO_2] + 2\,SO_2$	-6.4	-10.3	-16.7

Sample	$E_{electrostat.}$ / kJ mol^{-1}	$E_{disp.}$ / kJ mol^{-1}	$E_{tot.}$ / kJ mol^{-1}
$[P_{4,4,4,4}][C_5COO{-}SO_2]$ + 3 SO_2	1.2	-23.7	-22.5
$[P_{4,4,4,4}][C_5COO{-}SO_2]$ + 4 SO_2	-18.4	-22.4	-40.8
$[P_{4,4,4,4}][C_{11}COO{-}SO_2]$	-136.7	-7.3	-144.0
$[P_{4,4,4,4}][C_{11}COO{-}SO_2]$ + 1 SO_2	-25.3	-13.7	-38.9
$[P_{4,4,4,4}][C_{11}COO{-}SO_2]$ + 2 SO_2	-10.4	-34.2	-44.6
$[P_{4,4,4,4}][C_{11}COO{-}SO_2]$ + 3 SO_2	6.3	-30.8	-24.6
$[P_{4,4,4,4}][C_{11}COO{-}SO_2]$ + 4 SO_2	-1.0	-28.3	-29.3
$[P_{6,6,6,14}][C_{11}COO{-}SO_2]$	-55.3	-31.2	-86.5
$[P_{6,6,6,14}][C_{11}COO{-}SO_2]$ + 1 SO_2	-22.0	-30.5	-52.5
$[P_{6,6,6,14}][C_{11}COO{-}SO_2]$ + 2 SO_2	30.6	-61.9	-31.3
$[P_{6,6,6,14}][C_{11}COO{-}SO_2]$ + 3 SO_2	27.3	-43.9	-16.6
$[P_{6,6,6,14}][C_{11}COO{-}SO_2]$ + 4 SO_2	7.7	-48.6	-40.9
$[P_{4,4,4,4}][PhC_1COO{-}SO_2]$	-146.5	16.3	-130.3
$[P_{4,4,4,4}][PhC_1COO{-}SO_2]$ + 1 SO_2	-23.7	-6.7	-30.4
$[P_{4,4,4,4}][PhC_1COO{-}SO_2]$ + 2 SO_2	-17.2	-29.7	-46.9
$[P_{4,4,4,4}][PhC_1COO{-}SO_2]$ + 3 SO_2	-1.1	-32.6	-33.7
$[P_{4,4,4,4}][PhC_1COO{-}SO_2]$ + 4 SO_2	1.8	-31.8	-30.1
$[P_{4,4,4,4}][Me_4C_4COO{-}SO_2]$	-175.9	19.9	-156.0
$[P_{4,4,4,4}][Me_4C_4COO{-}SO_2]$ + 1 SO_2	-21.0	-8.6	-29.6
$[P_{4,4,4,4}][Me_4C_4COO{-}SO_2]$ + 2 SO_2	-18.1	-28.8	-46.9
$[P_{4,4,4,4}][Me_4C_4COO{-}SO_2]$ + 3 SO_2	3.5	-29.7	-26.2
$[P_{4,4,4,4}][Me_4C_4COO{-}SO_2]$ + 4 SO_2	-8.2	-15.7	-23.9
$[P_{6,6,6,14}][Me_4C_4COO{-}SO_2]$	-125.6	-4.8	-130.4
$[P_{6,6,6,14}][Me_4C_4COO{-}SO_2]$ + 1 SO_2	-17.5	-53.9	-71.4
$[P_{6,6,6,14}][Me_4C_4COO{-}SO_2]$ + 2 SO_2	-6.3	-24.7	-31.0
$[P_{6,6,6,14}][Me_4C_4COO{-}SO_2]$ + 3 SO_2	-22.0	-29.7	-51.7

Sample	$E_{electrostat.}$ / kJ mol^{-1}	$E_{disp.}$ / kJ mol^{-1}	$E_{tot.}$ / kJ mol^{-1}
$[P_{6,6,6,14}][Me_4C_4COO{-}SO_2]$ + 4 SO_2	-9.0	-48.7	-57.7

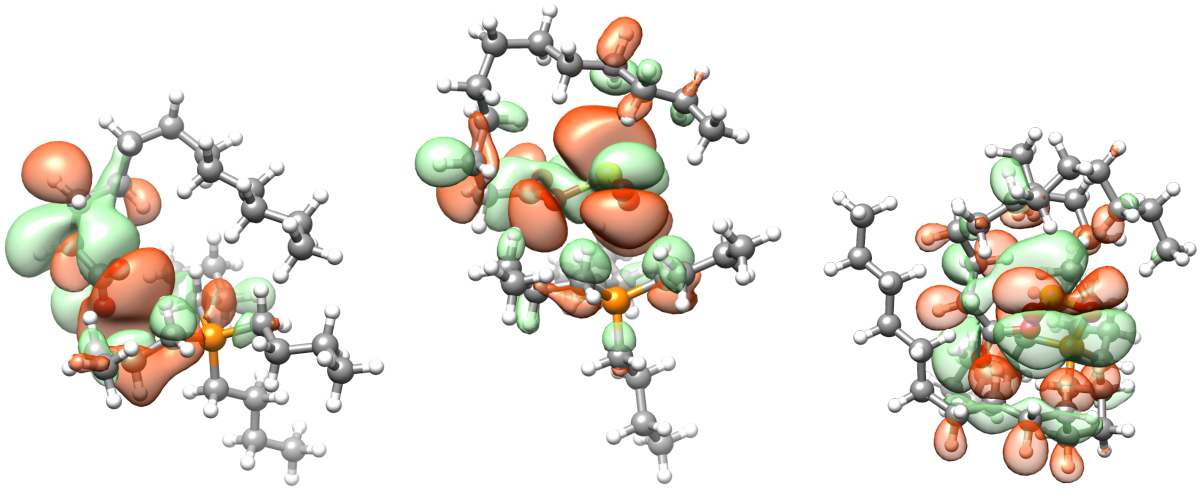

Figure S24 – Comparison of the HOMO in (left) $[P_{4,4,4,4}][C_{11}COO]$, (middle) $[P_{4,4,4,4}][C_{11}COO{-}SO_2]$ and (right) $[P_{6,6,6,14}][C_{11}COO{-}SO_2]$.

Table S6 – CM5 charges of the cation and the anion in the various ILs before and after reaction with SO_2, but also the charges of the solvated SO_2 as well as the related HOMO energy.

Sample	q(Cation) / e	q(Anion) / e	q(SO_2) / e	q(SO_2) / e	q(SO_2) / e	q(SO_2) / e	E(HOMO) / eV
$[P_{4,4,4,4}][2-ClPyCOO]$	0.73	-0.73	-	-	-	-	-7.78
$[P_{4,4,4,4}][2-ClPyCOO{-}SO_2]$	0.72	-0.72	-	-	-	-	-8.23
$[P_{4,4,4,4}][2-ClPyCOO{-}SO_2]$ + 1 SO_2	0.70	-0.64	-0.06	-	-	-	-8.33
$[P_{4,4,4,4}][2-ClPyCOO{-}SO_2]$ + 2 SO_2	0.70	-0.53	-0.06	-0.11	-	-	-8.45
$[P_{4,4,4,4}][2-ClPyCOO{-}SO_2]$ + 3 SO_2	0.72	-0.59	0.00	-0.12	-0.01	-	-8.49
$[P_{4,4,4,4}][2-ClPyCOO{-}SO_2]$ + 4 SO_2	0.59	-0.50	-0.03	0.00	-0.05	-0.01	-8.52
$[P_{4,4,4,4}][2-ClPhC_1OHCOO]$	0.76	-0.76	-	-	-	-	-7.47
$[P_{4,4,4,4}][2-ClPhC_1OHCOO{-}SO_2]$	0.68	-0.68	-	-	-	-	-7.92
$[P_{4,4,4,4}][2-ClPhC_1OHCOO{-}SO_2]$ 1 + SO_2	0.65	-0.59	-0.05	-	-	-	-8.26
$[P_{4,4,4,4}][2-ClPhC_1OHCOO{-}SO_2]$ 2 + SO_2	0.64	-0.58	-0.05	-0.01	-	-	-8.05
$[P_{4,4,4,4}][2-ClPhC_1OHCOO{-}SO_2]$ 3 + SO_2	0.64	-0.49	-0.03	-0.01	-0.11	-	-8.12
$[P_{4,4,4,4}][2-ClPhC_1OHCOO{-}SO_2]$ 4 + SO_2	0.66	-0.47	-0.04	-0.02	-0.09	-0.04	-8.11

Sample	q(Cation) e	q(Anion) e	$q(SO_2)$ e	$q(SO_2)$ e	$q(SO_2)$ e	$q(SO_2)$ e	E(HOMO) eV
$[P_{4,4,4,4}][PhSC_1COO]$	0.76	-0.76	-	-	-	-	-6.79
$[P_{4,4,4,4}][PhSC_1COO{-}SO_2]$	0.67	-0.67	-	-	-	-	-7.19
$[P_{4,4,4,4}][PhSC_1COO{-}SO_2] + 1\ SO_2$	0.76	-0.66	-0.10	-	-	-	-7.63
$[P_{4,4,4,4}][PhSC_1COO{-}SO_2] + 2\ SO_2$	0.68	-0.58	-0.06	-0.03	-	-	-7.86
$[P_{4,4,4,4}][PhSC_1COO{-}SO_2] + 3\ SO_2$	0.68	-0.51	-0.11	-0.03	-0.01	-	-7.28
$[P_{4,4,4,4}][PhSC_1COO{-}SO_2] + 4\ SO_2$	0.58	-0.52	-0.07	0.00	-0.01	0.01	-7.19
$[P_{4,4,4,4}][PhC_1COO]$	0.69	-0.69	-	-	-	-	-7.18
$[P_{4,4,4,4}][PhC_1COO{-}SO_2]$	0.67	-0.67	-	-	-	-	-7.79
$[P_{4,4,4,4}][PhC_1COO{-}SO_2] + 1\ SO_2$	0.71	-0.60	-0.11	-	-	-	-7.83
$[P_{4,4,4,4}][PhC_1COO{-}SO_2] + 2\ SO_2$	0.67	-0.62	-0.02	-0.03	-	-	-7.99
$[P_{4,4,4,4}][PhC_1COO{-}SO_2] + 3\ SO_2$	0.69	-0.47	-0.04	-0.10	-0.06	-	-7.96
$[P_{4,4,4,4}][PhC_1COO{-}SO_2] + 4\ SO_2$	0.72	-0.48	-0.02	-0.09	-0.01	-0.12	-8.68
$[P_{4,4,4,4}][C_5COO]$	0.74	-0.74	-	-	-	-	-7.48
$[P_{4,4,4,4}][C_5COO{-}SO_2]$	0.72	-0.72	-	-	-	-	-7.80
$[P_{4,4,4,4}][C_5COO{-}SO_2] + 1\ SO_2$	0.73	-0.63	-0.10	-	-	-	-8.15
$[P_{4,4,4,4}][C_5COO{-}SO_2] + 2\ SO_2$	0.74	-0.49	-0.16	-0.09	-	-	-8.52
$[P_{4,4,4,4}][C_5COO{-}SO_2] + 3\ SO_2$	0.76	-0.50	-0.16	-0.05	-0.04	-	-8.59
$[P_{4,4,4,4}][C_5COO{-}SO_2] + 4\ SO_2$	0.71	-0.47	-0.09	-0.07	-0.04	-0.04	-8.68
$[P_{4,4,4,4}][C_{11}COO]$	0.74	-0.74	-	-	-	-	-7.35
$[P_{4,4,4,4}][C_{11}COO{-}SO_2]$	0.72	-0.72	-	-	-	-	-7.95
$[P_{4,4,4,4}][C_{11}COO{-}SO_2] + 1\ SO_2$	0.73	-0.63	-0.10	-	-	-	-8.38
$[P_{4,4,4,4}][C_{11}COO{-}SO_2] + 2\ SO_2$	0.74	-0.49	-0.16	-0.09	-	-	-8.29
$[P_{4,4,4,4}][C_{11}COO{-}SO_2] + 3\ SO_2$	0.76	-0.50	-0.16	-0.05	-0.04	-	-8.55
$[P_{4,4,4,4}][C_{11}COO{-}SO_2] + 4\ SO_2$	0.62	-0.51	-0.02	-0.02	-0.03	-0.05	-8.73
$[P_{6,6,6,14}][C_{11}COO]$	0.75	-0.75	-	-	-	-	-7.35
$[P_{6,6,6,14}][C_{11}COO{-}SO_2]$	0.75	-0.75	-	-	-	-	-7.73
$[P_{6,6,6,14}][C_{11}COO{-}SO_2] + 1\ SO_2$	0.65	-0.50	-0.15	-	-	-	-8.59
$[P_{6,6,6,14}][C_{11}COO{-}SO_2] + 2\ SO_2$	0.60	-0.53	-0.07	0.00	-	-	-8.63

Sample	q(Cation)	q(Anion)	q(SO_2)	q(SO_2)	q(SO_2)	q(SO_2)	E(HOMO)
	e	e	e	e	e	e	eV
$[P_{6,6,6,14}][C_{11}COO{-}SO_2] + 3\ SO_2$	0.65	-0.61	-0.13	0.09	0.00	-	-8.57
$[P_{6,6,6,14}][C_{11}COO{-}SO_2] + 4\ SO_2$	0.63	-0.56	-0.03	0.04	-0.05	-0.03	-8.831
$[P_{4,4,4,4}][Me_4C_4COO]$	0.76	-0.76	-	-	-	-	-7.34
$[P_{4,4,4,4}][Me_4C_4COO{-}SO_2]$	0.77	-0.77	-	-	-	-	-7.76
$[P_{4,4,4,4}][Me_4C_4COO{-}SO_2] + 1\ SO_2$	0.78	-0.72	-0.06	-	-	-	-8.02
$[P_{4,4,4,4}][Me_4C_4COO{-}SO_2] + 2\ SO_2$	0.72	-0.61	-0.04	-0.07	-	-	-8.29
$[P_{4,4,4,4}][Me_4C_4COO{-}SO_2] + 3\ SO_2$	0.72	-0.56	-0.03	-0.13	-0.01	-	-8.46
$[P_{4,4,4,4}][Me_4C_4COO{-}SO_2] + 4\ SO_2$	0.71	-0.52	-0.03	0.00	-0.11	-0.04	-8.50
$[P_{6,6,6,14}][Me_4C_4COO]$	0.66	-0.66	-	-	-	-	-7.48
$[P_{6,6,6,14}][Me_4C_4COO{-}SO_2]$	0.71	-0.71	-	-	-	-	-7.89
$[P_{6,6,6,14}][Me_4C_4COO{-}SO_2] + 1\ SO_2$	0.66	-0.65	-0.01	-	-	-	-8.17
$[P_{6,6,6,14}][Me_4C_4COO{-}SO_2] + 2\ SO_2$	0.66	-0.62	-0.01	-0.03	-	-	-8.27
$[P_{6,6,6,14}][Me_4C_4COO{-}SO_2] + 3\ SO_2$	0.67	-0.52	0.02	-0.08	-0.09	-	-8.27
$[P_{6,6,6,14}][Me_4C_4COO{-}SO_2] + 4\ SO_2$	0.65	-0.54	-0.01	-0.06	-0.08	0.04	-8.53

References

(1) Scaglione, N.; Avila, J.; Padua, A. A. H.; Gomes, M. C. Tailored Carbon Dioxide Capacity in Carboxylate-Based Ionic Liquids†. *Faraday Discuss.* **2024**, Publisher: The Royal Society of Chemistry.

(2) Scaglione, N.; Wylie, L.; Padua, A.; Costa Gomes, M. *Submitted* **2024**, *00*, 000–000.

(3) Scaglione, N.; Avila, J.; Bakis, E.; Padua, A.; Gomes, M. C. Alkylphosphonium carboxylate ionic liquids with tuned microscopic structures and properties. *Phys. Chem. Chem. Phys.* **2023**, *25*, 15325–15339.

Part III

EXPLORATORY PROJECTS

7

ELECTROCHEMICAL PROPERTIES

Context

The study of the electrochemical properties of the new library of phosphonium carboxylate ILs was carried out to explore their applicability to other types of applications as they showed an interesting long-term thermal stability (Chapters 4 and 5). It also appeared as a way to complete their characterization to get a better understanding of their properties.

7.1 INTRODUCTION

Due to their unique structures, ILs are renowned for their interesting electrochemical properties. For example, pyridinium, pyrrolidinium, piperidinium, imidazolium or ammonium based ILs with bis(trifluoromethyl sulfonyl)imide ($[NTf_2]^-$) as anion find extensive use across diverse electrochemical applications [127–130]. One key characteristic is their wide electrochemical stability window [131], referring to the range of potentials over which they remain stable without undergoing decomposition. This property is crucial for electrochemical devices like batteries and supercapacitors, where the electrolyte must withstand high potentials without breaking down [132].

The electrochemical stability of aqueous solutions is notably low due to the narrow electrochemical stability window (ESW) of water, which stands at 1.23 V [133]. This, coupled with their low thermal stability and high corrosiveness, significantly restricts their practical applications.

Non-aqueous electrolytes have been consequently proposed, such as ammonium tetrafluoroborate salts in acetonitrile, but their ESWs remain limited due to the solvent [134]. Thank to their low vapor pressure and high stability, ILs appear as promising candidates to overcome these issues and obtain larger ESWs, despite that their conductivity is usually lower.

More particularly, imidazolium or phosphonium-based ILs paired with $[NTf_2]^-$ anions have been extensively studied for application in lithium-ion batteries. Their stability are very variable depending on the choice of the ions, with ESWs ranging from approximately 2.5 to 6.5 V [131, 135]. Some ILs showed promising stability, which allows their utilization of high-potential cathode materials, leading to enhanced energy density and performance. The electrochemical stability of halogen-free ILs are much less studied, with only a few examples reported in the literature. They usually have narrower ESWs, with the highest reported so far of approximately 3.5 V [136, 137].

It appears that because of the potential formation of N-heterocyclic carbenes upon reduction [138], imidazolium cations generally lead to narrower electrochemical windows [139] compared to that of phosphonium-based ILs [140]. On the other hand, ammonium cations associated with $[NTf_2]^-$ anion exhibit favorable electrochemical stability at r. t., but they demonstrate inferior

thermal stability compared to their phosphonium counterparts, making them less suitable as electrolytes for high-temperature applications [141, 142].

Due to their advantageous thermal, chemical and electrochemical stability [143, 144], phosphonium-based ILs have been considered as interesting candidates for many applications such as dye-sensitized solar cells [145], electrolytes in supercapacitors [146] or for electrochemical sensing [147].

Another important electrochemical property of ILs is their conductivity, due to the mobility of ions within their structure, which is crucial for efficient charge transport in electrochemical devices. A wide range of conductivities has been reported for ILs from 0.1 to 20 $\mathrm{mS\,cm^{-1}}$ [148]. It can influenced by many factors such as density, viscosity, ion size, charge delocalization or ionic motions [149]. It is essential to consider the viscosity for electrochemistry since it affects the ionic conductivity, diffusivity, dispersion, mixing, filtration, and even equipment selections.

Fluorinated anions are the most reported and more common anions for IL-based electrolytes because of their interesting electrochemical properties, but environmental concerns encouraged the need to design ILs with other anions.

Carboxylate-based ILs can be environmentally friendly and biodegradable, making them attractive alternatives to conventional organic solvents and electrolytes [146]. It should be highlighted that, as far as we know, the electrochemical properties of carboxylate-based ILs are not commonly reported in literature.

The new phosphonium carboxylate ILs under study have a great potential for electrochemical applications thanks to their favorable physico-chemical properties. Their electrochemical stability windows were assessed in order to evaluate their potential for electrochemical applications.

7.2 MATERIAL AND METHODS

The samples were degassed under primary vacuum for up to 48 hours before utilization. The electrochemical measurements were performed in a Faraday cage at various temperatures depending on the melting point of the IL. A SP-300 potentiostat from BioLogic was used in association with the EC-Lab software.

Cyclic voltammetry was performed with a three-electrode configuration. A silver wire was employed as pseudo-reference electrode, a Platinum wire as the auxiliary electrode and a glassy carbon working electrode was used (3 mm diameter, 0.07 $\mathrm{cm^{-2}}$). Once the IL was transferred to the measurement cell, argon was bubbled into the systems for at least 60 min to remove any traces of dissolved gases. The cyclic voltammograms showed were recorded at 100, 50, 25 and 10 $\mathrm{mV\,s^{-1}}$.

7.3 ELECTROCHEMICAL STABILITY

The ESWs of the ILs are estimated as the difference between the reduction potential at the cathode (E_C) and the oxidation potential at the anode (E_A) determined by the analysis of the voltammograms. It is important to note that the resulting ESWs listed in Table 7.1 are approximations. This is one of the first time that electrochemical stability of these types of

ILs is evaluated, so this constitutes a first approach to pave the way to future studies. The potential windows can be influenced by various parameters, with the type of working electrode being probably the most important factor. The scan rate was found to not be determinant for the determination of the ESWs (Table 7.1 and Figure A.1) as only small variations are observed at 10, 25, 50 and 100 mV s^{-1}.

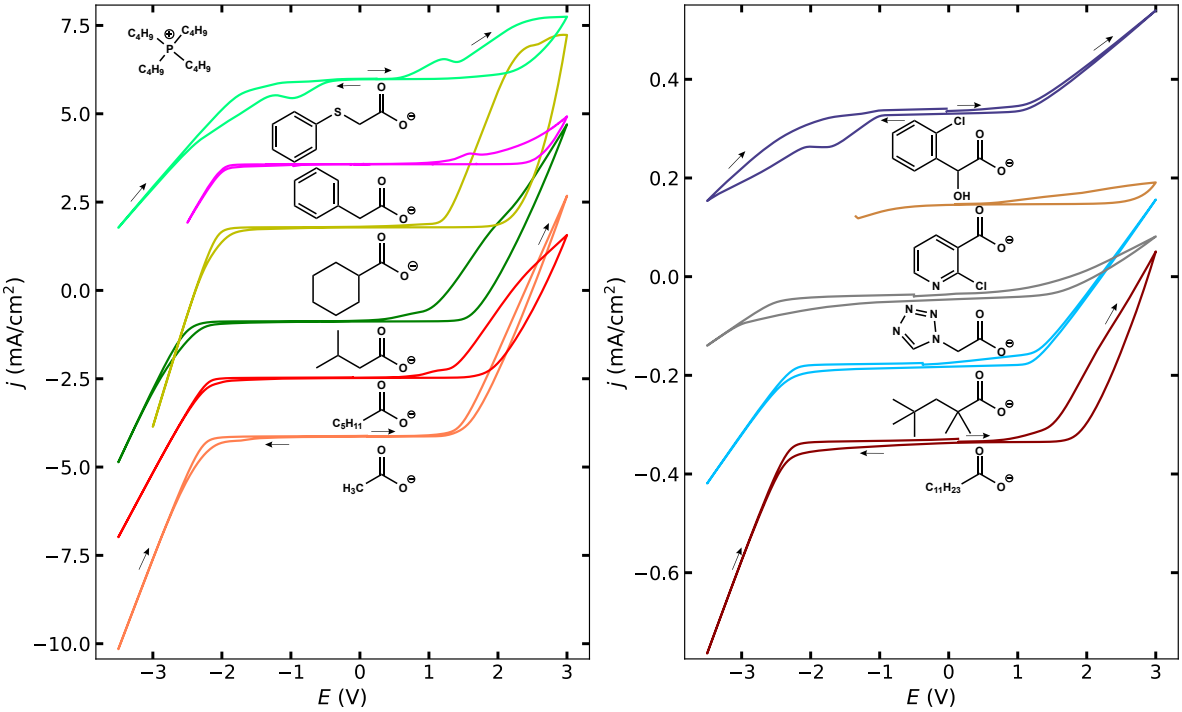

Figure 7.1 – Cyclic voltammetry of all the ILs under study with $[P_{4,4,4,4}]^+$ as common cation at 100 mV s^{-1}.

$[P_{4,4,4,4}][Me_4C_4COO]$ appears as the most electrochemically stable at the surface of glassy carbon electrode as depicted in Figure 7.1 with a ESW of 4.62 V which is higher than other imidazolium or phosphonium associated with $[NTf_2]^-$ [150, 151] or with flexible aromatic carboxylate anions [152]. It appears than the delocalization of the charge on the anion in aromatic carboxylate phosphonium ILs tend to widen the ESWs [153], but it was not observed here. For instance, $[P_{4,4,4,4}][TetrazC_1COO]$, whose negative charge is spread over the tetrazole ring, has a much smaller ESW of about 2.00 V.

It seems that the presence of aromatic rings as substituents in the carboxylate anion decreases the electrochemical stability of the IL as $[P_{4,4,4,4}][2-ClPyCOO]$, $[P_{4,4,4,4}][TetrazC_1COO]$, $[P_{4,4,4,4}][2-ClPhC_1OHCOO]$ and $[P_{4,4,4,4}][PhC_1COO]$ have a lower ESW, with the lowest observed for $[P_{4,4,4,4}][PhSC_1COO]$ (Table 7.1).

However, we can wonder if this lower stability is not due to the presence of trapped water as it is very difficult to completely remove traces of dispersed water molecules even with high temperature and vacuum treatments. This is due to the high affinity of water with carboxylate-based ILs due to the potential formation of strong hydrogen bonds. Indeed, a shoulder is noticed for several ILs upon oxidation in Figure 7.1. A similar feature has been previously attributed to

either the presence of methoxy groups in the phosphonium cations [151] or water resulting in its electrolysis at the electrode surface [154].

On the other hand, the presence of nitrogen atoms in the carboxylate substituent does not seem to significantly impact the anodic limit. The E_A of $[P_{4,4,4,4}][TetrazC_1COO]$ or $[P_{4,4,4,4}][2-ClPyCOO]$ is similar to that of aliphatic carboxylate-based ILs, provided no particular oxidation events occur. This is in contrast to findings for $[P_{4,4,4,4}][2,5-Pyra]$ and $[P_{4,4,4,4}][3-Pyra]$, where the presence of a second nitrogen atom lowered the anodic limit due to increased susceptibility to oxidation [137].

The oxidation events are shifted to lower potential and are also better defined by decreasing the scanning rate from 100 to 10 $mV\,s^{-1}$ as illustrated in Figure A.1 in Appendices. This is probably due to the fact that the oxidation reaction occurring is too slow to be complete for a high scanning rate [155]. Varying the scanning rate is consequently important to ensure that no electrochemical reaction is hidden due to slow kinetics.

Table 7.1 – Cathodic and anodic potential limits (E_C and E_A, respectively) and ESWs of the ILs with a glassy carbon working electrode. The measurements were carried out at various temperatures depending on the melting point of the ILs.

Sample	Rate / $mV\,s^{-1}$	E_C / V	E_A / V	ESW / V	Sample	Rate / $mV\,s^{-1}$	E_C / V	E_A / V	ESW / V
$[P_{4,4,4,4}][2-ClPyCOO]$	10	-0.73	1.23	1.95	$[P_{4,4,4,4}][C_1COO]$	10	-2.07	1.26	3.33
	25	-0.67	1.11	1.78		25	-2.07	1.20	3.26
	50	-0.54	0.90	1.44		50	-2.03	1.38	3.41
	100	-0.41	0.67	1.08		100	-2.01	1.35	3.36
$[P_{4,4,4,4}][TetrazC_1COO]$	10	-1.22	1.04	2.26	$[P_{4,4,4,4}][C_5COO]$	10	-2.01	1.10	3.11
	25	-1.17	0.94	2.11		25	-2.00	0.99	2.99
	50	-1.16	0.91	2.07		50	-1.98	0.99	2.97
	100	-1.14	0.85	1.99		100	-1.96	0.94	2.90
$[P_{4,4,4,4}][2-ClPhC_1OHCOO]$	10	-0.96	1.10	2.06	$[P_{4,4,4,4}][C_{11}COO]$	10	-2.05	1.19	3.24
	25	-0.96	0.99	1.95		25	-2.02	1.14	3.16
	50	-0.96	0.99	1.95		50	-1.99	1.12	3.11
	100	-0.96	0.99	1.95		100	-1.91	1.11	3.02
$[P_{4,4,4,4}][PhSC_1COO]$	10	-0.48	0.55	1.03	$[P_{6,6,6,14}][C_{11}COO]$	10	-1.37	0.81	2.18
	25	-0.48	0.55	1.03		25	-1.25	0.78	2.03
	50	-0.48	0.55	1.03		50	-1.20	0.70	1.90
	100	-0.48	0.59	1.07		100	-1.11	0.42	1.53
$[P_{4,4,4,4}][PhC_1COO]$	10	-1.55	0.96	2.51	$[P_{4,4,4,4}][Me_4C_4COO]$	10	-	-	-
	25	-1.35	0.94	2.29		25	-2.81	1.81	4.62
	50	-1.24	0.95	2.19		50	-2.82	1.81	4.63
	100	-1.15	0.95	2.10		100	-2.81	1.81	4.62
$[P_{4,4,4,4}][MeC_3COO]$	10	-2.26	0.98	3.24	$[P_{6,6,6,14}][Me_4C_4COO]$	10	-2.57	1.48	4.05
	25	-2.21	0.94	3.15		25	-2.54	1.45	3.99
	50	-2.19	0.67	2.86		50	-2.49	1.38	3.87
	100	-2.17	0.55	2.72		100	-2.30	1.40	3.70
$[P_{4,4,4,4}][c-C_6COO]$	10	-1.92	1.21	3.13					
	25	-1.89	1.19	3.08					
	50	-1.85	1.19	3.04					
	100	-1.80	1.17	2.97					

For the ILs with $[P_{4,4,4,4}]^+$ as cation, a continuous reduction below approximately −2 V is noticed on the cathodic scans. This phenomenon has been previously observed in other phosphonium-based ILs and is attributed to the presence of acidic H_α protons on the cation [142, 143, 153]. The type of alkyl substituent on the carboxylate anion does not seem to have a major impact on E_C (around 2.0 V), but an improved cathodic stability is noticed for $[P_{4,4,4,4}][Me_4C_4COO]$ with a E_C= −2.81 V. This could potentially be attributed to strong interactions with the carboxylate or strong hydrogen bonding, but further investigation is necessary to fully elucidate the underlying mechanisms.

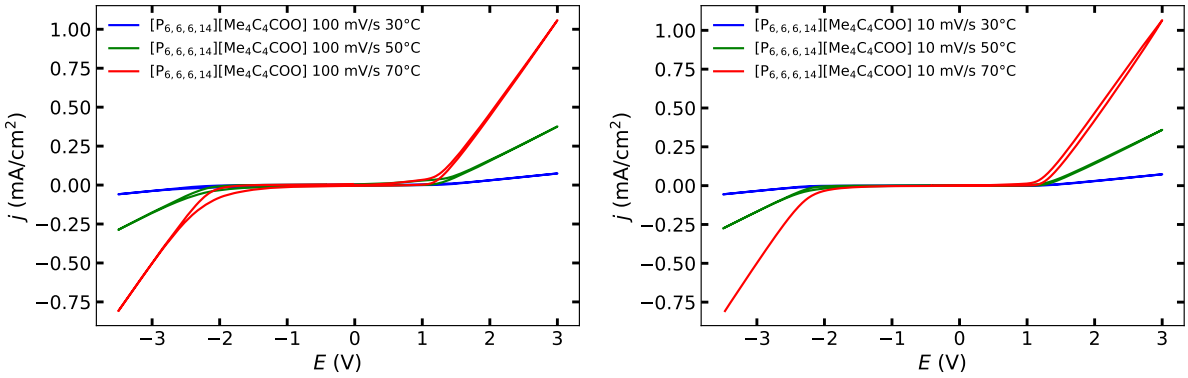

Figure 7.2 – Cyclic voltammetry of $[P_{6,6,6,14}][Me_4C_4COO]$ at (left) 100 and (right) 10 mV s^{-1} at — 30 °C, — 50 °C and — 70 °C.

On the contrary, the presence of other chemical functionalities in carboxylate substituents ($[2-ClPyCOO]^-$, $[TetrazC_1COO]^-$, $[2-ClPhC_1OHCOO]^-$ and $[PhSC_1COO]^-$) leads to a decrease of E_C. An irreversible reduction event is occurring at −1.71 and −0.98 V for $[P_{4,4,4,4}][2-ClPhC_1OHCOO]$ and $[P_{4,4,4,4}][PhSC_1COO]$, respectively, as depicted in Figure 7.1. Initially, it was hypothesized that this reduction could be due to the remaining dissolved oxygen in the ILs, but even after bubbling Ar for up to 12 h, the peak remained unchanged. These features might be due to small quantities of impurities remaining from the starting materials.

The presence of a bulkier phosphonium cation, with longer alkyl side chains, decreases both E_C and E_A. It leads to a narrower ESW as exemplified by comparison of the voltammogram of $[P_{4,4,4,4}][Me_4C_4COO]$ and $[P_{6,6,6,14}][Me_4C_4COO]$ in Figure 7.3, with a decrease of the ESWs from 4.62 to 3.70 V. The decrease is even more important for $[P_{4,4,4,4}][C_{11}COO]$ and $[P_{6,6,6,14}][C_{11}COO]$ (from 3.02 to 1.53 V, respectively). This might be due to the much lower conductivity of ILs based on $[P_{6,6,6,14}]^+$ as cation compared to the ones with $[P_{4,4,4,4}]^+$ as it was observed with various imidazolium ILs [156]. The increase of alkyl chain length in the cations does not seem to always decrease the electrochemical stability as the reverse trend was observed in imidazolium [157, 158] or other phosphonium-based ILs [159].

The impact of temperature on the ESWs was studied because it was necessary to heat a few ILs that are solid at r. t. and the effect was assessed using $[P_{6,6,6,14}][Me_4C_4COO]$ as a representative example (Figure 7.2). Only a small decrease of both E_C and E_A was observed upon heating leading to a slight narrowing of the ESW from 3.70 V at 30 °C to 2.87 V at 70 °C without any major effect of the scanning rate. This variation is certainly due to the decrease of viscosity upon heating which improves mass transport properties in the bulk of the IL, inducing more frequent

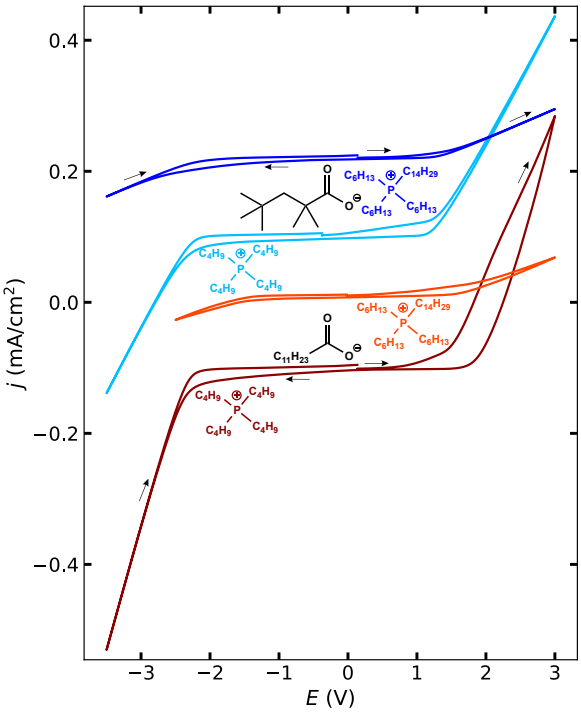

Figure 7.3 – Cyclic voltammetry of from bottom to top — $[P_{4,4,4,4}][C_{11}COO]$, — $[P_{6,6,6,14}][C_{11}COO]$, — $[P_{4,4,4,4}][Me_4C_4COO]$ and — $[P_{6,6,6,14}][Me_4C_4COO]$ at $100\,mV\,s^{-1}$.

interactions between the electrode and the ions [160]. Both cathodic and anodic peak current were much higher with increased temperature stemming from the decrease of viscosity [161].

A more important decrease of the ESW was found for other phosphonium carboxylate ILs, and no clear link between the thermal and the electrochemical stability was found contrary to what was reported for aromatic carboxylate phosphonium ILs [153].

Main ideas

The presence of aromatic substituents in the carboxylate anions and longer alkyl chains in the cations tends to decrease the electrochemical stability. The influence of alkyl chain length varies among ILs, highlighting the interplay between molecular structure and electrochemical behavior. Temperature appears to have only a minor effect, contrary to what was sometimes reported for other ILs. Further studies should be carried out to understand the origins of the events observed in the voltammograms with, for example, *in situ* spectroscopy. This is essential because if these events are due to the presence of impurity traces and not the IL itself, the real ESW of these ILs might be much larger which is crucial for their applications.

8

MIXTURES OF IONIC LIQUIDS

Context

In this chapter, an exploration of the effect of mixing ILs is proposed to fluidify viscous or solid ILs in order to broaden their liquid windows. The impact of adding a less viscous and denser IL on their physical and chemical properties has been thoroughly studied. The analysis of their excess molar volumes and viscosity deviations revealed unusual behaviors. The interactions between the ions were asses through the examination of the vibrational modes obtained by FT-IR measurements.

8.1 INTRODUCTION

The enhancement of the fluidity is an essential factor influencing the practical applicability of ILs in various processes, such as catalysis, electrochemistry, and separation technologies because high viscosity can impede mass transfer which limits the efficiency of these processes.

One way would be the incorporation of molecular co-solvents to the IL without modifying the combination of cations and anions [162, 163]. Intensive research has focused on exploring the solid-liquid phase behavior of such systems [164], but a major drawback of this approach is the potential loss of essential IL properties, such as non-volatility or high thermal stability.

An alternative strategy is the addition of another IL rather than a molecular solvent. Mixing a solid IL with a liquid one at r.t. might be a promising approach to widen the liquid window, while keeping the desired properties of ILs. It enables the tailoring of IL properties *via* mixture preparation, offering opportunities to improve and design the physicochemical characteristics of ILs as required while preserving their absorption capacity of gas.

Mixtures of $[P_{4,4,4,4}][c{-}C_6COO]$, $[P_{4,4,4,4}][PhSC_1COO]$, $[P_{4,4,4,4}][p{-}MeBzCOO]$ and $[P_{4,4,4,4}][MeC_3COO]$, with another phosphonium-based IL, $[P_{6,6,6,14}][NTf_2]$, were prepared. The densities and viscosities of the mixtures were initially measured to investigate their excess molar volumes and viscosity deviations from the average obtained by molar abundance averaging. FT-IR spectroscopy was employed to assess the interactions between the different components of the mixtures. The thermal properties were analyzed for selected mixtures using TGA and DSC to obtain insights into the impact of IL mixing on thermal stability and the liquid window.

It was not possible to calculate the excess molar properties and viscosity deviations of $\{[P_{4,4,4,4}][p{-}MeBzCOO]\}_x\{[P_{6,6,6,14}][NTf_2]\}_{1-x}$ mixtures because the density and the viscosity of the pure $[P_{4,4,4,4}][p{-}MeBzCOO]$ could not be determined due to its too high melting point (90.7 °C, from Chapter 3).

8.2 MATERIALS AND METHODS

Trihexyltetradecylphosphonium bis(trifluoromethyl sulfonylimide) ($[P_{6,6,6,14}][NTf_2]$, >98 % pure) was purchased from Iolitec. The synthesis and the characterization of the pure ILs are reported in Chapter 3 for $[P_{4,4,4,4}][c{-}C_6COO]$, $[P_{4,4,4,4}][p{-}MeBzCOO]$ and $[P_{4,4,4,4}][MeC_3COO]$ and in Chapter 5 for $[P_{4,4,4,4}][PhSC_1COO]$.

The ionic liquid mixtures were prepared by weighting the components, which were degassed for at least 72 h under a primary vacuum, using a New Classic MS Mettler Toledo balance with an accuracy of ± 0.01 mg inside a glove box GP (campus) Jacomex. The mixtures prepared and their exact composition are listed Table 8.1.

Chemicals	m_{IL1}	m_{IL2}	x_{IL1}
$\{[P_{4,4,4,4}][c{-}C_6COO]\}_{0.75}\{[P_{6,6,6,14}][NTf_2]\}_{0.25}$	1.15860	0.77762	0.74687
$\{[P_{4,4,4,4}][c{-}C_6COO]\}_{0.50}\{[P_{6,6,6,14}][NTf_2]\}_{0.50}$	0.70334	1.37050	0.50351
$\{[P_{4,4,4,4}][c{-}C_6COO]\}_{0.35}\{[P_{6,6,6,14}][NTf_2]\}_{0.65}$	0.65645	2.39012	0.35181
$\{[P_{4,4,4,4}][c{-}C_6COO]\}_{0.20}\{[P_{6,6,6,14}][NTf_2]\}_{0.80}$	0.27592	2.13189	0.20364
$\{[P_{4,4,4,4}][c{-}C_6COO]\}_{0.15}\{[P_{6,6,6,14}][NTf_2]\}_{0.85}$	0.19787	2.23685	0.14880
$\{[P_{4,4,4,4}][PhSC_1COO]\}_{0.80}\{[P_{6,6,6,14}][NTf_2]\}_{0.20}$	1.99826	0.90411	0.79830
$\{[P_{4,4,4,4}][PhSC_1COO]\}_{0.68}\{[P_{6,6,6,14}][NTf_2]\}_{0.32}$	1.34779	1.12110	0.68312
$\{[P_{4,4,4,4}][PhSC_1COO]\}_{0.50}\{[P_{6,6,6,14}][NTf_2]\}_{0.50}$	1.00490	1.79600	0.50049
$\{[P_{4,4,4,4}][PhSC_1COO]\}_{0.29}\{[P_{6,6,6,14}][NTf_2]\}_{0.71}$	0.51017	2.20520	0.29293
$\{[P_{4,4,4,4}][p{-}MeBzCOO]\}_{0.74}\{[P_{6,6,6,14}][NTf_2]\}_{0.26}$	1.16180	0.79050	0.73987
$\{[P_{4,4,4,4}][p{-}MeBzCOO]\}_{0.49}\{[P_{6,6,6,14}][NTf_2]\}_{0.51}$	1.15281	2.34765	0.48675
$\{[P_{4,4,4,4}][p{-}MeBzCOO]\}_{0.40}\{[P_{6,6,6,14}][NTf_2]\}_{0.60}$	0.60020	1.74652	0.39893
$\{[P_{4,4,4,4}][p{-}MeBzCOO]\}_{0.24}\{[P_{6,6,6,14}][NTf_2]\}_{0.76}$	0.26972	1.62441	0.24280
$\{[P_{4,4,4,4}][MeC_3COO]\}_{0.74}\{[P_{6,6,6,14}][NTf_2]\}_{0.26}$	1.55801	1.15664	0.74055

Table 8.1 – Composition of the ionic liquid mixtures prepared. $\{[IL_1]\}_x\{[IL_2]\}_{1-x}$ denotes that x of $[IL_1]$ is mixed with (1-x) of $[IL_2]$, in mole fraction.

The density, viscosity, FT-IR, TGA and DSC measurements used to characterize the mixtures were explained in detail in Chapter 3.

8.3 DENSITY AND VISCOSITY MEASUREMENTS

An ideal mixture is defined as a homogeneous mixture of substances that follows Raoult's Law and has physical properties linearly dependent to the properties of the pure components. The excess molar volume (V^E) is calculated according to the Equation 8.1 and it represents the difference between the volume of the mixture and that of the ideal mixture:

$$V^E = V_{mixture} - V_{ideal\ mixture}$$
$$V^E = \left(\frac{x_{IL1}M_{IL1} + x_{IL2}M_{IL2}}{\rho_{mix}}\right) - \left(\frac{x_{IL1}M_{IL1}}{\rho_{IL1}} + \frac{x_{IL2}M_{IL2}}{\rho_{IL2}}\right) \quad (8.1)$$

where V_{mixture} and $V_{\text{ideal mixture}}$ are the molar volumes of the mixture and the ideal mixtures, respectively. ρ_{mix} is the density of the mixture, ρ_{IL}, x_{IL} and M_{IL} are the density, the mole fraction and the molar mass of each pure IL, respectively.

V^{E} arises from structural contributions as well as interactions between the components of the liquid mixture. It results from the presence of suitable interstitial accommodations which stems from the size and the shape of the molecules involved leading to a more compact structure. Specific intermolecular interactions, such as charge-transfer or hydrogen bonding, are also contributing negatively to V^{E} which may result in a more efficient packing of the molecules. On the contrary, a positive V^{E} corresponds to an expansion of the mixing volume due to a looser microscopic structure.

The Redlich-Kister (RK) polynomial [165] (Equation 8.2) is used to fit the calculated V^{E} in which A_{i} are parameters obtained using a least-squares fitting procedure.

$$V^{\text{E}} = x_{\text{IL}}(1 - x_{\text{IL}}) \sum_{i=0}^{\text{n}} [A_{\text{i}}(1 - 2x_{\text{IL}})^{\text{i}}] \tag{8.2}$$

The examination of the average absolute deviation (AAD) is calculated following Equation 8.3:

$$AAD = \frac{100}{N} \sum \frac{|V^{\text{E}}_{\text{exp}} - V^{\text{E}}_{\text{calc}}|}{V^{\text{E}}_{\text{exp}}} \tag{8.3}$$

As expected, the density of the mixtures decreases with increasing temperature as depicted in Figure 8.1 (left) for some mixtures. All the measured densities are listed in Table B.1 in Appendices. The mixture densities increase as the proportion of $[P_{6,6,6,14}][NTf_2]$ increases because it is denser than the pure ILs used here.

The excess molar volumes of the $[P_{4,4,4,4}][c{-}C_6COO]$ mixtures with $[P_{6,6,6,14}][NTf_2]$ are positive for all the temperatures and for all the compositions studied as depicted in Figure 8.1 (top right) with the exact values reported in Table B.3. It suggests the presence of less favourable and weak interactions between the different ions compared to the ones in the ideal mixtures.

In Figure 8.1 (top right), an asymmetry of the curve is noticed with a maximum found around 0.35 mole fraction of $[P_{4,4,4,4}][c{-}C_6COO]$. It shows that a small addition of $[P_{4,4,4,4}][c{-}C_6COO]$ will disrupt more the organization of the mixture compared to ideality. The V^{E} slightly increases with higher temperatures which indicates that the mixtures are more expansible than the ideal mixtures. Similar features were found for the mixtures based on $[P_{4,4,4,4}][PhSC_1COO]$ with a likely asymmetry, but the V^{E} are smaller with a maximum at around $1.75\,\text{cm}^3\,\text{mol}^{-1}$ (Figure 8.1 (bottom)). The fitting curves depicted in Figure 8.1 (right) are RK polynomials of degree 2 with the fitting parameters reported in Table B.4 in Appendices.

A high V^{E} was calculated for $\{[P_{4,4,4,4}][MeC_3COO]\}_{0.74}\{[P_{6,6,6,14}][NTf_2]\}_{0.26}$ which is similar to the maximum found for $[P_{4,4,4,4}][c{-}C_6COO]$-based mixtures (Table B.3), but it was the only mixture based on $[P_{4,4,4,4}][MeC_3COO]$ prepared.

Usually, the V^{E} for mixtures of ILs found in literature are relatively small which means that the mixtures of ILs are close to ideality relatively to the mixing law. A few mixtures with V^{E}

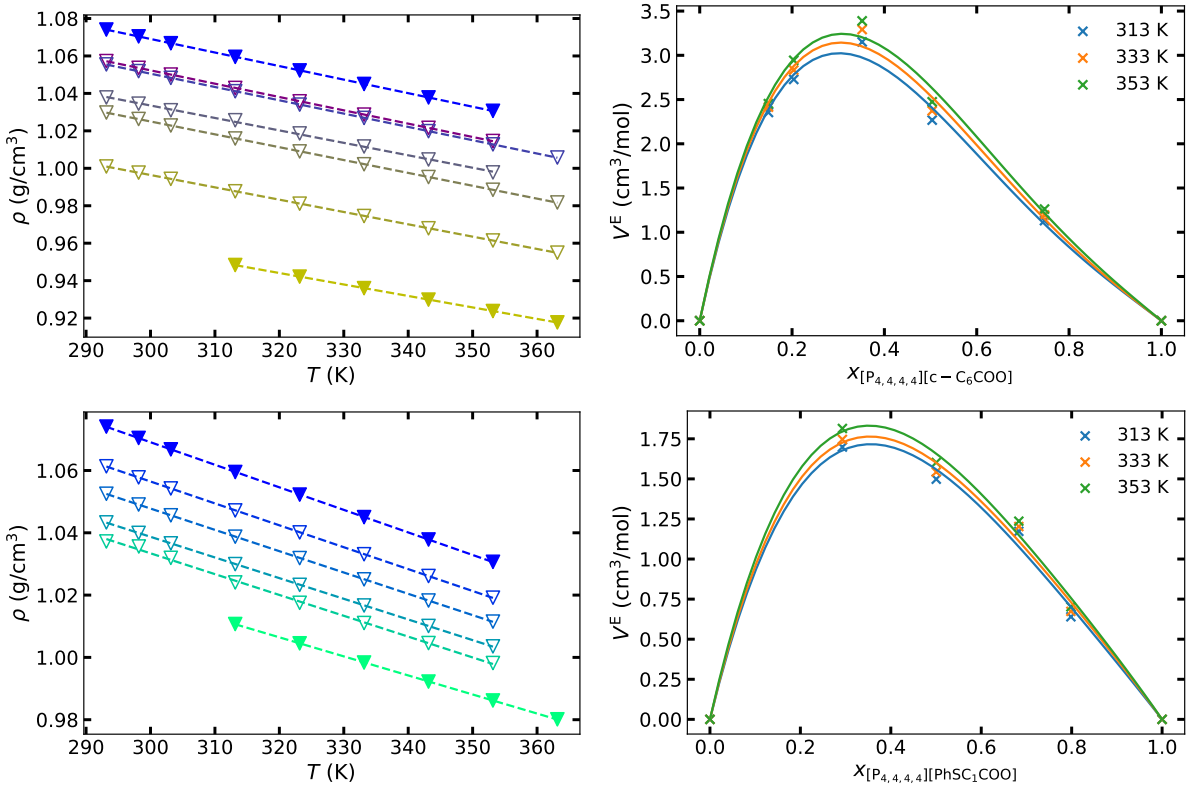

Figure 8.1 – Experimental densities of (top left) ▼ $[P_{4,4,4,4}][c{-}C_6COO]$, (bottom left) ▼ $[P_{4,4,4,4}][PhSC_1COO]$ and ▼ $[P_{6,6,6,14}][NTf_2]$ and their mixtures (▽ with the color gradient indicating the increasing mole fraction of $[P_{6,6,6,14}][NTf_2]$ from bottom to top) as a function of temperature. Dashed lines represent linear fits. Excess molar volume (V^E) as a function of (top right) $[P_{4,4,4,4}][c{-}C_6COO]$ and (bottom right) $[P_{4,4,4,4}][PhSC_1COO]$ mole fraction at × 313 K, × 333 K and × 353 K. Solid lines represent the RK polynomial fitting.

around 1.5 $cm^3\,mol^{-1}$ have been reported, and the first mixtures with $V^E > 3\,cm^3\,mol^{-1}$ have been reported recently [166]. They were based on various ammonium carboxylate ILs mixed with 1-butyl-3-methylimidazolium dimethylphosphate, which are ILs with lower molar volumes than the ILs studied herein.

As expected, the viscosity decreases with the increasing temperature following the VFT equation (Chapter 3) as illustrated in Figure 8.2 (left) and the values for all the mixtures are listed in Table B.5 in Appendices. The viscosity of a mixture depends on the liquid structure depending on the size, the shape and molecular interactions of the molecules. The viscosity is decreasing with the increasing amount of $[P_{6,6,6,14}][NTf_2]$ which acts as a fluidifying agent. It is interesting to highlight the fact that for $\{[P_{4,4,4,4}][c{-}C_6COO]\}_{0.15}\{[P_{6,6,6,14}][NTf_2]\}_{0.85}$ and $\{[P_{4,4,4,4}][c{-}C_6COO]\}_{0.20}\{[P_{6,6,6,14}][NTf_2]\}_{0.80}$, the viscosities are slightly lower than the one of $[P_{6,6,6,14}][NTf_2]$.

In order to have a better insight on the dynamic properties of ILs mixtures, the determination of the viscosity deviation ($\Delta\eta$) provides a way to asses how the mixtures behave compared to the viscosity of a mixture usually defined as a logarithm weighted average of the viscosity of each component [167, 168]. The deviation is calculated as depicted in Equation 8.4, where η_{mix} is the

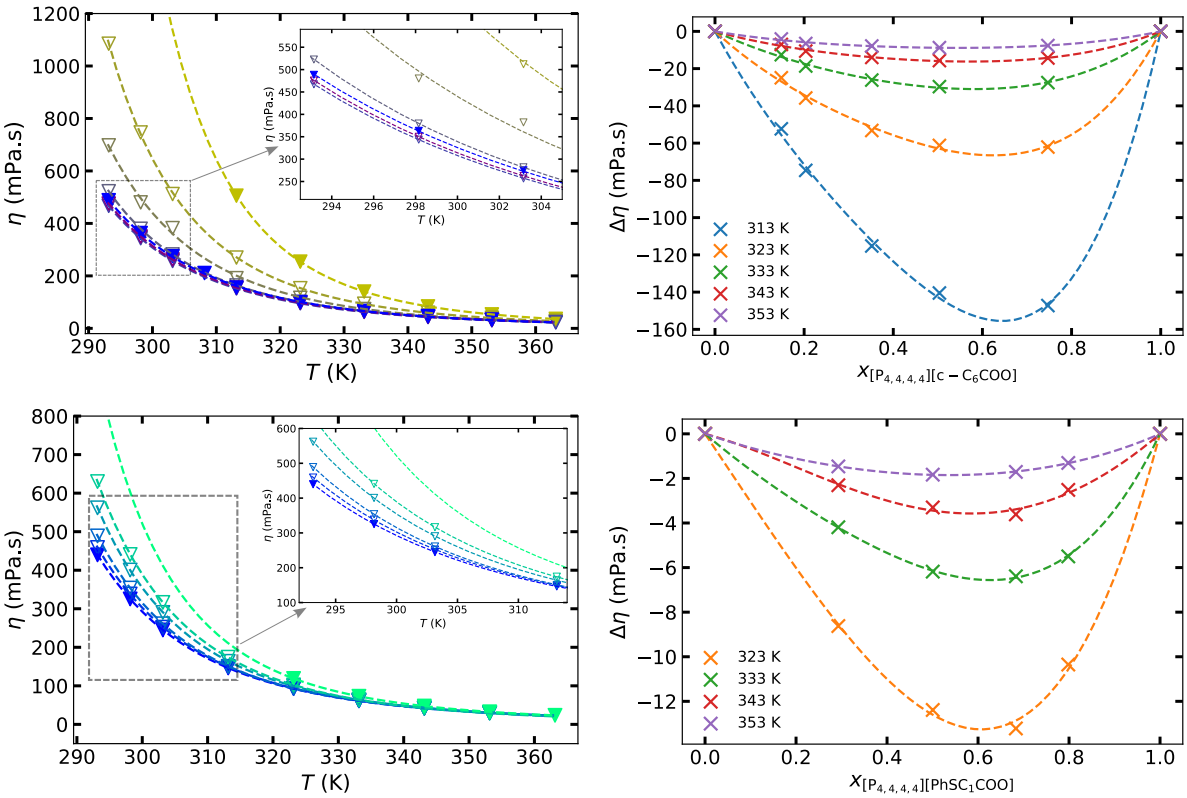

Figure 8.2 – Experimental viscosities of (top left) ▼ $[P_{4,4,4,4}][c{-}C_6COO]$, (bottom left) ▼ $[P_{4,4,4,4}][PhSC_1COO]$ and ▼ $[P_{6,6,6,14}][NTf_2]$ and their mixtures (▽ with the color gradient indicating the increasing mole fraction of $[P_{6,6,6,14}][NTf_2]$ from top to bottom) as a function of temperature. Dashed lines represent fits using the VFT equation. Viscosity deviations ($\Delta\eta$) as a function of (top right) $[P_{4,4,4,4}][c{-}C_6COO]$ and (bottom right) $[P_{4,4,4,4}][PhSC_1COO]$ mole fraction between 313–353 K. Dashed lines represent the RK polynomial fitting.

viscosity of the binary mixture, x_{IL} and η_{IL} are the mole fraction and the viscosity of the pure IL, respectively.

$$\Delta\eta = \eta_{mix} - x_{IL1}\eta_{IL1} - x_{IL2}\eta_{IL2} \tag{8.4}$$

The $\Delta\eta$ determined for the mixtures based on $[P_{4,4,4,4}][c{-}C_6COO]$ are much more negative than the ones for $[P_{4,4,4,4}][PhSC_1COO]$ and $[P_{4,4,4,4}][MeC_3COO]$-based mixtures as illustrated in Figure 8.2 (right) with the exact values reported in Table B.7 in Appendices. The negative deviations are representative of weak and non-specific interactions stemming from the size and the shape of the ions involved.

It is possible to notice the asymmetry of the fitting curve in both $[P_{4,4,4,4}][c{-}C_6COO]$ and $[P_{4,4,4,4}][PhSC_1COO]$ with a minimum found between 0.50 and 0.75 mole fraction of phosphonium carboxylate IL. A RK polynomial of degree 2 (Equation 8.2) is also used to fit the viscosity deviation with the obtained parameters reported in Table B.8 in Appendices. Nonetheless, the

asymmetric curve is shifted to the richer carboxylate-based IL composition side while the reverse was observed for the V^{E}.

Another way to have a better understanding of the dynamic properties of ILs mixtures is to consider the logarithm of the viscosity of the various mixtures as a function of the composition as expressed in Equation 8.5. A clear deviation of $\ln(\eta(x))$ of the mixtures is noticed in Figure 8.3 compared to the weighted average of the viscosity logarithm of its constituents (dashed lines). A third term , d, has been consequently added in the equation for viscosity [169] to take into consideration this deviation:

$$\ln(\eta(x)) = x_{IL1}\ln(\eta_{IL1}) - x_{IL2}\ln(\eta_{IL2}) + x_{IL1}x_{IL2}d \tag{8.5}$$

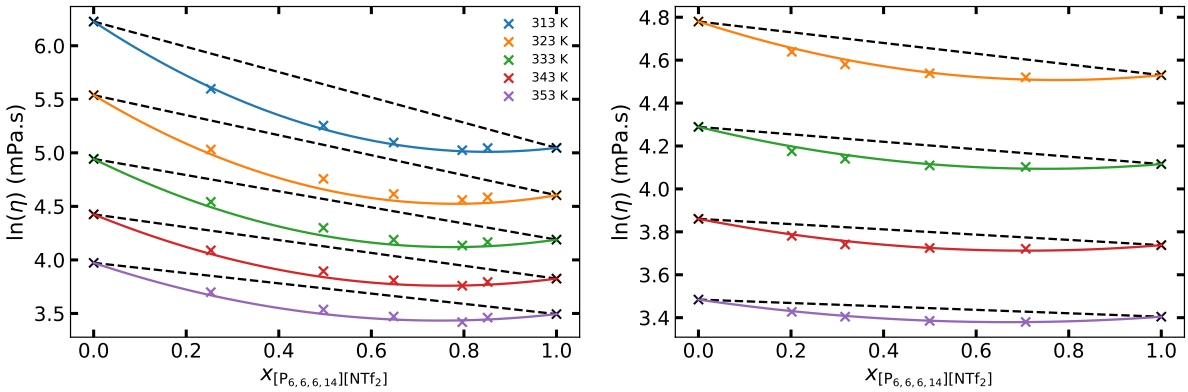

Figure 8.3 – Logarithm of the viscosity of (left) $\{[P_{4,4,4,4}][c{-}C_6COO]\}_x\{[P_{6,6,6,14}][NTf_2]\}_{(1-x)}$ and (right) $\{[P_{4,4,4,4}][PhSC_1COO]\}_x\{[P_{6,6,6,14}][NTf_2]\}_{(1-x)}$ as a function of composition between 313–353 K. The dashed lines represent the logarithm weighted average viscosity and the full lines are the fit to Equation 8.5. The value determined for d are (left) -2.02 at 313 K, -1.67 at 323 K, -1.37 at 333 K, -1.15 at 343 K and -0.96 at 353 K and (right) -0.45 at 323 K, -0.35 at 333 K, -0.30 at 343 K and -0.23 at 353 K.

Larger deviations are noticed at lower temperatures in Figures 8.2 (right) and 8.3, while the mixtures are getting closer to the logarithm weighted average viscosity for ILs mixtures when the temperature increases with a $\Delta\eta$ and a d value getting closer to 0. The greater $\Delta\eta$ and d values calculated for $\{[P_{4,4,4,4}][c{-}C_6COO]\}_x\{[P_{6,6,6,14}][NTf_2]\}_{(1-x)}$ are probably due to the less flexible structure of the cyclohexane substituent, on the carboxylate anion.

8.4 FT-IR MEASUREMENTS

FT-IR measurements were initially conducted on both the pure $[P_{4,4,4,4}][c{-}C_6COO]$ and $[P_{6,6,6,14}][NTf_2]$ compounds, but also on their mixtures to analyze the modification of the intermolecular interactions within the mixtures. For the sake of clarity, we chose to present only the FT-IR spectra of three mixtures ($x_{[P_{4,4,4,4}][c-C_6COO]}$= 0.75, 0.50, and 0.25). In Figure 8.4, only the major bands representing the most significant vibrational modes of both cations and anions were highlighted, and the rest of the spectra are depicted in Figure B.1 in Appendices.

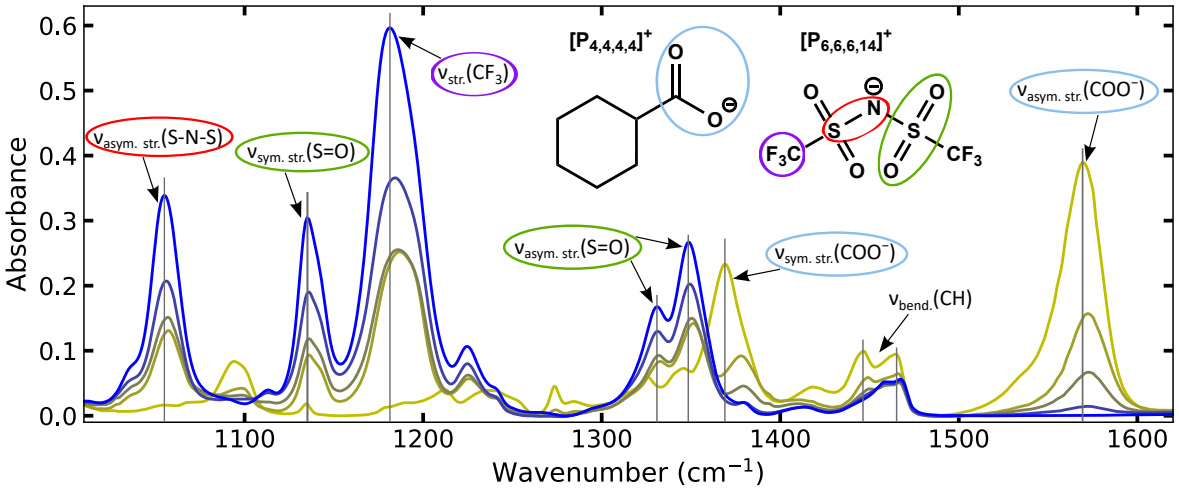

Figure 8.4 – FT-IR spectra of the pure $[P_{4,4,4,4}][c{-}C_6COO]$ and $[P_{6,6,6,14}][NTf_2]$ and 3 of their mixtures ($x_{[P_{4,4,4,4}][c-C_6COO]}$= 0.75, 0.50 and 0.20). The grey lines are guidelines to observe the shifts.

Observations reveal a noteworthy shift to higher wavenumbers, indicating higher energy (blue shift) in the vibrational modes associated of the $[NTf_2]^-$ anion as the proportion of $[P_{4,4,4,4}][c{-}C_6COO]$ increases. This shift is exemplified in Figure 8.4 with the S−N−S asymmetric stretching (in red), the CF_3 stretching (in purple), and the S=O asymmetric and symmetric stretching (in green). A similar trend is observed for the characteristic COO^- stretching modes (in light blue) of the $[c{-}C_6COO]^-$ anion as the proportion of $[P_{6,6,6,14}][NTf_2]$ increases.

The shifts arise from slightly longer distances between the anions and cations in the mixtures compared to the pure ILs. Specifically, in the mixture with $x_{[P_{4,4,4,4}][c-C_6COO]}$ = 0.20, the $[NTf_2]^-$ anions are closer to the cations, while in the mixture with $x_{[P_{4,4,4,4}][c-C_6COO]}$= 0.75, the $[c{-}C_6COO]^-$ anions are closer to the cations. This increase of ion distances aligns with the calculated excess molar volume (V^E), indicating volume expansion upon mixing.

In contrast to the behavior observed for the anions, red shifts are evident in the bands associated with the phosphonium cations. Peaks attributed to the asymmetric and symmetric stretching of CH_2 and CH_3 (Figure B.1), as well as those related to CH bending (Figure 8.4), exhibit lower energy shifts with increasing $x_{[P_{4,4,4,4}][c-C_6COO]}$. This phenomenon likely stems from the less energetically active vibrational modes of the $[P_{4,4,4,4}]^+$ cations compared to those of the $[P_{6,6,6,14}]^+$ cations, owing to higher symmetry.

Similar trends have been observed for mixtures based on $[P_{4,4,4,4}][PhSC_1COO]$ and $[P_{4,4,4,4}]$ $[p{-}MeBzCOO]$ with $[P_{6,6,6,14}][NTf_2]$ (Figures B.3 and B.2). Whereas, a blue shift is noticeable for bands associated with the $[NTf_2]^-$ anion, as well as those related to the $[PhSC_1COO]^-$ and $[p{-}MeBzCOO]^-$ anions with the increasing proportion of the carboxylate anion. Conversely, a red shift is observed for the vibrational modes belonging to both $[P_{4,4,4,4}]^+$ and $[P_{6,6,6,14}]^+$ cations.

The absence of new peaks or broadening of bands, but only shifts of the bands, suggests the absence of strong and specific interactions in the mixtures. This observation is consistent with the molar volume excess properties and viscosity deviations, indicating no significant effect from ion proximity or efficient packing in the mixtures.

8.5 THERMAL ANALYSIS

Having elucidated the intermolecular interactions through FT-IR measurements, we now turn our attention to the thermal properties of the mixtures. Understanding how these mixtures behave under different temperatures is crucial for assessing their suitability for various applications. Their phase transitions and thermal stability have been studied by DSC and TGA, respectively, to have a better understanding of the effect of $[P_{6,6,6,14}][NTf_2]$ as fluidifying agent and also to determine the temperature range in which these ILs are liquid.

As it was the case in Chapter 3, the onset temperature of the thermal event, labeled as (o), was preferentially reported, but if broad peaks were observed in the DSC thermograms, the maximum value of the signal was reported, labeled as (p), and all the results are reported in Table 8.2.

Table 8.2 – Glass transition temperatures (T_g), solid-solid transition temperatures (T_{s-s}), melting points (T_{fus}) and crystallization temperatures (T_{cr}) of the pure ILs and the mixtures prepared. The different temperatures reported were measured using DSC with a $10\,K\,min^{-1}$ heating rate. In order to facilitate the reading, when the onset temperature is reported, the value will be followed by (o) and when the peak temperature is reported, a (p) marker is used.

Sample	$\frac{T_g}{°C}$	$\frac{T_{s-s}}{°C}$	$\frac{T_{fus}}{°C}$	$\frac{T_{cr}}{°C}$
$[P_{4,4,4,4}][c-C_6COO]$ [170]	-44.6	61.8 (p)	46.3 (p)	
$\{[P_{4,4,4,4}][c-C_6COO]\}_{0.75}\{[P_{6,6,6,14}][NTf_2]\}_{0.25}$	-60.5	-	-	-
$\{[P_{4,4,4,4}][c-C_6COO]\}_{0.50}\{[P_{6,6,6,14}][NTf_2]\}_{0.50}$	-	-	-	-
$\{[P_{4,4,4,4}][c-C_6COO]\}_{0.35}\{[P_{6,6,6,14}][NTf_2]\}_{0.65}$	-	-	-	-
$\{[P_{4,4,4,4}][c-C_6COO]\}_{0.20}\{[P_{6,6,6,14}][NTf_2]\}_{0.80}$	-	-	-	-
$\{[P_{4,4,4,4}][c-C_6COO]\}_{0.15}\{[P_{6,6,6,14}][NTf_2]\}_{0.85}$	-	-	-	-
$[P_{4,4,4,4}][PhSC_1COO]$ [171]	-53.4	46.1 (o)	57.6 (o)	-19.1 (o)
$\{[P_{4,4,4,4}][PhSC_1COO]\}_{0.80}\{[P_{6,6,6,14}][NTf_2]\}_{0.20}$	-63.5	-	-	-
$\{[P_{4,4,4,4}][PhSC_1COO]\}_{0.68}\{[P_{6,6,6,14}][NTf_2]\}_{0.32}$	-66.8	-	-	-
$\{[P_{4,4,4,4}][PhSC_1COO]\}_{0.50}\{[P_{6,6,6,14}][NTf_2]\}_{0.50}$	-	-	-	-
$\{[P_{4,4,4,4}][PhSC_1COO]\}_{0.29}\{[P_{6,6,6,14}][NTf_2]\}_{0.71}$	-	-	-	-
$[P_{4,4,4,4}][p-MeBzCOO]$ [170]	-	-	90.7 (o)	11.6 (o)
$\{[P_{4,4,4,4}][p-MeBzCOO]\}_{0.74}\{[P_{6,6,6,14}][NTf_2]\}_{0.26}$	-62.6	27.2 (p)	67.9 (p)	-23.0 (p)
$\{[P_{4,4,4,4}][p-MeBzCOO]\}_{0.49}\{[P_{6,6,6,14}][NTf_2]\}_{0.51}$	-	-	-	-
$\{[P_{4,4,4,4}][p-MeBzCOO]\}_{0.40}\{[P_{6,6,6,14}][NTf_2]\}_{0.60}$	-	-	-	-
$\{[P_{4,4,4,4}][p-MeBzCOO]\}_{0.24}\{[P_{6,6,6,14}][NTf_2]\}_{0.76}$	-	-	-	-
$[P_{4,4,4,4}][MeC_3COO]$ [170]	-52.8	-8.0 (p)	66.0 (p)	-16.6 (p)
$\{[P_{4,4,4,4}][MeC_3COO]\}_{0.74}\{[P_{6,6,6,14}][NTf_2]\}_{0.26}$	-65.9	-	-	-
$[P_{6,6,6,14}][NTf_2]$ [172]	-75.1	-	-	-

The three pure carboxylate phosphonium ILs used here have a melting point (T_{fus}) above r.t., along with a clear crystallization point (T_{cr}) [170]. $[P_{6,6,6,14}][NTf_2]$ only presents a glass transition at −75.1 °C without any crystallization point [172].

The melting point of the mixtures based on $[P_{4,4,4,4}][p-MeBzCOO]$ is lowered from 90.7 to 67.9 °C for the mixture with $x_{[P_{4,4,4,4}][p-MeBzCOO]} = 0.74$. With a further increase in the proportion of $[P_{6,6,6,14}][NTf_2]$, no discernible melting point is observed. The gradual enrichment in $[P_{6,6,6,14}]^+$

and $[NTf_2]^-$ ions appears to impede crystallization, possibly due to unfavorable ion packing arising from differences in ion sizes and shapes. This observation is supported by the fact that the melting points of the other mixtures were not detected within the temperature range measured in the DSC (Table 8.2). Similar effects have been reported in mixtures based on pyrrolidinium [161] or imidazolium [173] ILs of varying sizes, as well as binary mixtures of imidazolium and pyridinium-based ILs [174].

The glass transition could only be detected at temperatures above −70 °C due to technical limitations. Only the mixtures with $x_{[P_{4,4,4,4}][RCOO]}$ exceeding approximately 0.7 exhibit a glass transition between −60 and −67 °C. The high asymmetry of the $[P_{6,6,6,14}]^+$ cation and the flexibility of the $[NTf_2]^-$ anion seem to hinder the ion packing, consequently lowering the lattice energy of the system [175].

The addition of $[P_{6,6,6,14}][NTf_2]$, even in small quantities, significantly reduces the IL's melting point, resulting in an expanded liquid window due to the absence of a crystalline phase.

Thermal stability stands as an essential property of ILs, particularly in applications where they serve as recyclable and reusable absorbents, often exposed to high temperatures during gas absorption processes. In Chapters 3 and 5, we extensively discussed the thermal stability of the pure ILs under both N_2 (for comparative purposes) and O_2 atmospheres. TGA measurements were not conducted on all mixtures under both atmospheres because the results we obtained were sufficient to assess the impact of IL mixing on the thermal stability.

The decomposition temperature (T_{dec}) corresponds to the upper limit of the usable IL liquid window. Herein, only the short-term thermal stability of the mixtures was studied. It is still important to keep in mind that it generally leads to an overestimation of the thermal stability in real conditions. All the T_{dec} are reported in Table B.9 in Appendices. They were determined at the intersection point of the tangents before and after the commencement of decomposition, influenced by the slope observed during the initial degradation step.

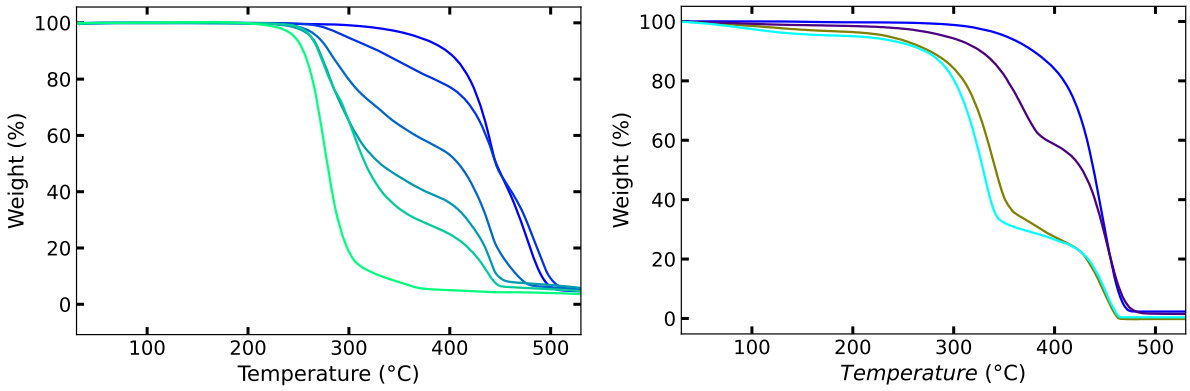

Figure 8.5 – TGA thermographs of (left) — $[P_{4,4,4,4}][PhSC_1COO]$ and its mixtures with — $[P_{6,6,6,14}][NTf_2]$ (with the color gradient indicating the increasing mole fraction of $[P_{6,6,6,14}][NTf_2]$ from (bottom to top) under O_2, and (right) of — $\{[P_{4,4,4,4}][p\text{−}MeBzCOO]\}_{0.24}\{[P_{6,6,6,14}][NTf_2]\}_{0.76}$, — $\{[P_{4,4,4,4}][c\text{−}C_6COO]\}_{0.75}\{[P_{6,6,6,14}][NTf_2]\}_{0.25}$, — $\{[P_{4,4,4,4}][MeC_3COO]\}_{0.74}\{[P_{6,6,6,14}][NTf_2]\}_{0.26}$ and — $[P_{6,6,6,14}][NTf_2]$ under N_2 with a heat rate of 10 °C min^{-1}.

All the pure ILs present a single decomposition step [170, 171], whereas the resulting mixtures are all exhibiting a complex two steps decomposition profile similar to the two independent ILs they are made of as depicted in Figure 8.5 (left) for $\{[P_{4,4,4,4}][PhSC_1COO]\}_x\{[P_{6,6,6,14}][NTf_2]\}_{1-x}$ under O_2 and (right) for $\{[P_{4,4,4,4}][MeC_3COO]\}_{0.74}\{[P_{6,6,6,14}][NTf_2]\}_{0.26}$, $\{[P_{4,4,4,4}][c{-}C_6COO]\}_{0.75}$ $\{[P_{6,6,6,14}][NTf_2]\}_{0.25}$ and $\{[P_{4,4,4,4}][p{-}MeBzCOO]\}_{0.24}\{[P_{6,6,6,14}][NTf_2]\}_{0.76}$ under N_2. It suggests the sequential thermal decomposition of the constituents without apparent effect of mixing on the short-term thermal stability of the resulting compound. The analysis of the decomposition paths of the pure ILs and the mixtures would be interesting.

A similar behavior was observed in various types of mixtures with different cations and anions. For example, with imidazolium [173] or pyrrolidinium [161, 176] based ILs, but also by mixing different types of cations such as pyridinium and imidazolium [174].

Therefore, it seems that mixing a tetrabutylphosphonium carboxylate IL with $[P_{6,6,6,14}][NTf_2]$ yield an intermediate thermal stability between the two parent ILs. It would be interesting to carry out a long-term stability study of the mixtures as it has been done in Chapters 4 and 5 for the pure ILs to verify if a similar phenomena is occurring.

Main ideas

The ILs which were solid at r. t. were successfully fluidized by addition of $[P_{6,6,6,14}][NTf_2]$ in various proportions and they were fully characterized. Important deviations from the mixing properties of an ideal mixture were found with the unexpectedly large excess molar volume V^E calculated compared to other mixtures of ILs. This is in accordance with the negative calculated viscosity deviations $\Delta\eta$ which accounts for weak and non-specific interactions.

FT-IR measurements have shed light on the modifications of the intermolecular interactions between the ions, providing valuable information for the comprehension of their physico-chemical properties. It confirmed the absence of strong and specific interactions in the mixtures.

Dynamic TGA measurements showed that mixing ILs the high thermal stability of the phosphonium carboxylate ILs is not affected by the addition of another IL with the clear consecutive degradation of both components of the mixture. DSC measurements revealed that the addition of $[P_{6,6,6,14}][NTf_2]$ drastically reduced the crystallisation point of the mixtures as they were not observable in the accessible temperature range. These two techniques permitted to attest the enlargement of the liquid window upon mixing.

Mixing ILs appear as a promising way to tune their properties as required offering a new way for their design for various applications ranging from catalysis to gas absorption technologies.

9

POROUS CARBOXYLATE IONIC LIQUIDS

Context

This chapter reports the first results on the use of the new phosphonium carboxylate ILs for the preparation of porous ILs (PoILs). The ILs were selected according to their ability to capture CO_2 or SO_2. The results provide the first insight on the impact of the carboxylate anion on the stability and properties of the porous IL suspensions of ZIF-8 and HKUST-1.

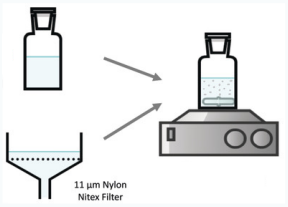

9.1 INTRODUCTION

The recent emergence of liquids possessing permanent porosity marks a significant transition from traditional solid microporous materials. While such materials have long found utility across diverse domains including gas capture [177], molecular separations [178], catalysis [179], and energy storage [180], the porous liquids open up new possibilities of exploration [181]. Unlike conventional liquids, which possess only transient porosity [182], porous liquids offer a unique combination of fluidity and microporous characteristics [183, 184]. Porous liquids offer the advantage of being easier to handle and store compared to porous solids. For example, liquid circulation systems, particularly in industrial settings such as post-combustion CCS applications, are simpler to implement [183].

Efforts have been made to integrate permanent porosity into liquids through various strategies. Four distinct types of porous liquids have been identified (illustrated in Figure 9.1). Type I comprises of pure molecular species with lasting liquid-state pores, close to room temperature. Type II involves solutions where microporous materials are dissolved in solvents that exclude cavities. Type III encompasses suspensions of microporous solids within liquids, also excluding cavities. Type IV consists of self-contained, meltable microporous extended frameworks.

In this study, our focus lies on type III porous liquids [186], prepared by dispersing chosen metal-organic frameworks (MOFs) into voluminous ILs [187, 188]. These porous ILs (PoILs) combine the advantages and the properties of both the porous solids and the ILs, resulting in a stable system with permanent porosity.

PoILs are of particular interest for us as they are media with promising properties for gas capture [189, 190] and separation [96, 191]. By increasing the free volume compared to the pure ILs, PoILs exhibit improved gas capture efficiency at similar gas partial pressures. However, selectivity may be low despite notable increases in gas uptake [188]. To address this limitation,

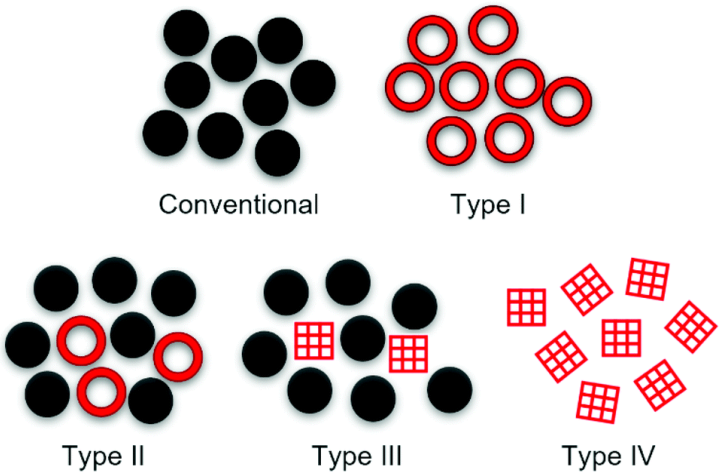

Figure 9.1 – Schematic representation of the conventional liquids lacking permanent intrinsic porosity with the four categories of porous liquids [185].

ILs can be designed to react selectively with gases like CO_2, thereby improving capture capacity and selectivity while reducing desorption energy for easier regeneration of the absorbent [96].

The potential design of the PoILs in tandem with our previous findings related to the effect of basicity of the carboxylate anions in phosphonium-based ILs on acid gas capture (Chapters 4-6) appears as a promising way to improve the capture capacity, the selectivity as well as the regeneration step. In what follows, we could not extensively study all the properties and the gas capture capacity for the PoILs. The purpose was to explore the potential of phosphonium carboxylate ILs to form PoILs useful for gas separations.

9.2 MATERIAL AND METHODS

ZIF-8 is a 2-methylimidazole zinc salt ($ZnIm_2$) with a major pore of 11.6 Å and an aperture of 3.4 Å [192]. HKUST-1 is a copper benzene-1,3,5-carboxylate ($Cu(BTC)_2$) with 9 Å main channels and tetrahedral-shaped 5.0 Å side-pockets, accessible through 3.0 Å triangular window [193]. They were both purchased from Sigma Aldrich.

The suspensions of either ZIF-8 or HKUST-1 in the pure $[P_{4,4,4,4}][2-ClPyCOO]$, $[P_{4,4,4,4}][C_{11}COO]$ and $[P_{4,4,4,4}][Me_4C_4COO]$ and in the mixture $\{[P_{4,4,4,4}][MeC_3COO]\}_{0.74}\{[P_{6,6,6,14}][NTf_2]\}_{0.26}$ were prepared at room temperature by weighing the components using a Mettler Toledo New Classic MS balance with an accuracy of ± 0.01 mg inside a glove box GP (campus) Jacomex. Both ZIF-8 and HKUST-1 have been passed through a Nylon Nitex 11 µm mesh to ensure a homogeneous size distribution of the solid particles. The samples were stirred at 400 – 500 rpm during 10 min. The pure chemicals were degassed for at least 72 h under a primary vacuum and the PoILs samples were also degassed under primary vacuum for up to 24 h before use. The prepared samples and their exact composition are listed in Table 9.1.

The density of the PoILs were measured as previously described in Chapter 3.

The CO_2 and SO_2 gas absorption measurements were performed following the procedures detailed in Chapter 4.

The electrochemical characterizations were realized similarly as explained in Chapter 7.

Table 9.1 – Composition of the porous ILs prepared.

Sample	m_{IL} / g	m_{MOF} / g	MOF w/w / %
$[P_{4,4,4,4}][2-ClPyCOO]$ + ZIF-8	2.95213	0.15212	5.1530
$[P_{4,4,4,4}][2-ClPyCOO]$ + HKUST-1	3.43051	0.17266	5.0330
$[P_{4,4,4,4}][C_{11}COO]$ + ZIF-8	3.69632	0.18456	4.9930
$[P_{4,4,4,4}][Me_4C_4COO]$ + ZIF-8	1.98908	0.09808	4.9309
$\{[P_{4,4,4,4}][MeC_3COO]\}_{0.74}\{[P_{6,6,6,14}][NTf_2]\}_{0.26}$ + ZIF-8	1.39715	0.05808	4.1570

9.3 PROPERTIES

The density of the pure ILs have been previously determined and discussed in Chapters 3 and 5, and in Chapter 8 for the mixture. The experimental values of the densities (ρ) of all the PoILs are represented in Figure 9.2 and listed in Table C.1 in Appendices together with the linear fits with temperature in Table C.2.

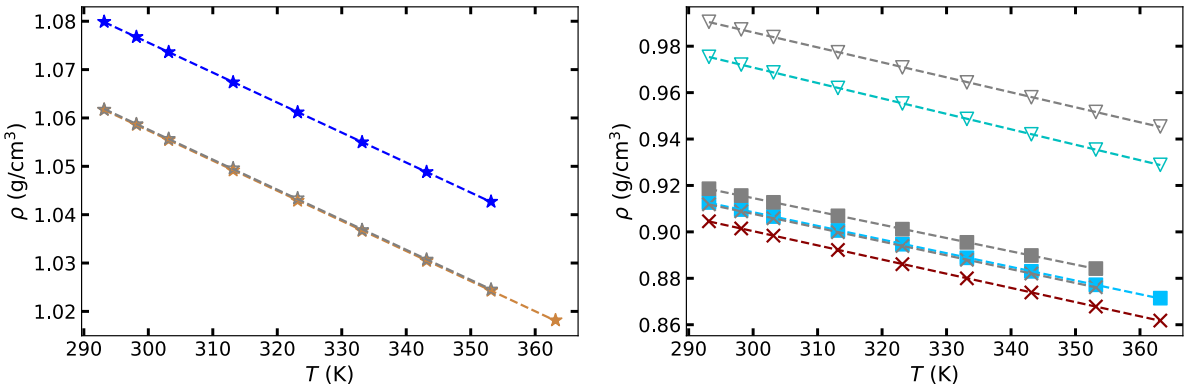

Figure 9.2 – Experimental densities of (left) ★ $[P_{4,4,4,4}][2-ClPyCOO]$, ★ $[P_{4,4,4,4}][2-ClPyCOO]$ + ZIF-8 5 % wt. and ★ $[P_{4,4,4,4}][2-ClPyCOO]$ + HKUST-1 5 % wt.; (right) ▽ $\{[P_{4,4,4,4}][MeC_3COO]\}_{0.74}\{[P_{6,6,6,14}][NTf_2]\}_{0.26}$, ■ $[P_{4,4,4,4}][Me_4C_4COO]$ and × $[P_{4,4,4,4}][C_{11}COO]$ and their corresponding PoILs with — ZIF-8 as a function of temperature, with linear fits (dashed lines).

As expected, the density of the PoILs is decreasing with temperature. The addition of both ZIF-8 or HKUST-1 results in an overall increase of the density of the PoILs, with the exception of $[P_{4,4,4,4}][2-ClPyCOO]$ + ZIF-8 5 % wt., for which the density remains similar to that of the corresponding pure IL.

The stability of the suspensions has only been assessed visually over several months (Figure 9.3). The addition of ZIF-8 to $[P_{4,4,4,4}][Me_4C_4COO]$ and $[P_{4,4,4,4}][2-ClPyCOO]$ led to the formation of a stable suspension for at least 6 months. Whereas after only 10 days, the segregation in two distinct phases is observable in the case of $[P_{4,4,4,4}][C_{11}COO]$ (Figure 9.3 (left)). The upper phase is transparent, while the lower phase, much more opaque, probably contain the majority of the

ZIF-8 due to a sedimentation process. A similar behavior is noticed for $[P_{4,4,4,4}][2-ClPyCOO]$ + HKUST-1 5 % wt., but a longer time (2 months) was necessary to observe the formation of two distinct phases (Figure 9.3 (right)).

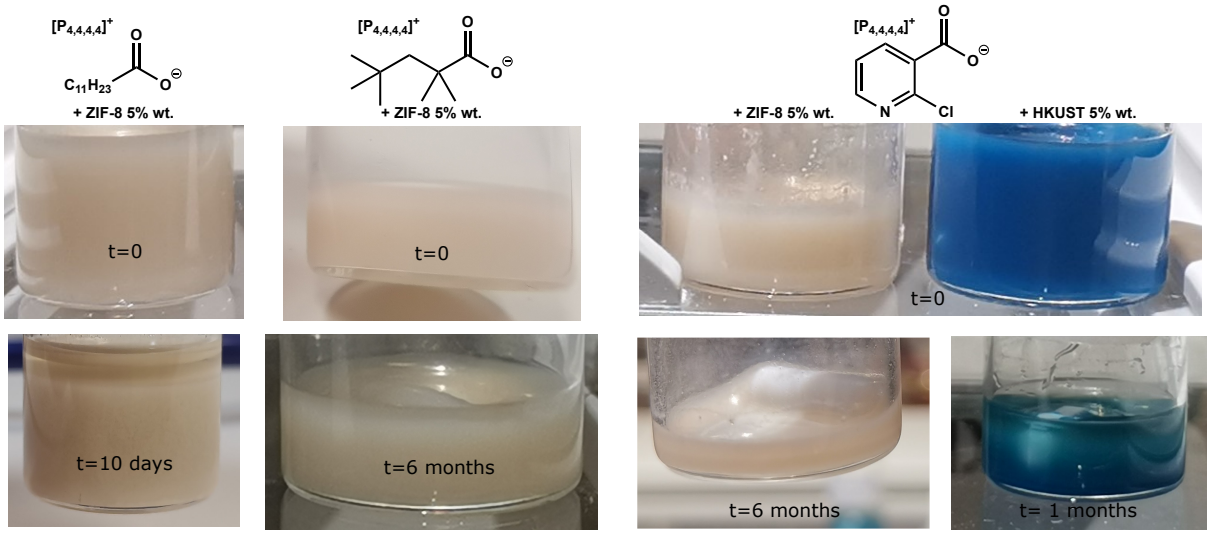

Figure 9.3 – Comparison of the physical aspects of the PoILs just after their preparation and after a certain period of time.

9.4 GAS CAPTURE

The CO_2 capacity capture of the PoILs was evaluated with a gravimetric method between 0–5 bar at either 303, 313, 323 or 343 K, with the results detailed in Table C.3 in Appendices. The CO_2 absorption is expressed in molality.

The CO_2 capture capacity of the PoILs based on $[P_{4,4,4,4}][2-ClPyCOO]$ and $[P_{4,4,4,4}][Me_4C_4COO]$ was measured as their carboxylate anions have the lowest and the highest basicity, respectively. The former is not reactive towards CO_2, while the latter demonstrated the highest capacity capture as discussed in Chapter 5. The $\{[P_{4,4,4,4}][MeC_3COO]\}_{0.74}\{[P_{6,6,6,14}][NTf_2]\}_{0.26}$ mixture was used to assess the effect of other ion types on porosity.

The addition of both ZIF-8 and HKUST-1 to $[P_{4,4,4,4}][2-ClPyCOO]$ leads to an increase of the CO_2 uptake at all the temperatures (Figures 9.4 (top) and Table C.3). This augmentation is relatively higher at high pressures, as anticipated, given that porous solids enhance the physical absorption of the gas which is more important at high pressures. This aligns with previous reports for PoILs only reliant on physical absorption of gas [188], indicating that the pores of both porous solids remain free and accessible in the suspension. At 303 K, the presence of HKUST-1 results in a more important increase in CO_2 uptake compared to ZIF-8, while at 313, 323 and 343 K, the opposite trend is observed. The improvement of the capture capacity is higher at lower temperatures, consistent with the diminished efficiency of the physical absorption process at higher temperatures due to its exothermic nature.

The gas uptake of the PoILs based on the reactive $[Me_4C_4COO]^-$ and $[MeC_3COO]^-$ anions (Figure 9.4 (bottom)) remains similar to that of their corresponding ILs at low pressures (around

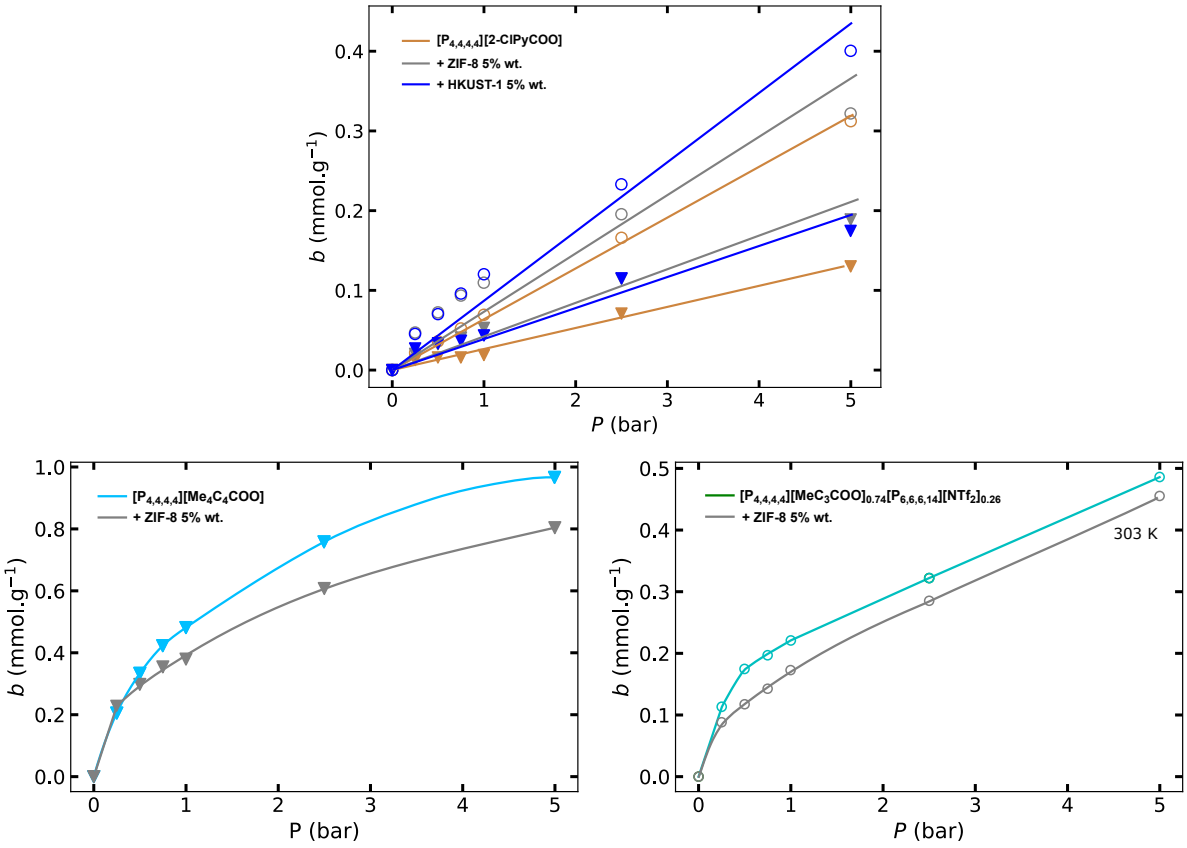

Figure 9.4 – Absorption of CO_2 in molality as a function of pressure between 0–5 bar at ○ 303 K and ▼ 343 K in (top) — $[P_{4,4,4,4}][2-ClPyCOO]$, (bottom left) — $[P_{4,4,4,4}][Me_4C_4COO]$ and (bottom right) — $\{[P_{4,4,4,4}][MeC_3COO]\}_{0.74}\{[P_{6,6,6,14}][NTf_2]\}_{0.26}$ and their corresponding PoILs, with either — ZIF-8 or — HKUST-1.

0.25 bar), with notable deviations from Henry's law showing that the gas is chemisorbed. A decrease of the CO_2 capacity is noticed for the suspensions at higher pressures, suggesting that the pores of ZIF-8 may not be fully available to host gases. Similar results were reported for phosphonium acetate-based ILs mixed with ZIF-8 [96]. It has been hypothesized that the acetic acid was small enough to enter the pores of ZIF-8, while the utilization of a larger carboxylate anion prevented the filling of the ZIF-8 pores. Both MeC_3COOH and Me_4C_4COOH are probably still not voluminous enough to completely prevent this phenomenon leading to non-porous suspensions.

The SO_2 capture capacity of these PoILs has only been assessed for $[P_{4,4,4,4}][2-ClPyCOO]$ and $[P_{4,4,4,4}][Me_4C_4COO]$ + ZIF-8 5 % wt. at a few pressures, with the results depicted in Figures 9.5 and C.1, respectively (exact values provided in Table C.4 in Appendices). Given that the reaction between SO_2 and phosphonium carboxylate ILs do not yield a carboxylic acid as side product (as discussed in Chapters 4 and 6), we hypothesized that the porosity would be maintained. The purpose was also to get insights into the effect of these porous solids on the absorption of a more acidic gas.

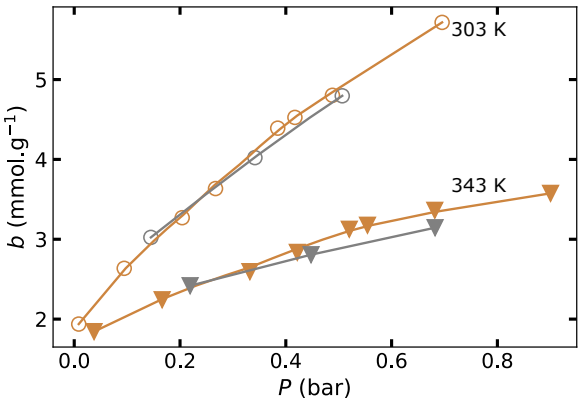

Figure 9.5 – Absorption of SO_2 by the — pure $[P_{4,4,4,4}][2-ClPyCOO]$ and the corresponding PoIL with — ZIF-8 at ◯ 303 K and ▼ 343 K up to a pressure of approximately 1 bar.

A slight decrease of the SO_2 uptake is observed upon addition of ZIF-8 to $[P_{4,4,4,4}][2-ClPyCOO]$ at 343 K for pressures above approximately 0.45 bar (Figure 9.5), while at 303 K, the SO_2 uptakes with or without ZIF-8 are similar. With only one measurement being performed with $[P_{4,4,4,4}][Me_4C_4COO]$ + ZIF-8 5 % wt. (Figure C.1), it appears that the addition of ZIF-8 leads to a slight increase of the SO_2 capture capacity. In both cases, the addition of ZIF-8 does not seem to have a major impact on the SO_2 capture, but more measurements are required to draw meaningful conclusions.

The absorption of a non-reactive gas, such as nitrogen, should be conducted on these PoILs to get a better insight of the availability of free pores in the suspensions.

Main ideas

The choice of both the IL and the porous solid is crucial for the preparation of stable suspensions. The addition of both ZIF-8 and HKUST-1 to a non-reactive carboxylate IL led to an increase in CO_2 capture capacity, particularly notable at high pressures. This is in contrast with the observed decrease in CO_2 uptake when ZIF-8 is mixed with reactive ILs, suggesting that the accessibility of ZIF-8 pores to gases is limited. SO_2 absorption appears to only be minimally affected by ZIF-8, but additional investigations are needed to confirm these findings.

Further investigations are required to deepen our understanding of the properties of this type of suspension, this study providing a first preliminary result for further exploration and innovation in the design and optimization of PoILs.

10

CONCLUSIONS AND PERSPECTIVES

CONCLUSIONS

A new library of phosphonium carboxylate ILs was successfully designed and prepared based on $[P_{4,4,4,4}]^+$ and $[P_{6,6,6,14}]^+$ cations and twelve carboxylate anions with different basicity, the pK_a of the conjugated carboxylic acid in water ranging from 2.07 to 6.51. Straightforward yet reliable methods, using readily available chemicals, were followed to synthesize the ILs with a high purity.

The ILs were thoroughly characterized and their viscosity were slightly higher than their imidazolium and ammonium counterparts, but they exhibited favorable properties, including larger liquid window and superior thermal stability compared to other ILs.

Through a combination of experimental and simulation studies, their complex and liquid-phase structures were carefully investigated and three distinct IL groups were found: carboxylate anions with linear, branched or cyclic substituents. $[P_{4,4,4,4}][TetrazC_1COO]$ appeared as an outlier due to its particular and unique anion-anion correlations.

$[P_{4,4,4,4}][TetrazC_1COO]$ emerged as a promising candidate for the reversible and selective SO_2 capture over CO_2, with one of the highest ideal selectivity reported so far, resulting from the low basicity of the carboxylate anion. It was also possible to regenerate the IL under mild conditions. An enhanced fluidity upon gas absorption was noticed, overcoming the important increase of viscosity that many ILs suffer from after absorption of acid gases.

Phosphonium carboxylate ILs appear as promising absorbents for CO_2 absorption. A clear trend was found between the pK_a of the acid precursors and the CO_2 capture capacity. If the carboxylate anions are not basic enough, the corresponding ILs were only depicting physical absorption of CO_2, while past the pK_a threshold of about 4, the ILs were reactive towards CO_2. The higher the pK_a, the higher the CO_2 uptake, with some exceptions highlighting the importance of the structure and properties of the ILs.

The chemical absorption was reversible with low equilibrium constants. This directly stems from the initial non thermodynamically favorable deprotonation of the H_α of the cation by the carboxylate anion. These findings allow the tuning of the reactivity towards CO_2 and the IL regeneration. Another major advantage compared to other ILs for carbon capture is that the studied ILs were fluidized upon CO_2 capture which is a crucial improvement.

The prepared ILs exhibited promising long-term thermal stability $T_{0.01/10}$ between 103–157 °C, surpassing those of many other ILs. A significant discrepancy between short and long-term sta-

bility was found, resulting from the overestimation of TGA measurements based on temperature ramps. The long-term thermal stability of ILs should be assess with isothermal measurements to provide a more accurate estimation of their long-time stability.

The impact of the carboxylate anion basicity and the size of the phosphonium cations on SO_2 absorption was subsequently explored. Minimal variations in gas uptake were observed upon modification of the size of the phosphonium cation or the basicity of the carboxylate anion. At low pressures, a thermodynamically favorable and exothermic chemical absorption led to high SO_2 capacity capture, while as pressure increased, physical absorption became increasingly significant.

The pK_a was found as crucial for IL regeneration and also to reach a high selectivity of SO_2 over CO_2. Carboxylate anions with aqueous pK_a below 3.7 offered milder regeneration conditions and much higher SO_2/CO_2 ideal selectivity.

The self-diffusion coefficients of both the cations and the anions increased upon SO_2 capture, even surpassing the enhancements observed with CO_2. This overcomes the substantial viscosity increase often reported for many other ILs. This is a major improvement as it might facilitate their utilization.

These four first Chapters constitute the cornerstone of this PhD, while the following Chapters delve into exploratory projects aimed at pointing to diverse properties and potential applications of this new library of phosphonium carboxylate ILs.

Investigations into the electrochemical behavior of the ILs provided valuable insights into their properties and aiding in the design of ILs for specific purposes. Some ILs exhibit a high electrochemical stability, with a minimal impact of temperature, a crucial attribute for a range of electrochemical applications.

Solid ILs were successfully fluidized by addition of $[P_{6,6,6,14}][NTf_2]$ in various proportions, opening avenues for the customization of IL properties. The mixing properties were carefully examined, revealing deviations from ideal mixtures, notably unexpected large excess molar volume (V^E) and negative viscosity deviations ($\Delta\eta$). This indicates the presence of weak and non-specific interactions, which were confirmed by FT-IR measurements.

The thermal stability of the mixtures was unaffected as showed by the apparition of two distinct decomposition steps probably due to the different ions degrading consecutively. DSC measurements highlighted a significant reduction in crystallization points. The addition of $[P_{6,6,6,14}][NTf_2]$ to phosphonium carboxylate ILs resulted in enhanced fluidity and an expanded liquid window, paving the way for the design of ILs and application-specific optimization.

The critical role of the selection of both the IL and the porous solid for the preparation of stable suspensions was underscored in the last Chapter. The addition of ZIF-8 or HKUST-1 yielded different stability, emphasizing the difficulty to predict the stability of the suspensions.

Addition of both porous solids to a non-reactive IL led to an increased CO_2 capture capacity, particularly at high pressures, attributed to improved physical absorption. The reverse was

observed for reactive ILs upon addition of ZIF-8, pointing towards pore hindrance. Suspended porous solids seem to have a minimal impact on SO_2 absorption, probably due to the different mechanism for this gas.

PERSPECTIVES

Plastic Crystals

The more careful analysis of the DSC curves made us think that among the $[P_{4,4,4,4}]^+$-based ILs under study, six of them may possess characteristics of plastic crystals: $[C_1COO]^-$, $[MeC_3COO]^-$, $[Me_4C_4COO]^-$, $[PhC_1COO]^-$, $[PhSC_1COO]^-$ and $[TetrazC_1COO]^-$. Plastic crystals are distinguished by a significant change in enthalpy during solid-solid transitions compared to fusion enthalpy [194]. These materials are promising for various applications owing to their mechanical flexibility and reversible phase transitions. Figure 10.1 depicts the DSC curve for $[P_{4,4,4,4}][TetrazC_1COO]$, used as representative example, with a solid-solid transition, at approximately 10 °C, which is characterised by a distinct narrow endothermic peak. The broader peak, at about 27 °C, corresponds to the melting point, whereas a regular salt usually depicts a narrow and well defined sharp melting point, not as wide as the one observed here. This DSC curve pattern is typical of plastic crystal materials [194].

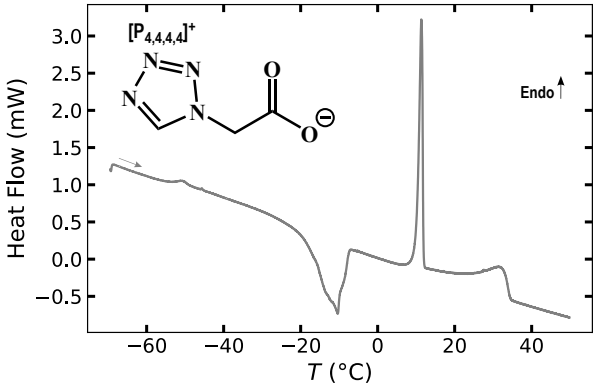

Figure 10.1 – DSC traces of — $[P_{4,4,4,4}][TetrazC_1COO]$ measured at $1\,K\,min^{-1}$.

It will be interesting to elucidate how variations in anion structure impact both crystal structure and molecular mobility within the crystal lattice. For that purpose, the concerned ILs have already been characterized by Raman spectroscopy and DSC.

In complement, the crystal structure at various temperatures, particularly before, during, and after the solid-solid transitions, utilizing temperature-controlled synchrotron WAXSwas tried for $[P_{4,4,4,4}][C_1COO]$, but problems with temperature control led to results that can not be exploited. A modification of the crystalline structure as a function of temperature was noted with the observation of two distinct structures as illustrated in Figure 10.2. The Raman spectra showed that the bands related to the rocking motion of CH_2 and CH_3 are shifted to higher wavenumber

upon heating during the solid-solid transition (II → I). It showed that a modification of the conformation of the alkyl chains of $[P_{4,4,4,4}]^+$ from gauche to trans was occurring.

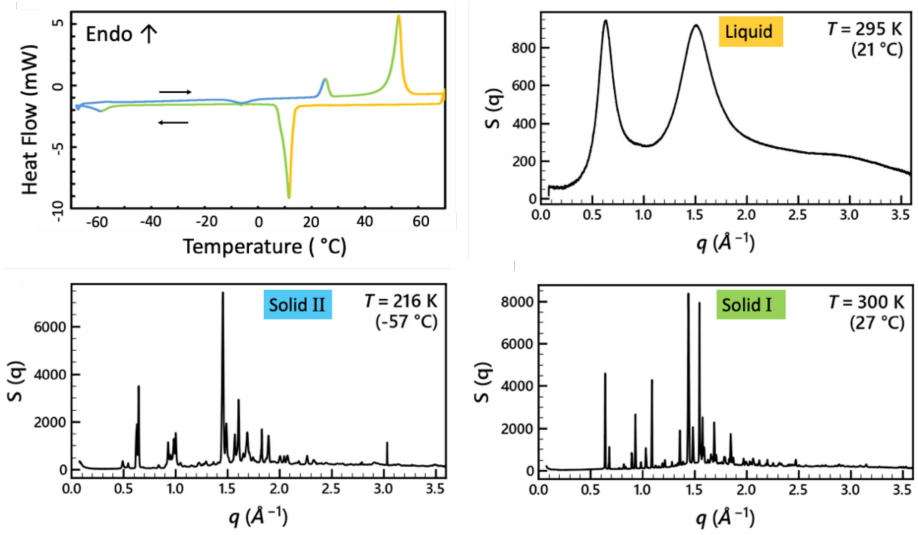

Figure 10.2 – (Top left) DSC traces of $[P_{4,4,4,4}][C_1COO]$ measured at $10\,K\,min^{-1}$. Experimental X-ray scattering structure factors, $S(q)$, of (top right) the liquid phase ■, (bottom left) the solid phase, labeled II ■, and (bottom right) the solid phase, labeled I ■.

Several collaborations were started to deepen our understanding of their plastic crystal behavior. The first one was with collaborators from the University of São Paulo, Brazil, specialized in Raman spectroscopy to study the modifications of the vibrational modes of the ILs as a function of temperature. Another one was initiated with a group specialised in solid state NMR at the Very High Field NMR Center (CRMN) in Lyon in order to identify the variation of internal degree of freedom during these transitions. A project proposal has been submitted to the ESRF to carry out WAXS experiments as a function of temperature to fully characterize and understand the solid-solid transitions, crystallization phenomena as well as their melting behaviours noticed in these ILs with potentially plastic crystal properties.

Other perspectives

- Design and extension of the library of phosphonium carboxylate ILs based on our discoveries to optimize their physico-chemical properties and their ability to selectively and reversibly capture gases
  - Carboxylate anion, within the same range of aqueous pK_a, containing different chemical functions and various structures
  - Phosphonium cations with different side chains, with for example the introduction of ether functions, to improve the viscosity
- Pursue the CO_2 and SO_2 absorption measurements to evaluate the effectiveness of the newly designed ILs, mainly in terms of capture capacity, selectivity and regeneration

- The first experiments carried out on the PoILs paved the way to numerous combinations of ILs and porous solids
  - Exploration of the effect of the addition of porous solids to both reactive and non-reactive ILs towards CO_2
  - Measurement of full SO_2 absorption isotherms to accurately assess the effect of addition of MOFs on SO_2 capture

APPENDIX

A

ELECTROCHEMICAL PROPERTIES

A.1 CYCLIC VOLTAMMETRY

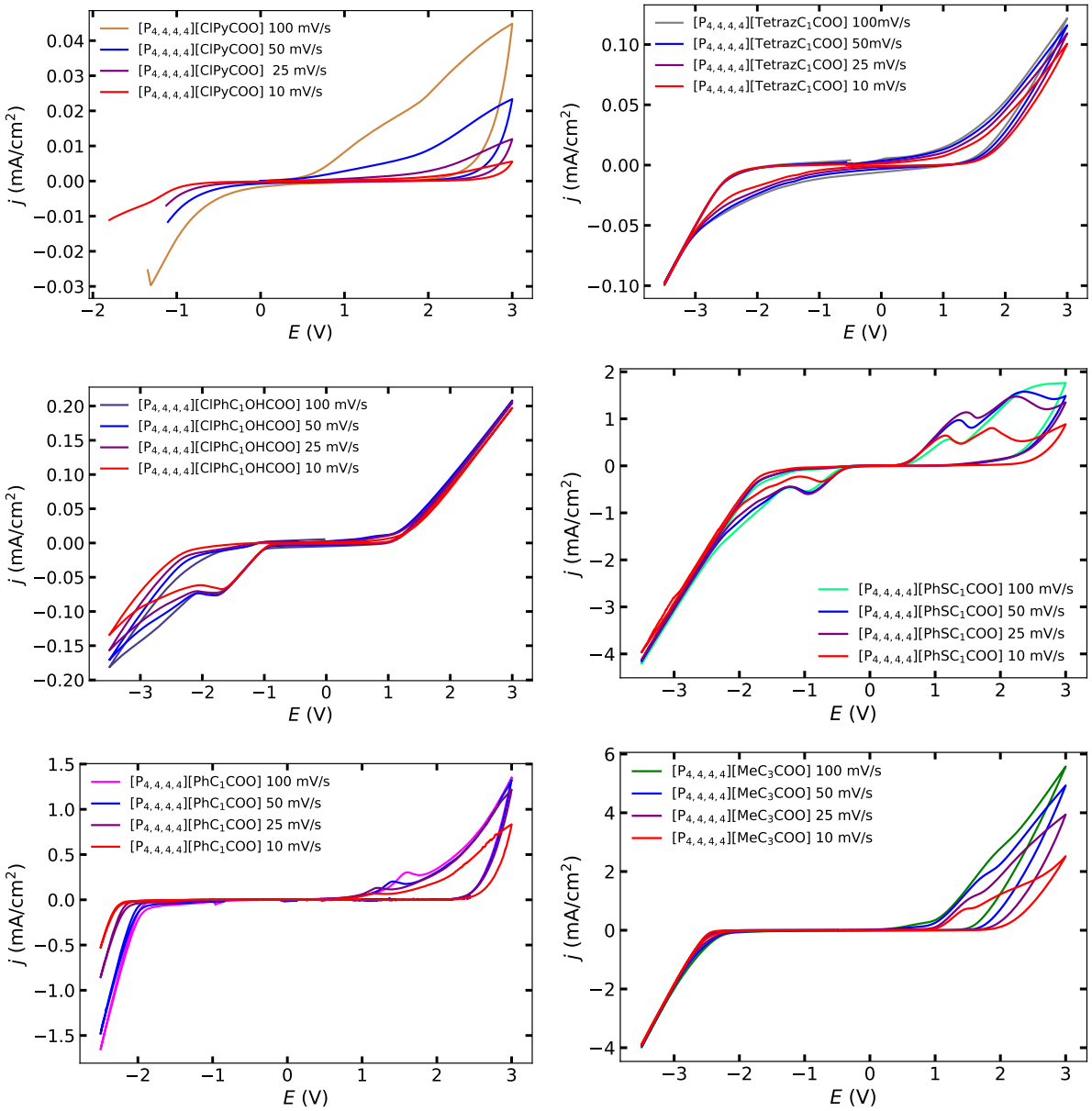

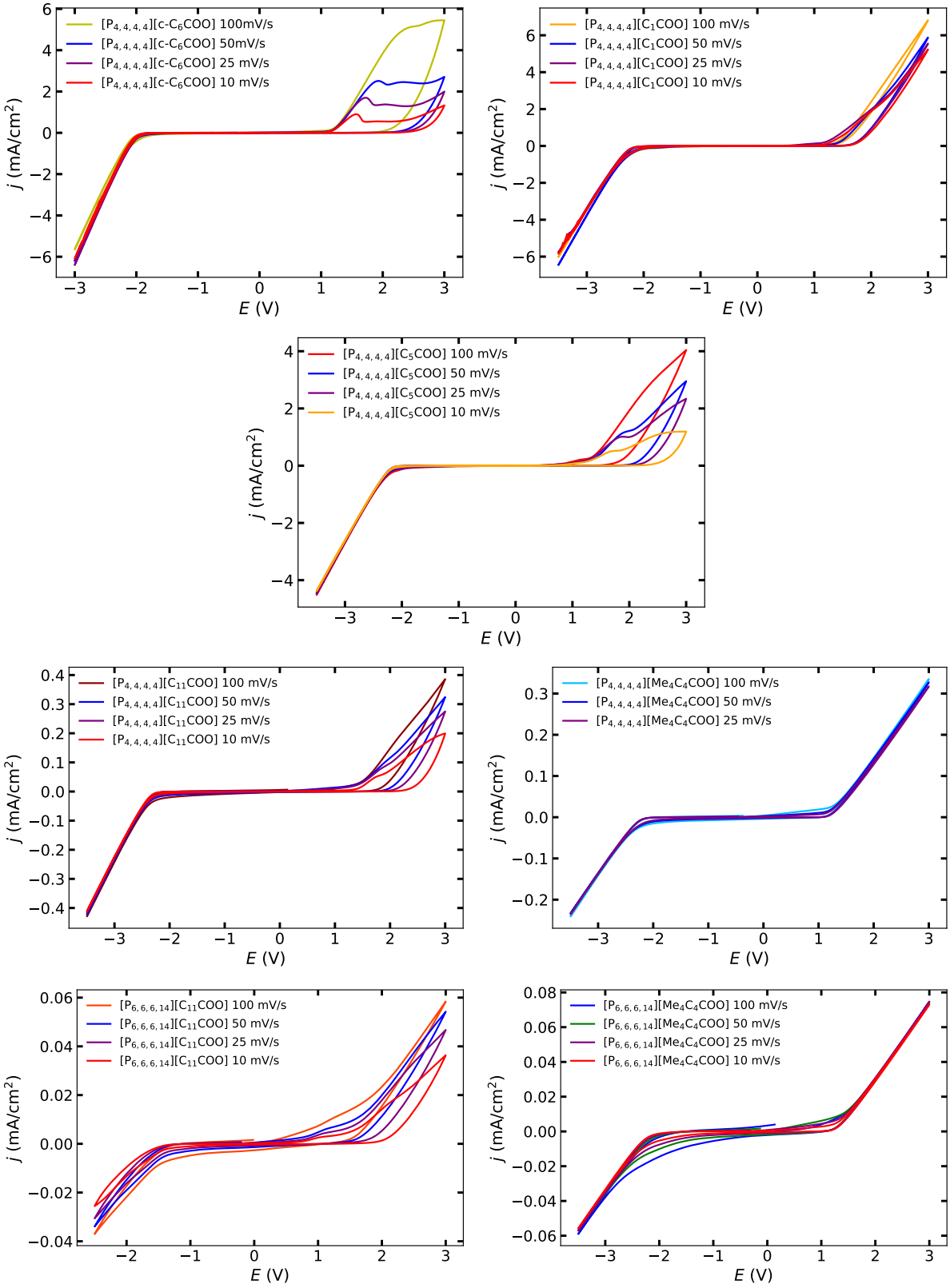

Figure A.1 – Cyclic voltammetry of the various ILs under study at at 100, 50, 25 and 10 mV s^{-1}.

B

MIXTURES OF IONIC LIQUDIS

B.1 DENSITY MEASUREMENTS AND EXCESS MOLAR VOLUMES

Table B.1 – Experimental densities of the mixtures in the temperature range of 293–363 K. The deviations (δ) reported are relative to the fittings with coefficients listed in Table B.2. Only the mole fraction of the phosphonium carboxylate IL is indicated for the sack of clarity.

$\frac{T}{\mathrm{K}}$	$\frac{\rho}{\mathrm{g\,cm^{-3}}}$	$\frac{\delta}{\%}$	$\frac{T}{\mathrm{K}}$	$\frac{\rho}{\mathrm{g\,cm^{-3}}}$	$\frac{\delta}{\%}$	$\frac{T}{\mathrm{K}}$	$\frac{\rho}{\mathrm{g\,cm^{-3}}}$	$\frac{\delta}{\%}$
$\{[P_{4,4,4,4}][c{-}C_6COO]\}_{0.75}$			$\{[P_{4,4,4,4}][c{-}C_6COO]\}_{0.50}$			$\{[P_{4,4,4,4}][c{-}C_6COO]\}_{0.35}$		
293.149	1.00096	0.004	293.153	1.02878	0.007	293.153	1.03784	0.005
298.152	0.99769	0.007	298.152	1.02534	0.007	298.151	1.03451	0.01
303.152	0.99436	0.002	303.151	1.02185	0.001	303.152	1.03099	0.01
313.152	0.98771	0.005	313.152	1.01491	0.006	313.152	1.02566	0.01
323.152	0.98110	0.007	323.151	1.00802	0.009	323.152	1.01862	0.02
333.152	0.97451	0.008	333.152	1.00115	0.009	333.152	1.01163	0.01
343.152	0.96796	0.005	343.151	0.99432	0.005	343.152	1.00470	0.0008
353.152	0.96144	0.002	353.152	0.98753	0.003	353.152	0.99780	0.01
363.152	0.95495	0.01	363.152	0.98080	0.01	-	-	-
$\{[P_{4,4,4,4}][c{-}C_6COO]\}_{0.20}$			$\{[P_{4,4,4,4}][c{-}C_6COO]\}_{0.15}$			$\{[P_{4,4,4,4}][PhSC_1COO]\}_{0.80}$		
293.149	1.05548	0.007	293.151	1.05724	0.006	293.149	1.03722	0.08
298.152	1.05189	0.004	298.151	1.05364	0.003	298.187	1.03560	0.09
303.152	1.04829	0.0005	303.152	1.05004	0.001	303.152	1.03196	0.06
313.152	1.04115	0.004	313.152	1.04290	0.004	313.152	1.02406	0.05
323.152	1.03400	0.007	323.151	1.03576	0.007	323.152	1.01752	0.04
333.152	1.02689	0.007	333.152	1.02865	0.005	333.152	1.01104	0.02
343.152	1.01982	0.004	343.152	1.02160	0.0002	343.152	1.00460	0.003
353.152	1.01278	0.002	353.152	1.01456	0.008	353.151	0.99819	0.03
363.152	1.00575	0.01	-	-	-	-	-	-
$\{[P_{4,4,4,4}][PhSC_1COO]\}_{0.68}$			$\{[P_{4,4,4,4}][PhSC_1COO]\}_{0.50}$			$\{[P_{4,4,4,4}][PhSC_1COO]\}_{0.29}$		
293.148	1.04333	0.007	293.151	1.05253	0.006	293.152	1.06134	0.006
298.152	1.03996	0.002	298.152	1.04907	0.003	298.152	1.05779	0.002
303.152	1.03660	0.002	303.152	1.04561	0.002	303.152	1.05424	0.001
313.152	1.02994	0.004	313.152	1.03874	0.004	313.152	1.04718	0.004

$\frac{T}{\mathrm{K}}$	$\frac{\rho}{\mathrm{g\,cm^{-3}}}$	$\frac{\delta}{\%}$	$\frac{T}{\mathrm{K}}$	$\frac{\rho}{\mathrm{g\,cm^{-3}}}$	$\frac{\delta}{\%}$	$\frac{T}{\mathrm{K}}$	$\frac{\rho}{\mathrm{g\,cm^{-3}}}$	$\frac{\delta}{\%}$
323.152	1.02328	0.007	323.152	1.03187	0.006	323.152	1.04013	0.006
333.152	1.01666	0.006	333.152	1.02505	0.005	333.152	1.03312	0.004
343.152	1.01009	0.0006	343.152	1.01825	0.0002	343.152	1.02613	0.0003
353.151	1.00353	0.008	353.151	1.01148	0.007	353.152	1.01917	0.007
$\{[P_{4,4,4,4}][p-MeBzCOO]\}_{0.74}$			$\{[P_{4,4,4,4}][p-MeBzCOO]\}_{0.49}$			$\{[P_{4,4,4,4}][p-MeBzCOO]\}_{0.40}$		
-	-	-	313.148	1.02602	0.0009	313.150	1.02934	0.002
323.148	0.99001	0.01	323.152	1.01925	0.001	323.152	1.02242	0.004
333.148	0.98409	0.002	333.152	1.01245	0.0007	333.152	1.01562	0.002
343.148	0.97829	0.02	343.152	1.00568	0.0008	343.152	1.00874	0.001
353.148	0.97227	0.01	353.152	0.99889	0.0003	353.152	1.00188	0.0003
363.152	0.96597	0.02	363.152	0.99210	0.0007	363.152	0.99502	0.0002
$\{[P_{4,4,4,4}][p-MeBzCOO]\}_{0.24}$			$\{[P_{4,4,4,4}][MeC_3COO]\}_{0.74}$					
293.149	1.05679	0.01	293.150	0.97542	0.006			
298.152	1.05355	0.01	298.152	0.97207	0.003			
303.152	1.04996	0.008	303.151	0.96872	0.001			
313.150	1.04284	0.003	313.152	0.96202	0.003			
323.152	1.03572	0.002	323.152	0.95533	0.007			
333.151	1.02861	0.005	333.152	0.94867	0.007			
343.152	1.02155	0.004	343.152	0.94205	0.004			
353.152	1.01452	0.0006	353.152	0.93546	0.001			
363.152	1.00750	0.004	363.152	0.92889	0.01			

Table B.2 – Fitting parameters A_0 and A_1 determined from the linear fitting of the experimental densities of the mixtures to $\rho = A_0 + A_1 T$ and the corresponding absolute average deviation (AAD).

Sample	$\frac{A_0}{\mathrm{g\,cm^{-3}}}$	$\frac{A_1}{\mathrm{g\,cm^{-3}\,K^{-1}}}$	$\frac{AAD}{\%}$
$\{[P_{4,4,4,4}][c{-}C_6COO]\}_{0.75}\{[P_{6,6,6,14}][NTf_2]\}_{0.25}$	1.19389	-6.5825×10^{-4}	0.004
$\{[P_{4,4,4,4}][c{-}C_6COO]\}_{0.50}\{[P_{6,6,6,14}][NTf_2]\}_{0.50}$	1.23103	-6.8678×10^{-4}	0.005
$\{[P_{4,4,4,4}][c{-}C_6COO]\}_{0.35}\{[P_{6,6,6,14}][NTf_2]\}_{0.65}$	1.23294	-6.6470×10^{-4}	0.04
$\{[P_{4,4,4,4}][c{-}C_6COO]\}_{0.20}\{[P_{6,6,6,14}][NTf_2]\}_{0.80}$	1.26373	-7.1069×10^{-4}	0.006
$\{[P_{4,4,4,4}][c{-}C_6COO]\}_{0.15}\{[P_{6,6,6,14}][NTf_2]\}_{0.85}$	1.26578	-7.1160×10^{-4}	0.006
$\{[P_{4,4,4,4}][PhSC_1COO]\}_{0.80}\{[P_{6,6,6,14}][NTf_2]\}_{0.20}$	1.23403	-6.6870×10^{-4}	0.005
$\{[P_{4,4,4,4}][PhSC_1COO]\}_{0.68}\{[P_{6,6,6,14}][NTf_2]\}_{0.32}$	1.23777	-6.6352×10^{-4}	0.005
$\{[P_{4,4,4,4}][PhSC_1COO]\}_{0.50}\{[P_{6,6,6,14}][NTf_2]\}_{0.50}$	1.25307	-6.8429×10^{-4}	0.004
$\{[P_{4,4,4,4}][PhSC_1COO]\}_{0.29}\{[P_{6,6,6,14}][NTf_2]\}_{0.71}$	1.26740	-7.0311×10^{-4}	0.004
$\{[P_{4,4,4,4}][p{-}MeBzCOO]\}_{0.74}\{[P_{6,6,6,14}][NTf_2]\}_{0.26}$	1.18367	-5.9901×10^{-4}	0.01
$\{[P_{4,4,4,4}][p{-}MeBzCOO]\}_{0.49}\{[P_{6,6,6,14}][NTf_2]\}_{0.51}$	1.23845	-6.7836×10^{-4}	0.001
$\{[P_{4,4,4,4}][p{-}MeBzCOO]\}_{0.40}\{[P_{6,6,6,14}][NTf_2]\}_{0.60}$	1.24414	-6.8599×10^{-4}	0.001
$\{[P_{4,4,4,4}][p{-}MeBzCOO]\}_{0.24}\{[P_{6,6,6,14}][NTf_2]\}_{0.76}$	1.26422	-7.0707×10^{-4}	0.006
$\{[P_{4,4,4,4}][MeC_3COO]\}_{0.74}\{[P_{6,6,6,14}][NTf_2]\}_{0.26}$	1.17038	-6.6525×10^{-4}	0.005

Table B.3 – Excess molar volumes V^{E} of the IL mixtures as a function of composition and temperature. Only the mole fraction of the phosphonium carboxylate IL is indicated for the sack of clarity.

	V^{E} / $\mathrm{cm^3\,mol^{-1}}$				
	$x_{[\mathrm{P_{4,4,4,4}}][\mathrm{c-C_6COO}]}$				
T / K	0.14880	0.20364	0.35181	0.50351	0.74687
313	2.354	2.727	3.152	2.268	1.131
323	2.394	2.782	3.234	2.315	1.156
333	2.415	2.834	3.291	2.373	1.195
343	2.436	2.887	3.343	2.420	1.227
353	2.453	2.944	3.389	2.475	1.262
	$x_{[\mathrm{P_{4,4,4,4}}][\mathrm{PhSC_1COO}]}$				
T / K	0.29393	0.50049	0.68312	0.7983	
313	1.699	1.498	1.173	0.640	
323	1.726	1.523	1.191	0.663	
333	1.746	1.543	1.203	0.674	
343	1.778	1.570	1.215	0.687	
353	1.815	1.602	1.236	0.702	
$x_{[\mathrm{P_{4,4,4,4}}][\mathrm{MeC_3COO}]}$					
T / K	0.74055				
323	3.197				
333	3.248				
343	3.313				
353	3.369				

Table B.4 – Fitting parameters A_0, A_1 and A_2 of the RK polynomial fitting of the experimental excess molar volume V^E at different temperatures and the corresponding absolute average deviation (AAD).

Sample	T / K	A_0 / cm^3 mol^{-1}	A_1 / cm^3 mol^{-1}	A_2 / cm^3 mol^{-1}	AAD / %
$\{[P_{4,4,4,4}][c-C_6COO]\}_x\{[P_{6,6,6,14}][NTf_2]\}_{1-x}$	313	9.69	10.05	4.30	4.3
	323	9.93	10.28	4.22	4.5
	333	10.17	10.33	4.16	4.4
	343	10.37	10.41	4.18	4.2
	353	10.58	10.46	4.16	3.9
$\{[P_{4,4,4,4}][PhSC_1COO]\}_x\{[P_{6,6,6,14}][NTf_2]\}_{1-x}$	313	6.24	3.95	1.33	7.3
	323	6.33	3.99	1.50	6.8
	333	6.41	4.03	1.53	6.6
	343	6.51	4.14	1.62	6.3
	353	6.63	4.23	1.67	6.1

B.2 VISCOSITY MEASUREMENTS AND DEVIATIONS

Table B.5 – Experimental viscosities of the mixtures in the temperature range of 293–363 K. The deviations (δ) reported are relative to the fittings with coefficients listed in Table B.6. Only the mole fraction of the phosphonium carboxylate IL is indicated for the sack of clarity.

T / K	ρ / g cm^{-3}	δ / %	T / K	ρ / g cm^{-3}	δ / %	T / K	ρ / g cm^{-3}	δ / %
$\{[P_{4,4,4,4}][c-C_6COO]\}_{0.75}$			$\{[P_{4,4,4,4}][c-C_6COO]\}_{0.50}$			$\{[P_{4,4,4,4}][c-C_6COO]\}_{0.35}$		
293.15	1085	0.2	293.15	697.5	0.4	293.15	522.6	0.01
298.15	746.7	0.9	298.15	480.2	3.2	298.15	379.6	0.001
303.15	512.0	0.9	303.15	382.1	5.6	303.15	281.8	0.1
313.15	269.8	0.4	313.15	191.3	5.0	313.15	163.4	0.1
323.15	153.1	0.2	323.15	116.4	2.1	323.15	101.0	0.2
333.15	93.89	1.1	333.15	73.67	0.3	333.15	65.93	0.2
343.15	59.7	0.7	343.15	49.14	2.2	343.15	45.12	0.2
353.15	40.39	1.9	353.15	34.35	5.5	353.15	32.18	0.9
363.15	28.49	3.2	363.15	24.84	8.8	-	-	-
$\{[P_{4,4,4,4}][c-C_6COO]\}_{0.20}$			$\{[P_{4,4,4,4}][c-C_6COO]\}_{0.15}$			$\{[P_{4,4,4,4}][PhSC_1COO]\}_{0.80}$		
293.15	467.1	0.01	293.15	475.6	0.01	293.15	630.0	0.02
298.15	343.6	0.09	298.15	350.0	0.02	298.15	440.8	0.07
303.15	256.8	0.2	303.15	262.6	0.04	303.15	316.4	0.04
313.15	152.1	0.07	313.15	155.2	0.2	313.15	174.3	0.4

$\frac{T}{\mathrm{K}}$	$\frac{\eta}{\mathrm{mPa\,s}}$	$\frac{\delta}{\%}$	$\frac{T}{\mathrm{K}}$	$\frac{\eta}{\mathrm{mPa\,s}}$	$\frac{\delta}{\%}$	$\frac{T}{\mathrm{K}}$	$\frac{\eta}{\mathrm{mPa\,s}}$	$\frac{\delta}{\%}$
323.15	95.56	0.4	323.15	97.95	0.2	323.15	103.4	0.1
333.15	62.49	0.3	333.15	64.48	0.1	333.15	65.06	1.2
343.15	42.91	0.2	343.15	44.43	0.06	343.15	43.87	0.04
353.15	30.53	0.2	353.15	31.85	0.3	353.15	30.79	0.7
363.15	22.48	0.2						
$\{[P_{4,4,4,4}][PhSC_1COO]\}_{0.68}$			$\{[P_{4,4,4,4}][PhSC_1COO]\}_{0.50}$			$\{[P_{4,4,4,4}][PhSC_1COO]\}_{0.29}$		
293.15	561.9	0.06	293.15	489.0	0.02	293.15	459.0	0.08
298.15	400.5	0.2	298.15	353.7	0.09	298.15	338.3	0.3
303.15	290.4	0.2	303.15	261.0	0.01	303.15	252.2	0.2
313.15	163.6	0.3	313.15	150.5	0.3	313.15	148.7	0.4
323.15	97.54	0.2	323.15	93.56	0.3	323.15	91.86	0.3
333.15	62.83	0.3	333.15	60.92	0.2	333.15	60.5,	0.2
343.15	42.14	0.03	343.15	41.45	0.2	343.15	41.31	0.2
353.15	30.1	0.5	353.15	29.52	0.1	353.15	29.37	0.5
$\{[P_{4,4,4,4}][p\text{−}MeBzCOO]\}_{0.74}$			$\{[P_{4,4,4,4}][p\text{−}MeBzCOO]\}_{0.49}$			$\{[P_{4,4,4,4}][p\text{−}MeBzCOO]\}_{0.40}$		
			313.15	185.7	0.01	313.15	176.6	0.009
			323.15	111.6	0.05	323.15	107.0	0.07
333.14	80.6	0.03	333.15	70.92	0.08	333.15	68.41	0.1
343.14	51.3	0.3	343.15	46.98	0.5	343.15	45.97	0.04
353.14	35.3	0.7	353.15	32.72	0.006	353.15	32.13	0.05
363.15	25.2	0.5	363.15	23.62	0.6	363.15	23.31	0.2
$\{[P_{4,4,4,4}][p\text{−}MeBzCOO]\}_{0.24}$			$\{[P_{4,4,4,4}][MeC_3COO]\}_{0.74}$					
293.15	438.4	0.04	293.15	480.0	0.2			
298.15	321.0	0.1	298.15	337.0	0.3			
303.15	238.7	0.1	303.15	242.1	0.6			
313.15	140.2	0.1	313.15	129.1	2.0			
323.15	86.99	0.2	323.15	76.47	1.3			
333.15	56.78	0.4	333.15	48.47	0.05			
343.15	38.97	0.05	343.15	32.58	2.1			
353.15	27.72	0.4	353.15	22.90	4.4			
363.15	20.44	1.3	363.15	16.76	7.0			

Table B.6 – Fitting parameters A, B and T_0 determined from the fitting of the experimental viscosities to the VFT function and the corresponding absolute average deviation (AAD).

Sample	$\frac{A}{\text{mPa s}}$	$\frac{B}{\text{K}}$	$\frac{T_0}{\text{K}}$	$\frac{AAD}{\%}$
$\{[P_{4,4,4,4}][c-C_6COO]\}_{0.75}\{[P_{6,6,6,14}][NTf_2]\}_{0.25}$	0.0066	1926.40	126.62	3.7
$\{[P_{4,4,4,4}][c-C_6COO]\}_{0.50}\{[P_{6,6,6,14}][NTf_2]\}_{0.50}$	0.0411	1349.15	150.40	0.2
$\{[P_{4,4,4,4}][c-C_6COO]\}_{0.35}\{[P_{6,6,6,14}][NTf_2]\}_{0.65}$	0.0338	1428.24	143.32	0.2
$\{[P_{4,4,4,4}][c-C_6COO]\}_{0.20}\{[P_{6,6,6,14}][NTf_2]\}_{0.80}$	0.0410	1379.90	145.71	0.1
$\{[P_{4,4,4,4}][c-C_6COO]\}_{0.15}\{[P_{6,6,6,14}][NTf_2]\}_{0.85}$	0.0115	1835.32	120.90	1.8
$\{[P_{4,4,4,4}][PhSC_1COO]\}_{0.80}\{[P_{6,6,6,14}][NTf_2]\}_{0.20}$	0.0339	1386.05	145.79	0.3
$\{[P_{4,4,4,4}][PhSC_1COO]\}_{0.68}\{[P_{6,6,6,14}][NTf_2]\}_{0.32}$	0.0495	1255.62	156.64	0.2
$\{[P_{4,4,4,4}][PhSC_1COO]\}_{0.50}\{[P_{6,6,6,14}][NTf_2]\}_{0.50}$	0.0475	1241.06	160.81	0.2
$\{[P_{4,4,4,4}][PhSC_1COO]\}_{0.29}\{[P_{6,6,6,14}][NTf_2]\}_{0.71}$	0.0248	1393.47	155.74	0.3
$\{[P_{4,4,4,4}][p-MeBzCOO]\}_{0.74}\{[P_{6,6,6,14}][NTf_2]\}_{0.26}$	0.3490	603.87	222.20	0.4
$\{[P_{4,4,4,4}][p-MeBzCOO]\}_{0.49}\{[P_{6,6,6,14}][NTf_2]\}_{0.51}$	0.0288	1422.16	151.03	0.2
$\{[P_{4,4,4,4}][p-MeBzCOO]\}_{0.40}\{[P_{6,6,6,14}][NTf_2]\}_{0.60}$	0.0377	1339.43	154.69	0.09
$\{[P_{4,4,4,4}][p-MeBzCOO]\}_{0.24}\{[P_{6,6,6,14}][NTf_2]\}_{0.76}$	0.0300	1419.40	145.12	0.3
$\{[P_{4,4,4,4}][MeC_3COO]\}_{0.74}\{[P_{6,6,6,14}][NTf_2]\}_{0.26}$	0.0237	1444.18	158.62	1.0

Table B.7 – Viscosity deviations ($\Delta\eta$) of the IL mixtures as a function of composition and temperature. Only the mole fraction of the phosphonium carboxylate IL is indicated for the sack of clarity.

$\frac{\Delta\eta}{\text{mPa s}}$

	$x_{[P_{4,4,4,4}][c-C_6COO]}$						$x_{[P_{4,4,4,4}][PhSC_1COO]}$			
$\frac{T}{\text{K}}$	0.14880	0.20364	0.35181	0.50351	0.74687	$\frac{T}{\text{K}}$	0.29393	0.50049	0.68312	0.7983
313	-52.3	-74.6	-115.2	-140.5	-147.2					
323	-24.9	-35.8	-53.2	-61.2	-62.1	323	-8.6	-12.4	-13.2	-10.3
333	-12.5	-18.6	-26.1	-29.7	-27.5	333	-4.2	-6.2	-6.4	-5.5
343	-7.0	-10.6	-14.0	-15.7	-14.3	343	-2.3	-3.3	-3.6	-2.5
353	-4.1	-6.5	-7.9	-8.7	-7.6	353	-1.5	-1.8	-1.7	-1.3

$\frac{T}{\text{K}}$	$x_{[P_{4,4,4,4}][MeC_3COO]}$ 0.74055
333	-7.8
343	-4.7
353	-3.0

Table B.8 – Fitting parameters A_0, A_1 and A_2 of the RK polynomial fitting of the experimental viscosity deviations $\Delta\eta$ at different temperatures and the corresponding absolute average deviation (AAD).

Sample	$\frac{T}{\mathrm{K}}$	$\frac{A_0}{\mathrm{mPa\,s}}$	$\frac{A_1}{\mathrm{mPa\,s}}$	$\frac{A_2}{\mathrm{mPa\,s}}$	$\frac{AAD}{\%}$
$\{[P_{4,4,4,4}][c{-}C_6COO]\}_x\{[P_{6,6,6,14}][NTf_2]\}_{1-x}$	313	-571.0	318.5	-187.5	1.9
	323	-251.3	110.9	-79.8	2.6
	333	-120.9	35.4	-24.9	2.5
	343	-63.7	14.8	-16.9	2.6
	353	-35.3	4.7	-10.2	3.1
$\{[P_{4,4,4,4}][PhSC_1COO]\}_x\{[P_{6,6,6,14}][NTf_2]\}_{1-x}$	323	-50.4	23.5	-3.5	2.2
	333	-24.5	12.5	-5.4	0.8
	343	-13.9	6.0	2.3	5.4
	353	-7.4	1.0	-0.6	0.8

B.3 FT-IR MEASUREMENTS

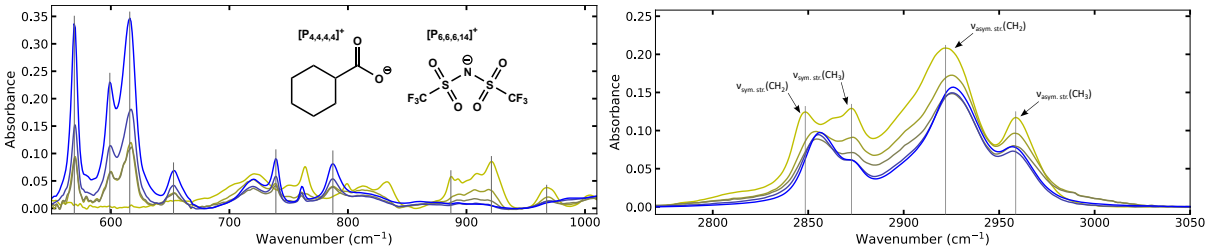

Figure B.1 – FT-IR spectra of the pure $[P_{4,4,4,4}][c{-}C_6COO]$ and $[P_{6,6,6,14}][NTf_2]$ and 3 of their mixtures ($x_{[P_{4,4,4,4}][c-C_6COO]}$= 0.75, 0.50 and 0.20). The grey lines are guidelines to observe the shifts.

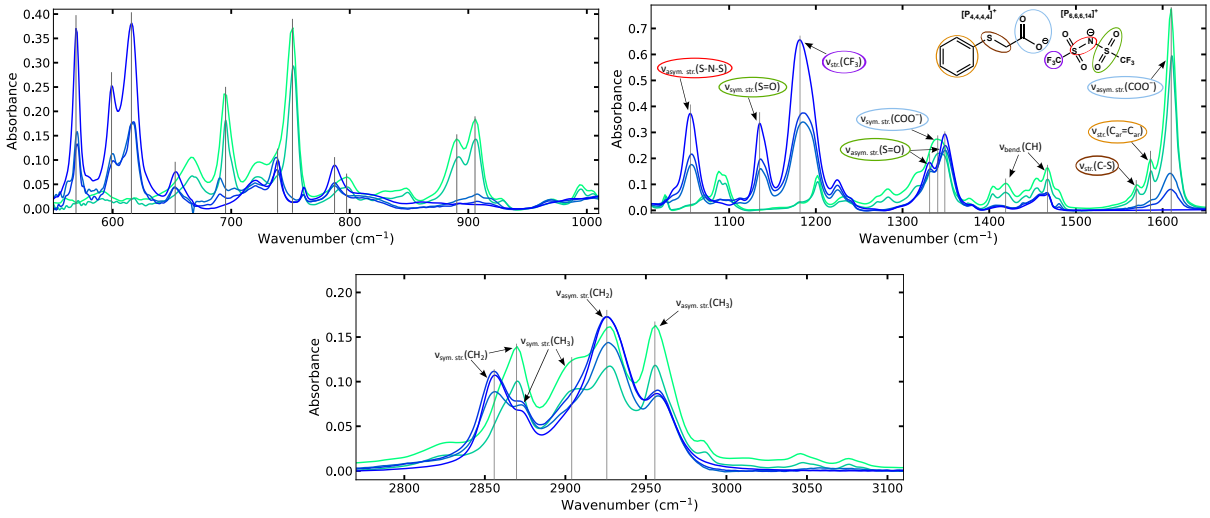

Figure B.2 – FT-IR spectra of the pure $[P_{4,4,4,4}][PhSC_1COO]$ and $[P_{6,6,6,14}][NTf_2]$ and 3 of their mixtures ($x_{[P_{4,4,4,4}][PhSC_1COO]}$= 0.80, 0.50 and 0.29). The grey lines are guidelines to observe the shifts.

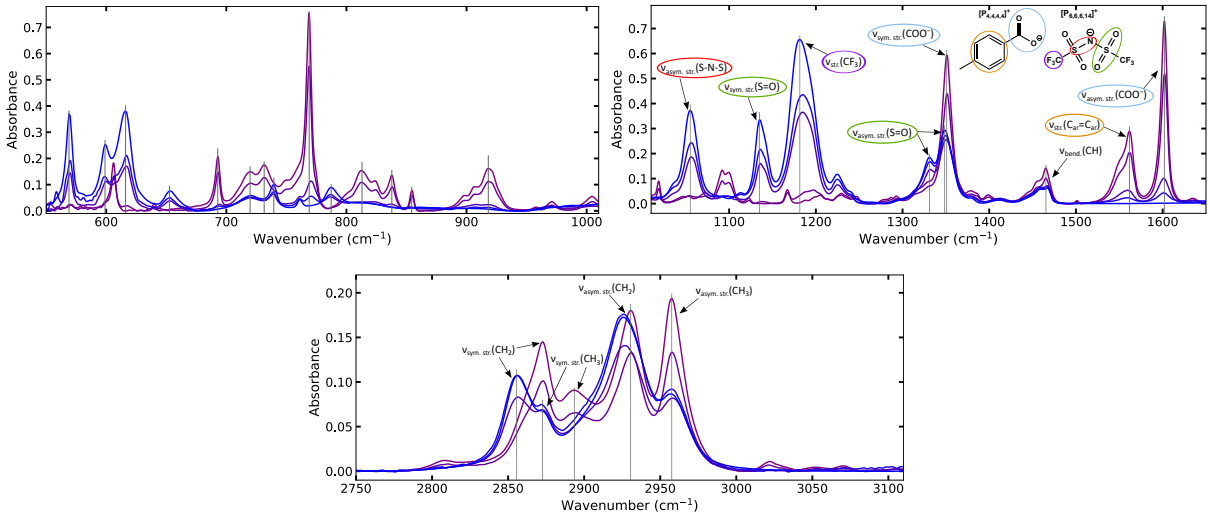

Figure B.3 – FT-IR spectra of the pure $[P_{4,4,4,4}][p-MeBzCOO]$ and $[P_{6,6,6,14}][NTf_2]$ and 3 of their mixtures ($x_{[P_{4,4,4,4}][p-MeBzCOO]}$= 0.74, 0.49 and 0.24). The grey lines are guidelines to observe the shifts.

B.4 THERMAL ANALYSIS

Table B.9 – Decomposition temperatures (T_{dec}) for a few ILs mixtures determined at 10 °C min^{-1} under a O_2 and N_2 atmosphere.

Sample	$T_{dec\ 1}$ / °C	$T_{dec\ 2}$ / °C
O_2 atmosphere		
$[P_{4,4,4,4}][c{-}C_6COO]$ [170]	336	-
$\{[P_{4,4,4,4}][c{-}C_6COO]\}_{0.35}\{[P_{6,6,6,14}][NTf_2]\}_{0.65}$	317	436
$\{[P_{4,4,4,4}][c{-}C_6COO]\}_{0.15}\{[P_{6,6,6,14}][NTf_2]\}_{0.85}$	315	441
$[P_{4,4,4,4}][PhSC_1COO]$ [171]	276	-
$\{[P_{4,4,4,4}][PhSC_1COO]\}_{0.80}\{[P_{6,6,6,14}][NTf_2]\}_{0.20}$	305	433
$\{[P_{4,4,4,4}][PhSC_1COO]\}_{0.68}\{[P_{6,6,6,14}][NTf_2]\}_{0.32}$	281	438
$\{[P_{4,4,4,4}][PhSC_1COO]\}_{0.50}\{[P_{6,6,6,14}][NTf_2]\}_{0.50}$	287	444
$\{[P_{4,4,4,4}][PhSC_1COO]\}_{0.29}\{[P_{6,6,6,14}][NTf_2]\}_{0.71}$	347	474
$[P_{6,6,6,14}][NTf_2]$	-	464
N_2 atmosphere		
$[P_{4,4,4,4}][c{-}C_6COO]$ [170]	303	-
$\{[P_{4,4,4,4}][c{-}C_6COO]\}_{0.75}\{[P_{6,6,6,14}][NTf_2]\}_{0.25}$	305	423
$[P_{4,4,4,4}][p{-}MeBzCOO]$ [170]	337	-
$\{[P_{4,4,4,4}][p{-}MeBzCOO]\}_{0.24}\{[P_{6,6,6,14}][NTf_2]\}_{0.76}$	326	429
$[P_{4,4,4,4}][MeC_3COO]$ [170]	292	-
$\{[P_{4,4,4,4}][MeC_3COO]\}_{0.74}\{[P_{6,6,6,14}][NTf_2]\}_{0.26}$	300	426
$[P_{6,6,6,14}][NTf_2]$	414	-

C

POROUS CARBOXYLATE IONIC LIQUIDS

C.1 DENSITY MEASUREMENTS

Table C.1 – Fitting parameters A_0 and A_1 determined from the linear fitting of the experimental densities to $\rho = A_0 + A_1 T$ and the corresponding absolute average deviation (AAD).

Sample	$\frac{A_0}{\mathrm{g\,cm^{-3}}}$	$\frac{A_1}{\mathrm{g\,cm^{-3}\,K}}$	$\frac{AAD}{\%}$
$[P_{4,4,4,4}][2-ClPyCOO]$ + ZIF-8 5 % wt.	1.2441	-6.2180 x 10^{-4}	0.009
$[P_{4,4,4,4}][2-ClPyCOO]$ + HKUST-1 5 % wt.	1.2616	-6.2013 x 10^{-4}	0.003
$[P_{4,4,4,4}][C_{11}COO]$ + ZIF-8 5 % wt.	1.0864	-5.9534 x 10^{-4}	0.003
$[P_{4,4,4,4}][Me_4C_4COO]$ + ZIF-8 5 % wt.	1.0865	-5.7331 x 10^{-4}	0.008
$\{[P_{4,4,4,4}][MeC_3COO]\}_{0.74}\{[P_{6,6,6,14}][NTf_2]\}_{0.26}$ + ZIF-8 4 % wt.	1.1796	-6.4556 x 10^{-4}	0.01

Table C.2 – Experimental densities of the PoILs in the temperature range of 293–363 K. The deviations (δ) reported are relative to the fitting polynomials with coefficients listed in Table C.2.

$\frac{T}{\mathrm{K}}$	$\frac{\rho}{\mathrm{g\,cm^{-3}}}$	$\frac{\delta}{\%}$	$\frac{T}{\mathrm{K}}$	$\frac{\rho}{\mathrm{g\,cm^{-3}}}$	$\frac{\delta}{\%}$
$[P_{4,4,4,4}][2-ClPyCOO]$ + ZIF-8 5 % wt.			$[P_{4,4,4,4}][2-ClPyCOO]$ + HKUST-1 5 % wt.		
293.15	1.06172	0.01	293.15	1.07989	0.005
298.15	1.05872	0.004	298.15	1.07675	0.002
303.15	1.05569	0.004	303.15	1.07362	0.0005
313.15	1.04960	0.02	313.15	1.06738	0.005
323.15	1.04340	0.02	323.15	1.06117	0.005
333.15	1.03683	0.02	333.15	1.05498	0.004
343.15	1.03073	0.004	343.15	1.04882	0.0001
353.15	1.02455	0.001	353.15	1.04269	0.007
$[P_{4,4,4,4}][C_{11}COO]$ + ZIF-8 5 % wt.			$[P_{4,4,4,4}][Me_4C_4COO]$ ZIF-8 5 % wt.		
293.15	0.91187	0.005	293.15	0.91858	0.01
298.15	0.90886	0.001	298.15	0.91564	0.004
303.15	0.90586	0.001	303.15	0.91272	0.002
313.15	0.89988	0.004	313.15	0.90691	0.01
323.15	0.89393	0.003	323.15	0.90116	0.01
333.15	0.88798	0.003	333.15	0.89548	0.006
343.15	0.88205	0.000	343.15	0.88981	0.001
353.15	0.87615	0.006	353.15	0.88418	0.01
$\{[P_{4,4,4,4}][MeC_3COO]\}_{0.74}$ $\{[P_{6,6,6,14}][NTf_2]\}_{0.26}$ + ZIF-8 4 % wt.					
293.15	0.99052	0.01			
298.15	0.98723	0.007			
303.15	0.98394	0.002			
313.15	0.97739	0.007			
323.15	0.97087	0.01			
333.15	0.96441	0.02			
343.15	0.95800	0.01			
353.15	0.95167	0.002			
363.15	0.94540	0.02			

C.2 GAS ABSORPTION DATA

Table C.3 – Absorption and desorption of CO_2 in the PoILs as a function of pressure from 0–5 bar at either 303 K, 313 K, 323 K or 343 K.

CO_2 - Absorption			CO_2 - Desorption		
$\frac{T}{\mathrm{K}}$	$\frac{P}{\mathrm{bar}}$	$\frac{b_{CO_2}}{\mathrm{mmol\,g^{-1}}}$	$\frac{T}{\mathrm{K}}$	$\frac{P}{\mathrm{bar}}$	$\frac{b_{CO_2}}{\mathrm{mmol\,g^{-1}}}$
$[P_{4,4,4,4}][2-ClPyCOO]$ + ZIF-8 5 % wt.					
303.06	0.0000	0.0000	303.06	0.0000	0.0000
303.14	0.2492	0.0471	303.15	0.2497	0.0510
303.15	0.4982	0.0724	303.15	0.4985	0.0763
303.15	0.7487	0.0935	303.16	0.7493	0.0962
303.14	0.9981	0.1097	303.16	0.9986	0.1137
303.15	2.4987	0.1955	303.13	2.4998	0.1971
303.14	4.9977	0.3219	303.14	4.9977	0.3219
313.05	0.0000	0.0000	313.05	0.0000	0.0000
313.11	0.2490	0.0431	313.08	0.2488	0.0459
313.14	0.4985	0.0630	313.10	0.4985	0.0695
313.11	0.7490	0.0818	313.07	0.7476	0.0855
313.11	0.9988	0.0959	313.06	0.9995	0.1003
313.13	2.4980	0.1729	313.12	2.4991	0.1779
313.11	4.9987	0.2819	313.11	4.9987	0.2819
322.12	0.0000	0.0000	322.12	0.0000	0.0000
323.12	0.2491	0.0246	323.12	0.2477	0.0312
323.12	0.4979	0.0395	323.09	0.4981	0.0486
323.14	0.7473	0.0516	323.13	0.7481	0.0610
323.04	0.9989	0.0625	323.08	0.9986	0.0708
323.10	2.4984	0.1321	323.12	2.4994	0.1376
323.11	4.9994	0.2269	323.11	4.9994	0.2269
341.12	0.0000	0.0000	335.09	0.0000	0.0000
343.11	0.2498	0.0243	343.03	0.2486	0.0272
343.08	0.4977	0.0364	343.12	0.4981	0.0396
343.10	0.7490	0.0444	343.12	0.7488	0.0472
343.11	0.9985	0.0554	343.06	0.9989	0.0587
343.09	2.4996	0.1181	343.13	2.4988	0.1224
343.15	4.9980	0.1915	343.15	4.9980	0.1915
$[P_{4,4,4,4}][2-ClPyCOO]$ + HKUST-1 5 % wt.					
303.09	0.0000	0.0000	303.09	0.0000	0.0000
303.15	0.2486	0.0453	303.14	0.2494	0.0386

CO_2 - Absorption			CO_2 - Desorption		
$\frac{T}{K}$	$\frac{P}{bar}$	$\frac{b_{CO_2}}{mmol\,g^{-1}}$	$\frac{T}{K}$	$\frac{P}{bar}$	$\frac{b_{CO_2}}{mmol\,g^{-1}}$
303.14	0.4984	0.0702	303.15	0.4984	0.0656
303.13	0.7488	0.096	303.14	0.7490	0.0896
303.15	0.9993	0.1202	303.14	0.9996	0.1131
303.13	2.4981	0.233	303.15	2.4978	0.2429
303.15	4.9982	0.4005	303.15	4.9982	0.4005
313.20	0.0000	0.0000	313.20	0.0000	0.0000
313.06	0.2491	0.0318	313.22	0.2492	0.0381
313.21	0.4975	0.0509	313.08	0.4988	0.0552
313.06	0.7483	0.0681	313.06	0.7493	0.0678
313.07	0.9982	0.0796	313.05	1.0000	0.0778
311.77	2.4969	0.1418	313.48	2.5003	0.1578
313.18	4.9939	0.2495	313.18	4.9939	0.2495
323.17	0.0000	0.0000	323.17	0.0000	0.0000
323.15	0.2497	0.0272	323.13	0.2492	0.0314
323.13	0.4992	0.0421	323.12	0.4992	0.0439
323.10	0.7463	0.0528	323.21	0.7491	0.0532
323.13	0.9989	0.0615	323.12	0.9996	0.0626
323.12	2.4996	0.1283	323.12	2.4992	0.1285
323.09	4.9993	0.2156	323.09	4.9993	0.2156
343.12	0.0000	0.0000	343.12	0.0000	0.0000
343.12	0.2495	0.0271	343.10	0.2498	0.0224
343.11	0.4990	0.0336	343.11	0.4978	0.0285
343.13	0.7493	0.0368	343.11	0.7487	0.0326
343.11	0.9999	0.0434	343.12	0.9995	0.0421
343.10	2.5002	0.1150	343.12	2.4976	0.1051
343.10	4.9976	0.1746	343.10	4.9976	0.1746
$[P_{4,4,4,4}][Me_4C_4COO]$ + ZIF-8 5 % wt.					
342.73	0.0000	0.0000	342.98	0.0000	0.0000
343.11	0.2491	0.2273	343.12	0.2487	0.2359
343.11	0.4988	0.2978	343.11	0.4977	0.3042
343.10	0.7486	0.3543	343.09	0.7484	0.3589
343.10	0.9995	0.3795	343.14	0.9989	0.3973
343.11	2.4991	0.6075	343.06	2.4992	0.6112
343.14	4.9986	0.8039	343.14	4.9986	0.8039
$\{[P_{4,4,4,4}][MeC_3COO]\}_{0.74}\{[P_{6,6,6,14}][NTf_2]\}_{0.26}$ + ZIF-8 4 % wt.					
303.70	0.0000	0.0000	303.15	0.0000	0.0000

CO_2 - Absorption			CO_2 - Desorption		
$\frac{T}{\mathrm{K}}$	$\frac{P}{\mathrm{bar}}$	$\frac{b_{CO_2}}{\mathrm{mmol\,g^{-1}}}$	$\frac{T}{\mathrm{K}}$	$\frac{P}{\mathrm{bar}}$	$\frac{b_{CO_2}}{\mathrm{mmol\,g^{-1}}}$
303.12	0.2497	0.0882	303.13	0.2486	0.1441
303.20	0.4993	0.1174	303.14	0.4974	0.1646
303.22	0.7486	0.1426	303.15	0.7481	0.1811
303.15	0.9971	0.1728	303.16	0.9993	0.1970
303.13	2.4999	0.2853	303.14	2.4982	0.2988
303.15	4.9980	0.4553	303.15	4.9980	0.4553

Table C.4 – SO_2 absorption expressed in molality (b_{SO_2}) in the PoILs under study as different pressures below 1 bar at 5 temperatures from 303 K to 343 K.

SO_2 absorption					
$\frac{T}{\mathrm{K}}$	$\frac{P}{\mathrm{mbar}}$	$\frac{b_{SO_2}}{\mathrm{mmol\,g^{-1}}}$	$\frac{T}{\mathrm{K}}$	$\frac{P}{\mathrm{mbar}}$	$\frac{b_{SO_2}}{\mathrm{mmol\,g^{-1}}}$
$[P_{4,4,4,4}][2-ClPyCOO]$ + ZIF-8 5 % wt.					
303.46	144.90	3.0235	313.37	164.93	2.8409
303.46	341.61	4.0222	313.37	372.51	3.5972
303.45	506.72	4.7965	313.35	558.13	4.2224
323.29	183.54	2.6855	333.21	201.64	2.5447
323.29	399.72	3.2741	333.21	424.67	3.0146
323.26	604.01	3.7706	333.14	644.92	3.4209
343.14	219.14	2.4183			
343.13	447.71	2.8067			
343.02	682.19	3.1449			
$[P_{4,4,4,4}][Me_4C_4COO]$ + ZIF-8 5 % wt.					
303.43	758.04	5.9875			
313.347	816.21	5.2562			
323.263	868.96	4.6837			
333.182	915.53	4.2715			
343.103	959.76	3.9286			

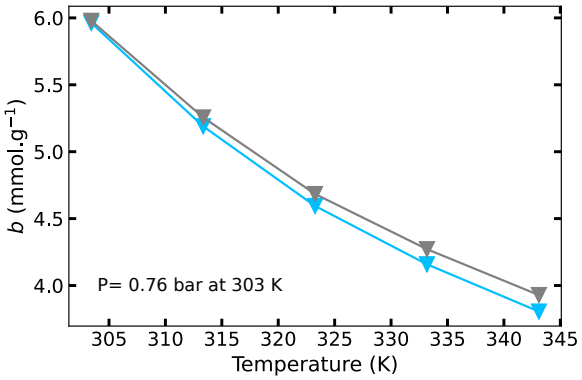

Figure C.1 – Absorption of SO_2 by the — pure $[P_{4,4,4,4}][Me_4C_4COO]$ and the corresponding PoIL, with — ZIF-8 between 303–343 K with an equilibrium pressure of 0.76 bar at 303 K.

[1] P. Styring, D. Jansen, CO2Chem – Carbon Capture and Utilisation in the green economy, **2011,** http://co2chem.co.uk/carbon-capture-and-utilisation-in-the-green-economy.

[2] P. Friedlingstein et al., *Earth System Science Data* **2023,** *15,* 5301–5369.

[3] European Environmental Bureau, Revised Industrial Emissions Directive and Regulation Establishing the Industrial Emissions Portal: outcomes and opportunities, https://eeb.org/library/revised-industrial-emissions-directive-and-regulation-establishing-the-industrial-emissions-portal-outcomes-and-opportunities/ (visited on 05/17/2024).

[4] Joint Research Centre, Institute for Energy and Transport, 2013 Technology map of the European Strategic Energy Technology Plan (SET-Plan) : technology descriptions. **2014,** http://op.europa.eu/en/publication-detail/-/publication/f5b60dd9-a0a1-447d-a64a-11c436f84492/language-en.

[5] R. A. Khatri, S. S. C. Chuang, Y. Soong, M. Gray, *Energy Fuels* **2006,** *20,* 1514–1520.

[6] *Climate Change 2013 - The Physical Science Basis: Working Group I Contribution to the Fifth Assessment Report of the Intergovernmental Panel on Climate Change,* (Ed.: Intergovernmental Panel on Climate Change), Cambridge University Press, Cambridge, **2014.**

[7] M. Vaccarelli, R. Carapellucci, L. Giordano, *Energy Procedia* **2014,** *45,* 1165–1174.

[8] J. D. Figueroa, T. Fout, S. Plasynski, H. McIlvried, R. D. Srivastava, *Int. J. Greenhouse Gas Control* **2008,** *2,* 9–20.

[9] IEA, Tracking Clean Energy Progress 2023, https://www.iea.org/reports/tracking-clean-energy-progress-2023.

[10] D. Y. C. Leung, G. Caramanna, M. M. Maroto-Valer, *Renew. Sust. Energ. Rev.* **2014,** *39,* 426–443.

[11] G. T. Rochelle, *Science* **2009,** *325,* 1652–1654.

[12] J. Gervasi, L. Dubois, D. Thomas, *Energy Procedia* **2014,** *63,* 1018–1028.

[13] P. Brandl, M. Bui, J. P. Hallett, N. Mac Dowell, *Int. J. Greenh. Gas Control.* **2022,** *120,* 103771.

[14] H. Yamada, *Polym. J.* **2021,** *53,* 93–102.

[15] K. A. Mumford, Y. Wu, K. H. Smith, G. W. Stevens, *Front. Chem. Sci. Eng.* **2015,** *9,* 125–141.

[16] P. Luis, *Desalination* **2016,** *380,* 93–99.

[17] R. S. Iglesias, J. M. Ketzer, C. L. Melo, R. Heemann, C. X. Machado, *Greenh. Gases: Sci. Technol.* **2015,** *5,* 119–130.

[18] G. T. Rochelle, *Curr. Opin. Chem. Eng.* **2012,** *1,* 183–190.

[19] S. B. Fredriksen, K.-J. Jens, *Energy Procedia* **2013,** *37,* 1770–1777.

[20] M. Bui et al., *Energy Environ. Sci.* **2018,** *11,* 1062–1176.

[21] H. H. Khoo, J. Bu, R. L. Wong, S. Y. Kuan, P. N. Sharratt, *Energy Procedia* **2011,** *4,* 2494–2501.

[22] Carbon Storage Program, netl.doe.gov, https://www.netl.doe.gov/coal/carbon-storage.

[23] A. A. Olajire, *J. Pet. Sci. Eng.* **2013,** *109,* 364–392.

[24] A. R. Kovscek, M. D. Cakici, *Energy Convers. Manag.* **2005,** *46,* 1941–1956.

[25] F. D. Meylan, V. Moreau, S. Erkman, *J. CO2 Util.* **2015,** *C,* 101–108.

[26] L. Brennan, P. Owende, *Renew. Sust. Energ. Rev.* **2010,** *14,* 557–577.

[27] H.-J. Ho, A. Iizuka, E. Shibata, *Ind. Eng. Chem. Res.* **2019,** *58,* 8941–8954.

[28] S. Bhoi, T. Banerjee, K. Mohanty, *Fuel Process. Technol.* **2016,** *151,* 1–10.

[29] A. Arif et al., *In: Conference of the National Association for Clean Air* **2015.**

[30] US EPA, OAR, Sulfur Dioxide (SO2) Pollution, **2016,** https://www.epa.gov/so2-pollution.

[31] WHO global air quality guidelines: particulate matter (PM2.5 and PM10), ozone, nitrogen dioxide, sulfur dioxide and carbon monoxide, en, https://www.who.int/publications-detail-redirect/9789240034228.

[32] J. Yang, H. Gao, G. Hu, S. Wang, Y. Zhang, *Energy Fuels* **2016,** *30,* 3205–3218.

[33] F. J. Gutiérrez Ortiz et al., *Ind. Eng. Chem. Res.* **2006,** *45,* 1466–1477.

[34] J. Rodríguez-Sevilla, M. Álvarez, M. C. Díaz, M. C. Marrero, *J. Chem. Eng. Data* **2004,** *49,* 1710–1716.

[35] R. Rogers, K. Seddon, *Science* **2003,** *302,* 792–3.

[36] Y. Marcus *Ionic Liquid Properties: From Molten Salts to RTILs,* Springer, **2016,** 123–220.

[37] K. R. Seddon, *J. Chem. Technol. Biotechnol.* **1997,** *68,* 351–356.

[38] P Wasserscheid, T Welton, *Ionic Liquids in Synthesis,* John Wiley & Sons, Ltd, **2002,** 380.

[39] T. Welton, *Biophysical Reviews* **2018,** *10,* 691–706.

[40] M. Kosmulski, J. Gustafsson, J. B. Rosenholm, *Thermochim. Acta* **2004,** *412,* 47–53.

[41] T. Welton, *Chem. Rev.* **1999,** *99,* 2071–2084.

[42] J. P. Hallett, T. Welton, *Chem. Rev.* **2011,** *111,* 3508–3576.

[43] R. D. Rogers, K. R. Seddon, S. Volkov, *Green Industrial Applications of Ionic Liquids,* Springer Netherlands, **2002.**

[44] M. J. Earle, K. R. Seddon, *Pure App. Chem.* **2000,** *72,* 1391–1398.

[45] M. Smiglak, A. Metlen, R. D. Rogers, *Acc. Chem. Res.* **2007,** *40,* 1182–1192.

[46] J. F. Brennecke, E. J. Maginn, *AIChE J.* **2001,** *47,* 2384–2389.

[47] K. Ghandi, *Green Sustain. Chem.* **2013,** *04,* 44–53.

[48] J. D. Seader, E. J. Henley, D. K. Roper, *Separation process principles: chemical and biochemical operations,* 3rd ed, Wiley, Hoboken, NJ, **2011,** 821 pp.

[49] M. Koel, *Crit. Rev. Anal. Chem.* **2005,** *35,* 177–192.

[50] M. J. Muldoon, S. N. V. K. Aki, J. L. Anderson, J. K. Dixon, J. F. Brennecke, *J. Phys. Chem. B* **2007,** *111,* 9001–9009.

[51] R. P. Swatloski, S. K. Spear, J. D. Holbrey, R. D. Rogers, *J. Am. Chem. Soc.* **2002,** *124,* 4974–4975.

[52] E. W. Castner, J. F. Wishart, H. Shirota, *Acc. Chem. Res.* **2007,** *40,* 1217–1227.

[53] L. F. Lepre et al., *ACS Sustain. Chem. Eng.* **2019,** *7,* 16900–16906.

[54] N. Meksi, A. Moussa, *J. Clean. Prod.* **2017,** *161,* 105–126.

[55] S. S. Y. Tan, D. R. MacFarlane, *Ionic Liquids in Biomass Processing,* (Ed.: B. Kirchner), Springer Berlin Heidelberg, Berlin, Heidelberg, **2010,** 311–339.

[56] I. M. Marrucho, L. C. Branco, L. P. N. Rebelo, *Annu. Rev. Chem. Biomol. Eng.* **2014,** *5,* 527–546.

[57] S. Sharma, A. S. Ivanov, C. J. Margulis, *J. Phys. Chem. B* **2021,** *125,* 6359–6372.

[58] J. N. A. Canongia Lopes, A. A. H. Pádua, *J. Phys. Chem. B* **2006,** *110,* 3330–3335.

[59] J. Dupont, *Acc. Chem. Res.* **2011,** *44,* 1223–1231.

[60] A. A. H. Pádua, M. F. Costa Gomes, J. N. A. Canongia Lopes, *Acc. Chem. Res.* **2007,** *40,* 1087–1096.

[61] Z. He, P. Alexandridis, *Phys. Chem. Chem. Phys.* **2015,** *17,* 18238–18261.

[62] L. A. Blanchard, Z. Gu, J. F. Brennecke, *J. Phys. Chem. B* **2001,** *105,* 2437–2444.

[63] S. G. Kazarian, B. J. Briscoe, T. Welton, *Chem. Commun.* **2000,** 2047–2048.

[64] C. Cadena et al., *J. Am. Chem. Soc.* **2004,** *126,* 5300–5308.

[65] S. N. V. K. Aki, B. R. Mellein, E. M. Saurer, J. F. Brennecke, *J. Phys. Chem. B* **2004,** *108,* 20355–20365.

[66] M. J. Muldoon, S. N. V. K. Aki, J. L. Anderson, J. K. Dixon, J. F. Brennecke, *J. Phys. Chem. B* **2007,** *111,* 9001–9009.

[67] D. Almantariotis, T. Gefflaut, A. A. H. Pádua, J.-Y. Coxam, M. F. Costa Gomes, *J. Phys. Chem. B* **2010,** *114,* 3608–3617.

[68] J. Huang, T. Rüther, *Aust. J. Chem.* **2009,** *62,* 298–308.

[69] E. D. Bates, R. D. Mayton, I. Ntai, J. H. Davis, *J. Am. Chem. Soc.* **2002,** *124,* 926–927.

[70] L. M. Galán Sánchez, G. W. Meindersma, A. B. de Haan, *Chem. Eng. J.* **2011,** *166,* 1104–1115.

[71] K. E. Gutowski, E. J. Maginn, *J. Am. Chem. Soc.* **2008,** *130,* 14690–14704.

[72] J. Zhang et al., *Chemistry* **2006,** *12,* 4021–4026.

[73] B. E. Gurkan et al., *J. Am. Chem. Soc.* **2010,** *132,* 2116–2117.

[74] J. F. Brennecke, B. E. Gurkan, *J. Phys. Chem. Lett.* **2010,** *1,* 3459–3464.

[75] B. F. Goodrich et al., *J. Phys. Chem. B* **2011,** *115,* 9140–9150.

[76] B. F. Goodrich et al., *Ind. Eng. Chem. Res.* **2011,** *50,* 111–118.

[77] J. L. McDonald, R. E. Sykora, P. Hixon, A. Mirjafari, J. H. Davis, *Environ. Chem. Lett.* **2014,** *12,* 201–208.

[78] B. Gurkan et al., *J. Phys. Chem. Lett.* **2010,** *1,* 3494–3499.

[79] H. Wu, J. K. Shah, C. M. Tenney, T. W. Rosch, E. J. Maginn, *Ind. Eng. Chem. Res.* **2011,** *50,* 8983–8993.

[80] B. E. Gurkan, T. R. Gohndrone, M. J. McCready, J. F. Brennecke, *Phys. Chem. Chem. Phys.* **2013,** *15,* 7796–7811.

[81] S. Seo et al., *J. Phys. Chem. B* **2014,** *118,* 5740–5751.

[82] G. Cui, J. Wang, S. Zhang, *Chem. Soc. Rev.* **2016,** *45,* 4307–4339.

[83] C. Wang et al., *Angew. Chem. Int. Ed.* **2011,** *50,* 4918–4922.

[84] C. Wang, H. Luo, D.-e. Jiang, H. Li, S. Dai, *Angew. Chem. Int. Ed.* **2010,** *49,* 5978–5981.

[85] D. J. Heldebrant, C. R. Yonker, P. G. Jessop, L. Phan, *Energy Environ. Sci.* **2008,** *1,* 487–493.

[86] C. Wang et al., *Green Chem.* **2010,** *12,* 870–874.

[87] M. Ramdin, T. W. de Loos, T. J. Vlugt, *Ind. Eng. Chem. Res.* **2012,** *51,* 8149–8177.

[88] D. Chinn, D. Vu, M. Driver, L. Boudreau (C. U. Inc), *US Pat.,* 20060251558A1, **2006.**

[89] E. J. Maginn, Design and evaluation of ionic liquids as novel CO2 absorbents, University of Notre Dame (US), **2004.**

[90] M. B. Shiflett, D. J. Kasprzak, C. P. Junk, A. Yokozeki, *J. Chem. Thermodyn.* **2008,** *40,* 25–31.

[91] M. B. Shiflett, D. W. Drew, R. A. Cantini, A. Yokozeki, *Energy Fuels* **2010,** *24,* 5781–5789.

[92] G. Gurau et al., *Angew. Chem. Int. Ed. Engl.* **2011,** *50,* 12024–12026.

[93] M. Besnard et al., *Chem. Commun. (Camb.)* **2012,** *48,* 1245–1247.

[94] W. Shi et al., *J. Phys. Chem. B* **2014,** *118,* 7383–7394.

[95] D. J. Yeadon, J. Jacquemin, N. V. Plechkova, M. Maréchal, K. R. Seddon, *ChemPhysChem* **2020,** *21,* 1369–1374.

[96] J. Avila et al., *Angew. Chem. Int. Ed.* **2021,** *60,* 12876–12882.

[97] T. R. Gohndrone et al., *ChemSusChem* **2014,** *7,* 1970–1975.

[98] S. Stevanovic, A. Podgoršek, A. A. H. Pádua, M. F. Costa Gomes, *J. Phys. Chem. B* **2012,** *116,* 14416–14425.

[99] G. Wang et al., *J. Chem. Eng. Data* **2011,** *56,* 1125–1133.

[100] Y. Yasaka, M. Ueno, Y. Kimura, *Chem. Lett.* **2014,** *43,* 626–628.

[101] X. Li, L. Zhang, Y. Zheng, C. Zheng, *Ind. Eng. Chem. Res.* **2015,** *54,* 8569–8578.

[102] S. F. R. Taylor et al., *Ind. Eng. Chem. Res.* **2018,** *57,* 17033–17042.

[103] W. Wu et al., *Angew. Chem. Int. Ed. Engl.* **2004,** *43,* 2415–2417.

[104] M. Jin et al., *J. Phys. Chem. B* **2011,** *115,* 6585–6591.

[105] K. Huang, J.-F. Lu, Y.-T. Wu, X.-B. Hu, Z.-B. Zhang, *Chem. Eng. J.* **2013,** *215-216,* 36–44.

[106] K. Huang et al., *RSC Adv.* **2013,** *3,* 16264–16269.

[107] G. Cui et al., *Angew. Chem. Int. Ed.* **2013,** *52,* 10620–10624.

[108] C. Wang et al., *J. Am. Chem. Soc.* **2011,** *133,* 11916–11919.

[109] L. Wang et al., *J. Hazard. Mater.* **2020,** *392,* 122504.

[110] S. Ren et al., *Ind. Eng. Chem. Res.* **2009,** *48,* 4928–4932.

[111] S. D. Tian, Y. C. Hou, W. Z. Wu, S. H. Ren, J. G. Qian, *Bull. Korean Chem. Soc.* **2014,** *35,* 2791–2796.

[112] K. Y. Lee, H. S. Kim, C. S. Kim, K.-D. Jung, *Int. J. Hydrogen Energy* **2010,** *35,* 10173–10178.

[113] J. Zhao, S. Ren, Y. Hou, K. Zhang, W. Wu, *Ind. Eng. Chem. Res.* **2016,** *55,* 12919–12928.

[114] M. B. Shiflett, A. Yokozeki, *Ind. Eng. Chem. Res.* **2010,** *49,* 1370–1377.

[115] X. L. Yuan, S. J. Zhang, X. M. Lu, *J. Chem. Eng. Data* **2007,** *52,* 596–599.

[116] K. Huang, Y.-T. Wu, X.-B. Hu, *Chem. Eng. J.* **2016,** *297,* 265–276.

[117] G. Cui et al., *ACS Sustain. Chem. Eng.* **2015,** *3,* 2264–2270.

[118] F. Zhang et al., *RSC Adv.* **2016,** *6,* 86082–86088.

[119] G. Cui et al., *Green Chem.* **2014,** *16,* 1211–1216.

[120] G. Cui et al., *Chemistry* **2015,** *21,* 5632–5639.

[121] K. Huang et al., *RSC Adv.* **2013,** *3,* 16264–16269.

[122] K. Huang et al., *Chem. Eng. J.* **2014,** *237,* 478–486.

[123] X. Meng et al., *Energy Fuels* **2018,** *32,* 1956–1962.

[124] J. Gao, S. Wang, B. Zhao, G. Qi, C. Chen, *Energy Fuels* **2011,** *25,* 5802–5809.

[125] G. García, M. Atilhan, S. Aparicio, *Phys. Chem. Chem. Phys.* **2017,** *19,* 5411–5422.

[126] A. H. Padua, Cl&Pol, **(accessed 2021).**

[127] T. Sato, G. Masuda, K. Takagi, *Electrochim. Acta* **2004,** *49,* 3603–3611.

[128] H. Sakaebe, H. Matsumoto, K. Tatsumi, *J. Power Sources* **2005,** *146,* 693–697.

[129] H. Matsumoto et al., *J. Power Sources* **2006,** *160,* 1308–1313.

[130] R. Kawano et al., *J. Photochem. Photobio. A* **2004,** *164,* 87–92.

[131] G. A. O. Tiago, I. A. S. Matias, A. P. C. Ribeiro, L. M. D. R. S. Martins, *Molecules* **2020,** *25,* 5812.

[132] J. R. Miller, P. Simon, *Science* **2008,** *321,* 651–652.

[133] R.-S. Kühnel et al., *Chem. Commun.* **2016,** *52,* 10435–10438.

[134] P. W. Ruch, D. Cericola, A. Foelske, R. Kötz, A. Wokaun, *Electrochim. Acta* **2010,** *55,* 2352–2357.

[135] A. Balducci, *Top. Curr. Chem.* **2017,** *375,* 20.

[136] A. Savateev et al., *Chem. Commun.* **2017,** *53,* 10192–10195.

[137] M. Ahmed, S. S. Rao, A. Filippov, P. Johansson, F. U. Shah, *Phys. Chem. Chem. Phys.* **2023,** *25,* 3502–3512.

[138] M. Kathiresan, D. Velayutham, *Chem. Commun.* **2015,** *51,* 17499–17516.

[139] R. Pauliukaite, A. P. Doherty, K. D. Murnaghan, C. M. A. Brett, *J. Electroanal. Chem.* **2008,** *616,* 14–26.

[140] K. Tsunashima, M. Sugiya, *Electrochem. Solid-State Lett.* **2007,** *11,* A17.

[141] K. Tsunashima, M. Sugiya, *Electrochem. Commu.* **2007,** *9,* 2353–2358.

[142] K. Tsunashima, M. Sugiya, *Electrochem.* **2007,** *75,* 734–736.

[143] K. J. Fraser, D. R. MacFarlane, *Aust. J. Chem.* **2009,** *62,* 309–321.

[144] K. Tsunashima, E. Niwa, S. Kodama, M. Sugiya, Y. Ono, *J. Phys. Chem. B* **2009,** *113,* 15870–15874.

[145] R. E. Ramírez, E. M. Sánchez, *Sol. Energy Mater. Sol. Cells* **2006,** *90,* 2384–2390.

[146] I. A. Khan, F. U. Shah, *ACS Sustainable Chem. Eng.* **2020,** *8,* 10212–10221.

[147] N. W. Duffy, A. M. Bond, *Electrochem. Commun.* **2006,** *8,* 892–898.

[148] A. Mohammad, D. Inamuddin, *Green Solvents II: Properties and Applications of Ionic Liquids,* Springer Science & Business Media, **2012.**

[149] W.-L. Yuan et al., *Front. Chem.* **2018,** *6.*

[150] S. Kazemiabnavi, Z. Zhang, K. Thornton, S. Banerjee, *J. Phys. Chem. B* **2016,** *120,* 5691–5702.

[151] N. De Vos, C. Maton, C. V. Stevens, *ChemElectroChem* **2014,** *1,* 1258–1270.

[152] M. Ahmed, S. Bhowmick, A. Filippov, P. Johansson, F. U. Shah, *Chem. - Eur. J.* **2023,** *29,* e202301000.

[153] I. A. Khan, O. I. Gnezdilov, Y.-L. Wang, A. Filippov, F. U. Shah, *J. Phys. Chem. B* **2020,** *124,* 11962–11973.

[154] D. S. Silvester, R. G. Compton, *Z. fur Phys. Chem.* **2006,** *220,* 1247–1274.

[155] N. Elgrishi et al., *J. Chem. Educ.* **2018,** *95,* 197–206.

[156] A. Fortunati et al., *Commun. Chem.* **2023,** *6,* 1–13.

[157] N. R. Pitawela, S. K. Shaw, *ACS Meas. Sci. Au* **2021,** *1,* 117–130.

[158] H. Li, F. Endres, R. Atkin, *Phys. Chem. Chem. Phys.* **2013,** *15,* 14624–14633.

[159] L. Sun, O. Morales-Collazo, H. Xia, J. F. Brennecke, *J. Phys. Chem. B* **2016,** *120,* 5767–5776.

[160] Y.-L. Wang, M. Golets, B. Li, S. Sarman, A. Laaksonen, *ACS Appl. Mater. Interfaces* **2017,** *9,* 4976–4987.

[161] J. S. Moreno et al., *Electrochim. Acta* **2015,** *151,* 599–608.

[162] H. Sifaoui, A. Ait-Kaci, A. Modarressi, M. Rogalski, *Thermochim. Acta* **2007,** *456,* 114–119.

[163] U. Domańska, I. Bakała, J. Pernak, *J. Chem. Eng. Data* **2007,** *52,* 309–314.

[164] U. Domańska, L. M. Casás, *J. Phys. Chem. B* **2007,** *111,* 4109–4115.

[165] O. Redlich, A. T. Kister, *Ind. Eng. Chem.* **1948,** *40,* 345–348.

[166] M. A. Martins et al., *Fluid Phase Equilibria* **2020,** *518,* 112621.

[167] H. Niedermeyer, J. P. Hallett, I. J. Villar-Garcia, P. A. Hunt, T. Welton, *Chem. Soc. Rev.* **2012,** *41,* 7780–7802.

[168] G. Chatel, J. F. B. Pereira, V. Debbeti, H. Wang, R. D. Rogers, *Green Chem.* **2014,** *16,* 2051–2083.

[169] L. Grunberg, A. H. Nissan, *Nature* **1949,** *164,* 799–800.

[170] N. Scaglione, J. Avila, E. Bakis, A. Padua, M. C. Gomes, *Phys. Chem. Chem. Phys.* **2023,** *25,* 15325–15339.

[171] N. Scaglione, J. Avila, A. A. H. Padua, M. C. Gomes, *Faraday Discuss.* **2024,** –.

[172] R. A. Faria, M. N. da Ponte, E. Bogel-Łukasik, *Fluid Ph. Equilibria* **2015,** *385,* 1–9.

[173] G. Huang, W.-C. Lin, P. He, Y. Pan, C.-M. Shu, . *Mol. Liq.* **2018,** *272,* 37–42.

[174] P. Navarro, M. Larriba, J. García, F. Rodríguez, *J. Chem. Thermodyn.* **2014,** *76,* 152–160.

[175] G. B. Appetecchi et al., *Electrochim. Acta* **2011,** *56,* 1300–1307.

[176] O. Stolarska, H. Rodríguez, M. Smiglak, *Fluid Ph. Equilib.* **2016,** *408,* 1–9.

[177] A. H. Farmahini, S. Krishnamurthy, D. Friedrich, S. Brandani, L. Sarkisov, *Chem. Rev.* **2021,** *121,* 10666–10741.

[178] Q. Qian et al., *Chem. Rev.* **2020,** *120,* 8161–8266.

[179] A. Dhakshinamoorthy, Z. Li, H. Garcia, *Chem. Soc. Rev.* **2018,** *47,* 8134–8172.

[180] K. Zhang et al., *ACS Appl. Mater. Interfaces* **2020,** *12,* 27821–27852.

[181] N. O'Reilly, N. Giri, S. L. James, *Chem. - Eur. J.* **2007,** *13,* 3020–3025.

[182] A. Pohorille, L. R. Pratt, *J. Am. Chem. Soc.* **1990,** *112,* 5066–5074.

[183] N. Giri et al., *Nature* **2015,** *527,* 216–220.

[184] T. D. Bennett, F.-X. Coudert, S. L. James, A. I. Cooper, *Nat. Mater.* **2021,** *20,* 1179–1187.

[185] B. D. Egleston, A. Mroz, K. E. Jelfs, R. L. Greenaway, *Chem. Sci.* **2022,** *13,* 5042–5054.

[186] W. Shan et al., *ACS Appl. Mater. Interfaces* **2018,** *10,* 32–36.

[187] M. Costa Gomes, L. Pison, C. Červinka, A. Padua, *Angew. Chem. Int. Ed.* **2018,** *57,* 11909–11912.

[188] J. Avila, C. Červinka, P.-Y. Dugas, A. A. H. Pádua, M. Costa Gomes, *Adv. Mater. Interfaces* **2021,** *8,* 2001982.

[189] J. Cahir et al., *Chem. Sci.* **2020,** *11,* 2077–2084.

[190] J. Avila, R. Clark, A. A. H. Pádua, M. C. Gomes, *Mater. Adv.* **2022,** *3,* 8848–8863.

[191] M. Z. Ahmad, A. Fuoco, *Curr. Res. Green Sustain. Chem* **2021,** *4,* 100070.

[192] K. S. Park et al., *Proc. Natl. Acad. Sci. U. S.* **2006,** *103,* 10186–10191.

[193] J. Getzschmann et al., *Micropor. Mesopor. Mat.* **2010,** *136,* 50–58.

[194] S. Das, A. Mondal, C. M. Reddy, *Chem. Soc. Rev.* **2020,** *49,* 8878–8896.

Abstract

The capture of polluting gases such as CO_2 and SO_2 presents a significant challenge in mitigating the environmental impact of human activities. To address this challenge, we propose the development of new materials based on reactive ionic liquids (ILs) as absorbents, with low environmental impact and cost-effectiveness.

ILs are non-volatile compounds with a melting temperature below 100 °C, capable of dissolving a wide range of substances due to their versatile cation-anion combinations. With unique properties like low flammability, high conductivity, and thermal stability, ILs hold promise for various applications, including gas absorption. The wide range of possible combinations of cations and anions allow for the design of a multitude of ionic solvents with tunable properties.

A novel family of ILs comprising carboxylate anions and phosphonium cations for the selective separation of CO_2 and SO_2 has been developed and prepared. Through rigorous experimental and computational analyses, we investigated their physicochemical properties, thermal behavior, and microscopic structure. They notably displayed promising thermal stability and a large liquid window. It was possible to distinguish the microscopic structure of the ILs based on the substituents of the carboxylate anions. $[P_{4,4,4,4}][TetrazC_1COO]$ appeared as an outlier with peculiar anion-anion correlations.

Measurements of gas absorption as a function of temperature and partial pressure revealed the crucial role of carboxylate anion basicity in CO_2 capture capacity, but not in SO_2 capture. The pK_a of corresponding carboxylic acids in water of each carboxylate anion was nonetheless determinant for the reversibility of SO_2 capture, and crucial for achieving high selectivity over CO_2. The related thermodynamics properties were carefully studied and interpreted based on the equilibrium constants and Henry's law constants, obtained from the absorption isotherm fittings, and *ab initio* simulations.

Exploratory projects were carried out to consider other potential applications of these ILs and their mixtures in electrochemistry due to their high electrochemical stability, but also as plastic crystals.

These studies pave the way for understanding the properties of these ILs, guiding future research in this field.

Key words: Ionic liquids, tunable, physico-chemical properties, gas absorption, CO_2, SO_2, selectivity, basicity, molecular dynamics, *ab initio* simulations, porous liquids, electrochemistry

Résumé

La capture des gaz polluants tels que le dioxyde de carbone (CO_2) et le dioxyde de soufre (SO_2) reste un défi majeur dans les efforts visant à atténuer l'impact des activités humaines sur l'environnement. Nous proposons le développement de nouveaux matériaux absorbants à base de liquides ioniques (LIs) réactifs, avec un faible impact environnemental et un coût réduit.

Les LIs, des sels dont la température de fusion est inférieure à 100 °C, sont une classe de composés non volatils capables de dissoudre une grande variété de substances. La multitude de combinaisons de cations et d'anions permet de concevoir une large gamme de solvants ioniques aux propriétés modulables. Grâce à leurs propriétés uniques, telles qu'une faible inflammabilité, une volatilité négligeable, une conductivité élevée ainsi qu'une excellente stabilité thermique et électrochimique, les LIs sont des milieux prometteurs pour de nombreuses applications, et plus particulièrement, ils sont des candidats intéressants pour l'absorption de gaz polluants.

Une nouvelle famille de LIs composés d'anions carboxylates et de cations phosphoniums pour la séparation sélective de CO_2 et SO_2 a été conçue et préparée. Leurs propriétés physico-chimiques et thermiques ainsi que leur structure microscopique ont été étudiées en détail à l'aide de méthodes expérimentales et computationnelles. Ils ont notamment démontré une stabilité thermique prometteuse et une large fenêtre liquide. Il a été possible de distinguer la structure microscopique des LIs en fonction des substituants des anions carboxylates. $[P_{4,4,4,4}][TetrazC_1COO]$ est apparu comme un cas particulier avec des corrélations anion-anion singulières.

L'absorption de CO_2 et de SO_2 a été mesurée en fonction de la température et de la pression partielle des gaz pour chacun des LIs. La sélectivité a été calculée à partir du rapport des ratios molaires de chaque gaz absorbé. Les propriétés thermodynamiques d'absorption ont été obtenues à partir des isothermes d'absorption à différentes températures et de simulations *ab initio*.

La basicité de l'anion carboxylate est un facteur déterminant dans la capture de CO_2, mais pas pour SO_2. Le pK_a dans l'eau de l'acide carboxylique correspondant à chaque anion carboxylate a une influence sur la réversibilité de la capture de SO_2, et sur la capture sélective de SO_2 par rapport à CO_2.

Des projets exploratoires ont été menés en parallèle afin d'envisager d'autres applications potentielles de ces LIs et leurs mélanges en électrochimie grâce à leur bonne stabilité électrochimique, mais aussi en tant que cristaux plastiques.

Ces études ouvrent la voie à de futures recherches pour la compréhension des propriétés de ces LIs.

Mots clés : Liquides ioniques, design, propriétés physico-chimiques, absorption de gaz, CO_2, SO_2, sélectivité, basicité, dynamique moléculaire, simulations *ab initio*, liquids poreux, électrochimie